Nonlinear truss modelling of masonry infill frames towards sustainable residential buildings

By

Peter Binali Kamowa Mbewe

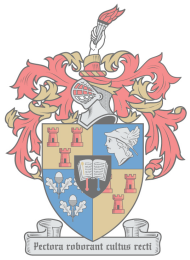

UNIVERSITEIT
iYUNIVESITHI
STELLENBOSCH
UNIVERSITY

Dissertation presented for the degree of

Doctor of Philosophy in Civil Engineering

at Stellenbosch University

Promotor

Prof. G.P.A.G van Zijl, DEng, PhD, PrEng

March 2018

DECLARATION

By submitting this dissertation electronically, I declare that the entirety of the work contained therein is my own, original work, that I am the sole author thereof (save to the extent explicitly otherwise stated), that reproduction and publication thereof by Stellenbosch University will not infringe any third-party rights and that I have not previously in its entirety or in part submitted it for obtaining any qualification.

Date:…….. Signature:…….

March 2018

Plagiaatverklaring / Plagiarism *Declaration*

1 Plagiaat is die oorneem en gebruik van die idees, materiaal en ander intellektuele eiendom van ander persone asof dit jou eie werk is.
Plagiarism is the use of ideas, material and other intellectual property of another's work and to present is as my own.

2 Ek erken dat die pleeg van plagiaat 'n strafbare oortreding is aangesien dit 'n vorm van diefstal is.
I agree that plagiarism is a punishable offence because it constitutes theft.

3 Ek verstaan ook dat direkte vertalings plagiaat is.
I also understand that direct translations are plagiarism.

4 Dienooreenkomstig is alle aanhalings en bydraes vanuit enige bron (ingesluit die internet) volledig verwys (erken). Ek erken dat die woordelikse aanhaal van teks sonder aanhalingstekens (selfs al word die bron volledig erken) plagiaat is.
Accordingly all quotations and contributions from any source whatsoever (including the internet) have been cited fully. I understand that the reproduction of text without quotation marks (even when the source is cited) is plagiarism.

5 Ek verklaar dat die werk in hierdie skryfstuk vervat, behalwe waar anders aangedui, my eie oorspronklike werk is en dat ek dit nie vantevore in die geheel of gedeeltelik ingehandig het vir bepunting in hierdie module/werkstuk of 'n ander module/werkstuk nie.
I declare that the work contained in this assignment, except where otherwise stated, is my original work and that I have not previously (in its entirety or in part) submitted it for grading in this module/assignment or another module/assignment.

PBK Mbewe	March 2018
Voorletters en van / *Initials and surname*	**Datum / *Date***

ABSTRACT

With significant international efforts focused on sustainable development goals, the role of engineers in achieving sustainable infrastructure development cannot be over-emphasised. However, one of the challenges in ensuring implementation of sustainable infrastructure development for building infrastructure among engineers is lack of clear integrated structural performance and sustainability performance assessment. This research work is part of the effort in establishing a proper linkage between structural performance and sustainability performance of building infrastructure. Both structural performance and sustainability performance are evaluated on a building structure with clear definition of its structural topology, building materials and construction, use of the building and all relevant information about the location. Sustainability assessment requires further information on the material sourcing and the processes involved in material production and the supply chain. Thus, a case-study-based evaluation approach is adopted to ensure an integrated approach for structural and sustainability performance is conducted. Infill RC framed residential buildings in Western Cape, South Africa are selected for evaluation, but the approach can be applied to load-bearing masonry buildings, of which a significant stock currently exists in the region. The region is susceptible to moderate seismic events. A simplified nonlinear structural performance evaluation procedure for the infill RC frames is developed through evaluation of the infill behaviour and the bare frame behaviour. Both experimental and numerical data is used to verify the proposed procedure. Two modelling approaches for the infill RC frames are used, the truss system and frame-strut system.

Infill frame modelling utilises the equivalent strut concepts, with the cross-sectional areas for the equivalent strut established using existing models in literature. Models that incorporate the contribution of the frame stiffness and the infill wall to the equivalent strut width or cross-sectional area are considered. Use of the equivalent struts for the infill is a simplification, developed based on observed infill behaviour when subjected to lateral loading. Thus, it provides an 'averaged' behaviour at macro-level concealing the detailed behaviour at micro-level. Notwithstanding this weakness, the equivalent strut modelling offers a simplified approach for infill frame modelling. Much research has been done on the improvement of the macro-modelling of the infill frames, with various configurations for the equivalent struts being suggested, such as single strut, double strut, multi-struts and incorporation of shear links within the equivalent strut. Some of these models are reviewed in this study. Analytical relationships for the equivalent strut behaviour are developed based on the key infill failure modes, namely corner crushing, diagonal compression or cracking and sliding shear failures. Stress zones representing these dominant stress behaviours are used to evaluate the infill behaviour. A parametric study for the infill RC frames is conducted to develop and calibrate the analytical models for the equivalent struts.

Apart from examining the behaviour for the infill, parametric evaluation of the bare frame behaviour is performed. Second moment of areas and the lengths for the beam and the columns are varied using the second moment ratios and aspect ratios respectively, to cover what may be an inclusive range in applied infill frame geometries and configurations encountered in practice. The behaviour of the bare frame is captured through the yield and ultimate strength, and their respective deformations. Trends in the yield and ultimate strength and their deformations across the aspect ratios and the second moment of area ratios of the beam and columns are used to develop analytical relationships for the bare frame behaviour. The bare frame lateral deformation characteristics can be represented by a truss system, where a diagonal strut is introduced. Apart from the parametric-based definition for the diagonal strut behaviour,

the diagonal behaviour is also calibrated based on the column properties. This assumes that column properties have significant contribution to the lateral behaviour for the bare frames.

The truss and frame-strut system models for the infill RC frames are validated using experimental and numerical data for the infill RC frames. These models utilise the infill strut properties while the truss modelling also incorporates the diagonal strut properties used to convert the frame into a truss. Though the truss model gives higher values of resistance than the frame-strut model, both models give reasonable predictions. It is recommended that improvements in material behaviour characterisation, infill frame experimental evaluation can improve the model predictions and refine the analytical relationships proposed.

Integration of structural performance assessment with sustainability performance assessment for development of sustainable infrastructure is possible. Work by Lepech et al. (2015) provides the basis for the integration, with structural performance generating the timeline (durability) with which the sustainability impacts are measured. The sustainability impact of the building from construction to end of its life and incorporating the structural repairs can be established using probabilistic approaches. However, this approach requires more data for probabilistic characterisation of both the impacts and the timelines for specific activities within the life cycle of the building.

The dissertation presents a simplified assessment method of structural walling systems of infrastructure, which is intended to enable assessment of complex structural systems in either the conceptual design stage, or possibly for existing structures at the stage of structural renovation or rehabilitation. Whilst complex nonlinear finite element approaches could be performed instead, the simple, but nevertheless rigorously derived proposed approach, enables feasible analysis and assessment of structural performance, be it capacity for lateral, seismic resistance, or other regional dominating actions like high wind or even flooding and subsidence. The feasible approach is argued to enable incorporation of structural integrity in broader sustainability assessment frameworks for appropriate decision making by potential or existing owners and their professional teams.

OPSOMMING

Met noemenswaardige internasionale navorsingsaktiwiteit gefokus op volhoubare ontwikkelingsdoelwitte, kan die rol van ingenieurs in die bereiking van volhoubare infrastruktuur nie genoeg beklemtoon word nie. Een van die uitdagings in implementering van volhoubare infrastruktuurontwikkeling deur ingenieurs, is egter die gebrek aan geïntegreerde assessering van struktuurgedrag én volhoubaarheid van geboue. Beide struktuurgedrag en volhoubaarheid van ’n gebou-struktuur word hier evalueer, met duidelike definisie van die strukturele topologie, boumateriale en konstruksie, gebruik van die gebou en alle relevante inligting oor die lokasie. Volhoubaarheidsassessering verg verdere inligting oor bronne van materiaal, en die prosesse betrokke in materiaalprosessering in materiaalvervaardiging, en die toevoerketting. Dus word ’n gevallestudie-benadering gevolg vir strukturele gedrag- en volhoubaarheidsassessering. Messelwerk invul gewapende beton (RC) residensiële geboue in die Wes-Kaap, Suid-Afrika word geselekteer vir evaluering, maar die benadering kan toegepas word op lasdraende messelwerk muur geboue, waarvan ’n groot aantal in die streek voorkom. Die streek val in ’n ligte tot matige seismiese gebied. ’n Vereenvoudigde nie-lineêre struktuurgedrag evalueringsprosedure vir die invul RC rame word ontwikkel deur evaluering van die invul gedrag, en afsonderlik dié van die RC rame. Beide eksperimentele en numeriese data word gebruik om die voorgestelde prosedure te verifieër. Twee modelleringsbenaderings vir die invul RC rame word gebruik, naamlik die vakwerk sisteem, en ’n raam-diagonale stut sisteem.

Invul raam modellering maak gebruik van die ekwivalente diagonale stut konsep, en die dwarssnit afmetings vir die stut word bepaal met bestaande modelle in die literatuur. Modelle wat die bydrae van die raamstyfheid en die invul muur tot die ekwivalente stut inagneem, word beskou. Gebruik van die ekwivalente stut vir die invul is ’n vereenvoudiging, ontwikkel op basis van waargenome invul gedrag onderhewig aan dwarsbelasting. Dit voorsien dus ‘n ‘gemiddelde’ gedrag op makro-vlak, sonder om gedetaileerde gedrag op mikro-vlak te onthul. Nieteenstaande hierdie swakheid, bied die ekwivalente stut modellering ’n vereenvoudigde benadering vir die invul raam modellering. Veel navorsing is gedoen ter verbetering van die makro-modellering van die invul rame, en verskeie konfigurasies is voorgestel vir die ekwivalente stut, insluitend ’n enkel stut, ’n dubbel stut, veelvoudige stutte, en inkorporering van skuifweerstand in die ekwivalente stut. Van hierdie modelle word in hierdie studie bestudeer. Analitiese verwantskappe vir die ekwivalente stutgedrag word ontwikkel op basis van die sleutel invul falingsmodes, naamlik hoekvergruising, diagonale vergruising/kraakvorming, en skuif-glip falings. Spanningsones wat dominante spanningsgedrag verteenwoordig word gebruik ter evaluering van die invul gedrag. ’n Parametriese studie word vir die invul RC rame uitgevoer, ter ontwikkeling en kalibrasie van die analitiese modelle vir die ekwivalente stutte.

Benewens die bestudering van die invul gedrag, is parametrise evaluering van die RC rame afsonderlik uitgevoer. Tweede momente van area en die lengte van die balk en kolomme word geverifieër met gebruik van tweede moment van area verhoudings en aspekverhoudings onderskeidelik, om wat beskou word as ’n inklusiewe bereik van invul rame en konfigurasies in die praktyk, in te sluit. Die gedrag van die kaal rame word verteenwoordig deur die vloei- en ultieme weerstand, en geassosieerde deformasies. Tendense in die vloei- en ultieme weerstand en ooreenstemmende deformasies oor die spektrum van verhoudings in tweede momente van area van die balk en kolomme word gebruik om analitiese verbande vir die kaal raamgedrag te ontwikkel. Die kaal raam se dwarsdeformasie karakteristieke kan verteenwoordig word deur ’n vakwerk sisteem, waarin ’n diagonale stut geplaas word. Afgesien van die geparametriseerde definisie vir die diagonale stut se gedrag, word die stut se gedrag ook gekalibreer

op grond van die kolom eienskappe. Dit aanvaar dat die kolom noemenswaardig bydra tot die dwarsverplasingsgedrag van die kaal rame.

Die vakwerk en raam-stut sisteem modelle vir invul RC rame word valideer deur gebruik van eksperimentele en numeriese data vir invul RC rame. Hierdie modelle gebruik die invul stut eienskappe, terwyl die vakwerk modellering ook die diagonal stut-eienskappe gebruik om die raam na ’n vakwerk om te skakel. Al gee die vakwerkmodel hoër waardes van weerstand as die raam-stut model, gee beide modelle redelike voorspellings. Dit word aanbeveel dat verbeteringe in materiaalgedrag karakterisering en invul raam eksperimentele evaluering kan help om die modelvoorspellings te verbeter, en om die voorgestelde analitiese verwantskappe te verfyn.

Integrasie van strukturele gedrag-assessering met volhoubaarheidsassessering vir die ontwikkeling van volhoubare infrastruktuur is moontlik. Navorsing van Lepech et al. (2015) voorsien ‘n basis vir integrasie, met struktuurgedrag wat die tydslyn (duursaamheid) skep, waarteen die volhoubaarheidsimpak gemeet word. Die volhoubaarheidsimpak van die gebou vanaf konstruksie tot einde van sy leeftyd en inkorporasie van strukturele herstel kan beskryf word aan die hand van waarskynlikheidsbenaderings. Hierdie benadering verg egter meer data vir die karakterisering van beide die impak en tydslyn vir spesifieke aktiwiteite in die lewensiklus van die gebou.

Die proefskrif bied ‘n vereenvoudigde assesseringsmetode vir strukturele muursisteme vir infrastruktuur, wat die assessering van komplekse strukturele sisteme in óf die konsepontwerp fase, óf die strukturele renovering of rehabilitering van bestaande geboue moontlik maak. Terwyl komplekse nie-lineêre eindige element benaderings uitgevoer sou kon word, maak die vereenvoudigde maar sorgvuldig afgeleide voorgestelde benadering die analise en assessering van struktuurgedrag koste-effektief uitvoerbaar, hetsy dit die kapasiteit onder seismiese opwekking is, of ander streeksgebonde dominerende aksies soos hoë windsnelheid en selfs vloede en versakking. Dit word aangevoer dat die uitvoerbare benadering die inkorporasie van strukturele integriteit in breër volhoubaarheidsassessering raamwerke moontlik maak, vir geskikte besluitneming deur potensiële eienaars en hulle professionele spanne.

ACKNOWLEDGEMENTS

I would like to express my heartfelt gratitude to my promoter, Prof GPAG van Zijl, for his guidance and continual support throughout my research. The comments and discussions I had with him throughout the research were very helpful. Furthermore, the financial support which he offered me through his research funds and an opportunity to work with the JENGA and LIANE projects made it possible for me to pursue my studies. In the same vein, I would like to express my appreciation to Wibke de Villiers, the project leader for the JENGA and LIANE projects for engaging me. Dr TN Haas and Etienne van der Klashorst also helped me with ABAQUS and Matlab respectively, for which I am grateful.

I thank my wife, Lydia, for her support throughout my studies, and also for taking care of our two daughters, Isabel and Florence, while I was away most of the time during my studies.

I am grateful to God for His faithfulness throughout my life. May He receive all the glory!

TABLE OF CONTENTS

LIST OF FIGURES

LIST OF TABLES

LIST OF SYMBOLS, ABBREVIATIONS AND DEFINITIONS

Symbols

A Area

A_c Column cross-sectional area

A_{cc} Cross-sectional area for the infill corner crushing stress zone

A_d Diagonal strut cross-sectional area

A_{dc} Cross-sectional area for the infill diagonal compressive or cracking stress zone

A_m Infill masonry wall cross-sectional area

A_o Original cross-sectional area for homogenised elements

A_{kp1}, A_{kp} and A_{kp0} Constants for plastic stiffness ratio coefficient

A_{pr1}, A_{pr} Constants for plastic stiffness ratio, K_{pF}

A_{ke}, K_{er0} Constants for elastic stiffness ratio coefficient

A_{ss} Cross-sectional area for the infill sliding shear stress zone

a_u Normalised horizontal infill-to-frame contact length

a_v Normalised vertical infill-to-frame contact length

a_ε, b_ε, c_ε Constants for yield and ultimate strain coefficients

b Breadth

b_β A parameter of the function relating the displacement to the spectral acceleration

C_f Correction factor due to randomness in the demand and capacity of a structure

C_H Correction factor due to uncertainty in the ground motion hazard curve

C_n Normal stress distribution factor

C_s Shear stress distribution factor

C_x Correction factor due to the uncertainty in the demand and capacity

D_{fe1}, D_{fe}, D_{fe0} Constants for strut yield strength coefficient

D_{fu1}, D_{fu}, D_{fu0} Constants for strut ultimate strength coefficient

D_g Flexural/longitudinal reinforcement diameter

D_s Shear reinforcement diameter

d_{cc} Length of infill corner crushing stress zone

d_{dc} Length of infill diagonal compressive or cracking stress zone

d_n, d_f Displacement vectors

d_{ss} Length of infill sliding shear stress zone

E Young's modulus

E_b Young's modulus for beam

E_c Young's modulus for concrete

E_{cc} Young's modulus for the infill corner crushing stress zone

E_{ce} Young's modulus for column

E_{dc} Young's modulus for the infill diagonal compressive or cracking stress zone

E_{de} Diagonal strut elastic modulus

E_{du} Diagonal strut plastic modulus

E_s Young's modulus for steel

E_{ss} Young's modulus for the infill sliding shear stress zone

E_w Young's modulus for infill masonry (taken at right angles to the masonry bed)

E_θ Transformed Young's modulus along the infill diagonal

e Eccentricity

ef_i Material conversion factor for LCIA

F_{de} Strut yield strength

F_{der} Strut yield strength coefficient

F_{du} Strut ultimate strength

F_{dur} Strut ultimate strength coefficient

F_e Lateral yield strength for the frame

F_j Applied lateral force at step j

F_u Lateral ultimate strength for the frame

f_{b0} Initial equi-biaxial compressive yield stress

f_c Compressive strength

f_{cc} Confined concrete compressive strength

f_{ccr} Residual compressive strength for confined concrete

f_{c0} Initial uniaxial compressive yield stress

f_{cw} Infill compressive strength

f_{le} Confining pressure due to the reinforcement

G Shear modulus

G_w Infill wall shear modulus

g Acceleration due to gravity

$\tilde{H}(s_a^{\tilde{C}})$ Median value of the hazard function at the spectral acceleration $s_a^{\tilde{C}}$

h Height

h_p Height of masonry prism

h_w Infill wall height

I_b Second moment of area for beam

I_c Second moment of area for column

I_i Cumulative sustainability indicator impact

i_{rk} Characteristic impact for structural repair

K Stiffness

K_{cc} Stiffness for corner crushing stress zone

K_{cf} Condensed frame lateral flexural stiffness

K_{dc} Stiffness for diagonal compressive or cracking tress zone

K_{de} Diagonal strut elastic stiffness

K_{du} Diagonal strut plastic stiffness

K_{eF} Elastic stiffness ratio

K_{er} Elastic stiffness ratio coefficient

K_{fs} Frame-transformed elastic stiffness for the diagonal strut

K_{pF} Plastic stiffness ratio

K_{ss} Stiffness for sliding shear stress zone

K_x Standardised normal variate associated with probability x of not being exceeded

K_σ Ratio of second stress invariant on tensile meridian to that on compressive meridian at initial yield for any given value of pressure invariant

k_β A parameter of the hazard function

k_{ff}, k_{nn}, k_{fn}, k_{nf} Stiffness submatrices

k_{TM} Stiffness conversion parameter

L Length

L_b Beam length

L_c Column length

L_d Diagonal strut length

l_w Infill wall length

M_{mb} Beam moment

M_{mc} Column moment

M_{mi} Beam-column joint resisting moment

m Steel to concrete Young's modulus ratio

P Applied point load

$P_{PL,x}$ x confidence level estimate of the annual probability of exceedance of a given performance level

q Behaviour factor

R Strength reduction factor

r_a Aspect ratio of the frame

S_a Spectral acceleration

$s_a^{\tilde{C}}$ Spectral acceleration corresponding to the median displacement capacity $\tilde{C}$

S_{ae} Elastic spectral acceleration

S_d Spectral displacement

S_{de} Elastic spectral displacement

s_s Shear link spacing

T Period of a structure under dynamic loading

t_{el} End of life time for a system or structure

t_p Thickness of the masonry prism

t_{rk} Characteristic timeline for structural repair

t_w Infill wall thickness

t_0 Initial construction time

u_i Horizontal displacement

v_i Vertical displacement

w_d	Infill diagonal strut width
α_{cc}	Ratio of the length of a corner crushing zone to the total diagonal strut length
α_{cj}	Ratio of instantaneous Young's modulus to elastic Young's modulus for concrete in compression
α_{tj}	Ratio of instantaneous Young's modulus to elastic Young's modulus for concrete in tension
β_{CR}	Dispersion measure for randomness in displacement capacity
β_{CU}	Dispersion measure for uncertainty in top displacement capacity
β_{DR}	Dispersion measure for randomness in displacement demand
β_{DU}	Dispersion measure for uncertainty in top displacement demand
β_H	Dispersion measure for hazard
β_i	Reliability index
$\beta_{\min}$	Scaling factor
δ_e	Lateral yield deformation for the frame
δ_u	Lateral ultimate deformation for the frame
ΔF	Change in applied force
ε_{cc}	Strain at peak confined compressive strength
ε_{ccu}	Ultimate compressive strain for confined concrete
ε_{de}	Diagonal strut yield strain
ε_{der}	Yield strain coefficient
ε_{du}	Diagonal strut ultimate strain
ε_{dur}	Ultimate strain coefficient
ξ	Beam-to-column stiffness ratio
ξ_{cc}	Compression zone length factor
σ_{bi}	Beam-infill uniform normal stress at peak load
σ_{ci}	Column-infill uniform normal stress at peak load
σ_{de}	Diagonal strut yield stress
σ_{du}	Diagonal strut ultimate stress
σ_{oj}	Homogeneous stress
η_{cj}	Compressive behaviour Young's modulus homogenisation factor for the j^{th} stress-strain state
η_{tj}	Tensile behaviour Young's modulus homogenisation factor for the j^{th} stress-strain state
θ	Angle of inclination for the diagonal strut with the horizontal axis
ρ_g	Flexural reinforcement density (per unit cross-sectional area)
ρ_s	Shear reinforcement density (per unit volume)
τ_{bi}	Beam-infill uniform shear stress
τ_0	is initial shear strength
ψ	Dilation angle
μ	Friction coefficient
χ_b	Reduction factors for the beam intermediate bending moment
χ_c	Reduction factors for the column intermediate bending moment

Abbreviations

A-D	Acceleration-displacement
AExe	Net avoided exergy consumption
AF	Acidification factor
AP	Acidification potential
BoQs	Bills of quantities
CC	Corner crushing
CF	Carbon footprint
CP	Collapse prevention
Cov	Coefficient of variation
DC	Diagonal compression or cracking
EE	Embodied energy
FE	Finite element
F-δ	Force vs. deformation
GWP	Global warming potential
IDA	Incremental dynamic analysis
IO	Immediate occupancy
IN2	Incremental N2
LCI	Life cycle inventory
LCA	Life cycle assessment
LS	Life safety
PGA	Peak ground acceleration
SS	Sliding shear
Std dev	Standard deviation
WG	Waste generation

Definitions

Sustainable development: Development that meets the needs of the present generation without compromising the ability of future generations to meet their own needs accordingly (WCED, 1987).

Sustainable site: Protecting the natural habitat, keeping open spaces, dealing with rainwater and heat island and light pollution reduction.

CHAPTER 1

1.0 INTRODUCTION

1.1 BACKGROUND INFORMATION

Man's aspirations for social and economic fulfilment have led to development of infrastructure that supports his well-being. With increase in population and corresponding demand for infrastructure, the concept of sustainable development has evolved in all fields of human endeavour. In the built environment, sustainability is being championed with the aim of achieving a balance in infrastructure development and the environmental and social demands (Watermeyer, 2006; Watermeyer & Pham, 2011). Broad themes that are commonly considered by many proponents and pioneers of building sustainability as summarised by Rosa & Haddad (2013) are operation investments and expenses, eco-management, water use, energy use, material and resource use, waste and pollution, sustainable site(i.e. sustainability of the environment surrounding the building), comfort and health and safety. Due to generality of these items, many agencies that promote building sustainability through green building ratings have identified specific indicators within each theme for building sustainability.

There is a growing interest, among structural engineers, to develop and incorporate more building assessment indicators that deal with structural engineering (Chaudhary & Piracha, 2013; Watermeyer, 2006; Watermeyer & Pham, 2011; Weisenberger, 2011). Some of the structural engineering aspects that are gaining interest with building sustainability are: (i) base line material usage-this may include use of structural systems that require minimal amount of material usage such as thin shell concrete structures, concrete bubble decks, castellated steel beams and high strength materials; (ii) structural robustness and resilience - this can be done by use of performance based design for sustaining the brunt of seismic, blast and hurricane loads in prone areas (structures which are robust and resilient to extreme environmental and accidental loads offer indirect benefits to sustainability by reducing the wastage of embodied energy that would have gone into the rebuilding of damaged/collapsed buildings and infrastructure); (iii) structural adaptability and reuse - this can be done through promotion of design for deconstruction and reuse and it has potential of minimising the amount of embodied energy lost through demolition and non-usage of demolished materials; and, (iv) structural durability - shorter life span of structures result in a higher embodied material energy per year.

With divergent and isolated methodologies for assessing the structural performance of a building towards sustainability, there is a need to work towards the development of a unified approach to building sustainability assessment regarding structural performance of the building and its related environmental impacts. One way to handle building performance evaluation is through consideration of a building as a system with various sub-systems. Structural system performance attributes can be systematically evaluated so that an attribute that fairly depicts the structural performance and integrity of the building is identified and used in building sustainability assessment. In addition to identification of a reliable structural performance indicator for use in sustainability based structural performance, there are other items that can only be captured through consideration of a whole building life cycle i.e. initial construction, building operation and building deconstruction phases. Current research carried out at Stellenbosch University on environmental performance of buildings at pre-use phase, operational phase and end-of-life phase in South Africa has indicated the potential for use and promotion of alternative building materials in ensuring building sustainability (Brewis & Boshoff, 2010; Brewis, 2011; Brits, 2012; De Villiers, 2012).

One of the challenges in promoting a strong drive towards alternative building systems and any other environmentally sustainable structural systems has been lack of rational and reliable evaluation parameters that can link structural performance to sustainability. Providing a procedure for the building structures that incorporates sustainability, or evaluation of sustainability that incorporate structural performance of the buildings, would help in promoting sustainability in building structures. It is anticipated that varying useful structural performance parameters should influence the sustainability of a structure even when same building materials are used. Primary structural performance parameters such as strength, durability and ductility and secondary parameters of buildability, maintainability should all be considered in ensuring that a structure is well characterised for sustainability evaluation. In order to fully explore and work towards structural performance evaluation procedure that integrates building sustainability, an infill-framed building structure is selected.

Since building exposure to environmental loads may impact its durability and hence the life span of various building parts, incorporation of sustainability into structural performance evaluation requires case by case evaluation for specific material, structural system and the environmental exposure and the building usage. In this research, a fictitious masonry infill framed residential building constructed in the south western region of the Western Cape, that experiences moderate seismic activities, has been considered. Masonry is a commonly used construction material which is locally available in most regions in southern Africa. Reinforced concrete frames with masonry infill have been used in areas that experience moderate seismic events in South Africa. This thesis provides a comprehensive structural performance evaluation for the infill framed structures subjected to seismic action with an objective of generating simplified structural performance evaluation parameters that can be incorporated in sustainability evaluation of building structures. An integrated evaluation procedure is proposed and implemented using a case study of a fictitious residential building located in the south western region of the Western Cape.

1.2 PROBLEM STATEMENT

Modelling the structural performance of the Infill frames may involve the use of macro-models, meso-models or micro-models. When any of these approaches is used, current structural performance evaluation practice ensures that the structure is safe and fit for use. This conventional approach does not consider the impact of the structural system on the building sustainability. The need to balance any infrastructure development with environmental and social pressures has ignited interest among researchers to incorporate building sustainability in all phases of a building life cycle. The contribution of structural engineers within building sustainability is limited to material selection with emphasis on embodied energy of building materials (Weisenberger, 2011). This approach to building sustainability overlooks the influence of structural system performance to building sustainability i.e. building maintenance, construction method and materials for building envelope. This has been the case because of lack of a unified approach to structural performance evaluation of structural systems and understanding of the influence of structural performance on the overall building sustainability performance. This research contributes to the efforts by structural engineering experts to bridge this knowledge gap.

1.3 RESEARCH HYPOTHESIS

Since building sustainability involves evaluation of any activity/system about its environmental and socio-economic impact, selection of any structural system should be based not only on the current sustainability assessments that ignore the inherent structural performance and its influence on the overall sustainability performance of the system. The proposed research assumes that ignoring the

structural performance in evaluating the sustainability of the building may have a consequence on the predictability of maintenance demands and overall building performance, as structures are assumed to suffer no major damage within the considered period of sustainability evaluation. Integration of sustainability assessment with structural performance evaluation at the conceptual design stage can help identify sustainable alternatives for consideration in the detailed design, thus promoting sustainable infrastructure development.

Various nonlinear analysis procedures for structural systems subjected to a seismic load exist in literature. These procedures are classified into two main categories, namely (a) dynamic analysis procedures and (b) static analysis procedures. A brief outline for each of these two procedures is given in Chapter 2. While the dynamic analysis procedures offer more accurate results when adequate seismic data is available, the simplicity and robustness of nonlinear static analysis procedures make them equally competitive. The nonlinear static analysis has an appeal for viable design office application, while the dynamic analysis should currently still be performed by specialists in important cases. The static analysis offers simple and cost-effective means of seismic design of regular structures. With the advent of displacement-based design of structures subjected to seismic loading, efforts in developing more robust methods in nonlinear static procedures become worthwhile.

1.4 RESEARCH SIGNIFICANCE

Structural and non-structural performances of buildings have been assessed through various methodologies that are developed with the aim of achieving specific objective functions. According to current design practice, the selection and design of appropriate building structural system is influenced by the need to have safe and serviceable system at a lower cost (meeting a lower cost would entail use of locally available resources-labour and materials). While efforts to incorporate building sustainability are being made by different professionals within the building construction sector, little has been done to develop a comprehensive evaluation methodology for structural system performance that incorporates structural system safety and integrity and its overall influence on the environmental and economic sustainability of the building. With lack of a unified structural system evaluation framework, it is difficult to appraise any (new) structural system in terms of its influence on the overall building sustainability performance and hence its appropriateness to a specific building system. This research aims at developing a unified structural performance evaluation framework that incorporates building sustainability.

1.5 RESEARCH SCOPE

The major themes of this research can be broken into two, namely, structural performance of structural systems, and environmental performance of building systems. Structural systems are a product of assembly of structural elements formed from various structural materials. Different structural materials display different structural behaviour when subjected to various loads (load events). The behaviour of a structural system could be assumed to be influenced by the material it is made of, structural topology and construction methods used to assemble the system. Due to abundant number of available structural systems and possible load events when evaluation structural performance, a case study based approach is adopted for sustainability evaluation while a simplified evaluation procedure for the infill framed structures subjected to seismic loading is developed. The case study based approach also affords identification of common building model(s) with enough detailed information for sustainability assessment.

1.6 RESEARCH OBJECTIVES

The overall objective of this research is to develop a structural system performance evaluation framework for infill framed structures that incorporates building sustainability. By integrating structural performance into the building sustainability assessment, sustainable options of structural systems and building envelope can be selected for individual cases. While integration of the structural behaviour to the sustainability evaluation has not been comprehensively dealt with, the structural performance factors/indicators are helpful towards development of a comprehensive framework. The research is divided into two sub tasks, namely, structural system performance evaluation and building environmental and economic sustainability evaluation.

Sub task one*:* Structural system performance evaluation for infill framed structures
This aims at developing a unified structural system performance evaluation methodology that should generate comparable structural performance indicator(s) for the infill frames subjected to seismic loading. Specific objectives under sub task one are:

(a) Development of analytical models for evaluation of the structural performance of the infill frame system;

(b) Numerical modelling and evaluation of key aspects of a subsystem's structural performance;

(c) Subsystem and material behaviour characterisation and verification through laboratory experimental data; and

(d) Verification of analytical and numerical models for structural performance evaluation.

Sub task two: Building environmental sustainability evaluation
This task aims at identifying an appropriate sustainability assessment approach from state-of-the-art research that can be integrated with structural performance parameters of the building structure through building life cycle evaluation. It is a literature-based study, with most of the work reported in Chapter 2 under literature review. The following specific objectives are considered:

(a) Identification of common building models that represent residential building topologies for single storey and multi-storey buildings for the specified study region;

(b) Evaluation of the state of the art literature on building sustainability assessment; and

(c) Evaluation of building sustainability with incorporation of structural performance for common building models.

1.7 CHALLENGES

Building sustainability is a multi-disciplinary field and its incorporation into structural performance evaluation of structural systems would require the use of fundamental principles within the concerned fields of study. This offers challenges in both research execution and derivation of unified parameters that can be used to measure sustainability. Different sustainability indicators are measured in different units. Aggregation of various sustainability indicators has been possible by normalisation of impacts. Another challenge arises in deciding the balance between environmental pressures of any infrastructural development against the socio-economic needs of a society. This is influenced by the current socio-economic status and priorities of a society. Different weightage for various indicators can be used to reflect the society's priorities and goals within the sustainability framework.

While consideration of building life cycle offers a unified framework for evaluation of building sustainability performance, there is always a challenge to reliably predict the unfolding of future events that may affect maintenance demand, building operation and labour and material costing. This research

will use state-of-the-art information in handling these challenges. Furthermore, comparing building sustainability performances of various construction materials and structural systems require conversion of building structures so that they all have functionally equivalent structural systems and building envelop. While this may not be a challenge in a multi-disciplinary industry with architects and engineers working together for a building project, it is challenging to a structural engineering researcher. It is anticipated that collaboration with architects in future endeavours will help solve this challenge.

1.8 DISSERTATION OUTLINE

This study develops analytical models for the evaluation of the infill frames, with an objective of incorporating the resisting contribution of the infill, thus reducing the amount of materials for construction. Optimum use of building materials, using reliable design tools can enhance sustainability in buildings. Chapter 1 introduces the study, summarising existing challenges in structural evaluation for the infill frames and available sustainability tools. It highlights identified research gaps. A comprehensive evaluation of existing studies on infill frame behaviour evaluation and building sustainability evaluation procedures is provided in Chapter 2. Chapter 3 provides a detailed discussion of the research problem and comprehensive methodological approach followed. Three research studies for development of structural performance evaluation procedures for the infill frames are discussed, namely, analytical, experimental and numerical studies. The material characterisation for the infill frame macro-modelling is provided in Chapter 4. Since the macro-models are used in the structural evaluation of the infill frames in this study, parametric evaluation of bare frames, identifying key parameters for use in establishing diagonal strut properties is provided in Chapters 5 while calibration parameters are developed in Chapter 6. Chapter 7 provide the structural evaluation procedure that utilises the truss analogy, validating all the proposed modelling procedures. Integration of the structural performance with sustainability evaluation, through a case study-based approach, is provided in Chapter 8. Chapter 9 summarises the key findings and draws the conclusion and recommendations drawn from the research study.

CHAPTER 2

2.0 LITERATURE REVIEW

2.1 INTRODUCTION

There is a general interest to promote sustainability globally. In civil and building infrastructure development, significant research effort is devoted towards development and implementation of sustainable infrastructure. This work is one of such efforts in developing appropriate means of promoting sustainability through structural performance evaluation. As stated in Chapter 1, there are two key issues of interest, namely structural performance and sustainability. Since sustainability is measured within properly defined boundary conditions, the work considers the residential buildings within the south western region of the Western Cape in South Africa. This region is susceptible to moderate seismic events (PGA ranges from 0.1g to 0.15g) and one of the commonly used structural systems is the infill RC frames. Thus, the behaviour of the infill RC frames subjected to the seismic events is explored. Various macro-modelling techniques for the infill frames are considered before examining the existing procedures for seismic evaluation of structures.

Sustainability in building infrastructure involves adequate consideration for environmental, social and economic impact of the buildings at design, construction, operation and end of life stages. Thus, from extraction of raw materials to end of life management of the infrastructure, any sustainable building system must meet the desirable goals of improved environmental, social, and economic performance (Elkington, 1994). Civil and building infrastructures form a critical part of the global human essential systems that support our quality of life and enable global development and progress while consuming vast amounts of material resources and energy (Lepech, et al., 2015), thus the need for sustainability incorporation. Careful evaluation of the sustainability assessment methods is undertaken, with emphasis on the integration of the structural performance of structures.

2.2 INFILL RC FRAME BEHAVIOUR

The significance of the infill walls in modifying the structural performance of infill framed structures has widely been studied. While some building standards do not incorporate the effects of infill, various research conducted over the past five decades indicate that infill walls significantly affect the strength and stiffness of infill frames (Saneinejad & Hobbs, 1995; Smith, 1962; Crisafulli, 1997; Lavanya, et al., 2015). With proper detailing, infills can increase the lateral stiffness/resistance of framed structures and reduce the p-Δ effects. It is argued that inclusion of the infill walls to assess the seismic resistance of existing buildings that were designed before the seismic codes might enable the buildings to meet the current code requirements (Saneinejad & Hobbs, 1995). The sections that follow evaluate the material behaviour of the constituents of the infill RC frames, the structural system behaviour for the RC frames and examine the existing methods used for infill frame behaviour modelling.

2.2.1 Material behaviour

RC infill frames comprises mainly the RC frame and the masonry panel. While the overall behaviour of the infill frame is not the summation of each of its constituents, understanding the behaviour of each of the constituents is crucial in evaluating the overall system behaviour. This section discusses the material behaviour characterisation and modelling of the masonry, normal concrete and reinforced concrete under the anticipated loads when the structure is subjected to seismic loading.

2.2.1.1 Masonry

Masonry is a composite material comprising the assemblage of the brick units with mortar. Due to this nature of assemblage, masonry behaves anisotropically. However, for simplified modelling purposes, masonry can be considered as an orthotropic material displaying different behaviour only in the orthogonal axes. Material behaviour of masonry that are considered as having effects on the infill lateral resistance are the compressive behaviour, tensile behaviour and the shear behaviour and are discussed in the subsequent paragraphs. While this section provides the behaviour of masonry under uniaxial load, the nature of loading the infill is subjected to during any seismic event may generate biaxial stresses. The work of Page (1981; 1983) on the behaviour of masonry under biaxial loading showed variations in the principal stresses along different orientations of the loading with respect to the material axes. It is thus prudent that modelling of the infill masonry subjected to seismic loading should incorporate the effects of biaxial stresses.

(a) Compressive behaviour of masonry

To establish the behaviour of masonry under compression, either the uniaxial compression test or the biaxial compression tests can be conducted depending on the nature of loading under investigation. Determination of the uniaxial compressive strength of masonry is carried out using conventional methods as outlined in various standards such as the EN 1052 (1998). Extensive experimental research on the behaviour of masonry under uniaxial compression revealed that the compressive strength is influenced by the confining effects during testing and that the strength varies with respect to the aspect ratio of the wall/prism. It is therefore, not surprising that most experimental work on the uniaxial compressive behaviour of masonry recommends the use of higher aspect ratio to estimate the compressive behaviour of masonry wall. The ACI (1992) recommends the use of two brick prism while several researchers recommend the use of 5 bricks (Amrhein, 1992; Page & Marshall, 1985).

Due to the variations in the methods employed to establish the uniaxial compressive behaviour of masonry, correction factors are used to generate normalised compressive strength. Table 2.1 provides a summary of the correction factors for compressive strength from various authors. The prism aspect ratio of 5 is considered as standard unit geometric size for all the masonry units except for the concrete block as noted by the correction factor by the ACI (1992) in the Table 2.1. In addition to aspect ratios, the compressive strength is influenced by the properties of its constituent materials (masonry unit strength, mortar strength, mortar joint thickness, water retentivity and water absorption) and the type/manner of loading (static loading, cyclic loading, direction of compression loading with respect to bed joint), construction related factors (workmanship, patterns and method of bonding).

Table 2.1: Correction factors of compressive strength of masonry for different aspect ratios of test masonry prisms

Researcher/Building standard specification	**Aspect ratio of masonry prism (h_p/t_p)**									
	0.4	0.7	1.0	1.33	2.0	2.5	3.0	4.0	4.5	≥5.0
ACI(1992) –Clay bricks	-	-	-	-	0.82	0.85	0.88	0.94	0.97	1.00
ACI (1992) - Concrete block	-	-	-	0.75	1.0	-	1.07	1.15	-	1.22
Page & Marshall (1985)[1]	0.5	0.6	0.7	-	-	-	0.85	-	-	1.00
Drysdale et al. (1994)[1]	-	-	0.7	-	-	-	-	-	-	1.00

[1]For use on both clay bricks and concrete blocks

(b) Compressive stress-strain modelling

Masonry is a quasi-brittle material, typically non-elastic, non-homogeneous and anisotropic. Its main constituents, brick and mortar display different properties, with bricks typically stiffer and less ductile than mortar. A stress-strain relationship for masonry wall is influenced by material and geometric properties of its constituents. Figure 2.1 shows typical compressive stress-strain curves for mortar, brick and masonry. The findings of Atkinson et al. (1989) revealed that the shape of the stress-strain curve is affected by the strength and Young's modulus of mortar. Significant softening occurs when the mortar strength decreases.

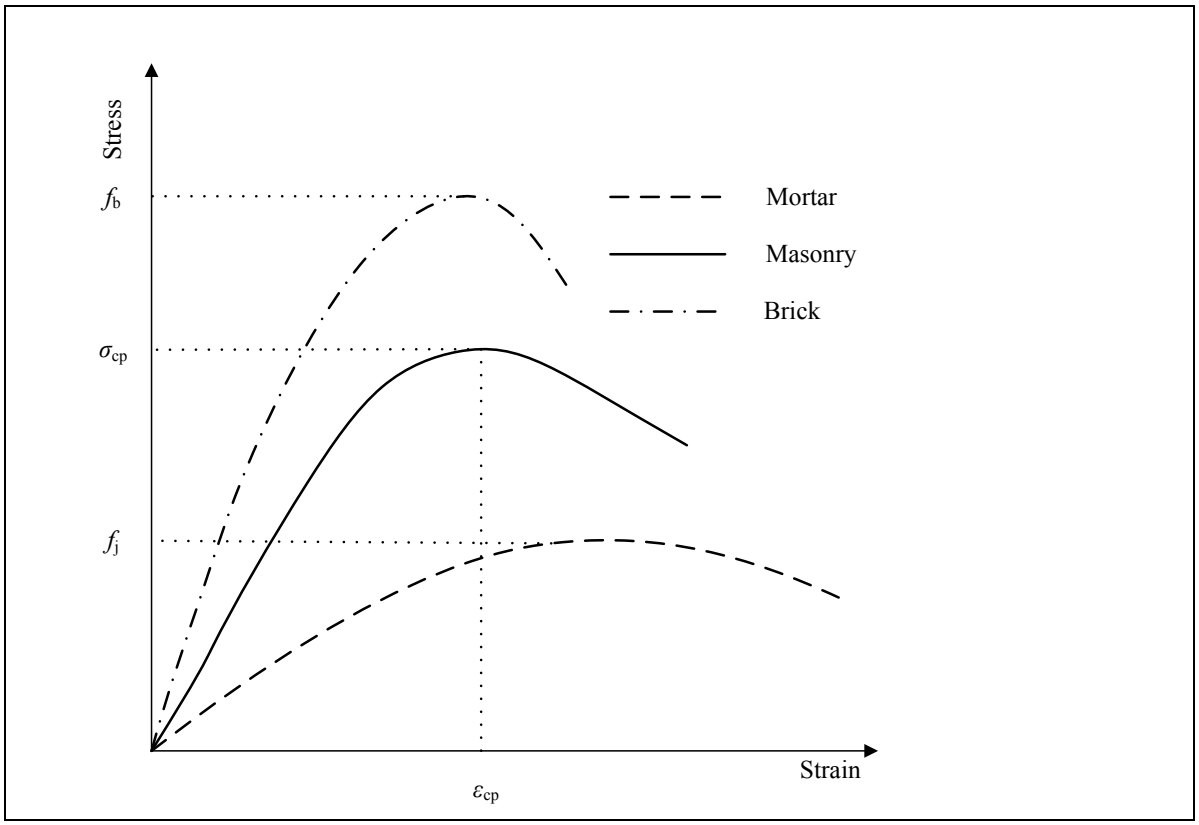

Figure 2.1: Typical compressive stress-strain curves for mortar, brick and masonry (Paulay & Priestley, 1992)

Under lateral loads, masonry behave inelastically even in the range of small deformations (Kaushik, et al., 2007). Various researchers have tried to find mathematical relationship between the compressive stress and strain. Ewing & Kowalsky (2004) and Paulay & Priestley (1992) proposed the use of a *modified* Kent-Park (Park, et al., 1982) model that is normally used for concrete to predict the unconfined masonry compressive stress-strain behaviour. The model consists of three parts, namely; a parabolic rising curve, a linear falling branch and a final horizontal plateau of constant stress at 20% masonry prism strength as provided in equation 2.1.

$$\frac{\sigma_c}{\sigma_{cp}} = \begin{cases} 1.067\left[2\left(\frac{\varepsilon_c}{0.002}\right) - \left(\frac{\varepsilon_c}{0.002}\right)^2\right] & \text{for } \varepsilon_c \le 0.0015 \text{ (rising curve)} \\ 1 - Z_m\left(\varepsilon_c - 0.0015\right) & \text{up to } \frac{\sigma_c}{\sigma_{cp}} = 0.2 \text{ (descending curve)} \\ 0.2 & \text{residual stress} \end{cases} \quad (2.1)$$

where

$$Z_m = \frac{0.5}{\left(\frac{3 + 0.29 f_j}{145 f_j - 1000}\right) - 0.002}$$

f_j is compressive strength of mortar

σ_{cp} is peak compressive stress of masonry

A parabolic stress-strain proposed by Powell & Hodgkinson (Hendry, 1990) for the ascending part as given in equation 2.2 is widely accepted by researchers (Paulay & Priestley, 1992; Priestley & Elder, 1983; Kaushik, et al., 2007; Sawko & Rouf, 1984). Kaushik, et al. 2007 proposed that the curve can be extended beyond the peak until stress drops to 90% of peak stress. Beyond this point a linear relationship is used to describe the descending part up to 20% of peak stress (residual strength) of masonry.

$$\frac{\sigma_c}{\sigma_{cp}} = 2\frac{\varepsilon_c}{\varepsilon_{cp}} - \left(\frac{\varepsilon_c}{\varepsilon_{cp}}\right)^2 \quad (2.2)$$

The compressive strain at maximum residual strength ($0.20\sigma_{cp}$) can be assumed to be 2.0 times the strain at peak stress ($2.0\varepsilon_{cp}$) and 2.75 time the strain at peak stress ($2.75\varepsilon_{cp}$) for mortar without lime and mortar with lime respectively (Kaushik, et al., 2007).

Binda et al. (1988) proposed a material law that recognized two equal phases within the pre-peak stress. The initial state, representing the stress-strain relationship up to half the strain at peak stress is defined as:

$$\frac{\sigma_c}{\sigma_{cp}} = \frac{3\varepsilon_c}{2\varepsilon_{cp}} \quad (2.3)$$

The last state representing the remaining half of the strain before peak stress is reached is defined by the analytical law:

$$\frac{\sigma_c}{\sigma_{cp}} = -0.50 + 3.5\frac{\varepsilon_c}{\varepsilon_{cp}} - 2\left(\frac{\varepsilon_c}{\varepsilon_{cp}}\right)^2 \quad (2.4)$$

Concrete compressive stress-strain law developed based on tests results conducted by Vecchio & Collins (1986) and adopted by Ibrahim & Suter (1994) for concrete masonry that incorporates the effects of tensile stresses when masonry is subjected to biaxial loading. The analytical model for principal compressive stress (see equation 2.5) incorporates the effects of principal tensile stresses in reducing the magnitude of principal compressive stress-strain behaviour.

$$\frac{\sigma_c}{\sigma_{cp}} = \frac{1}{\beta_{ft}}\left(2\left(\frac{\varepsilon_c}{\varepsilon_{cp}}\right) - \left(\frac{\varepsilon_c}{\varepsilon_{cp}}\right)^2\right) \quad (2.5)$$

where

$\beta_{ft} = 0.8 - 0.34\left(\frac{\varepsilon_{tp}}{\varepsilon_{cp}}\right) \geq 1$; and

ε_{tp} is principal tensile strain in the direction normal to that being considered.

Ewing & Kowalsky (2004) proposed limit states that can be used to describe the stress-strain behaviour of masonry. Based on these limit states, Kaushik et al. (2007) identified six control points that represent significant change in material behaviour, namely;

(a) $0.33\sigma_{cp}$: This represents the stress-strain point beyond which the initial elastic behaviour changes to nonlinear behaviour. The nonlinear behaviour is characterized by development of cracks in masonry;

(b) $0.75\sigma_{cp}$: At this point, the masonry starts developing vertical splitting cracks. The masonry still resists the applied load without much stiffness deterioration;

(c) $0.90\sigma_{cp}$: This represents the stress-strain point just before failure of masonry. The vertical splitting cracks propagate excessively generating great stiffness degradation of masonry.

(d) σ_{cp}: This is the ultimate compressive stress of masonry. The stress-strain curve starts to drop and exhibits sudden increase in the strains beyond this point.

(e) $0.50\sigma_{cp}$: This is a key point in the post cracking stress-strain curve (descending curve) as it represents the maximum possible dependable compressive strength of masonry;

(f) $0.20\sigma_{cp}$: This stress represents the maximum residual compressive stress for masonry. This point is useful for numerical purposes as the material is assumed to have infinite residual strength.

The discussed mathematical relationships between stress and strain are empirical in nature and do not capture any physical/scientific mechanisms that influence the stress-strain behaviour. Nevertheless, such relationships enable nonlinear modelling of masonry structure that requires the full stress-strain behaviour when only the peak compressive stress and strain are available. The stress-strain behaviour normalised by respective peak stress and corresponding strain for respective analytical models is shown in Figure 2.2. Tangential modulus of elasticity can be determined by differentiating the stress functions with respect to strain $(E_t = \partial\sigma_c / \partial\varepsilon_c)$. The results show key relationship between the tangential modulus of elasticity and the maximum compressive stress of masonry. The *modified* Kent-Park (Park, et al., 1982) model gives $E_t = 1067\sigma_{cp}$, the Powell & Hodgkinson model gives $E_t = 1000\sigma_{cp}$, Ibrahim & Suter (1994) model gives $E_t = 833\sigma_{cp}$ and Binda eta al. (1988) model gives $E_t = 750\sigma_{cp}$ for strain between zero strain and half the strain at maximum stress and $E_t = 1750\sigma_{cp}$ for the remaining strain state before the peak. All the models show slight decrease in the Young's moduli except for the model by Binda et al. (1988) which shows increased stiffness. The behaviour depicted by Binda et al. (1988) model does not represent the usual masonry behaviour as masonry's stiffness degrades towards the peak stress.

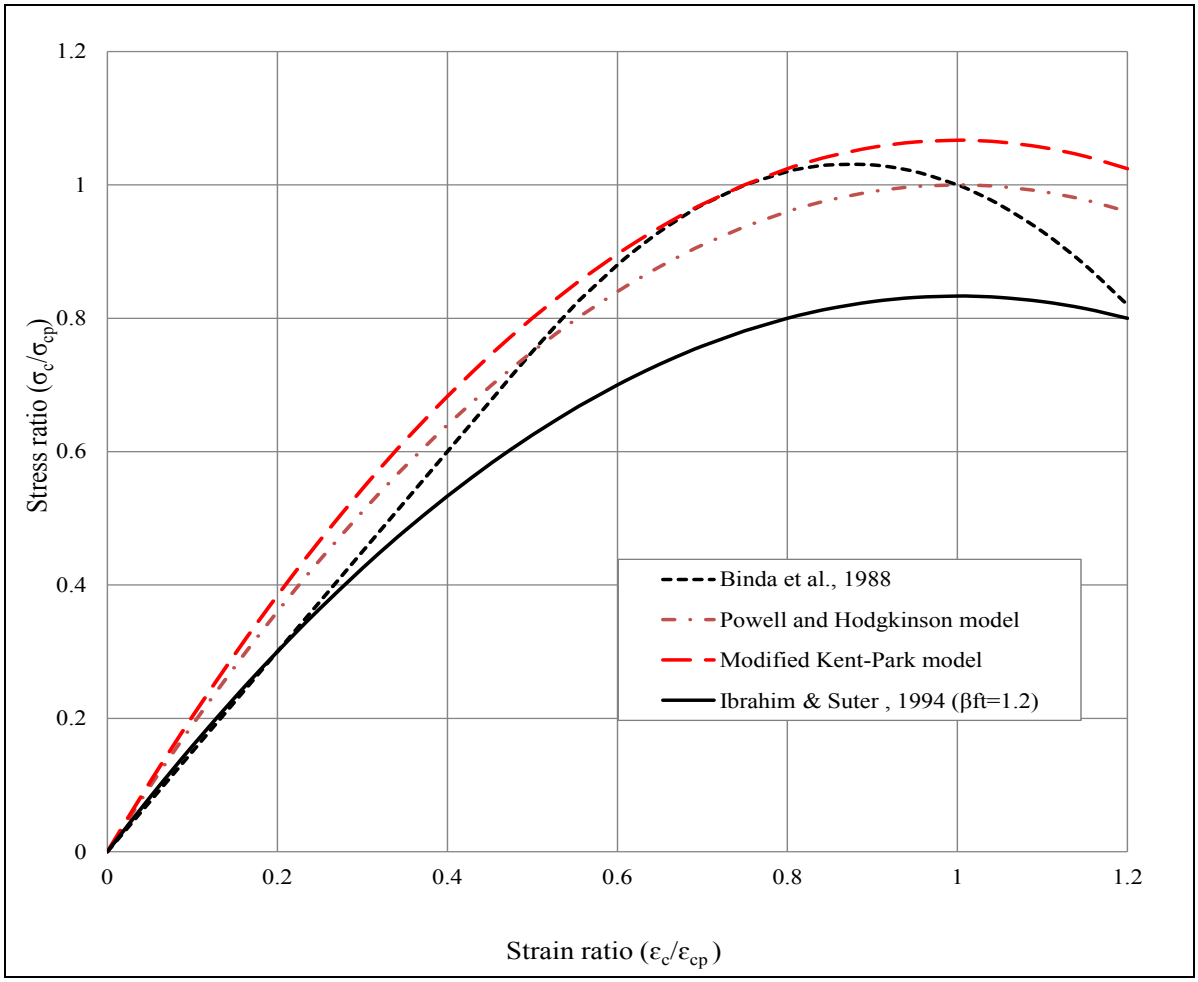

Figure 2.2: Comparison of analytical models for compressive stress-strain relations for masonry

Different approaches have been attempted by researchers to relate the Young's modulus of masonry with its compressive strength. As noted with the variations in the tangential moduli predictions from the stress-strain relationships, the empirical relationships for the Young's modulus vary significantly, within the range of $210\sigma_{cm} < E_{cm} < 1670\sigma_{cm}$ for clay brick masonry (Grimm, 1984) and $400\sigma_{cm} < E_{cm} < 1290\sigma_{cm}$ for concrete masonry (Hamid, et al., 1987). Some of the analytical relationships for the Young's modulus derived as a function of prism compressive strength, σ_{cm} are summarised in Table 2.2. Variability in the material properties, measurements methods and actual panel construction may be some of the sources of uncertainty that generates such variations.

Table 2.2: Young's modulus for masonry

Author	Analytical relationship
Paulay & Priestley (1992)	$E_{cm} = 750\sigma_{cm}$
San Bartolome (in Amrhein, 1992)	$E_{cm} = 500\sigma_{cm}$
Sinha & Pedreschi (1983)	$E_{cm} 1180\sigma_{cm}^{0.33}$
Schubert (in Sinha & Pedreschi, 1983)	$E_{cm} = 2116\sqrt{\sigma_{cm}}$
Paulay & Priestley (1992)	$E_{cm} = 1000\sigma_{cm}$

Apart from the use of the masonry compressive stress-strain to establish tangential modulus, the Young's modulus for the brick and mortar can be used to estimate the Young's modulus for the masonry. Analytical expression for the determination of masonry Young's modulus from the moduli of bricks and mortar was developed using principles of deformation and mix combination by various researchers as given in equation 2.6 (Ameny, et al., 1983; Binda, et al., 1988; Drysdale, et al., 1994). The effect of confinement is insignificant (about 2%) as investigated by Ameny et al. (1983). The Young's modulus of masonry, bricks and mortar are usually estimated from the stress-strain data, at 30% to 33% of peak strength (Amrhein, 1992; Binda, et al., 1988).

$$E_{cm} = E_{cb} \frac{1 + h_b / j}{E_{cb} / E_{cj} + h_b / j} \tag{2.6}$$

where

j is mortar joint thickness;

h_b is brick thickness;

E_{cb} is Young's modulus of the brick;

E_{cj} is Young's modulus of mortar; and

E_{cm} is Young's modulus of the masonry.

An evaluation of these models regarding their variability and stiffness degradation as determined by linearised instantaneous tangential moduli of elasticity for specific stress-strain points is carried out. Since comparison of tangential modulus degradation is possible if dimensionless parameters are used, an instantaneous tangential modulus factor, α_{ci}, is given by equation 2.7.

$$\alpha_{ci} = \frac{E_{ci}\varepsilon_{cp}}{\sigma_{cp}} \Leftrightarrow E_{ci} = \frac{\alpha_{ci}\sigma_{cp}}{\varepsilon_{cp}} \tag{2.7}$$

where E_{ci} is an instantaneous tangential modulus considered to be constant within each stress-strain state.

For the initial stress-strain state, this modulus of elasticity is the same as the secant modulus of elasticity for masonry. Key control points as identified by Kaushik et al. (2007) are used to determine the linearised instantaneous tangential modulus. There are four key control points before post-peak behaviour of masonry that are considered, based on stress values and are defined as $0.33\sigma_{cp}$, $0.75\sigma_{cp}$, $0.90\sigma_{cp}$ and $1.0\sigma_{cp}$. Post peak behaviour is usually defined by a linear relationship up to residual stress as defined by equation 2.1. A multi-linear stress-strain law of masonry in compression can be approximated based on these four material points up to peak stress as shown in Figure 2.3. Variations in the linearised tangential moduli for masonry up to peak compressive stress for various analytical relationships are indicated in Table 2.3 while strain limits for corresponding stress-strain state are provided in Table 2.4.

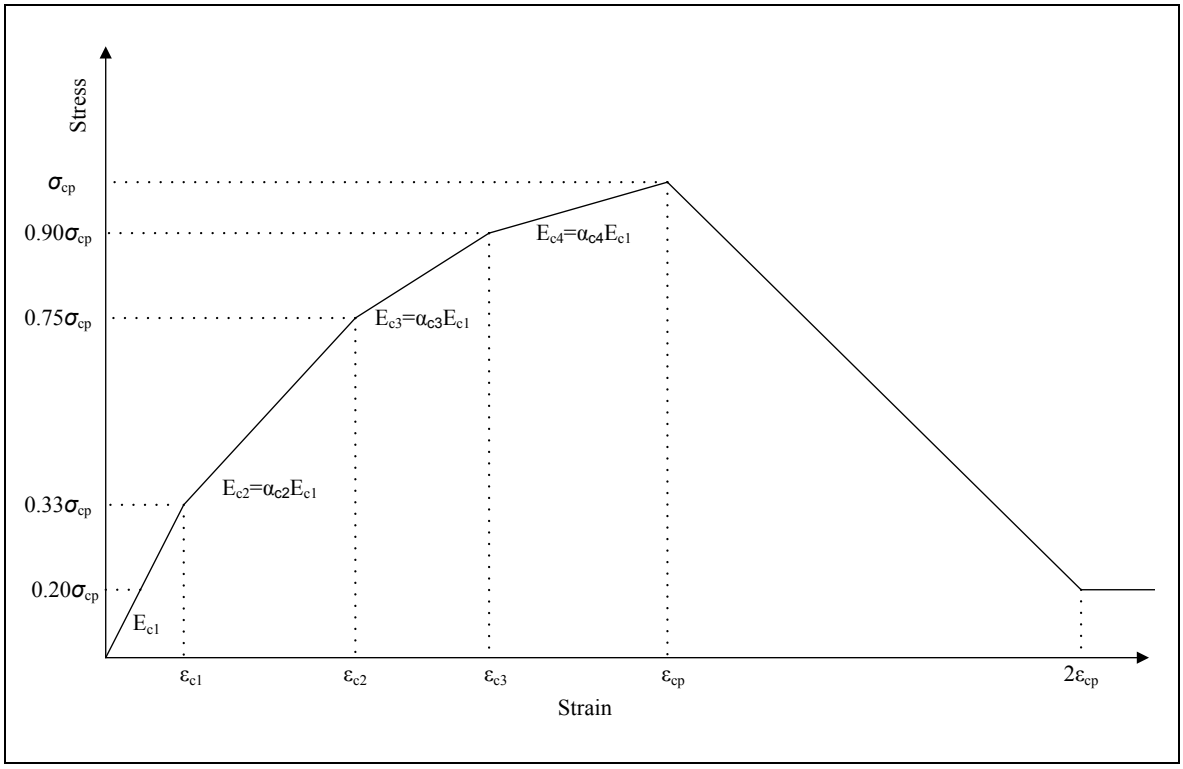

Figure 2.3: Typical multi-linear stress–strain curve

Table 2.3: Average instantaneous modulus of elasticity for stress states before peak stress

Analytical model authors or source	**Stage 1 stress state,** E_{c1}	**Stage 2 stress state**		**Stage 3 stress state**		**Stage 4 stress state**	
		E_{c2}	α_{c2}	E_{c3}	α_{c3}	E_{c4}	α_{c4}
Binda et al. (1988)	$750\sigma_{cp}$	$750\sigma_{cp}$	1.0	$631\sigma_{cp}$	0.842	$381\sigma_{cp}$	0.508
Powell & Hodgkinson	$908\sigma_{cp}$	$658\sigma_{cp}$	0.725	$408\sigma_{cp}$	0.449	$158\sigma_{cp}$	0.174
Modified Kent-Park (Park, et al., 1982)	$976\sigma_{cp}$	$733\sigma_{cp}$	0.751	$502\sigma_{cp}$	0.514	$645\sigma_{cp}$	0.353

Table 2.4: Stress states strain limits for different analytical models

Analytical model	**Stage 1 strain limit**	**Stage 2 strain limits**	**Stage 3 strain limits**	**Stage 4 strain limits**
Binda et al. (1988)	$\varepsilon_c \le 0.2222\varepsilon_{cp}$	$0.2222\varepsilon_{cp} < \varepsilon_c \le 0.50\varepsilon_{cp}$	$0.50\varepsilon_{cp} < \varepsilon_c \le 0.619\varepsilon_{cp}$	$0.619\varepsilon_{cp} < \varepsilon_c \le 0.750\varepsilon_{cp}$ *1
Powell & Hodgkinson	$\varepsilon_c \le 0.1835\varepsilon_{cp}$	$0.1835\varepsilon_{cp} < \varepsilon_c \le 0.50\varepsilon_{cp}$	$0.50\varepsilon_{cp} < \varepsilon_c \le 0.684\varepsilon_{cp}$	$0.684\varepsilon_{cp} < \varepsilon_c \le 1.0\varepsilon_{cp}$
Modified Kent-Park (Park, et al., 1982)	$\varepsilon_c \le 0.1708\varepsilon_{cp}$	$0.171\varepsilon_{cp} < \varepsilon_c \le 0.455\varepsilon_{cp}$	$0.455\varepsilon_{cp} < \varepsilon_c \le 0.604\varepsilon_{cp}$	$0.684\varepsilon_{cp} < \varepsilon_c \le 0.75\varepsilon_{cp}$ *2

*1Theoretical peak stress is $1.03\sigma_{cp}$ and occurs between $0.75\varepsilon_{cp}$ and ε_{cp} (these strains have respective stress of $1.0\sigma_{cp}$ each); *2Peak stress is assumed to occur at a lower strain than the theoretical strain, ε_{cp}

(c) Tensile behaviour of masonry

Masonry, like concrete, is brittle in tension. Masonry is also orthotropic, with low tensile strength normal to bed joints (about 5% of its capacity in compression), and somewhat higher parallel to bed joints (about 10% of its capacity in compression) (Mohamad, et al., 2017; Khalaf, et al., 1992; Page, 1983). After peak, masonry display softening behaviour as tensile cracks increase. Since the post peak tensile behaviour is marred with crack formation and propagation, most of the tensile behaviour models are based on crack width formulations. Due to versatility of stress-strain modelling in finite elements, researchers have developed stress-strain relationships for the post peak tensile behaviour. These models are used in finite element modelling utilising the smeared cracking material behaviour. Most of the models for masonry in tension have been developed from concrete tensile models, due to the similarity in brittle behaviour. However, the orthotropic behaviour of masonry makes it necessary for modification of the concrete models. Gopalaratnam & Shah (1985) proposed the following uniaxial tensile stress-strain model for masonry:

$$\frac{\sigma_t}{\sigma_{tp}} = 1 - \left(1 - \frac{\varepsilon_t}{\varepsilon_{tp}}\right)^{A_t} \quad \text{for } \varepsilon_t \le \varepsilon_{tp} \tag{2.8}$$

where

σ_t is tensile stress;

σ_{tp} is peak tensile stress;

ε_t is tensile strain;

ε_{tp} is tensile strain at peak tensile stress;

$A_t = E_t \varepsilon_{tp} / \sigma_{tp}$; and

E_t is initial tangent modulus

Stavridis & Shing (2008) considered elastic tensile behaviour up to peak (assumed cracking), followed by an exponential decline up to residual strength (see Figure 2.4). The declining relationship is defined by equation 2.9.

$$\frac{\sigma_t}{\sigma_{tp}} = r_t + (1 - r_t)\exp\left(\frac{-\alpha_1(\varepsilon_t - \varepsilon_{tp})}{\sigma_{tp}}\right) \tag{2.9}$$

where

r_t is proportion of residual tensile strength –typically, the value ranges from 0.05 to 0.2 and is used for computational stability in finite element modelling. This parameter can be ignored for the case of macro-modelling; and

α_1 represents a calibration parameter that controls the rate of decline of the softening curve and is expressed in stress unit. Lofti & Shing (1991) used 250 ksi (1723.69 MPa) for α_1 .

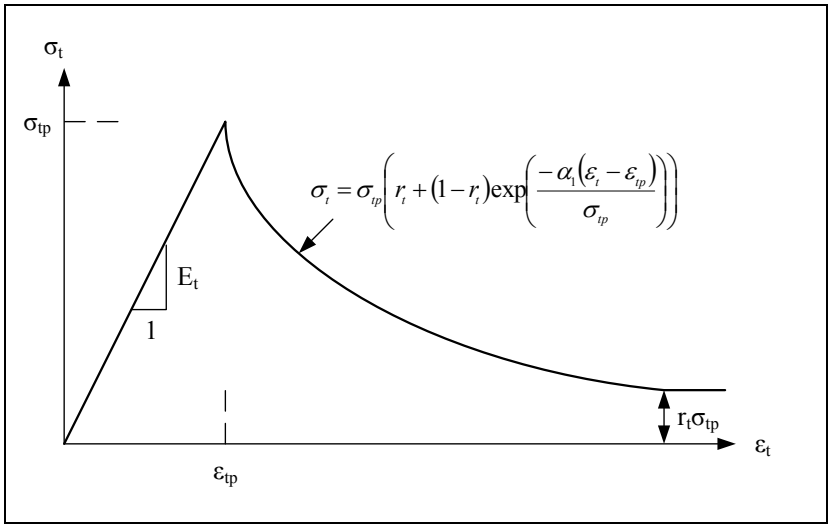

Figure 2.4: Tensile model of masonry with softening behaviour (Stavridis & Shing, 2008)

(d) Shear behaviour of masonry

Infill masonry can fail through sliding shear. Experimental studies were conducted to establish and characterise the shear behaviour of masonry joint. Atkinson, et al. (1989) reported that experimental data that can be useful to develop analytical models to simulate shear response under seismic loading condition should have (1) shear stiffness for both initial and repeated loading states; (2) peak and residual strength values; (3) normal load and stiffness effects on shear stiffness and dilatancy; (4) repeated shear reversals; and (5) dynamic effects.

Van der Pluijm (1993; 1998) examined the shear behaviour of masonry joint by subjecting the joint interface to shear forces at various confining pressures. It was found that within the elastic range, the maximum shear stress increases linearly with increase in confining pressure while the shear stiffness seemed to be constant. Thus, Coulomb friction model can be used to adequately describe the shear behaviour of masonry joints subjected to any level of confining stress. It was also observed that the shear fracture energy (G_f^{II}) increases linearly with increase in the confining pressure. Atkinson et al. (1989) examined the horizontal bed joint shear failure mode and shear load-displacement behaviour of clay masonry during both static and cyclic loading. Laboratory tests were conducted on masonry samples using a servo-controlled direct shear apparatus. Under cyclic shear loading, masonry bed joints showed peak strength for the first cycle followed by residual shear strength. The peak and residual shear strengths could be represented by the Mohr Coulomb criterion, with friction coefficients ranging between 0.64 and 0.75. The post-peak relationship between shear stiffness and relative horizontal displacement could be approximated by an exponential function to represent the softening behaviour (see Figure 2.5a). A full description of the experimental set-up and results can be found in Atkinson et al. (1989). The sliding shear stress along the masonry interface (τ_p) is, therefore, related to the confining stress (σ_p) using coulomb friction relationship given in equation 2.10. Figure 2.5b illustrates the relationship between the shear and the confining pressure.

$$\tau_p = \tau_0 + \sigma_p \tan\phi_i \Leftrightarrow \tau_p = \tau_0 + \mu_i \sigma_p \qquad (2.10)$$

where

τ_0 is initial shear strength;

ϕ_i is angle of friction; and

$\mu_i = \tan\phi_i$

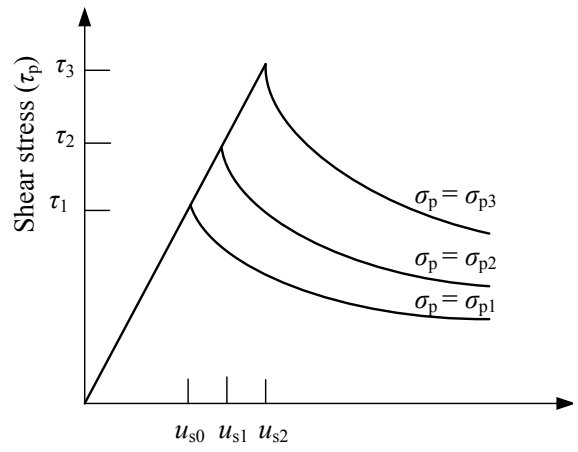

(a) Typical bed-joint shear stress vs. displacement at different confining pressures

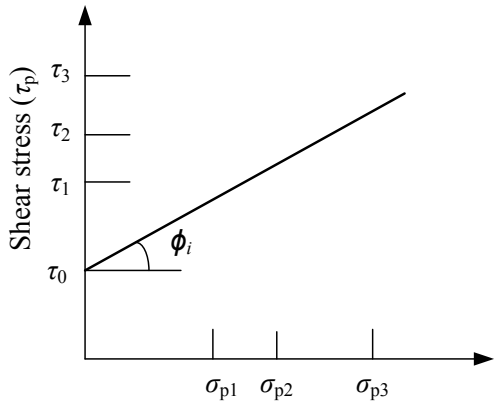

(b) Typical joint shear stress vs. confining pressure

Figure 2.5: Typical shear behaviour of masonry (Van der Pluijm, 1998; Van der Pluijm, 1993)

2.2.1.2 Concrete

Concrete is a quasi-brittle material, displaying high compressive resistance as compared to the tensile resistance. The behavior of concrete is well established, with numerous material models developed to predict its behaviour. Most of the models presented under masonry were developed from concrete behaviour, for example, equations 2.1 and 2.2. In this study, concrete is used for the RC frames that are subjected to seismic loading. Thus, the effects of reinforcement on the behaviour of concrete in both compression and tension are discussed and existing modelling approaches highlighted.

(a) Confined concrete in compression

Various studies have established that the presence of transverse reinforcement in concrete columns provides confinement to the compressed concrete, prevents premature buckling of compressed longitudinal bars and act as shear reinforcement (Mander, et al., 1988; Sheikh & Uzumeri, 1982; Vallenas, et al., 1977). Transverse reinforcement can increase the strength and ductility of the confined concrete. Compressive stress-strain models that capture the influence of transverse reinforcement have been developed (Mander, et al., 1988; Sheikh & Uzumeri, 1982; Vallenas, et al., 1977). The *modified* Kent-Park. (Park, et al., 1982) model, Mander et al. (1988) model, The Eurocode 2 (2004) model and Vallenas et al. (1977) model are considered in this study, and are shown in Figure 2.6. Key parameters defining each model are summarized in Table 2.5.

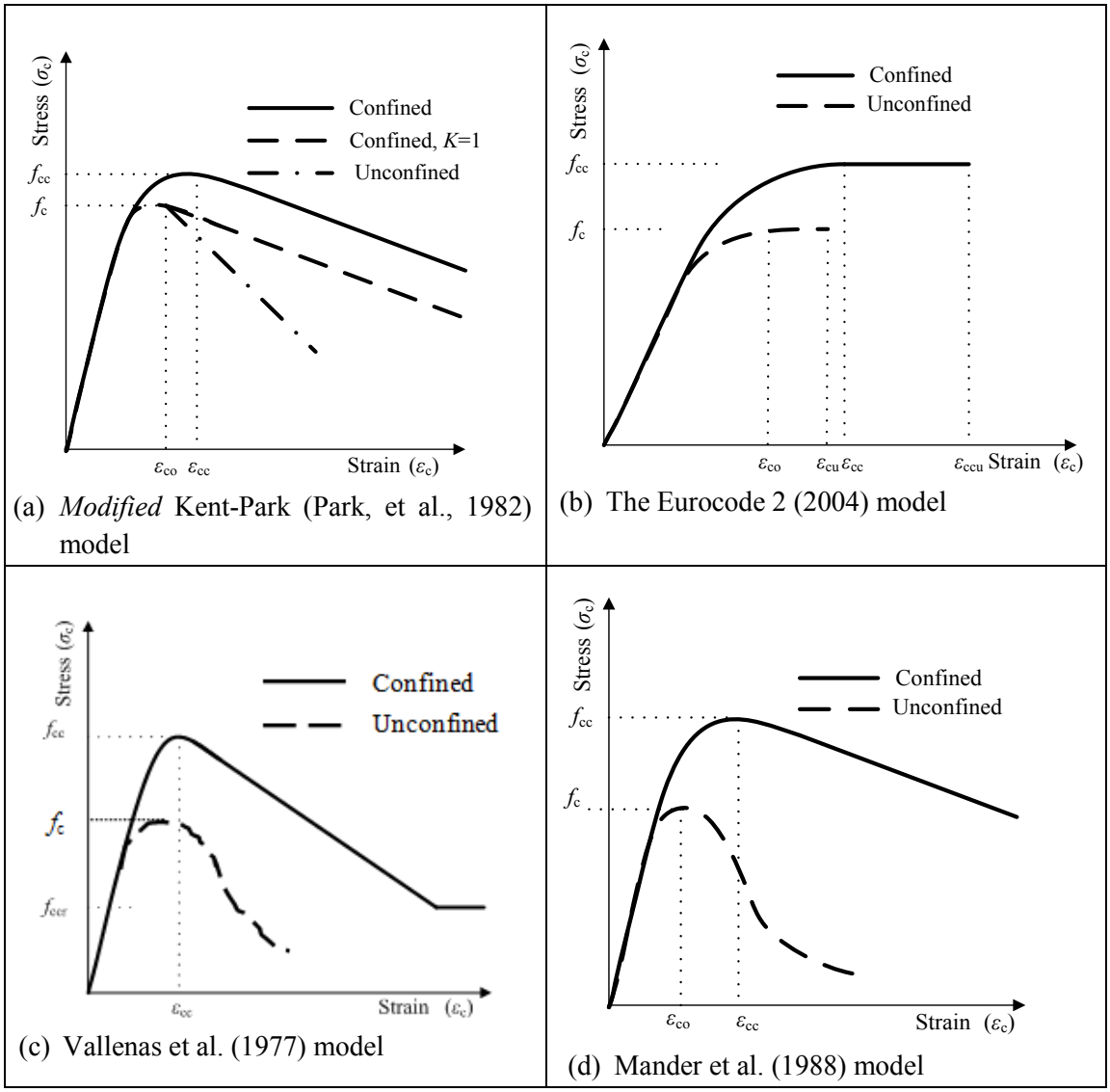

(a) *Modified* Kent-Park (Park, et al., 1982) model

(b) The Eurocode 2 (2004) model

(c) Vallenas et al. (1977) model

(d) Mander et al. (1988) model

Figure 2.6: Uniaxial compressive stress-strain models for confined concrete

Table 2.5: Confined compressive stress-strain analytical models

Model	**Analytical model expression**	**Parameters or comments**
Modified Kent-Park (Park, et al., 1982) model	$0 \le \varepsilon_c \le \varepsilon_{cc}$ $\frac{\sigma_c}{f_{cc}} = 2\frac{\varepsilon_c}{\varepsilon_{cc}} - \left(\frac{\varepsilon_c}{\varepsilon_{cc}}\right)^2$ $\varepsilon_c > \varepsilon_{cc}$ $\frac{\sigma_c}{f_{cc}} = 1 - Z\varepsilon_{cc}\left(\frac{\varepsilon_c}{\varepsilon_{cc}} - 1\right)$ $f_{ccr} = 0.2 f_{cc}$	$K = 1 + \frac{\rho_s f_{sy}}{f_c}$; $f_{cc} = Kf_c$; $\varepsilon_{cc} = K\varepsilon_{co}$ $Z = \frac{0.5}{\frac{3 + 0.29 f_c}{145 f_c - 1000} + \frac{3}{4}\rho_s\sqrt{\frac{b_0}{s_s}} - \varepsilon_{cc}}$
Eurocode 2 (2004)	$0 \le \varepsilon_c \le \varepsilon_{ccu}$ $\frac{\sigma_c}{f_c} = \frac{n_1\left(\frac{\varepsilon_c}{\varepsilon_{cc}}\right) - \left(\frac{\varepsilon_c}{\varepsilon_{cc}}\right)^2}{1 + (n_1 - 2)\left(\frac{\varepsilon_c}{\varepsilon_{cc}}\right)}$	$n_1 = 1.05\frac{E_c\varepsilon_{cc}}{f_{cc}}$; $\varepsilon_{cc} = \varepsilon_{co}\left(\frac{f_{cc}}{f_c}\right)^2$; $f_{cc} = \begin{cases} f_c(1 + 5 f_{le}/f_c) & \text{for } f_{le} \le 0.05 f_c \\ f_c(1.125 + 2.5 f_{le}/f_c) & \text{for } f_{le} > 0.05 f_c \end{cases}$; $\varepsilon_{ccu} = \varepsilon_{cu} + 0.2 f_{le}/f_c$
Vallenas et al. (1977) model	$0 \le \varepsilon_c \le \varepsilon_{cc}$ $\frac{\sigma_c}{f_c} = \frac{n\left(\frac{\varepsilon_c}{\varepsilon_{cc}}\right) - K\left(\frac{\varepsilon_c}{\varepsilon_{cc}}\right)^2}{1 + \left(\frac{n}{K} - 2\right)\left(\frac{\varepsilon_c}{\varepsilon_{cc}}\right)}$ $\varepsilon_c > \varepsilon_{cc}$ $\frac{\sigma_c}{f_{cc}} = 1 - Z\varepsilon_{cc}\left(\frac{\varepsilon_c}{\varepsilon_{cc}} - 1\right)$ $f_{ccr} = 0.3 f_{cc}$	$n = \frac{E_c\varepsilon_{c0}}{f_c}$; $E_c \approx 3820\sqrt{f_c}$ MPa; $f_{cc} = Kf_c$ $Z = \frac{0.5}{\frac{3 + 0.29 f_c}{145 f_c - 1000} + \frac{3}{4}\frac{\rho_s}{\sqrt{\varsigma}} - \varepsilon_c}$; $\varsigma = \frac{s_s}{\min(b, h)}$; $\varepsilon_{cc} = \varepsilon_{co} + 0.005(1 - 0.734\varsigma)\rho_s\frac{f_{sy}}{\sqrt{f_c}}$; $\varepsilon_{co} = 0.0024$; $K = 1 + 0.1091(1 - 0.245\varsigma)\left(\rho_s + \frac{D_s}{D_g}\rho_g\right)\frac{f_{sy}}{\sqrt{f_c}}$
Mander et al. (1988) model	$\frac{\sigma_c}{f_{cc}} = \frac{c\zeta_c}{c - 1 + \zeta_c^c}$	$c = \frac{E_c}{E_c - \left(\frac{f_{cc}}{\varepsilon_{cc}}\right)}$; $\zeta_c = \frac{\varepsilon_c}{\varepsilon_{cc}}$; $f_{cc} = Kf_c$; $\varepsilon_{co} = 0.002$; $E_c \approx 4700\sqrt{f_c}$ MPa ; $\varepsilon_{cc} = 0.002\left[1 + 5\left(\frac{f_{cc}}{f_c} - 1\right)\right]$; $\varepsilon_{ccu} = 0.004 + 1.4\rho_s(f_{sy}/f_{cc})\varepsilon_{sm}$; $\varepsilon_{cu} = 0.004$

where

f_{cc} is confined concrete compressive strength; f_{ccr} is the residual compressive strength for the confined concrete; ε_{cc} strain at peak confined compressive strength; ε_{ccu} ultimate compressive strain for the confined concrete; f_c and ε_c are the unconfined compressive strength and its corresponding strain; f_{sy} yield strength for the shear links; s_s spacing for the shear links; b and h are breadth and height of the

RC section; f_{le} is the confining pressure due to the reinforcement; ρ_s amount of shear reinforcement per unit volume; ρ_g is amount of longitudinal reinforcement per unit area; D_s and D_g are the diameter for the shear link and the longitudinal reinforcement respectively

(b) Tensile behaviour and modelling of concrete with flexural reinforcement

As a quasi-brittle material, unreinforced concrete cracks when subjected to tensile forces at a lower capacity as compared to its compressive capacity (about a tenth). In flexure, unreinforced concrete exhibit localized crack formation and propagation. However, the presence of flexural reinforcement generates tensile stiffening, increasing the ductility of the concrete (Gilbert & Warner, 1978; Lin & Scordelis, 1975; Beebay, et al., 2005). Tension stiffening occurs due to the bond between the concrete and the reinforcing bars. Various approaches have been devised to integrate the effect of tension stiffness when modelling RC elements, such as the use of an equivalent moment of inertia of the cracked section of a beam (Branson, 1968) and the modification of the constitutive models of concrete in tension (Beebay, et al., 2005; Schnobrich, 1985; Lam, et al., 2010). In this study, some of the tension-stiffening models that integrate the tension stiffening by modifying the tensile stress–strain behaviour are considered and are shown in Figure 2.7.

Beebay et al. (2005) model prescribes a lower tensile strength followed by a more ductile post peak bilinear behaviour with a prescribed ultimate strain (see Figure 2.7a). Schnobrich (1985) developed a bilinear model, comprising elastic behaviour up to peak followed by linear softening to an ultimate strain that depends on the strain at peak (see Figure 2.7b). Gilbert & Warner (1978) proposed a model that allows for adjustment of key stress-strain point (see Figure 2.7c). Lin & Scordelis (1975) proposed a model comprising of linear behaviour up to peak followed by an exponential softening up to ultimate strain (see Figure 2.7d). Ng et al. (2010) used a similar model to that proposed by Beebay et al. (2005) and found that the key stress-strain points may vary depending on the type of loading (distributed and point load); the amount of reinforcement does not significantly affect the ultimate strain (for 0.5% to 2% of reinforcement tested).

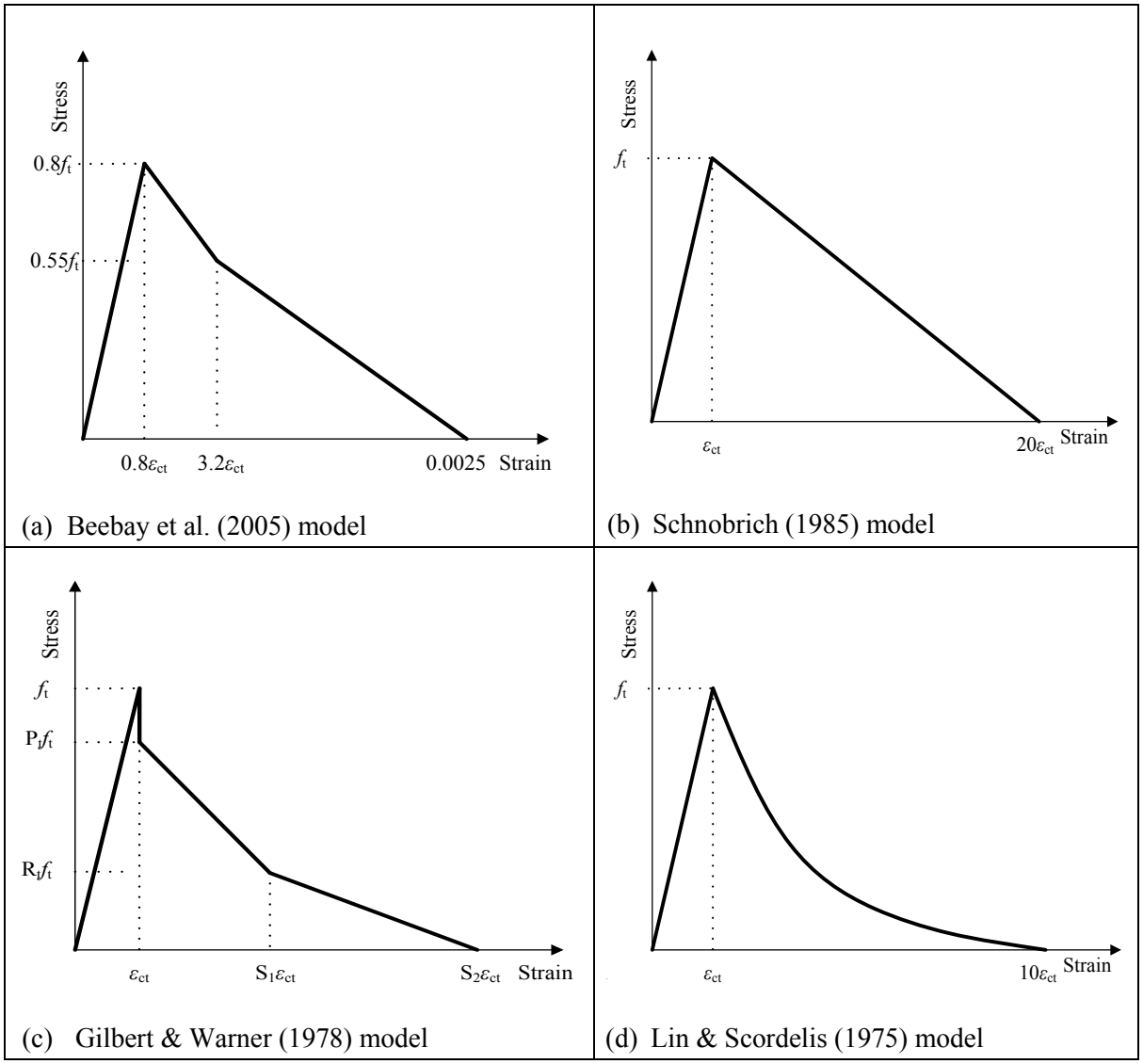

Figure 2.7: Various tension stiffening models for concrete

2.2.2 Structural system behaviour

An extensive research on the behaviour of RC infill frames over the past five decades has established five major modes of failure associated with masonry infill RC frame as summarized by El-Dakhakhni et al. (2003) and Asteris et al. (2011). These modes of failure, as illustrated in Figure 2.8, are:

(a) Corner crushing (CC) mode: infill masonry wall fails due to compression as at least one of its loaded corners crushes (see Figure 2.8(a)). This mode of failure is associated with weak infill masonry blocks surrounded by a frame with weak joints and strong members.

(b) Diagonal compression (DC) mode: infill masonry wall fails by crushing of its central region of the wall (see Figure 2.8(a)). It is associated with relatively slender infill wall, where failure results from out-of-plane buckling instability of the infill wall.

(c) Sliding shear (SS) mode: infill masonry wall fails due to horizontal sliding shear through bed joints (see Figure 2.8(b)). This mode of failure is associated with infill of weak mortar joints and a strong frame. This occurs for low normal compressive stresses and masonry with weak joints. Debonding at interface is followed by sliding. Failure occurs along a single weak bed or in stepped manner following head joints.

(d) Frame failure (FF) mode: failure occurs in the frame as plastic hinges form in the column or beam or the beam-column connection (see Figure 2.8(b)). This mode of failure is associated with a weak frame or a frame with weak joints and strong members infilled with strong masonry wall.

(e) Diagonal cracking (DK) mode: infill masonry wall develops a diagonal crack across its loaded corners (see Figure 2.8(b)). This failure mode is associated with a weak frame or a frame with weak joints and strong members infilled with a strong infill masonry wall. This is diagonal tension failure due to combination of compressive and shear stresses in the masonry. This occurs for medium to high values of normal stress. The shear strength of the mortar joints increases with increase in the normal compressive stress and bricks crack as a result of tensile stresses induced by the shear-compressive stress state. Cracks follow head joints and pass through bricks with an inclination which depends on the inclination of principal stresses in the brick.

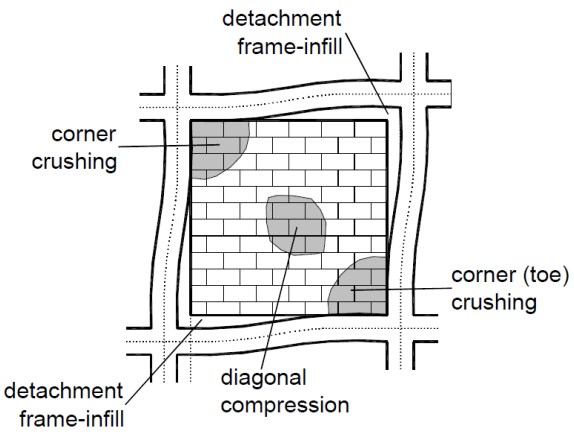

(a) Corner crushing (CC) and Diagonal compression (DC) modes

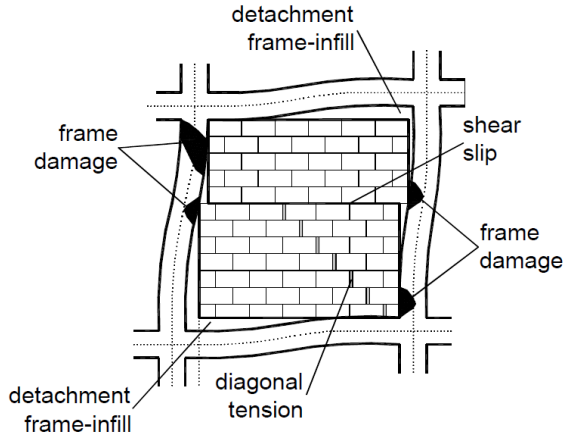

(b) Sliding shear (SS), Frame failure (FF) and Diagonal cracking (DK) modes

Figure 2.8: Typical modes of failure for infill masonry frames (taken from Asteris, et al., 2011)

Modelling of the infill RC frame to evaluate its behaviour requires establishing the characteristic material behaviour of all the constituent materials of the structural system. The material behaviour of concrete and reinforcement has been widely explored while more research is being conducted on the behaviour of masonry. The complexity of masonry behaviour is attributed to its anisotropic nature. Thus, the material behaviour characterisation for masonry is discussed in subsequent subsections to explore existing characterisation methods and analytical models that have been developed.

2.3 INFILL RC FRAME EVALUATION MODELLING

Having considered the general behaviour of the infill frame that is subjected to lateral loading (seismic load) in the previous section, existing modelling approaches for the infill frame behaviour is reviewed. This section discusses only the macro-modelling of the infill frame as it is subjected to an incremental lateral load. Both the micro-models and meso-models were reviewed but could not be considered for structural and sustainability performance integration due to computational complexities as compared to the macro-models. During the initial stages of lateral deformation, an infill frame subjected to an in-plane lateral load behaves like a solid cantilever with an initial bond at frame-wall interface (Polyakov, 1963). A non-integral infill wall (not connected to the frame with shear connectors) debonds from the

frame at diagonally opposite corners subjected to tension as the applied lateral load is increased (with increased deformation). The lateral load is transferred from the frame along the contact region with the wall. The wall behaves like an axial element under compression. Based on this behaviour, macro-models were developed that represent the infill using equivalent struts. Through this approach, various truss configurations and material behaviour calibrations for the struts have been proposed as discussed in the subsequent subsections.

2.3.1 Geometric configuration and models for macro-modelling

Based on this physical behaviour of the infill, Holmes (1961) proposed replacing the wall panel with an equivalent strut along the diagonal under compression. While the single strut models could predict the deformation characteristics of the frames, they failed to predict the stress and moment distributions within the frame elements. Multi-struts models such as (a) two-strut model, (b) three-strut model, multi-strut model and (d) multi-strut models with shear springs were developed by various researchers (Liauw & Kwan, 1985; Saneinejad & Hobbs, 1995; Adukadukam & Sengupta, 2013). Figure 2.9 provides some of the common macro-models that have been developed. Key parameters in the macro-models are geometric properties such as the effective contact area that transmits the lateral load from the frame to the infill wall, effective area of the infill wall that can be considered as resisting the lateral load and strut layout and material properties that include strength properties of the equivalent strut(s).

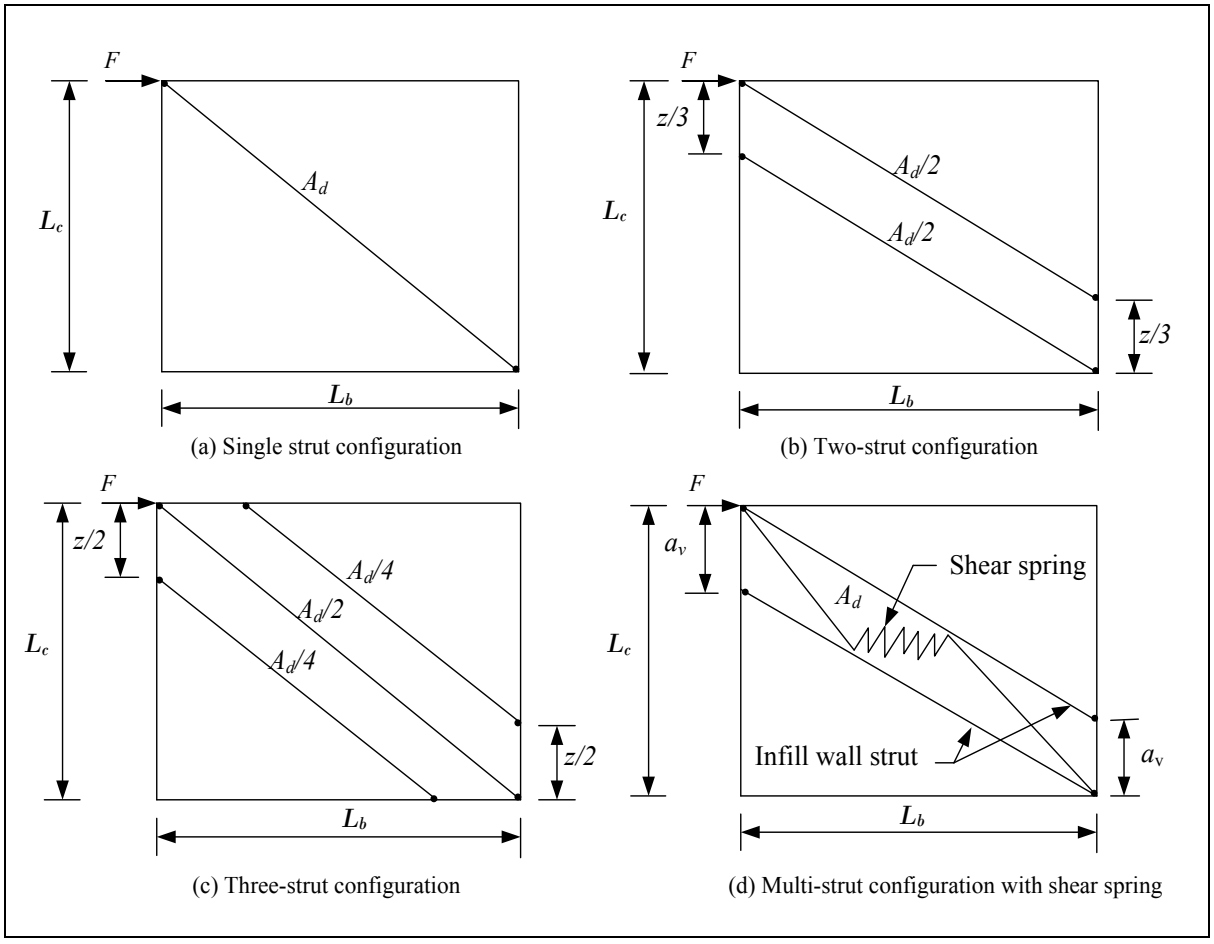

Figure 2.9: Infill macro-model geometric configurations (Crisafulli, 1997)

Macro-models for infill masonry define the geometric properties of the equivalent strut. These geometric properties depend on a few factors such as the type of analysis to be used (when linear elastic

analysis is used, only strut area, diagonal strut length/contact length and the Young's modulus are required while for nonlinear analysis may require, in addition to the above parameters, the full axial force-deformation characteristics), the type of loading: the loading can be monotonic, cyclic or dynamic. For cyclic or dynamic loading, hysteretic behaviour must be established.

The cross-sectional area of the equivalent strut, as a product of width and thickness, is mainly influenced by the choice of the model that defines the width of the strut. Usually, the equivalent strut is assumed to have the same thickness as that of the wall. The width of the equivalent strut can be established using either empirical methods which are based on experimental studies or using analytical procedures that use finite element analysis or elastic or plastic theories. The location of struts (in the case of multi-strut models), can also be determined based on contact lengths shown in Figure 2.10 Table 2.6 provides a summary of the formulae used to determine the strut width and the length of infill/frame contact zones.

Table 2.6: A summary of strut width formulation and length of infill/frame contact zone

Method or Author	**Strut width,** w_d	**Contact length factor,** z	**Parameter definition and comments**
FEMA 356 (2000) model	$w_d = 0.175(\lambda_1 L_c)^{-0.4} L_d$	$z = \frac{\pi}{2\lambda_1}$	$\lambda_1 = \left(\frac{E_w t_w Sin(2\theta)}{4E_f I_c h_w}\right)^{0.25}$
Holmes (1961) model	$w_d = \frac{L_d}{3}$	Not applicable	Constant width
Paulay & Priestley (1992) model	$w_d = \frac{L_d}{4}$	Not applicable	Recommended at 50% lateral loading of ultimate lateral capacity of the wall
Mainstone (1971) model	$w_d = 0.16(\lambda)^{-0.3} L_d$	$z = \frac{\pi L_c}{2\lambda}$	$\lambda = L_c\left(\frac{E_w t_w Sin(2\theta)}{4E_{ce} I_c h_w}\right)^{0.25}$
Liauw & Kwan (1985) model	$w_d = \frac{0.95 h_w Cos(\theta)}{\sqrt{\lambda}}$	$z = \frac{\pi L_c}{2\lambda}$	$\lambda = L_c\left(\frac{E_w t_w Sin(2\theta)}{4E_{ce} I_c h_w}\right)^{0.25}$
Decanini & Fantin model (in Crisafulli, 1997)	$w_d = \left(\frac{0.748}{\lambda} + 0.085\right) L_d$	$z = \frac{\pi L_c}{2\lambda}$	Uncracked section, $\lambda \le 7.85$; $\lambda = L_c\left(\frac{E_w t_w Sin(2\theta)}{4E_{ce} I_c h_w}\right)^{0.25}$ Use uncracked E_w
	$w_d = \left(\frac{0.393}{\lambda} + 0.13\right) L_d$	$z = \frac{\pi L_c}{2\lambda}$	Uncracked section, $\lambda > 7.85$ Use uncracked E_w
	$w_d = \left(\frac{0.707}{\lambda} + 0.010\right) L_d$	$z = \frac{\pi L_c}{2\lambda}$	Cracked section, $\lambda \le 7.85$ Use cracked E_w
	$w_d = \left(\frac{0.470}{\lambda} + 0.040\right) L_d$	$z = \frac{\pi L_c}{2\lambda}$	Cracked section, $\lambda > 7.85$ Use cracked E_w
Bazan & Meli model (in Crisafulli, 1997)	$w_d = (0.35 + 0.22\lambda_2) h_w$	-	$\lambda_2 = \frac{E_{ce} A_c}{G_w A_m}$, $A_m = l_w t_w$
Saneinejad & Hobbs (1995)	$w_d = \frac{(1-\lambda_c)\lambda_c L_c \frac{\sigma_{ci}}{f_{cw}} + \lambda_b L_b \frac{\tau_{bi}}{f_{cw}}}{Cos(\theta)}$	$a_u = \lambda_b L_c$ $a_v = \lambda_c L_b$	$\lambda_b = \sqrt{\frac{2(M_{mi} + \chi_b M_{mb})}{\sigma_{bi} t_w L_b^2}} \le 0.4$; $\lambda_c = \sqrt{\frac{2(M_{mi} + \chi_c M_{mc})}{\sigma_{ci} t_w L_c^2}} \le 0.4$

where

w_d and L_d are equivalent diagonal strut width and length respectively;

L_c, L_b, h_w, l_w and t_w are column height, beam length, infill masonry height, length and thickness respectively;

E_{ce}, E_w, G_w are Young's moduli for the column and masonry, and the shear modulus for the masonry respectively;

a_u, a_v are the normalised horizontal and vertical infill-to-frame contact lengths respectively

I_c is second moment of area for the column;

f_{cw}, σ_{ci}, σ_{bi}, τ_{bi} are compressive strength of the infill, column-infill and bam-infill uniform normal stress at peak and beam-infill uniform shear stress respectively;

M_{mb}, M_{mc}, M_{mi} are the beam, the column and the joint resisting moments respectively;

χ_b, χ_c are reduction factors for the frame intermediate bending moments; and

θ is the angle of inclination of the diagonal strut to the horizontal axis.

2.3.2 Material modelling

Various material models for the equivalent strut behaviour exist. Some material models are developed based on compressive strength of masonry infill and they ignore the influence of horizontal sliding and diagonal cracking, some of the key failure modes as discussed in Section 2.2.2. Furthermore, significant strength degradation which the infill may undergo through is rarely incorporated during pre-peak stage and may only be incorporated towards failure in post peak stage. The material models for strut behaviour use maximum strength and modulus of elasticity for complete definition of material behaviour. They implicitly assume brittle models (with elastic-brittle behaviour as shown in Figure 2.10a). However, there have been efforts to improve the behaviour characteristic of the equivalent strut by incorporating pre-peak strength points that could define different stress states for the masonry. Adukadukam & Sengupta (2013) proposed three stress states before peak strength, representing limits of respective performance levels namely, immediate occupancy (IO) level, life safety level (LS) and collapse prevention level (CP) as shown in Figure 2.10b. The model assumes brittle failure beyond collapse prevention limit.

Some researchers have proposed nonlinear material models that consider gradual decline of masonry stiffness before failure. Radić et al. (2016) proposed the use of post peak stiffness to model the gradual strength degradation of the infill before reaching its residual strength (see Figure 2.10d). Key parameters for this model are infill yielding point (F_y, δ_y), peak strength point (F_m, δ_m) and post-peak residual strength (F_{res}, δ_{res}). Rodrigues et al. (2010) proposed an infill panel model that is defined by four support struts with rigid behaviour and a central strut element where nonlinear hysteretic behaviour is concentrated (see Figure 2.9d). The nonlinear behaviour of the central strut is characterised by a multi-linear force–deformation behaviour defined by nine parameters, namely cracking force and displacement (F_{cr}, δ_{cr}), yielding force and displacement (F_y, δ_y), maximum strength and corresponding displacement (F_m, δ_m), residual strength and its corresponding displacement (F_{res}, δ_{res}) and the fifth branch is defined by the stiffness, K_r.

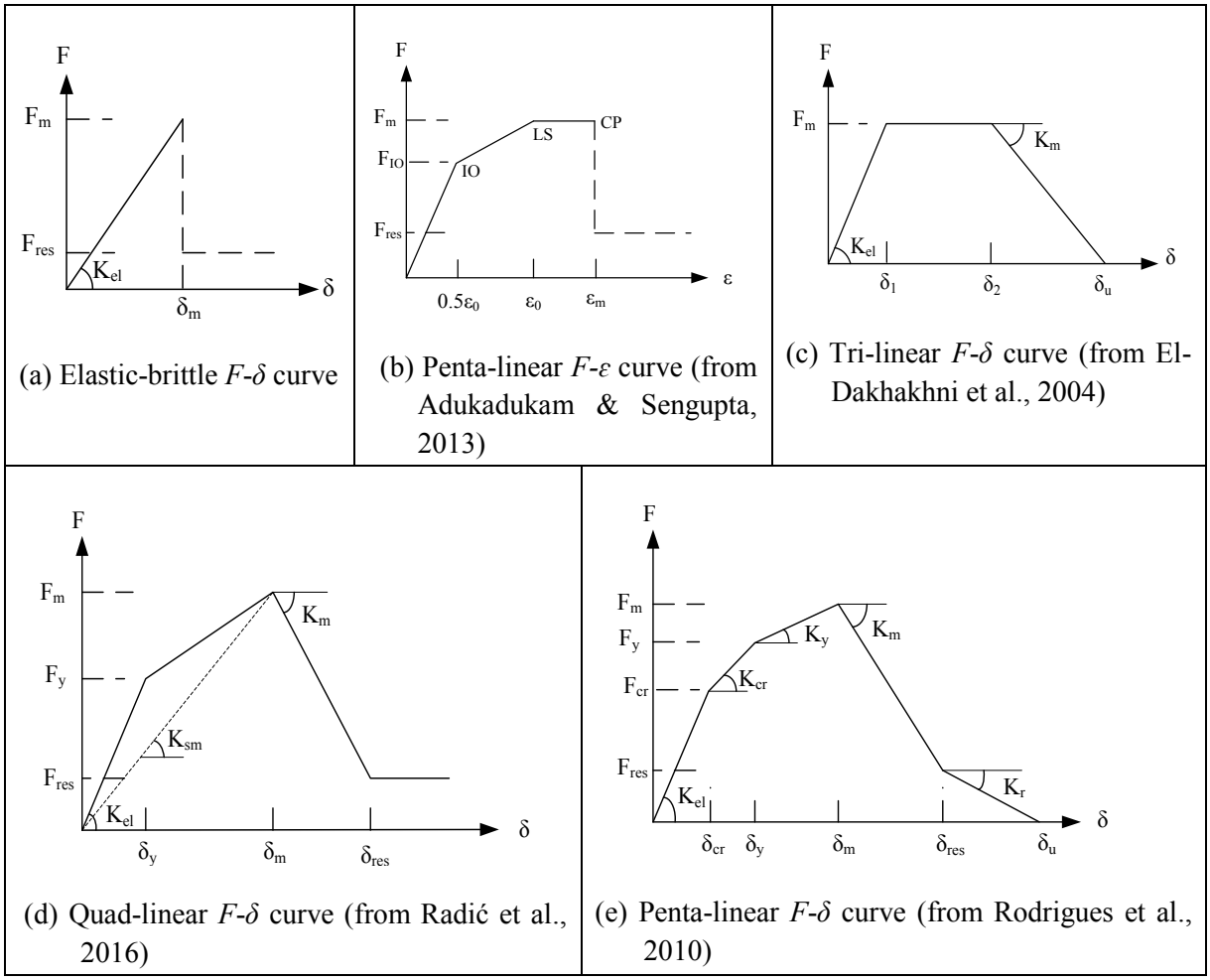

(a) Elastic-brittle *F-δ* curve

(b) Penta-linear *F-ε* curve (from Adukadukam & Sengupta, 2013)

(c) Tri-linear *F-δ* curve (from El-Dakhakhni et al., 2004)

(d) Quad-linear *F-δ* curve (from Radić et al., 2016)

(e) Penta-linear *F-δ* curve (from Rodrigues et al., 2010)

Figure 2.10: Various material models for the equivalent strut

Strength characterisation of the equivalent struts based on the ultimate carrying capacity of the infill wall proposed by Saneinejad & Hobbs (1995) incorporates the aspect ratio of the infilled panel, interface stresses due to the frame-wall interaction and the flexural capacities of the bounding frame. With this approach, specific failure modes of the infill wall such as corner crushing (CC), shear cracking or sliding shear (SS) and diagonal compression (DC) failure load can be predicted using expressions given in equation 2.11 (Saneinejad & Hobbs, 1995). Saneinejad & Hobbs (1995) observed that diagonal tensile cracking could be ignored in the failure analysis as higher load could be applied beyond tensile cracking. A minimum diagonal force established by equation 2.11 determines the type of failure and the capacity of the infill. The formulation procedure could be assumed to have been developed based on a force-controlled approach where failure is assumed upon reaching maximum strength. Infill ductility is ignored.

$$F_d = \begin{cases} \dfrac{(1-\alpha_c)\alpha_c t_w h_f \sigma_c + \alpha_b t_w l_f \tau_{wb}}{\cos\theta} & \text{for local crushing at the loaded corners, } F_{d,cc} \\ \dfrac{\tau_{mn} t_w l_w}{(1-0.45\tan\theta_{ed})\cos\theta} & \text{for shear cracking along the bed joint, } F_{d,ss} \\ \dfrac{0.5 h_w t_w l_w f_{ad}}{\cos\theta} & \text{for diagonal compression, } F_{d,dc} \end{cases} \quad (2.11)$$

where

σ_c is normal contact stress for the infill/column;

τ_{wb} is the beam/infill shear contact/bond strength;

$\theta_{ed} = \tan^{-1}\left[(1-\alpha_c)\frac{h_w}{l_w}\right]$;

τ_{mm} is infill shear strength;

$f_{ad} = f_c^{'}\left[1-\left(\frac{l_{ef}}{40t_w}\right)^2\right]$, where $f_c^{'}$ is factored compressive strength of infill defined by ACI 318-1 (1999)as $f_c^{'} = 0.6\phi f_{cw}$ and $\phi = 0.65$, f_{cw} is prism strength of masonry, $l_{ef} = l_w/\cos\theta_{ed}$. Note that the derivation for f_{ad} is positive only for $l_{ef} > 40t_w$.

Saneinejad & Hobbs (1995) assumed that the corner crushing occurs due to a combination of normal stress and contact stresses between the frame and the infill. However, other researchers developed analytical models for corner crushing that assumes failure is because of biaxial compressive stresses at loaded corners. Thus, biaxial strength approximation can be used to determine the compressive capacity of the corner crushing zone and subsequent capacity for the infill. Lourenco et al. (2006) proposed adopting a simplified analytical relationship that is used for concrete as provided in the CEB-FIP (1993) which relates the maximum biaxial compressive strength ($f_{c,bi}$), at an angle Θ, to uniaxial compressive strength (f_{cw}) as:

$$f_{c,bi} = \frac{1+3.65\tan\theta}{(1+\tan\theta)^2} f_{cw} \qquad (2.12)$$

The weakness of adopting concrete models is that masonry is at best orthotropic and at worst anisotropic material and hence the models are not a fair representation of masonry behaviour. Based on biaxial stress distributions on each edge of the infill, an average biaxial stress can be used to determine the crushing failure horizontal force using equation 2.13.

$$F_{h,cc} = Min\begin{cases} f_{c,biav}a_v t_w & \text{stress acting on the infill/column contact zone} \\ \dfrac{f_{c,biav}a_u t_w}{\tan\theta} & \text{stress acting on the infill/beam contact zone} \end{cases} \qquad (2.13)$$

Rewriting equation 2.13 in the form of diagonal force gives;

$$F_{d,cc} = Min\begin{cases} \dfrac{f_{c,biav}a_v t_w}{\cos\theta} & \text{stress acting on the infill/column contact zone} \\ \dfrac{f_{c,biav}a_u t_w}{\cos\theta} & \text{stress acting on the infill/beam contact zone} \end{cases} \qquad (2.14)$$

where θ is the angle of inclination for the diagonal strut and $f_{c,biav}$ is the average biaxial strength applied uniformly across the infill/frame contact zones. For an assumed triangular distribution, $f_{c,biav} = 0.5f_{c,bi}$. A factor other than 0.5 can be used to establish an average biaxial stress for masonry when biaxial stress distribution is not triangular.

Crisafulli (1997) proposed analytical models for determining the equivalent strut strength when the infill fails in shear and diagonal tension. Determination of the sliding shear failure and diagonal tension

failure is done by stress/vector transformation and assuming the principal compressive stress corresponds to the diagonal strut resistance. Equations 2.15 and 2.16 provide the formula used for the strut strength derived from shear resistance and diagonal tensile resistance respectively. Diagonal strength in terms of stress is determined independent of geometric properties of the equivalent strut. The axial strength, in terms of load, is then determined using strut equivalent cross-sectional area, A_d, as indicated in equation 2.17.

$$f_{d,ss} = \frac{\tau_0^*}{\sin\theta\left(\cos\theta - \mu^* \sin\theta\right)} \tag{2.15}$$

$$f_{d,dk} = \frac{f_{tb}}{\sin\theta\left(C_s \cos\theta - 0.27\sin\theta\right)} \tag{2.16}$$

where

τ_0^* is the reduced cohesion of masonry, defined by $\tau_0^* = \tau_0\left(1+\mu C_n h_b / l_b\right)^{-1}$

μ^* is reduced Poisson ratio of masonry, defined by $\mu^* = \mu\left(1+\mu C_n h_b / l_b\right)^{-1}$

τ_0, μ, C_n, h_b and l_b are masonry cohesion, masonry Poisson ratio, normal stress distribution factor, shear stress distribution factor, brick height and brick length respectively;

f_{tb} is uniaxial tensile strength of a brick; and

θ is the angle of inclination of the diagonal strut with respect to the horizontal axis.

The axial strut load determined from sliding shear failure and diagonal tension failure is defined respectively as:

$$F_{d,ss} = f_{d,ss} A_d \text{ and } F_{d,dk} = f_{d,dk} A_d \tag{2.17}$$

where

$A_d = w_d t_w$, is equivalent strut cross-sectional area with w_d and t_w are its width and thickness respectively.

Infill strength formulae proposed by Saneinejad & Hobbs (1995) incorporate the geometric properties of the infill and infill/frame mechanisms while the formulae proposed by Lourenco et al. (2006) and Crisafulli (1997) are based on the material behaviour and diagonal angle and are formulated independent of the possible diagonal strut geometric properties (usually width, w_d or cross-sectional area, A_d). Thus, it is difficult to compare the performance of these formulas through evaluation of the formulae with linkage to the geometry of the infill.

El-Dakhakhni (2003) proposed the use axis transformation matrix to establish the Young's modulus along the diagonal direction of the infill. Since the masonry infill behaves orthotropically at best and anisotropically at worst, axis transformation matrix that incorporates orthotropic behaviour of masonry offers a better approximation for the diagonal strut behaviour. The key material parameters for generating the diagonal strut Young's modulus (E_θ) for orthotropic plates are vertical Young's modulus (E_{90}), horizontal Young's modulus (E_0), shear modulus (G) and Poisson's ratio (v_{0-90}) (see equation 2.18). A simplified way of establishing the peak strength for the diagonal strut ($f_{m\theta}$) is by applying the same factor used in generating the diagonal Young's modulus (E_θ / E_{90}) from the vertical compressive strength (see equation 2.19). However, this approximation neglects the shear effects and biaxial stress effects at the corners.

$$E_\theta = \frac{1}{\frac{\cos^4\theta}{E_0} + \left(-\frac{2\upsilon_{0-90}}{E_0} + \frac{1}{G}\right)\cos^2\theta\sin^2\theta + \frac{\sin^4\theta}{E_{90}}} \tag{2.18}$$

$$f_{m\theta} = \frac{E_\theta}{E_{90}} f_{cw} \tag{2.19}$$

Modelling infill frames using the macro-models, in most cases, involves performing a preliminary evaluation to assess the mode of failure of the infill, from which an appropriate material model for the equivalent strut behaviour is established. A pre-analysis evaluation to establish possible failure mode is conducted on 10 infill frame samples taken from literature (see Sections 3.5.2.1 and 3.5.2.2 for full details). Table 2.7 shows the results of the pre-analysis evaluation, where strut area is determined by the FEMA method. There is variation in the equivalent strut capacity as determined by each of the four approaches discussed, with Crisafulli (1997) generating low capacities for the infill while the rest generating high values. Based on the preliminary analysis, most of the samples would fail in shear and or diagonal cracking. Though equation 2.19 considers the orthotropic properties of the infill, the equivalent strut capacity predicted by the analytical relationship are all high. Due to the ease in generating parameters for equation 2.19 coupled with the orthotropic consideration in the formulation, this study adopts and modifies the equation in material characterisation of the infill provided in Chapter 4. A comprehensive evaluation of implementation of all the other analytical material models is also provided in the Chapter 4.

Table 2.7: Pre-analysis results for the selected infill frame experimental sample

Sample notation	**CC mode (equation in bracket) – MPa**		**SS mode (equation in bracket) – MPa**		**DC or DK mode (equation in bracket) – MPa**		$f_{m\theta}$ **MPa** (2.19)
	CC (2.11)	CC (2.14)	SS (2.11)	SS (2.11)	DC (2.11)	DK (2.16)	
G3	14.9	11.1	5.6	1.07	21.4	2.00	15.5
G4(1)	13.3	15.9	4.1	1.42	26.1	1.60	12.4
G4(2)	9.9	12.0	3.8	1.42	17.7	1.64	8.7
G4(3)	8.8	10.6	3.9	1.42	15.9	1.64	7.8
G4(4)	9.4	11.0	4.1	1.42	18.5	1.60	8.7
G4(5)	12.1	14.3	4.1	1.42	24.2	1.60	11.3
G4(6)	7.9	12.7	3.7	1.38	5.8	1.88	8.2
G4(7)	9.5	14.8	4.0	1.38	7.7	1.83	10.5
G4(8)	7.8	11.8	4.2	1.38	6.6	1.83	8.9
G4(9)	10.1	12.9	3.5	1.42	15.9	1.64	8.3

2.4 PROBABILISTIC ASSESSMENT OF STRUCTURAL PERFORMANCE OF THE INFILL FRAME STRUCTURES

The main objective of the study is to integrate structural performance of the infill frame structures with the sustainability performance. As it is noted in Section 2.5, a possible way of integrating structural performance with the sustainability is the establishment of the structure's service life, a structural performance property. A reliable way of establishing the structure life is the use of reliability-based design, where structural performance functions are expressed as a function of time, allowing integration of the deterioration of the structure. When reliability-based assessment is required, the issue of model uncertainty becomes an important issue of concern for most of the macro-models. The variations in material modelling make it difficult to link the existing infill material models discussed in Section 2.3.2

and identify a robust mean of addressing the uncertainties across the material characterisation processes. For example, the infill strength formulae proposed by Saneinejad & Hobbs (1995) incorporate the geometric properties of the infill and infill/frame mechanisms while the formulae proposed by Lourenco et al. (2006) and Crisafulli (1997) are based on the material behaviour and diagonal angle and are formulated independent of the possible diagonal strut geometric properties (usually width, w_d or cross-sectional area, A_d).

There are two main approaches for the evaluation of structures under seismic loading, namely (a) deterministic approaches and (b) probabilistic approaches. The SAC-FEMA method (Cornell, et al., 2002) is a typical example of a closed-form probabilistic based evaluation of structures while the N2 method is a deterministic method (Fajfar, 2000). The probabilistic–based assessment methods requires establishment of seismic demand and capacity at different levels of seismic intensity. The SAC-FEMA method estimates the seismic demand and capacity for different levels of seismic intensity using incremental dynamic analysis (IDA) method developed by Vamvatsikos & Cornell (2002). The IDA requires many inelastic time-history analyses to generate the IDA curves. As Dolšek& Fajfar (2008) have shown, it is possible to generate a summarised IDA curves with less input and data using an incremental N2 method. The N2 method is a practice-oriented nonlinear method based on the pushover analysis and the inelastic response spectrum (Dolšek & Fajfar, 2008; Dolšek & Fajfar, 2004; Dolšek & Fajfar, 2007). A simplified probabilistic assessment that combines the SAC-FEMA method, with the N2 method (N2 replacing the IDA) proposed by Dolšek& Fajfar (2004; 2007) is adopted due to its simplicity in the amount of data required and its capability to generate the probability based results. A detailed discussion of this simplified approach is given in the subsequent subsections, starting with the N2 method, the general probabilistic assessment approach and the simplified probabilistic approach.

2.4.1 N2 method for the seismic assessment

The N2 method for the assessment of structures compares the seismic demand of a given seismic intensity with the capacity corresponding to a given performance level (limit state). When probabilistic assessment approaches are used, the relationship between the seismic demand and corresponding seismic intensity is established for different values of the seismic intensity. The incremental N2 method can be used to establish this relationship in the form of the incremental N2 (IN2) curve (Dolšek & Fajfar, 2004; Dolšek & Fajfar, 2005). The seismic intensity measure can be represented by the spectral acceleration or the velocity of a SDOF model while the seismic demand can be represented by the roof displacement, the maximum storey drift, rotation at a column or beam end or the shear force. The use of spectral acceleration at the natural period of the SDOF model and the roof displacement for the seismic intensity measure and the engineering demand respectively are the most convenient parameters as it allows the visualisation of the procedure in the acceleration-displacement (A-D) format (Dolšek & Fajfar, 2007). The shape of the IN2 curve depends on the inelastic spectra applied in the N2 method, which are based on the three interrelated parameters, namely, the strength reduction factor (R), the ductility (μ) and the period (T), using appropriate $R-\mu-T$ relation. For a typical 2D analysis of a structure, the procedure for establishing an IN2 curve is summarised as:

(a) Select the ground motion intensity measure and the demand measure (e.g. select the spectral acceleration and the top (roof) displacement respectively);
(b) Identify a series of relevant ground motion intensities (spectral accelerations);
(c) For each of the chosen spectral acceleration, draw A-D curve;
(d) Establish the period, T of the structure using the equation:

$$T = 2\pi\sqrt{\frac{m^{*}\delta_e}{F_e}} \tag{2.24}$$

where $m*$ is equivalent mass, δ_e is yield displacement, and F_e is the yield force

(e) Draw a radial line of the period, T on the A-D curves. The intersection of the period line with the A-D curve gives the elastic seismic demand in terms of elastic spectral acceleration, S_{ae} and corresponding elastic spectral displacement S_{de};

(f) Draw the capacity curve for the equivalent SDOF structural system, using the pushover analysis;

(g) From the capacity curve, identify the yield acceleration, S_{ay} and yield displacement, S_{dy};

(h) Determine the strength reduction factor (R) using values obtained in steps (e) and (g) as follows:

$$R = \frac{S_{ae}}{S_{ay}} \tag{2.25}$$

Note that the value of R does not consider the reduction due to the over-strength as is the case with the behaviour factor, q, in the SANS 10160-4 (2011) and the Eurocode 8 (2004).

(i) Establish the ductility (μ) using the R value obtained in steps (h) and relevant $R-\mu-T$ relation, that depends on the type of the structural system under consideration.

(j) Draw corresponding inelastic spectrum using the strength reduction factor and the ductility obtained in steps (h) and (i) respectively;

(k) Draw a horizontal line through the yield point of the capacity curve. The intersection of the horizontal line with the inelastic spectrum gives the corresponding inelastic displacement demand, S_d;

(l) Draw a vertical line through the inelastic displacement demand. Where the line meets with the elastic spectral acceleration of the A-D curve is the point along the IN2 curve (a point on the IN2 curve is defined by the elastic spectral acceleration and corresponding inelastic displacement demand);

(m) Perform steps (c) to (l) for all the spectral accelerations considered until a complete IN2 curve is draw/established. A schematic construction of the IN2 curve for a SDOF model in acceleration-displacement (A-D) format is presented in Figure 2.11b, where two ground motion intensities are considered (and are represented by point A_1 and A_2 on the IN2 curve).

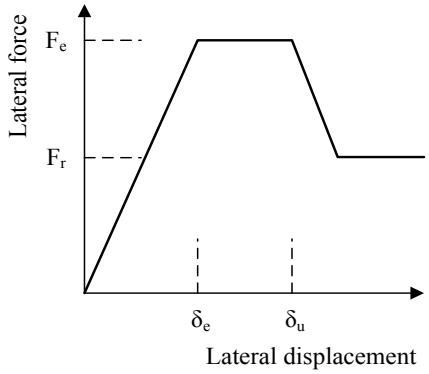

(a) Idealised force-displacement relation for an infill RC frame (Dolšek & Fajfar, 2004)

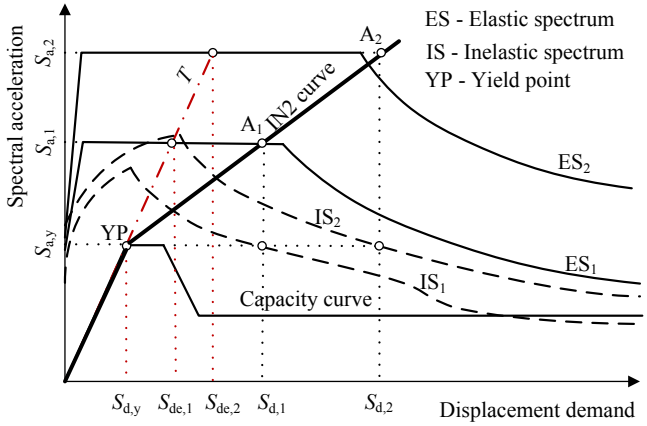

(b) Schematic construction of an IN2 curve (Dolšek & Fajfar, 2004)

Figure 2.11: (a) Idealised force-displacement relation for an infill RC frame, and (b) Schematic construction of an IN2 curve

2.4.2 Probability assessment in closed form

The SAC-FEMA (Cornell, et al., 2002) probabilistic assessment method can be used to assess the performance of a structure under seismic events. The ground motion intensity is characterised by the level of spectral acceleration at approximately the first period of the structure and 5% damping, while the engineering demand parameter is defined by the roof displacement (Dolšek & Fajfar, 2007). Based on the SAC-FEMA approach, the *x* confidence level estimate of the annual probability of exceedance of a given performance level, $P_{PL,x}$ can be determined by the analytical expression as follows (Cornell, et al., 2002):

$$P_{PL,x} = \tilde{H}(s_a^{\tilde{C}})C_H C_f C_x \tag{2.26}$$

where

$\tilde{H}(s_a^{\tilde{C}})$ is the median value of the hazard function at the spectral acceleration $s_a^{\tilde{C}}$;

$s_a^{\tilde{C}}$ is the spectral acceleration corresponding to the median displacement capacity $\tilde{C}$;

C_H is the correction factor due to uncertainty in the ground motion hazard curve, defined as:

$$C_H = \exp\left(\frac{1}{2}\beta_H^2\right) \tag{2.27}$$

C_f is the correction factor due to the randomness in the demand and capacity and is defined as:

$$C_f = \exp\left[\frac{k_\beta^2}{2b_\beta^2}\left(\beta_{DR}^2 + \beta_{CR}^2\right)\right] \tag{2.28}$$

C_x is the correction factor due to the uncertainty in the demand and capacity and is defined as:

$$C_x = \exp\left[K_x\sqrt{\frac{k_\beta^2}{b_\beta^2}\left(\beta_{DU}^2 + \beta_{CU}^2\right)}\right] \tag{2.29}$$

k_β is a parameter of the hazard function (see equation 2.30);

b_β is a parameter of the function relating the displacement to the spectral acceleration;

K_x is the standardized normal variate associated with probability *x* of not being exceeded;

β_H is the dispersion measure for hazard;

β_{DR} and β_{CR} are the dispersion measures for randomness in displacement demand and capacity respectively; and

β_{CU} and β_{DU} are the dispersion measures for uncertainty in top displacement demand and capacity respectively.

$\tilde{H}(s_a^{\tilde{C}})$ provides the median estimate of the annual probability that the spectral acceleration will be equal to or exceed the spectral acceleration, $s_a^{\tilde{C}}$ while the product $\tilde{H}(s_a^{\tilde{C}})C_H$ represents the mean value of the hazard function. The values of β_{DR} and β_{CR} are obtained from an IDA analysis while determination of β_{CU} and β_{DU} requires additional analyses or else, the predetermined default values can be used as in the SAC-FEMA approach (Dolšek & Fajfar, 2007; Yun, et al., 2002). The probability of exceedance of a given limit state as provided in equation 2.20 was derived on the assumption that the hazard curve, $\tilde{H}(s_a)$ and the median IDA curve $\tilde{D}(s_a)$ can be approximated as (Dolšek & Fajfar, 2007):

$$\tilde{H}(s_a) = k_0.(s_a)^{-k_\beta} \tag{2.30}$$

$$\tilde{D}(s_a) = a.(s_a)^{b_\beta} \tag{2.31}$$

where

$\tilde{H}(s_a)$ is the median annual probability that the spectral acceleration s_a will be exceeded; and

$\tilde{D}(s_a)$ is the median displacement as a function of s_a.

The spectral acceleration and displacement distributions are assumed log-normal while the dispersion measures, β_{DR}, β_{CR}, β_{CU} and β_{DU} are quantified as standard deviations (Std dev) of the natural logarithm. Parameters, k_0 and k_β, determining the hazard curve are determined from any two points on the actual hazard curve. Parameters, *a* and b_β, determining the IDA curve are determined from two points on the IDA curve. b_β is typically assumed as 1.0 (FEMA 350, 2000).

2.4.3 Simplified probabilistic performance assessment based on Dolšek &Fajfar (2007)

The simplified approach proposed by Dolšek & Fajfar (2007) uses incremental N2 (IN2) approach instead of the IDA to establish the relationship between the spectral acceleration at the period of the equivalent SDOF system and seismic demand. The IN2 curve is used to represent the relationship between the spectral acceleration and the seismic demand (in terms of the top displacement) as shown in Figure 2.11b. The determination of the IN2 curve is summarized in Section 2.4.1. For common structural systems with moderate or long fundamental period(s), the 'equal displacement rule' applies, resulting in a straight line IN2 curve (b_β=1.0) up to the 'failure' point, which is typically represented by the near collapse (NC) limit state (Dolšek & Fajfar, 2004). The IN2 curve becomes a horizontal line beyond the NC limit state. The IN2 curve approximates a summarised IDA curve, thus it is difficult to measure the dispersion measures of randomness, β_{DR} and β_{CR}. Dolšek and Fajfar estimated the β_{DR} and β_{CR} values from the coefficient of variation for the displacement of the SDOF system, for which $R-\mu-T$ relation was determined. The default values for dispersion of randomness in the displacement

capacity β_{CR} can be obtained by IDA analyses of typical structural systems. Alternatively, the dispersion values can be approximately determined for the specific structure by using a nonlinear dynamic analysis of an equivalent SDOF system (Vamvatsikos & Cornell, 2005; Han & Chopra, 2006). Appropriate dispersion values for β_{CU} and β_{DU} can be prescribed based on the typical structural systems and materials, if specific values are not available. FEMA 350 (2000) proposed typical dispersion values for steel frames.

2.5 SUSTAINABILITY AND STRUCTURAL PERFORMANCE

Effective evaluation and integration of sustainability and building structural performance involves development of overall system modelling approaches that incorporate expertise in materials deterioration science, structural behaviour and damage modelling and industrial ecology. Since sustainability incorporates different fields from which performance indicators are drawn, there is always a challenge of bridging different aspects of the sustainability into an effective and reliable system evaluation procedure, considering that different methods of indicator evaluation and units of measure are employed. Much research has been carried out to develop building sustainability evaluation procedures, using either analysis-oriented approach (WCED, 1987; Liu, et al., 2010; Hischier, et al., 2010) or application-oriented approach (Liu, et al., 2010).

Both analysis-oriented methods and application-oriented methods utilise set sustainability indicators that are derived from the consideration of the overall building life cycle, from the pre-use phase through the use phase to the end-of-life phase (see Figure 2.12). Application of these methods emphasized the need to meet environmental sustainability of buildings (Chaudhary & Piracha, 2013). For example, in the current state of promotion of green building through green rating by major rating agencies such as LEED (USGBC, 2009), BREEAM (BRE Global, 2008), Green Star SA (GBCSA, 2009) and Green Star Australia (GBCA, 2008), six broad categories for sustainability are considered as (i) site selection and urban connectivity, (ii) water conservation, (iii) energy efficiency, (iv) building material efficiency, (v) indoor air quality and occupant comfort, and (vi) innovation and exemplary performance. An evaluation of common rating systems by Chaudhary & Piracha (2013) revealed that the contribution of structural engineering in sustainable construction is minimal compared to other professionals. The minimal credits given to items under structural engineering has been attributed to the generally lower structural cost of most buildings and the little involvement of structural engineers in the development and implementation of building sustainability concepts within the built environment. There are high prospects of structural engineers' contributions in sustainable construction in the future due to current technological advancements towards energy efficient and net zero buildings as the importance of embodied energy in buildings would increase to up to 20-25% of total energy of a building (Chaudhary & Piracha, 2013).

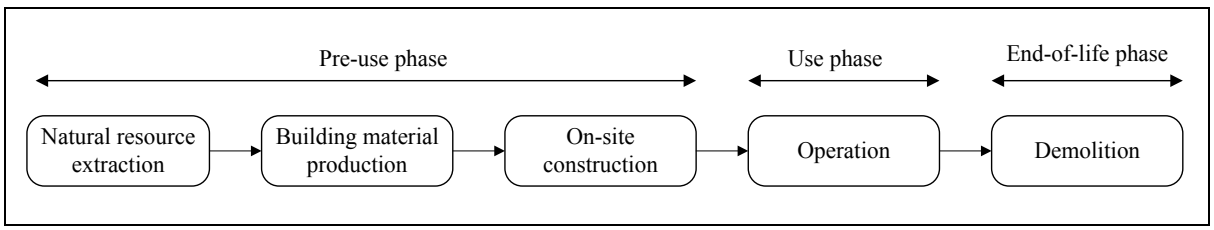

Figure 2.12: Building life cycle (adopted from Wang, et al. (2005))

The application-based methods promote sustainability through adherence to set checklists and use green building ratings. The methods focus on the environmental sustainability of buildings. The application-based methods are widely used by green rating agencies such as the BREEAM (BRE Global, 2008),

LEED (USGBC, 2009), Green Star Australia (GBCA, 2008), and Green Star South Africa (GBCSA, 2009). These rating agencies have come up with six broad categories for sustainability assessment from which a checklist of specific application-based activities is derived, namely:

(a) site selection and urban connectivity;
(b) water conservation;
(c) energy efficiency;
(d) building material efficiency;
(e) indoor air quality and occupant comfort; and
(f) innovation and exemplary performance.

While such methods have helped in promoting environmental friendly buildings through adherence to the specified activities from design, use and end of life, it is difficult to measure whether such methods provide optimum benefits since it is difficult to measure their impact. A checklist of activities for the selected indicators can be used to generate a scorecard from which a spidergram representation is drawn to illustrate the general sustainability adherence. A typical illustration of the spidergram is shown in Figure 2.13, drawn from a qualitative assessment of urban sustainability in Kigali, Rwanda (LIANE, 2015).

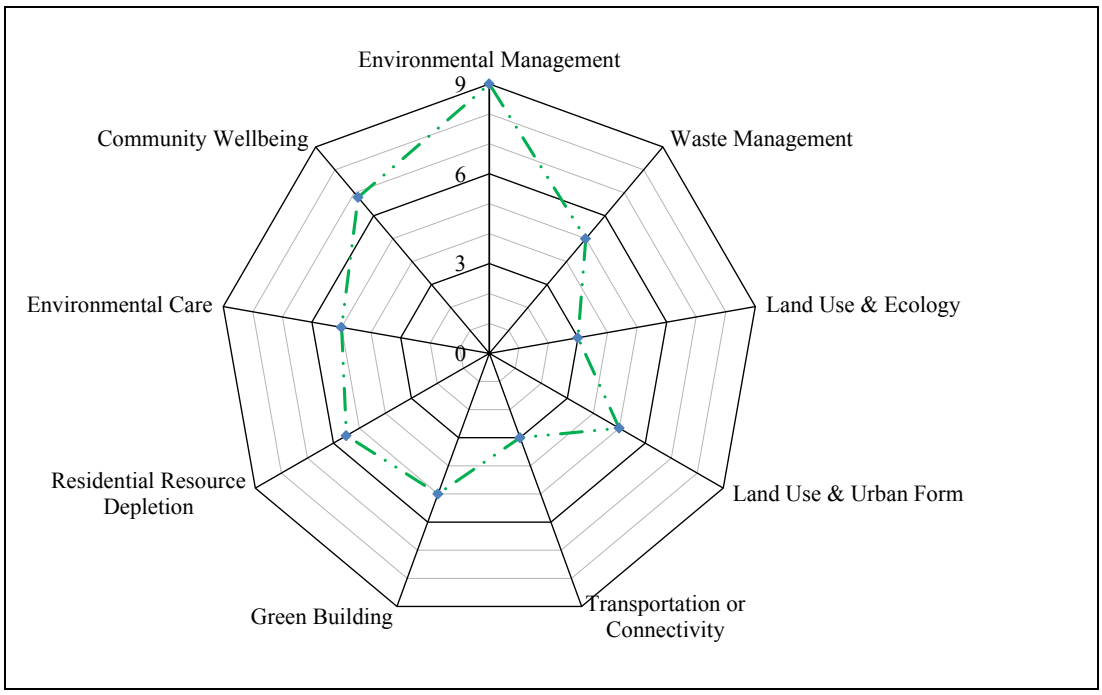

Figure 2.13: Typical spidergram representation of urban sustainability assessment (LIANE, 2015)

Analysis oriented assessment methods offer a scientific hence rational means of assessing the environmental impacts. Results of the analysis-based evaluation are usually considered separately from structural performance indicators. This approach ignores the interactions between the sustainability performance of the building and the structural performance. In recent years, more work is conducted to link the sustainability of infrastructure to the structural performance of the structures. The advantage of analysis-based methods is that they are quantitative and are based on life cycle analyses, thus, offering opportunities for integration with structural performance through the common property of time. It is noteworthy that probability-based structural performance evaluation methods are time-based, through

service life design approaches, and hence ideal for possible integration of structural performance and sustainability indicators.

Significant research effort is devoted to sustainability modelling for structures; with the *fib* developing a model code (*fib*, 2012) providing guidance on service life design, the work of *fib* committee on service life design (*fib*, 2006) and the work of Lepech et al. (2015) that developed a probabilistic design approach for sustainable repair and rehabilitation of civil and building structures. The framework developed by Lepech et al. (2015) provides a state-of-the art approach in ensuring that the targeted improvements in quantitative sustainability indicators are achieved through proper repair strategies. Two types of models are considered and integrated, namely:

(a) Service life prediction models: They estimate the age at which first repair may be required and the time for subsequent repairs, considering the structural conditions after repair. The models are based on existing infrastructure deterioration models such as those reported in the *fib* Model code for service life and the models developed by Lepech et al. (2015).
(b) Life cycle assessment (LCA) models. They estimate the environmental, social, and economic impact of a given repair, rehabilitation, or strengthening based on a process-based LCA of individual repair activities. Models for the environmental impact assessment have widely been developed and used in sustainability assessment, unlike the social and economic impact indicators. The environmental impact assessment models are based on the ISO 14040 (2006) and ISO 14044 (2006) LCA protocols and mostly use midpoint environmental impact indicators.

2.5.1 Structural repair and sustainability integration framework

Lepech et al. (2015) developed a framework that integrates the structural repair and rehabilitation of civil infrastructure with the sustainability requirements. Quantitative sustainability methods using the LCA methods are adopted. The framework is based on the service life design provided in the *fib* standards (*fib*, 2006; *fib*, 2012). Incorporation of the service life design models is essential in determining the end of life of a structure, beyond which repair is needed. Figure 2.14 illustrates the concept of the end of life (service life), defined as the probability of load exceeding capacity reaching an unacceptable level. It should be noted that the structural repair falls within the use phase of the structure, with individual repair considered to span within the use of the structure and end of life prediction due to that repair event.

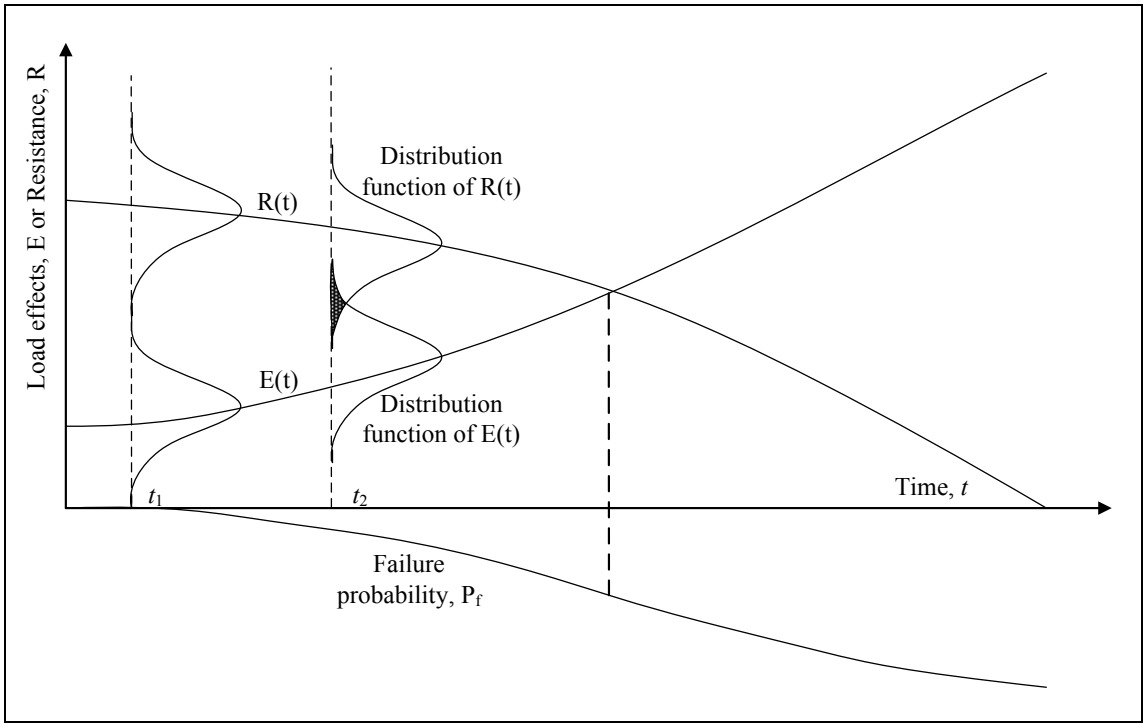

Figure 2.14: Probabilistic Service Life Design (Lepech, et al., 2015)

The general procedure for the sustainability-based structural repair evaluation framework as proposed by Lepech et al. (2015) is:

(a) Measure and plot the cumulative sustainability indicator impacts of a repair and rehabilitation timeline up to the time of functional obsolescence (see Figure 2.15a). The cumulative impacts are expressed as midpoint environmental indicators such as global warming potential, polluted water produced, solid waste generated, or total primary energy consumed.

(b) Characterise the probability distribution function of the structure reaching a service life limit at each time of repair, t_{rk} (see probability functions imposed on the cumulative impact vs. time in Figure 2.4a). The service life limit is either based on the provisions in the codes or the accepted standards by the owner. The probabilistic time between repairs ($t_{rk+1} - t_{rk}$) is based on several factors such as the chosen repair strategy, the quality of the repair work, the variable nature of exposure and load conditions and the limit state.

(c) Characterise the probability distribution function of the amount of impact of each repair event, i_{rk} (see Figure 2.15b). Note that the Gaussian distribution is assumed for both i_{rk} and t_{rk} and is for illustrative purposes). The uncertainties in the actual repair construction processes used, supply chain of repair materials, effects of the repair works on the infrastructure users affect the stochastic modelling of the impact for each repair. The cumulative impact of the repair timeline, I_i, is defined as:

$$I_i = \sum_{k=1}^{n} i_{rk}(t) \tag{2.32}$$

where

$i_{rk}(t)$ is the impact due to the k^{th} repair event measured using the LCA methods provided in the ISO 14040 (2006).

(d) Establish an aggregated probabilistic distribution for the cumulative impact of the repaired structure at any time, from initial construction to the time of functional obsolescence. This is done as follows:

a. Combine the probabilistic models for both repair timeline (t_{rk}) and amount of impact (i_{rk}), by drawing them on the same cumulative vs. time curve (see Figure 2.16)
b. Construct a probabilistic envelope for the entire infrastructure service life (shown with the strong dotted line in Figure 2.16)
c. Based on the boundaries of the envelope in step b, establish an aggregated probabilistic assessment for cumulative impact at any time, t , for the repaired structure (illustrated by the distribution function along time in Figure 2.16).

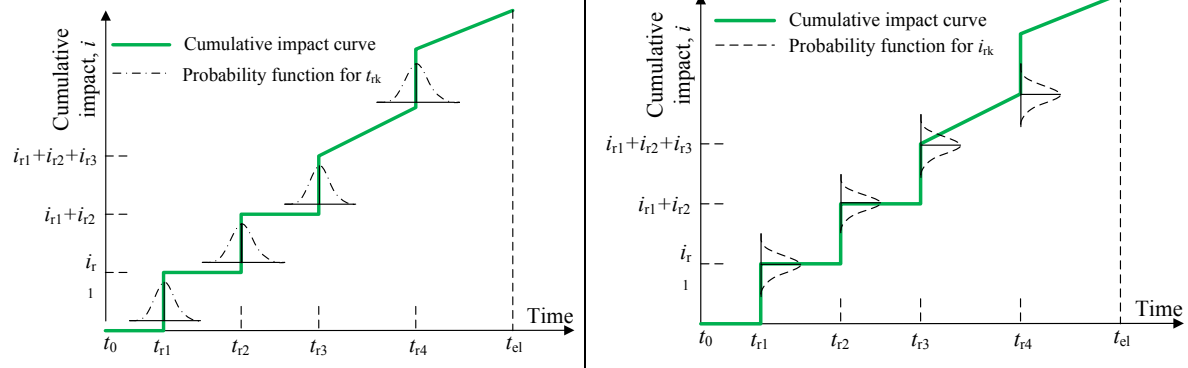

(a) Probabilistic characterisation of a repair timeline, t_{rk} and the cumulative impact

(b) Probabilistic characterisation of repair impacts, i_{rk} and the cumulative impact

Figure 2.15: Probabilistic characterisation of (a) repair timeline, t_{rk} and, (b) repair impact, i_{rk} for cumulative impact determination (Lepech, et al., 2015)

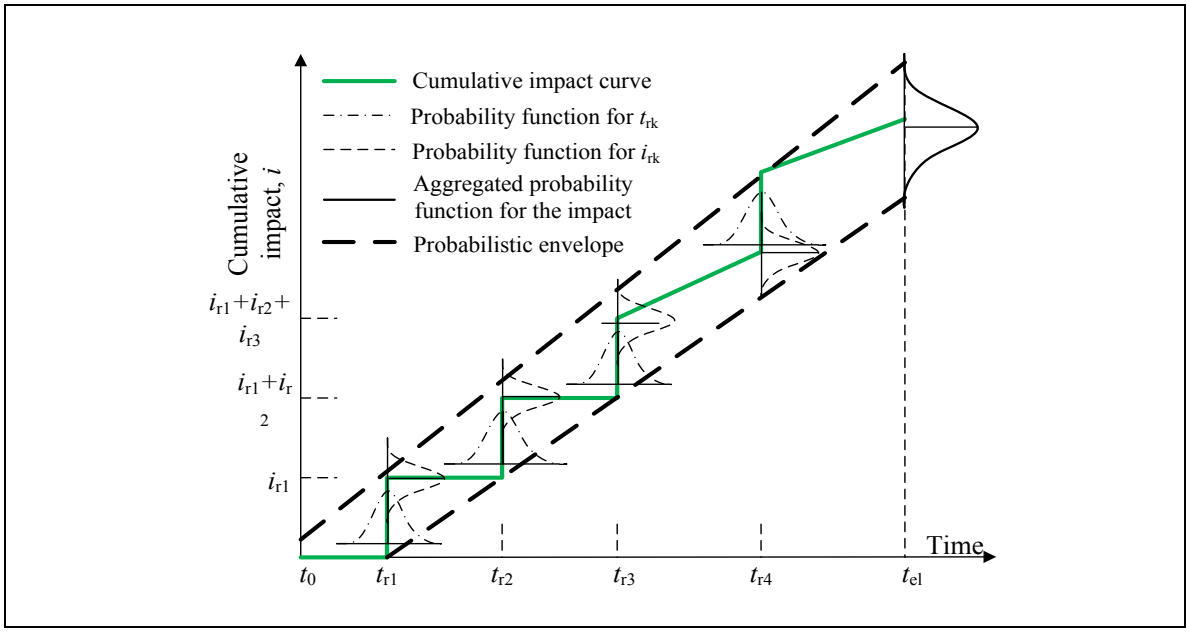

Figure 2.16: Construction of a probabilistic envelope of cumulative impact of repairs after initial construction (t_o) to functional obsolescence (t_{el}) (Lepech, et al., 2015)

(e) Recall the limit states for sustainability as determined by relevant professionals (ecologists, climate scientists and policymakers), conduct various repair alternatives and compare their performance with the limit states. Establishment of a sustainable repair strategy involves an iterative process.

While steps (a) to (e) highlight repair alternatives in achieving sustainable infrastructure, alternative structural systems, building envelope and initial construction techniques can be considered for the full building life. The overall framework and the integration of all applicable models for life cycle assessment of sustainable repair of civil infrastructure as proposed by Lepech et al. (2015) is shown in Figures 2.17 and 2.18 respectively.

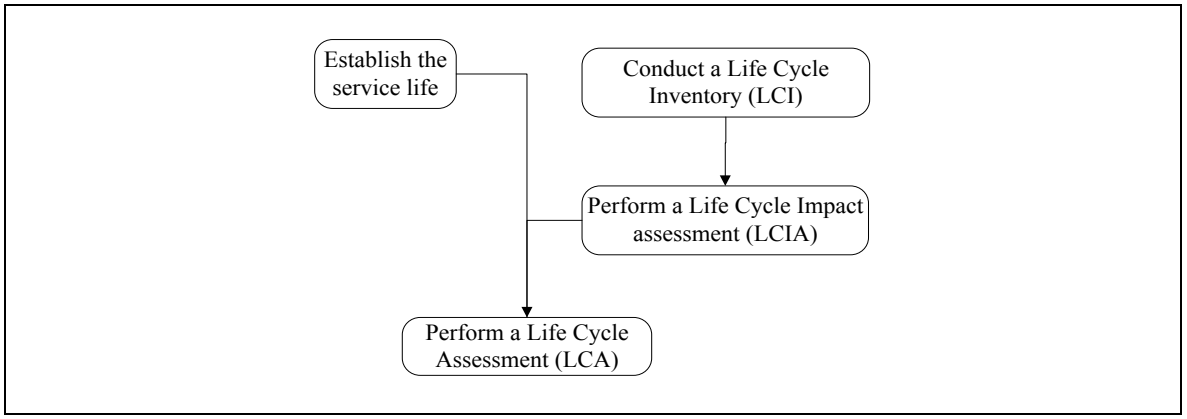

Figure 2.17: A simplified framework for the life cycle assessment of sustainable repair of civil infrastructure proposed by Lepech et al. (2015)

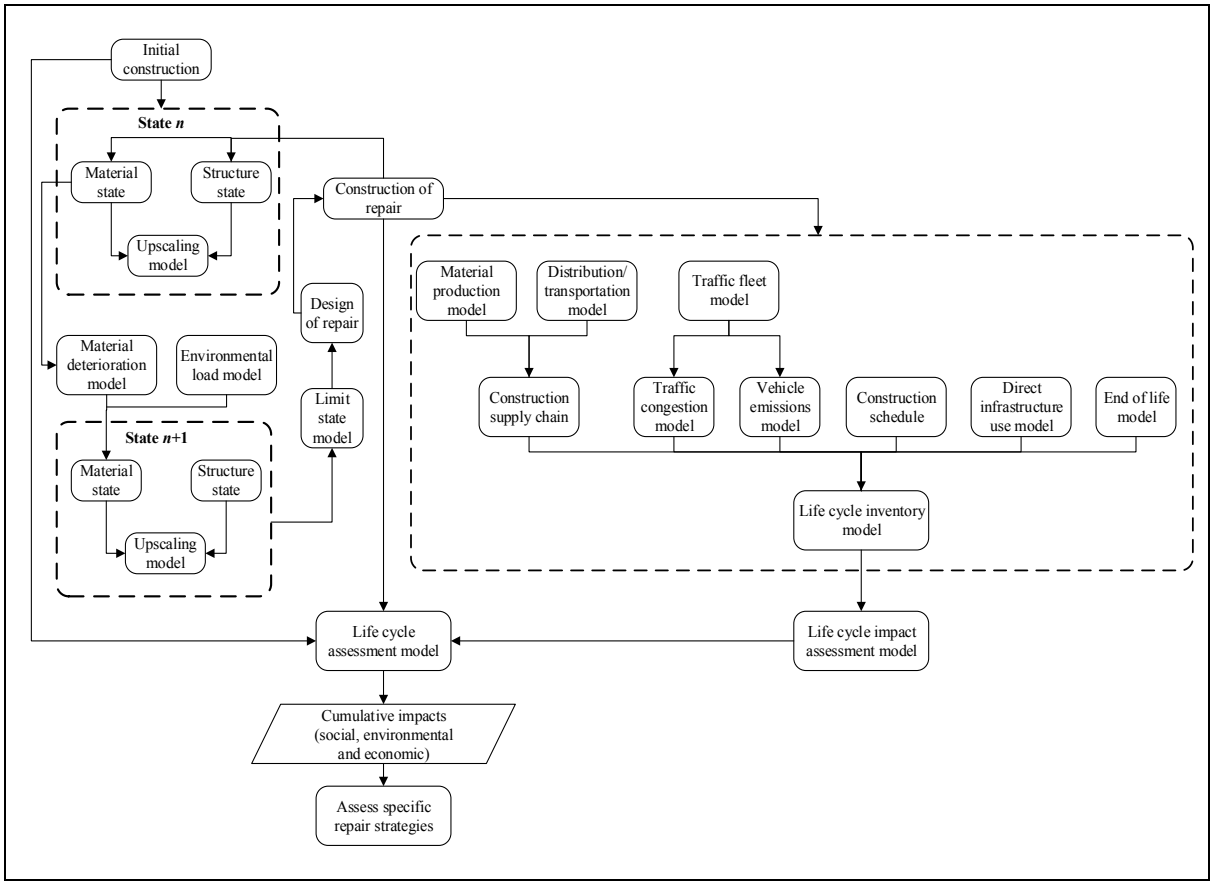

Figure 2.18: A detailed framework and model integration for life cycle assessment of sustainable repair of civil infrastructure proposed by Lepech et al. (2015)

2.5.2 Structural performance deterioration models and limit states

As noted in the integrated framework shown in Figure 2.18, structural performance of a repair strategy is modelled based on its deterioration over time. For probability-based design, the duration of use of the structure after the repair event is estimated by a specified structural performance limit described in terms of probability of failure. Deterioration models and structural performance limit states are required and are reviewed in subsequent subsections.

2.5.2.1 Deterioration models

Deterioration models quantify the performance deterioration of a structure over time. These deterioration models are either phenomenological-based or multi-physics based. Phenomenological-based models consider deterioration phenomenon. Corrosion initiation model is an example of a phenomenological-based deterioration model for the RC structures. Multi-physics models consider the actual physics involved in the deterioration process. For example, multi-physics based deterioration model for the RC concrete would incorporate analytical relationships that describe transport of heat and matter, reinforcement corrosion, and corrosion-induced concrete damage (Lepech, et al., 2015).

(a) Phenomenological-based corrosion initiation model

The corrosion initiation model can be used for the service design of RC structures as provided in the 2006 *fib* Model Code for Service Life Design of Reinforced Concrete (2006). This model can be implemented using Monte Carlo analysis. A probabilistic quantification of the corrosion initiation and

progress of chloride induced reinforcement corrosion as a function of time is derived as used for service life design.

(b) Multi-physics based deterioration model

The model combines coupled transport of heat and matter, reinforcement corrosion and corrosion-induced concrete damage, described using analytical relationships. Initially, a solution for the transport and distribution of heat and matter is generated together with the corrosion potential and corrosion current density. Corrosion-induced concrete damage is simulated using the data generated from the distribution of heat, matter, corrosion potential, and corrosion current density. Corrosion-induced deformations and cracks are then incorporated in the final simulation of heat, matter, and reinforcement corrosion. Corrosion initiation can be modelled by defining a chloride threshold. Further details on this deterioration modelling can be found in specialised literature (Flint, et al., 2013; Pease, et al., 2012; Michel, et al., 2012; Lepech, et al., 2015). This process models the structural deterioration behaviour over time.

2.5.2.2 Limit states

Establishment of a limit state for the sustainability development definition is crucial in the overall evaluation of the infrastructure sustainability. However, as Lepech et al. (2015) argued, the decision to decide the sustainable level of impact should be left up to ecologists, climate scientists, and policymakers. When a limit state is defined, the engineers can measure and design for impact reduction. As noted in Figure 2.14, the time for repair is reached when a structure deteriorates to a specified unacceptable level of probability of failure. This specified level of failure is defined by a limit state function. Either a material-focused limit state or a structure-focused limit state can be used. A materials-focused limit state defines the limit based on attainment of a material deterioration process. In RC structures, for example, the limit state can be represented by material based deterioration models for corrosion initiation due to the chloride ingress. Probability of surpassing the corrosion initiation is determined using appropriate service life design model such as the *fib* Model Code for Service Life Design of Reinforced Concrete (*fib*, 2006). The material-focused limit states can be considered as only inferring probable structural service performance level attainment. However, structure-focused limit state, considered on the ultimate limit state, characterise the probability of the structural capacity over time. The characterised structural behaviour over time is compared to the time-dependent probabilistically characterised load effect function, from which a reliability index, β_i is computed. The time at which the acceptance reliability index is exceeded is considered as time for repair. The increase in the probability of failure with time as shown in Figure 2.14 is indicative of a decline in reliability index.

Structural repair performance characterisation

Initially, the environmental loads that contribute to the deterioration of the structure must be identified. Deterioration of RC structures due to the corrosion is one such example. Based on the nature of the environmental loads, various repair methods and strategies can be devised for the maintenance of the RC structures. In the case of the RC structures affected by corrosion, some repair strategies are provided in the British standards (BS EN 1504-9, 2008).

2.5.3 Sustainability evaluation

Life cycle assessment methods are used to evaluate the sustainability of the infrastructure. The general life cycle assessment procedure as outlined in the ISO 14040:2006 (2006) can be summarised as follows:

(a) The goal and scope definition: This defines the target audience and the boundary conditions.
(b) Inventory analysis: This involves the quantification of relevant input and output data. Material quantities can be established from the bills of quantities while impact potentials are established from the impact characterisation factors.
(c) Impact assessment: This involves the quantification and assessment of the environmental impacts and can be carried out as summarised by Hischier & Weidema (2010) as follows:
    a. calculation of environmental impact potentials;
    b. normalisation of environmental impact potentials calculated in Step a; and
    c. application of weighing factors to compare impacts relative to one another.
(d) Interpretation of results.

LCA models are used to quantify the environmental, social and economic impacts of an infrastructure. A typical illustration of the system boundary definition highlighting possible inputs, out puts and interactions is shown in Figure 2.19. Due to the availability of data and limitation of time, only the environmental impacts relevant to the building infrastructure are considered.

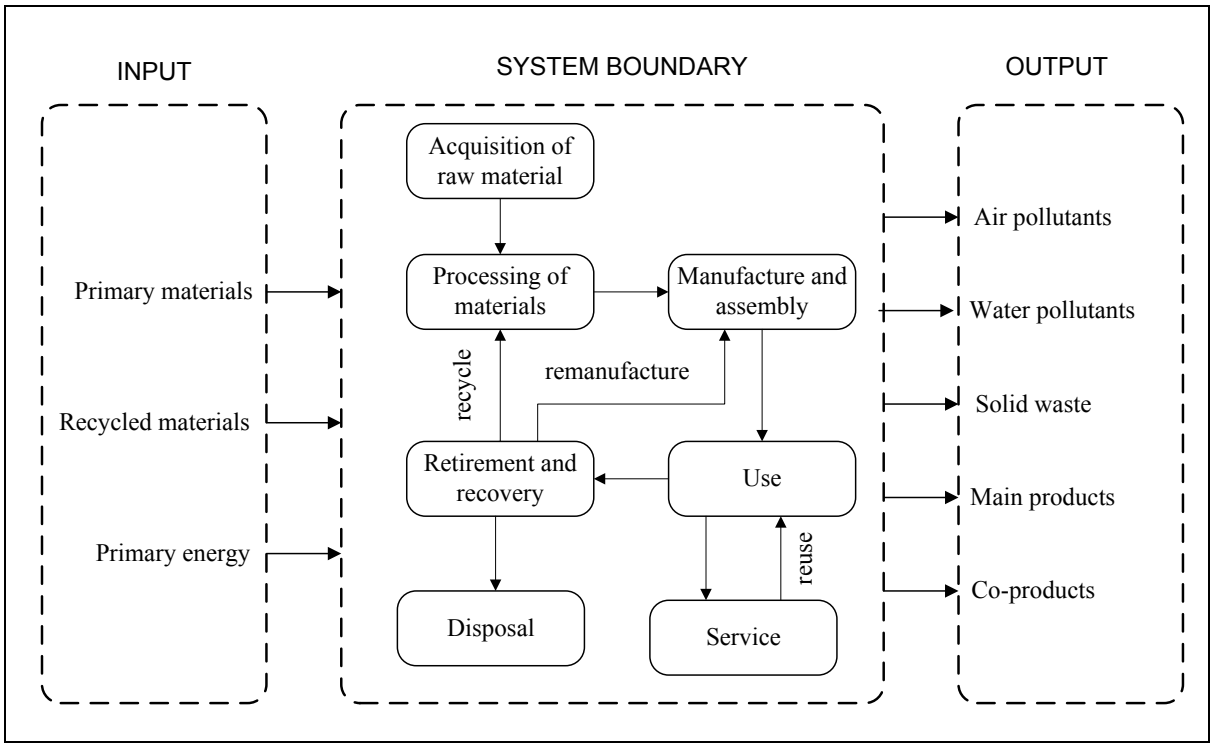

Figure 2.19: Schematic representation of a typical LCA model (Lepech, et al., 2015)

Brewis (2011) outlined three environmental impact that are relevant to the built environmental in South Africa, namely emissions, resource depletion and waste generation. Quantification of emissions is carried out using carbon footprint for greenhouse gases impacting on climate change, and human health and acidification potentials for its impact on ecosystem quality. Increased acidity of water and soil can consequently increase corrosion of man-made structures (Azapagic, et al., 2004), apart from its impact on the quality of the ecosystem. Relevant substances that are considered in the built environment are given in Table 2.8 including conversion factors (Azapagic, et al., 2004; Pachauri & Reisinger, 2007) and other quantification procedures. Resource depletion may be quantified using cumulative exergy, that considers the embodied energy of the concerned materials throughout their life span and convert them to exergy using appropriate conversion factors (Dewulf, et al., 2009; De Meester, et al., 2009).

Waste generation comprises construction waste and demolition waste which are generated at pre-use phase and end-of-life phase respectively. The amount of waste from demolition works is estimated after a materials inventory study for demolition is carried out. This process involves materials classification and separation into three classes, namely; hazardous waste, recyclable waste, and waste to be disposed. Solís-Guzmán et al. (2009) proposed a three-step procedure of quantifying the amount of waste as (a) classification system–put together similar materials of same unit; (b) determination of the quantity of each item per m^2 of the building; and (c) calculation of the expected waste.

Table 2.8: Indicator quantification for selected environmental impacts (Brewis, 2011)

Environmental impact	**Indicator (unit)**	**Elements/ substance**	**Conversion factors**	**Quantification**
Emission	Carbon footprint – CF (CO_{2e})	CO_2	$GWP_{100} = 1$	$CF = \sum_{i=1}^{n} GWP_i EM_i$ $EM_i = e_i m_i$
		CH_4	$GWP_{100} = 25$	
		N_2O	$GWP_{100} = 310$	
	Acidification potential-AP (SO_{2e})	SO_2	AF=1	$AP = \sum_{i=1}^{n} AF_i EM_i$
		NO_x	AF=0.7	
Resource depletion	Exergy (Exe-Jex) Embodied energy (*EE*)	Materials & processes	X_i[1] ef_i[2]	$Exe = \sum_{i=1}^{n} X_i EE_i$ $EE_i = ef_i m_i$
Waste generation	Demolition, packaging & Wreckage (WG)	Materials	W_i[1]	$WG = \sum_{i=1}^{n} W_i EM_i$ $EM_i = M_i - M_{ri}$
	Net avoided exergy consumption (AExe)	Recovered materials (M_{ri}): C_{av}, C_{disp} & C_{rec}	X_i[1] ef_i[2]	$AExe = \sum_{i=1}^{n} X_i \left(C_{(av)i} + C_{(disp)i} - C_{(rec)i}\right)$ $C_i = ef_i m_{ri}$

[1] Material quantity; [2] Material conversion factor

2.6 CONCLUSION

The behaviour of the infill RC frames is reviewed. The effects of the infills in seismic behaviour evaluation of the (integrated) infill RC frames behaviour cannot be ignored. Micro-models for the infill RC frames provide more accurate results. However, macro-models provide comparable results, with notable uncertainties arising from the infill modelling using the equivalent struts. This study aims at developing an evaluation framework that considers the structural performance and sustainability performance of the buildings together. Such an approach, which would be implemented at the preliminary design stage, may favour the use of simplified structural performance evaluation procedures. Thus, macro-models for the infill RC frames have been reviewed, identifying opportunities and challenges of the modelling approach.

Since seismic evaluation of the infill RC frames requires knowledge of the deformation characteristics of the structure, material behaviour characteristics with full stress-strain behaviour is required. It is common to find only the strength characteristics of the material without the full stress-strain data. For concrete and masonry, a wide range of both analytical and empirical relationships have been developed that can be used to establish missing data within each material behaviour. For compressive behaviour, for example, the Young's modulus can be related to strength and stress-strain relationships can be

established using the peak stress and strain at the peak stress; the compressive strength can be related to the tensile strength, and the Young's modulus can be related to the shear modulus. Such relationships help reduce the amount of data required for structural analysis and design.

The equivalent struts have been developed by various researchers, providing adequate information on the geometry and the material properties. Empirical models for the infill have specified calibrated parameters that were derived from specific experimental data by the respective authors. In this study, structural evaluation of the infill RC frames is sought for probabilistic approaches. Thus, any specified model for use in the probabilistic evaluation of the structures should have known model uncertainties. The use of the infill modelling based on material parameter transformation, as provided by El-Dakhakhni (2003) offers better opportunities in calibrating the infill behaviour from the basic material behaviours.

Incorporation of sustainability in structures may involve identifying the possible linkage between structural performance and the sustainability performance indicators. One such linkage is where the structural performance influences the life span of the structure and the life span influences the duration within which a sustainability performance indicator (or impact) can be assessed. The work of Lepech et al. (2015) on structural repair and sustainability provides a good basis for the integration of the structural performance with sustainability. The relationship of structural repair and sustainability is dynamic over time and hence time-based structural evaluation approaches and sustainability evaluation methods can be integrate these items. Available case studies on the integration of structural repair and sustainability (Lepech, et al., 2015) and general LCA of buildings (Bayer, et al., 2010) show that there is great opportunity in integrating the full structural system performance from design state to end of life of the building. An iterative procedure in identifying a more sustainable repair strategy is indicative that any structural system evaluation that integrates sustainability will be iterative. Furthermore, sustainability is considered in the context of specified boundary conditions. Therefore, the specified environmental loads, the use and the exposure of a structure would guide the sustainability evaluation process. In the case of structural behaviour evaluation, simple structural evaluation methods may be helpful at conceptual stage where iterative process is carried out to identify a sustainable infrastructure solution. It is against this background that a simplified structural system evaluation procedure is proposed for lateral load resistance of the infill framed structures for structures in moderate seismic region of the south western region of the Western Cape in South Africa.

CHAPTER 3

3.0 RESEARCH METHODOLOGY

3.1 INTRODUCTION

This chapter describes the detailed methodology used to achieve the two main goals of this research, namely (a) the development and validation of the truss-based structural evaluation procedure; and (b) establishment of a sustainability-based evaluation framework that incorporate the structural performance of the building. The proposed structural evaluation procedure is used for infill RC framed structures subjected to seismic loading. Deformation characteristics of the infilled RC frames are evaluated using a macro-modelling strategy where the infill is represented by equivalent struts. The frame is converted to a truss and together with the equivalent strut, that represents the infill, forms a new structural system idealisation as a complete truss. The simplified structural system can also be evaluated for its robustness. The incorporation of the infill to offer structural resistance of the infilled frames may enhance material resource efficiency towards sustainable housing. Thus, a proposed simple but adequate structural evaluation procedure for infill framed structures subjected to horizontal loading may be useful in promoting sustainable use of structural material resources. To achieve this goal, four key activities are conducted which are:

(a) Development of an analytical procedure for evaluation of the infilled RC frames using truss analogy elaborated in Section 3.2;
(b) Equivalent strut characterisation for the infill, explained in Section 3.3;
(c) Transformation of the bare frame behaviour to equivalent truss behaviour, expanded in Section 3.4; and
(d) Evaluation and validation of the truss-based evaluation procedure discussed in Section 3.5.

The analytical procedure for the evaluation of the infilled RC frames establishes the deformation characteristics of the infilled RC frame (i.e. force-deformation curve). The force vs. deformation curve is treated as the capacity curve for the infill RC frame and can be used in the preliminary evaluation of the structures under seismic load using the methods discussed in Section 2.4.1.

A structural performance evaluation framework that incorporates sustainability performance, based on the work of Lepech et al. (2015), is proposed as explained in Section 3.6. Life cycle assessment methods are adopted while probabilistic methods for both sustainability quantification and structural performance are adopted as discussed in Section 2.5.1. A case study-based evaluation of the proposed framework is adopted.

3.2 DEVELOPMENT OF A TRUSS-BASED STRUCTURAL SYSTEM EVALUATION PROCEDURE

A truss-based structural system offers simplicity in evaluation procedure and ability to capture key structural performance indicators that can be used for sustainability evaluation of structures. Just as any trussed system, pin connections are used for all element to element connections and the support connections. Thus, the structure does not support any moment and shear transfer, but only axial forces. For the analytical procedure proposed, the linearised material characteristics for the truss members are assumed. Each linear segment of the stress-strain curve has its own stress gradient (instantaneous Young's modulus) that can be used for structural evaluation. For the linearised material properties of truss members, there is proportional change in stress and strain within each stress state. These characteristics for the truss members allow for the development of the structural evaluation procedure

where displacement-control or force-control may be used. Where an increase in the applied force generates corresponding increase in displacement, force-control is used (Region A in Figure 3.1). When an increase in displacement generates no change in resistance (region B) or gradual reduction in resistance (region D), displacement-control is used. A third scenario involves a sharp change (increase or reduction) in loading that does not correspond to any change in displacement (region C in Figure 3.1). This scenario can be solved by using force-control, with some modifications.

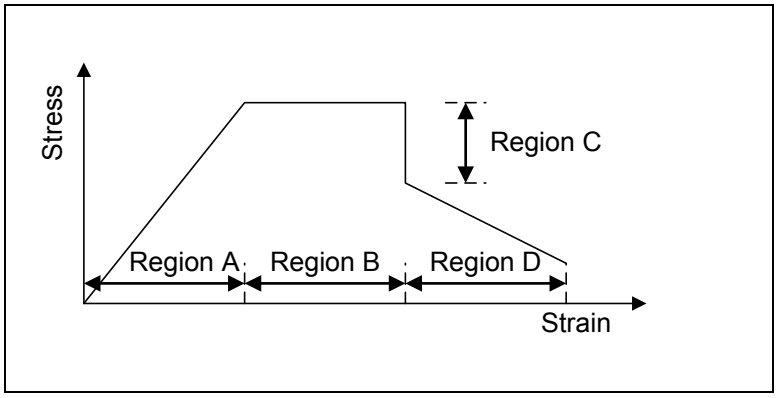

Figure 3.1: Typical stress state regions for a truss element

The proposed evaluation procedure would be useful in establishing the lateral force-deformation curve that can be used in seismic analysis of structures. Two broad categories for analysis of structures subjected to seismic forces that can use the force-deformation curves derived from the proposed procedure are:

a. load-based seismic evaluation; and
b. displacement-based evaluation.

The proposed procedure, which is strain-based, would be very helpful in displacement-based analysis of the structures as illustrated under the application of the procedure in Section 7.6.

3.3 EQUIVALENT STRUT CHARACTERISATION

Equivalent strut characterisation involves establishment of two main parameters for the struts. These are geometric properties (usually the cross-sectional area for the strut) and the material behaviour characterisation. The existing equivalent strut characterisation models, reviewed in Section 2.3, may generate diverse solutions for the same infill, thereby making it difficult to identify appropriate material and geometric model parameters. This study, therefore, utilises the fundamental principles and the observed infill behaviour to develop a new approach for characterising the equivalent struts. The proposed analytical model characterises the material and geometric properties of the equivalent strut. It is developed based on zoning the masonry infill into representative stress zones along the diagonal of the infill and calibrating the nonlinear stiffness of these zones using experimental data. Using nonlinear springs to represent the behaviour of each zone, a subsystem is assembled to calibrate the behaviour of the equivalent strut. Three key activities are conducted for the development and validation of the equivalent strut characterisation; namely analytical study, experimental study and numerical study (see Figure 3.2).

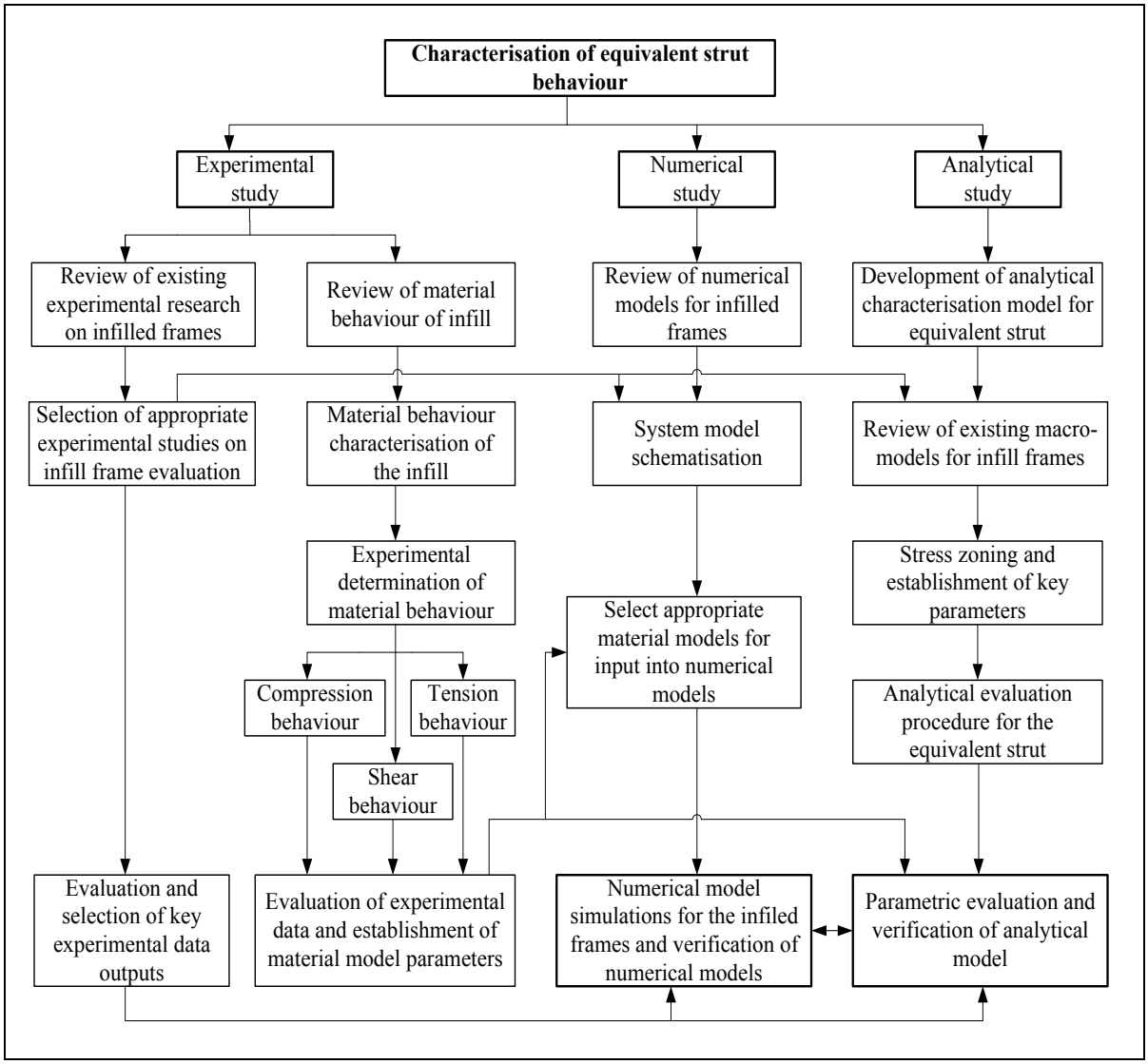

Figure 3.2: Equivalent strut characterisation process

3.3.1 Analytical study

An evaluation of existing macro-models for the infilled RC framed structures in Section 2.3 provides an insight into the basis of the formulation, application and respective advantages and disadvantages of these models. While micro-models offer more accurate and detailed results, the amount of time required, the requirement for special skills and specialised finite element programmes make it difficult to motivate practising engineers to use the modelling procedure for practical purposes, especially where regular and simple structures are involved. On the other hand, macro-models, if properly implemented, may be easier and sufficiently reliable for the evaluation of global behaviour of structural systems. In macro-modelling, the local effects are usually ignored and only the global effects are captured to minimise computational efforts while maintaining the system behaviour at global scale. Current efforts towards the establishment of better macro-models have seen the development of macro-models that can be used in nonlinear analysis of infill frames as discussed in Section 2.3. These macro-models have varying abilities to reliably predict the infill frame performance due to simplifications in both geometric and material properties. Macro-models, therefore, possess uncertainties resulting from these simplifications in addition to inherent uncertainties in material behaviour and its characterisation.

Most of the macro-models that utilise equivalent strut for the infill predetermine the probable mode of infill failure, from which the appropriate infill equivalent strut material properties are derived. The assumed mode of failure is pre-determined based on existing geometric and material elastic properties. Various experimental studies have established that infill frames subjected to incremental lateral displacement can display more than one mode of failure. This study, therefore, seeks to incorporate possible multiple failure modes in infill frame analysis through characterisation of the equivalent strut nonlinear behaviour. The key parameters that link the equivalent strut properties to the observed key infill behaviour when the system is subjected to a pushover analysis are derived. Both displacement-control and force-control load approaches are adopted that rely on the stress-strain states to update the equivalent strut subsystem stiffness. Five activities are conducted for the analytical study as summarised below:

(a) Establish various failure modes of the infill and corresponding dominant stresses. The failure modes considered are the corner crushing (CC), Diagonal cracking (DK), diagonal compression (DC) and sliding shear (SS) as shown in Figure 3.3;
(b) Establish stress zone boundaries;
(c) Workout stress homogenization of each zone and convert the zones' properties to equivalent nonlinear elements whose orientations align with infill diagonal;
(d) Establish zone stiffness along the infill diagonal orientation; and
(e) Assemble the zones' stiffness for the 'equivalent strut subsystem' and analyse the 'subsystem' for the determination of characterised material behaviour of the equivalent strut.

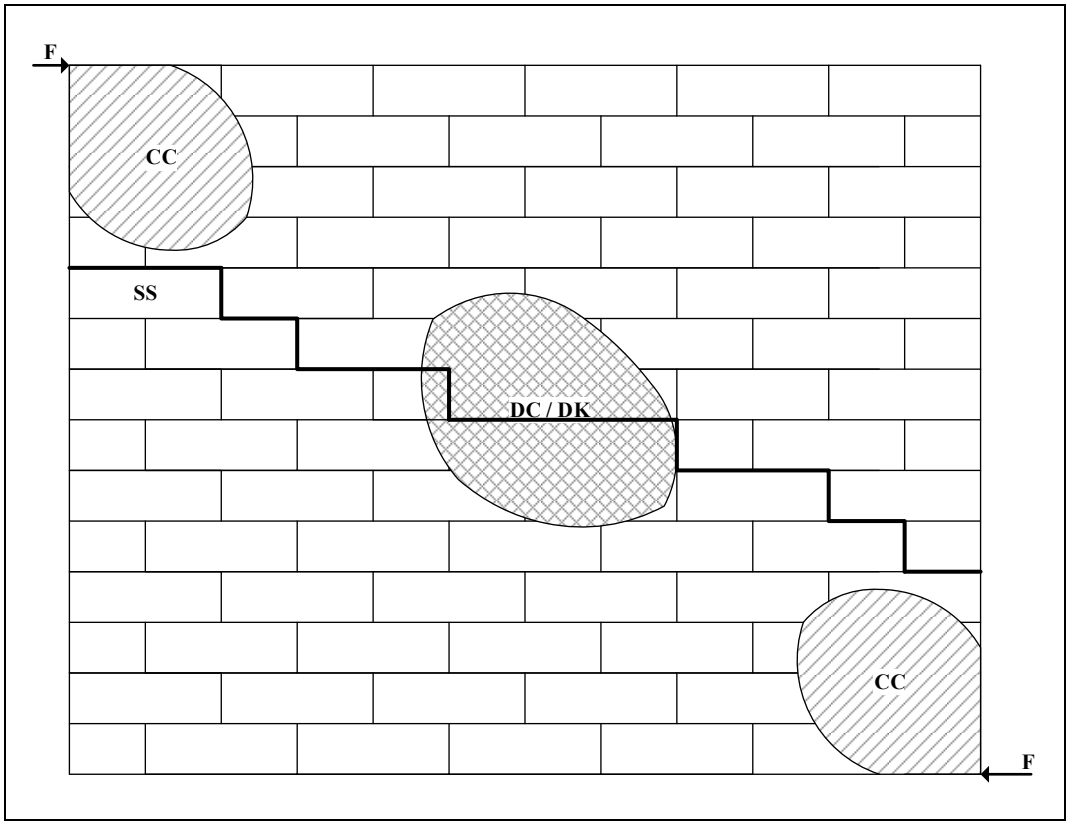

Figure 3.3: Key infill failure modes considered for stress zoning (frame not shown)

The assumptions and hypotheses for zoning and characterisation of individual zones are:

(a) The diagonal stretch of the infill provides substantial resisting force compared to other regions, making the infill resistance contribution equivalent to diagonal strut action.

(b) The failure of the infill along the most loaded zone (i.e. along the diagonal) can be assumed to occur in three regions, namely two zones at opposite corners of the loaded diagonal and the middle region of the loaded diagonal. The corner crushing occurs due to biaxial loading of the loaded corners and diagonal compression or cracking failure occurs due to diagonal compression forces and or diagonal cracking at the mid region of the infill.
(c) Hypothetically, any seismic action generates lateral loads that can be applied statically and incrementally at the loading corners of the infill frame (i.e. through push over analysis). These lateral loads can cause de-bonding and shear slip between the frame and the infill making subsequent lateral loading transferred through contact surfaces at the loading corners of the infill frame.
(d) Due to the topological configuration and material properties of the infill and frame, masonry and mortar can experience de-bonding and shearing along the bed and head joints. Thus, lateral resistance from the infill can also be provided by the bonding and shear resistance of the mortar and brick. The infill can fail due to de-bonding and shear slip when shear stresses exceed the shear capacity of the infill.
(e) In the case when de-bonding and shear slip failure occurs within the infill, the edges adjacent to shear slip zone in contact with the frame can experience excessive contact stress concentration capable of inducing frame failure. Thus, an infill frame that experiences excessive shear slip may be prone to frame failure.

3.3.2 Experimental study

The objective of the experimental study is to select relevant experimental data for the infill RC frames subjected to seismic representative loading (using either cyclic loading or incremental horizontal loading). The experimental data is used both for the model calibration and verification of the equivalent strut characterisation procedure and the calibration of numerical models that are used in the numerical study for structural system evaluation. Two types of experimental data required for this exercise are material characterisation data and infill RC frame verification data.

3.3.2.1 Material characterisation data

For infill RC frames, three distinct materials are involved, namely infill masonry, concrete and reinforcing bars. The characteristic material behaviour for each of these materials is established using relevant methods provided in material standards. In this study, the material characterisation data is obtained from experimental studies available in literature. Due to variability in the methods for establishing the material behaviour for each material, a guideline for the selection of the relevant material is used as provided in Section 3.3.2.3. Nonetheless, a brief discussion of some of the commonly used methods for material characterisation for each material is provided.

(a) Infill masonry

The infill masonry material behaviour is established by considering the masonry behaviour subjected to loading action in compression, tension and shear. These three material behaviours are useful in understanding the behaviour of the infill masonry when subjected to in plane lateral loading. The conventional material characterisation tests can be used to establish the behaviour of critical zones for the infill. Experimental data on the behaviour of masonry units, mortar and masonry panels derived from either standardised methods or author-specified methods are available in literature. As an assumed orthotropic material, masonry panels are subjected to biaxial tests with loading applied at varying angles to the bed joints to establish the behaviour of masonry along different loading planes. Other tests involve uniaxial behaviour evaluation such as vertical and horizontal compressive tests for masonry panels, and tensile and shear tests conducted by applying a diagonal load (see Figure 3.4 for typical test set-up).

Experimental methods for these tests are typically provided in standards such as the Eurocode (e.g. EN 772-1; EN 1052-1, EN 1052-2, EN 1052-5) and American Standards (e.g. ASTM C1006; ASTM C140/C140M-17a). For this research, material characterisation experimental data obtained by Crisafulli (1997), Mehrabi et al. (1996) and Dawe & Seah (1989) is considered.

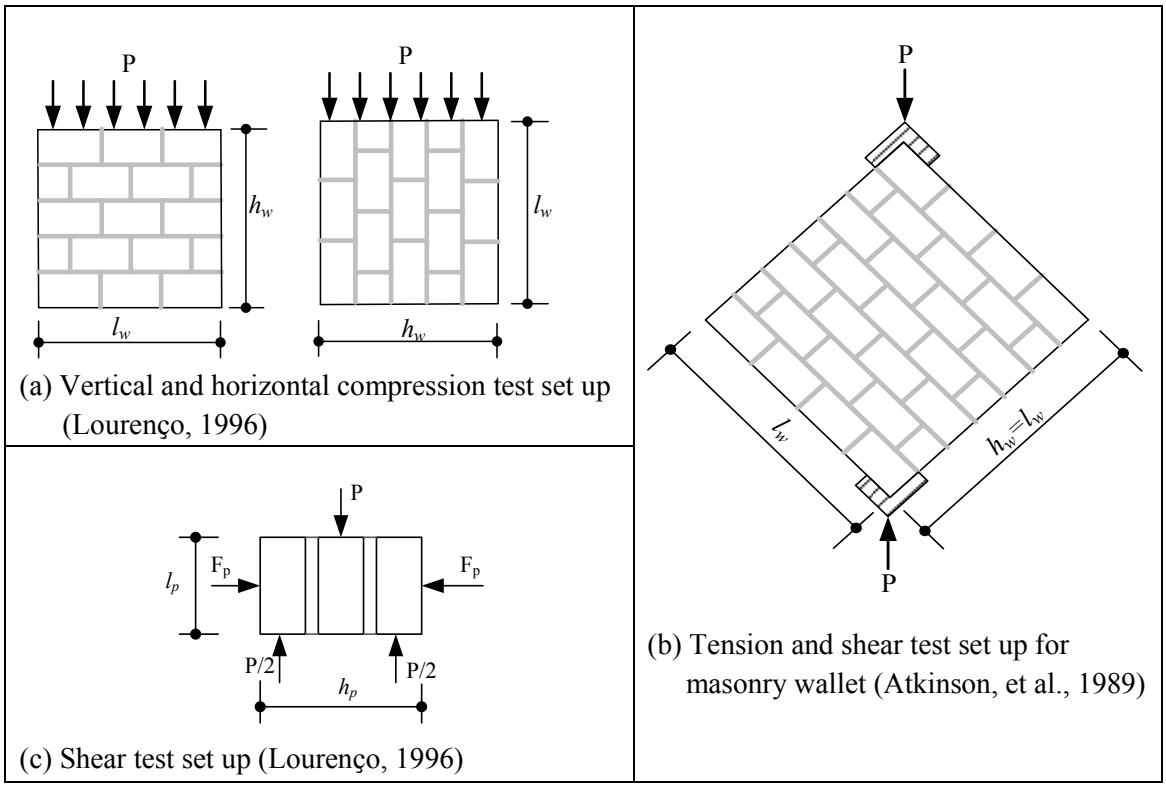

Figure 3.4: Masonry material behaviour characterisation test configurations

For the compressive behaviour, six control data points on the stress-strain curve are used to describe key events of the compressive behaviour of masonry as proposed by Ewing & Kowalsky (2004). These are three pre-peak points and two post peak points in addition to peak strength parameters (see Section 2.2.1.1). A penta-linear material model connecting these key points is selected as an ideal compressive material behaviour. The linearised tangential stiffness values make it possible to use the proposed nonlinear displacement control analysis procedure. Tension characterisation requires parameters for elastic behaviour (usually Young's modulus and tensile strength) and post peak tensile behaviour. Some of the available data in literature may not provide all the data points for a full stress-strain curve. In this case, complete compressive stress-strain curve may be obtained using a parabolic analytical model followed by a straight line up to failure (see Section 2.2.1.1). The post-peak tensile stress-strain curve may be obtained using either equation 2.8 or 2.9 provided in Section 2.2.1.1 or any appropriate analytical relationships provided in the literature.

(b) Concrete

Concrete is used for the frame construction. Three main material behaviour tests for concrete are compression, tension and shear tests. As a quasi-brittle material, most of the tests currently adopted for masonry were originally developed for concrete. The behaviour of concrete in these three material modes changes to a varying degree when it is used together with reinforcement. In addition to bridging mode I (tensile) and mode II (shear-slip) cracks in concrete, reinforcement introduces confinement in concrete, especially for RC frame members subjected to axial compressive forces such as the columns.

In tension, reinforcing bars introduce strengthening and stiffening of the tensile behaviour, enabling the reinforced concrete to transfer tensile stresses at greater deformation than what is normally the case for unreinforced concrete.

Standard tests for concrete compressive behaviour are provided in various material codes. The common test is uniaxial compression tests. These tests generate the stress-strain behaviour for concrete from which compressive strength and corresponding strain and Young's modulus can be calculated. The Young's modulus is calculated at 33% to 40% of the ultimate compressive strength for most of the codes while some literature indicates the Young's modulus calculated at 45% of the ultimate compressive strength (Mehrabi, et al., 1996). Availability of the full stress-strain behaviour of concrete is useful for this study. However, most literature reports the compressive strength and the Young's modulus only or even the compressive strength only. When such a situation arises; appropriate standard guidelines are used to establish the missing data in addition to the use of appropriate analytical models for stress-strain behaviour as discussed in Section 2.2.1.1. For unconfined concrete in compression the Kent & Park (1971) analytical model is adopted, while for confined concrete, the *modified* Kent-Park (Park, et al., 1982) model is adopted.

Tensile behaviour of concrete is established using various methods such as the direct uniaxial tension test and the splitting test. The relationship of the tensile strengths obtained using these methods have been widely reported in literature (Eurocode 2, 2004). Each method has its own advantages and disadvantages. Uniaxial direct tension testing, for example, offers a better means of establishing the uniform tensile behaviour of concrete but practical implementation of the test set-up is challenging. The splitting test does not give direct tensile stresses but allows determination of tensile stress that develops due to splitting force application. Typical tension test-set ups are shown in Figure 3.5.

In addition to the uniaxial tests in compression and tension used for concrete, biaxial tests are also conducted to establish the capacity of concrete when it is subjected to biaxial loads. In the most practical case, concrete may not be subjected to a purely axial load only but other load combinations exist. Furthermore, when concrete is modelled in finite element programs, shell elements may be used. The behaviour of shell elements involves the biaxial characteristics of the material such as f_{b0}/f_{c0} ratios for concrete.

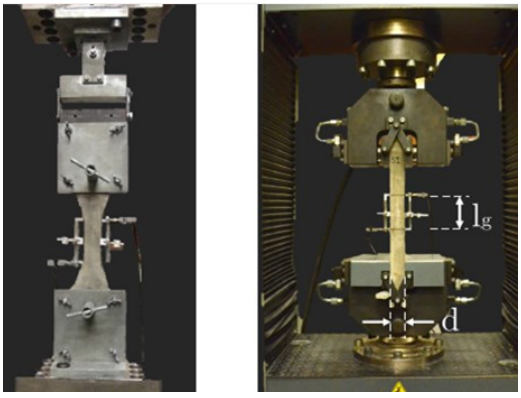

(a) Direct tension test set-up (De Beer, 2016)

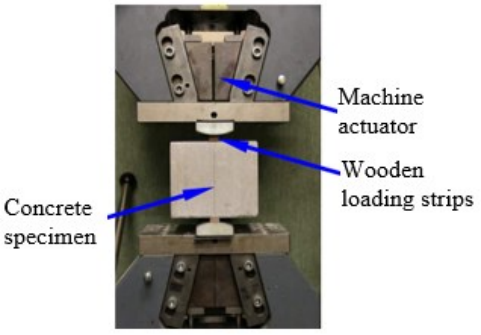

(b) Splitting test set-up (De Villiers J, 2015)

Figure 3.5: Various tension test set up (direct test and splitting tests)

(c) Reinforcing bars

Reinforcing bars help improve the tensile and shear behaviour of concrete used for frame construction. Tensile behaviour tests for steel bars do not vary significantly across various testing methods standards. Usually the tensile behaviour for steel is similar to the compressive behaviour, if buckling can be avoided. The typical tensile behaviour for reinforcing bars used in the selected experiments is indicated in Figure 3.6. Since a linearised material behaviour is required for the proposed analytical models, the behaviour of reinforcing steel is linearised either using the Eurocode 2 (2004) or as indicated in Figure 3.6(b).

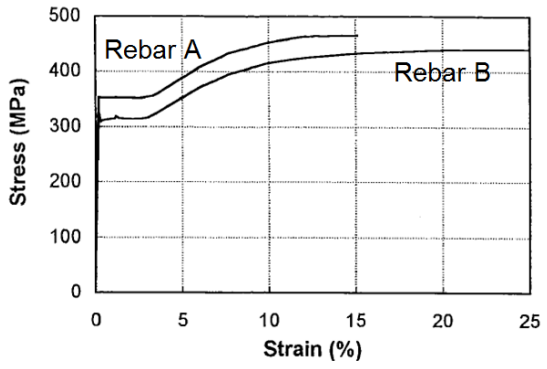

(a) Typical tensile behaviour for steel bars(taken from Crisafulli, 1997)

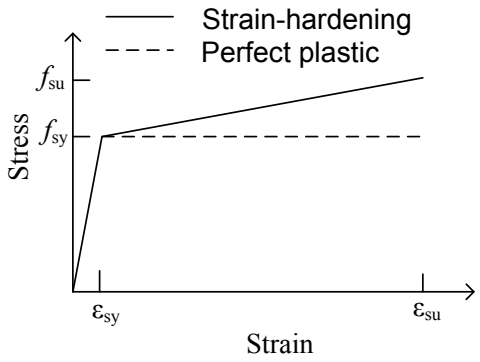

(b) Simplified constitutive model for steel in tension (Eurocode 2, 2004)

Figure 3.6: (a) Typical tensile behaviour for steel reinforcing bars and (b) simplified constitutive models

3.3.2.2 Verification data

Both the bare frame and infill frame behaviour experimental data are obtained from literature and used for verification of the proposed strut characterisation procedure, calibration of numerical models that have been used in performing parametric studies and lastly, for verification of the structural system evaluation procedures proposed in this study. The key structural behaviour data obtained from the experiments is the force vs. deformation characteristics, from which the following parameters are extracted for use in both model calibration and validation:

(a) initial or elastic stiffness (K_e);
(b) peak elastic lateral strength (F_e);
(c) lateral deformation at peak elastic strength (δ_e);
(d) ultimate lateral strength (F_u); and
(e) lateral deformation at the ultimate lateral strength (δ_u).

Experimental data available in literature involve single-storey single-bay infill RC frames. The single-storey single-bay infill RC frames and corresponding bare frames are adopted as standard structural topology for the calibration and verification exercise. Due to possible uncertainties when using different sources of data, a simple experimental data selection procedure is used as discussed in Section 3.3.2.3.

3.3.2.3 Infill frame experimental data selection procedure

This research utilises experimental data from various sources in literature. The fact that the experiments were conducted in different laboratories, possibly using different experimental set-ups and testing methodologies, causes uncertainty about the data. Information is also required about the way the

experiments were conducted, the type of data captured and any report of observed behaviour during experimentation. Such amount of information would be helpful in deciding whether the results from such data source would be helpful in model verification for both material characterisation and structural evaluation. Preliminary evaluation of the existing experimental data for infill RC frames is conducted for data selection. The procedure for the selection of experimental data used in this research is based on three key steps (see Figure 3.7), namely:

(a) qualitative evaluation of the available data;
(b) streamlining of the data based on consistency and or restricted coefficient of variation; and
(c) data normalisation to extract trends in behaviour.

Qualitative data evaluation: The qualitative evaluation ensures completeness of data for use in the study. It is based on the following items:

(a) Availability of material characterisation data. The material characterisation data is useful as input into both the numerical and analytical modelling procedures. For concrete, masonry and reinforcing bars (rebars), the checklist given in Table 3.1 is used. In addition to the type of data stated in Table 3.1, the methods used for establishing respective material behaviour characteristics are required. When non-codified procedure is used, there is a need for a full description of the method so that it can be compared to codified methods.

Table 3.1: Required material characterisation data

Material	**Data type**										
	Compression				Tension			Shear			Biaxial
Concrete	f_{cp}	ε_{cp}	ε_{cu}	E_c	f_{tp}	ε_{tp}	ε_{tu}	μ_0	τ_0	ϕ	f_{b0}/f_{c0}
Masonry	f_{cp}	ε_{cp}	ε_{cu}	E_c	f_{tp}	ε_{tp}	ε_{tu}	μ_0	τ_0	ϕ	f_{b0}/f_{c0}
Rebars	f_{cy}	ε_{cy}	f_{sk}	ε_{sk}	f_{su}	ε_{su}	E_s	N/A	N/A	N/A	N/A

(b) Availability of the bare and infill RC frame structural behaviour data. While most of the experimental programmes reported in literature consider bare frame experiments as control, in this study, the behaviour of bare frames is useful for both control (for comparison with and evaluation of the infill RC frames) and verification of the frame-to-truss transformation procedure. The infill RC frame data is used for calibration of the equivalent strut behaviour, infill frame behaviour evaluation procedure verification and calibration of numerical models used in parametric studies. Specific data for each experimental type is summarised in Table 3.2. A full description for the experimental set up, data acquisition and processing is required. In addition to the quantified data output stated in Table 3.2, there is need for descriptive data of the observed structural behaviour during experimentation. For the infill RC frame, the observations can include but are not limited to the key points of substantial stiffness degradation (through cracking or crushing of concrete or and masonry), failure progression pattern, ultimate failure mode, frame/infill detachment.

Table 3.2: Required structural behaviour evaluation data (indicated with a tick)

Structural system	**Elastic behaviour**			**Plastic behaviour**		
	K_e	F_e	δ_e	F_u	δ_u	Length of infill/frame contact
Bare frame	✓	✓	✓	✓	✓	N/A
Infill RC frame	✓	✓	✓	✓	✓	✓

Data categorisation and consistency evaluation: A simple evaluation of the single bay single storey infill RC frames is conducted to establish an empirical relationship between the bare frame capacity and the infill frame capacity. This process is fully discussed in Section 4.4.1. Categorisation of data based on the type of infill used and the RC frame properties such as the support conditions and connections types between frame members and loading types are used to determine possible relationships between the bare frame and the infill RC frame behaviour. The assumptions/hypothesis and the reasons behind such data selection/sampling procedure are:

(a) Categorisation would enable sampling of data that is consistent with specified procedures and hence more reliable;
(b) Data within the same category, if fully established using similar methods would enable easier and direct relationship between the infill RC frame and the bare frame behaviours;
(c) An empirical relationship is developed using qualified data sets. Due to possible challenges in maintaining uniform and consistent infill frame construction, any data that fails the empirical relationship is considered as an outlier and discarded, unless adequate data is available to justify its inclusion. While this is good for calibration and potential use of various existing infill frame behaviour models, such removal of data may alter the actual behaviour of the infill RC frame that represents the unique behaviour of the system. Nevertheless, such consistency factor may help develop quality control measures for infill RC frame construction. It is assumed that data from the same source would have been treated equally as compared to data from multiple sources. In this research, experimental data is obtained from multiple sources. Thus, the data set from each source is analysed separately before being lumped to generate overall general behaviour of the infill RC frames.

Data normalisation: This procedure is usually used for material data that is established using non-standard methods. For example, infill masonry compression tests can be carried out using different sample dimensions. The compressive behaviour of masonry walls varies with the slenderness ratio. Due to variations in the brick sizes, different slenderness ratios can be used for compressive behaviour testing. When such a scenario exists, there is need to normalise the compressive strength. This is discussed in Chapter 2. Another example is that of shear properties of masonry. As proposed by Crisafulli (1997), the friction factor (μ_0) and shear strength (τ_0) can be normalised to generate average properties across the brick.

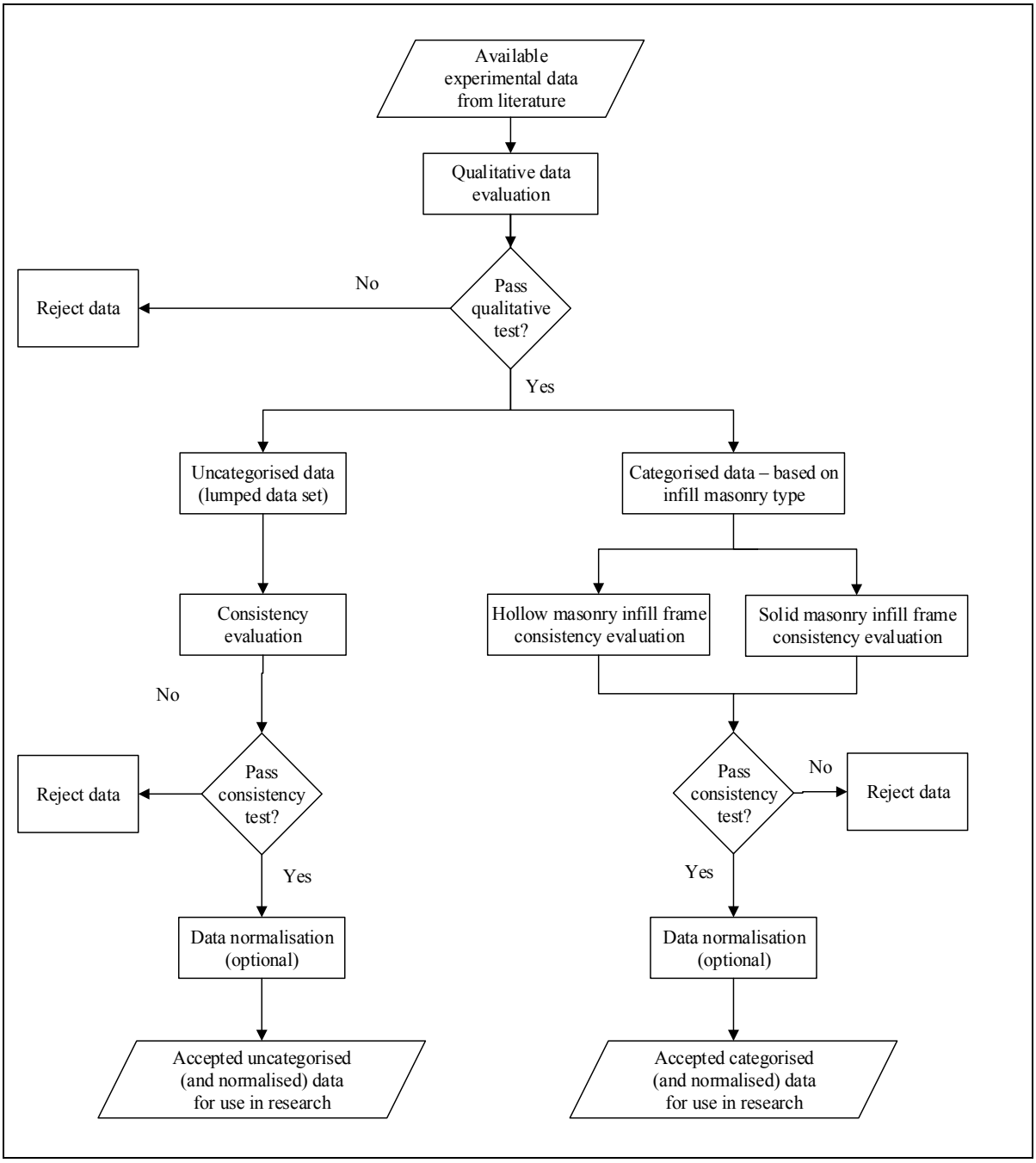

Figure 3.7: Experimental data selection procedure

3.3.3 Numerical study

Available experimental data on infill RC frame behaviour is limited and usually not tailored to the specific requirements for this research. To conduct a comprehensive parametric study that can assess the performance of the proposed characterisation procedure, finite element modelling is performed in ABAQUS (2011). A preliminary numerical study involves experimental data from Crisafulli (1997). Actual material properties for both the infill and frame are considered constant (as it is only one case study used for calibration and parametric evaluation) while geometric configuration is varied by changing the angle of diagonal inclination.

The stress zones discussed in Section 3.3.1 are assumed to be related using the shear factor, γ_{ss} and the compression factor, γ_{cc}. These two material model parameters are varied to evaluate the behaviour of the infill under varying stress dominance. Table 3.3 provides a summary of the parametric study programme for the numerical evaluation used for the equivalent strut characterisation. Ten variations of the compression factor and six variations of the shear factor are used to generate sixty samples for the numerical simulation, where each sample is denoted by X_{ij} in Table 3.3.

Table 3.3: Numerical experimentation matrix for the equivalent strut characterisation

Shear factor, γ_{ss} & ith term		**Compression factor, γ_{cc} and jth term**									
		1	2	3	4	5	6	7	8	9	10
ith term	Factor	0.50	0.60	0.70	0.80	0.90	1.00	1.10	1.15	1.25	1.40
1	0.15	$X_{1,1}$	$X_{2,1}$	$X_{3,1}$	$X_{4,1}$	$X_{5,1}$	$X_{6,1}$	$X_{7,1}$	$X_{8,1}$	$X_{9,1}$	$X_{10,1}$
2	0.25	$X_{1,2}$	$X_{2,2}$	$X_{3,2}$	$X_{4,2}$	$X_{5,2}$	$X_{6,2}$	$X_{7,2}$	$X_{8,2}$	$X_{9,2}$	$X_{10,2}$
3	0.35	$X_{1,3}$	$X_{2,3}$	$X_{3,3}$	$X_{4,3}$	$X_{5,3}$	$X_{6,3}$	$X_{7,3}$	$X_{8,3}$	$X_{9,3}$	$X_{10,3}$
4	0.50	$X_{1,4}$	$X_{2,4}$	$X_{3,4}$	$X_{4,4}$	$X_{5,4}$	$X_{6,4}$	$X_{7,4}$	$X_{8,4}$	$X_{9,4}$	$X_{10,4}$
5	0.65	$X_{1,5}$	$X_{2,5}$	$X_{3,5}$	$X_{4,5}$	$X_{5,5}$	$X_{6,5}$	$X_{7,5}$	$X_{8,5}$	$X_{9,5}$	$X_{10,5}$
6	0.80	$X_{1,6}$	$X_{2,6}$	$X_{3,6}$	$X_{4,6}$	$X_{5,6}$	$X_{6,6}$	$X_{7,6}$	$X_{8,6}$	$X_{9,6}$	$X_{10,6}$

3.4 TRANSFORMATION OF THE KEY FRAME BEHAVIOUR TO EQUIVALENT TRUSS BEHAVIOUR

Frames and trusses are fundamentally different in the type of internal forces and stresses involved. When infill frames are subjected to seismic loading, the lateral force transfer mechanism changes from a predominant frame action to a predominant truss action (Catherin, et al., 2013; Murty & Jain, 2000). The lateral frame resisting mechanism is transformed into a lateral truss resisting mechanism, considering both the elastic and inelastic behaviours. As is the case for the characterisation of the infill frame, single storey single bay bare frames are used as a basic geometric unit for the transformation of the frame to truss. Key geometric properties for the truss are developed during the elastic transformation procedure using basic mechanics of structures theories, while inelastic behaviour is calibrated through experimental/numerical evaluation. The bare frame is considered fixed at the support boundaries to reflect the experimental set ups available in literature for model verification. However, pinned support formulations are considered as well, since most of the foundation types are considered pinned for practical purposes. A numerical model is developed for a truss-based system to verify/validate the established truss parameters. However, due to the limitations in the availability and detailed output from RC frame experiments, numerical models are used for the frame for some of the verification exercise.

3.4.1 Elastic behaviour transformation

The seismic loading is generated from the inertial forces of the mass of the frame, the masses are assumed to be lumped at each floor level in lateral DOFs, which is the general practice in dynamic evaluation of structures. This assumption ensures that all the rotational DOFs do not support any inertial force, thus allowing for condensation of these DOFs into lateral DOFs. The inertial force from the lumped mass is then replaced with a lateral force as shown in Figure 3.8. The frame is assumed to be axially stiff. This ensures that simplified relationships can be developed. However, as it will be noted later, the simplification generates slightly stiffer equivalent lateral truss resisting systems. Key parameters for elastic behaviour of the frame are the Young's modulus, cross-sectional properties (second moment of area, *I*, for axially stiff frame and area, *A*, if axial stiffness are to be incorporated)

and respective lengths for the beam and column. Furthermore, appropriate boundary conditions for the frame must be used.

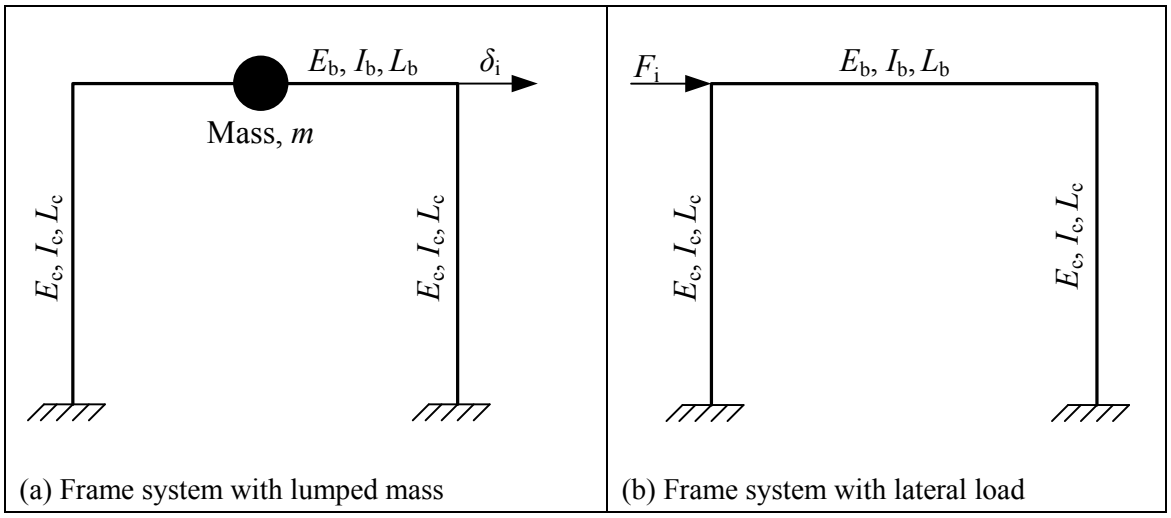

(a) Frame system with lumped mass (b) Frame system with lateral load

Figure 3.8: Idealised single-storey single-bay bare frame subjected to seismic load

The elastic and geometric properties for the truss are developed from the frame using stiffness based force equilibrium and kinematics equations. Verification and validation are based on the use of experimental and numerical data. Experimental data, where available, are used to calibrate the numerical models for the frame.

3.4.2 Parametric studies for bare frame's diagonal strut behaviour calibration

As discussed in literature, the structural behaviour of the frame subjected to horizontal loading may be influenced by both the material, geometric and topological features of the frame. The relationship of the key parameters that define the structural behaviour of the frame can be used to calibrate the material behaviour of the diagonal strut when used in a truss. Thus, the parametric studies are conducted to examine the effects of the second moment of areas and the aspect ratio on the structural behaviour characteristics of the RC frames. The patterns in the behaviour of the frame would help formulate possible calibration of the diagonal strut properties. There are four key parameters that have been used to describe the structural behaviour of the frame under lateral load; namely, the yield strength (F_e), the deformation at yield strength (δ_e), the ultimate strength (F_u) and the deformation at ultimate strength (δ_u). Material data obtained from a single experiment is used for the parametric studies. Thus, considering material behaviour constant, four variables are considered in the parametric evaluation, namely; length of the beam (L_b), height of the column (L_c) and the second moment of area for the beam and column (I_b and I_c). Four possible combinations (A - D) are generated as shown in Table 3.4.

Table 3.4: Combinations for consideration for parametric studies using numerical analysis

Constant structural topological parameter	**Constant cross-sectional parameter**	
	Column second moment of area, I_c	Beam second moment of area, I_b
Column length, L_c	L_c , I_c constant (Case A)	L_c , I_b constant (Case B)
Beam length, L_b	L_b , I_c constant (Case C)	L_b , I_b constant (Case D)

Parametric evaluation of each of the category of frame based on the combinations in Table 3.4 is conducted considering the four variables (I_b , I_c , L_b and L_c). These four parameters are captured using their respective ratios, I_b/I_c and L_c/L_b (aspect ratio). For the second moment of area, the ratio I_b/I_c is used and either I_b or I_c is made constant for a numerical analysis. Likewise, for the member length, the aspect ratio, r_a , ($r_a = L_c/L_b$) is used and either L_b or L_c is made constant for a numerical analysis. Thus, four groups of combinations exist as shown in the Tables 3.5 to 3.8. In this numerical experimentation, the aspect ratios of 1.5, 1.0, 0.665, 0.5 and 0.2 are used while the I_b/I_c ratios of 1.0, 2.5, 5.0, 10.0 and 20.0 are used. Thus, for a choice of I_c , the beam-to-column stiffness ratio, ξ , $\left(\xi = \left(E_b I_b/L_b^3\right)/\left(E_c I_c/L_c^3\right)\right)$ would range from 0.2 to 30.0. For cases A and B, a constant square column section is used together with square beams of corresponding stiffness. Cases C and D use a constant rectangular beam section against square RC column with corresponding stiffness.

Table 3.5: Case A - numerical experimentation matrix considering I_c and L_c as constant

I_c (mm^4) x10^8	$\frac{I_b}{I_c}$	L_c (mm)	Samples for respective aspect ratios, r_a (ξ in brackets)					
			$r_a = 1.5$	$r_a = 1.0$	$r_a = 0.75$	$r_a = 0.665$	$r_a = 0.50$	$r_a = 0.2$
2.31	1.0	1537	A_{11}(1.50)	A_{12}(1.0)	A_{13}(0.75)	A_{14}(0.665)	A_{15}(0.50)	A_{16}(0.20)
2.31	2.5	1537	A_{21}(3.75)	A_{22}(2.50)	A_{23}(1.875)	A_{24}(1.6625)	A_{25}(1.25)	A_{26}(0.50)
2.31	5.0	1537	A_{31}(7.50)	A_{32}(5.0)	A_{33}(3.75)	A_{34}(3.335)	A_{35}(2.50)	A_{36}(1.00)
2.31	10.0	1537	A_{41}(15.0)	A_{42}(10.0)	A_{43}(7.50)	A_{44}(6.65)	A_{45}(5.00)	A_{46}(2.00)
2.31	20.0	1537	A_{51}(30.0)	A_{52}(20.0)	A_{53}(15.0)	A_{54}(13.30)	A_{55}(10.0)	A_{56}(4.0)

Table 3.6: Case B - numerical experimentation matrix considering I_c and L_b as constant

I_c (mm^4) x10^8	$\frac{I_b}{I_c}$	L_b (mm)	Samples for respective aspect ratios, r_a (ξ in brackets)					
			$r_a = 1.5$	$r_a = 1.0$	$r_a = 0.75$	$r_a = 0.665$	$r_a = 0.50$	$r_a = 0.2$
2.31	1.0	2311	B_{11}(1.50)	B_{12}(1.00)	B_{13}(0.75)	B_{14}(0.665)	B_{15}(0.50)	B_{16}(0.20)
2.31	2.5	2311	B_{21}(3.75)	B_{22}(2.50)	B_{23}(1.875)	B_{24}(1.6625)	B_{25}(1.25)	B_{26}(0.50)
2.31	5.0	2311	B_{31}(7.50)	B_{32}(5.00)	B_{33}(3.75)	B_{34}(3.335)	B_{35}(2.50)	B_{36}(1.00)
2.31	10.0	2311	B_{41}(15.0)	B_{42}(10.0)	B_{43}(7.50)	B_{44}(6.65)	B_{45}(5.00)	B_{46}(2.00)
2.31	20.0	2311	B_{51}(30.0)	B_{52}(20.0)	B_{53}(15.0)	B_{54}(13.30)	B_{55}(10.00)	B_{56}(4.0)

Table 3.7: Case C - numerical experimentation matrix considering I_b and L_c as constant

I_b (mm^4) x10^8	$\frac{I_b}{I_c}$	L_c (mm)	Samples for respective aspect ratios, r_a (ξ in brackets)					
			$r_a = 1.5$	$r_a = 1.0$	$r_a = 0.75$	$r_a = 0.665$	$r_a = 0.50$	$r_a = 0.2$
46.20	1.0	1537	C_{11}(1.50)	C_{12}(1.00)	C_{13}(0.75)	C_{14}(0.665)	C_{15}(0.50)	C_{16}(0.20)
46.20	2.5	1537	C_{21}(3.75)	C_{22}(2.50)	C_{23}(1.875)	C_{24}(1.6625)	C_{25}(1.25)	C_{26}(0.50)
46.20	5.0	1537	C_{31}(7.50)	C_{32}(5.00)	C_{33}(3.75)	C_{34}(3.335)	C_{35}(2.50)	C_{36}(1.00)
46.20	10.0	1537	C_{41}(15.0)	C_{42}(10.0)	C_{43}(7.50)	C_{44}(6.65)	C_{45}(5.00)	C_{46}(2.00)
46.20	20.0	1537	C_{51}(30.00)	C_{52}(20.00)	C_{53}(15.00)	C_{54}(13.30)	C_{55}(10.00)	C_{56}(4.0)

Table 3.8: Case D - numerical experimentation matrix considering I_b and L_b as constant

I_b (mm^4) x10^8	$\frac{I_b}{I_c}$	L_b (mm)	Samples for respective aspect ratios, r_a (ξ in brackets)					
			r_a = 1.5	r_a = 1.0	r_a = 0.75	r_a = 0.665	r_a = 0.50	r_a = 0.2
46.20	1.0	2311	D_{11}(1.50)	D_{12}(1.00)	D_{13}(0.75)	D_{14}(0.665)	D_{15}(0.50)	D_{16}(0.20)
46.20	2.5	2311	D_{21}(3.75)	D_{22}(2.50)	D_{23}(1.875)	D_{24}(1.6625)	D_{25}(1.25)	D_{26}(0.50)
46.20	5.0	2311	D_{31}(7.50)	D_{32}(5.00)	D_{33}(3.75)	D_{34}(3.335)	D_{35}(2.50)	D_{36}(1.00)
46.20	10.0	2311	D_{41}(15.0)	D_{42}(10.0)	D_{43}(7.50)	D_{44}(6.65)	D_{45}(5.00)	D_{46}(2.00)
46.20	20.0	2311	D_{51}(30.00)	D_{52}(20.00)	D_{53}(15.00)	D_{54}(13.30)	D_{55}(10.00)	D_{56}(4.0)

The parametric studies are designed in such a way that contribution to the cross-sectional stiffness, through the second moment of area, is proportional for both the reinforcement and the concrete sections. The reinforcements are provided in the numerical model by use of two layers embedded at a distance of d_1 from the section centroid to each of the two edges of the frame element respectively. The second moment of area of the section is calculated using $I_i = I_0 + (m-1)A_s d_1^2$. Varying the second moment of the section, I, involving varying the actual section dimensions and amount of reinforcement. In this study, it is assumed that the section properties are changed by the same factor to both the concrete section stiffness contribution (assumed as I_0) and the reinforcement section contribution (assumed as $I_\rho = (m-1)A_s d_1^2$). A beam or column and reinforcement cross-sectional dimensions are determined from the respective new second moment of areas. The details of the calculations for the parameters used in the study are provided in Tables A1.1-A1.4 in Appendix A1.1. The parametric design results in varying the amount of reinforcement as a proportion to the cross-sectional area. Samples with I_b/I_c ratios of 1.0, 2.5, 5.0, 10.0 and 20.0 have amount of reinforcement of 2.79%, 2.94%, 3.12% and 3.84% respectively.

3.4.3 Finite element model for the frame

ABAQUS is used for finite element modelling in this study. 2D plane stress shell elements are used for concrete frame elements while truss elements are used for the reinforcing longitudinal bars. A 4-node bilinear plane stress quadrateral element (CPS4R) with reduced integration is used for concrete columns and beams. Approximate mesh size of 80 mm is used for all the frame elements while the thickness of the element depends on the respective thickness of the frame members. For reinforcing bars, 2-node linear shear flexible beam elements (B21) in a plane are used. Approximate mesh size for the reinforcing bar elements is 80mm. The reinforcement is layered in the frame elements through embedment. The cross-sectional properties of the elements are calculated from combined reinforcement bar areas for each layer since the frame is modelled in two dimensions (2D).

Frame members (i.e. the columns, beams and reinforcement bars) are modelled separately and assembled together in assembly module of the ABAQUS using appropriate definition of constraints. For beam-column connection, tie connections are used that allow for constraining rotational DOFs while reinforcing bars are constrained using embedment options where rebars are defined as an embedded region and column/beam as the host region. In both constraint types, default values are used for tolerance definition. Typical assembly for the single storey is shown in Figure 3.9.

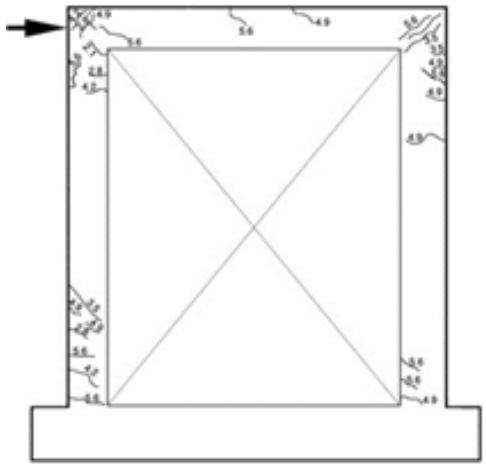

(a) Typical experimental set up (taken from Abdel-Hafez et al. (2015)

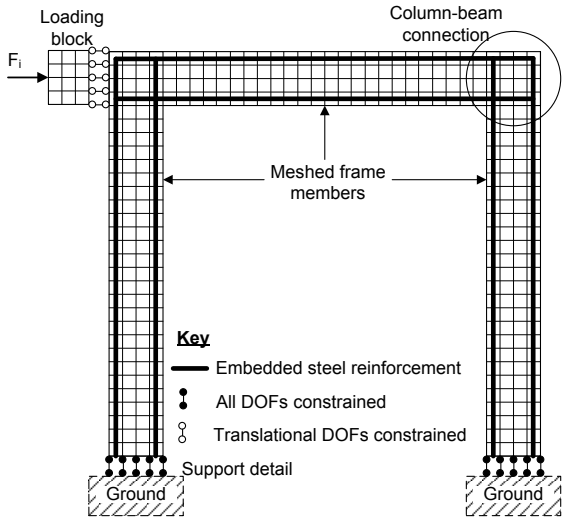

(b) Typical finite element model representation

Figure 3.9: Geometric model for a typical RC bare frame subjected to a lateral load

A concrete damaged plasticity model is used for concrete with plasticity data for dilation angle (ψ), eccentricity (ϵ), the ratio of initial equi-biaxial compressive yield stress to initial uniaxial compressive yield stress (f_{b0}/f_{c0}), K_σ (the ratio of the second stress invariant on the tensile meridian to that on the compressive meridian at initial yield for any given value of the pressure invariant as discussed in ABAQUS documentation (ABAQUS, 2011) assumed as 31°, 0.1, 1.16 and 0.667 respectively. No viscosity is assumed (i.e. zero value is adopted). Yield stress and inelastic strain for concrete in compression and the yield stress and cracking stress in tension are derived from material data established from experimental tests in the literature. For most of the relevant experimental data in this research work reported in literature, not all stress-strain points are readily available. In the case of concrete in compression, the Kent & Park (1971) and the *modified* Kent-Park (Park, et al., 1982) models are selected for unconfined concrete and confined concrete stress-strain behaviour respectively. The confined concrete compressive stress-strain is used for the columns subjected to axial compressive force while the unconfined concrete compression is used for the beams.

Unreinforced concrete is brittle in tension. Provision of reinforcement in concrete improves the softening behaviour due to stiffening effects of the reinforcement. Thus, tensile models with reduced brittleness can be used for the reinforced concrete. In this research a tensile model proposed by Schnobrich (1985) is adopted for all the concrete. Usually very brittle concrete models affect the convergence of the numerical model, hence preventing the generation of a complete solution. However, the model proposed by Schnobrich (1985) offered minimal convergence problems, especially for lowly reinforced concrete sections, while also providing results in close agreement with experimental data. The numerical output for the force vs. deformation characteristics and stress distribution is compared to the experimental output for the force vs. deformation characteristics and crack formation and distribution, wherever available. An elastic perfect plastic material model is used for reinforcing bars. The model requires the Young's modulus of elasticity and the yield stress and plastic ultimate strain data. All this data is taken from experimental tests available in the literature. The typical stress-strain behaviour and corresponding material behaviour for the reinforcing bars used for input into the numerical model are shown in Figure 3.6.

3.4.4 Finite element model for the truss

A trussed system that represents the lateral resistance of the frame is modelled in 2D using wire elements in ABAQUS (2011). Considering that a truss will have uniform sectional stresses (axial stresses), the composite behaviour for the RC frame elements is homogenised first so that uniform stress-strain behaviour for each truss element can be used. The homogenisation of the composite behaviour of the RC elements is provided in Section 5.2.

A2-node linear 2D truss element (T2D2) is used for all the truss members. The length of each truss member is used as mesh size for the respective member since truss elements do not support bending and shear stresses, and load variations within the element due to self-weight are ignored. The geometric data used for the truss is the cross-sectional area of each element. While truss elements representing the columns and the beam use the respective cross-sectional areas as given in the experimental data/parametric definition, the cross-sectional area for the diagonal struts are determined through the frame-truss transformation process discussed in Section 5.3.

A typical finite element model for the truss would be either the use of a single diagonal-strut (DS) or double diagonal-strut (DS1 and DS2) configurations as shown in Figure 3.10. Since the use of the diagonal struts is an approximation based on the force-deformation behaviour, it is assumed that when double diagonal struts are used to represent a bare frame, they should have similar properties. Thus, the material behaviour for either single or double struts is similar with the cross-sectional area the only property that differentiates the two struts configurations. Pinned supports are used for the truss system.

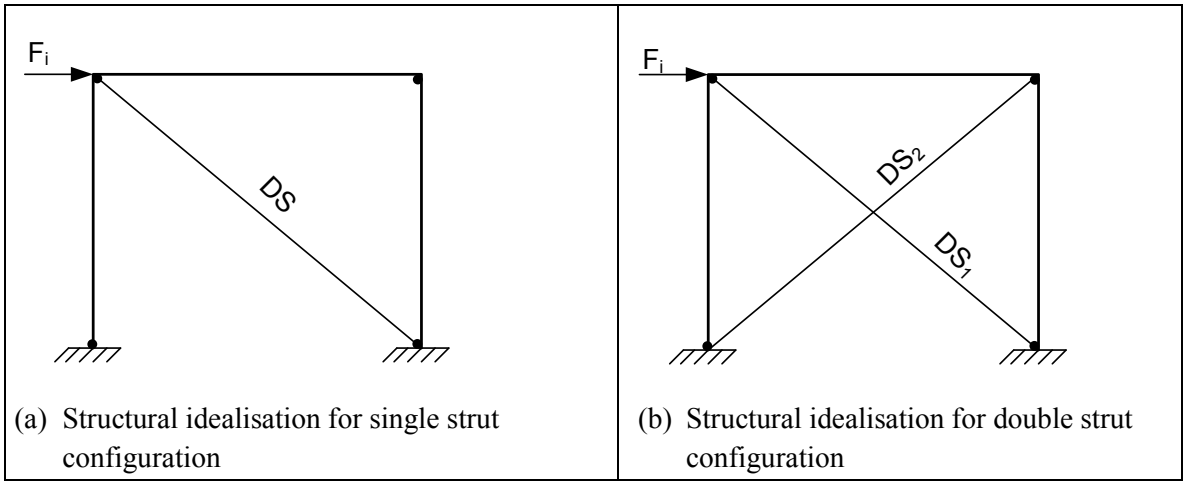

(a) Structural idealisation for single strut configuration

(b) Structural idealisation for double strut configuration

Figure 3.10: Idealisation for a truss model

3.4.5 Evaluation, calibration and verification/validation for the transformed material parameters

Calibration and verification data for the transformed truss system is obtained from both the experimental and numerical studies. Numerical studies offer a wide range of relevant data for calibration and then verification. A set of experimental case studies are identified from literature involving bare frame behaviour. These samples are used to calibrate finite element model for each case study. Having calibrated the numerical model, different factors/features of the FE model are varied to generate data for parametric evaluation. Transformed material behaviour parameters for the truss are determined using different procedures for elastic and plastic behaviours.

Calibration of the diagonal struts used to generate equivalent lateral deformation characteristics for the frame is carried out considering single frame behaviour. Figure 3.11 shows the behaviour of a typical frame subjected to a lateral load. With respect to Figure 3.11, the following deformation and load relationships for the diagonal struts are used:

The length of the diagonal, L_d, is defined as

$$L_d = \frac{L_c}{\sin\theta} \tag{3.1}$$

For an instantaneous horizontal displacement, δ_i, an equivalent displacement the diagonal, δ_{di}, is defined as:

$$\delta_{di} = \delta_i \cos\theta \tag{3.2}$$

The axial strain for the diagonal, ε_{di}, is calculated using equations 3.1and 3.2 as:

$$\varepsilon_{di} = \frac{\delta_{di}}{L_d} = \frac{\delta_i}{L_c} \sin\theta\cos\theta \tag{3.3}$$

The strains at peak elastic deformation and ultimate strength are determined using respective horizontal deformations, δ_e and δ_u in equation 3.3.

For an instantaneous horizontal load, F_i, an equivalent diagonal load, F_{di}, is defined as:

$$F_{di} = \frac{F_i}{\cos\theta} \tag{3.4}$$

The axial stress for the diagonal, σ_{di}, can be calculated considering a diagonal cross-section area, A_d, that is determined using elastic properties of the frame:

$$\sigma_{di} = \frac{F_{di}}{A_d} = \frac{F_i}{A_d \cos\theta} \tag{3.5}$$

The stresses at peak elastic strength and ultimate strength are determined using respective loads, F_e and F_u in equation 3.5.

Using either experimental or numerical data, stress-strain data is established for the equivalent diagonal with a fixed cross-sectional area. This data is used for calibration of the diagonal strut as used from column and beam material properties.

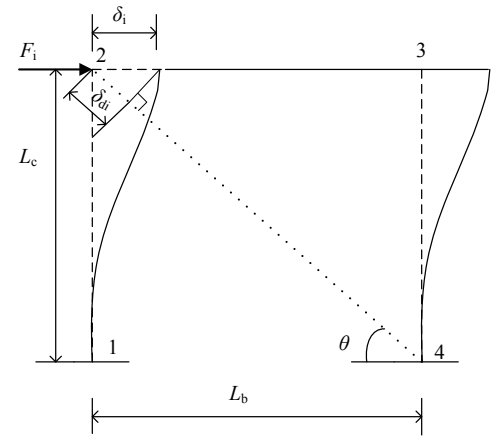

(a) Lateral loading and frame deformation (assuming a stiff beam)

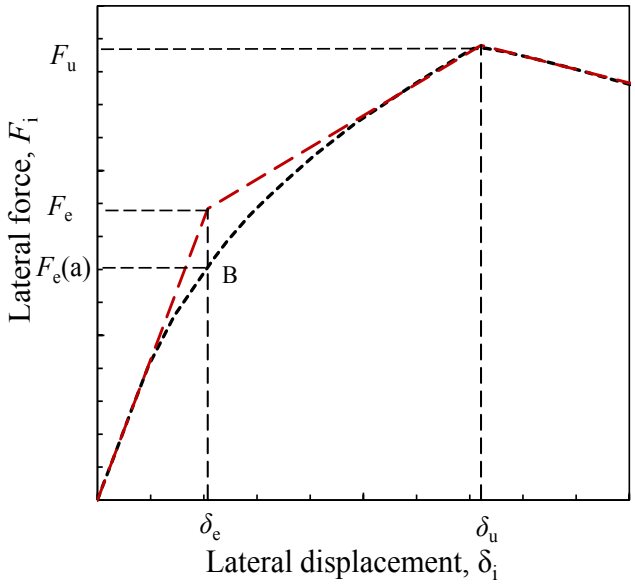

(b) Typical lateral force vs. deformation characteristic for the bare frame

Figure 3.11: Deformation characteristics for the bare frame subjected to a lateral load

Two approaches that are used to establish the key evaluation data from the force-deformation curve for the bare frame, namely:

(a) Tangential stiffness definition; and
(b) Secant stiffness definition.

For the tangential stiffness definition, a tangential line for the initial stiffness, K_e, is defined as the gradient of the curve in the initial third of the curve. Likewise, the plastic tangential stiffness, K_p, that connects the ultimate strength (known) with peak elastic strength (unknown) is established by calculating the gradient of the curve in the last third of the curve from the ultimate value. Mathematically, these definitions can be expressed as follows:

$$K_e = \frac{F_1 - 0}{\delta_1 - 0} \tag{3.6}$$

$$K_p = \frac{F_u - F_2}{\delta_u - \delta_2} \tag{3.7}$$

where

$\delta_1 = \delta_u/3$ and F_1 is the lateral force at the deformation δ_1; and

$\delta_2 = 2\delta_u/3$ and F_2 is the lateral force at the deformation δ_2.

The yielding values (F_e, δ_e) for a tangential stiffness definition are defined by the point where the two tangential lines meet (see Figure 3.11b). However, this approach over-predicts the yield strength as shown (since the deformation curve usually curves downwards). The secant stiffness definition uses the yield deformation point established by the tangential stiffness. The yield strength is then defined by the intersection of the yield deformation line with the force-deformation curve (point B). Secant stiffness lines connect with this intersection point. Mathematically, these definitions are expressed as:

$$K_e = \frac{F_e(a) - 0}{\delta_e - 0} \tag{3.8}$$

$$K_p = \frac{F_u - F_e(a)}{\delta_u - \delta_e} \tag{3.9}$$

where

$F_e(a)$ and δ_e is force and deformation respectively for the intersection point B as shown in Figure 3.11 (b).

Elastic and plastic stiffness for the diagonal strut, defined based on the linearised *F*-δ curve for the strut are calculated using equations 3.10 and 3.11 respectively.

$$K_{de} = \frac{F_{de}}{\delta_{de}} \tag{3.10}$$

$$K_{du} = \frac{F_{du} - F_{de}}{\delta_{du} - \delta_{de}} \tag{3.11}$$

3.5 EVALUATION AND VALIDATION OF THE TRUSS-BASED ANALYSIS PROCEDURE FOR THE INFILLED RC FRAMES

Experimental results for the infill RC single storey single bay frames are used for verification of truss-based system. Since this allows only single storey single bay frames, other structural topologies such as multi-storeys and multi-bays are considered using numerical models. These numerical models are calibrated using experimental data for the single storeys. For the single storey single bay RC frames, the structural behaviour for the frames are established using three distinct methods, namely:

(a) the proposed analytical/semi-analytical method;
(b) the experimental method; and
(c) the numerical methods.

3.5.1 Analytical study (semi-analytical method-proposed method)

The proposed analytical methods determine force or displacement gradients depending on whether force control or displacement control is used. Then, these small changes are scaled using known material properties for the truss elements. The detailed procedure discussion is provided in Section 7.4. The analytical method is implemented in Matlab (see Appendix A2.2 for the pseudo-code used).

3.5.2 Experimental study

Four main experimental data sets are selected from literature for use in this study. They comprise of steel infill frames and RC infill frames as summarised in Table 3.9. Both the steel infill frames and the RC infill frames are used for the evaluation of the proposed model. Steel frames are incorporated for elastic behaviour evaluation only to examine the elastic behaviour transformation for the bare frames. Elastic behaviour of steel is more linear than that of RC. All the selected experimental data involve single storey single bay frames.

Table 3.9: Selected experimental research from literature

Sample Notation	Source of the data	Description	Use of the experimental data
G1	Markulak et al. (2013)	1 sample, steel bare frame	Elastic stiffness evaluation (frame-to-truss transformation)
G2	Dawe & Seah (1989)	1 sample, steel bare frame	Elastic stiffness evaluation (frame-to-truss transformation)
G3	Crisafulli (1997)	1 sample, RC bare- and infill frames	Elastic and plastic behaviour evaluation for both bare and infill frames
G4	Mehrabi et al. (1996)	9 samples, RC bare- and infill frames	Elastic and plastic behaviour evaluation for both bare and infill frames

3.5.2.1 Steel frames experimental data (sample group G1 and G2)

Two samples for steel frames from Markulak et al. (2013) and Dawe & Seah (1989) are used for evaluation of the elastic behaviour of the bare frames. Material properties similar for column and beam, steel sections are used (see Table 3.10).

Table 3.10: Experimental data for steel frames

Characteristics	Sample G1	Sample G2
Material properties	Steel	Steel
Sectional properties	Beam - HEA120 Column - HEA120	Beam - W200 x 46 Column - W250 x 58
Topological properties	L_c = 2167 mm c/c, L_b = 2176 mm c/c, fixed support assumed	L_c = 2800 mm c/c, L_b = 3350 mm c/c, fixed support assumed

3.5.2.2 Crisafulli (1997) experiment description (Sample group G3)

An infill RC frame representing a lower part of a two-storey structure was constructed to a scale of 3/4. RC column and beam with dimensions of 150 mm x 150 mm and 150 mm x 200 mm, respectively, contained the same amount of longitudinal reinforcement (4 No. of 10 mm diameter high strength steel bars (4D10)). D6 (6 mm diameter high strength steel bars) stirrups were spaced between 75 mm c/c to 150 mm c/c, with close spacing around the column-beam connection where a plastic hinge could develop, were used. A summary of the geometric and material properties is given in Table 3.11. The RC infill frame was subjected to a simulated seismic loading. A comprehensive description of the experimental set-up, including loading configuration can be found in Crisafulli (1997).

Table 3.11: Experimental data for RC infill frame (from Crisafulli, 1997)

Attributes	**RC Frame**	**Masonry wall**
Geometric properties	Frame size (c/c): L_c = 2.10 m, L_b = 2.67 m Column: • 150 mm x 150 mm • 4 No. D10 longitudinal rebars • 19D6 stirrups @ 75 mm c/c, • 6D6 stirrups @ 150 mm c/c • d' = 25 mm; d = 125 mm (assumed) Beams: • 150 mm x 200 mm • 4 No. D10 longitudinal rebars • 26 D6 stirrups @ 100 mm c/c • d' = 25 mm; d_{eff} = 175 mm (assumed)	Masonry wall size (edges): • h_w = 2.00 m, l_w = 2.52 m t_w = 0.09 m Solid concrete brick size: • l_b = 230 mm, b = 90 mm, t_b = 75 mm Mortar joint size: • t_j = 10 mm thick
Material properties	Concrete properties at test: • f_{cp} = 22.5 MPa, f_{tp} = 2.4 MPa • E_c = 22.1 GPa Reinforcing steel (D10) • f_{cy} = 323 MPa, ε_{sy} = 0.0016 • E_s = 201.9 GPa • f_{sh} = 323 MPa, ε_{sh} = 0.026 • f_{su} = 441 MPa, ε_{su} = 0.253 Reinforcing steel (D6) • f_{cy} = 353 MPa, ε_{sy} = 0.0017 • E_s = 207.6 GPa • f_{sh} = 353 MPa, ε_{sh} = 0.031 • f_{su} = 466 MPa, ε_{su} = 0.151	Masonry brick: • f_{cp} = 26.2 MPa, E_c =12.9 GPa, • f_{tp} = 2.8 MPa Mortar: • f_{cp} = 8.0 MPa, E_c = 8.54 MPa Masonry prism (h_p/b_p=2.72): • f_{cp} = 19.3 MPa • E_c = 11.55 GPa • τ_o = 0.41 MPa, μ_0 = 0.70

3.5.2.3 Mehrabi et al. (1996) experiment description (Sample group G4)

Mehrabi et al. (1996) conducted experimental research involving infill RC frames. A summary of key data obtained from the experiment is provided in Table 3.12. It should be noted that samples G4(1) to G4(8) were assumed to be weak and had similar amounts and arrangements of reinforcement, while sample G4(9) was assumed to be strong and had different amounts of reinforcement as stated in Table 3.13. Three different reinforcement sizes were used as summarised in Table 3.12. These reinforcement types had the following properties:

(a) Type Y1 had yield strength of 420.7 MPa and ultimate strength of 662.1 MPa;
(b) Type Y2 had yield strength of 413.8 MPa and ultimate strength of 662.1 MPa; and
(c) Type R had yield strength of 367.6 MPa and ultimate strength of 49.6 MPa.

The lengths of the beams and columns (measured centre-to-centre) for samples G4(1) - G4(5), G4(9) are 2311 mm and 1537 mm respectively and for samples G4(6) - G4(8) are 3124 mm and 1537 mm respectively. The breadth and depth of the beam for all the samples are 152 mm x 229 mm respectively,

square columns are used, with size of 203 mm side for sample G4(9) and 178 mm side for the rest of the samples. The infill for samples G4(1), G4(5), G4(8), G4(7) are solid and the rest are hollow.

Table 3.12: Infill RC frame experimental data used for sample group G4 (from Mehrabi et al. 1996) - concrete and masonry

Sample notation	Material properties (f_{cp}, f_{tp}, E_c and τ_0 in MPa)								
	Concrete				Masonry				Brick
	f_{cp}	ε_{cp}	E_c	f_{tp}	f_{cp}	E_c	τ_0	μ_0	f_{cp}
G4(1)	30.87	0.0018	21910	3.29	13.17	9515	0.37	0.65	15.57
G4(2)	26.80	0.0027	17225	2.76	9.26	4596	0.37	0.65	16.47
G4(3)	26.80	0.0027	17225	2.76	8.30	5099	0.37	0.65	16.47
G4(4)	26.80	0.0027	17225	2.76	9.26	8234	0.37	0.65	15.57
G4(5)	20.87	0.0026	18052	1.81	12.09	8943	0.37	0.65	15.57
G4(6)	26.87	0.0021	20119	2.98	9.26	3941	0.37	0.65	16.47
G4(7)	26.87	0.0021	20119	2.98	11.85	7331	0.37	0.65	15.57
G4(8)	25.70	0.0028	18121	3.09	9.98	9598	0.37	0.65	15.57
G4(9)	25.84	0.0024	19843	3.13	8.84	4196	0.37	0.65	16.47

Table 3.13: Infill RC frame experimental data used for sample group G4 (from Mehrabi et al. 1996) - longitudinal and shear reinforcement

Sample notation	Member	Longitudinal reinforcement			Shear reinforcement		
		Number	Type	Size* (mm)	Type	Size*(mm)	Spacing (mm, c/c)
All except G4(9)	Column	8	Y1	12.7	R	6.35	64
	Beam	4	Y2	15.9	R	6.35	76
G4(9)	Column	8	Y2	15.9	R	6.35	76 and 38
	Beam	4	Y2	15.9	R	6.35	76 and 38

*Diameter of the reinforcement

3.5.3 Numerical study

Finite element models calibrated using the experimental data provided under Section 3.5.2, are used to evaluate the structural performance of single storey single bay frames, assumed, in this study, as a basic unit for understanding the behaviour of any structural topology. The four key data points, namely F_e, δ_e, F_u and δ_u are used for verification exercise in addition to the stiffness values along the force-deformation curves.

3.6 SUSTAINABILITY BASED STRUCTURAL EVALUATION FRAMEWORK FOR RESIDENTIAL BUILDINGS

Life cycle assessment procedures are adopted for the sustainability assessment. Integration of the structural performance and the sustainability evaluation is based on the influence of the structural system on the durability or service life of the structure. The integration of the sustainability and structural performance is based on the work of Lepech et al. (2015) for a sustainable repair framework. The basic framework considers probabilistic approaches for the determination of repair impacts and timelines as discussed in Section 2.5.1. Based on the building life cycle as illustrated by Figure 2.12, it

can be assumed that the work of Lepech et al. (2015) tackles the operation phase (excluding the impact from the actual use of the building) and end of life phase. This study uses the framework proposed by Lepech et al. (2015) and includes sustainability evaluation of buildings from pre-use phase of the building. The full integrated framework and its implementation is provided in Chapter 8.

Due to the limitation of the data available and time constraint, only the environmental aspects of the sustainability are considered. A case study-based evaluation of the proposed procedure is carried out as sustainability evaluation requires case-based analysis for implementation. Infill RC framed structures are selected to enable implementation of the proposed structural performance evaluation procedure with sustainability analysis. The residential buildings under study are from the Western Cape Province in South Africa that experience natural seismic activities as illustrated by the seismic hazard map of South Africa provided in the SANS 10160-4 (2011) (see Figure 3.12). The peak ground accelerations with a probability of exceedance of 10% in 50 years are shown. A fictitious multi-storey residential building assumed to exist within the south western region of the Western Cape Province is selected and used for common building modelling. Environmental indicators selected for this case study are emissions, resource depletion and waste generation, prioritised for the building sustainability in the targeted region as proposed by Brewis (2011).

3.6.1 Scope and limitations for the sustainability-based structural system evaluation

(a) The sustainability framework is implemented on infill RC framed residential buildings where buildings are designed based on two design approaches, namely:
    a. incorporation of the contribution of the infill in design
    b. ignoring the contribution of the infill in design

(b) A single deterioration mechanism is considered along with a series of limit states for defining the service life model. Initiation of corrosion due to chloride ingress is the only limit state considered.

(c) Environmental impacts of the selected system from construction, repair (during operation) are considered but impacts associated with individual persons are excluded.

(d) Comparison of the considered structural system is assumed on the compliance of each system with the code requirements for structural design and construction and subsequent repairs through the building life. Thus, a minimum level of structural safety required by the codes is maintained throughout the infrastructure life cycle.

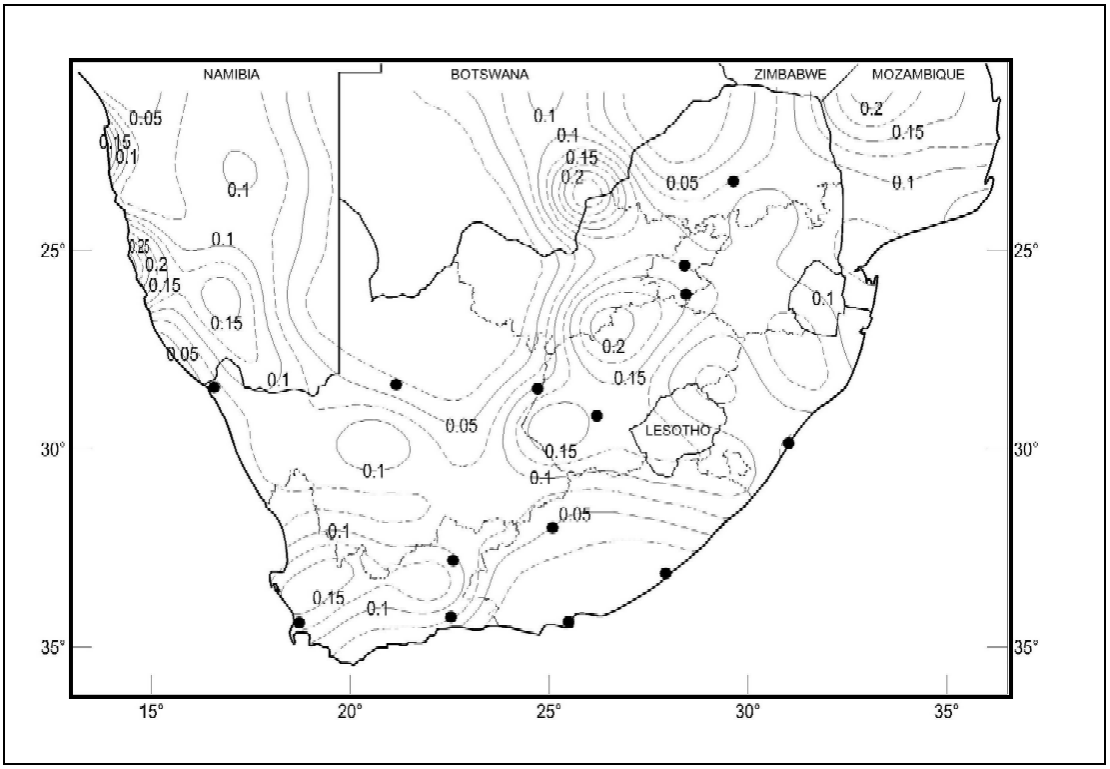

Figure 3.12: Seismic hazard map of South Africa - peak ground acceleration is expressed in earth gravity acceleration, *g* (SANS 10160-4, 2011)

3.7 SUMMARY

A comprehensive methodology is developed to allow for a systematic development of analytical models for material characterisation and infill frame behaviour evaluation. Detailed procedures followed for validation of the proposed models have been discussed. The inconsistencies of the experimental data for infill frames have been addressed by specifically limiting acceptable variability using consistency factor. While such a development removes extremely variant experimental data, which can be assumed to occur due to construction or production errors, there is a need for a comprehensive evaluation of more data so that mean consistency factors are derived from a population of the respective category. Furthermore, there is need for provision of practical implication when using the proposed models validated from specifically qualified data.

CHAPTER 4

4.0 MATERIAL BEHAVIOUR CHARACTERISATION OF MASONRY INFILL FOR MACRO-MODELLING

4.1 INTRODUCTION

As has been highlighted in Chapter 2, various analytical models exist that can be used for the determination of both the material and geometric properties of equivalent struts of the infill frame macro-models. Most of these models were developed based on either the elastic properties of the frame and infill, or the plastic properties of the frame and infill. While elastic-to-brittle failure behaviours for the infill are implicitly assumed for most of these infill behaviour models, those that assume non-brittle behaviour are developed based on assumed overall infill behaviour of the infill and not the behaviour of infill within each zone of critical stress dominance. This generates variability in model predictions and makes it difficult to establish a reliable and generalised material model for the equivalent strut that can be useful in the post-elastic behaviour for the infill. Furthermore, the existing macro-models consider only the governing failure mode. This essentially removes the possibility of observing multi-mode behaviour of the infill with increase in lateral load. It is against this background that this paper seeks to establish a feasible and rational means of characterising the equivalent strut properties so that the material behaviour of the equivalent strut can reflect multiple dominant modes of failure during nonlinear analysis of the infill frames.

Since existing literature already establishes the key infill behaviour observed through experimental work and numerical studies, this paper uses the observed physical behaviour to model the infill as a layered material with various zones that reflect the major stress states. The use of an equivalent strut along the diagonal makes the zoning of the infill along the diagonal phenomenologically acceptable. Therefore, corner crushing zones, and diagonal compression or cracking zones can be treated as individually homogenised elements in series, while shear sliding occurs along the entire length enhancing the stiffness of the infill through a parallel resisting system.

Systematically selected experimental data from literature (Crisafulli, 1997; Mehrabi, et al., 1996; Dawe & Seah, 1989; Markulak, et al., 2013) have been used to validate the proposed method and help calibrate the finite element models. The FE models are used to increase the amount of available data for parametric evaluation of the proposed characterisation procedure for the equivalent strut. A FEM capable of predicting the pre-peak and post-peak response of masonry walls subjected to lateral-in-plane loading, with boundary confinement due to surrounding frame can be used to expand available experimental data for masonry infills. Either a discrete crack approach or smeared crack approach is used for the analysis of structures made of quasi-brittle materials such as masonry and concrete (Lofti & Shing, 1991). A smeared crack approach is simpler and has a better computational efficiency than a discrete method. However, the smeared crack model has some challenges that must be considered when it is used. These challenges include mesh-size dependency of the numerical solution, failure to capture diagonal shear cracking, directional bias and spurious kinematic modes and stress locking (Bazant, 1976; Cervenka & Gerstle, 1972; Rots & Blaauwendraad, 1989). Various solutions have been proposed and outlined in literature to overcome the challenges (Bazant, 1985; Bazant & Oh, 1983). In the numerical study, numerical simulations for masonry behaviour are carried out using ABAQUS (2011). Non-linear behaviour for concrete (and reinforced concrete) and other quasi-brittle materials is modelled using the damaged plasticity models.

4.2 EQUIVALENT STRUT MACRO-MODEL CHARACTERISATION

The proposed material behaviour characterisation for the equivalent strut is developed based on the following premises:

(a) The behaviour of the infill is dominated by the failure modes established in literature. Thus, corner crushing mode (CC) for the loaded corners which are subjected to biaxial compressive stresses and any other contact stresses; diagonal compression mode (DC) for the middle zone subjected to diagonal compressive stresses and shear sliding mode (SS) for the whole length of the infill subjected to shear sliding stresses. These zones are demarcated as shown in Figure 4.1.

(b) The equivalent strut width, w_d, is incorporated in the overall strut property characterisation process so that various analytical models that give variations in the strut width can be re-calibrated to give similar behaviour through material behaviour normalisation. Typically, the stress flow in the plates follows the Flamant-Boussinesq distribution (Flamant, 1892). However, the assumption of a constant cross section, with width, w_d, considers an average and constant stress distribution both across the section and along the length of the equivalent strut. This assumption has been widely used by various researchers as it provides a reasonable approximation of the overall infill behaviour (Adukadukam & Sengupta, 2013; Catherin, et al., 2013; Crisafulli, 1997; FEMA 356, 2000; Liauw & Kwan, 1985; Mainstone, 1971).

(c) Each stress zone must have its length. The determination of the length of each stress zone is important in establishing the overall equivalent strut stiffness and stiffness degradation. A multi-linear stress-strain material model for each stress zone is used in developing an equivalent strut multi-linear stress-strain curve.

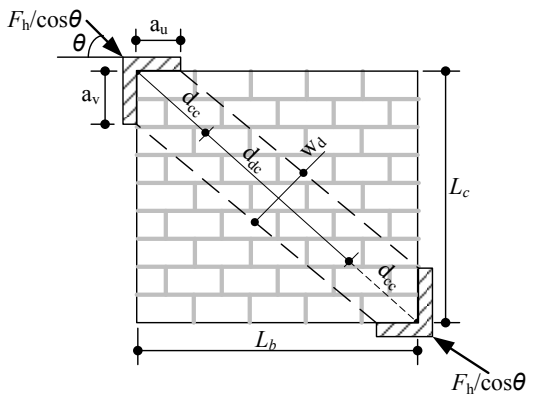

(a) Configuration for the derivation of macro-model equivalent strut parameters (for *CC* and DC modes)

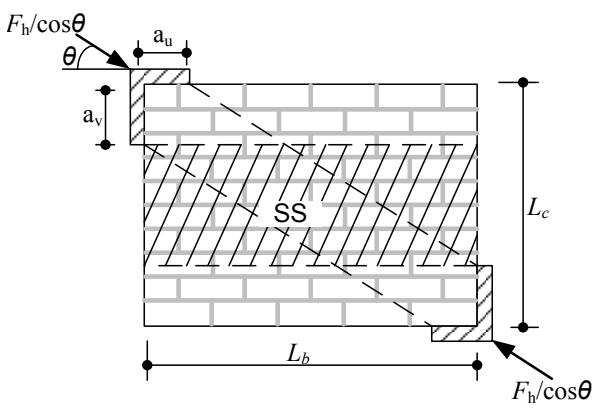

(b) Configuration for the derivation of macro-model equivalent strut parameters (for *SS* mode effective region)

Figure 4.1: Configuration for the derivation of macro-model equivalent strut parameters

4.2.1 Determination of the length of each dominant stress zone

The total equivalent strut (infill diagonal) length, L_d, is divided into three lengths comprising corner crushing region (d_{cc}) and diagonal compression region (d_{dc}) based on common infill behaviour as discussed in Section 2.2.2 (see Figure 4.1). Thus,

$$L_d = 2d_{cc} + d_{dc} \Rightarrow L_d = \sqrt{L_b^2 + L_c^2} \qquad (4.1a,b)$$

where

$d_{cc} = \alpha_{cc} L_d$ and $d_{dc} = (1 - 2\alpha_{cc}) L_d$; and (4.2a, b)

d_{cc} is the length of the corner crushing region;

α_{cc} is the ratio of the length of a corner crushing zone to the total diagonal strut length; and

d_{dc} is the length of equivalent strut portion representing the region under diagonal compression.

The value of α_{cc} can be determined through numerical calibration for individual cases. However, an approximation of d_{cc} can be determined by assuming that d_{cc} is the diagonal length of a rectangular corner region formed by the contact lengths as follows:

$$d_{cc} \approx \sqrt{a_u^2 + a_v^2} \tag{4.3}$$

where

$a_u = \lambda_b L_b$ and $a_v = \lambda_c L_c$ (4.4a,b)

λ_b and λ_c are contact length parameters determined using expressions given in Table 2.6 ($\lambda_c = \pi / 2\lambda$).

Substituting equation 4.4 into equation 4.3 and then substituting for d_{cc} and L_d in equation 4.2a gives the expression for α_{cc} as follows:

$$\alpha_{cc} = \sqrt{\frac{\alpha_b^2 + r_a^2 \alpha_c^2}{1 + r_a^2}} \tag{4.5}$$

where r_a is the infill frame aspect ratio, L_c / L_b .

A fixed value for the corner crushing zone length factor, α_{cc}, is assumed across all stress states. However, it is possible to implement a flexible length factor that can vary across various stress states.

4.2.2 Material characterisation of dominant stress zones

Existing material characterisation for the infill that has been developed to both identify the mode of failure and the capacity of the infill has been adopted with minor modifications. The choice and modification are based on the ability of the analytical model to capture the possible forces involved in the failure mode and allow transformation of that force into the axial load. For corner crushing and diagonal compression failure, relevant expressions (equations 2.11 and 2.14) may be used to evaluate the relevant failure behaviour. The failure formulations for both corner crushing and diagonal compression can be assumed to represent local behaviour and hence ideal for characterising the material behaviour in the respective stress zones. The shear failure formulation proposed by Crisafulli (1997) as provided in equations 2.15 and 2.16 provides a systematic evaluation of shear behaviour from principally a material point of view without incorporation of the geometric properties of the infill and the equivalent diagonal strut. Failure of the analytical model to incorporate the actual shear slip surface makes it difficult to evaluate the shear force contribution by the infill and compare its performance with other models through physical interpretation of the behaviour. The shear-slip failure model as proposed by Crisafulli (1997) is modified to incorporate the shear slip surface and hence link with the diagonal strut width as discussed in the next subsection.

4.2.2.1 Sliding shear failure

While some material properties and geometric properties were derived independent of each other, the concept of equivalent strut should fundamentally link material and geometric properties together as it

is premised on stiffness contribution of the infill. Figure 4.2 illustrates the possible linkages between geometric properties and material properties to establish the axial resisting force of the equivalent strut. Note that only a plane of shear failure is indicated with the assumed shear and normal forces acting on the plane.

From the figure, the width of the plane of normal stress and shear stress are related to the width of the equivalent strut as:

$$w_n = w_{ss} = \frac{w_d}{\sin\theta} \tag{4.6}$$

Therefore, the shear resisting force represented in the transformed diagonal stress relates to the area $w_n t_w$, where w_n is the length of effective shear stress region. An evaluation of shear stress development using numerical studies is conducted to establish the shear stress patterns; influencing normal stresses and tipping point of failure that should help establish the mean shear strength that can be used in equivalent strut modelling. Once an improved and systematic shear zone is established through this process, linkage with equivalent diagonal properties is developed.

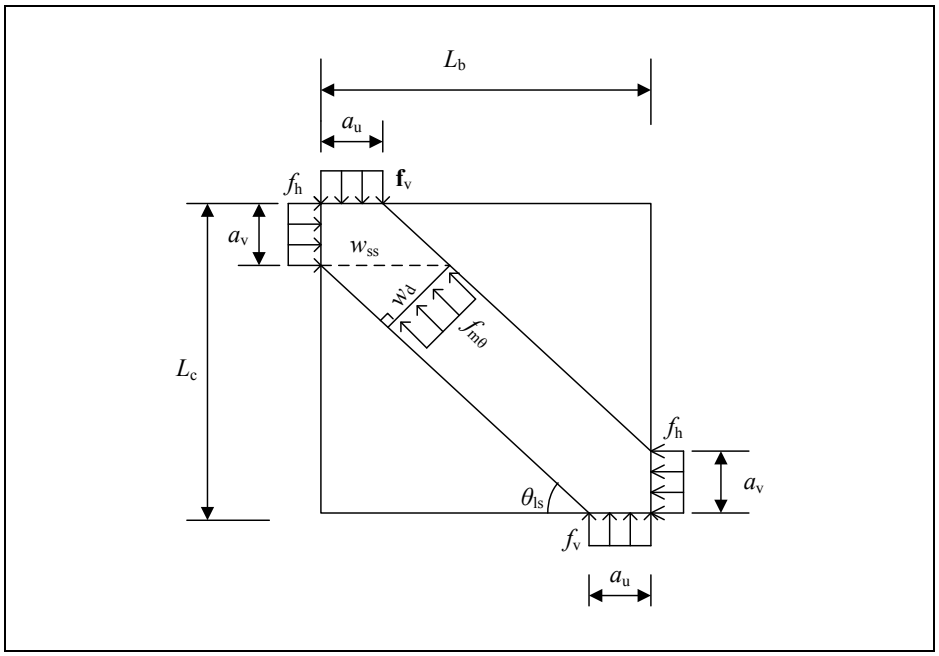

Figure 4.2: Typical equivalent diagonal strut geometric properties

Lack of direct relationship between the equivalent strut width (area) and the material properties may be one of the sources of uncertainties and variations in the equivalent strut shear-based strength predictions for the existing equivalent-strut material models. This section proposes some linkage between the geometric properties and material properties for the equivalent strut models through zoning and improved calibration of material zone properties and subsequent overall strut properties.

The shear slip failure of the infill can occur along the horizontal bed joint of the masonry or through stepped form. In this formulation, it is assumed that the shear slip failure is initiated adjacent to the applied horizontal load (point A_1, Figure 4.3(a)) and can progress through following different averaged

paths. It is assumed that the slip failure path can occur at angle Θ_{ss}, where the angle ranges from 0 to Θ_{ef} as shown in Figure 4.3(b).

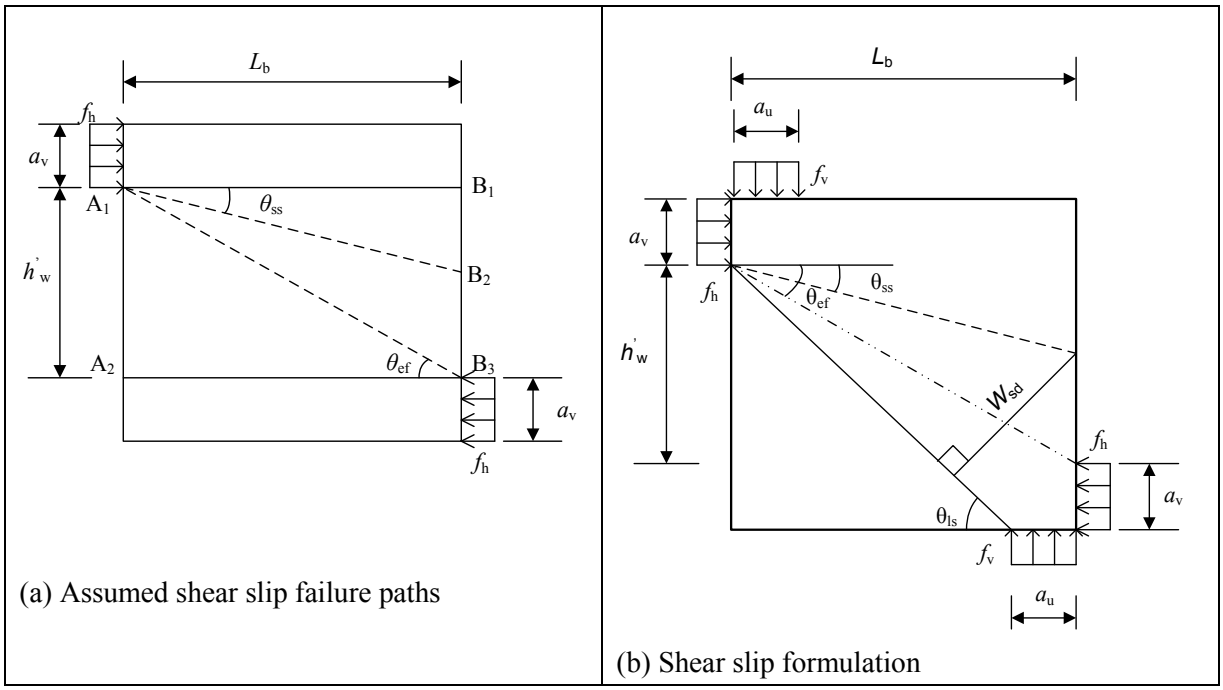

(a) Assumed shear slip failure paths

(b) Shear slip formulation

Figure 4.3: Sliding shear zone material formulation

With respect to Figure 4.3(b), if the shear strength is considered along the shear slip failure zone, that normal compressive stress is applied normal to the plane of shear slip failure and following the procedure used by Crisafulli (1997), key parameters are derived as follows:
The length of shear slip zone, w_{ss}, and its corresponding equivalent width for the diagonal strut, w_{sd}, are defined respectively using equations 4.7 and 4.8:

$$w_{ss} = \frac{l_w}{\cos\theta_{ss}} \tag{4.7}$$

$$w_{sd} = w_{ss}\sin(\theta_{ls} - \theta_{ss}) \tag{4.8}$$

where shear slip angle, Θ_{ss}, varies from 0 to Θ_{ef}

For the equivalent strut width, w_d, determined using any method (based on various failure modes), a relationship with the strut width derived from the shear zone is proposed so that equivalent strut width is kept constant while changing the shear strength parameters.

Shear force per unit width, f_{sh} is defined as:

$$f_{sh} = \tau_0 w_{ss} \tag{4.9}$$

Equivalent diagonal force per unit width reflecting the shear force as in equation 4.9 is:

$$f_{m\theta}^{ss} = f_{m\theta} w_{sd} = f_{m\theta}\xi_{ss} w_d \tag{4.10}$$

where

$$\xi_{ss} = \frac{w_{sd}}{w_d};\ \tau_{av}^{*} = \xi_{ss}\tau_0^{*};\ \text{and}\ f_{m\theta}^{ss} = \frac{\tau_{av}^{*}}{\sin\theta\left(\cos\theta - \mu^{*}\sin\theta\right)}$$

Factor ξ_{ss} is used to ensure that the width of the diagonal strut is the same for all zones. The diagonal axial force from shear slip resistance is given by equation 4.11.

$$F_{m\theta}^{ss} = f_{m\theta} w_d t_w \tag{4.11}$$

4.2.3 Determination of equivalent strut stiffness

Equivalent strut material behaviour can be established by considering the stiffness contribution from each stress zone. Each zone is assumed to have unique stress-strain behaviour that contributes to instantaneous stiffness (tangential stiffness) of the zone at various deformation levels. The equivalent strut material behaviour is calibrated from a stiffness-based formulation, with each zone's instantaneous stiffness represented by a nonlinear spring. The instantaneous stiffness for each of the nonlinear springs are K_{cc}, K_{dc} and K_{ss} representing corner crushing zone, diagonal compression zone and shear sliding zone respectively. The nonlinear springs for the corner crushing zone and that of diagonal compression are connected in series while the nonlinear spring representing shear sliding is connected parallel to the corner crushing and diagonal compression springs in a 1D problem (see Figure 4.4).

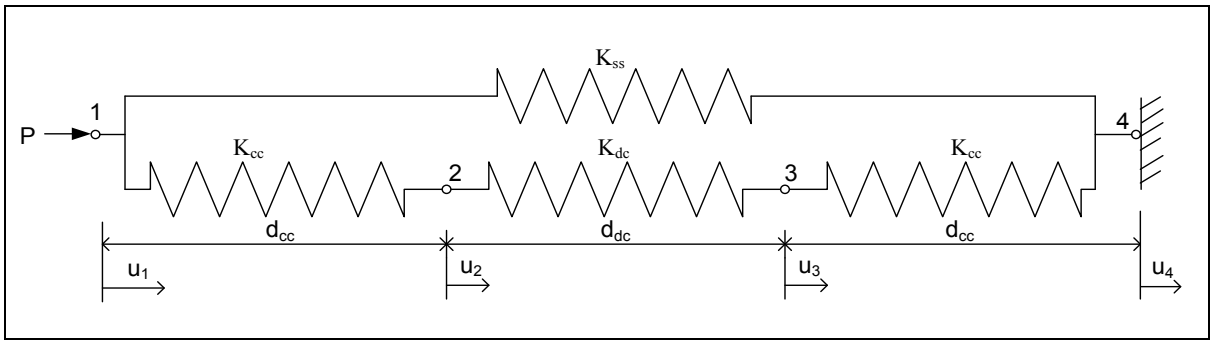

Figure 4.4: One-dimensional idealization for dominant stress-based zones

With respect to Figure 4.4, the overall strut system stiffness within elastic range is derived as follows:

$$\begin{Bmatrix} P \\ 0 \\ 0 \\ F_4 \end{Bmatrix} = \begin{bmatrix} K_{cc}+K_{ss} & -K_{cc} & 0 & -K_{ss} \\ -K_{cc} & K_{cc}+K_{dc} & -K_{dc} & 0 \\ 0 & -K_{dc} & K_{dc}+K_{cc} & -K_{cc} \\ -K_{ss} & 0 & -K_{cc} & K_{cc}+K_{ss} \end{bmatrix} \begin{Bmatrix} u_1 \\ u_2 \\ u_3 \\ 0 \end{Bmatrix} \tag{4.12}$$

Ignoring the fourth row and column and corresponding force, F_4, in order to condense degree of freedom (DOFs) u_2 and u_3 into DOF u_1:

$$\{P\} = \left[K_{cc}+K_{ss}\right]\{u_1\} + \begin{bmatrix} -K_{cc} & 0 \end{bmatrix}\begin{Bmatrix} u_2 \\ u_3 \end{Bmatrix} \tag{4.13}$$

$$\begin{Bmatrix} 0 \\ 0 \end{Bmatrix} = \begin{bmatrix} -K_{cc} \\ 0 \end{bmatrix}\{u_1\} + \begin{bmatrix} K_{cc}+K_{dc} & -K_{dc} \\ -K_{dc} & K_{cc}+K_{dc} \end{bmatrix}\begin{Bmatrix} u_2 \\ u_3 \end{Bmatrix} \tag{4.14}$$

Making $\{u_2\ u_3\}^{\mathrm{T}}$ the subject in equation (4.14) gives

$$\begin{Bmatrix} u_2 \\ u_3 \end{Bmatrix} = -\left[\begin{bmatrix} K_{cc}+K_{dc} & -K_{dc} \\ -K_{dc} & K_{cc}+K_{dc} \end{bmatrix}^{-1}\begin{bmatrix} -K_{cc} \\ 0 \end{bmatrix}\right]\{u_1\} \tag{4.15}$$

Substituting equation (4.15) into (4.13) gives

$$\{P\}=\left(\left[K_{cc}+K_{ss}\right]+\left[-K_{cc}\quad 0\right]\left[\begin{matrix}K_{cc}+K_{dc} & -K_{dc}\\ -K_{dc} & K_{cc}+K_{dc}\end{matrix}\right]^{-1}\left[\begin{matrix}-K_{cc}\\ 0\end{matrix}\right]\right)\{u_1\} \tag{4.16}$$

The effective equivalent strut stiffness (K_{seq}) in the condensed DOF u_1 is as follows:

$$K_{seq}=K_{cc}+K_{ss}-\frac{K_{cc}^2\left(K_{cc}+K_{dc}\right)}{K_{cc}^2+2K_{cc}K_{dc}}=\frac{K_{cc}K_{ss}+K_{cc}K_{dc}+2K_{dc}K_{ss}}{K_{cc}+2K_{dc}} \tag{4.17}$$

Thus $P=K_{seq}u_1$ (4.18)

For the elastic loading range, all these stiffness values are constant. When these regions enter the nonlinear loading range, the stiffness will change to reflect the instantaneous tangential stiffness of the current stress state. Thus, a stress-strain material model representative of each region is used to establish instantaneous stiffness for each region. If the nodal displacement in the local strut axis at the point of load application is known (u_1), the local strains in the corner crushing zone and diagonal compression zone can be determined as:

$$\varepsilon_{cc}=\frac{-K_{dc}}{\left(K_{cc}+2K_{dc}\right)}\frac{u_1}{d_{cc}} \tag{4.19}$$

$$\varepsilon_{dc}=\frac{-K_{cc}}{\left(K_{cc}+2K_{dc}\right)}\frac{u_1}{d_{dc}} \tag{4.20}$$

$$\varepsilon_{ss}=\frac{u_1}{d_s} \tag{4.21}$$

The stiffness method involving nonlinear springs connected in series may require more detailed and sometimes different formulations to that given in the above due to variations in the stress-state combinations. For a tri-linear material model with each zone as assumed in Section 4.2.4, there could be up to nine (9) possible combinations of the stress states which the nonlinear springs may experience during compressive loading as summarised in Table 4.1. The combinations are derived from the assumed material model for the springs. Each loading state or case is discussed, and relevant formulae are derived for effective spring stiffness for the series. The stiffness and strain formulae are determined based on force equilibrium and strain compatibility principles. Table 4.1 also provides useful conditions within which these formulae are derived as discussed in subsequent paragraphs. It should be noted that all formulations assume a constant cross-sectional area and uniform stress for each zone throughout all the stress states. Thus, the stress-strain characteristic is like the force-deformation characteristic for each respective stress zone. The loading state cases stated in the Table 4.1 are illustrated in Figure 4.5.

Table 4.1: Possible loading states for the nonlinear springs in series

Diagonal compression element (DC zone)	**Compression crushing element (CC zone)**		
	Ascending curve	Constant curve*	Descending curve
Ascending curve	Case 1: stiffness useful; load increment	Case 2: stiffness not useful; constant load; $u_{DC}=0$	Case 3: stiffness useful; pre-peak elastic load reversal for DC
Constant curve*	Case 4: stiffness not useful, constant load; $u_{CC}=0$	Case 5: zero stiffness, constant load	Case 6: stiffness useful; post-peak elastic reversal for DC
Descending curve	Case 7: stiffness useful pre-peak elastic load reversal for CC	Case 8: stiffness useful; post-peak elastic reversal for CC	Case 9: stiffness useful; load increment

*For perfect plastic material behaviour

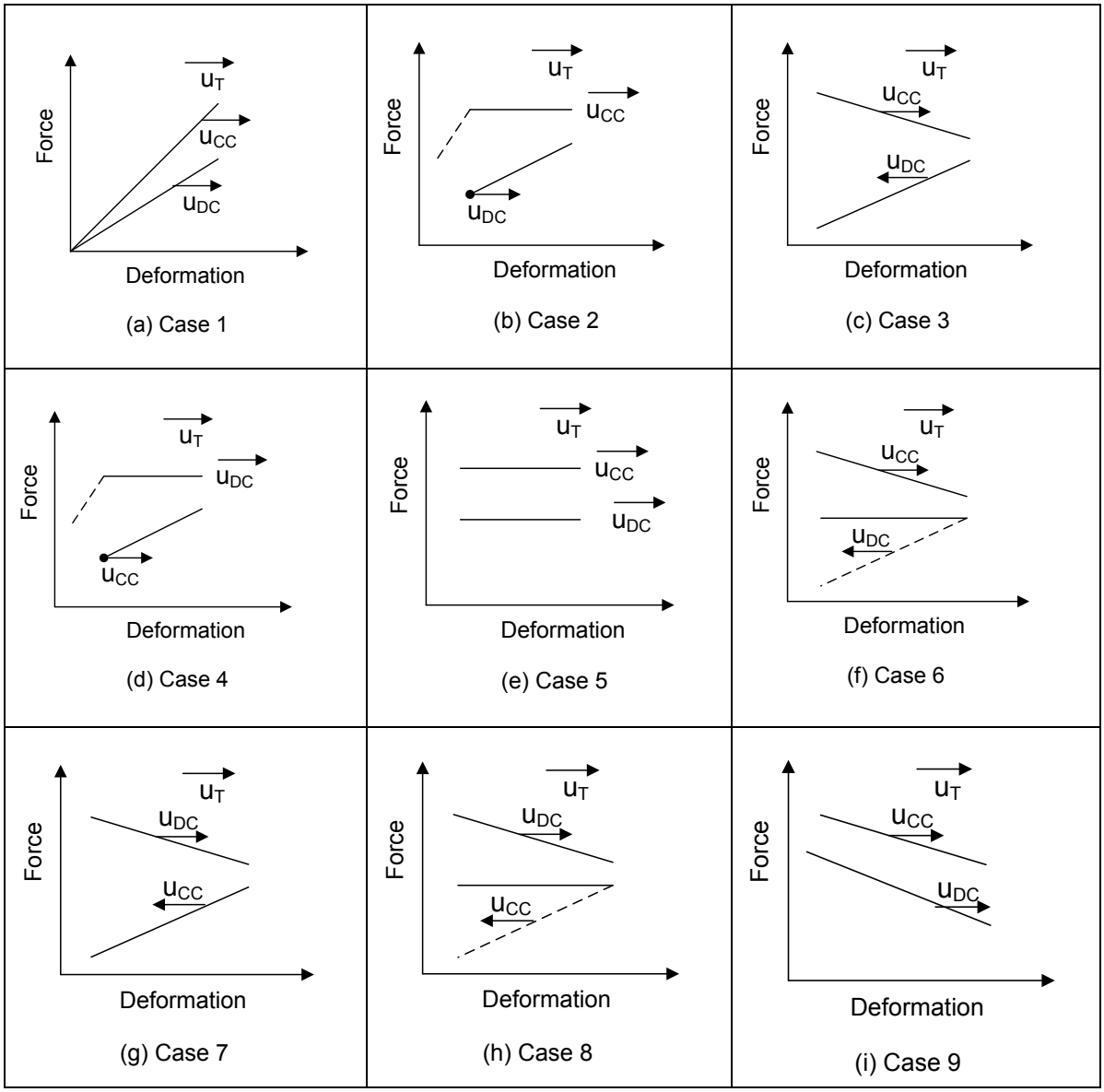

Figure 4.5: Possible stress state combinations for two non-linear springs connected in series

Case 1: Ascending curves for both CC and DC zones

In this loading regime, both zones have positive stiffness and therefore they will resist any applied load. An increment in deformation generates additional load to the series system. This is a typical elastic stiffness problem. Considering symmetry, the equilibrium of forces and kinematic principles (as illustrated in Figure 4.5a) are used to derive effective series spring stiffness, strains for each zone and overall strut stiffness as follows:

Equilibrium of forces:

$$F_{CC} = F_{DC} = F_T \tag{4.22}$$

Kinematic principle

$$u_T^* = u_{CC} + u_{DC} \tag{4.23}$$

Each deformation can be expressed in terms of the applied force and corresponding stiffness:

$$u_T^* = \frac{F_T}{K_{seq}^*};\ u_{CC} = \frac{F_T}{K_{cc}};\ u_{DC} = \frac{F_T}{K_{dc}^*} \tag{4.24}$$

where

K_{seq}^* is effective stiffness for the symmetric portion of the series springs

$K_{cc} = \frac{E_{cc}A_{cc}}{d_{cc}}$ is the stiffness for the full CC zone;

$K_{dc}^* = \frac{E_{DC}A_{DC}}{0.5d_{CC}} = 2K_{dc}$ is the stiffness for the symmetrical section of the DC zone (i.e. half zone length) and K_{dc} is the stiffness of the full length of the DC zone;

Substituting equation 4.24 into 4.23 and solving for K_{seq}^* gives

$$K_{seq}^* = \frac{2K_{cc}K_{Ddc}}{K_{cc} + 2K_{dc}} \tag{4.25}$$

The effective stiffness for the full subsystem in series (K_{seq}) is determined as follows:

$$\frac{1}{K_{seq}} = \frac{2}{K_{seq}^*} \Leftrightarrow K_{seq} = \frac{K_{cc}K_{dc}}{K_{cc} + 2K_{dc}} \tag{4.26}$$

Incorporating the shear stiffness, K_{ss} , acting in parallel, the overall stiffness for the equivalent strut, K_{eq}, is

$$K_{eq} = K_{SS} + \frac{K_{cc}K_{dc}}{K_{cc} + 2K_{dc}} \tag{4.27}$$

Strain in each zone is calculated as follows:

$$\varepsilon_{cc} = \frac{u_T K_{seq}}{d_{cc}K_{cc}} = \frac{u_T}{d_{cc}} \frac{K_{dc}}{K_{cc} + 2K_{dc}};\ \varepsilon_{dc} = \frac{u_T K_{seq}}{d_{dc}K_{dc}} = \frac{u_T}{d_{dc}} \frac{K_{cc}}{K_{cc} + 2K_{dc}};\ \varepsilon_{SS} = \frac{u_T}{d_{SS}} \tag{4.28}$$

where

$\varepsilon_{cc}, \varepsilon_{dc}$ and ε_{SS} are the strains for the CC zone, DC zone and SS zone respectively;

d_{cc}, d_{dc} and d_{SS} are the lengths for the CC zone, DC zone and SS zone respectively.

Case 2: Ascending curve for DC zone and constant curve for CC zone

Case 2 loading regime describes a scenario whereby CC zone reaches perfect plastic state while DC zone is still in elastic state. Since any increase in system deformation would have no corresponding load increase in CC zone due as it is perfect plastic, no increment in deformation is expected in DC zone to ensure force equilibrium. Therefore, in this loading regime system stiffness will not be useful for deformation or strain calculation. Considering symmetry, the equilibrium of forces and kinematic principles (as illustrated in Figure 4.5b), the following relationships are established:

Equilibrium of forces:

$$F_{CC} = F_{DC} = F_T \text{ (constant)} \tag{4.29}$$

Kinematic principle

$$u_T^* = u_{CC} + u_{DC} \tag{4.30}$$

Assuming $u_{DC} = 0$; $\therefore u_T^* = u_{CC} \Leftrightarrow u_{CC} = 0.5u_T$ (4.31)

Therefore, the strains in CC zone, DC zone and SS zone are respectively as follows:

$$\varepsilon_{cc} = \frac{0.5u_T}{d_{cc}} \; ; \; \varepsilon_{dc} = 0 \text{ and } \varepsilon_{ss} = \frac{u_T}{d_{ss}} \tag{4.32}$$

Case 3: Ascending curve for DC zone and descending curve for CC zone

In this loading regime, DC zone is in elastic stress state while CC zone is in post peak state, whereby it is releasing the load with increment in deformation. To ensure that force equilibrium is achieved, the DC zone releases the load but with reduction in the deformation. Thus, the direction of deformation in these zones will be opposite to each other (see Figure 4.5c). Considering symmetry, the equilibrium of forces and kinematic principles are used to derive effective series spring stiffness, strains for each zone and overall strut stiffness:

Equilibrium of forces:

$$F_{CC} = F_{DC} = F_T \tag{4.33}$$

Kinematic principle

$$u_T^* = u_{CC} - u_{DC} \tag{4.34}$$

Each deformation can be expressed in terms of the applied force and corresponding stiffness as:

$$u_T^* = \frac{F_T}{K_{seq}^*} \; ; \; u_{CC} = \frac{F_T}{K_{cc}} \; ; \; u_{DC} = \frac{F_T}{K_{dc}^*} \tag{4.35}$$

Substituting equation 4.35 into 4.34 and solving for K_{seq}^* gives

$$K_{seq}^* = \frac{2K_{cc}K_{dc}}{K_{cc} - 2K_{dc}} \tag{4.36}$$

The effective stiffness for the full subsystem in series (K_{seq}) is:

$$\frac{1}{K_{seq}} = \frac{2}{K_{seq}^*} \Leftrightarrow K_{seq} = \frac{K_{cc}K_{dc}}{K_{cc} - 2K_{dc}} \tag{4.37}$$

Incorporating the shear stiffness, K_{ss} , acting in parallel, the overall stiffness for the equivalent strut, K_{eq}, is

$$K_{eq} = K_{ss} + \frac{K_{cc}K_{dc}}{K_{cc} - 2K_{dc}} \tag{4.38}$$

The strain in each zone is calculated using equation 4.39:

$$\varepsilon_{cc} = \frac{u_T}{d_{cc}} \frac{K_{dc}}{K_{cc} - 2K_{dc}} ; \varepsilon_{dc} = \frac{u_T}{d_{dc}} \frac{K_{cc}}{K_{cc} - 2K_{dc}} \; ; \; \varepsilon_{ss} = \frac{u_T}{d_{ss}} \tag{4.39}$$

Case 4: Ascending curve for CC zone and constant curve for DC zone

This case involves the CC zone in elastic state with DC in perfect plastic state. Like Case 2, this is a special case involving a perfect plastic material characterisation model for the stress zones. Any increase in system deformation would have no corresponding load increase in DC zone due as it is perfect plastic. To ensure force equilibrium, DC zone is assumed not to undergo any increment in deformation. Thus, series zones' stiffness is not used for deformation and force calculations. Considering symmetry, the

equilibrium of forces and kinematic principles (as illustrated in Figure 4.5d), the following relationships are established:

Equilibrium of forces:

$$F_{CC} = F_{DC} = F_T \text{ (constant)} \tag{4.40}$$

Kinematic principle

$$u_T^* = u_{CC} + u_{DC} \tag{4.41}$$

Assuming $u_{CC} = 0$; $\therefore u_T^* = u_{DC} \Leftrightarrow u_{DC} = 0.5u_T$ (4.42)

Therefore, the strains in CC zone, DC zone and SS zone are respectively:

$$\varepsilon_{dc} = \frac{0.5u_T}{d_{dc}} \; ; \; \varepsilon_{cc} = 0 \text{ and } \varepsilon_{ss} = \frac{u_T}{d_{ss}} \tag{4.43}$$

Case 5: Constant curves for both CC and DC zones

This is a special case where both zones have zero stiffness and are at the perfect plastic loading regime. The zones can support the same amount of load while undergoing increased deformation. Deformation characteristics are based on the applied deformation only. Considering the equilibrium of forces and kinematic principles (as illustrated in Figure 4.5e), the following relationships are established:

Equilibrium of forces:

$$F_{CC} = F_{DC} = F_T \text{ (constant)} \tag{4.44}$$

Kinematic principle

$$u_T^* = u_{CC} + u_{DC} \tag{4.45}$$

$$K_{cc} = 0 \; ; \; K_{dc} = 0 \tag{4.46}$$

Uniform strain is assumed across all the zones in series. Therefore, the strains in CC zone, DC zone and SS zone are respectively as follows:

$$\varepsilon_{cc} = \frac{u_T}{L_d} \; ; \; \varepsilon_{dc} = \frac{u_T}{L_{ds}} \text{ and } \varepsilon_{ss} = \frac{u_T}{d_{ss}} \tag{4.47}$$

where L_d is the total strut length (equal to d_{ss})

Case 6: Descending curve for CC zone and constant curve for DC zone

DC zone is in perfect plastic stress state while CC zone is in post peak strain softening state. Increase in deformation reduces the load resistance for zone CC hence DC zone must release its load to ensure that force equilibrium is achieved. Thus, the direction of deformation in these zones will be opposite to each other (see Figure 4.5f). The release of the load for DC zone is assumed to follow elastic stiffness path (indicated with dotted lines in Figure 4.5f). Considering symmetry, the equilibrium of forces and kinematic principles are used to derive effective series spring stiffness, strains for each zone and overall strut stiffness as follows:

Equilibrium of forces:

$$F_{CC} = F_{DC} = F_T \tag{4.48}$$

Kinematic principle

$$u_T^* = u_{CC} - u_{DC} \tag{4.49}$$

Each deformation can be expressed in terms of the applied force and corresponding stiffness:

$$u_T^* = \frac{F_T}{K_{seq}^*} \; ; \; u_{CC} = \frac{F_T}{K_{Ccc}} \; ; \; u_{DC} = \frac{F_T}{K_{dc}^*} \tag{4.50}$$

Note that K_{dc}^{*} is calculated using elastic modulus of elasticity.

Substituting equation 4.50 into equation 4.49 and solving for K_{seq}^{*} gives

$$K_{seq}^{*} = \frac{2K_{cc}K_{dc}}{K_{cc} - 2K_{dc}} \tag{4.51}$$

The effective stiffness for the full subsystem in series (K_{seq}) is:

$$\frac{1}{K_{seq}} = \frac{2}{K_{seq}^{*}} \Leftrightarrow K_{seq} = \frac{K_{cc}K_{dc}}{K_{cc} - 2K_{dc}} \tag{4.52}$$

Incorporating the shear stiffness, K_{ss}, acting in parallel, the overall stiffness for the equivalent strut, K_{eq}, is

$$K_{eq} = K_{ss} + \frac{K_{cc}K_{dc}}{K_{cc} - 2K_{dc}} \tag{4.53}$$

The strain in each zone is calculated as follows:

$$\varepsilon_{cc} = \frac{u_T}{d_{cc}}\left(\frac{K_{dc}}{K_{cc} - 2K_{dc}}\right);\ \varepsilon_{dc} = \frac{u_T}{d_{Ddc}}\left(\frac{K_{cc}}{K_{cc} - 2K_{dc}}\right);\ \varepsilon_{ss} = \frac{u_T}{d_{ss}} \tag{4.54}$$

Case 7: Ascending curve for CC zone and descending curve for DC zone

Stress zone CC is in elastic stress state while DC zone is in post peak strain softening state. Force equilibrium is achieved by allowing elastic release of load from zone CC through reduction in its deformation. Thus, the direction of deformation in these zones will be in opposite directions (see Figure 4.5g). Considering symmetry, the equilibrium of forces and kinematic principles are used to derive effective series spring stiffness, strains for each zone and overall strut stiffness as follows:

Equilibrium of forces:

$$F_{CC} = F_{DC} = F_T \tag{4.55}$$

Kinematic principle

$$u_T^{*} = u_{CC} - u_{DC} \tag{4.56}$$

Each deformation can be expressed in terms of the applied force and corresponding stiffness as follows:

$$u_T^{*} = \frac{F_T}{K_{seq}^{*}};\ u_{CC} = \frac{F_T}{K_{cc}};\ u_{DC} = \frac{F_T}{K_{dc}^{*}} \tag{4.57}$$

Substituting equation 4.57 into 4.55 and solving for K_{seq}^{*} gives

$$K_{seq}^{*} = \frac{2K_{cc}K_{dc}}{2K_{dc} - K_{cc}} \tag{4.58}$$

The effective stiffness for the full subsystem in series (K_{seq}) is:

$$\frac{1}{K_{seq}} = \frac{2}{K_{seq}^{*}} \Leftrightarrow K_{seq} = \frac{K_{cc}K_{dc}}{2K_{dc} - K_{cc}} \tag{4.59}$$

Incorporating the shear stiffness, K_{ss}, acting in parallel, the overall stiffness for the equivalent strut, K_{eq}, is

$$K_{eq} = K_{ss} + \frac{K_{cc}K_{dc}}{2K_{dc} - K_{cc}} \tag{4.60}$$

The strain in each zone is calculated as follows:

$$\varepsilon_{cc} = \frac{u_T}{d_{cc}}\left(\frac{K_{dc}}{2K_{dc} - K_{cc}}\right);\ \varepsilon_{dc} = \frac{u_T}{d_{dc}}\left(\frac{K_{cc}}{2K_{dc} - K_{cc}}\right);\ \varepsilon_{ss} = \frac{u_T}{d_{ss}} \tag{4.61}$$

Case 8: Descending curve for DC zone and constant curve for CC zone

Stress zone CC is in a perfect stress state while DC zone is in post peak strain softening state. Force equilibrium is achieved by elastic release of the load from zone CC through reduction in its deformation. The elastic release of the load is selected due to its simplicity as is indicated using dotted lines in Figure 4.5h. The direction of deformation in these zones will be in opposite directions. Considering symmetry, the equilibrium of forces and kinematic principles are used to derive effective series spring stiffness, strains for each zone and overall strut stiffness as follows:

Equilibrium of forces:

$$F_{CC} = F_{DC} = F_T \tag{4.62}$$

Kinematic principle

$$u_T^* = u_{CC} - u_{DC} \tag{4.63}$$

Each deformation can be expressed in terms of the applied force and corresponding stiffness as follows:

$$u_T^* = \frac{F_T}{K_{seq}^*};\ u_{CC} = \frac{F_T}{K_{cc}};\ u_{DC} = \frac{F_T}{K_{dc}^*} \tag{4.64}$$

Substituting equation 4.64 into 4.63 and solving for K_{seq}^* gives

$$K_{seq}^* = \frac{2K_{cc}K_{dc}}{2K_{dc} - K_{cc}} \tag{4.65}$$

The effective stiffness for the full subsystem in series (K_{seq}) is:

$$\frac{1}{K_{seq}} = \frac{2}{K_{seq}^*} \Leftrightarrow K_{seq} = \frac{K_{cc}K_{dc}}{2K_{dc} - K_{cc}} \tag{4.66}$$

Incorporating the shear stiffness, K_{ss} , acting in parallel, the overall stiffness for the equivalent strut, K_{eq}, is

$$K_{eq} = K_{ss} + \frac{K_{cc}K_{dc}}{2K_{dc} - K_{cc}} \tag{4.67}$$

Strain in each zone is calculated as follows:

$$\varepsilon_{cc} = \frac{u_T}{d_{cc}}\left(\frac{K_{dc}}{2K_{dc} - K_{cc}}\right);\ \varepsilon_{dc} = \frac{u_T}{d_{dc}}\left(\frac{K_{cc}}{2K_{dc} - K_{cc}}\right);\ \varepsilon_{ss} = \frac{u_T}{d_{ss}} \tag{4.68}$$

Case 9: Descending curves for both CC and DC zones

Both zones have negative stiffness and therefore any increment in deformation results in loss of resistance for both zones. Considering symmetry, the equilibrium of forces and kinematic principles (as illustrated in Figure 4.5i) are used to derive effective series spring stiffness, strains for each zone and overall strut stiffness as follows:

Equilibrium of forces:

$$F_{CC} = F_{DC} = F_T \tag{4.69}$$

Kinematic principle

$$u_T^* = u_{CC} + u_{DC} \tag{4.70}$$

Each deformation can be expressed in terms of the applied force and corresponding stiffness as follows:

$$u_T^* = \frac{F_T}{K_{seq}^*};\ u_{CC} = \frac{F_T}{K_{cc}};\ u_{DC} = \frac{F_T}{K_{dc}^*} \tag{4.71}$$

Substituting equation 4.71 into 4.70 and solving for K_{seq}^* gives

$$K^*_{seq} = \frac{2K_{cc}K_{dc}}{K_{cc}+2K_{dc}} \tag{4.72}$$

The effective stiffness for the full subsystem in series (K_{seq}) is determined as:

$$\frac{1}{K_{seq}} = \frac{2}{K^*_{seq}} \Leftrightarrow K_{seq} = \frac{K_{cc}K_{dc}}{K_{cc}+2K_{dc}} \tag{4.73}$$

Incorporating the shear stiffness, K_{ss}, acting in parallel, the overall stiffness for the equivalent strut, K_{eq}, is

$$K_{eq} = K_{ss} + \frac{K_{cc}K_{dc}}{K_{cc}+2K_{dc}} \tag{4.74}$$

The strain in each zone is calculated as follows:

$$\varepsilon_{cc} = \frac{u_T}{d_{cc}}\left(\frac{K_{dc}}{K_{cc}+2K_{dc}}\right);\quad \varepsilon_{dc} = \frac{u_T}{d_{dC}}\left(\frac{K_{cc}}{K_{cc}+2K_{dc}}\right);\ \varepsilon_{ss} = \frac{u_T}{d_{ss}} \tag{4.75}$$

4.2.4 Analysis procedure for evaluation of strut force vs. deformation characteristics

A stiffness modification method for nonlinear structural evaluation of truss systems as presented in this section is used to establish the force deformation characteristics of the equivalent strut. Displacement control method based on displacement scaling factor, β_{min}, is used to establish stress-strain state for each element. A tri-linear full stress-strain material model shown in Figure 4.6(a) for each stress zone is adopted to illustrate the formulation procedure. The assumed stiffness for each stress zone is shown in Figure 4.6(b). The initial geometric properties are kept constant throughout the analysis while degradation factor α_{ji} is be used to incorporate material stiffness degradation.

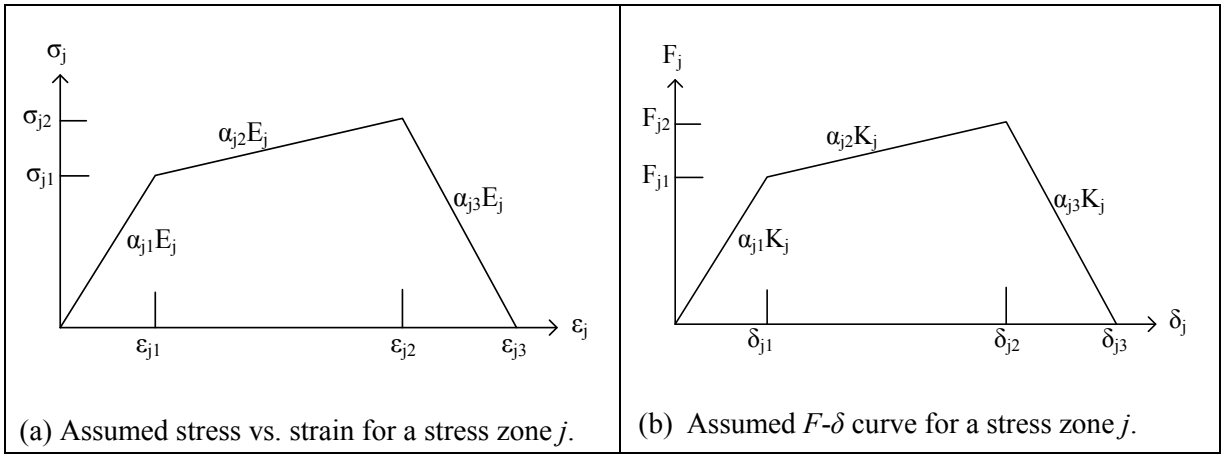

(a) Assumed stress vs. strain for a stress zone *j*.

(b) Assumed *F*-δ curve for a stress zone *j*.

Figure 4.6: Assumed tri-linear material model and key material model parameters

An incremental load and deformation adjustment are adopted as shown in equation 4.76 with additional force determined based on tangential stiffness (α_i) as shown in equation 4.77.

$$F_i = K_{(i\text{-}1)}d_{0(i\text{-}1)} + \Delta F_i \tag{4.76}$$

where

$$\Delta F_i = \alpha_i \Delta d_i \tag{4.77}$$

Appropriate adjustment of the nodal displacement and nodal forces and subsequent element deformation is performed using a deformation scaling factor, β_{min} as follows:

$$\beta_{\min} = \begin{cases} Min\left(\dfrac{\{\varepsilon_{0i}\}}{\{\varepsilon_i\}}\right) & \text{for initial step} \\ Min\left(\dfrac{\{\varepsilon_{0i}\}-\{\varepsilon_i\}}{\{\Delta\varepsilon_i\}}\right) & \text{for all other steps} \end{cases} \tag{4.78}$$

where

$$\{\varepsilon_i\} = [C_\varepsilon]\{d_i\} \tag{4.79}$$

$$\{\Delta\varepsilon_i\} = [C_\varepsilon]\{\Delta d_i\} \tag{4.80}$$

ε_{0i} are strains at which the stress/strain gradient changes (e.g. at cracking, yielding or ultimate strains)

$[C_\varepsilon]$ is a system matrix assembled from individual element transformation as follows:

$$C_{\varepsilon(element)} = \left\{-\frac{1}{L} \quad \frac{1}{L}\right\} \tag{4.81}$$

Nodal force at any change in stress-strain gradient of elements, $\{F_{0i}\}$, corresponding nodal displacements $\{d_{0i}\}$ and elements strains $\{\varepsilon_{0i}\}$ can be determined respectively as follows:

$$d_{0i} = d_{0(i\text{-}1)} + \beta_{\min}\Delta d_i\ ;\ \varepsilon_{0i} = \varepsilon_{0(i\text{-}1)} + \beta_{\min}\Delta\varepsilon_i\ ;\ \Delta F_{0i} = K_{seq}\beta_{\min}\Delta d_i\ ;\ F_{0i} = F_{0(i\text{-}1)} + \beta_{\min}\Delta F_i \tag{4.82}$$

Element stiffness for the biaxially loaded zone (K_{cc}) and diagonally loaded zone (K_{dc}) and shear slip region (K_{ss}) can be calculated respectively as follows:

$$K_{cc} = \frac{E_{cc}A_{cc}}{d_{cc}};\ K_{dc} = \frac{E_{dc}A_{dc}}{d_{dc}} \text{ and } K_{ss} = \frac{E_{ss}A_{ss}}{d_{ss}} \tag{4.83}$$

A summary of the general procedure for nonlinear evaluation of the strut system using displacement control approach are:

(a) Establish initial elements' stiffness using equation 4.77 and calculate assembled stiffness, K_{seq} based on respective stress-strain state as discussed;
(b) Considering an arbitrary incremental displacement, Δd_j, determine corresponding element strains, $\Delta\varepsilon_j$;
(c) Determined the scaling factors, β_{min}, using equation 4.78. Identify the element undergoing change in stiffness;
(d) Determine yield point for the system using equation 4.82;
(e) Adjust the system stiffness, K_{seq}, by replacing the stiffness of the yielded element with the new tangential stiffness;
(f) Repeat steps (b) to (e) until the full force deformation characteristics of the equivalent strut 'system' are established.

A pseudo-code for the material characterisation procedure is developed and used to programme the procedure in Matlab (2015) (see Appendix A2.1).

4.3 PRELIMINARY EVALUATION OF THE PROPOSED INFILL CHARACTERISATION MODEL

A preliminary evaluation of the proposed material characterisation procedure is carried out. Experimental data reported by Crisafulli (1997) is selected for use in this process. Since the proposed

material characterisation procedure incorporates all possible failure modes, the variations in model predictions can be attributed to the variations in the cross-sectional area definitions. Existence of variations formulations for failure mode determination generates additional variability in model prediction as noted in Section 2.3.2. In this section, three formulations for the equivalent strut cross-sectional area were adopted from FEMA 356 (2000), Mainstone (1971) and Liauw & Kwan (1985).

The objective of this section is to evaluate the proposed model, considering the zone material properties established from the analytical material models discussed in Section 2.3.2. This is a useful step towards modifications in material behaviour modelling and calibration of material models. The data from Crisafulli is used for both implementation and evaluation of the proposed procedure. Detailed experimental set-up, execution of the experimental program and full results are reported in Crisafulli (1997). In this study, the following information has been used:

(a) RC frame

Frame height and length were 2.1 m and 2.67 m c/c respectively; each column is 150 mm square with 4No D10 longitudinal bars and D6 stirrups spaced between 75 mm and 150 mm c/c; the beam's depth and width are 200 mm and 150 mm respectively and it is reinforced with 4No D10 longitudinal bars and D6 stirrups spaced at 100 mm c/c. Concrete with a compressive strength, tensile strength and Young's modulus of 22.5 MPa, 2.4 MPa and 22.1 GPa respectively is used. D10 reinforcing bars had yield stress of 323 MPa at strain of 0.0016 and 0.0026 and ultimate stress of 441 MPa at strain of 0.253. D6 stirrups had yield stress of 353 MPa at strain of 0.0017 and 0.0031 and ultimate stress of 466 MPa at strain of 0.151.

(b) Infill masonry wall

The height, length and thickness of the infill wall were 2.00 m, 2.52 m and 0.09 m respectively; the thickness of the mortar joint is 10 mm. The compressive strength and Young's modulus for the brick units were 26.2 MPa and 12.98 GPa while the compressive strength and Young's modulus for the masonry prism (with aspect ratio of 2.72) were 19.3 MPa and 11.55 GPa respectively; the mortar had compressive strength and Young's modulus of 8.0 MPa and 8.54 GPa respectively. The brick/mortar joint properties were 0.41 MPa and 0.70 for initial shear strength and angle of friction respectively.

In this preliminary evaluation, each of the three geometry defining approaches (FEMA, Mainstone and Liauw & Kwan), four material combinations are used to generate appropriate equivalent strut properties as follows:

(a) Case 1: CC (Saneinejad & Hobbs, 1995) - DC (Saneinejad & Hobbs, 1995) & SS (Saneinejad & Hobbs, 1995)
(b) Case 2(a): CC (Lourenco et al., 2006) - DK (Crisafulli, 1997) & SS (Crisafulli, 1997)
(c) Case 2(b): CC (Lourenco et al., 2006) - DK (Crisafulli, 1997) & SS (Modified-stepped slip)
(d) Case 2(c): CC (Lourenco et al., 2006) - DK (Crisafulli, 1997) & SS (Modified-horizontal slip)

The sliding shear capacity determined using the analytical model by Crisafulli (1997) is modified to incorporate geometry dependence as outlined in Section 4.2.1. Detailed discussion of the implementation of the proposed procedure and the results of these four material combinations is provided in subsequent sections. Considering these four material combinations, evaluation of the equivalent strut model is conducted, with stress-strain points adopted based on the Powell & Hodgkinson (reported in Hendry, 1990) analytical model stated in Section 2.2.1.1. It should be noted that Matlab (2015) is used for the implementation of the proposed characterisation procedure.

4.3.1 FEMA based macro-modelling evaluation

Based on FEMA 356, the cross-sectional area for the equivalent strut is calculated as 0.0230 m^2, thus equivalent width of 256 mm and infill thickness of 90 mm adopted for the equivalent strut as well. Using various material analytical models for corner crushing, sliding shear and diagonal compression or cracking failure, the calculated maximum axial capacity for each stress zone is summarised in Table 4.2.

Table 4.2: Maximum axial capacity of each stress zone based on FEMA 356 (2000) model

Stress zone	Maximum force (N)	Maximum stress (MPa)
CC-Saneinejad & Hobbs (1995)	343612	14.91
CC-Lourenco et al. (2006)	256106	11.11
SS- Saneinejad & Hobbs (1995)	129235	5.61
SS-Crisafulli (1997)	24646	1.07
SS-Modified-stepped slip	37577	1.63
SS-Modified-horizontal slip	192239	8.34
DC-Saneinejad & Hobbs (1995)	492965	21.39
DK-Crisafulli (1997)	74223	3.22

An analysis of the equivalent strut behaviour using the proposed method is conducted in Matlab (2015) and the summary of the stress-strain behaviour generated by the various material combinations is provided in Figure 4.7. The following observations are noted:

(a) Case 1 generates a maximum axial force of 471.28 kN at deformation of 0.0038 m. Key strain points leading to failure (peak equivalent strut stress) are strains at peak sliding shear followed by strain at peak corner crushing. The overall peak equivalent strut occurs at peak corner crushing stress.

(b) Case 2a generates a maximum axial force of 92.40 kN at deformation of 0.0057 m with diagonal compression failure as predicted failure mode. Key strain points leading to failure are strains at peak sliding shear followed by strain at peak diagonal compression.

(c) Case 2b generates a maximum axial force of 103.35 kN at deformation of 0.0039 m. Key strain points leading to failure are strains at peak sliding shear followed by strain preceding peak diagonal compression. Thus, overall equivalent strut strength does not reflect the peak stress of any of the zone but general decline in degradation of the DC zone just before reaching its peak strength.

(d) Case 2c generates a maximum axial force of 256.87 kN at deformation of 0.0037 m with sliding shear failure as predicted failure mode. Degradation in the stiffness of the DC zone before reaching its peak followed by strain at peak sliding shear stress leads to the failure of the equivalent strut.

A parametric study on the effects of varying the lengths of CC and DC zones for Case 1 material combination under the FEMA-based property is conducted by varying the length of the corner crushing zone using a compression zone length factor ξ_{cc} applied to a compression zone length factor α_{cc} defined in Section 4.2.1. The values of 0.5, 0.75, 1.0, 1.25 and 1.5 are used for the factor ξ_{cc}. Results of the parametric study are shown in Figure 4.7(b). The equivalent strength of the cases with length factors of 0.5, 0.75, 1.0, 1.25 and 1.5 are 463.58 kN, 4 69.66 kN, 471.28 kN, 468.24 kN and 465.21 kN respectively. Changing the length of each of DC and CC zones using a corner crushing length factor, ξ_{cc} has minimal effects on the magnitude of the peak strength for the equivalent strut.

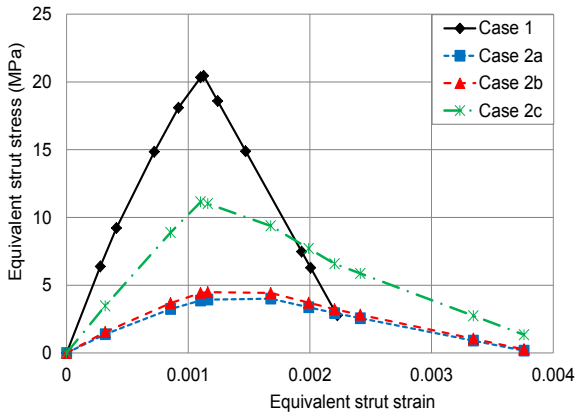

(a) Stress-strain curves for various material combinations

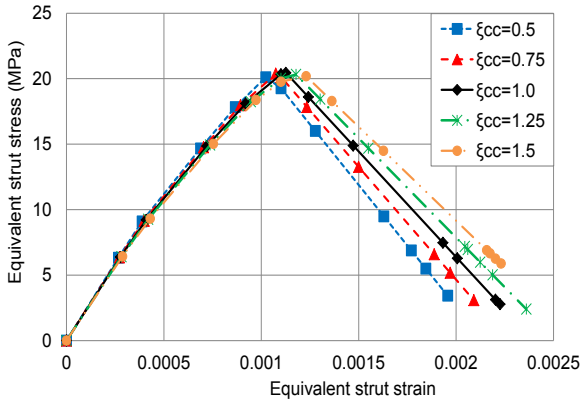

(b) Case 1 stress–strain curves, varying the zone length using factor, ξ_{cc}

Figure 4.7: Stress-strain curves for various cases using FEMA defined cross-sectional area

4.3.2 Mainstone macro-modelling evaluation

The equivalent strut cross-sectional area is calculated using Mainstone analytical model. The cross-sectional area is 0.0257 m^2 with a strut width of 286 mm. Table 4.3 provides a summary of the equivalent strut capacities calculated using the analytical models for corner crushing, sliding shear and diagonal compression or cracking failure.

Table 4.3: Maximum axial capacity of each stress zone based on Mainstone (1971) model

Stress zone	Maximum force (N)	Maximum stress (MPa)
CC-Saneinejad & Hobbs (1995)	343612	13.39
CC-Lourenco et al. (2006)	256106	9.98
SS- Saneinejad & Hobbs (1995)	129235	5.04
SS-Crisafulli (1997)	27439	1.07
SS-Modified-stepped slip	37577	1.46
SS-Modified-horizontal slip	192239	7.49
DC-Saneinejad & Hobbs (1995)	492965	19.21
DK-Crisafulli (1997)	82634	3.22

Using the stress zone strengths provided in the Table 4.3 and combining materials for the strut formulation as stated in Section 4.5, an evaluation of the equivalent strut behaviour is performed to generate the stress-strain behaviour. The following observations are noted:

(a) Case 1 generates a maximum axial force of 471.28 kN at deformation of 0.0038 m. The key strain points leading to failure are strains at peak sliding shear followed by strain at peak corner crushing. The overall peak equivalent strut occurs at peak corner crushing stress.

(b) Case 2a generates a maximum axial force of 102.78 kN at deformation of 0.0057 m with diagonal compression failure as predicted failure mode. The key strain points leading to failure are strains at peak sliding shear followed by strain at peak diagonal compression.

(c) Case 2b generates a maximum axial force of 110.82 kN at deformation of 0.0040 m. The key strain points leading to failure are strains at peak sliding shear followed by strain preceding peak diagonal compression. Thus, overall equivalent strut strength does not reflect the peak

stress of any of the zone but general decline in degradation of the DC zone just before reaching its peak strength.

(d) Case 2c generates a maximum axial force of 263.95 kN at deformation of 0.0037 m with sliding shear failure as predicted failure mode. Degradation in the stiffness of the DC zone before reaching its peak followed by strain at peak sliding shear stress leads to the failure of the equivalent strut.

A parametric study on the effects of varying the lengths of CC and DC zones for Case 1 material combination under the Mainstone-defined strut cross section is conducted by varying the length of the corner crushing zone using a compression zone length factor ξ_{cc} as defined in Section 4.2.1. The values of 0.5, 0.75, 1.0, 1.25 and 1.5 are used for the factor ξ_{cc}. Results of the parametric study are shown in Figure 4.8(b). The equivalent strength of the cases with length factors of 0.5, 0.75, 1.0, 1.25 and 1.5 are 463.58 kN, 469.66 kN, 471.28 kN, 468.24 kN and 465.21 kN respectively.

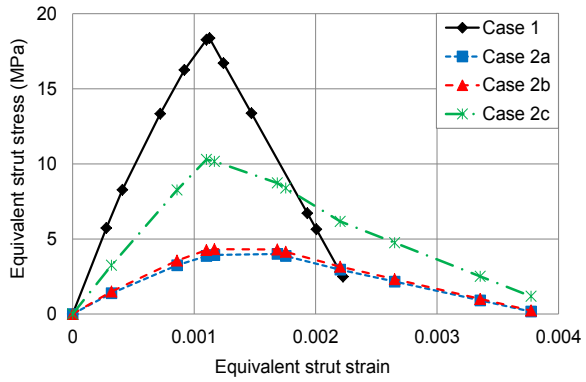

(a) Stress-strain curves for various material combinations

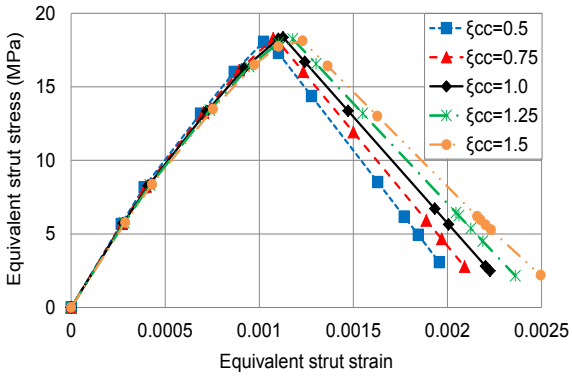

(b) Case 1 stress–strain curves, varying the zone length using factor, ξ_{cc}

Figure 4.8: Stress-strain curves for various cases using Mainstone defined cross-sectional area

4.3.3 Liauw & Kwan (1985) macro-modelling evaluation

The equivalent strut cross-sectional area for the based on Liauw & Kwan (1985) analytical model is 0.050 m^2, with a strut width of 556 mm. Table 4.4 provides a summary of the equivalent strut capacities calculated using the analytical models for corner crushing, sliding shear and diagonal compression or cracking failure.

Table 4.4: Maximum axial capacity of each stress zone based on Liauw & Kwan (1985) model

Stress zone	Maximum force (N)	Maximum stress (MPa)
CC-Saneinejad & Hobbs (1995)	343612	6.87
CC-Lourenco et al. (2006)	256106	5.12
SS- Saneinejad & Hobbs (1995)	129235	2.58
SS-Crisafulli (1997)	53503	1.07
SS-Modified-stepped slip	37577	0.75
SS-Modified-horizontal slip	192239	3.84
DC-Saneinejad & Hobbs (1995)	492965	9.85
DK-Crisafulli (1997)	161124	3.22

Using the stress zone strengths provided in the Table 4.4 and combining materials for the strut formulation as stated in Section 4.3, an evaluation of the equivalent strut behaviour is performed to generate the stress-strain behaviour. The following observations are noted:

(a) Case 1 generates a maximum axial force of 471.28 kN at deformation of 0.0038 m. The key strain points leading to failure are strains at peak sliding shear followed by strain at peak corner crushing. The overall peak equivalent strut occurs at peak corner crushing stress.

(b) Case 2a generates a maximum axial force of 198.27 kN at deformation of 0.0060 m with diagonal compression failure as predicted failure mode. The key strain points leading to failure are strains at peak sliding shear followed by strain at peak diagonal compression.

(c) Case 2b generates a maximum axial force of 187.20 kN at deformation of 0.0060 m. The key strain points leading to failure are strains at peak sliding shear followed by strain at peak diagonal compression. The diagonal compression failure is the dominant failure mode.

(d) Case 2c generates a maximum axial force of 326.61 kN at deformation of 0.0037 m with sliding shear failure as predicted failure mode. Degradation in the stiffness of the DC zone before reaching its peak followed by strain at peak sliding shear stress led to the failure of the equivalent strut.

A parametric study on the effects of varying the lengths of CC and DC zones for Case 1 material combination under the Liauw & Kwan (1985)-defined strut cross section is conducted by varying the length of the corner crushing zone using a compression zone length factor ξ_{cc} as defined in Section 4.2.1. The values of 0.5, 0.75, 1.0, 1.25 and 1.5 are used for the factor ξ_{cc}. Results of the parametric study are shown in Figure 4.9(b). The equivalent strength of the cases with length factors of 0.5, 0.75, 1.0, 1.25 and 1.5 are 463.58 kN, 469.66 kN, 471.28 kN, 468.24 kN and 465.21 kN respectively.

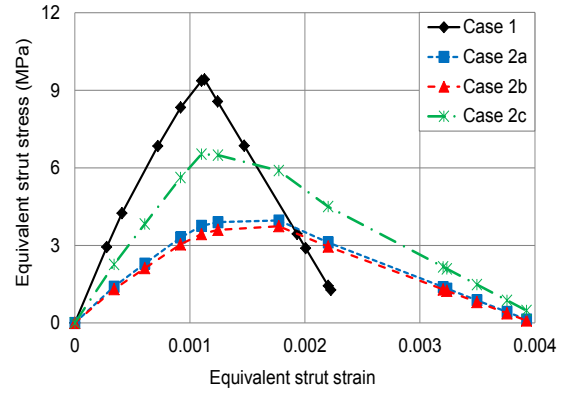

(a) Stress-strain curves for various material combinations

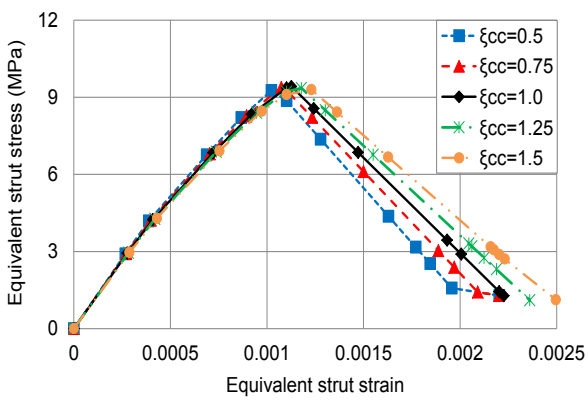

(b) Case 1 stress–strain curves, varying the zone length using factor, ξ_{cc}

Figure 4.9: Stress-strain curves for various cases using Liauw & Kwan (1985) defined cross-sectional area

4.3.4 Comparison of the model predictions and evaluation

Based on experimental data from Crisafulli (1997) from which these material characteristics are derived, the infill frame subjected to cyclic loading is provided. The maximum capacity observed for the RC infill frame is 45.5 kN at a lateral displacement of 0.0063 m. The infill frame started to

experience notable stiffness degradation at a lateral force of 10 kN with substantial change in stiffness occurring at a lateral force and displacement of 31.6 kN and 0.00032 m respectively. Crisafulli (1997) noted that the RC infill frame failed mainly by horizontal shear along the infill bed close to the beam, with stepped cracking at the end. Thus, the models predicting a SS failure mode could be adopted (Cases 2c for all the geometric definitions) and used for subsequent calibration, validation and parametric evaluation using both numerical methods using experimental data from Crisafulli.

In a typical evaluation of frames, identification of the mode of failure is a preliminary step before selection of the appropriate axial capacity to use in the analysis. As noted in Section 2.3.2, the minimum axial capacity is usually adopted. Thus, Case 2a for the FEMA and Mainstone geometric definitions and Case 2b for Liauw & Kwan is adopted for subsequent analysis of the infill as they have the least axial resistance. Under the FEMA model, the infill is predicted to fail in diagonal compression mode, and after maximum shear capacity is exceeded. Similar failure progression is observed under the Mainstone model, and the Liauw & Kwan model. Since Case 2a is one of the three modifications adopted to address the sliding shear mode, all the cases are used in the FE analysis of the infill frame as discussed in subsequent sections.

4.3.4.1 Evaluation of the infill frame-Case study of the data from Crisafulli

A numerical model is developed for the RC infill frame tested by Crisafulli (1997). A bare frame generates a lateral capacity of 13.77 kN at a lateral displacement of 26.78 mm. This compares well with a lateral resistance of 14.5 kN for the experimental results reported in literature for this frame. A single strut macro-model is used to evaluate the infill frame behaviour under incremental lateral load. Figure 4.10(a) shows the force vs. deformation behaviour for the RC infill frame considering the sliding shear mode (Case 2c) as reported from experimental results. The infill frame resistance for the Case 2c under the FEMA, Mainstone and Liauw & Kwan are 187.83 kN, 187.77 kN and 187.68 kN respectively, with respective deformations at peak of 7.56 mm, 7.39 mm and 6.55 mm.

As noted, the sliding shear failure mode does not represent the minimum strut capacity for each case. Another numerical simulation is performed involving minimum equivalent strut capacity for each category (i.e. Case 2a for FEMA and Mainstone and Case 2b for Liauw & Kwan) and the results are reported in Figure 4.10(b). The infill frame capacity for FEMA Case 2a is 76.82 kN at displacement of 5.74 mm with initial stiffness of 19,500 N/mm; the infill frame capacity for Mainstone Case 2a is 86.30 kN at a displacement of 7.65 mm with initial stiffness of 21,300 N/mm; and the infill frame capacity for Liauw & Kwan Case 2b is 152.16 kN at a displacement of 9.17 mm with initial stiffness of 33,500 N/mm. Experimental results from Crisafulli (1997) indicated infill frame capacity of 45.5 kN at a horizontal displacement of 6.325 mm with initial stiffness of 372,911 N/mm.

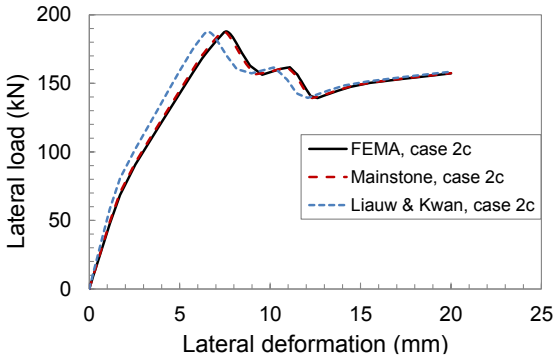

(a) Sliding shear failure mode

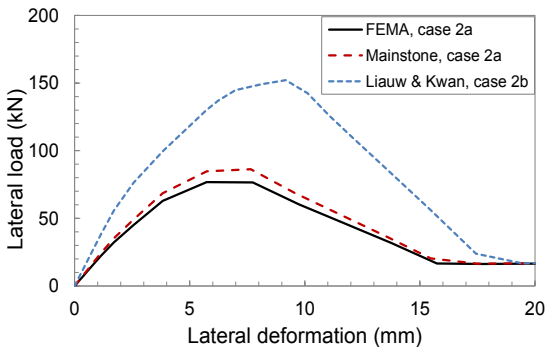

(b) Diagonal compression failure mode-minimum strut capacity

Figure 4.10: Infill frame behaviour generated using finite element macro-model

The deviations of the non-calibrated proposed characterisation models for the cases considered are summarised in Table 4.5. An average strength over-prediction factor of 4.13 with coefficient of variation (Cov) of 0.04% is obtained for shear dominated failure modes (Case 2c). An average deformation over-prediction of 1.13 with a coefficient of variation of 7.55% is obtained for the same shear dominated failure mode. When minimum axial capacity cases are considered (Cases 2a for FEMA and Mainstone and Case 2b for Liauw & Kwan), average over-prediction for strength and deformation are 2.31 (Cov of 39.05%) and 1.19 (Cov of 22.85%) respectively.

Table 4.5: Comparison of predicted strength and displacement with experimental data

Considered case	**Predicted values**		**Predicted-to-experimental value ratio**	
	Strength	Deformation	Strength ratio	Deformation ratio
FEMA, Case 2c	187.84 kN	7.56 mm	4.13	1.19
Mainstone, Case 2c	187.77 kN	7.39 mm	4.13	1.17
Liauw &Kwan, Case 2c	187.68 kN	6.55 mm	4.12	1.03
FEMA, Case 2a	76.82 kN	5.74 mm	1.69	0.91
Mainstone, Case 2a	86.30 kN	7.65 mm	1.90	1.21
Liauw & Kwan, Case 2b	152.16 kN	9.17 mm	3.34	1.45

From the brief statistical analysis of these results, a few possible means to address the variability and predictability of the model through calibration can be noted as follows:

(a) The choice of minimum strut capacity determined from the characterisation process that incorporates the existing material models may generate high coefficient of variation;
(b) The choice of the strut capacity based on predetermined failure mode offers a better mean of model calibration due to the minimal variability in the results;
(c) A clear and reliable identification of possible failure mode as a preliminary analysis is vital if (b) is to be adopted;
(d) Better material models may have to be examined before the use of minimum strut capacity can either refined and or rejected;
(e) More experimental case studies are required to establish whether the trend noted using Crisafulli experimental data may be applicable to other experimental data sets. This would help

in calibration of the proposed model. Section 4.3.4.2 provides an evaluation of the proposed model prediction using more experimental data taken from literature.

4.3.4.2 General evaluation of the infill frames under the FEMA, Mainstone and Liauw & Kwan analytical models

Preliminary evaluation of the proposed method using experimental data from Crisafulli gives general observations that cannot be relied on for calibration of the proposed modelling, as only one experimental data set is used. In this section, an evaluation of additional nine (9) experimental case studies taken from Mehrabi et al. (1996) is reported. Full details of the experimental set up, material data and experimental results analysis are not reported here, but can be found in Mehrabi et al. (1996). The increase in the number of experimental data sets would help improve the quality of numerical output and statistical significance for calibration purposes.

A pre-analysis failure identification process conducted to establish the possible failure mode for each sample is summarised in Table 2.7 (Section 2.3.2). Considering only FEMA based cross-sectional area definition, detailed failure progression with specific material combinations is summarised in Table 4.6. Amongst the three geometric definitions (FEMA, Mainstone and Liauw & Kwan), FEMA gives the least cross-sectional area, close to that defined by Mainstone. Thus, the capacities established using FEMA definitions would be lower for material analytical models that are geometric property independent.

Table 4.6: Pre-analysis results for identification of failure mode/progression

Sample notation	**Strut capacity for least resistance case**		**Strut capacity with SS mode**	
	Capacity (kN)	Failure progression – Material combination	Capacity (kN)	Material combination
G4(1)	73.74	SS, DC* - Case 2a	103.43, 225.24	Cases 2b, 2c
G4(2)	80.55	SS, DC*- Case 2a	117.09, 229.88	Cases 2b, 2c
G4(3)	76.52	SS, DC* - Case 2a	112.36, 227.17	Cases 2b, 2c
G4(4)	77.22	SS, DC* - Case 2a	106.30, 229.75	Cases 2b, 2c
G4(5)	67.21	SS, DC* - Case 2a	96.75, 220.81	Cases 2b, 2c
G4(9)	92.73	SS, DC*- Case 2a	142.96, 238.75	Cases 2b, 2c
G4(6)	125.74	SS, DC,DC* - Case 2a	248.19	Case 2c
G4(7)	98.05	SS, DC* - Case 2a	125.00, 235.31	Cases 2b, 2c
G4(8)	99.16	SS,DC,DC* - Case 2a	234.8	Case 2c

Numerical analyses are conducted for each of the nine samples using ABAQUS (2011). Each sample has at least two simulations representing the data for Cases 2a, 2b and 2c where applicable. The results of the numerical analysis are shown in Table 4.7. Case 2a generates lower strength prediction values, which are lower than the experimental values for most of the samples. The average ratio of predicted strength to experimental strength is 0.563 with a coefficient of variation of 43.8%. However, Cases 2b and 2c predict higher strength values than Case 2a with average ratio for the predicted strength to experimental strength of 0.591 (Cov of 38.1%) and 0.994 (Cov of 32.5%) respectively. A summary the deformation characteristics for the infill as observed from experimental studies compared with the numerical results is summarised in Table 4.8. It should be noted that for experimental data taken from cyclic experiments, only the deformation at initial peak strength reached during the cyclic loading is considered. The average ratio for the predicted deformation to experimental deformation at peak

strength for Cases 2a, 2b and 2c were 1.211 (Cov of 69.6%), 0.85 (Cov of 55.6%) and 0.659 (Cov of 47.7%) respectively.

Table 4.7: Strength evaluation for the numerical studies

Sample notation	Infill frame strength (kN) - experimental	Infill frame strength (kN) - numerical			Predicted-to-experimental strength ratio		
		Case 2a	Case 2b	Case 2c	Case 2a	Case 2b	Case 2c
G4(1)	277.7	104.63	118.39	202.15	0.38	0.43	0.73
G4(2)	153.5	108.61	128.69	206.92	0.71	0.84	1.35
G4(3)	190.0	100.57	123.36	202.48	0.53	0.65	1.07
G4(4)	292.0	101.98	119.42	204.27	0.35	0.41	0.70
G4(5)	232.3	89.03	107.59	193.32	0.38	0.46	0.83
G4(9)	188.2	162.85	178.39	237.35	0.87	0.95	1.26
G4(6)	156.2	159.51	-	240.15	1.02	-	1.54
G4(7)	355.6	124.68	143.15	224.2	0.35	0.40	0.63
G4(8)	276.0	133.68	-	232.97	0.48	-	0.84

Table 4.8: Deformation evaluation for the numerical studies

Sample notation	Deformation at peak strength (mm) - experimental	Deformation at peak strength (mm) - numerical			Predicted-to-experimental deformation ratio		
		Case 2a	Case 2b	Case 2c	Case 2a	Case 2b	Case 2c
G4(1)	3.30	10.00	5.50	4.00	3.03	1.67	1.21
G4(2)	7.11	9.33	5.33	5.33	1.31	0.75	0.74
G4(3)	13.97	7.33	5.33	5.33	0.53	0.38	0.38
G4(4)	7.37	7.33	5.33	5.33	1.00	0.72	0.72
G4(5)	15.24	5.33	5.33	5.33	0.35	0.35	0.35
G4(9)	8.89	12.88	11.38	5.38	1.45	1.28	0.61
G4(6)	6.10	11.46	-	6.46	1.88	-	1.06
G4(7)	8.13	6.66	6.66	4.44	0.82	0.82	0.55
G4(8)	17.02	9.17	-	5.17	0.54	-	0.30

Evaluation of the existing models provided in the current section and use of various material models in the evaluation of infill frame resistance using the proposed material characterisation show great variability. The high variability in model prediction increases the model uncertainty. This could be one of the reasons for the use of high material safety factors in the design of masonry structures in general and sometimes completely ignoring the structural contribution of masonry in the infill frame structures. The model uncertainty can be reduced either by improvements in material characterisation for the masonry, or by improving the models used for infill frame strength prediction. The reduction in the model variability could improve the structural resistance contribution for the infill and may allow for the reduced use of material to achieve a specific reliability factor; thus, improving material efficiency.

To identify a common approach to material characterisation for macro-modelling of the infill frames, equivalent strut behaviour established using the matrix transformation is considered. The elastic diagonal strut properties as defined in equations 2.18 and 2.19 incorporate important properties for the masonry as an orthotropic material, hence its choice. Since the axial compressive strength along the

diagonal is a single value, it is considered that this value should represent the nominal strength for DC zone. The strength for the CC and SS zones are related to this nominal capacity using factors, γ_{cc} and γ_{ss} respectively (see Section 4.4.2).

A comparison with other material predictions is carried out. The results for FEMA defined geometric definition are summarised in Table 4.9. The equivalent strut capacity determined based on biaxial stress approximation (equation 2.14) predicts lower stress values than the diagonal compression capacity (F_{sa}) established through stress matrix transformation. The mean ratio for the biaxial prediction to diagonal stress transformation is 0.84 with coefficient of variation of 7.3%. While the results shown are for the FEMA definition only, similar evaluation carried out with Mainstone and Liauw & Kwan geometric definitions, give similar ratios. This is the case because the material analytical model that defines the corner crushing is independent of geometric variations. Saneinejad analytical material models, developed based on contact stresses (equation 2.11), provide almost the same capacity of compression strut as that of the transformed diagonal strut, with F_{cc}/F_{Θ} mean ratio of 1.06 and coefficient of variation of 6.6%. The choice of geometric models (cross-sectional area of strut) does not affect the compression zone capacity for the Saneinejad compression crushing zone analytical model as similar results were obtained for other geometric definitions.

A comparison of the transformed diagonal compressive strength with the predicted capacity for the sliding shear zone showed significant variations across various material definitions. For example, the mean ratio of sliding shear capacity to transformed diagonal compressive strength are 0.39, 0.76, 2.09 and 1.37 for SS failure defined by Crisafulli (normal SS failure), horizontal SS failure, stepped SS failure and SS failure defined by Saneinejad (equation 2.11) respectively. Similar ratios were observed when comparing across geometric definitions except for the normal SS failure. The use of SS failure modifications (Section 4.2.2.1) becomes vital where geometric models that give varying cross-sectional areas are to be used and expected to give similar resistance. However, the challenge with such normalization of SS failure is the choice of whether horizontal sliding will dominate or stepped sliding shear would dominate the failure.

The extent of inherent variations in the material model definitions for SS mode can be noted in Table 4.9. With such variations, the expected predictions across both the material and geometric definitions cannot be similar. It is useful to establish any relationship of key material parameters that are used in modelling with material data that can be established from experiments. In some cases, available experimental data may not be adequate in describing complete material behaviour for an element. Thus, modelling the structural behaviour of such an element would require either additional and sometimes, complex experimentation to capture all the required data or use of well verified and calibrated analytical models. It is thus decided that the use of transformed diagonal compression resistance be adopted to establish a common material definition for strut behaviour. The strut behaviour evaluation considering the transformed diagonal compression resistance as nominal diagonal strength is reported in Section 2.3.2.

Table 4.9: Strength ratios for compression crushing (F_{cc}) and sliding shear (F_{ss}) to diagonal matrix-transformed compression (F_{Θ}) strengths

Sample Notation	F_{cc}/F_{θ} (equation in bracket)		F_{ss}/F_{θ} (equation in bracket)			
	CC - (2.11)	CC – (2.14)	SS[1] – (2.15)	SS[2] – (2.11)	SS[3] – (2.11)	SS – (2.11)
G4(1)	1.01	0.81	0.41	0.82	2.39	1.49
G4(2)	1.02	0.83	0.39	0.86	2.19	1.36
G4(3)	1.03	0.83	0.40	0.85	2.22	1.38
G4(4)	1.02	0.81	0.41	0.81	2.42	1.52
G4(5)	1.01	0.80	0.41	0.80	2.43	1.52
G4(9)	1.03	0.88	0.39	0.96	1.99	1.21
G4(6)	1.15	0.93	0.39	0.74	1.62	1.20
G4(7)	1.14	0.89	0.41	0.70	1.80	1.35
G4(8)	1.14	0.87	0.41	0.67	1.89	1.42
G3	1.14	0.71	0.25	0.38	1.92	1.29
Mean	1.06	0.84	0.39	0.76	2.09	1.37
Std dev.	0.070	0.061	0.051	0.158	0.285	0.117
Cov	0.066	0.073	0.131	0.208	0.136	0.085

[1] Normal shear slip; [2] Stepped shear slip; [3] Horizontal shear slip

4.4 PARAMETRIC EVALUATION, CALIBRATIONAND VALIDATION OF THE PROPOSED METHOD

The proposed strut characterisation is implemented and validated using existing experimental data. As a starting point, the material strengths for each stress zone are taken from available analytical models in literature. Since the proposed procedure assumes stress zones in series and parallel, there is need to calibrate the material strengths for each zone. Adjustment of material characterisation data is carried out through an optimisation process. A basic optimisation process that uses a single calibration factor for the strut strength for each stress zone is used. Thus, the corner crushing strength is related to the diagonal compressive strength using compression factor, γ_{cc} while the sliding shear strength is related to the diagonal compressive strength by a sliding shear factor, γ_{ss}.

4.4.1 Infill frame experimental data evaluation

A preliminary evaluation of the existing experimental data for infill frames is conducted to establish reliable data sets that can be used for subsequent model verification and validation. A detailed procedure for selection of experimental data for use in this research is based on firstly, qualitative evaluation of the available data followed by streamlining of the data based on consistency and or restricted coefficient of variation and lastly, data normalisation as discussed in Section 3.3.2.3.

The experimental data consistency evaluation procedure is developed to make sure that only the experimental data whose consistency factor, N_f, as established using equation 4.84 lies within a prescribed range of mean consistency factor, $\overline{N}_f$. The consistency factor is developed on the basis that infill frame strength is influenced by frame properties (bare frame), slenderness ratio of the frame and the infill compressive strength (see equation 4.84).

$$N_f = \frac{F_{\text{infra}}}{F_{\text{bare}} f_{cw}} r_w \tag{4.84}$$

where

F_{infra} is the capacity of the infill frame;

F_{bare} is the capacity of the bare frame;

f_{cw} is the normalised compressive strength of infill wall; and

$r_w = \frac{h_w}{l_w}$ is slenderness the ratio of the infill wall.

Establishment of the consistency factor, N_f, requires the use of the infill frame capacity whose frame properties have been used to generate the bare frame capacity. For this to be achieved, the amount of concrete batch mixed at a time should be large enough to cast two RC frames. In the experimental design conducted by Mehrabi et al. (1996), such is not the case (to the best knowledge of the author) as it is resource demanding. However, a single RC frame was cast and tested to establish the bare frame capacity. Furthermore, material characteristics data for all the frames used in the experiments were obtained. The concrete frames used in the experimental study by Mehrabi et al. (1996) have variations in the material characteristic values. This would result in possible variations in the respective bare frame capacity for each sample. A numerical model is used to generate the respective bare frame capacities so that additional data that is not available from experimental data is produced. Both the experimental data and numerical data for the bare frame capacity are used to calculate the consistency factor.

The respective average value for the consistency factors for all the samples using numerical bare frame data and experimental bare frame data are 0.153 and 0.133 with coefficient of variation of 25.2% and 25.9% respectively. Two actions are taken to reduce the coefficient of variation; namely (a) categorisation of the samples based on masonry type (solid masonry and hollow masonry) and (b) removal of samples that generate excessively low or high values (outliers). While the second option is carried out to improve statistical quality of data, there is need for comprehensive data evaluation with the objective of understanding the cause of large variations in the infill behaviour. However, in this study no further evaluation of the 'outliers' is carried out.

The $\overline{N}_f$ values for the solid infill frames using numerical and experimental data are 0.158 (Cov of 9.6% and 0.134 (Cov of 10.0%). For hollow infill frames, the respective average values for consistency factor, $\overline{N}_f$, using numerical and experimental data are 0.105 (Cov of 12.8%) and 0.093 (Cov of 15.4%). A maximum cut-off point for the outliers is chosen to be at a coefficient of variation of 16% for the respective mean consistency factors. By ignoring the outliers, the respective average value for the consistency factors for all the samples (uncategorised) using numerical bare frame data and experimental bare frame data are 0.143 (Cov of 22.3%) and 0.125 (Cov of 23.6%).

Table 4.10: Infill frame experimental data consistency evaluation

Sample notation	F_{infra} - kN	F_{bare} – kN		f_{cw} - Mpa	Aspect ratio, r_w	Consistency factor, N_f	
		numerical	experimental			numerical	Experimental
G4(1)	277.7	94	106	13.17	0.667	0.150	0.133
G4(2)	153.5	92	106	9.26	0.667	0.120	0.104
G4(5)	232.3	88	106	12.09	0.667	0.146	0.121
G4(9)	188.2	138	145	8.84	0.667	0.103	0.098
G4(10)	445	138	145	11.85	0.667	0.181	0.173
G4(3)	190	92	106	8.30	0.667	0.166	0.144
G4(4)	292	92	106	9.26	0.667	0.228	0.198
G4(6)	156.2	87	106	9.26	0.483	0.094	0.077
G4(8)	276	88	106	9.98	0.483	0.152	0.126
G4(7)	355.6	79	106	11.85	0.483	0.183	0.137
G3	45.5	14	14.5	16.00	0.794	0.161	0.156

In the absence of adequate data equation 4.85 can be used to evaluate the infill frame capacity for the single bay single storey infill frame. The results for the infill frame capacities established using equation 4.85 using the experimental data is reported in Table 4.11.

$$F_{\text{infra}}(\text{kN}) = \frac{\overline{N}_f F_{bare} f_{cw}}{r_w} \tag{4.85}$$

where

F_{bare} and f_{cw} are bare frame capacity in KN and infill compressive strength in MPa respectively.

Table 4.11: Results of the preliminary evaluation of the experimental infill frame data

Sample name	Loading type	Infill category	Infill frame capacity (kN)		
			Experimental	Categorised	Un-categorised
G4(1)	Static	Solid	277.7	281.3	261.4
G4(5)	Cyclic	Solid	232.3	258.2	239.9
G4(8)	Cyclic	Solid	275.9	294.5	273.6
G4(7)	Cyclic	Solid	355.6	349.5	324.7
G3	Cyclic	Solid	45.5	39.3	36.5
G4(10)	Cyclic	Solid	445.0	346.2	321.6
G4(3)	Static	Hollow	190.0	122.7	164.7
G4(2)	Cyclic	Hollow	153.5	136.9	183.8
G4(9)	Cyclic	Hollow	188.2	178.8	240.0
G4(6)	Cyclic	Hollow	156.2	189.1	253.8

4.4.2 Parametric evaluation and calibration of the proposed evaluation procedure

As stated in Section 4.2, three zones make up the equivalent strut, namely the corner crushing and diagonal compression zone acting in series and sliding shear zone acting in parallel. The material behaviour of each zone is expressed as a function of the diagonal compressive strength as determined using equation 2.19. This assumption is made to simplify the material behaviour modelling procedure

by reducing the number of variables. This simplification also follows conventional standards where knowledge of compressive material behaviour can be used to extrapolate other material behaviours. Thus, diagonal compressive strength, $f_{m\theta}$ as determined by equation 2.19 is a standard material property for the diagonal compression zone, DC. The compressive strength for the corner crushing zone is assumed to be linked to the strength $f_{m\theta}$ using compression factor, γ_{cc} and shear factor, γ_{ss} respectively. Therefore, establishing the values and behaviours for the compression and shear factors is vital towards calibrating of the equivalent strut material characterisation.

A tri-linear perfect plastic material behaviour is adopted for each zone. Furthermore, the strain limits established for the diagonal strut are adopted for all the zones. With these assumptions, both the strength and Young's modulus for each zone can be related to the general diagonal properties.

For diagonal compression zone, the strength and Young's modulus are:

$$f_{dc} = f_{m\theta} \text{ and } E_{dc} = E_{m\theta} \tag{4.86}$$

For corner crushing zone, the strength and Young's modulus are:

$$f_{cc} = \gamma_{cc} f_{m\theta} \text{ and } E_{cc} = \gamma_{cc} E_{m\theta} \tag{4.87}$$

For sliding shear zone, the strength and Young's modulus are:

$$f_{ss} = \gamma_{ss} f_{m\theta} \text{ and } E_{ss} = \gamma_{ss} E_{m\theta} \tag{4.88}$$

A parametric study to establish the influence of compression and shear factors is conducted for each sample using finite element modelling. Each sample has sixty cases, representing ten variations of the compression factor, γ_{cc} and six (6) variations of the shear factor, γ_{ss} as outlined in Table 4.12. The value of γ_{cc} ranges from 0.50 to 1.4 and that of γ_{ss} from 0.15 to 0.8. These values are considered as broad enough to enable the prediction of relevant axial resistance. When the required axial resistance is outside the range of the selected values, linear interpolation or extrapolation is used. The results of the numerical experimentation are used to establish the trend of the infill frame behaviour or identify probable relationships for subsequent derivation of empirical relationships. Nine samples are used for this exercise while additional samples from different sources are used for validation of the proposed procedure.

Table 4.12: Numerical experimentation matrix

Shear factor, γ_{ss} & ith term		**Compression factor, γ_{cc} and jth term**									
		1	2	3	4	5	6	7	8	9	10
ith term	Factor	0.50	0.60	0.70	0.80	0.90	1.00	1.10	1.15	1.25	1.40
1	0.15	$X_{1,1}$	$X_{2,1}$	$X_{3,1}$	$X_{4,1}$	$X_{5,1}$	$X_{6,1}$	$X_{7,1}$	$X_{8,1}$	$X_{9,1}$	$X_{10,1}$
2	0.25	$X_{1,2}$	$X_{2,2}$	$X_{3,2}$	$X_{4,2}$	$X_{5,2}$	$X_{6,2}$	$X_{7,2}$	$X_{8,2}$	$X_{9,2}$	$X_{10,2}$
3	0.35	$X_{1,3}$	$X_{2,3}$	$X_{3,3}$	$X_{4,3}$	$X_{5,3}$	$X_{6,3}$	$X_{7,3}$	$X_{8,3}$	$X_{9,3}$	$X_{10,3}$
4	0.50	$X_{1,4}$	$X_{2,4}$	$X_{3,4}$	$X_{4,4}$	$X_{5,4}$	$X_{6,4}$	$X_{7,4}$	$X_{8,4}$	$X_{9,4}$	$X_{10,4}$
5	0.65	$X_{1,5}$	$X_{2,5}$	$X_{3,5}$	$X_{4,5}$	$X_{5,5}$	$X_{6,5}$	$X_{7,5}$	$X_{8,5}$	$X_{9,5}$	$X_{10,5}$
6	0.80	$X_{1,6}$	$X_{2,6}$	$X_{3,6}$	$X_{4,6}$	$X_{5,6}$	$X_{6,6}$	$X_{7,6}$	$X_{8,6}$	$X_{9,6}$	$X_{10,6}$

The parametric studies are divided into two phases, namely equivalent strut material behaviour established using characterisation programme in Matlab (2015) and infill frame structural behaviour

evaluation established using finite element analysis in ABAQUS (2011). Under material characterisation studies, the equivalent strut strength variation with varying compression and shear strength factors, γ_{cc} and γ_{ss} is presented for sample G4(1) in Table 4.13. For any compression factor, the equivalent strut resistance increases with increase in shear factor, γ_{ss}. However, for a shear factor, γ_{ss}, the strut resistance increases with increase in compression factor up to a compression factor of 1.0. Beyond the compression factor of 1.0, there is no increase in strut resistance. Similar trends are noted for all the other samples as shown for samples G4(7) and G4(8) in Figure 4.11.

Table 4.13: Overall strut characteristics - Maximum strut resistance for sample G4(1)

Shear factor, γ_{ss}	**Strut resistance (kN) at compression factor, γ_{cc}**									
	0.50	0.60	0.70	0.80	0.90	1.00	1.10	1.15	1.25	1.40
0.15	190.1	220.6	250.0	279.4	308.8	338.2	338.2	338.2	338.2	338.2
0.25	218.8	250.0	279.5	308.9	338.3	367.7	367.7	367.7	367.7	367.7
0.35	247.5	279.4	308.9	338.3	367.7	397.1	397.1	397.1	397.1	397.1
0.50	290.5	323.5	353.0	382.4	411.8	441.2	441.2	441.2	441.2	441.2
0.65	333.6	367.7	397.1	426.5	455.9	485.3	485.3	485.3	485.3	485.3
0.80	376.6	411.8	441.2	470.6	500.0	529.4	529.4	529.4	529.4	529.4

The plot for the axial capacities vs. shear factor, γ_{ss}, shows a linear relationship within the range of factors considered (Figure 4.11a and c). A linear relationship between the axial resistance and the compression factor exists up to compression factor of 1.0 (see Figure 4.11 b and d). These trends are noted for all the other sample studies (see results in Appendix A3.1). The mode of failure does not influence the observed linear relationship that exists between both the compression factor and the shear factor.

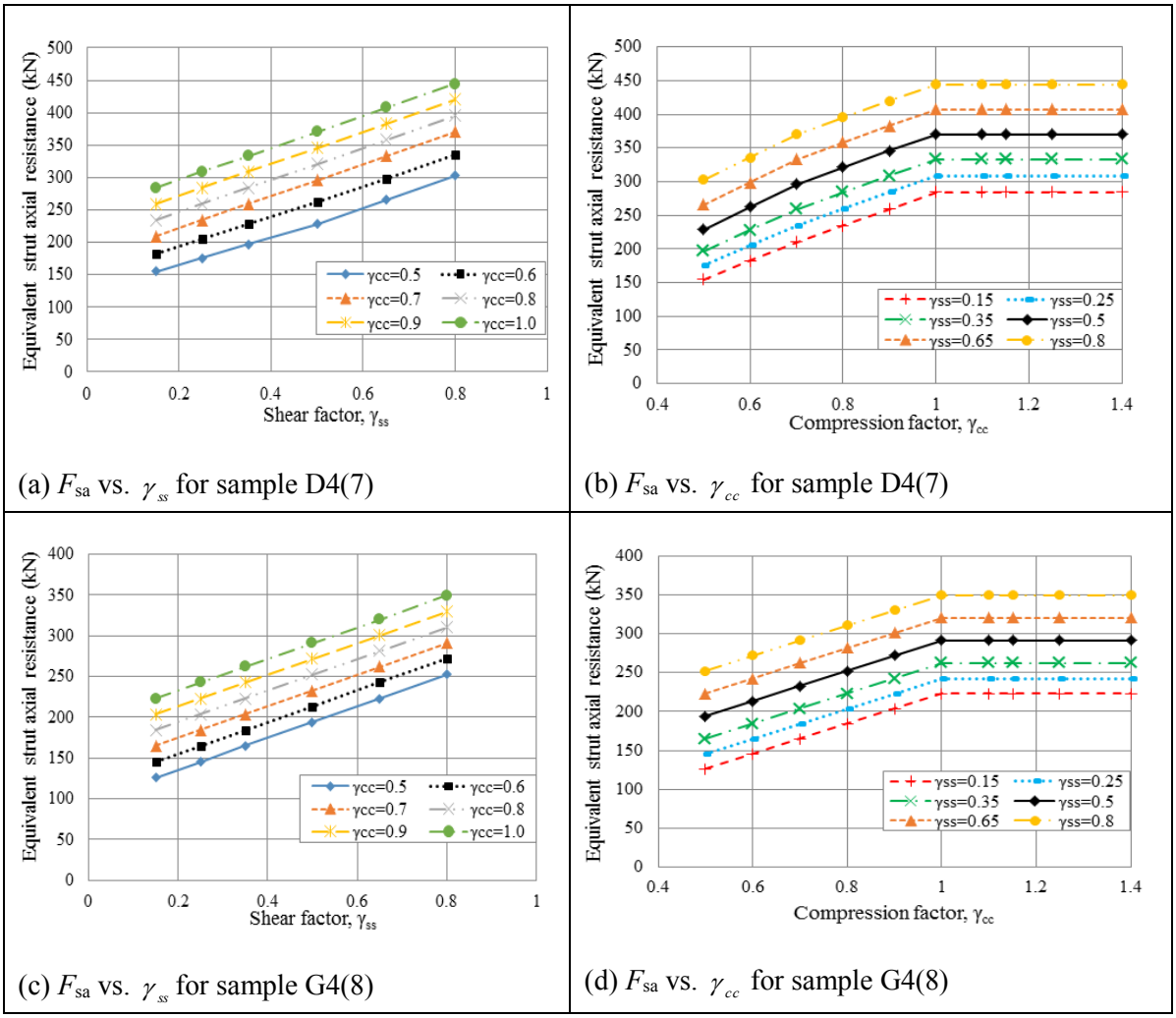

(a) F_{sa} vs. γ_{ss} for sample D4(7)

(b) F_{sa} vs. γ_{cc} for sample D4(7)

(c) F_{sa} vs. γ_{ss} for sample G4(8)

(d) F_{sa} vs. γ_{cc} for sample G4(8)

Figure 4.11: Typical results from a parametric study for samples G4(7) and G4(8)

The observed trend, however, does not provide full details into the stress-strain behaviour for each combination. It is observed that the stress-strain relationships vary considerably with some combinations showing more ductile behaviour than the other (see Figure 4.12). Lower values for the compression factor generates less ductile behaviour. Typical results for numerical evaluation of the infill frames using macro-models (single strut) with strut material characteristics shown in Figure 4.12(a) are shown in Figure 4.12(b).

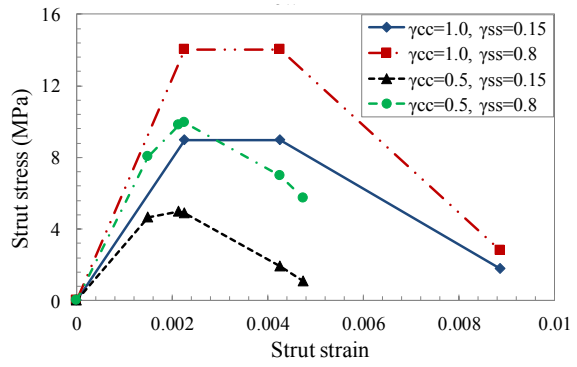

(a) Typical material characterisation behaviour (stress-strain relationship)

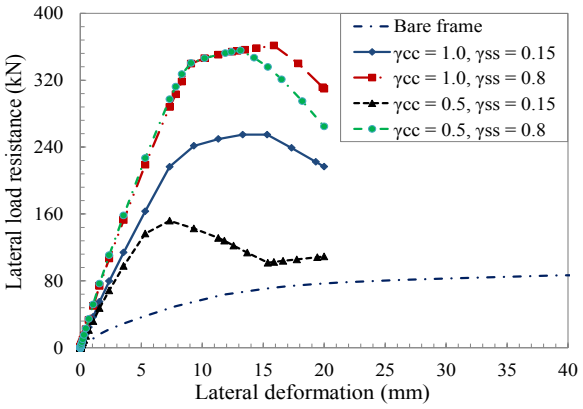

(b) Typical lateral force vs. deformation behaviour for the infill frame from numerical analysis

Figure 4.12: Equivalent strut material behaviour and infill frame behaviour for sample G4(3)

Since the axial resistance is defined by two variables, γ_{cc} and γ_{ss}, a simple linear relationship given by equation 4.89 is proposed. A subsequent process of generating relevant coefficients for the linear relationship and linking and calibrating the coefficients with material properties is presented in subsequent paragraphs.

$$F_{sa} = A_{\gamma}\gamma_{ss} + B_{\gamma}\gamma_{cc} \tag{4.89}$$

The coefficients A_{γ} and B_{γ} are assumed to represent the respective force contribution from the SS zone and the overall CC - DC zones respectively. Assuming that elastic properties can fairly predict the axial resistance, F_{sa}, the coefficients A_{γ} and B_{γ} is defined by the effective peak strains for SS zone and CC zone, $\varepsilon_{A\gamma}$ and $\varepsilon_{B\gamma}$ respectively as:

$$A_{\gamma} = E_{\theta}\varepsilon_{A\gamma}A_d \text{ and } B_{\gamma} = E_{\theta}\varepsilon_{B\gamma}A_d \tag{4.90}$$

From which effective peak strains $\varepsilon_{A\gamma}$ and $\varepsilon_{B\gamma}$ are:

$$\varepsilon_{A\gamma} = \frac{A_{\gamma}}{E_{\theta}A_d} \text{ and } \varepsilon_{B\gamma} = \frac{B_{\gamma}}{E_{\theta}A_d} \tag{4.91}$$

A summary of raw values for coefficients A_{γ} and B_{γ} established from the regression analysis are provided in Table 4.14. These coefficients are established by a three-step process:

(a) Establish a linear relationship for the axial resistance with shear factor for a compression factor in the form: $F_{sa} = A_{\gamma}\gamma_{ss} + C$ (i.e. the expression defining the material trend shown in Figure 4.6.3a and c);

(b) For all the values of C, establish a linear relationship of C as a function of compression factor in the form: $C = B_{\gamma}\gamma_{cc}$; and

(c) Substitute C established in step (b) into the axial expression established from step (a) generating the equation format as equation 4.89.

Comparison of the effective strains, A_{γ} and B_{γ} with actual elastic strain at peak compression stress,

ε_1, is provided through the strain ratio defined by equation 4.92.

$$\text{Strain ratio} = \frac{0.5\left(\varepsilon_{A\gamma} + \varepsilon_{B\gamma}\right)}{\varepsilon_1} \quad (4.92)$$

An average strain ratio for all the samples altogether is 0.758 with a coefficient of variation of 15.5%. However, an improved coefficient of variation of 7.0% and 8.5% corresponding to the average ratios of 0.649 and 0.855 for hollow infill frame samples and solid infill frame samples respectively are obtained.

Table 4.14: Equivalent strut elastic properties and initial empirical relationship coefficients

Sample name	Equivalent strut elastic properties			Coefficients & effective elastic strains				Strain ratio
	E_θ (MPa)	A_d (m^2)	ε_1 (10^{-3})	A_γ (N)	B_γ (N)	$\varepsilon_{A\gamma}$ (10^{-3})	$\varepsilon_{B\gamma}$ (10^{-3})	
G4(1)	8921	0.0238	1.77	292956	294128	1.38	1.39	0.782
G4(2)	4309	0.0261	3.03	220186	226615	1.96	2.02	0.655
G4(5)	8385	0.0232	1.70	262113	262218	1.35	1.35	0.791
G4(9)	3934	0.0298	3.21	244470	246722	2.09	2.11	0.652
G4(3)	4780	0.0256	2.26	197796	199558	1.62	1.63	0.720
G4(6)	3500	0.0262	3.70	201891	215434	2.20	2.35	0.615
G4(8)	8523	0.0219	1.08	194055	194061	1.04	1.04	0.962
G4(7)	6510	0.0235	2.23	241429	245984	1.58	1.61	0.713
G3	11159	0.0234	1.77	353332	359637	1.35	1.38	0.889

Since strain ε_1 is derived from actual material properties, the empirical relationship for the effective strut axial resistance as defined by equation 4.89 is calibrated to incorporate actual material behaviour parameters and is simplified as:

$$F_{sa} = F_{a\varepsilon}\left(\gamma_{cc} + \gamma_{ss}\right) \quad (4.93)$$

where coefficient $F_{a\varepsilon}$ calibrated based on the infill masonry material properties is defined as:

$$F_{a\varepsilon} = E_\theta A_d \varepsilon_{1c}; \quad (4.94)$$

and ε_{1c} is a calibrated elastic strain at peak compressive strength for either hollow masonry or solid masonry and is calculated as:

$\varepsilon_{1c} = 0.649\varepsilon_1$ for hollow masonry (4.95a)

$\varepsilon_{1c} = 0.855\varepsilon_1$ for solid masonry (4.95b)

ε_1 is the elastic strain at peak elastic compressive strength.

Elastic strain at peak compressive strength, ε_1, is defined based on a tri-linear material model (see Figure 4.6 in Section 4.2.4). When strain values are not available, El-Dakhakhni et al. (2003) proposed a simple way of generating both the total strain at peak strength, ε_{cp}, and elastic strain at peak strength, ε_1, and strain at ultimate strength, ε_2, for the generalised diagonal compression strut behaviour as:

$$\varepsilon_{cp} = \frac{f_{m\theta}}{E_p};\ \varepsilon_1 = \varepsilon_{cp} - 0.001 \text{ and } \varepsilon_2 = \varepsilon_{cp} + 0.001 \quad (4.96)$$

where E_p is secant modulus at peak strength is assumed as half of the elastic Young's modulus for the diagonal strut, $E_{m\Theta}$ (i.e. $E_p = 0.5E_{m\theta}$).

A summary of the calibrated factors, $F_{a\varepsilon}$, ε_{1c}, diagonal elastic modulus and equivalent strut cross-sectional area for the various samples under study is provided in Table 4.15.

Table 4.15: Calibrated equivalent strut elastic properties

Sample Name	E_θ (MPa)	A_d (m^2)	ε_{1c} (10^{-3})	$F_{a\varepsilon}$ (N)
G4(1)	8921	0.0238	1.48	313819
G4(2)	4309	0.0261	1.97	221323
G4(5)	8385	0.0232	1.46	283454
G4(9)	3934	0.0298	2.09	244653
G4(3)	4780	0.0256	1.46	179228
G4(6)	3500	0.0262	2.40	220318
G4(8)	8523	0.0219	0.92	172510
G4(7)	6510	0.0235	1.91	292127
G3	11159	0.0203	1.51	343020

4.4.3 Evaluation of the strut behaviour using the proposed model

FE models for the infill frame are developed for all the selected samples. Infill contribution is modelled by using a single strut whose material characteristics are derived from the proposed procedure. Numerical experimentation matrix provided in Table 4.12 indicates 60 possible combinations. Considering the observed trend of the strut resistance behaviour (see Figure 4.11), two sets of cases are selected from the numerical simulation matrix provided in Table 4.12. The first set comprises the lower resistance values taken at compression factor, γ_{cc} of 0.5 while the other one comprises the upper strut resistance values taken at compression factor, γ_{cc} of 1.0 or greater. The first set consists of cases $X_{1,1}$ (i.e. γ_{cc} = 0.5 and γ_{ss} = 0.15) and $X_{1,6}$ (i.e. γ_{cc} = 0.5 and γ_{ss} = 0.8) and the second set consists of cases $X_{6,1}$ (i.e. γ_{cc} = 1.0 and γ_{ss} = 0.15) and $X_{6,6}$ (i.e. γ_{cc} = 1.0 and γ_{ss} = 0.8).

Using the stress-strain behaviour generated from the selected four cases and evaluating a numerical model of the infill frame in ABAQUS generates the infill frame capacity for the respective material behaviour. Since the choice of the factors γ_{cc} and γ_{ss} is arbitrary, the resulting infill frame resistance taken from the numerical simulation can be either higher or lower than the expected resistance. Linear interpolation/extrapolation to establish the strut resistance that gives corresponding infill frame resistance from experiment is used. Once the target strut resistance is established, the corresponding shear factor, is determined from either equation 4.93 or through extrapolation or interpolation as shown in Table 4.16 or Figure 4.13a) for sample G4(3) since is known for this case.

Table 4.16 together with Figure 4.13(a) provide an illustration for the determination of the target strut resistance and corresponding compression and shear factors for sample G4(3). The sample has an infill frame resistance of 190.0 kN determined in a laboratory experiment. The target axial strut resistance is determined using interpolation/extrapolation between infill frame resistance and axial strut resistance values. With the target axial strut resistance known, the corresponding sum of the shear and compression factors can be established using either extrapolation/interpolation or by using equation 4.93. When equation 4.93 is used the shear factor of 0.342 is established for a compression factor of 0.5. It should be noted that the values for the coefficient $F_{a\varepsilon}$ can be calculated using the diagonally transformed

Young's modulus (E_θ), equivalent strut cross-sectional area (A_d) and calibrated elastic strain at peak strength, ε_{1c} (in this example the value of $F_{a\varepsilon}$ can be taken from Table 4.15).

Table 4.16: Experimental evaluation for G4(3) infill frame

Compression factor γ_{cc}	**Infill frame resistance** F_{infra} **(kN)**	**Axial strut resistance** F_{sa} **(kN)**	**Shear factor** γ_{ss}
0.5	151.92	128.06	0.15
	190.00	[150.99] *	[0.342]**
	355.47	250.63	0.8
1.0	190.00	[150.561]*	[-0.16]**
	254.83	229.515	0.15
	361.38	359.286	0.8

*Linear extrapolation/interpolation used; **Equation 4.93 used

As noted, the value of the shear factor is established for a selected compression factor. For equation 4.93 to be true and to allow variations in the values for both the compression factor and the shear factor, the sum of any chosen values of γ_{cc} and γ_{ss} must always be constant. The sum of the compression factor and shear factor for sample G4(3) that establishes target axial strut resistance is 0.842 (for γ_{cc} = 0.5 and γ_{ss} = 0.342) or 0.84 (for γ_{cc} = 1.0 and γ_{ss} = -0.16) as determined using the empirical expression (equation 4.93). For practical purposes, a negative value should not be used as it has no physical meaning.

Having established the summation for γ_{cc} and γ_{ss} values, four combinations for material characterisation data established from different values of γ_{cc} and γ_{ss} are established for sample G4(3). These are γ_{cc} = 0.5 and γ_{ss} = 0.342, γ_{cc} = 0.6 and γ_{ss} = 0.242, γ_{cc} = 0.7 and γ_{ss} = 0.142 and γ_{cc} = 0.8 and γ_{ss} = 0.042. The generated stress-strain behaviours for these cases show minimal variations as seen in Figure 4.13(b).

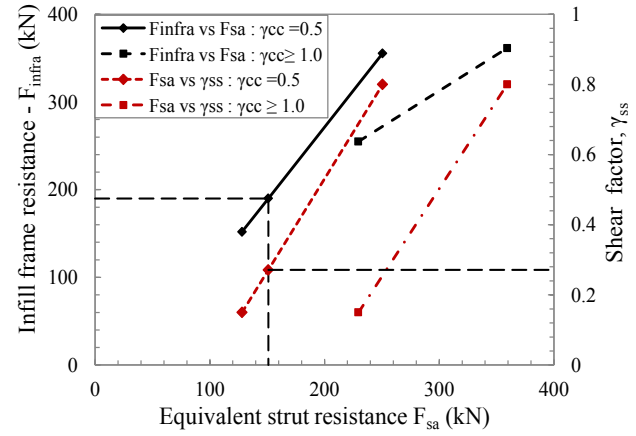

(a) Identification of equivalent strut resistance

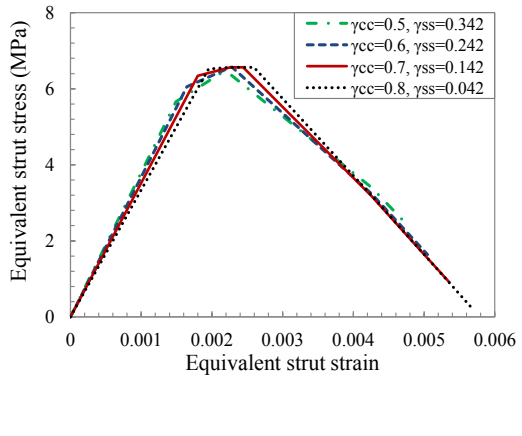

(b) Trial material characterisation options

Figure 4.13: Identification of equivalent strut resistance and possible stress-strain behaviour for sample G4(3) infill RC frame

The four material possible material combinations for the equivalent strut for sample G4(3) are used in a numerical evaluation of the infill frame. Force vs. deformation characteristics of the infill frame are shown in Figure 4.14. The infill frame numerical model with the equivalent strut material characterisation defined by γ_{cc} = 0.5 and γ_{ss} = 0.342 generates resistance of 181.0 kN at deformation of 7.33 mm. With factors γ_{cc} = 0.6 and γ_{ss} = 0.242 the numerical model generates infill frame resistance of 181.2 kN at deformation of 7.33 mm. Infill frame resistance and deformation at peak of 183.1 kN at 7.333 mm and 187.8 kN at 9.33 mm are established for strut material characterisation defined by with γ_{cc} = 0.7, γ_{ss} = 0.142 and γ_{cc} = 0.8 and γ_{ss} = 0.042 respectively.

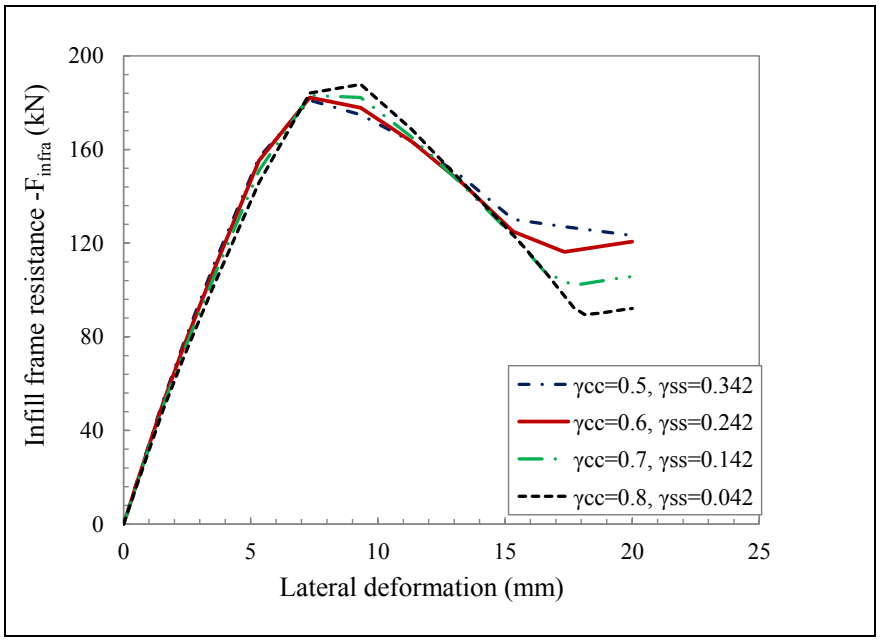

Figure 4.14: Infill frame behaviour for predicted strut material behaviour for sample G4(3)

The process of establishing the target strut resistance and then determining the respective sum of compression and shear factors is carried out for other samples. Strut material characteristics established from various combinations of the compression and shear factors are used for numerical evaluation of the infill frames. A summary of the results of the study is provided in Table 4.17. The proposed procedure generates more accurate predictions for the infill with the ratio of the predicted infill frame capacity to the experimental infill capacity ranging from 0.85 to 1.05 for the samples under study. A key feature of the proposed procedure is the establishment of both the target strut resistance and the corresponding sum of compression and shear factors. These values show significant variations across the samples.

Table 4.17: Results of experimental evaluation for various samples using the proposed procedure

Sample notation	**Infill frame strength (kN), $F_{infra(exp)}$ – Experimental**	**Target strut resistance, F_{sa} (kN)**	$\gamma_{cc}+\gamma_{ss}$	**Infill frame strength (kN), $F_{anfare(pred)}$ - predicted**	$\frac{F_{\inf ra(\text{pred})}}{F_{\inf ra(\exp)}}$
G4(1)	277.7	294.0	0.918	262.0	0.94
G4(2)	153.5	132.9	0.600	158.0	1.03
G4(5)	232.3	243.0	0.858	223.0	0.96
G4(9)	188.2	104.0	0.425	184.0	0.98
G4(3)	190.0	151.0	0.842	184.0	0.97
G4(4)	292.0	340.0	1.480	297.0	1.02
G4(6)	156.2	108.0	0.492	140.0	0.89
G4(8)	276.0	247.0	1.429	289.0	1.05
G4(7)	355.6	347.0	1.189	301.0	0.85
G3	45.5	58.0	0.168	41.0	0.89

Target strut resistance helps identify the infill contribution in the infill frame lateral resistance. An evaluation of the infill resistance with the sum of the compression and shear factors ($\gamma_{cc}+\gamma_{ss}$) is performed to identify possible relationships. Three possibilities of linking the target strut resistance with the $\gamma_{cc}+\gamma_{ss}$ are examined, namely:

(a) the variation of the F_{sa} with $\gamma_{cc}+\gamma_{ss}$;

(b) the variation of the F_{sa} with the product of the infill compressive strength, f_{cw} and $\gamma_{cc}+\gamma_{ss}$; and

(c) the variation of the F_{sa} with the product of the equivalent diagonal strut strength, determined by stress transformation as proposed by El-Dakhakhni et al. (2003), $f_{m\theta}$ and $\gamma_{cc}+\gamma_{ss}$.

Figure 4.15 shows the scatter of the target strut strength with the three possible representations of the $\gamma_{cc}+\gamma_{ss}$. The analytical relationships derived from the two possible linkages, (b) and (c) show better correlation (see Figure 4.15b). Thus, the target strut resistance, which represents the equivalent strut resistance, F_{sa}, is defined by equation 4.97. The R^2 for both equations is 0.92. However, sample G4(8) is far below the regression line, thus for a specified $f_{cw}(\gamma_{cc}+\gamma_{ss})$ or $f_{m\theta}(\gamma_{cc}+\gamma_{ss})$ the equation over predicts sample G4(8) target strut resistance.

$$F_{sa}=\begin{cases}24.875 f_{m\theta}(\gamma_{cc}+\gamma_{ss}) & \text{when } f_{m\theta} \text{ is used}\\ 22.769 f_{cw}(\gamma_{cc}+\gamma_{ss}) & \text{when } f_{cw} \text{ is used}\end{cases} \tag{4.97}$$

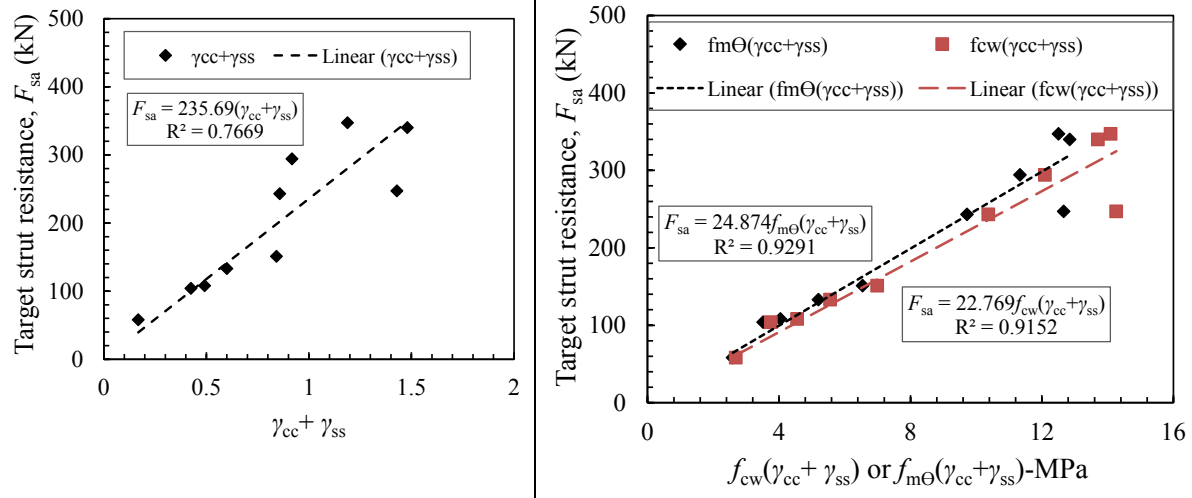

(a) Variation of F_{sa} with $\gamma_{cc}+\gamma_{ss}$

(b) Variation of F_{sa} with $f_{cw}(\gamma_{cc}+\gamma_{ss})$ and $f_{m\theta}(\gamma_{cc}+\gamma_{ss})$

Figure 4.15: Variation and relationship of the target strut resistance, F_{sa}, with $\gamma_{cc}+\gamma_{ss}$, $f_{cw}(\gamma_{cc}+\gamma_{ss})$ and $f_{m\theta}(\gamma_{cc}+\gamma_{ss})$

The variation of the infill compressive strength, f_{cw} and the transformed strut strength, $f_{m\theta}$ with the sum of the compression and the shear factors, $\gamma_{cc}+\gamma_{ss}$ is shown in Figure 4.16. The variation of the compressive strength with the $\gamma_{cc}+\gamma_{ss}$ is considered for each category of masonry as solid or hollow. There is correlation between the compressive strength of solid masonry with $\gamma_{cc}+\gamma_{ss}$ while hollow masonry shows little correlation. Thus, the compressive strength of masonry can be used to estimate the value of $\gamma_{cc}+\gamma_{ss}$ for the solid masonry while more mechanisms should be examined for the hollow masonry. Using regression analysis, linear relationships are developed for both the infill compressive strength and the transformed strut strength and are given in equations 4.98 and 4.99 respectively for the solid masonry.

$$f_{cw} = -4.833(\gamma_{cc}+\gamma_{ss})+16.925 \quad (4.98)$$

$$f_{m\theta} = -5.129(\gamma_{cc}+\gamma_{ss})+16.368 \quad (4.99)$$

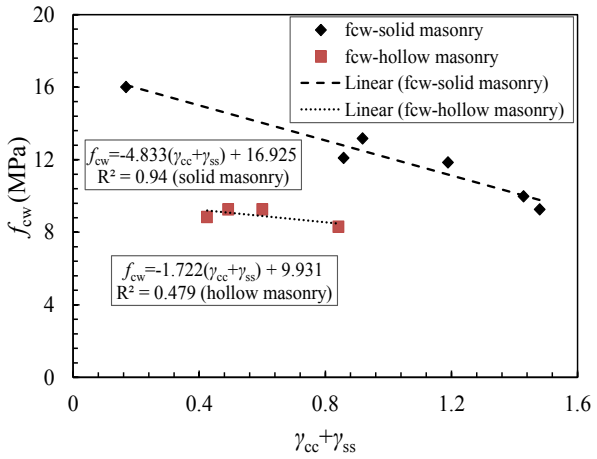

(a) Infill compressive strength variation with $\gamma_{cc}+\gamma_{ss}$

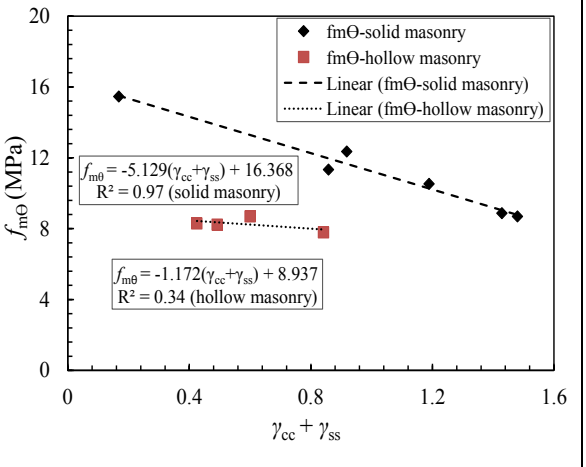

(b) The transformed strut strength variation with $\gamma_{cc}+\gamma_{ss}$

Figure 4.16: Variation and relationship of the infill compressive strength and the transformed strut strength with $\gamma_{cc}+\gamma_{ss}$

4.5 DISCUSSIONS AND CONCLUSION

A new infill frame macro modelling procedure that utilises the stress zoning of the infill has been provided. A preliminary evaluation of the proposed macro-modelling procedure utilises the existing analytical models in determining both the strut cross-sectional area and the capacity. It is noted, however, that utilizing the existing analytical models (FEMA, Mainstone, and Liauw & Kwan models) produces results that vary considerably, making it difficult to establish a common correction factor. A parametric study is conducted to both examine the behaviour of the infill, through macro-modelling, under various structural topological variations. Key parameters that define the infill strut capacity are identified as the target strut resistance, F_{sa}, the compression zone strength factor, γ_{cc}, and the shear sliding strength factor, γ_{ss}. Thus, the infill strut characterisation process can be summarised as follows:

(a) Recall the infill compressive strength, f_{cw}, or determine the transformed strut strength, $f_{m\theta}$;
(b) Determine the transformed diagonal Young's modulus, E_{θ};
(c) Establish the value of $\gamma_{cc}+\gamma_{ss}$ using the value calculated in (a) and either equation 4.98 or 4.99;
(d) Calculate the strut target strength, F_{sa}, using the value from (c) and equation 4.97;
(e) Determine the calibrated elastic strain at peak compressive strength, ε_{1c} using equation 4.95;
(f) Calculate the coefficient, $F_{a\varepsilon}$, by using the parameters calculated in (c) and (d) and using equation 4.94;
(g) Establish the cross-sectional area for the diagonal strut, A_d, using parameters calculated in (b), (e) and (f);
(h) Estimate the stress zone lengths, d_{cc} and d_{dc} using values of infill-frame contact lengths, a_u and a_v established using either FEMA, Mainstone or Liauw and Kwan formulations and equations 4.2 and 4.3;
(i) Using the diagonal strut peak stress (F_{sa}/A_d), the transformed Young's modulus, E_{θ}, the $\gamma_{cc}+\gamma_{ss}$ value and the linearised stress-strain analytical relationships as denoted by Figure 2.3 in Section 2.2.1.1, establish the stress-strain points for each of the stress zones; generate the

stress-strain behaviour for the infill equivalent strut, using characterisation procedure provided in Section 4.2.4.

Notwithstanding the above steps, once the target strut resistance is established, one can use any diagonal strut strength and cross-sectional area in any macro-model, if the parameters generate the same target strut resistance as established in (d). Apart from the infill characterisation, an analytical relationship that estimates the infill frame capacity is proposed. The analytical relationship requires prior knowledge of the bare frame capacity. The capacity of the bare frame is evaluated using appropriate analytical relations derived in Chapter 5. The expressions derived in these sections are based on the data obtained from literature comprising assumed to represent mean or most probable value for each case. Since the empirical models are sensitive to the nature of data used, only mean value should be used. Furthermore, the analytical model for establishing the value of $\gamma_{cc} + \gamma_{ss}$ has an implicit maximum limit of the masonry compressive strength (about 16.9 MPa) beyond which the model generates negative contribution from the infill, which does not have physical meaning.

CHAPTER 5

5.0 BARE FRAME ELASTIC BEHAVIOUR TRANSFORMATION TO EQUIVALENT TRUSS SYSTEM FOR LATERAL RESISTANCE EVALUATION

5.1 INTRODUCTION

Use of a complete truss-based evaluation system for the infill RC frames requires conversion of the frame into a truss that is then combined with the infill strut. Diagonal struts are used to transform the frame into a truss. The behaviour of frame elements and that of truss elements is fundamentally different. The axial resistance of the truss element depends on the stiffness of each section and generates uniform stress across the section. The flexural resistance depends significantly on the depth of the section and generates non-uniform stresses across the section. Thus, from a local material point, there is no way flexural stresses could be transformed into axial stresses. However, when lateral load is applied to both the truss and the frame, it is possible to calibrate the axial properties of the truss so that both systems generate the same force vs. deformation characteristics. The calibration of this behaviour would depend on the material, geometric and topological properties of these systems. For a nonlinear analysis of a truss, useful parameters are elastic and plastic behaviour characteristics (material behaviour characterisation) and cross-sectional area (geometric property) and the length and orientation of individual element (topological properties). This chapter provides the initial phase in the development and calibration of the truss material behaviour and considers two hypotheses to achieve this, namely:

(a) Lateral deformation characteristics within the elastic regime of the frame can be used to generate the equivalent elastic properties for the diagonal strut.
(b) Material and geometric properties of the column dominate the lateral deformation characteristics of the frame and hence the diagonal struts can be modelled using the material properties (both elastic and plastic) of the column.

The use of a truss for framed structural system has both merits and demerits. Its simplicity in determining the stress and strain states makes the use of strain-based nonlinear procedures possible, or easier. However, the loss of flexural DOFs modifies the actual stress states of the element at local level. Some of the challenges that must be resolved before a truss-based system is used to evaluate the bare frame's behaviour under seismic loading are:

(a) Loss of rotational DOFs, thus there is no moment resistance at the fixed connections.
(b) Loss of flexural stresses. The existence of flexural stresses in a frame allows for understanding of the frame behaviour at local level and possible contribution of system failure due to a local failure mechanism. Flexural stresses may vary across the element section and along the length of the element.
(c) Since truss/bar elements are used for material modelling, composite materials such as RC requires homogenised material behaviour to use for the bar elements.

The loss of rotational degrees of freedom and overall flexural resistance might excessively reduce the capacity of the frame to resist lateral loads. It is proposed that diagonal struts be used to represent the overall flexural resistance lost using a truss system. The diagonal struts are modelled to replicate the flexural behaviour of the frame. In the case of RC frames, the heterogeneous material composition across the section of the RC elements should be addressed if bar elements are to replace these RC elements. A composite material homogenisation procedure is used to transform the composite behaviour of respective elements into a uniform cross-sectional behaviour.

5.2 HOMOGENISATION OF COMPOSITE SECTIONS

A truss analogy uses bar elements. Since reinforced concrete elements constitute more than one element, a homogeneous material is developed to model the material behaviour of the composite material. For axially loaded composite elements, a homogenised material model is developed based on the following assumptions:

(a) The composite elements are subjected to the same axial deformation and there is no slippage between the interfaces of the composite members. For a typical tri-linear material model for both concrete and reinforcement bars in both compression and tension, representation of stress-strain at different stress states is as shown in Figure 5.1. It should be noted that the sequence of occurrence follows typical behaviour of concrete and steel and may not always be as assumed, and hence specific formulation may apply.

(b) The area of the homogenous material is constant throughout the full stress-strain spectrum.

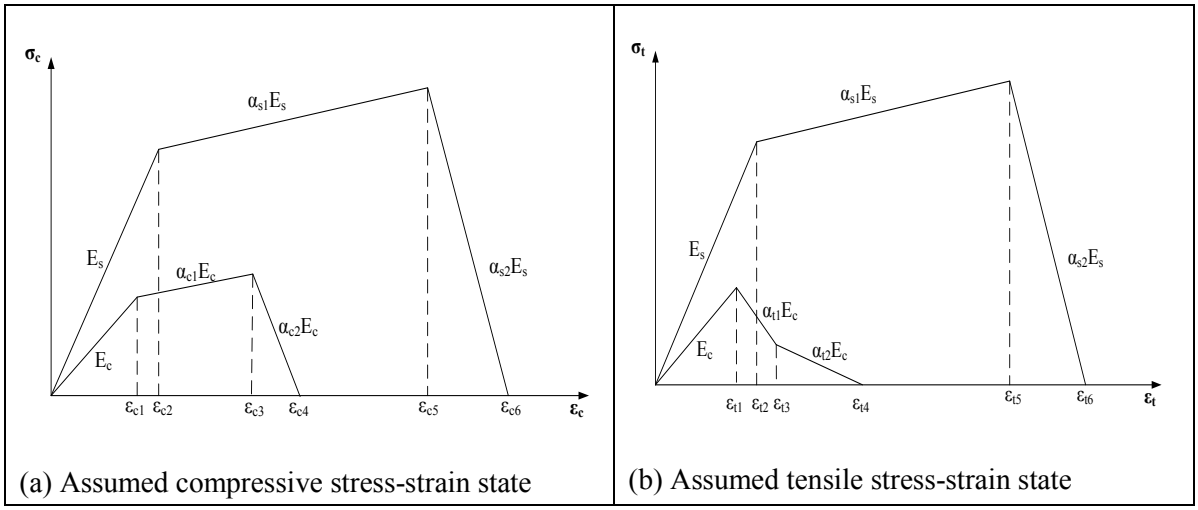

(a) Assumed compressive stress-strain state

(b) Assumed tensile stress-strain state

Figure 5.1: Assumed stress-strain state combinations for RC section under axial compression and tension load

For RC in compression, a homogeneous material model is derived with respect to Figure 5.1(a). Change in axial force (ΔF) is determined by the stiffness relationship for a homogeneous material in equation 5.1. Note that a common strain to both materials and homogeneous material is used as the materials experience the same change in length.

$$\Delta F = \frac{AE_{cj}}{L}\Delta d = AE_{cj}\Delta\varepsilon_{cj} = \Delta\sigma_{cc}A_c + \Delta\sigma_{sc}A_s \tag{5.1}$$

The homogeneous material is assumed to use concrete Young's modulus, E_c,

for $0 < \varepsilon_c \leq \varepsilon_{c1}$ *(elastic state):*

$$\Delta F_1 = E_c\Delta\varepsilon_c A_c + E_s\Delta\varepsilon_c A_s = E_c\Delta\varepsilon_c\left(A_c + mA_s\right) \tag{5.2}$$

'Homogeneous stress', $\Delta\sigma_{o1}$, based on original cross-sectional area, A_o, is

$$\Delta\sigma_{o1} = \frac{\Delta F_1}{A_o} = \frac{E_c\Delta\varepsilon_c\left(A_o - A_s + mA_s\right)}{A_o} = E_c\Delta\varepsilon_c\left(1 + \rho_g(m-1)\right) \tag{5.3}$$

Young's modulus homogenisation factor for the elastic state, η_{c1}, is

$$\eta_{c1} = 1 + \rho_g (m\text{-}1) \tag{5.4}$$

and the modified Young's modulus, $E_{c1} = \eta_{c1} E_c$

For the initial stress state, parameters that can be used in the analysis are E_{c1}, ε_{c1} and A_o representing the Young's modulus, the initial yield strain and the cross-sectional area respectively.

for $\varepsilon_{c1} < \varepsilon_c \leq \varepsilon_{c2}$ *(second stress-strain state):*

$$\Delta F_2 = \alpha_{c1} E_c \Delta\varepsilon_c A_c + E_s \Delta\varepsilon_c A_s = E_c \Delta\varepsilon_c \left(\alpha_{c1} A_o + A_s (m\text{-}\alpha_{c1})\right) \tag{5.5}$$

'Homogeneous stress', $\Delta\sigma_{o2}$, based on original cross-sectional area, A_o, is

$$\Delta\sigma_{o2} = \frac{\Delta F_2}{A_o} = \frac{E_c \Delta\varepsilon_c \left(\alpha_{c1} A_o \text{-} \alpha_{c1} A_s + m A_s\right)}{A_o} = E_c \Delta\varepsilon_c \left(\alpha_{c1} + \rho_g (m \text{-} \alpha_{c1})\right) \tag{5.6}$$

Young's modulus homogenisation factor for the second stress-strain state, η_{c2}, is

$$\eta_{c2} = \alpha_{c1} + \rho_g (m \text{-} \alpha_{c1}) \tag{5.7}$$

The modified tangential Young's modulus, $E_{c2} = \eta_{c2} E_c$.

for $\varepsilon_{c2} < \varepsilon_c \leq \varepsilon_{c3}$ *(Third stress-strain state):*

$$\Delta F_3 = \alpha_{c1} E_c \Delta\varepsilon_c A_c + \alpha_{s1} E_s \Delta\varepsilon_c A_s = E_c \Delta\varepsilon_c \left(\alpha_{c1} A_o + A_s (\alpha_{s1} m \text{-} \alpha_{c1})\right) \tag{5.8}$$

Homogeneous stress, $\Delta\sigma_{o3}$, based on original cross-sectional area, A_o, is

$$\Delta\sigma_{o3} = \frac{\Delta F_3}{A_o} = \frac{E_c \Delta\varepsilon_c \left(\alpha_{c1} A_o \text{-} \alpha_{c1} A_s + \alpha_{s1} m A_s\right)}{A_o} = E_c \Delta\varepsilon_c \left(\alpha_{c1} + \rho_g (\alpha_{s1} m \text{-} \alpha_{c1})\right) \tag{5.9}$$

Young's modulus homogenisation factor for the third stress-strain state, η_{c3}, is

$$\eta_{c3} = \alpha_{c1} + \rho_g (\alpha_{s1} m \text{-} \alpha_{c1}) \tag{5.10}$$

The modified tangential Young's modulus, $E_{c3} = \eta_{c3} E_c$.

for $\varepsilon_{c3} < \varepsilon_c \leq \varepsilon_{c4}$ *(fourth strain state):*

$$\Delta F_4 = \alpha_{c2} E_c \Delta\varepsilon_c A_c + \alpha_{s1} E_s \Delta\varepsilon_c A_s = E_c \Delta\varepsilon_c \left(\alpha_{c2} A_o + A_s (\alpha_{s1} m\text{-}\alpha_{c2})\right) \tag{5.11}$$

'Homogeneous stress', $\Delta\sigma_{o4}$, based on original cross-sectional area, A_o, is

$$\Delta\sigma_{o4} = \frac{\Delta F_4}{A_o} = \frac{E_c \Delta\varepsilon_c \left(\alpha_{c2} A_o \text{-} \alpha_{c2} A_s + \alpha_{s1} m A_s\right)}{A_o} = E_c \Delta\varepsilon_c \left(\alpha_{c2} + \rho_g (\alpha_{s1} m \text{-} \alpha_{c2})\right) \tag{5.12}$$

Young's modulus homogenisation factor for the fourth stress-strain state, η_{c4}, is

$$\eta_{c4} = \alpha_{c2} + \rho_g(\alpha_{s1}m - \alpha_{c2}) \tag{5.13}$$

The modified tangential Young's modulus, $E_{c4} = \eta_{c4}E_c$.

for $\varepsilon_{c4} < \varepsilon_c \leq \varepsilon_{c5}$ *(fifth strain state):*

$$\Delta F_5 = \alpha_{c3}E_c\Delta\varepsilon_c A_c + \alpha_{s1}E_s\Delta\varepsilon_c A_s = E_c\Delta\varepsilon_c\left(\alpha_{c3}A_o + A_s(\alpha_{s1}m\text{-}\alpha_{c3})\right) \tag{5.14}$$

'Homogeneous stress', $\Delta\sigma_{o5}$, based on original cross-sectional area, A_o, is

$$\Delta\sigma_{o5} = \frac{\Delta F_5}{A_o} = \frac{E_c\Delta\varepsilon_c\left(\alpha_{c3}A_o - \alpha_{c3}A_s + \alpha_{s1}mA_s\right)}{A_o} = E_c\Delta\varepsilon_c\left(\alpha_{c3} + \rho_g(\alpha_{s1}m - \alpha_{c3})\right) \tag{5.15}$$

Young's modulus homogenisation factor for the fifth stress-strain state, η_{c5}, is

$$\eta_{c5} = \alpha_{c3} + \rho_g(\alpha_{s1}m - \alpha_{c3}) \tag{5.16}$$

Considering that α_{c3}=0, the above expression simplifies to

$$\eta_{c5} = \alpha_{s1}m\rho_g \tag{5.17}$$

The modified tangential Young's modulus, $E_{c5} = \eta_{c5}E_c$.

for $\varepsilon_{c5} < \varepsilon_c \leq \varepsilon_{c6}$ *(sixth stress-strain state):*

$$\Delta F_6 = \alpha_{s2}E_s\Delta\varepsilon_c A_s = E_c\Delta\varepsilon_c\alpha_{s2}mA_s \tag{5.18}$$

'Homogeneous stress', $\Delta\sigma_{o6}$, based on original cross-sectional area, A_o, is

$$\Delta\sigma_{o6} = \frac{\Delta F_6}{A_o} = \frac{\alpha_{s2}E_s\Delta\varepsilon_c A_s}{A_o} = E_c\Delta\varepsilon_c\alpha_{s2}m\rho_g \tag{5.19}$$

Young's modulus homogenisation factor for sixth stress-strain state, η_{c6}, is

$$\eta_{c6} = \alpha_{s2}m\rho_g \tag{5.20}$$

The modified tangential Young's modulus, $E_{c6} = \eta_{c6}E_c$.

In the same way, the Young's moduli for various states of tensile strains are derived and the coefficient factors based on initial concrete modulus. Thus, the general formula for Young's modulus of a homogenous material representing a RC section subjected to axial forces only, taking concrete as reference material, is as follows:

Homogenised RC element in compression,

$$E_{cj} = \eta_{cj}E_c \tag{5.21}$$

where

$$\eta_{cj} = \alpha_{ci} + \rho_g\left(\alpha_{si} m - \alpha_{ci}\right) \begin{cases} \text{for } j=1; \alpha_{ci}=1,\ \alpha_{si}=1 \\ \text{for } j=2; \alpha_{ci}=\alpha_{c1},\ \alpha_{si}=1 \\ \text{for } j=3; \alpha_{ci}=\alpha_{c1}, \alpha_{si}=\alpha_{s1} \\ \text{for } j=4; \alpha_{ci}=\alpha_{c2}, \alpha_{si}=\alpha_{s1} \\ \text{for } j=5; \alpha_{ci}=0, \alpha_{si}=\alpha_{s1} \\ \text{for } j=6; \alpha_{ci}=0, \alpha_{si}=\alpha_{s2} \end{cases} \tag{5.22}$$

RC in tension,

$$E_{tj} = \eta_{tj} E_c \tag{5.23}$$

where

$$\eta_{tj} = \alpha_{ti} + \rho_g\left(\alpha_{si} m - \alpha_{ti}\right) \begin{cases} \text{for } j=1; \alpha_{ti}=1,\ \alpha_{si}=1 \\ \text{for } j=2; \alpha_{ti}=\alpha_{t1},\ \alpha_{si}=1 \\ \text{for } j=3; \alpha_{ti}=\alpha_{t1}, \alpha_{si}=\alpha_{s1} \\ \text{for } j=4; \alpha_{ti}=\alpha_{t2}, \alpha_{si}=\alpha_{s1} \\ \text{for } j=5; \alpha_{ti}=0, \alpha_{si}=\alpha_{s1} \\ \text{for } j=6; \alpha_{ti}=0, \alpha_{si}=\alpha_{s2} \end{cases} \tag{5.24}$$

5.3 FLEXURAL BEHAVIOURTRANSFORMATION FOR A FIXED FRAME

Transformation of the frame into a truss involves removal of the rotational degrees of freedom and ensuring that the lateral resistance is offered by the axial forces only. For this exercise, a single storey single bay bare frame is used for the derivation and validation of the proposed parameters. Verification uses both the experimental and numerical data. Conversion of the frame's elastic behaviour into a diagonal struts elastic behaviour utilises the method of static condensation. The static condensation method, as used in dynamic analysis of structures, is applied to eliminate the DOFs to which zero mass is assigned and then identify an overall stiffness value in the DOF supporting masses (or inertial-forces) (Chopra, 2007). Since the masses are used for seismic loading analysis, the method is ideal for lumping the flexural stiffness into respective lateral DOFs. Using an 'equivalent truss-structural system', the structural stiffness of axial elements can be determined that replace flexural stiffness contribution. The structural frame is assumed to be axially stiff so that only the flexural stiffness contribution is considered when converting the frame to axial diagonal elements.

5.3.1 Derivation of transformed elastic behaviour parameters for the fixed frame

A single-bay single-storey fixed supported frame structure is assumed as a basic structural configuration to derive relevant parameters for generating the truss equivalence, for use in fixed supported systems. While real structures may have more degrees of freedom, a single storey single bay offers invaluable information to understand the system's behaviour. Furthermore, most of the experimental studies on multi-storey and multi-bay structures are conducted on a single bay single storey structural representation. It is assumed that the formulations developed for the single bay single storey provide the basic formulations that can be modified or calibrated for other structural frame configurations. Figure 5.3 shows all the key parameters, definition of boundary conditions for the frame system and the

diagonal struts that provide equivalent resistance to the rotational DOF. The columns have the same geometric and material properties. The vertical translations at nodes 2 and 3 are made zero to ensure that the solution represents that of a structural system with axially stiff members. The use of rollers at nodes 2 and 3 is for structural clarity to ensure that the vertical DOF for the nodes are fully restrained.

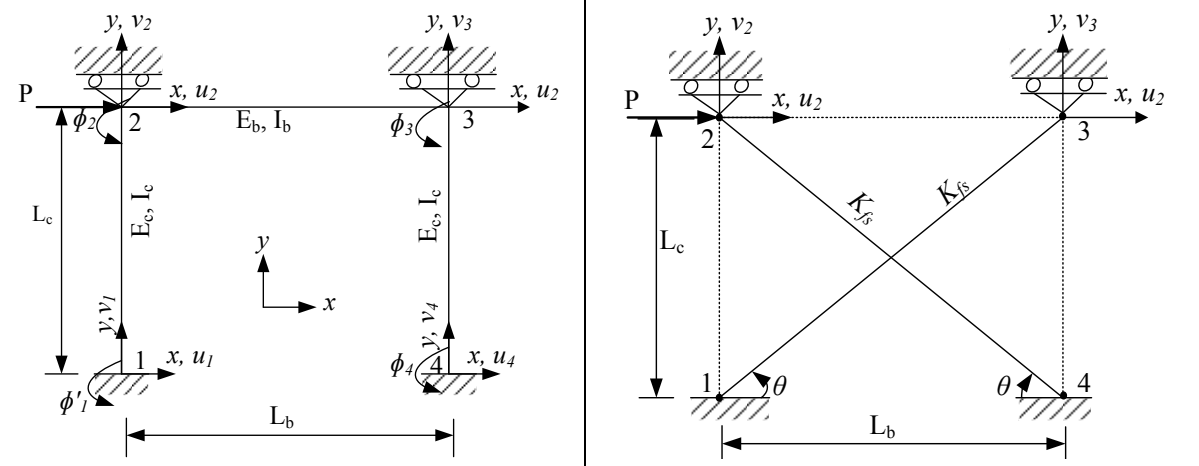

Figure 5.2: Elastic behaviour transformation for a single-storey single-bay fixed supported frame

Considering the stiffness for the non-zero DOFs only, the fixed frame system stiffness, assuming no subsidence, is assembled and used in the force-displacement equation as follows:

$$\begin{Bmatrix} P \\ 0 \\ 0 \end{Bmatrix} = \begin{bmatrix} \frac{24E_cI_c}{L_c^3} & \frac{6E_cI_c}{L_c^2} & \frac{6E_cI_c}{L_c^2} \\ \frac{6E_cI_c}{L_c^2} & \frac{4E_cI_c}{L_c}+\frac{4E_bI_b}{L_b} & \frac{2E_bI_b}{L_b} \\ \frac{6E_cI_c}{L_c^2} & \frac{2E_bI_b}{L_b} & \frac{4E_cI_c}{L_c}+\frac{4E_bI_b}{L_b} \end{bmatrix} \begin{Bmatrix} u_2 \\ \phi_2 \\ \phi_3 \end{Bmatrix} \tag{5.25}$$

Rearranging and partitioning the stiffness into those that support an applied force (k_{ff}) and those that have zero external forces (k_{nn}) gives the following equation:

$$\begin{Bmatrix} P \\ 0 \end{Bmatrix} = \begin{bmatrix} k_{ff} & k_{fn} \\ k_{nf} & k_{nn} \end{bmatrix} \begin{Bmatrix} d_f \\ d_n \end{Bmatrix} \tag{5.26}$$

The force/displacement equations can be re-written separately as follows:

$$P = k_{ff}d_f + k_{fn}d_n \text{ , and} \tag{5.27}$$

$$0 = k_{nf}d_f + k_{nn}d_n \tag{5.28}$$

Since no external forces are associated with DOFs d_n, a static relationship between d_n and d_f is developed from equation 5.28 as follows:

$$d_n = -k_{nn}^{-1}k_{nf}d_f \tag{5.29}$$

Substituting equation 5.29 into equation 5.27 becomes

$$P = \left(k_{ff} - k_{fn} k_{nn}^{-1} k_{nf}\right) d_f \tag{5.30}$$

The factor of DOF d_f in equation 5.30 is the condensed lateral stiffness matrix, K_{cf} and is expressed as follows:

$$K_{cf} = \left(k_{ff} - k_{fn} k_{nn}^{-1} k_{nf}\right) \tag{5.31}$$

Establishing the frame element's stiffness based on the material properties given in Figure 5.3 and substituting them into equation 5.31 gives the equivalent lateral stiffness for the fixed frame as follows:

$$K_{cf} = \frac{24 E_c I_c}{L_c^3}\left(\frac{6\xi + 1}{6\xi + 4}\right) \tag{5.32}$$

where

$$\xi = \frac{\frac{E_b I_b}{L_b}}{\frac{E_c I_c}{L_c}} \tag{5.33}$$

ξ is the beam-to-column stiffness ratio for the single bay single storey frame.

Considering the column as the source of the basic material and geometric properties for the diagonal strut, equation 5.32 can be generalised to comprise the column flexural stiffness, K_c defined by $24E_c I_c / L_c^3$ and the stiffness conversion parameter, k_{TM}, in this case defined as

$$k_{TM} = (6\xi + 1)/(6\xi + 4) \tag{5.34}$$

Thus, equation 5.32 can be redefined as follows:

$$K_{cf} = K_c k_{TM} \tag{5.35}$$

The lateral force applied to a frame must be resisted by the action of the truss mechanism when a truss is used. As a starting point, it is assumed that the lateral resistance in the truss is given by the diagonal struts as shown in Figure 5.2(b). Considering that each of the diagonal struts has an axial stiffness of K_{fs}, a relationship is developed to link the condensed lateral stiffness of the frame, K_{cf} and the diagonal strut stiffness, K_{fs} for either a single strut truss or a double strut truss as provided in equations 5.36 and 5.37 respectively.

$$K_{fs} = \frac{K_{cf}}{2Cos^2\theta} \quad \text{(when two diagonal struts are used- see Figure 5.2)} \tag{5.36}$$

$$K_{fs} = \frac{K_{cf}}{Cos^2\theta} \quad \text{(when only one diagonal strut is used)} \tag{5.37}$$

Considering the stiffness of each diagonal for respective boundary conditions, the cross-sectional area for a diagonal strut is calculated as:

$$A_d = \frac{K_{fs} L_c}{E_{de} \sin\theta} \tag{5.38}$$

where E_{de} is the diagonal strut elastic modulus.

The formulations given under this section assume the use of axially stiff elements and that no prescribed initial deformation due to the foundation subsidence or any other load effects is considered. In practice, all members in a frame resist axial forces and hence the overall stiffness of the frame is influenced by the axial stiffness of respective elements. It can be stated that the lower the axial stiffness of the frame elements the lower the overall lateral stiffness of the frame.

5.3.2 Evaluation and verification of transformed elastic behaviour parameters for the fixed frame

The expressions developed in Section 5.3.1 seek to generate a truss system that offers the same elastic lateral stiffness as that of the frame. Ignoring the contribution of the axial resistance in the formulation already makes the truss stiffer than the frame. Furthermore, the elastic behaviour of the frame may only be experienced for a small load regime as both material and geometric nonlinearity may affect the deformation characteristics for the frame. Both the tangential stiffness and secant stiffness (as defined in Section 3.4.5) are used for verification of the proposed relationships. It is assumed that the lateral deformation/behaviour of the frame is influenced by the column properties. To test this hypothesis, the material properties of the column are used to generate the diagonal strut for the truss. Force-deformation characteristics for the frame are generated using the truss system. Key deformation characteristics, namely yield strength and the yield deformations are used to test the hypotheses.

In this section, the diagonal strut elastic modulus, E_{de}, is assumed to have the same magnitude as that of the column. Thus, the cross-sectional area for a diagonal strut becomes a function of the sectional and geometric properties of the frame:

$$A_d = \frac{12 I_c}{L_c^2 \cos^2\theta \sin\theta}\left(\frac{6\xi + 1}{6\xi + 4}\right) \tag{5.39}$$

(a) Elastic stiffness evaluation

Finite element analysis in ABAQUS, using both the frame idealisation and the truss idealisation for the bare frames is used to evaluate the behaviour of the bare frame. Inputs for the finite element models for the truss are derived from the five experimental data sets selected from literature comprising two steel framed experiments (Markulak, et al., 2013; Dawe & Seah, 1989) and three RC framed experiments (Crisafulli, 1997; Mehrabi, et al., 1996) as shown in Table 5.1. The steel frames are incorporated in the evaluation of the elastic stiffness as they offer more linear behaviour and hence better chances of generating close values to the proposed analytical approximations.

Table 5.1: Input data for truss evaluation

Sample notation	Frame material and column section shape		Single diagonal strut properties		
	Material	Section shape	E_{de} (MPa)	A_d	Strength
G1	Steel	H-section - A120	200000	94	Steel column*
G2	Steel	H–section - W250 x 58	200000	130	Steel column*
G3	RC	Rectangular	22100	554	RC column*
G4(4)	RC	Rectangular	17225	2481	RC column*
G4(9)	RC	Rectangular	19843	3722	RC column*

*Material properties provided in Section 3.5.2

The input material behaviour for the RC truss model is based on homogenisation. Figure 5.3 illustrates the diagonal strut material behaviour used for the model. Confined compressive strength is used for concrete, considering that columns are subjected to axial compressive stresses that, together with the shear reinforcement, enhance their compressive strength. A tri-linear material model is used for the steel sections, steel reinforcement and concrete, with a descending line up to 20% of the material strength. Due to the homogenisation process, the overall material behaviour for the RC element is multi-linear as shown in Figure 5.3b.

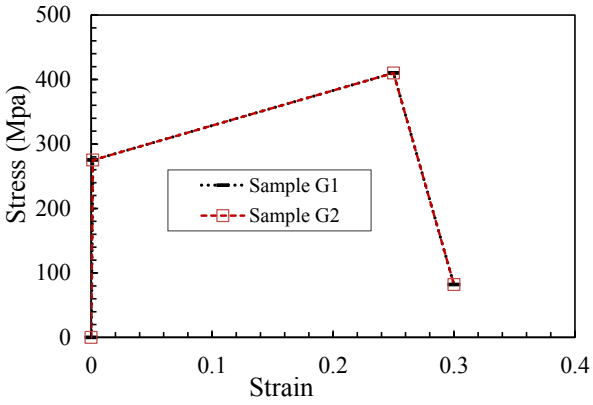

(a) Diagonal strut behaviour for the steel frames

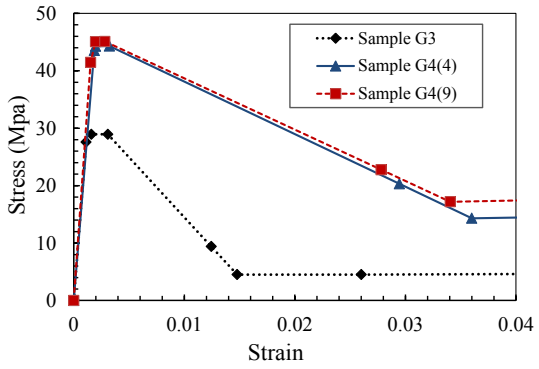

(b) Diagonal strut behaviour for the RC frames

Figure 5.3: Diagonal strut assumed material behaviour

Table 5.2 shows the initial stiffness established from the numerical frame model and the experimental data (when available). The elastic stiffness values extracted from the force-deformation curve of the experimental data are calculated at 33% of the peak load. However, the stiffness value given for the sample G4(4) was calculated at 50% peak load, as provided in the literature as such corresponding stiffness from the numerical frame model is used for comparison. Notwithstanding the scarcity of experimental data, steel frame elastic stiffness behaviour is closer to that of the numerical frame model as compared to the RC frame behaviour as expected.

Table 5.2: Comparison of the elastic behaviour of the frame between the frame model and experimental data

Sample notation	Elastic stiffness (kN/mm)		Numerical / Experimental
	Experimental	Numerical frame model	
G1	Not available	4.03	-
G2	3.50	3.58	1.02
G3	Not available	1.87	-
G4(4)	4.21	6.46	1.53
G4(9)	Not available	16.47	-

Evaluation of the frame elastic stiffness behaviour is conducted using the frame and truss numerical models. Both tangential stiffness (calculated at the initial behaviour force-deformation gradient of the force-deformation curve) and normal elastic stiffness (calculated at 33% of peak load) are established as summarised in Table 5.3. Truss approximation for the tangential stiffness is better than for the elastic stiffness at 33% peak load for the RC frames due to nonlinear behaviour of the RC frames. The truss model mean over-prediction ratio is 1.030 (Cov of 16.97%) for the tangential stiffness and 1.094 (Cov of 17.36%) for the elastic stiffness at 33% peak load. As expected, the steel frames show similar values for the tangential and elastic stiffness at 33% peak load.

Table 5.3: Elastic stiffness for the fixed supported frame for the frame model and truss model

Sample notation	Tangential elastic stiffness*			Elastic stiffness** (kN/mm)		
	Frame model	Truss model	Truss / Frame	Frame model	Truss model	Truss / Frame
G1	4.03	4.45	1.104	4.03	4.45	1.104
G2	3.56	3.66	1.028	3.56	3.66	1.028
G3	1.87	2.21	1.182	1.83	2.21	1.208
G4(4)	14.42	10.57	0.733	12.98	10.57	0.814
G4(9)	16.47	18.18	1.104	13.83	18.18	1.315

*Initial stiffness, calculated as a tangent at the beginning of the for-deformation curve
**Elastic stiffness calculated at 33% of the peak load

(b) Force-deformation characteristics for the fixed frame

As noted in Section 5.3.1, the truss model can either be a single strut or a double strut. In this analysis, both the single and double struts approaches are used. Both approaches give the same deformation characteristics. The force-deformation characteristics for the numerical frame and truss models are presented in Figure 5.4. While the truss system provides comparable prediction to the frame model for the tangential stiffness (with truss-to-frame ratio ranging from 0.73 to 1.18 as noted under (a)), there are significant variations in the overall deformation characteristics and the ultimate strength values. Since this is a preliminary step in the calibration of conversion factors for the truss, it is clear that changing only stiffness without modifying the other material data may not be representative of the overall frame behaviour. In the case of the RC frames, the truss system gives closer values to the numerical frame model, while the steel truss under-predicts the strength as can be noted in Figure 5.4. Thus, it is necessary to calibrate the material characteristics for the diagonal strut if the modelling approach is to be used either for the steel frames or the RC frames.

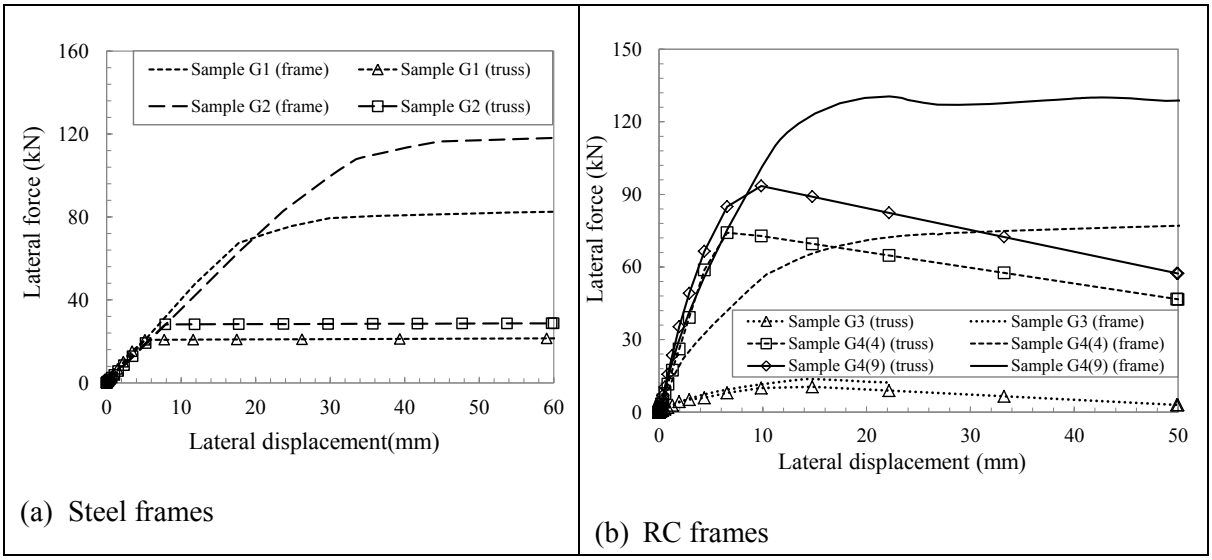

Figure 5.4: Force-deformation characteristics from the preliminary analysis of the fixed bare frames

5.4 FLEXURALBEHAVIOUR TRANSFORMATION FOR A PINNED FRAME

While most of the experimental study on the behaviour of the infill frames is carried out on fixed frame system, frames with pad foundations, which are commonly used, can be considered as pined frames. Thus, understanding the structural behaviour of the pinned frame is essential in developing models that can be used for the pin supported frames. Using a similar approach to that reported in Section 5.3, elastic parameters for the pin supported frames are provided in this section. Numerical data is used to verify the proposed analytical relationships.

5.4.1 Derivation of transformed elastic behaviour parameters for the pinned frame

A single-bay, single-storey frame structure is assumed as a basic structural configuration to derive relevant parameters for the pin supported frames. Figure 5.5 shows all the key parameters, definition of boundary conditions for the frame system and the diagonal struts that provide equivalent resistance to the rotational DOF. The columns have the same geometric and material properties. To ensure that the solution represents that of a structural system with axially stiff members, the vertical translations at nodes 2 and 3 are assumed to be zero.

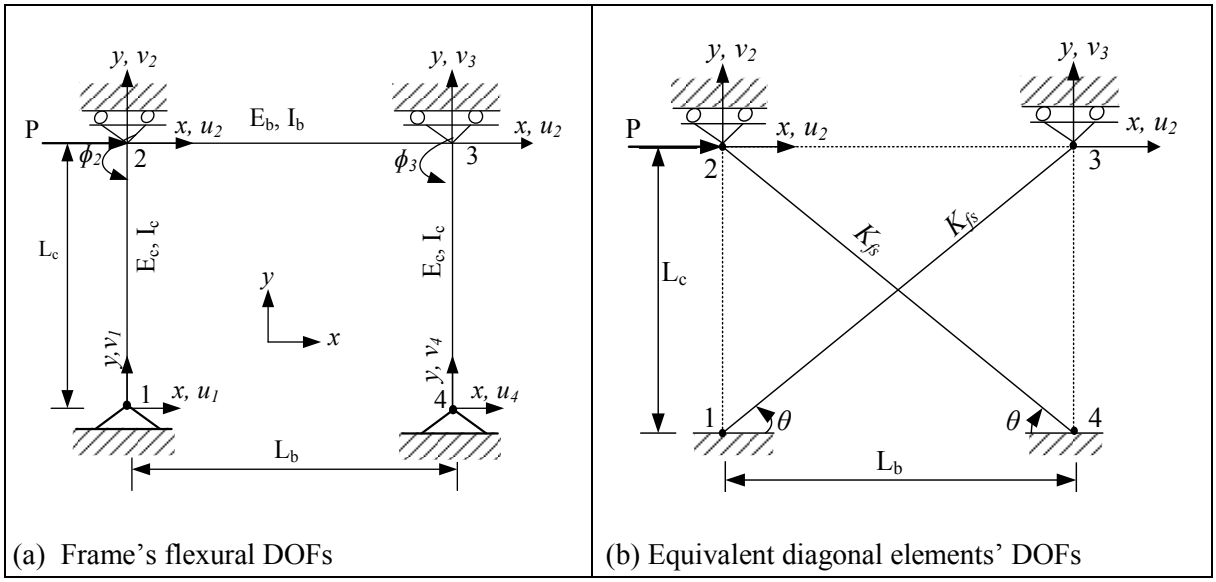

Figure 5.5: Elastic behaviour transformation for a single-storey single-bay pin supported frame

Considering the stiffness for the non-zero DOFs only, the pinned frame system stiffness, assuming no subsidence, is assembled and used in the force-displacement equation as:

$$\begin{Bmatrix} P \\ 0 \\ 0 \\ 0 \\ 0 \end{Bmatrix} = \begin{bmatrix} \frac{24E_cI_c}{L_c^3} & \frac{6E_cI_c}{L_c^2} & \frac{6E_cI_c}{L_c^2} & \frac{6E_cI_c}{L_c^2} & \frac{6E_cI_c}{L_c^2} \\ \frac{6E_cI_c}{L_c^2} & \frac{4E_cI_c}{L_c} & \frac{2E_cI_c}{L_c} & 0 & 0 \\ \frac{6E_cI_c}{L_c^2} & \frac{2E_cI_c}{L_c} & \frac{4E_cI_c}{L_c}+\frac{4E_bI_b}{L_b} & \frac{2E_cI_c}{L_c} & 0 \\ \frac{6E_cI_c}{L_c^2} & 0 & \frac{2E_cI_c}{L_c} & \frac{4E_cI_c}{L_c}+\frac{4E_bI_b}{L_b} & \frac{2E_cI_c}{L_c} \\ \frac{6E_cI_c}{L_c^2} & 0 & 0 & \frac{2E_cI_c}{L_c} & \frac{4E_cI_c}{L_c} \end{bmatrix} \begin{Bmatrix} u_2 \\ \phi_1 \\ \phi_2 \\ \phi_3 \\ \phi_4 \end{Bmatrix} \tag{5.40}$$

Rearranging and partitioning the stiffness into those that support an applied force (k_{ff}) and those that have zero external forces (k_{nn}) gives the equation:

$$K_{cf} = \frac{24E_cI_c}{L_c^3}\left(\frac{16\xi^2+11\xi+3}{64\xi^2+80\xi+36}\right) \tag{5.41}$$

Thus, the stiffness conversion parameter, k_{TM} , for the pinned frame, is:

$$k_{TM} = \left(\frac{16\xi^2+11\xi+3}{64\xi^2+80\xi+36}\right) \tag{5.42}$$

A comparison of the stiffness conversion parameter for the fixed and pin supported frames is conducted as shown in Figure 5.6. The ratios of the of stiffness conversion parameter for the pinned frame to that of the fixed frame at various beam-to-column stiffness ratios are also indicated in Figure 5.6. Fixed frames have a higher stiffness conversion factor than those with pin supports as expected. The stiffness conversion factor for the fixed frames with columns that are stiffer than beams vary from 0.25 to 0.7, while it approaches 1 for the beam-to-column stiffness ratio greater than 10 (at $\xi = 10$, k_{TM} is 0.95). The

stiffness conversion parameters for the pinned frame follow the same pattern as that of the fixed frame, with values approximately a quarter of the fixed frame conversion parameter as indicated by the pinned-to-fixed frame conversion ratio.

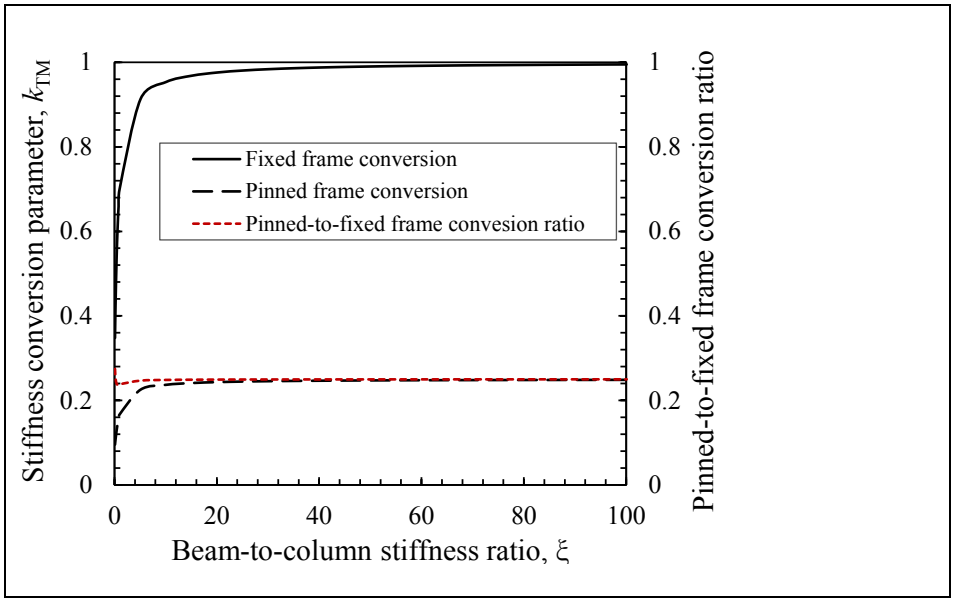

Figure 5.6: Effect of the beam-to-column stiffness ratio on the lateral stiffness

5.4.2 Evaluation and verification of transformed elastic behaviour parameters for the pinned frame

The elastic behaviour for the diagonal derived for the pin supported frames is verified using five samples that were used for the fixed frame. Table 5.4 summarises the diagonal strut properties. Note that the single diagonal strut cross-sectional area is determined using equations 5.37 and 5.41. Both the elastic stiffness and the general force-deformation characteristics are used to compare the behaviour of the frame derived from both the truss and frame numerical models. The input material behaviour for the RC truss model is based on homogenisation and is the same as that of the fixed frame presented in Section 5.4.2 (see Figure 5.3).

Table 5.4: Input data for truss evaluation for the pinned frame

Sample notation	**Frame material and column section shape**		**Single diagonal strut properties**		
	Material	Section shape	E_{de} (MPa)	A_d (mm^2)	Strength
G1	Steel	H-section-A120	200000	22	Steel column*
G2	Steel	H–section - W250x58	200000	31	Steel column*
G3	RC	Rectangular	22100	134	RC column*
G4(4)	RC	Rectangular	17225	592	RC column*
G4(9)	RC	Rectangular	19843	882	RC column*

*Material properties provided in Section 3.5.2

(a) Elastic stiffness evaluation

Finite element analysis in ABAQUS, using both the frame idealisation and the truss idealisation for the pin supported bare frames is used for the verification. Both tangential stiffness (calculated at the initial behaviour force-deformation gradient of the force-deformation curve) and normal elastic stiffness (calculated at 33% of peak load) are established as summarised in Table 5.5. Truss approximation for

the tangential stiffness is better than for the elastic stiffness at 33% peak load for the RC frames due to nonlinear behaviour of the RC frames. The truss model mean over-prediction ratio is 1.002 (Cov of 17.60%) for the tangential stiffness and 1.055 (Cov of 14.91%) for the elastic stiffness at 33% peak load. As expected, the steel frames show similar values for the tangential and elastic stiffness at 33% peak load. Comparison of the ratios of the stiffness values from the pinned to the fixed support frames agrees with the analytical relationship illustrated in Figure 5.6 (see Table 5.6).

Table 5.5: Elastic stiffness for the pin supported frame for the frame model and truss model

Sample notation	Tangential elastic stiffness*			Elastic stiffness** (kN/mm)		
	Frame model	Truss model	$\frac{\text{Truss}}{\text{Frame}}$	Frame model	Truss model	$\frac{\text{Truss}}{\text{Frame}}$
G1	0.96	1.058	1.103	0.96	1.058	1.103
G2	0.89	0.883	0.988	0.89	0.883	0.988
G3	0.47	0.538	1.152	0.47	0.538	1.157
G4(4)	3.60	2.541	0.705	3.12	2.541	0.815
G4(9)	4.11	4.357	1.060	3.60	4.357	1.210

*Initial stiffness, calculated as a tangent at the beginning of the force-deformation curve
**Elastic stiffness calculated at 33% of the peak load

Table 5.6: Pinned frame-to-fixed frame stiffness ratios

Sample notation	Tangential stiffness ratio		Elastic stiffness ratio	
	$\frac{\text{Pinned}}{\text{Fixed}}$ (Frame model)	$\frac{\text{Pinned}}{\text{Fixed}}$ (Truss model)	$\frac{\text{Pinned}}{\text{Fixed}}$ (Frame model)	$\frac{\text{Pinned}}{\text{Fixed}}$ (Truss model)
G1	0.24	0.24	0.24	0.24
G2	0.25	0.24	0.25	0.24
G3	0.25	0.24	0.25	0.24
G4(4)	0.25	0.24	0.24	0.24
G4(9)	0.25	0.24	0.26	0.24

(b) Force-deformation behaviour for the pin supported frames

The force-deformation characteristics for the numerical frame and truss models for the pin supported frames are presented in Figure 5.7. Just like with the fixed frames, there are large variations in the overall deformation characteristics derived from these two approaches. In the case of the RC frames, the truss system gives closer values to the numerical frame model, while the steel truss under-predicts the strength.

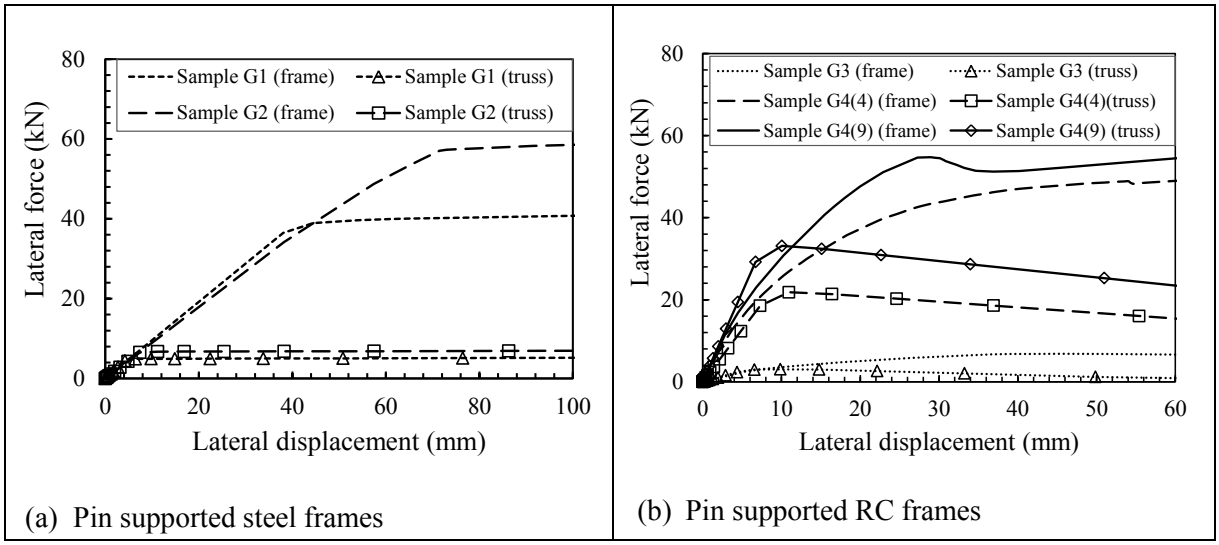

(a) Pin supported steel frames

(b) Pin supported RC frames

Figure 5.7: Force-deformation characteristics from the preliminary analysis of the pin supported bare frames

5.5 EVALUATION AND CALIBRATIONOF PEAK ELASTIC STRENGTH AND DEFORMATION PARAMETERS

The evaluation of the truss behaviour provided in Sections 5.3.2 and 5.4.2 has shown two key findings regarding the hypotheses proposed in Section 5.1, namely:

(a) The lateral deformation characteristics within the elastic regime of the frame can be used to generate the equivalent elastic properties for the diagonal strut. The lateral deformation characteristic is captured by elastic stiffness, where either the tangential or the secant stiffness values are used. The results in Tables 5.3 and 5.5 confirm this hypothesis, with variability emanating from the nonlinearity of the materials and the structural system assemblage.

(b) Material and geometric properties of the column dominate the lateral deformation characteristics of the frame and hence the diagonal struts can be modelled using the elastic material properties of the column. Non-calibrated plastic properties, including the peak elastic stresses/strain from the column cannot be used to model the diagonal strut behaviour. This is shown through Figures 5.4 and 5.7.

This section provides a preliminary evaluation of the diagonal strut material behaviour for the peak elastic strength towards material calibration for both the pinned and the fixed frames.

5.5.1 Peak elastic strength and deformation evaluation for the fixed frames

The peak elastic strength and corresponding deformation for both the frame idealisation and truss idealisation are summarised in Table 5.7. The frame-to-truss ratios for the strength and the deformations show variability, with overall mean of 0.640 (Cov of 56.29%) and 0.520 (Cov of 49.95%) for the strength ratios and deformation ratios respectively. Steel frames have mean ratios of 0.252 (Cov of 5.81%) and 0.237 (Cov of 0.35%) for the strength and the deformation ratios respectively. RC frames have mean ratios of 0.898 (Cov of10.22%) and 0.708 (Cov of 5.14%) for the strength and the deformation ratios respectively.

Table 5.7**:** Peak elastic behaviour for the fixed frames

Sample notation	**Peak elastic strength, F_e (kN)**		$\frac{F_e - \text{Truss}}{F_e - \text{Frame}}$	**Displacement at F_e, δ_e (mm)**		$\frac{\delta_e - \text{Truss}}{\delta_e - \text{Frame}}$
	Frame model	Truss model		Frame model	Truss model	
G1	79.7	20.9	0.262	19.8	4.7	0.237
G2	116.8	28.2	0.241	32.6	7.7	0.236
G3	12.2	9.7	0.793	6.6	4.4	0.667
G4(4)	74.1	69.4	0.937	9.1	6.6	0.725
G4(9)	123.7	119.3	0.965	9.0	6.6	0.733

Parametric evaluation of the peak elastic strength and the corresponding deformation is conducted to establish possible relationships that can be used to calibrate the respective parameters for use in the truss-based analysis. The truss-to-frame ratios of the peak elastic strengths (F_{eR}) and the deformation at peak elastic strength (δ_{eR}) are plotted against the product of the transformation factor, k_{TM} defined by equations 5.34 and 5.42 and the Young's modulus for the column section ($k_{TM}.E_{ce}$) as shown in Figure 5.8. Using regression analysis, analytical relationships are established for both the yield strength and the corresponding deformation (equations 5.43 and 5.44 respectively). Both expressions show good correlation, with correlation factor R^2 greater than 0.99.

$$F_{eR} = 3.69\left(k_{TM}E_{ce}\right)^{-0.54} \tag{5.43}$$

$$\delta_{eR} = 2.36\left(k_{TM}E_{ce}\right)^{-0.46} \tag{5.44}$$

The yield stress for the diagonal (σ_{de}) and its corresponding strain (ε_{de}) can be calibrated from the column properties using the following relationships:

$$\sigma_{de} = \frac{\sigma_{cy}}{F_{eR}} \tag{5.45}$$

$$\varepsilon_{de} = \frac{\varepsilon_{cy}}{\delta_{eR}} \tag{5.46}$$

Equations 5.45 and 5.46 are applicable for both the fixed and the pinned frames. The diagonal yield stress, σ_{de} , is a function of the cross-sectional area derived from Sections 5.3.1 and 5.4.1 for the fixed and pinned frames respectively.

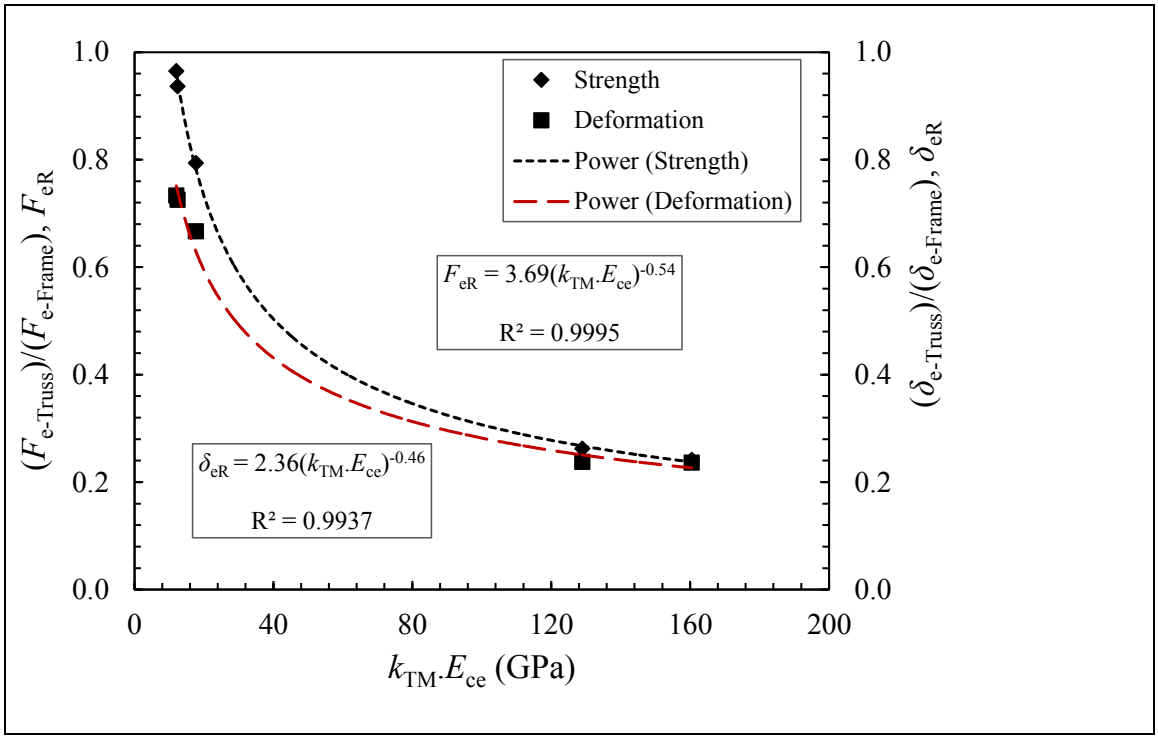

Figure 5.8: Peak elastic strength and deformation evaluation and calibration for the fixed frame

5.5.2 Peak elastic strength and deformation evaluation for the pinned frames

Table 5.8 summarises the peak elastic strength (yield strength) and corresponding deformation for both the frame idealisation and truss idealisation. The overall mean of frame-to-truss ratios for the strength and the deformations are 0.320 (Cov of 62.61%) and 0.306 (Cov of 62.35%) respectively. Steel frames have mean of 0.115 (Cov of 6.71%) and 0.110 (Cov of 1.61%) for the strength ratios and the deformation ratios respectively. RC frames have mean of 0.457 (Cov of 21.82%) and 0.437 (Cov of 20.99%) for the strength and the deformation ratios respectively.

Table 5.8: Peak elastic behaviour for the pinned frames

Sample notation	**Peak elastic strength, F_e (kN)**		$\frac{F_e - \text{Truss}}{F_e - \text{Frame}}$	**Displacement at F_e, δ_e (mm)**		$\frac{\delta_e - \text{Truss}}{\delta_e - \text{Frame}}$
	Frame model	Truss model		Frame model	Truss model	
G1	41.6	5.0	0.120	43.4	4.7	0.108
G2	61.3	6.7	0.109	68.6	7.6	0.111
G3	4.7	1.8	0.387	10.2	3.4	0.333
G4(4)	44.9	18.5	0.413	14.4	7.3	0.507
G4(9)	51.1	29.2	0.571	14.2	6.7	0.472

Parametric evaluation of the peak elastic strength and the corresponding deformation for the pined frames, similar to that for the fixed frames is performed and generated analytical relationships provided in equation 5.47 and 5.58. Figure 5.9 shows the correlation for the analytical expressions, generated using regression analysis. The R^2 for each case is greater than 0.98.

$$F_{eR} = 0.909(k_{TM}E_{ce})^{-0.59} \quad (5.47)$$

$$\delta_{eR} = 0.873(k_{TM}E_{ce})^{-0.59} \quad (5.48)$$

The yield stress for the diagonal strut (σ_{de}) and its corresponding strain (ε_{de}) can be calibrated from the column properties using equations 5.45 and 5.46 where F_{eR} and δ_{eR} are defined by equation 5.47 and 5.48 respectively.

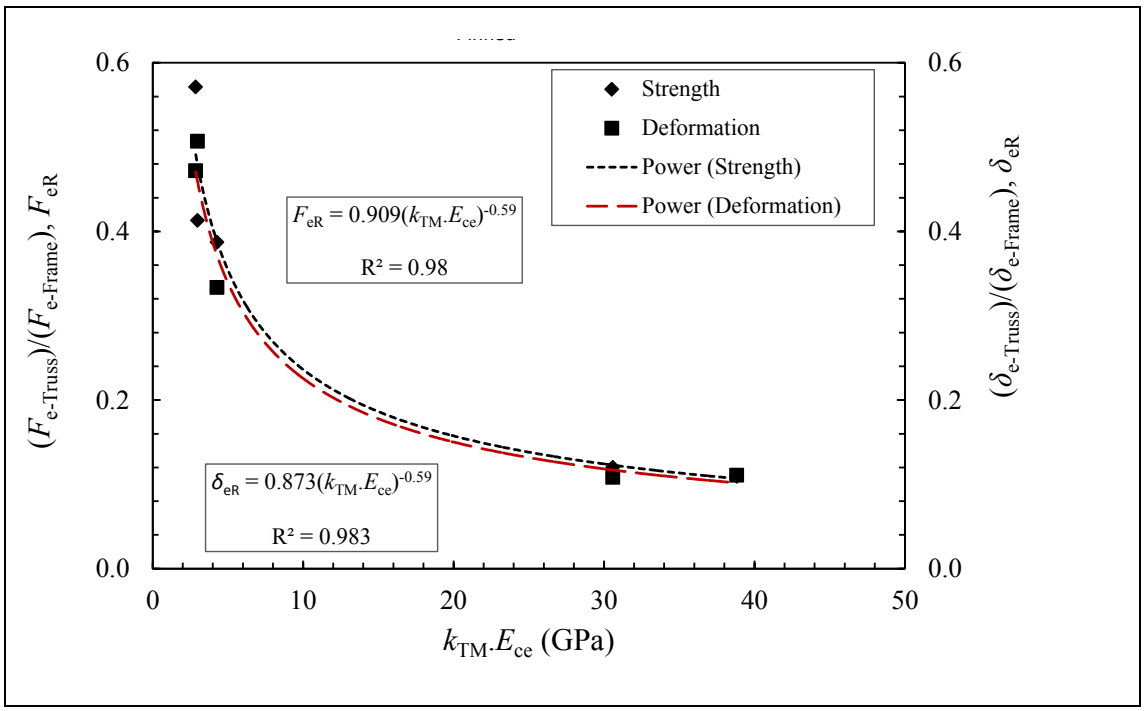

Figure 5.9: Peak elastic strength and deformation evaluation and calibration for the pinned frame

5.5.3 Validation of the peak elastic strength and deformation calibration

Calibration process for the diagonal strut elastic properties provided in Section 5.5.1 and 5.5.2 is based on the column properties. Samples G4(1), G4(6) and G4(8) are used to examine the validity of the calibration process. The yield stress and strain for the diagonal is calculated from the yield stress and strain of the column section. The overall procedure for the determination of the diagonal strut properties is summarised as follows:

(a) Determine the value of $k_{TM}.E_c$ using either equation 5.34 (fixed frames) or equation 5.42 (pinned frames) to calculate k_{TM} ;

(b) Using the values from (a), calculate the factor, F_{eR} using either equation 5.43 (fixed frames) or equation 5.47 (pinned frames);

(c) Using the values from (a), calculate the factor, δ_{eR} using either equation 5.44 (fixed frames) or equation 5.48 (pinned frames);

(d) Calculate the yield stress and corresponding strain for the diagonal using equations 5.45 and 5.46 respectively; and

(e) Establish the Young's modulus for the diagonal strut using values obtained in (d).

Material properties of the diagonal struts for the selected samples are established and used in a FE analysis for each frame conducted in ABAQUS (2011). Diagonal strut material properties, assuming a single strut, are reported in Tables A1.5 and A1.6 in Appendix A1.1. Perfect plastic material behaviour is assumed for the diagonal. Results of the peak elastic strength and the corresponding deformation are summarised in Table 5.9. The truss-based evaluation over predicts the yield strength and the

deformations for the fixed frames, with mean truss-to-frame yield strength and deformation ratios of 1.13 (Cov of 9.58%) and 1.32 (Cov of 11.53%) respectively. The model is conservative for the pinned frames, with mean truss-to-frame yield strength and deformation ratios of 0.81 (Cov of 8.87%) and 0.78 (Cov of 13.66%) respectively.

Table 5.9: Peak elastic behaviour for the fixed and pinned frames using calibrated parameters

Sample notation	**Fixed frame (Frame model)**		**Fixed frame (Truss model)**		**Pinned frame (Frame model)**		**Pinned frame (Truss model)**	
	F_e (kN)	δ_e (mm)	F_e (kN)	δ_e (mm)	F_e (kN)	δ_e (mm)	F_e (kN)	δ_e (mm)
G4(1)	76.8	5.0	91.5	7.3	46.2	12.1	40.8	10.9
G4(6)	70.6	5.4	87.5	7.3	46.1	14.9	35.3	10.9
G4(8)	77.0	6.3	84.4	7.3	45.3	15.4	34.2	10.9

5.6 DISCUSSIONS AND CONCLUSIONS

Transformation of the frame lateral deformation characteristics to an equivalent truss lateral deformation characteristic is provided in this Chapter. Emphasis is placed on the determination and calibration of the elastic and the geometric properties for the diagonal strut. The properties considered are the Young's modulus, the yield stress and its corresponding strain and the cross-sectional area for the diagonal strut. Two hypotheses assumed in Section 5.1 are evaluated. The use of the column properties for the diagonal strut provides a good starting point to understanding the frame to-truss transformation mechanism. Non-calibrated material properties for the column generate considerable variability. To manage such variability, a simple calibration process is proposed and used for the establishment of the diagonal strut elastic properties. The analytical models used for the calibration of the diagonal strut elastic properties are validated using data obtained from the numerical analysis, using both the frame modelling and truss modelling.

The variability in the truss-model predictions, when non-calibrated properties are used may signal that not only the column properties dominate the lateral deformation behaviour of the frames. The factor, $k_{TM}.E_{ce}$ used in the calibration incorporates the beam flexural stiffness (through the beam-to-column stiffness ratio). A comprehensive parametric evaluation for the bare frames is conducted in Chapter 6 to establish analytical relations for the full stress-strain behaviour of the diagonal strut. The transformed truss, together with equivalent strut properties established in Chapter 4 is used for evaluation of the infill RC frames reported in Chapter 7.

CHAPTER 6

6.0 PARAMETRIC EVALUATION AND CALIBRATION OF DIAGONAL STRUT BEHAVIOUR FOR THE BARE FRAME

6.1 INTRODUCTION

This chapter provides a parametric evaluation of the behaviour of the bare frame subjected to horizontal loading. The results of the parametric study are used to calibrate the behaviour of the diagonal strut that is used to transform the frame into a truss system. From the evaluation of the frame behaviour reported in Section 5.3, there are important points that help define the parametric study namely:

(a) There is a marked difference in both the stiffness and strength properties of the fixed and pin supported frames. This difference in the diagonal strut behaviour is illustrated in Figure 5.6. Thus, pin support and fixed support frames may have to be considered separately for diagonal strut behaviour evaluation and calibration.

(b) The structural deformation characteristics for the steel frames are different from that of RC frames when a truss system is used. While such a difference should be obvious, the capacity of steel frames evaluated using the non-calibrated material parameters in for the truss system is significantly lower than that obtained from the frame numerical analysis. For the RC frame, the capacity derived using a truss system is closer to that obtained from frame numerical analysis. Results from the calibrated elastic material properties give some improvements in the variability for both the steel frames and the RC frames. While the variability may be significant, it is acceptable considering that the overall lateral resistance of the RC infill frames comprises the contribution of the infill and the frame. Furthermore, the proposed modelling is designed for use in the preliminary evaluation of the structural system.

(c) It should be noted that the considered case studies have different aspect ratios, a structural topological property that has not been evaluated so far. The effect of the aspect ratio on the frame behaviour, thus diagonal strut behaviour, should be considered based on varying both the length of the beam and the height of the column.

(d) Effects of the structural layout, the number of storeys and bays (structural topology) were not comprehensively studied in the experimental works from which the case studies are selected. It is noted, however, that some experimental set-ups considered multi-storey effects by incorporating extra constant vertical load to the single storey single bay frame configuration (Mehrabi, et al., 1996).

(e) The beam-to-column stiffness ratio variation may have some effects on the behaviour of the frame, especially for $\xi \leq 10$, as noted with the behaviour of the fixed frame as shown in Figure 5.6. The five case studies consider a fixed ratio for each case and they do not give a systematic evaluation of the effect the beam-to-column stiffness ratio. To isolate each of the parameters that constitute this ratio, second moment of area and the lengths of the frames members can be considered separately. Thus, the aspect ratio, as discussed in (c) is considered separately from the I_b/I_c ratio and the material parameter E_b/E_c. In this study it is assumed that each frame comprises of members with the same value for the Young's modulus. Thus, the beam-to-column Young's modulus ratio (E_b/E_c) is 1.0.

(f) The experimental data from selected from literature was generated by testing frames under either a cyclic load or a quasi-static incremental lateral load.

The parametric study identifies the effects of the second moment of areas and the aspect ratio on the structural behaviour of the RC frames. Notable patterns in the behaviour of the frame are used to

formulate analytical relationships that are used in calibrating the diagonal strut properties. For the calibration of material parameters useful for practical applications, pin supported frames are considered in the parametric evaluation. Furthermore, only RC frames are targeted for material parameter calibration as they will be considered in subsequent evaluation. In subsequent parametric evaluation, basic frame properties of group G4 samples are used (sample groups G1 and G2 could not be considered as they are not RC frames while sample group G3 had numerical convergence challenges beyond certain lower applied displacement; any sample from the sample group G4 would have to be used for subsequent studies). Thus, a square column section is used together with a rectangular beam section as initial configuration. A full description of the parametric study program is given in Section 3.4.2.

6.2 PARAMETRIC RESULTS AND DISCUSSIONS FOR THE FIXED SUPPORTED FRAMES

Numerical simulations involving four case study parametric programmes (Cases A – D) comprising fixed supported frame are considered in this section. As stated in Section 3.4.2, the four case studies are devised based on the key parametric variables of I_b, I_c, L_b and L_c. These four variables are evaluated using four structural performance indicators from the lateral force-deformation (F-δ) curve, namely:

(a) Yield strength (F_e);
(b) Yield deformation (δ_e);
(c) Ultimate strength (F_u); and
(d) Ultimate deformation (δ_u)

This section provides the results and discussions for Case A samples, while the results for the other cases are provided in the Appendix A1.2.

6.2.1 Yield strength (F_e) results and discussions for Case A

Case A numerical simulations involve bare frames with constant second moment of area and height for the columns. Yield strength results from the numerical analysis for the bare frames conducted in ABAQUS are discussed in this section. As discussed in Section 3.4.5, the yield strength value can be established using either the linearised curve, where the initial stiffness line converges with the plastic stiffness line, or the actual curve, where a vertical line drawn from the elastic deformation meets with the actual curve (see Figure 3.11b in Section 3.4.5). The variation of the yield strength for the frame across various ratios of $I_b/I_c(I_b)$ (where I_b is varied) is shown in Figure 6.1. There is steeper increase in the yield strength for $I_b/I_c(I_b)$ less than 5.0 while the yield strength gradually increases or reduces for $I_b/I_c(I_b)$ > 5.0 (see Figure 6.1). The variation of the yield strength obtained from the linearised F-δ curve with that obtained from the actual F-δ curve (derived from the numerical results) reflects the extent of nonlinearity in the RC frame behaviour and indicates possible challenges using the linearised curve to approximate such nonlinear structural behaviour.

Figure 6.2 illustrates the scatter of the yield strength across various values of the aspect ratio of the frame, $r_a(L_b)$ (where L_b is varied). There is some pattern in the variation of the yield strength with the aspect ratio. A summary of mean values, standard deviation (Std dev) and coefficient of variation (Cov) for the yield strength under each category of aspect ratio, $r_a(L_b)$ (for respective beam length, L_b) across the $I_b/I_c(I_b)$ ratio is provided in Table 6.1. There is lower variability of the yield strength across the various values of the aspect ratio, $r_a(L_b)$ when the samples with $I_b/I_c(I_b)$ of 1.0 are removed. Overall Cov of 9.23% and 7.74% for linearised and actual curve points respectively are obtained as compared

to the Cov of 6.24% and 4.81% for linearised and actual curve points respectively when samples with $I_b/I_c(I_b)$ of 1.0 are removed.

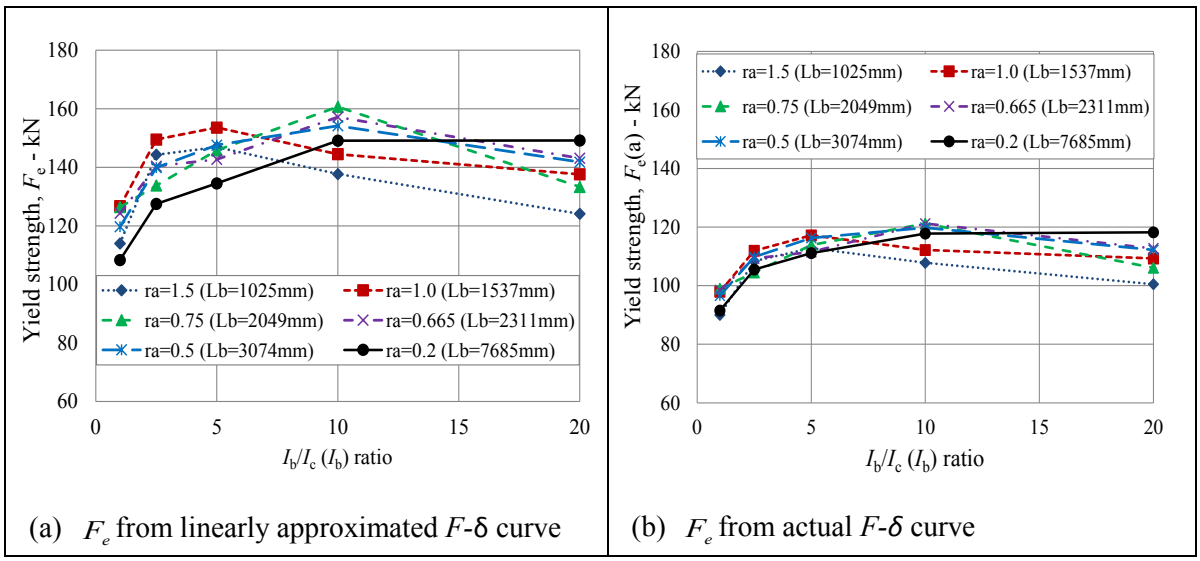

(a) F_e from linearly approximated F-δ curve (b) F_e from actual F-δ curve

Figure 6.1: Typical variation of the yield strength with the $I_b/I_c(I_b)$ ratio for Case A

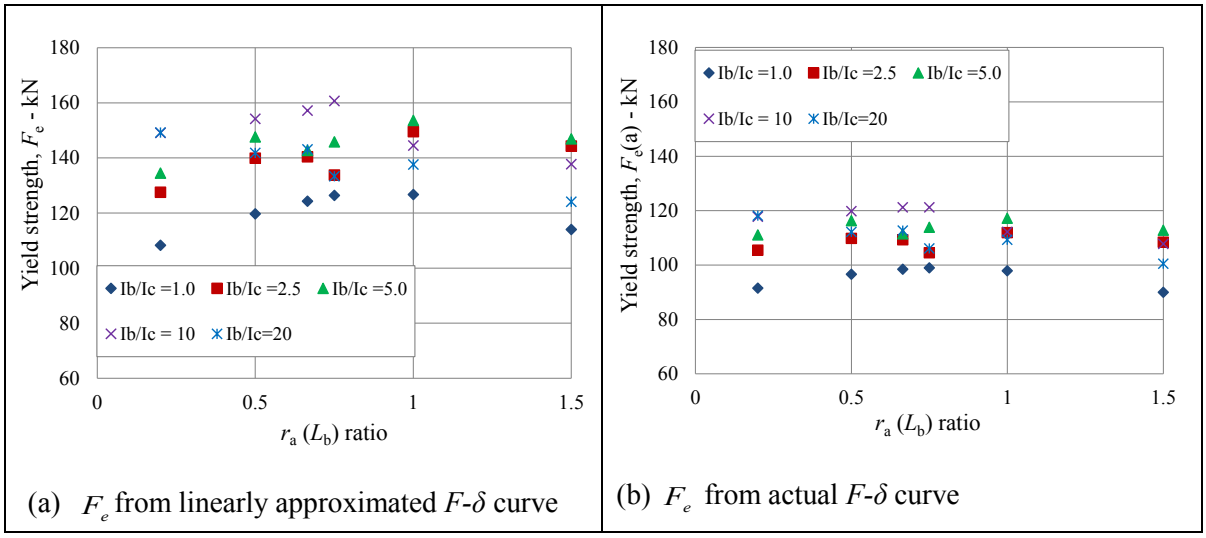

(a) F_e from linearly approximated F-δ curve (b) F_e from actual F-δ curve

Figure 6.2: Typical variation of the yield strength with the aspect ratio, $r_a(L_b)$ for Case A

Table 6. 1: Yield strength mean values, standard deviation and coefficient of variation for each aspect ratio, $r_a(L_b)$ sample category

Sample category	F_e from linearly approximated F-δ curve			F_e (a) from the actual F-δ curve		
	Mean (kN)	Std dev	Cov	Mean (kN)	Std dev	Cov
A_{i1}	133.4	13.99	0.1048	103.9	8.94	0.0860
A_{i2}	142.4	10.60	0.0745	109.7	7.19	0.0655
A_{i3}	140.0	13.51	0.0965	108.9	8.68	0.0797
A_{i4}	141.5	11.70	0.0827	110.6	8.15	0.0737
A_{i5}	140.6	12.97	0.0922	110.9	8.88	0.0801
A_{i6}	133.7	17.04	0.1274	108.8	11.01	0.1012
A_{ij}*	138.6	12.79	0.0923	108.8	8.42	0.0774
A_{ij}**	143.3	8.95	0.0624	112.1	5.39	0.0481

*Overall results; ** Overall results excluding samples for which $I_b/I_c(I_b)$=1.0

6.2.2 Yield deformation (δ_e) results and discussions for Case A

Results of the yield deformation for Case A samples are obtained and evaluated across the $I_b/I_c(I_b)$ ratio and the aspect ratio, $r_a(L_b)$. Figure 6.3 shows the variation of the yield deformation with the $I_b/I_c(I_b)$ ratio. The yield deformation for the frame across various ratios of $I_b/I_c(I_b)$ reduces at a steeper rate for the $I_b/I_c(I_b)$ less than 5.0 and there is a slower reduction in the yield strength for $I_b/I_c(I_b) >$ 5.0 (see Figure 6.3a). The yield deformation reduces with increase in the aspect ratio, $r_a(L_b)$ (see Figure 6.3b).

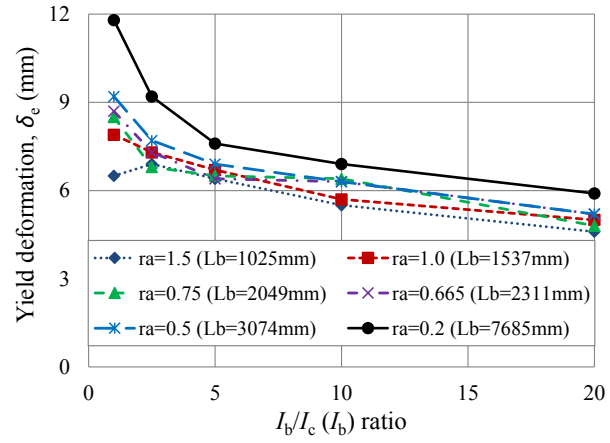

(a) Variation of the yield deformation with the $I_b/I_c(I_b)$ ratio

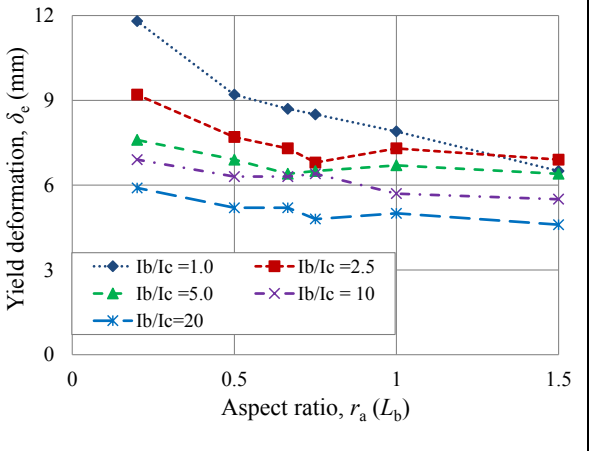

(b) Variation of the yield deformation with the aspect ratio, $r_a(L_b)$

Figure 6.3: Variation of the yield deformation with $I_b/I_c(I_b)$ and the aspect ratio, $r_a(L_b)$ for Case A

6.2.3 Ultimate strength (F_u) results and discussions for Case A

The ultimate strength for each numerical simulation data is established using either the linearised F-δ curve, where the pre-peak plastic stiffness line converges with the post-peak plastic stiffness line, or the actual F-δ cure where a vertical line drawn from the ultimate deformation meets with the actual curve (see Figure 3.11).

The ultimate strength for the frame across various ratios of $I_b/I_c(I_b)$ is shown in Figure 6.4. There is a steeper increase in the ultimate strength with increase in the $I_b/I_c(I_b)$ ratio when $I_b/I_c(I_b)$ is less than 5.0 while a gradual or no increase for $I_b/I_c(I_b)$ > 5.0 is observed (see Figure 6.4). Figure 6.5 illustrates the scatter of the ultimate strength across various values of the aspect ratio of the frame, $r_a(L_b)$. There is some pattern between the variations in the ultimate strength with the aspect ratio, $r_a(L_b)$. A summary of mean values, standard deviation and coefficient of variation for the ultimate strength under each category of aspect ratio, $r_a(L_b)$ across the $I_b/I_c(I_b)$ ratio is provided in Table 6.2. There are minimal differences in the variability of the ultimate strength obtained from either the linearised curve or the actual curve. The overall Cov of 5.87% and 4.64% for linearised and actual curve points respectively are obtained.

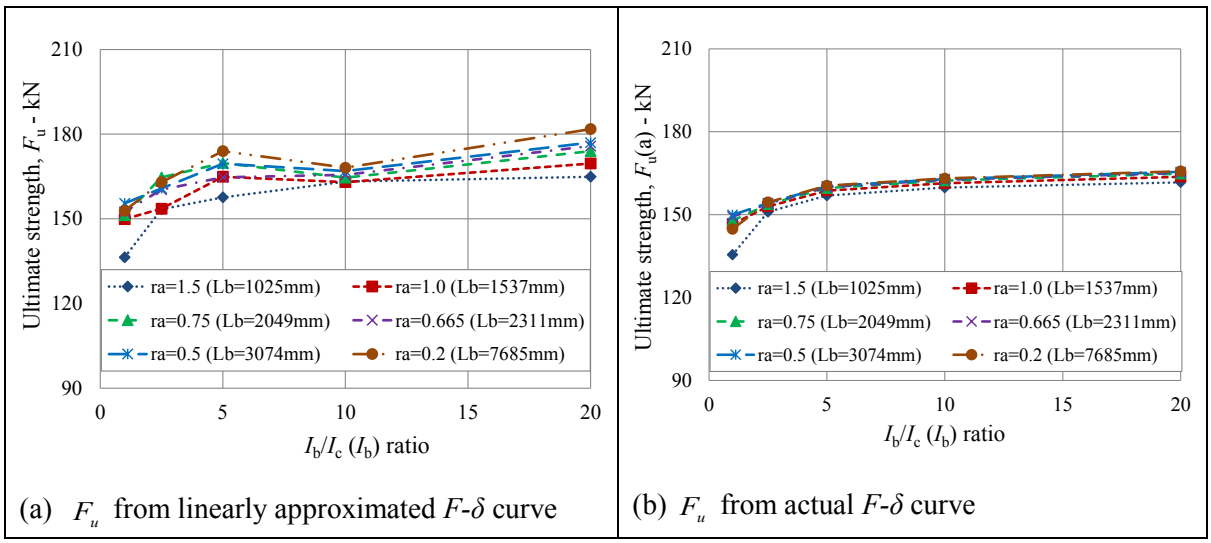

(a) F_u from linearly approximated *F-δ* curve (b) F_u from actual *F-δ* curve

Figure 6.4: Typical variation of the ultimate strength with the $I_b/I_c(I_b)$ ratio for Case A

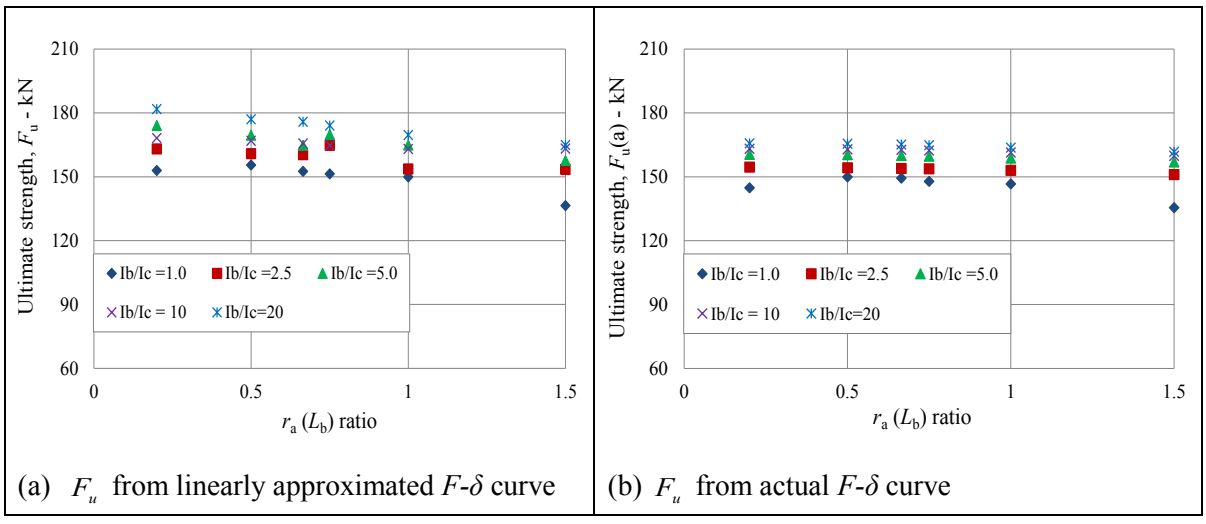

(a) F_u from linearly approximated *F-δ* curve (b) F_u from actual *F-δ* curve

Figure 6.5: Typical variation of the ultimate strength with the aspect ratio, $r_a(L_b)$ for Case A

Table 6.2: Ultimate strength mean values, standard deviation and coefficient of variations for each aspect ratio, $r_a(L_b)$ sample category

Sample category	F_u from linearly approximated F-δ curve			F_u (a) from the actual F-δ curve		
	Mean (kN)	Std dev	Cov	Mean (kN)	Std dev	Cov
A_{i1}	155.1	11.41	0.0735	153.0	10.58	0.0691
A_{i2}	160.2	8.18	0.0511	156.7	6.91	0.0441
A_{i3}	164.9	8.54	0.0518	157.6	6.88	0.0436
A_{i4}	163.8	8.49	0.0518	158.2	6.47	0.0409
A_{i5}	165.9	8.24	0.0496	158.6	6.40	0.0404
A_{i6}	168.0	10.95	0.0652	157.7	8.33	0.0528
A_{ij}*	163.0	9.57	0.0587	157.0	7.29	0.0464

*Overall results

6.2.4 Ultimate deformation (δ_u) results and discussions for Case A

The variations in the ultimate deformation with the $I_b/I_c(I_b)$ ratio and the aspect ratio, $r_a(L_b)$, are presented in Figure 6.6. The ultimate deformation reduces with increase in the $I_b/I_c(I_b)$ ratio, with a steeper decline for the $I_b/I_c(I_b)$ ratio less than 5.0 (see Figure 6.6a).When the ultimate deformations are plotted against the aspect ratios, $r_a(L_b)$, there is reduction in the ultimate deformation with increase in the aspect ratio, $r_a(L_b)$ (see Figure 6.6b). However, sample with the $I_b/I_c(I_b)$ ratio of 1.0 show a steeper reduction in the ultimate deformation with increase in the aspect ratio than the rest.

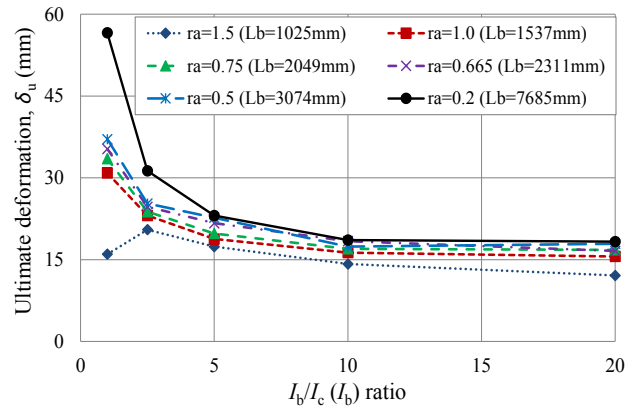

(a) Variation of the ultimate deformation with the $I_b/I_c(I_b)$ ratio

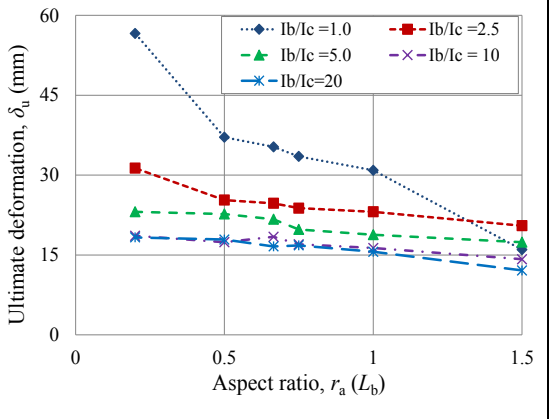

(b) Variation of the ultimate deformation with the aspect ratio, $r_a(L_b)$

Figure 6.6: Typical ultimate deformation variation with the $I_b/I_c(I_b)$ ratio and the aspect ratio, $r_a(L_b)$ for Case A

6.2.5 Discussions for the typical behaviour of the fixed frames

Results of the typical behaviour of the fixed frame are discussed in Sections 6.2.1 – 6.2.4 for Case A while for Cases B – D are provided in Appendix A1.2. The following points summarise the general behaviour of the bare frames subjected to the incremental lateral load:

(a) Both the yield strength and the ultimate strength reduce with reduction in the $I_b/I_c(I_b)$ ratio for $I_b/I_c(I_b) \leq 5.0$ and are almost constant for $I_b/I_c(I_b) > 5.0$. This trend is observed when either the beam length or the column length is varied (Cases A and B). There is no significant

variation of both the yield strength and ultimate strength with the aspect ratio $r_a(L_b)$ (for Case A) while increase in the aspect ratio, $r_a(L_c)$ significantly reduces the yield strength and the ultimate strength (Case B).

(b) There is a general reduction in both the yield and ultimate deformations with increase in the $I_b/I_c(I_b)$, with steeper reduction observed for $I_b/I_c(I_b) \leq 5.0$ for Cases A and B. Both the yield and the ultimate deformations decrease with increase in the aspect ratio $r_a(L_b)$ and increase with increase in the aspect ratio $r_a(L_c)$ for Cases A and B respectively.

(c) Both the yield and the ultimate strengths reduce with increase in the $I_b/I_c(I_c)$ ratio. This trend is observed when either the beam length or the column length is varied (Cases C and D). There is no significant variation of both the yield strength and ultimate strength with the aspect ratio $r_a(L_b)$ (for Case C) while increase in the aspect ratio, $r_a(L_c)$ reduces the yield strength and the ultimate strength (Case D).

(d) There is a general increase in both the yield and ultimate deformations with increase in $I_b/I_c(I_c)$ for $I_b/I_c(I_c) \leq 5.0$, with insignificant change for $I_b/I_c(I_c) > 5.0$ for Cases C. However, samples for Case D increase in both the yield and ultimate deformation for all the ratios of $I_b/I_c(I_c)$ considered. Both the yield and the ultimate deformations decrease with increase in the aspect ratio $r_a(L_b)$ and increase with increase in the aspect ratio $r_a(L_c)$ for Cases C and D respectively.

Both the yield and ultimate strengths are calculated using either the linearised or the actual *F-δ* curve. In all the cases the linearised approach over-estimates the yield strengths. Table 6.2 summarises the mean values of the strength for each case, highlighting possible variations emanating from the linear approximation. The linearised *F-δ* curve over-estimates the yield strength by an average of 24%, the ultimate strength by an average of 2%. The average F_e-to-F_u(a) ratio ranges from 0.77 to 0.92. Thus, a bilinear perfect-plastic force-deformation curve can be used as a conservative choice for the deformation characteristics of the fixed RC bare frames.

Table 6.3: Mean strength values from the linearised and the actual *F-δ* curves for fixed frames

Sample Group	Yield strength, kN		F_e – Linear	Ultimate strength, kN		F_u – Linear	F_e – Linear
	F_e-Linear	F_e(a)-actual	$F_e(a)$ – Actual	F_u-Linear	F_u(a)-Actual	$F_u(a)$ – Actual	$F_u(a)$ – Actual
A	138.6	108.8	1.27	163.0	157.0	1.04	0.88
B	132.4	104.4	1.27	147.3	144.2	1.02	0.92
C	252.6	212.5	1.19	344.3	342.1	1.01	0.74
D	245.8	203.1	1.21	320.8	318.8	1.01	0.77

6.3 PARAMETRIC RESULTS AND DISCUSSIONS FOR PIN SUPPORTED FRAMES

Numerical analyses are conducted on pin supported bare frames from the four case study groups outlined in Section 3.4.2. Four key variables, namely; I_b, I_c, L_b and L_c are considered to establish typical behaviours of bare frames subjected to incremental horizontal forces. The typical behaviour for the bare frame with pin supports is captured using the four key performance indicators of the structural frame, namely; F_e, δ_e, F_u and δ_u. In this section, only the results and discussions for Case A samples are provided while the results for the other cases are reported in Appendix A1.3. Case A pin-supported bare frames comprise of columns with constant second moment of area (I_c = 2.31 x 10^8 mm^4) and

height (L_c = 1537 mm). The geometric properties of the beam are varied, the length is determined by varying the aspect ratio $r_a(L_b)$, from 0.2 to 1.5 and the second moment of area is established by varying the $I_b/I_c(I_b)$ ratio from 1.0 to 20.The results and discussions for each of the four structural behaviour indicators (F_e, δ_e, F_u and δ_u) are summarised in this section.

6.3.1 Yield strength (F_e) and deformation (δ_e) results and discussions for Case A

Results of the yield strength and yield deformation are reported in this section. The yield strengths are established based on both the linearised and the actual *F*-*δ* curves.

(a) Yield strength behaviour for the pinned frames

Yield strength results from the numerical analyses are shown in Figure 6.7. The yield strength increases with increase in the $I_b/I_c(I_b)$ ratio, with steeper increase for $I_b/I_c(I_b)$ ratio less than 5.0. Figure 6.8 illustrates the scatter of the yield strength across various values of the aspect ratio of the frame, $r_a(L_b)$. There is consistent and gradual reduction in the yield strength with increase in the aspect ratio, $r_a(L_b)$ except for samples with $I_b/I_c(I_b)$ of 1.0. A summary of mean values, standard deviation and coefficient of variationfor the yield strength under each category of aspect ratio (for respective beam length) across the $I_b/I_c(I_b)$ ratio is provided in Table 6.4. Sample A_{11} has excessively low strength value compared to the rest. There is lower variability of the yield strength across the various values of the aspect ratio, $r_a(L_b)$ when sample A_{11} is removed compared to the overall variability. The overall Cov of 9.40% and 10.55% for linearised and actual curve points respectively are obtained as compared to the Cov of 6.67% and 8.59% for linearised and actual curve points respectively when sample A_{11} is removed.

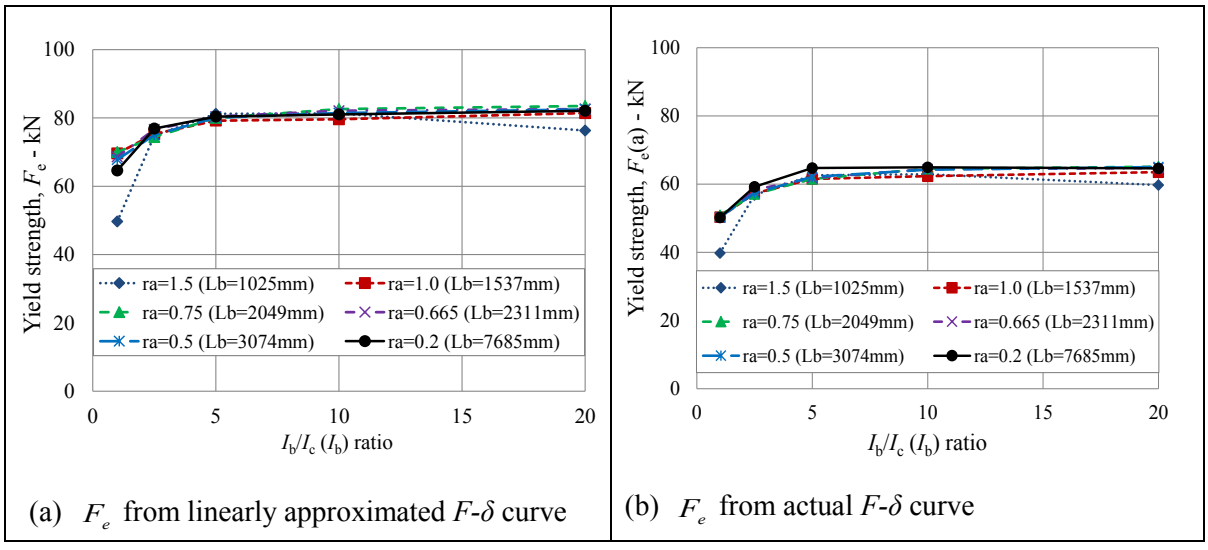

(a) F_e from linearly approximated *F*-*δ* curve

(b) F_e from actual *F*-*δ* curve

Figure 6.7: Typical variation of the yield strength with the $I_b/I_c(I_b)$ ratio for Case A

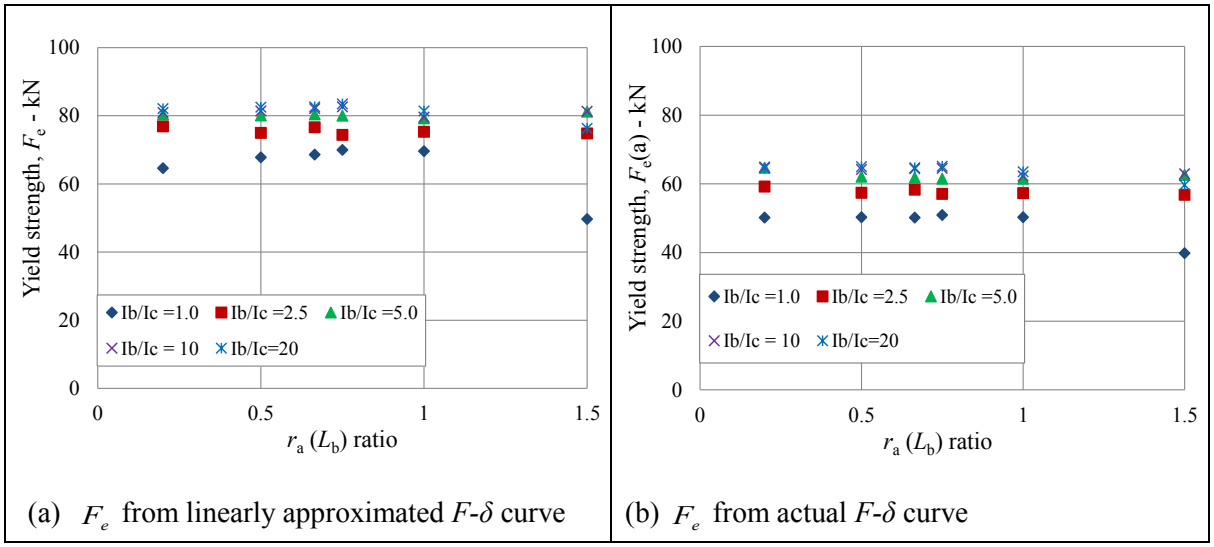

(a) F_e from linearly approximated F-δ curve (b) F_e from actual F-δ curve

Figure 6.8: Typical variation of the yield strength with the aspect ratio, $r_a(L_b)$ for Case A

Table 6.4: Yield strength mean values, standard deviation and coefficient of variation for each aspect ratio, $r_a(L_b)$ sample category

Sample category	**F_e from linearly approximated F-δ curve**			**F_e (a) from the actual F-δ curve**		
	Mean (kN)	Std dev	Cov	Mean (kN)	Std dev	Cov
A_{i1}	72.7	13.16	0.1811	56.4	9.58	0.1700
A_{i2}	77.0	4.71	0.0611	59.0	5.38	0.0913
A_{i3}	78.1	5.75	0.0736	59.8	5.91	0.0987
A_{i4}	78.1	5.79	0.0742	59.9	5.99	0.1000
A_{i5}	77.4	6.07	0.0784	59.8	6.08	0.1016
A_{i6}	77.0	7.20	0.0935	60.7	6.35	0.1046
A_{ij}*	76.7	7.21	0.0940	59.3	6.25	0.1055
A_{ij}**	77.6	5.18	0.0667	59.9	5.15	0.0859

*Overall results; ** Overall results excluding sampleA_{11}

(b) Yield deformation behaviour for the pinned frames

Yield deformations for Case A analyses are shown in Figure 6.9. Except for sample A_{11}, all the other samples show reduction in the yield deformation with increase in the $I_b/I_c(I_b)$ ratio, with a steeper reduction for $I_b/I_c(I_b) < 5.0$. The yield deformations gradually reduce with increase in the aspect ratio, $r_a(L_b)$.

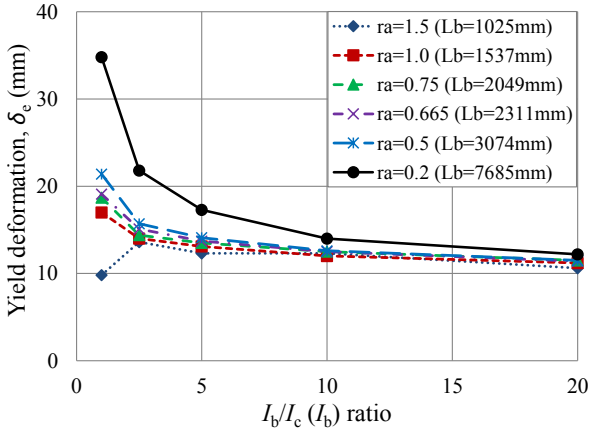

(a) Variation of the yield deformation with the $I_b/I_c(I_b)$ ratio

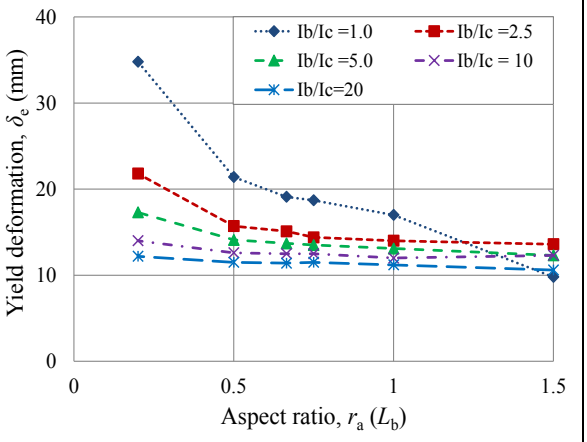

(b) Variation of the yield deformation with the aspect ratio, $r_a(L_b)$

Figure 6.9: Variation of the yield deformation with $I_b/I_c(I_b)$ ratio and the aspect ratio, $r_a(L_b)$ for Case A

6.3.2 Ultimate strength (F_u) and deformation (δ_u) results and discussions for Case A

Results of the ultimate strength and deformation are reported in this section. The ultimate strengths are established based on both the linearised and the actual *F*-δ curves.

(a) Ultimate strength (F_u) behaviours

The ultimate strengths for bare frames with different configurations as stated for Case A samples were established using finite element analyses and the results are shown in Figure 6.10. The ultimate strength increases with increase in the $I_b/I_c(I_b)$ ratio, with steeper increase for $I_b/I_c(I_b)$ < 5.0. Figure 6.11 illustrates the scatter of the ultimate strength across various values of the aspect ratio of the frame, $r_a(L_b)$. There is notable pattern of change in the ultimate strength with change in the aspect ratio, $r_a(L_b)$. A summary of mean values, standard deviation and coefficient of variation for the ultimate strength under each category of aspect ratio, $r_a(L_b)$ across the $I_b/I_c(I_b)$ ratio is provided in Table 6.5. There are minimal differences in the variability of the ultimate strength obtained from either the linearised curve or the actual curve across all the samples. The overall Cov of 5.79% and 6.18% for linearised and actual curve points respectively are obtained.

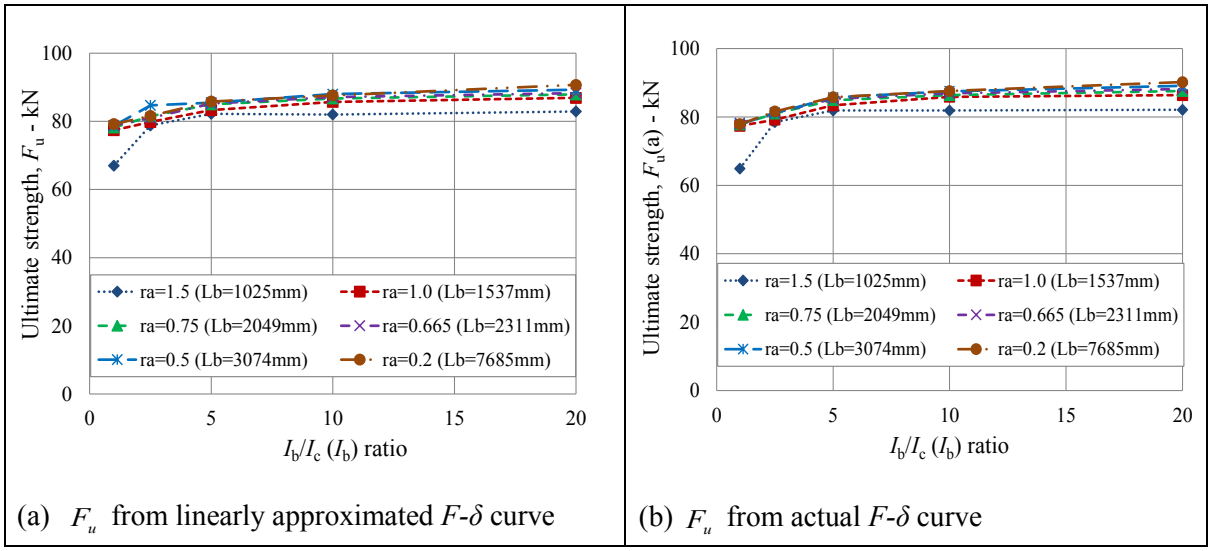

(a) F_u from linearly approximated F-δ curve (b) F_u from actual F-δ curve

Figure 6.10: Typical variation of the ultimate strength with the $I_b/I_c(I_b)$ ratio for Case A

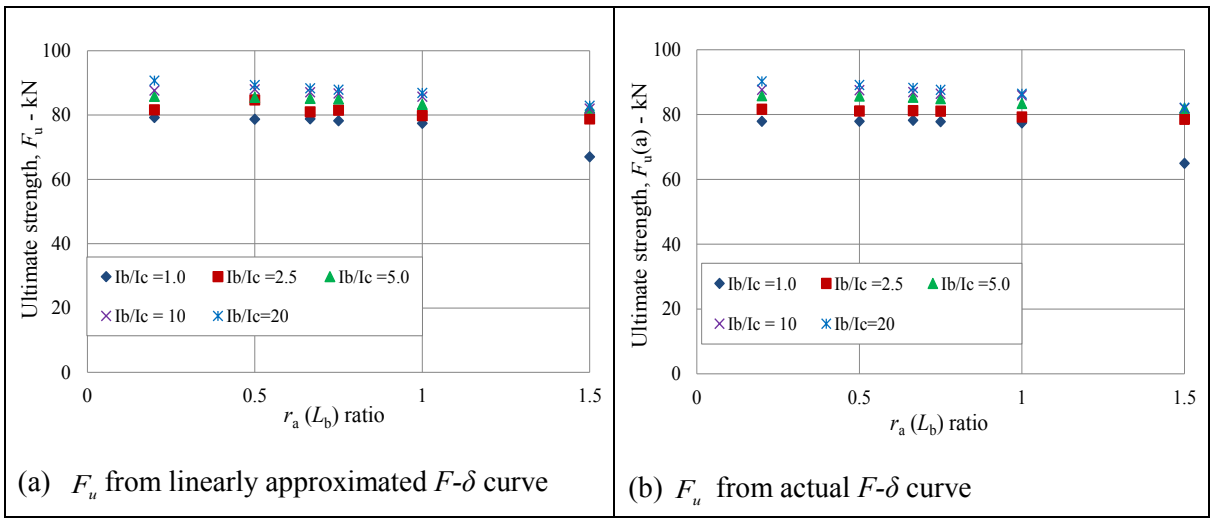

(a) F_u from linearly approximated F-δ curve (b) F_u from actual F-δ curve

Figure 6.11: Typical variation of the ultimate strength with the aspect ratio, $r_a(L_b)$ for Case A

Table 6.5: Ultimate strength mean values, standard deviation and coefficient of variation for each aspect ratio, $r_a(L_b)$ sample category

Sample category	***F*u from linearly approximated *F*-δ curve**			***F*u (a) from the actual *F*-δ curve**		
	Mean (kN)	Std dev	Cov	Mean (kN)	Std dev	Cov
A_{i1}	78.6	6.66	0.0848	77.9	7.40	0.0950
A_{i2}	82.6	3.98	0.0482	82.5	4.01	0.0487
A_{i3}	83.9	3.98	0.0474	83.5	4.06	0.0486
A_{i4}	84.1	4.05	0.0481	84.0	4.16	0.0495
A_{i5}	85.2	4.10	0.0481	84.3	4.65	0.0552
A_{i6}	85.0	4.61	0.0543	84.6	4.89	0.0578
A_{ij}*	83.2	4.82	0.0579	82.8	5.12	0.0618

*Overall results

(b) Ultimate deformation behaviour

Numerical results showing the variation of the ultimate deformation with $I_b/I_c(I_b)$ ratio and the aspect ratio, $r_a(L_b)$ are shown in Figure 6.12. Apart from sample A_{11}, there is a reduction in the ultimate deformation with an increase in the $I_b/I_c(I_b)$ ratio, with a wiggled increase observed for $I_b/I_c(I_b) < 5.0$. There is a reduction in the ultimate deformation with increase in the aspect ratio, $r_a(L_b)$ (see Figure 6.12b).

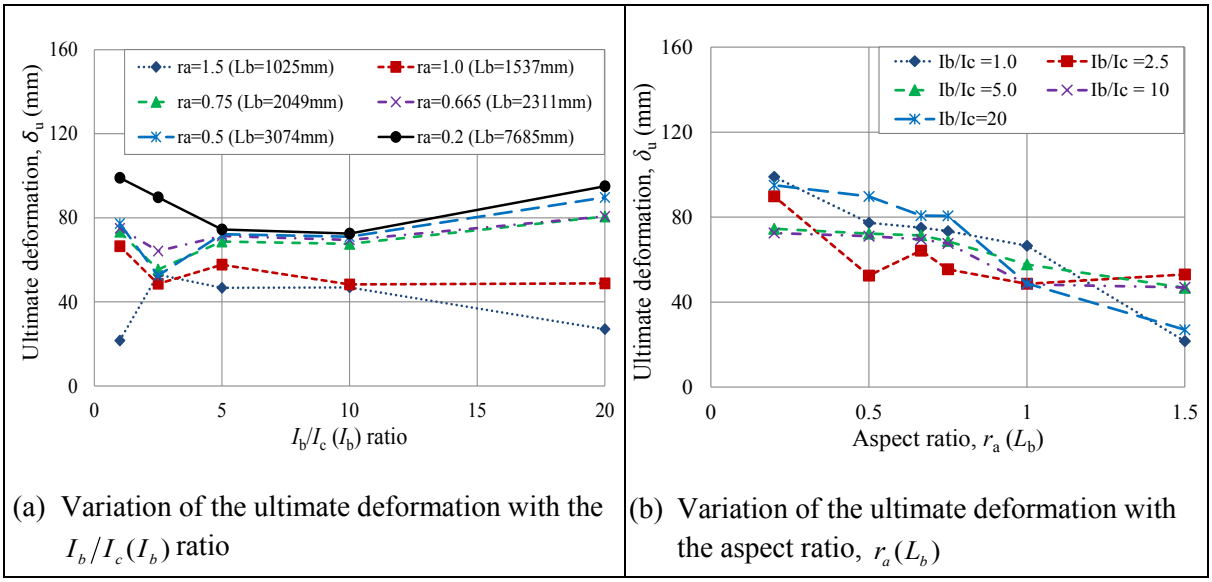

(a) Variation of the ultimate deformation with the $I_b/I_c(I_b)$ ratio

(b) Variation of the ultimate deformation with the aspect ratio, $r_a(L_b)$

Figure 6.12: Typical ultimate deformation variation with the $I_b/I_c(I_b)$ ratio and the aspect ratio, $r_a(L_b)$ for Case A

6.3.3 Discussions for the typical behaviour of the pinned frames

This section summarises the general behaviour of the pinned frames as observed through the evaluation of Cases A - D. The detailed evaluations for Case A are provided in Sections 6.3.1 and 6.3.2 and, for Cases B - D are reported in Appendix A1.3. The following points summarise the general behaviour of the bare frames subjected to the incremental lateral load:

(a) Both the yield strength and the ultimate strength decrease with reduction in the $I_b/I_c(I_b)$ ratio for $I_b/I_c(I_b) \leq 5.0$ and are almost constant for $I_b/I_c(I_b) > 5.0$. This trend is observed when either the beam length or the column length is varied (Cases A and B). There is no significant variation of both the yield strength and ultimate strength with the aspect ratio $r_a(L_b)$ (for Case A) while increase in the aspect ratio, $r_a(L_c)$ significantly reduces the yield strength and the ultimate strength (Case B).

(b) There is a gradual reduction in both the yield and ultimate deformations with increase in $I_b/I_c(I_b)$ for $I_b/I_c(I_b) \leq 5.0$ while the deformations are almost constant for $I_b/I_c(I_b) > 5.0$ for Cases A and B. Both the yield and ultimate deformations decrease with increase in the aspect ratio $r_a(L_b)$ and increase with increase in the aspect ratio $r_a(L_c)$ for Cases A and B respectively.

(c) For most of the samples in Case C, the yield strength increases with increase in the $I_b/I_c(I_c)$ ratio, for $I_b/I_c(I_c \leq 2.5)$ and decreases for increase in the $I_b/I_c(I_c)$ ratio, for $I_b/I_c(I_c) > 2.5$. Both the yield strength and ultimate strength for Case D and the ultimate strength for Case C

decrease gradually with increase in the $I_b/I_c(I_c)$ ratio. There is no significant variation of both the yield strength and ultimate strength with the aspect ratio $r_a(L_b)$ (for Case C) and both the yield and the ultimate strengths decreases with increase in the aspect ratio, $r_a(L_c)$ (Case D).

(d) There is a gradual increase in both the yield and ultimate deformations with increase in $I_b/I_c(I_c)$ for Cases C and D. Both the yield and the ultimate deformations decrease with increase in the aspect ratio $r_a(L_b)$ and increase with increase in the aspect ratio $r_a(L_c)$ for Cases C and D respectively.

Table 6.6 summarises the mean values of the strength for each case, highlighting possible variations emanating from the linear approximation. It should be noted that the analytical relations developed from the parametric studies are based on the data from the linearised curves. The linearised *F-δ* curve over-estimates the yield strength by an average of 26%. The average F_e-to-F_u(a) ratio ranges from 0.84 to 0.93, with overall mean of 0.89. Thus, a bilinear perfect-plastic force-deformation curve can be used as conservative choice for the deformation characteristics of the RC pinned bare frames.

Table 6.6: Mean strength values from the linearised and the actual *F-δ* curves for pinned frames

Sample	Yield strength, kN		F_e – Linear	Ultimate strength, kN		F_u – Linear	F_e – Linear
Group	F_e-Linear	F_e(a)-actual	$F_e(a)$ – Actual	F_u-Linear	F_u(a)-Actual	$F_u(a)$ – Actual	$F_u(a)$ – Actual
A	76.7	59.3	1.29	83.2	82.8	1.00	0.93
B	83.4	65.7	1.27	91.9	91.3	1.01	0.91
C	74.2	60.5	1.23	88.8	88.4	1.00	0.84
D	90.8	73.3	1.24	103.9	103.8	1.00	0.87

6.4 CALIBRATION OF DIAGONAL STRUT BEHAVIOUR

The results of the parametric study presented in Sections 6.2 and 6.3 have shown that there is a general trend in the behaviour of the bare frame when various topological and geometric properties are varied. This section establishes the parameters that define the diagonal strut behaviour. The parameters are expressed in terms of analytical relationships between the key structural performance indicators (F_e, δ_e, F_u and δ_u) and the geometric and topological factors (I_b/I_c and L_b/L_c) using the following iterative process:

(a) Establish the diagonal strut behaviour from the frame behaviour using appropriate expressions provided in Section 3.4.5;
(b) Plot the diagonal strut behaviour indicator against a specific variable geometric or topological variable;
(c) Identify the general trend for the plot in (b) based on average (mean) values over the specified variable using the regression analysis;
(d) The process in (c) is carried out for all the four case study groups (A-D). Identify common trends across the four cases, based on commonality of the variables. Based on the common trends, propose generalised formulae that capture the common trends across the cases;
(e) Calibrate all the constants and/or coefficients used to describe the relationship in (c); and
(f) Compare the analytical expression with the data plot in step (a). If there is inadequate correlation, start again with step (c).

For practical considerations, only pin supported frames are considered for the diagonal strut behaviour evaluation. A bilinear material model is used to characterise the diagonal strut behaviour (see

Figure 6.13). Key parameters for the bilinear material model are the yield stress, σ_{de}, yield strain, ε_{de}, ultimate stress, σ_{du}, and the ultimate strains, ε_{du}. Elastic Young's modulus, E_{de} (derived from the elastic stiffness, K_{de}), and plastic Young's modulus, E_{du} (derived from the plastic stiffness, K_{du}) for the diagonal strut, as indicated in Figure 6.13, are evaluated in this section.

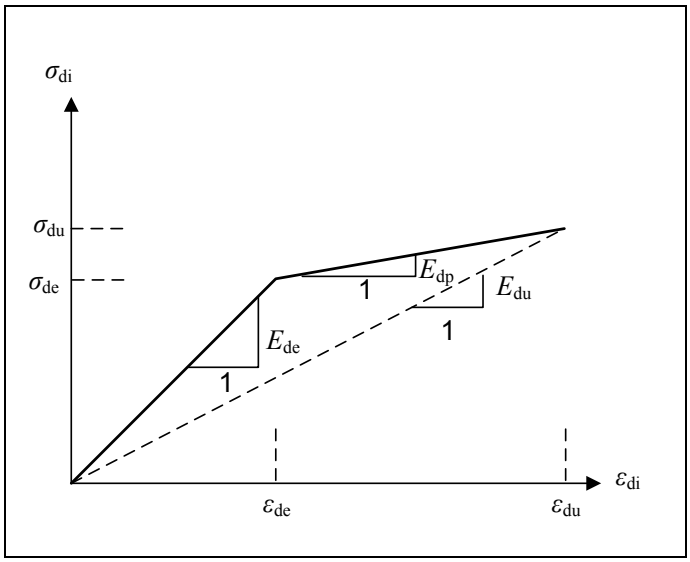

Figure 6.13: Assumed bilinear stress-strain behaviour for the diagonal strut

Considering these possible variations in the determination of the strut stress properties, diagonal strut strains are considered first as they do not depend on any modifications of either the elastic Young's modulus or the diagonal strut cross-sectional area.

6.4.1 Yield strain and ultimate strain calibration for the diagonal strut of the pinned frames

The diagonal strains are calculated from the frame's lateral deformations using equation 3.3 as discussed in Section 3.4.5. Analytical relationships of the diagonal strains with respective geometric and topological properties of the frame are developed and presented in the subsequent paragraphs. This section provides details for the analytical relations derived from Case A samples, the analytical relations for the rest of the cases is summarised in Section 6.4.4.

(a) Calibration of yield strains from Case A

Case A samples comprises constant parameters of I_c and L_c. Mean values of the diagonal yield strains are plotted against the $I_b/I_c(I_b)$ ratio with the range in the yield strain for each data point indicated in Figure 6.14(a). Considering the pattern of variation of the mean yield strains, an analytical relationship is proposed to link the yield strains with the $I_b/I_c(I_b)$ ratio as follows:

$$\varepsilon_{de} = \varepsilon_{der}\left(\frac{I_b}{I_c}(I_b)\right)^{-0.15} \tag{6.1}$$

where ε_{der} is the yield strain coefficient and is a function of the aspect ratio, $r_a(L_b)$, defined as:

$$\varepsilon_{der} = a_\varepsilon r_a^2(L_b) + b_\varepsilon r_a(L_b) + c_\varepsilon \tag{6.2}$$

and a_ε, b_ε and c_ε are coefficients for specific cases. The values of coefficients a_ε, b_ε and c_ε are -0.004, 0.008 and 0.0017 respectively. The proposed analytical relationships show some correlation with typical values from the numerical data as shown in Figure 6.14.

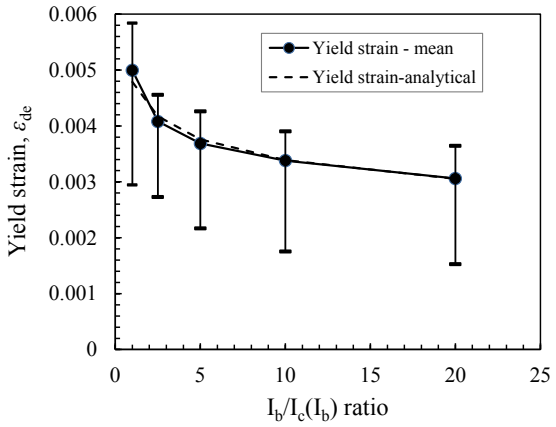

(a) Yield strain variation and relationship with the $I_b/I_c(I_b)$ ratio

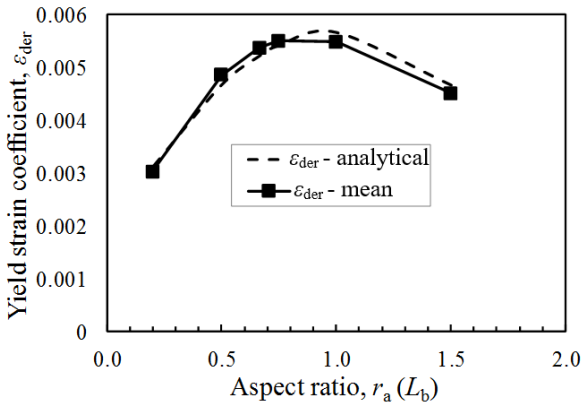

(b) Variation of the yield strain coefficient, ε_{der}, with the aspect ratio, $r_a(L_b)$

Figure 6.14: (a) Yield strain variation and relationship with the $I_b/I_c(I_b)$ ratio and, (b) the variation of the yield strain coefficient (ε_{der}) with the aspect ratio, $r_a(L_b)$ for Case A

(b) Calibration of ultimate strains for Case A

Mean values of the diagonal ultimate strains are plotted against the $I_b/I_c(I_b)$ ratio with the range in the ultimate strain for each data point indicated in Figure 6.15(a). Considering the pattern of variation of the mean ultimate strains, an analytical relationship is proposed to link the ultimate strains with the $I_b/I_c(I_b)$ ratio as:

$$\varepsilon_{du} = \varepsilon_{dur}\left(\frac{I_b}{I_c}(I_b)\right)^{-0.15} \tag{6.3}$$

where ε_{dur} is the ultimate strain coefficient and is a function of the aspect ratio, $r_a(L_b)$, defined as:

$$\varepsilon_{dur} = a_\varepsilon r_a^2(L_b) + b_\varepsilon r_a(L_b) + c_\varepsilon \tag{6.4}$$

and a_ε, b_ε and c_ε are coefficients established as -0.030, 0.051 and 00079 respectively for this case. The proposed analytical relationships show some correlation with typical values from the numerical data as shown in Figure 6.15.

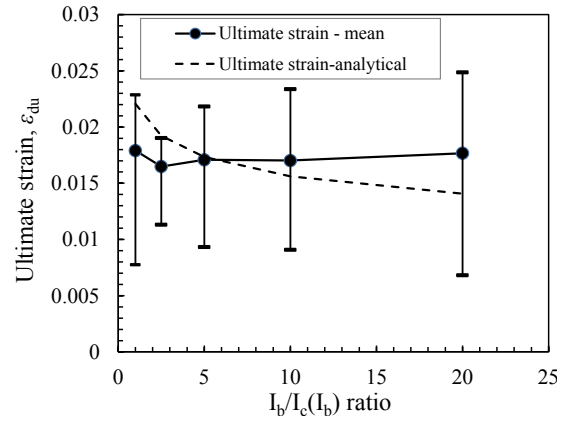

(a) Ultimate strain variation and relationship with the $I_b/I_c(I_b)$ ratio

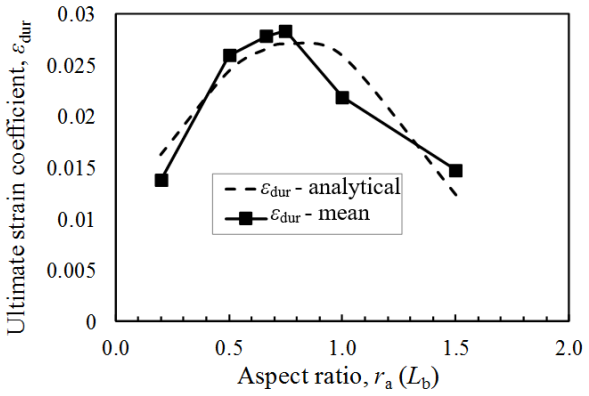

(b) Variation of the ultimate strain coefficient, ε_{dur}, with the aspect ratio, $r_a(L_b)$

Figure 6.15: (a) Ultimate strain variation and relationship with the $I_b/I_c(I_b)$ ratio and, (b) the variation of the ultimate strain coefficient (ε_{dur}) with the aspect ratio, $r_a(L_b)$ for Case A

6.4.2 Yield strength and elastic stiffness calibration for the diagonal strut of the pinned frames

The diagonal strut yield strength and the elastic stiffness are evaluated and calibrated in this section. The diagonal strength is calculated from the frame lateral yield strength using equation 3.4 and the elastic stiffness is calculated using equation 3.10 as reported in Section 3.4.5. Non-calibrated elastic stiffness of the single strut truss for a pin supported frame is established using equations 5.37 and 5.41 (see Sections 5.3.1 and 5.41). The diagonal stiffness is calibrated using the numerical data obtained from the parametric study using an elastic stiffness ratio, K_{eF}, defined as:

$$K_{eF} = \frac{K_{de}(numerical)}{K_{de}(calculated)} \tag{6.5}$$

(a) Calibration of strut yield strength (F_{de}) and elastic stiffness (K_{de}) for Case A

The mean values of the diagonal yield strength for Case A samples are plotted against the $I_b/I_c(I_b)$ ratio with the range in the yield strength for each data point indicated in Figure 6.16(a). Considering the pattern of variation of the mean yield strength for the diagonal, an analytical relationship is proposed to link the yield strength with the $I_b/I_c(I_b)$ ratio as:

$$F_{de} = F_{der}\left(\frac{I_b}{I_c}(I_b)\right)^{0.04} \tag{6.6}$$

where F_{der} is the strut yield strength coefficient dependent on the aspect ratio, $r_a(L_b)$ and is:

$$F_{der} = D_{fe} r_a(L_b) + D_{fe0} \tag{6.7}$$

D_{fe} and D_{fe0} constants for specific established as 38.7 kN and 63.4 kN respectively for this case. The proposed analytical relationships show some correlation with typical values from the numerical data as shown in Figure 6.16.

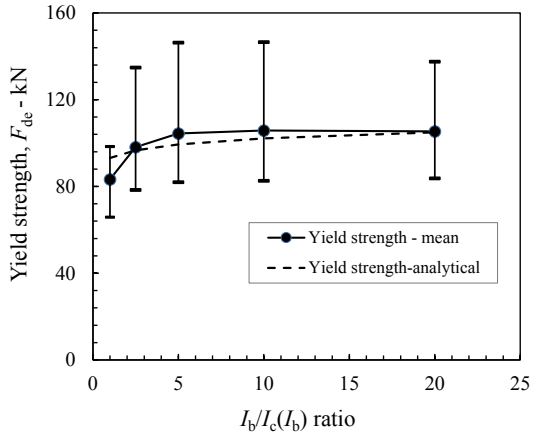

(a) Strut yield strength variation and relationship with the $I_b/I_c(I_b)$ ratio

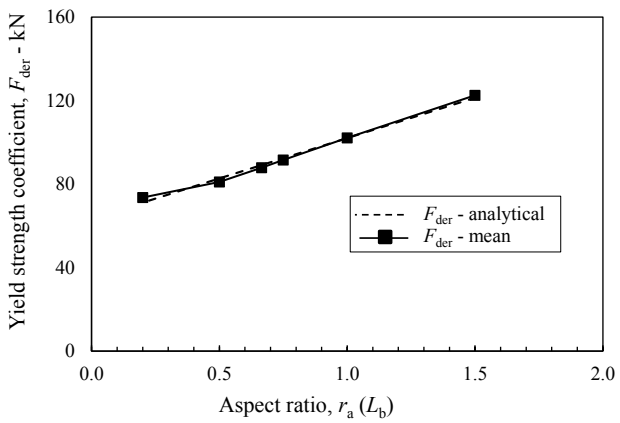

(b) Variation of the strut yield strength coefficient, F_{der}, with the aspect ratio, $r_a(L_b)$

Figure 6.16: (a) Diagonal strut yield strength variation and relationships with the $I_b/I_c(I_b)$ ratio and, (b) the variation of the strut yield strength coefficient with the aspect ratio, $r_a(L_b)$ for Case A

The mean values of the strut elastic stiffness calculated from both the numerical data and using elastic stiffness methods for Case A samples are plotted against the $I_b/I_c(I_b)$ ratio and the aspect ratio, $r_a(L_b)$ as shown in Figure 6.17. The variation of the elastic stiffness is similar for both methods of calculation, with that established using elastic stiffness being consistently higher than the numerical value.

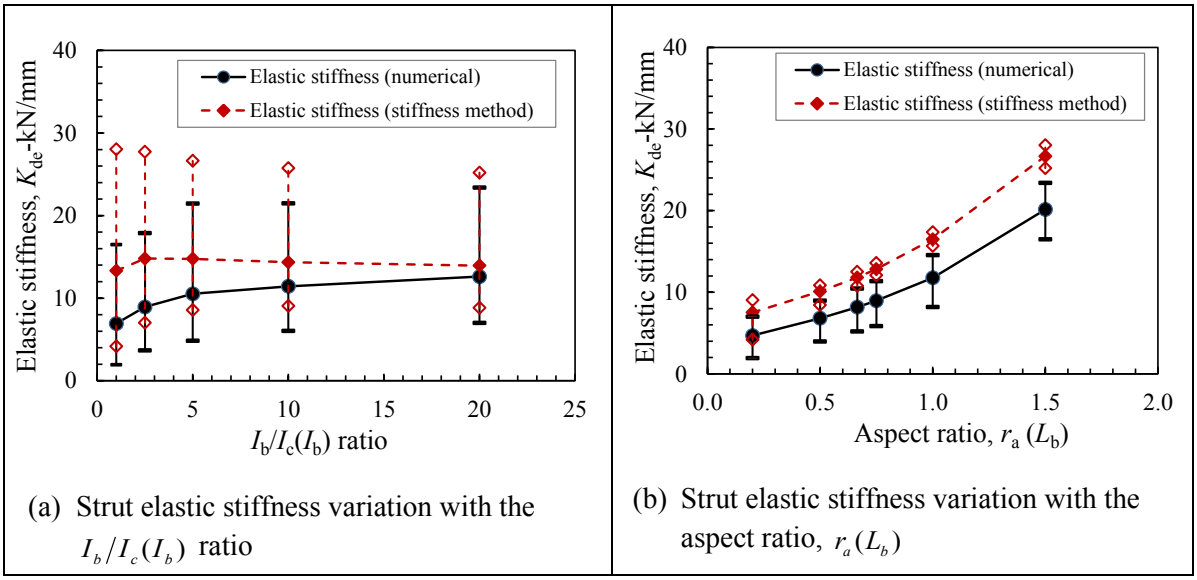

(a) Strut elastic stiffness variation with the $I_b/I_c(I_b)$ ratio

(b) Strut elastic stiffness variation with the aspect ratio, $r_a(L_b)$

Figure 6.17: (a) Diagonal strut elastic stiffness variation with the $I_b/I_c(I_b)$ ratio and, (b) diagonal strut elastic stiffness variation with the aspect ratio, $r_a(L_b)$ for Case A

The ratio of the elastic stiffness obtained from the numerical data to the elastic stiffness obtained using the stiffness method, K_{eF}, for each data point is established using equation 6.5. The variation of the elastic stiffness ratio K_{eF} is plotted against the $I_b/I_c(I_b)$ ratio as shown in Figure 6.18. Considering the pattern of variation of the elastic stiffness ratio, K_{eF}, an analytical relationship is proposed to link the elastic stiffness ratio, K_{eF} with the $I_b/I_c(I_b)$ ratio as:

$$K_{eF} = K_{der}\left(\frac{I_b}{I_c}(I_b)\right)^{0.20} \tag{6.8}$$

where K_{der} is the elastic stiffness ratio coefficient dependent on the aspect ratio, $r_a(L_b)$. The elastic stiffness ratio coefficient is:

$$K_{der} = A_{ke} r_a(L_b) + K_{er0} \tag{6.9}$$

and, A_{ke} and K_{er0} are constants and are 0.085 and 0.4285 respectively. The proposed analytical relationships show some correlation with typical values from the numerical data as shown in Figure 6.18.

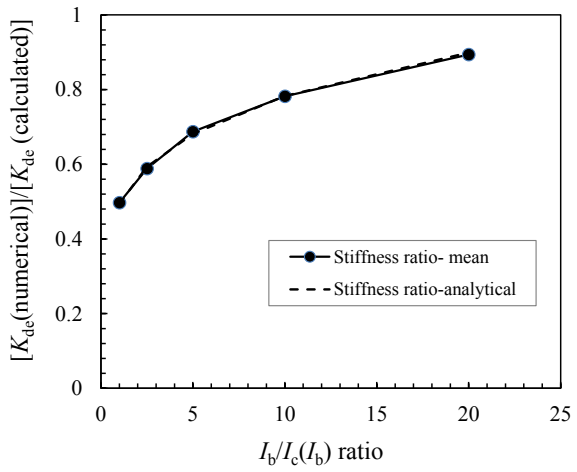

(a) Strut elastic stiffness ratio variation with the $I_b/I_c(I_b)$ ratio

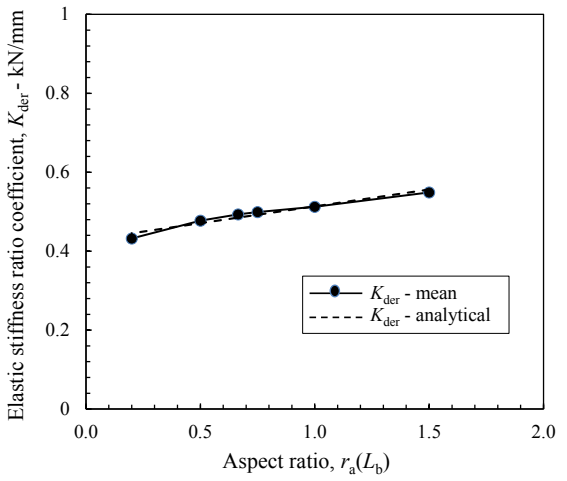

(b) Variation of the strut elastic stiffness ratio coefficient, K_{der}, with the aspect ratio, $r_a(L_b)$

Figure 6.18: (a) Diagonal strut elastic stiffness ratio variation and relationships with the $I_b/I_c(I_b)$ ratio and, (b) the variation of the strut elastic stiffness ratio coefficient with the aspect ratio, $r_a(L_b)$ for Case A

6.4.3 Ultimate strength and plastic stiffness calibration for the diagonal strut of the pinned frames

The diagonal strut ultimate strength and the plastic stiffness are evaluated and calibrated in this section. The strut ultimate strength is calculated from the frame lateral ultimate strength using equation 3.4 and the plastic stiffness is calculated using equation 3.10 as reported in Section 3.4.5. The plastic stiffness of the single strut truss for a pin supported frame is calibrated both the elastic and plastic stiffness obtained from the numerical data using a plastic stiffness ratio, K_{pF}, defined as follows:

$$K_{pF} = \frac{K_{du}(numerical)}{K_{de}(numerical)} \tag{6.10}$$

(a) Calibration of strut ultimate strength (F_{du}) and plastic stiffness (K_{du}) for Case A

The mean values of the diagonal ultimate strength for Case A samples are plotted against the $I_b/I_c(I_b)$ ratio with the range in the ultimate strength for each data point indicated (see Figure 6.19(a)). Considering the pattern of variation of the mean ultimate strength for the diagonal, an analytical relationship is proposed to link the ultimate strength with the $I_b/I_c(I_b)$ ratio as:

$$F_{du} = F_{dur}\left(\frac{I_b}{I_c}(I_b)\right)^{0.04} \tag{6.11}$$

where F_{dur} is the strut ultimate strength coefficient and is dependent of the aspect ratio, $r_a(L_b)$ and is:

$$F_{dur} = D_{flu} r_a(L_b) + D_{fle0} \tag{6.12}$$

and D_{fe} and D_{fe0} are constants for specific case and are established as 40.5 kN and 69.9 kN respectively for this case. The proposed analytical relationships show some correlation with typical values from the numerical data as shown in Figure 6.19.

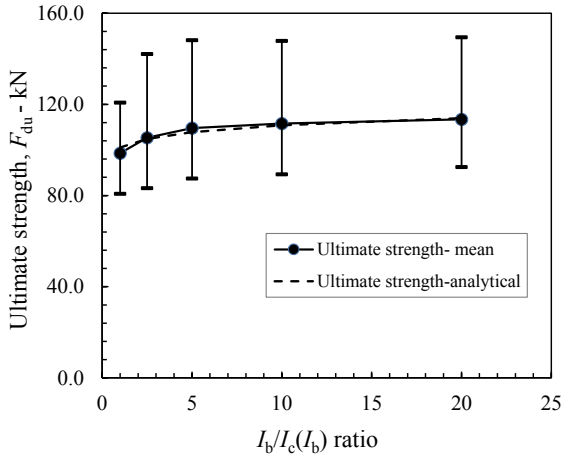

(a) Strut ultimate strength variation and relationship with the $I_b/I_c(I_b)$ ratio

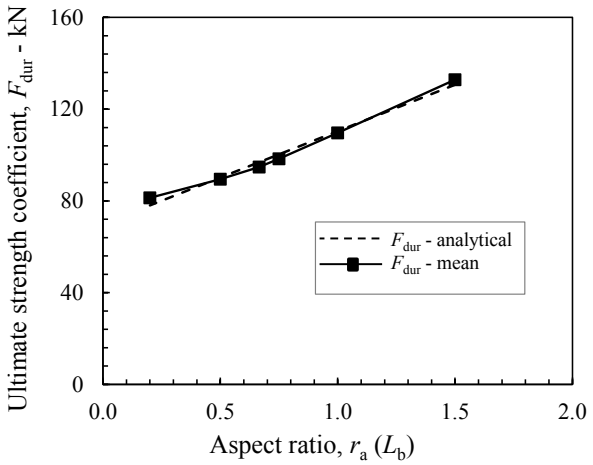

(b) Variation of the strut ultimate strength coefficient, F_{dur}, with the aspect ratio, $r_a(L_b)$

Figure 6.19: (a) Diagonal strut ultimate strength variation and relationships with the $I_b/I_c(I_b)$ ratio and, (b) the variation of the strut ultimate strength coefficient with the aspect ratio, $r_a(L_b)$ for Case A

Mean values of the strut plastic stiffness calculated from the numerical data for Case A samples are plotted against the $I_b/I_c(I_b)$ ratio and the aspect ratio, $r_a(L_b)$ with the range in the plastic stiffness for each data point indicated as shown in Figure 6.20. The plastic stiffness gradually increases with increase in the $I_b/I_c(I_b)$ ratio but it significantly increases with increase in the aspect ratio, $r_a(L_b)$.

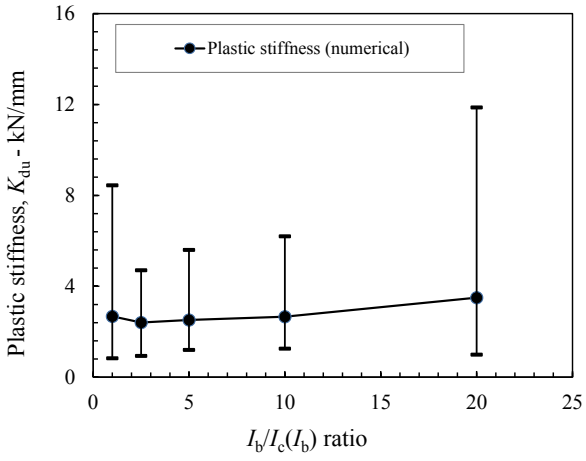

(a) Strut plastic stiffness variation with the $I_b/I_c(I_b)$ ratio

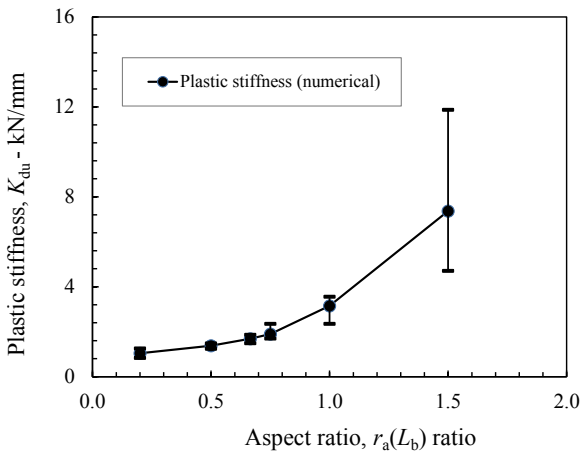

(b) Strut plastic stiffness variation with the aspect ratio, $r_a(L_b)$

Figure 6.20: Diagonal strut plastic stiffness variation with (a) the $I_b/I_c(I_b)$ ratio and, (b) the aspect ratio, $r_a(L_b)$ for Case A

The ratio of the plastic stiffness to the elastic stiffness, K_{pF}, for each data point is established and plotted against the $I_b/I_c(I_b)$ ratio as shown in Figure 6.21. Considering the pattern of variation of the plastic stiffness ratio, K_{pF}, with the $I_b/I_c(I_b)$ ratio, an analytical relationship is proposed to link the plastic stiffness ratio, K_{pF} with the $I_b/I_c(I_b)$ ratio as:

$$K_{pF} = K_{dur}\left(\frac{I_b}{I_c}(I_b)\right)^{-0.15} \tag{6.13}$$

where K_{dur} is the plastic stiffness ratio coefficient dependent on the aspect ratio, $r_a(L_b)$ and is:

$$K_{dur} = A_{kp1}r_a^2(L_b) + A_{kp}r_a(L_b) + A_{kp0} \tag{6.14}$$

A_{kp1}, A_{kp} and A_{kp0} are constants and are determined as 0.225, -0.250 and 0.344 respectively for this case. The proposed analytical relationships show some correlation with typical values from the numerical data as shown in Figure 6.21.

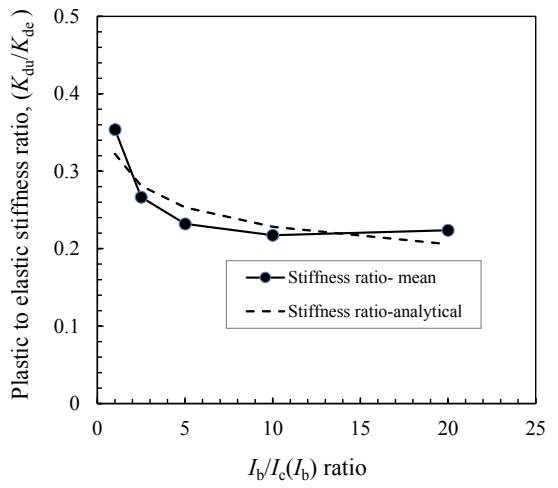

(a) Strut plastic stiffness ratio variation and relationship with the $I_b/I_c(I_b)$ ratio

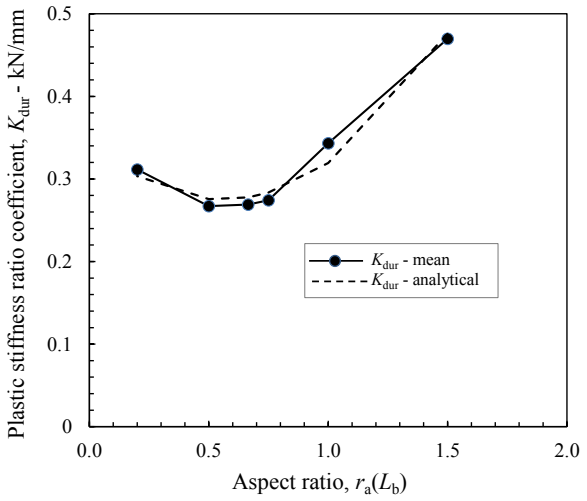

(b) Variation of the strut plastic stiffness ratio coefficient, K_{dur}, with the aspect ratio, $r_a(L_b)$

Figure 6.21: Diagonal strut plastic stiffness ratio variation and relationships with the $I_b/I_c(I_b)$ ratio and, (b) the variation of the strut plastic stiffness ratio coefficient with the aspect ratio, $r_a(L_b)$ for Case A

6.4.4 Calibration of diagonal strut properties for Cases B – D of the pinned frames

Using the same process illustrated through the analytical relations derivation for Case A, the analytical relations for the diagonal strut material parameters are derived for Cases B – D and summarised in Table 6.7. Detailed information of the comparison of the analytical relations with the numerical data through illustrative figures is reported in Appendix A1.4 – A1.6.

Table 6.7: Analytical relationships for the fixed supported bare frame

Item	Case B	Case C	Case D
ε_{de}	$\varepsilon_{de} = \varepsilon_{der}\left(\frac{I_b}{I_c}(I_b)\right)^{-0.15}$ $\varepsilon_{der} = a_\varepsilon r_a^2(L_c) + b_\varepsilon r_a(L_c) + c_\varepsilon$ a_ε = -0.003; b_ε = 0.013; c_ε = -0.0019	$\varepsilon_{de} = \varepsilon_{der}\left(\frac{I_b}{I_c}(I_c)\right)^{0.25}$ $\varepsilon_{der} = a_\varepsilon r_a^2(L_b) + b_\varepsilon r_a(L_b) + c_\varepsilon$ a_ε = -0.0011; b_ε = 0.0007; c_ε = -0.0020	$\varepsilon_{de} = \varepsilon_{der}\left(\frac{I_b}{I_c}(I_c)\right)^{0.25}$ $\varepsilon_{der} = a_\varepsilon r_a^2(L_c) + b_\varepsilon r_a(L_c) + c_\varepsilon$ a_ε = -0.002; b_ε = 0.005; c_ε = 0.0001
ε_{du}	$\varepsilon_{du} = \varepsilon_{dur}\left(\frac{I_b}{I_c}(I_b)\right)^{-0.15}$ $\varepsilon_{dur} = a_\varepsilon r_a^2(L_c) + b_\varepsilon r_a(L_c) + c_\varepsilon$ a_ε = -0.003; b_ε = 0.080; c_ε = -0.0128	$\varepsilon_{du} = \varepsilon_{du0}\left(\frac{I_b}{I_c}(I_c)\right)^2 + \varepsilon_{du1}\left(\frac{I_b}{I_c}(I_c)\right) + \varepsilon_{dur}$ $\varepsilon_{dur} = a_\varepsilon r_a^2(L_b) + b_\varepsilon r_a(L_b) + c_\varepsilon$ ε_{du0} = 6x10^{-6}; ε_{du1} = 0.0005 a_ε = -0.012; b_ε = 0.0516; c_ε = 0.0007	$\varepsilon_{du} = \varepsilon_{du0}\left(\frac{I_b}{I_c}(I_c)\right)^2 + \varepsilon_{du1}\left(\frac{I_b}{I_c}(I_c)\right) + \varepsilon_{dur}$ $\varepsilon_{dur} = a_\varepsilon r_a^2(L_c) + b_\varepsilon r_a(L_c) + c_\varepsilon$ ε_{du0} = 8x10^{-5}; ε_{du1} = -0.00008 a_ε = -0.026; b_ε = 0.055; c_ε = 0.0090
F_{de} (kN)	$F_{de} = F_{der}\left(\frac{I_b}{I_c}(I_b)\right)^{0.04}$ $F_{der} = D_{fe1} r_a^2(L_c) + D_{fe} r_a(L_c) + D_{fe0}$ D_{fe1} = 85.0 kN; D_{fe} = -230.0 kN; D_{fe0} = 205.3 kN	$F_{de} = F_{der}\left(\frac{I_b}{I_c}(I_c)\right)^{-0.15}$ $F_{der} = D_{fe1} r_a^2(L_b) + D_{fe} r_a(L_b) + D_{fe0}$ D_{fe1} = -70.0 kN; D_{fe} = 130.0 kN; D_{fe0} = 72.4 kN	$F_{de} = F_{der}\left(\frac{I_b}{I_c}(I_c)\right)^{-0.15}$ $F_{der} = D_{fe1} r_a^2(L_c) + D_{fe} r_a(L_c) + D_{fe0}$ D_{fe1} = 136.0 kN; D_{fe} = -345.0 kN; D_{fe0} = 298.0 kN
K_{eF}	$K_{eF} = K_{der}\left(\frac{I_b}{I_c}(I_b)\right)^{0.20}$ $K_{der} = A_{ke} r_a(L_c) + A_{ke0}$ A_{ke} = -0.040; A_{ke0} = 0.5276	$K_{eF} = K_{der}\left(\frac{I_b}{I_c}(I_c)\right)^{0.50}$ $K_{der} = A_{ke} r_a(L_b) + A_{ke0}$ A_{ke} = 0.120; A_{ke0} = 0.0313	$K_{eF} = K_{der}\left(\frac{I_b}{I_c}(I_c)\right)^{0.60}$ $K_{der} = A_{ke} r_a(L_c) + A_{ke0}$ A_{ke} = 0.087; A_{ke0} = 0.0131
F_{du} (kN)	$F_{du} = F_{dur}\left(\frac{I_b}{I_c}(I_b)\right)^{0.04}$ $F_{dur} = D_{fu1} r_a^2(L_c) + D_{fu} r_a(L_c) + D_{fu0}$ D_{fu1} = 101.0 kN; D_{fu} = -265.0 kN; D_{fu0} = 230.0 kN	$F_{du} = F_{dur}\left(\frac{I_b}{I_c}(I_c)\right)^{-0.15}$ $F_{dur} = D_{fu1} r_a^2(L_b) + D_{fu} r_a(L_b) + D_{fu0}$ D_{fu1} = -70.0 kN; D_{fu} = 133.0 kN; D_{fu0} = 92.6 kN	$F_{du} = F_{dur}\left(\frac{I_b}{I_c}(I_c)\right)^{-0.15}$ $F_{dur} = D_{fu1} r_a^2(L_c) + D_{fu} r_a(L_c) + D_{fu0}$ D_{fu1} = 206.0 kN; D_{fu} = -500.0 kN; D_{fu0} = 383.2 kN
K_{pF}	$K_{pF} = K_{dur}\left(\frac{I_b}{I_c}(I_b)\right)^{-0.15}$ $K_{dur} = A_{kp1} r_a^2(L_c) + A_{kp} r_a(L_c) + A_{kp0}$ A_{kp1} = 0.380; A_{kp} = -0.670; A_{kp0} = 0.567	$K_{pF} = K_{dur}\left(\frac{I_b}{I_c}(I_c)\right)^{-0.20}$ $K_{dur} = A_{kp1} r_a^2(L_b) + A_{kp} r_a(L_b) + A_{kp0}$ A_{kp1} = 0.530; A_{kp} = -0.815; A_{kp0} = 0.861	$K_{pF} = A_{pr1}\left(\frac{I_b}{I_c}(I_c)\right)^2 + A_{pr}\left(\frac{I_b}{I_c}(I_c)\right) + K_{dur}$ $K_{dur} = A_{kp1} r_a^2(L_c) + A_{kp} r_a(L_c) + A_{kp0}$ A_{pr1} = -0.001; A_{pr} = 0.24; A_{kp1} = 0.530; A_{kp} = 1.080; A_{kp0} = 0.674

6.4.5 Evaluation of the frames with fixed supports – towards calibration of the respective diagonal strut behaviour

This section provides a summary of the evaluation of the fixed frames behaviour for use in diagonal strut evaluation for the frames with fixed supports. It should be noted that all the experimental data available in this research are conducted for the frames with fixed supports. Thus, the analytical relationships for the frames with fixed supports, similar to that discussed in Sections 6.4.1- 6.4.3 for the diagonal are developed. A summary of the analytical relationships is provided in Table 6.8, while detailed figures illustrating the correlation for each analytical expression are provided in Appendix A1.7. The coefficients provided in the table are for the linearised force–deformation curve of the bare frame.

Table 6.8: Analytical relationships for the bare frames with fixed supports

Item	Case A	Case B	Case C	Case D
F_e (kN)	$F_e = F_{er}\left(\frac{I_b}{I_c}(I_b)\right)^{0.04}$ $F_{er} = D_{fe} r_a(L_b) + D_{fe0}$ D_{fe} = -3.8 kN; D_{fe0} = 133.0 kN	$F_e = F_{er}\left(\frac{I_b}{I_c}(I_b)\right)^{0.04}$ $F_{er} = D_{fe} r_a(L_c) + D_{fe0}$ D_{fe} = -94.0 kN; D_{fe0} = 196.7 kN	$F_e = F_{er}\left(\frac{I_b}{I_c}(I_c)\right)^{-0.40}$ $F_{er} = D_{fe} r_a(L_b) + D_{fe0}$ D_{fe} = -142.0 kN; D_{fe0} = 542.0 kN	$F_e = F_{er}\left(\frac{I_b}{I_c}(I_c)\right)^{-0.40}$ $F_{er} = D_{fe} r_a(L_c) + D_{fe0}$ D_{fe} = -336.0 kN; D_{fe0} = 607.0 kN
δ_e (mm)	$\delta_e = \delta_{er}\left(\frac{I_b}{I_c}(I_b)\right)^{-0.15}$ $\delta_{er} = b_\varepsilon r_a(L_b) + c_\varepsilon$ b_ε = -1.85 mm; c_ε = 10.0 mm	$\delta_e = \delta_{er}\left(\frac{I_b}{I_c}(I_b)\right)^{-0.15}$ $\delta_{er} = b_\varepsilon r_a(L_c) + c_\varepsilon$ b_ε = 34.4 mm; c_ε = -11.5 mm	$\delta_e = \delta_{er}\left(\frac{I_b}{I_c}(I_c)\right)^{0.25}$ $\delta_{er} = b_\varepsilon r_a(L_c) + c_\varepsilon$ b_ε = -2.7 mm; c_ε = 5.6 mm	$\delta_e = \delta_{er}\left(\frac{I_b}{I_c}(I_c)\right)^{0.25}$ $\delta_{er} = b_\varepsilon r_a(L_b) + c_\varepsilon$ b_ε = 9.3 mm; c_ε = -1.5 mm
F_u (kN)	$F_u = F_{ur}\left(\frac{I_b}{I_c}(I_b)\right)^{0.04}$ $F_{ur} = D_{fu} r_a(L_b) + D_{fu0}$ D_{fu} = -9.6 kN; D_{fu0} = 160.3 kN	$F_u = F_{ur}\left(\frac{I_b}{I_c}(I_b)\right)^{0.04}$ $F_{ur} = D_{fu} r_a(L_c) + D_{fu0}$ D_{fu} = -104.0 kN; D_{fu0} = 218.0 kN	$F_u = F_{ur}\left(\frac{I_b}{I_c}(I_c)\right)^{-0.4}$ $F_{ur} = D_{fu} r_a(L_b) + D_{fu0}$ D_{fu} = -112.0 kN; D_{fu0} = 652.0 kN	$F_u = F_{ur}\left(\frac{I_b}{I_c}(I_c)\right)^{-0.4}$ $F_{ur} = D_{fu} r_a(L_c) + D_{fu0}$ D_{fu} = -434.0 kN; D_{fu0} = 861.0 kN
δ_u (mm)	$\delta_u = \delta_{ur}\left(\frac{I_b}{I_c}(I_b)\right)^{-0.15}$ $\delta_{ur} = b_\varepsilon r_a(L_b) + c_\varepsilon$ b_ε = 11.0 mm; c_ε = 36.2 mm	$\delta_u = \delta_{ur}\left(\frac{I_b}{I_c}(I_b)\right)^{-0.15}$ $\delta_{ur} = b_\varepsilon r_a(L_c) + c_\varepsilon$ b_ε = 196.3 mm; c_ε = -72.5 mm	$\delta_u = \delta_{ur}\left(\frac{I_b}{I_c}(I_c)\right)^{0.4}$ $\delta_{ur} = b_\varepsilon r_a(L_b) + c_\varepsilon$ b_ε = 8.3 mm; c_ε = 17.4 mm	$\delta_u = \delta_{ur}\left(\frac{I_b}{I_c}(I_c)\right)^{0.5}$ $\delta_{ur} = a_\varepsilon r_a^2(L_c) + b_\varepsilon r_a(L_c) + c_\varepsilon$ a_ε = -11.7 mm; b_ε = 36.3 mm; c_ε = 5.3 mm

6.4.6 Validation of the bare frame parameters

This section validates the analytical relationships developed in Sections 6.4.1 - 6.4.5. The behaviour of the bare frames is evaluated by the truss idealisation for the frame with the diagonal strut properties established using the proposed analytical relationships. Results of the frame behaviour are compared with the available experimental data, and where not available, results from the finite element models of the frame idealisation are used. The yield strain and the ultimate strains for the diagonal struts are

evaluated in Section 6.4.1. In addition to these material parameters, the Young's modulus of elasticity, the cross-sectional area, yield stresses and the ultimate stresses are required. Evaluation of the diagonal strut Young's modulus, cross-sectional area, yield stress and the ultimate stress is provided first.

6.4.6.1 Diagonal strut Young's modulus of elasticity, cross-sectional area, yield stress, ultimate stress evaluation

Diagonal strut stresses are a function of both the diagonal force and the cross-sectional area. The diagonal strut geometric properties are developed based on stiffness equivalence. As noted in Section 5.3, the cross-sectional area and the Young's modulus are the only parameters of the diagonal strut that can be modified to establish the appropriate stiffness. It is proposed that the establishment of the cross-sectional area and/ or the Young's modulus for the diagonal strut be conducted considering the elastic behaviours. In this study, three possible ways of modifying the stiffness parameters for the diagonal struts are considered, namely;

(a) consider the elastic Young's modulus as constant and modify the cross-sectional area of the diagonal strut
(b) consider the cross-sectional area of the diagonal strut as constant and modify the elastic Young's modulus
(c) modify both the elastic Young's modulus and the cross-sectional area for the diagonal

Since both the diagonal strut yield strength, F_{de}, and the diagonal strut yield strain are already established, by choosing diagonal cross-sectional area, A_d to be similar to that of the column, A_c, the following expressions can be established:

(a) Determine the diagonal strut stresses:

Yield stress, $\sigma_{de} = \frac{F_{de}}{A_d}$ (6.15a)

Ultimate stress, $\sigma_{du} = \frac{F_{du}}{A_d}$ (6.15b)

(b) Determine the diagonal strut elastic and plastic modulus from the stress-strain relationship:

Elastic modulus, $E_{de} = \frac{\sigma_{de}}{\varepsilon_{de}}$ (6.16a)

Plastic modulus, $E_{du} = \frac{\sigma_{du}}{\varepsilon_{du}}$ (6.16b)

(c) Determine the diagonal strut elastic and plastic modulus from the stiffness relationship:

Elastic modulus, $E_{de} = \frac{K_{de}L_d}{A_d}$ (6.17a)

Plastic modulus, $E_{du} = \frac{K_{du}L_d}{A_d}$ (6.17b)

(d) The values obtained in (b) must be the same as that obtained in (c). likewise, equating the right-hand sides of each respective equation gives a credible relationship as follows:

$$\frac{K_{de}L_d}{A_d} = \left(\frac{F_{de}}{A_d}\right)\frac{1}{\varepsilon_e} \Leftrightarrow F_{de} = K_{de}\left(L_d\varepsilon_{de}\right) = K_{de}\delta_{de} \quad (6.18a)$$

$$\frac{K_{du}L_d}{A_d} = \left(\frac{F_{du}}{A_d}\right)\frac{1}{\varepsilon_e} \Leftrightarrow F_{du} = K_{du}\left(L_d\varepsilon_{du}\right) = K_{du}\delta_{du} \quad (6.18b)$$

Thus, any cross-sectional area can be selected if the values used for both the yield and ultimate stresses determination are based on the calibrated strength parameters.

The parameters derived in Sections 6.4.1 - 6.4.5 were derived based on the numerical data generated using the four case study groups, with key structural parameter linked, first with the second moment of area ratio, $I_b/I_c(I_b)$ or $I_b/I_c(I_c)$ and then deriving any relevant coefficients from such a relationship to depend on the aspect ratio, $r_a(L_b)$ or $r_a(L_c)$. However, application of these formulas starts in the opposite as follows:

(a) Establish the aspect ratio, $r_a(L_b)$ and $r_a(L_c)$;
(b) Establish the second moment of area ratios, $I_b/I_c(I_b)$ and $I_b/I_c(I_c)$;
(c) Establish the relevant coefficients for the parameter in question;
(d) Establish the structural parameter using relevant equations; and
(e) If none of the sectional and geometric properties of the frame coincides with the values under study, linear interpolation is used to establish the appropriate parameter. This is illustrated in the validation of the bare frame parameters in the next section.

6.4.6.2 Validation of pinned bare frame parameters

The diagonal strut properties are derived from the frame behaviour/parameters. To validate the proposed analytical relationships, the diagonal to frame transformation equations reported in Section 3.4.5 are used. Bare frames that were not used for the derivation of the analytical relationships are used for validation. These comprise bare frames from Crisafulli (1997) (sample G3) and Mehrabi et al. (1996) (samples G4(1), G4(2), G4(5), G4(6) and G4(8)). It should be noted that sample G4(9) is used as a basic frame from which all the numerical data is established as discussed in Sections 6.4.1 - 6.4.4. Based on the steps provided in Section 6.4.6.1, the aspect ratio, considering the dimensions of the frame for analysis and the corresponding dimensions with the basic frame (L_c/L_b, $I_b/I_c(I_b)$ and $L_c/L_b(L_c)$ respectively) are established. Furthermore, the second moment of area ratios, considering the respective I of the frame members for analysis and the corresponding I with the basic frame (I_b/I_c, $I_b/I_c(I_b)$ and $I_b/I_c(I_c)$) are established. A summary of these parameters, which are used as input for frame evaluation in the subsequent paragraphs, is provided in Table 6.9. Numerical data is used for the validation of the proposed analytical models, considering the lateral frame yield and ultimate deformations and corresponding strengths.

Table 6.9: The aspect ratio and the second moment of area ratios

Sample notation	L_c **(mm)**	L_b **(mm)**	$r_a=\frac{L_c}{L_b}$	$r_a=\frac{L_c}{L_b}(L_b)$	$r_a=\frac{L_c}{L_b}(L_c)$	I_c **x10^8 (mm^4)**	I_b **x10^8 (mm^4)**	$\frac{I_b}{I_c}$	$\frac{I_b}{I_c}(I_b)$	$\frac{I_b}{I_c}(I_c)$
G3	2100	2670	0.787	0.576	0.909	0.485	1.143	2.355	0.495	95.30
G4(1)	1537	2311	0.665	0.665	0.665	1.188	2.059	1.733	0.891	38.91
G4(2)	1537	2311	0.665	0.665	0.665	1.296	2.224	1.716	0.962	35.67
G4(5)	1537	2311	0.665	0.665	0.665	1.273	2.188	1.719	0.947	36.31
G4(6)	1537	3124	0.492	0.492	0.665	1.223	2.113	1.727	0.914	37.79
G4(8)	1537	3124	0.492	0.492	0.665	1.271	2.186	1.720	0.946	36.37

(a) Diagonal strut elastic strain and lateral yield deformations for the pinned frames

The diagonal strain analytical models proposed for all the cases (A - D) are used to determine the elastic strains for the diagonal struts. The strains from all the four cases are interpolated to generate an actual strain for the respective frame. Linear interpolation is used. Table 6.10 provides a summary of the elastic

strains for the validation samples established using the proposed analytical expressions. The G4 samples reported in the table have the elastic strain of 0.0054 or 0.0051 while sample G3 has the elastic strain of 0.0073, signifying a probable more ductile frame. It should be noted that samples G4 comprised of the same amount of reinforcement, and column and beam sectional properties with only the concrete strength and Young's modulus varying from 20.87 MPa to 30.87 MPa and 17.23 GPa to 21.91 GPa respectively.

Table 6.10: Diagonal strut yield strains

Sample notation	**Calculated yield strains from the four cases**				**Predicted strain (interpolated), ε_{de}**
	Case A- $\varepsilon_{de}(A)$	Case B - $\varepsilon_{de}(B)$	Case C - $\varepsilon_{de}(C)$	Case D - $\varepsilon_{de}(D)$	
G3	0.0055	0.0083	0.0064	0.0093	0.0073
G4(1)	0.0053	0.0055	0.0049	0.0063	0.0054
G4(2)	0.0053	0.0055	0.0048	0.0062	0.0054
G4(5)	0.0053	0.0055	0.0049	0.0062	0.0054
G4(6)	0.0047	0.0055	0.0052	0.0063	0.0051
G4(8)	0.0047	0.0055	0.0051	0.0062	0.0051

The elastic strains are used to calculate the lateral yield deformations for the frames using equation 3.3 (see Section 3.4.5). The predicted lateral yield deformations are compared to the lateral deformations established from either the experimental data or numerical data. Table 6.11 provides a summary of the predicted and actual lateral deformations for the bare frames.The $I_b/I_c(I_c)$ for all the samples are higher than the range considered, with sample G3 having excessively high ratio. Sample G4(5) had problems with numerical convergence. The overall mean of the analytical model over-prediction ratio is 1.81 with Cov of 42.10%. However, removing two samples of concern (G3 and G4(5)) gives mean over-prediction ratio of 1.34 with Cov of 8.30%. Thus, a correction factor of 0.75 (1/1.34) can be applied.

Table 6.11: Comparison of the analytical and numerical lateral yield deformations

Sample notation	**Lateral yield deformations (mm)**		$\frac{\delta_e(\textbf{analytical})}{\delta_e(\textbf{numerical})}$
	Analytical	Numerical	
G3	31.44	10.2	3.08
G4(1)	18.11	12.1	1.50
G4(2)	17.90	14.4	1.24
G4(5)	17.94	7.4	2.42
G4(6)	19.89	14.9	1.34
G4(8)	19.78	15.4	1.28

(b) Diagonal strut yield strength and lateral yield strength for the pinned frames

The predicted yield strengths are established using the proposed analytical relationships and the results are presented in Table 6.12. The yield strengths are used to calculate the predicted lateral yield strength for the frames using equation 3.4 (see Section 3.4.5). The strengths for G4 samples vary from 85.6 kN to 89.1 kN while G3 has strength of 71.2 kN. The predicted lateral yield strengths are compared to the lateral yield strength established from the numerical data. Table 6.13 provides a summary of the predicted and actual lateral yield strength for the bare frames.The overall mean for over-prediction ratio is 3.65 with Cov of 111.17%. However, removing two samples of concern (G3 and G4(5)) gives mean

over-prediction ratio of 1.65 with Cov of 2.40%. Thus, a correction factor of 0.60 (1/1.65) can be applied.

Table 6.12: Diagonal strut yield strength

Sample notation	**Calculated yield strength from the four cases (kN)**				**Predicted strength (interpolated), kN**
	Case A- $F_{de}(A)$	Case B - $F_{de}(B)$	Case C - $F_{de}(C)$	Case D - $F_{de}(D)$	
G3	83.3	64.6	62.6	48.9	71.2
G4(1)	88.7	89.5	73.9	74.3	88.8
G4(2)	89.0	89.8	74.8	75.3	89.1
G4(5)	88.9	89.7	74.6	75.1	89.0
G4(6)	82.1	89.6	69.3	74.6	85.6
G4(8)	82.3	89.7	69.7	75.1	85.7

Table 6.13: Comparison of the predicted and numerical lateral yield strength

Sample notation	**Lateral yield strength, F_e (kN)**		$\frac{F_e(\text{analytical})}{F_e(\text{numerical})}$
	Analytical	Numerical	
G3	55.9	4.7	11.80
G4(1)	73.9	46.2	1.60
G4(2)	74.2	44.9	1.65
G4(5)	74.1	21.2	3.50
G4(6)	76.8	46.1	1.67
G4(8)	76.9	45.3	1.70

(c) Diagonal strut ultimate strains and lateral ultimate deformations for the frames

The predicted ultimate strains are established using the proposed analytical relationships and the results are presented in Table 6.14. The ultimate strains are used to calculate the predicted lateral ultimate deformations for the frames using equation 3.3. The predicted lateral ultimate deformations are compared to the lateral ultimate deformations established from the numerical data. Table 6.15 provides a summary of the predicted and actual lateral ultimate deformations for the bare frames. The overall mean for over-prediction ratio is 2.60 with Cov of 59.88%. However, removing two samples of concern (G3 and G4(5)) gives mean over-prediction ratio of 1.77 with Cov of 15.11%. Thus, a correction factor of 0.56 (1/1.77) can be applied.

Table 6.14: Diagonal strut ultimate strains

Sample notation	**Calculated ultimate strains from the four cases**				**Predicted strain (interpolated), ε_{du}**
	Case A- $\varepsilon_{du}(A)$	Case B - $\varepsilon_{du}(B)$	Case C - $\varepsilon_{du}(C)$	Case D - $\varepsilon_{du}(D)$	
G3	0.0225	0.0638	0.0551	0.6699	0.0548
G4(1)	0.0218	0.0398	0.0223	0.1061	0.0315
G4(2)	0.0216	0.0393	0.0206	0.0893	0.0310
G4(5)	0.0216	0.0394	0.0209	0.0925	0.0311
G4(6)	0.0189	0.0396	0.0218	0.1001	0.0299
G4(8)	0.0188	0.0394	0.0211	0.0928	0.0297

Table 6.15: Comparison of the predicted and numerical lateral ultimate deformations

Sample notation	**Lateral ultimate strain, δ_u (mm)**		$\frac{\delta_u\,(\textbf{analytical})}{\delta_u\,(\textbf{numerical})}$
	Analytical	Numerical	
G3	236.9	42.2	5.61
G4(1)	105.1	56.1	1.87
G4(2)	103.2	61.8	1.67
G4(5)	103.6	35.5	2.08
G4(6)	116.2	55.8	2.32
G4(8)	115.2	79.0	1.46

(d) Diagonal strut ultimate strength and lateral ultimate strength for the pinned frames

The predicted ultimate strengths are established using the proposed analytical relationships and the results are presented in Table 6.16. The ultimate strengths are used to calculate the predicted lateral ultimate strengths for the frames using equation 3.4. The predicted lateral ultimate strengths are compared with the lateral ultimate strengths established from the numerical data (see Table 6.17). The overall mean for over-prediction ratio is 3.52 with Cov of 105.30%. However, removing two samples of concern (G3 and G4(5)) gives mean over-prediction ratio of 1.93 with Cov of 2.11%. Thus, a correction factor of 0.52 (1/1.93) can be applied to get the right ultimate strength.

Table 6.16: Diagonal strut ultimate strength

Sample notation	**Calculated ultimate strength from the four cases (kN)**				**Predicted strength (interpolated), kN**
	Case A- $F_{du}(A)$	Case B - $F_{du}(B)$	Case C - $F_{du}(C)$	Case D - $F_{du}(D)$	
G3	90.6	70.6	73.7	50.0	77.6
G4(1)	96.4	98.0	86.7	81.9	96.9
G4(2)	96.7	98.3	87.8	82.9	97.2
G4(5)	96.6	98.2	87.6	82.7	97.2
G4(6)	89.5	98.1	81.8	82.2	93.5
G4(8)	89.6	98.2	82.3	82.7	93.7

Table 6.17: Comparison of the predicted and numerical lateral ultimate strength

Sample notation	**Lateral ultimate strength, F_u (kN)**		$\frac{F_u\,(\textbf{analytical})}{F_u\,(\textbf{numerical})}$
	Analytical	Numerical	
G3	77.6	7.0	11.09
G4(1)	96.9	49.8	1.94
G4(2)	97.2	49.2	1.98
G4(5)	97.2	41.8	2.33
G4(6)	93.5	48.7	1.92
G4(8)	93.7	49.8	1.88

6.4.6.3 Validation of fixed bare frame parameters

The diagonal strut properties are derived from the analytical models proposed for the fixed frame behaviour/parameters provided in Section 6.4.5. Just like for the pinned frames, the bare frames that were not used for the derivation of the analytical relationships are used for validation. Input parameters for the models as summarised in Table 6.8 are used.

(a) Diagonal strut elastic strain and lateral yield deformations for the fixed frames

The frame elastic deformation analytical models proposed for all the cases (A - D) are used to determine the elastic strains for the diagonal struts using equations provided in Table 6.8 and equation 3.3 (see Section 3.4.5). The strains from all the four cases are interpolated to generate the predicted strain for the respective frame. Linear interpolation is used. Table 6.18 provides a summary of the elastic strains for the validation samples established using the proposed analytical expressions. The yield strains vary from 0.0027 to 0.0041.

Table 6.18: Diagonal strut yield strains

Sample notation	**Calculated yield strains from the four cases**				**Predicted strain (interpolated),** ε_{de}
	Case A- $\varepsilon_{de}(A)$	Case B - $\varepsilon_{de}(B)$	Case C - $\varepsilon_{de}(C)$	Case D - $\varepsilon_{de}(D)$	
G3	0.0023	0.0051	0.0029	0.0050	0.0041
G4(1)	0.0027	0.0035	0.0029	0.0035	0.0031
G4(2)	0.0026	0.0034	0.0028	0.0034	0.0030
G4(5)	0.0027	0.0034	0.0028	0.0035	0.0030
G4(6)	0.0024	0.0030	0.0027	0.0030	0.0027
G4(8)	0.0024	0.0030	0.0027	0.0030	0.0027

Lateral frame deformations at yield point are estimated using the expressions given in the Table 6.8. A summary of the yield deformations for each sample, compared to the numerical values are given in Table 6.19. The overall mean of the analytical model over-prediction ratio is 2.11 with Cov of 36.17%. However, removing two samples of concern (G3 and G4(5)) gives mean over-prediction ratio of 1.68 with Cov of 24.73%. Thus, a correction factor of 0.59 (1/1.68) can be applied.

Table 6.19: Comparison of the predicted and numerical lateral yield deformations

Sample notation	**Lateral yield deformations (mm)**		$\frac{\delta_e(\textbf{analytical})}{\delta_e(\textbf{numerical})}$
	Analytical	Numerical	
G3	17.5	6.6	2.66
G4(1)	10.3	5.0	2.05
G4(2)	10.1	9.1	1.11
G4(5)	10.2	3.1	3.28
G4(6)	10.4	5.4	1.92
G4(8)	10.3	6.3	1.64

(b) Lateral yield strength for the fixed frames

The predicted lateral yield strengths are established using the proposed analytical relationships provided in Table 6.8 and the results are presented in Table 6.20. The lateral yield strength for the G4 samples vary is 131 kN while the predicted strength for sample G3 is 114 kN. The predicted strength is compared with the yield strength obtained from the numerical analysis (see Table 6.21). The overall mean for over-prediction ratio is 3.28 with Cov of 92.190%. However, removing two samples of concern (G3 and G4(5)) gives mean over-prediction ratio of 1.76 with Cov of 4.14%. Thus, a correction factor of 0.57 (1/1.76) can be applied.

Table 6.20: Bare frame yield strength

Sample notation	Calculated yield strength from the four cases (kN)				Predicted strength (interpolated), kN
	Case A- $F_e(A)$	Case B - $F_e(B)$	Case C - $F_e(C)$	Case D - $F_e(D)$	
G3	127.2	107.5	74.4	48.7	113.7
G4(1)	129.9	132.9	103.5	88.7	130.6
G4(2)	130.3	133.3	107.1	91.8	131.1
G4(5)	130.2	133.2	106.4	91.2	131.0
G4(6)	130.7	133.0	110.4	89.7	131.1
G4(8)	130.8	133.2	112.1	91.1	131.3

Table 6.21: Comparison of the predicted and numerical lateral yield strength

Sample notation	Lateral yield strength, F_e (kN)		$\frac{F_e(\text{analytical})}{F_e(\text{numerical})}$
	Analytical	Numerical	
G3	113.7	12.2	9.32
G4(1)	130.6	76.84	1.70
G4(2)	131.1	74.09	1.77
G4(5)	131.0	39.25	3.34
G4(6)	131.1	70.63	1.86
G4(8)	131.3	76.96	1.71

(c) Diagonal strut ultimate strains and lateral ultimate deformations for the fixed frames

The ultimate deformation analytical models proposed for all the cases (A - D) are used to determine the elastic strains for the diagonal struts using equations provided in Table 6.8 and equation 3.3 (see Section 3.4.5). The strains from all the four cases are interpolated to generate the predicted strain for the respective frame. Linear interpolation is used. Table 6.22 provides a summary of the elastic strains for the validation samples established using the proposed analytical expressions. The yield strains vary from 0.0132 to 0.0215. Lateral frame ultimate deformations are estimated using the expressions given in the Table 6.8. A summary of the ultimate deformations for each sample, compared to the numerical values are given in Table 6.23. The overall mean of the analytical model over-prediction ratio is 3.10 with Cov of 55.37%. However, removing two samples of concern (G3 and G4(5)) gives mean over-prediction ratio of 2.40 with Cov of 58.22%.

Table 6.22: Diagonal strut ultimate strains

Sample notation	Calculated ultimate strains from the four cases				Predicted strain (interpolated), ε_{du}
	Case A- $\varepsilon_{du}(A)$	Case B - $\varepsilon_{du}(B)$	Case C - $\varepsilon_{du}(C)$	Case D - $\varepsilon_{du}(D)$	
G3	0.0109	0.0272	0.0318	0.0407	0.0215
G4(1)	0.0133	0.0177	0.0297	0.0256	0.0158
G4(2)	0.0131	0.0175	0.0287	0.0245	0.0156
G4(5)	0.0132	0.0176	0.0289	0.0247	0.0156
G4(6)	0.0109	0.0152	0.0237	0.0217	0.0132
G4(8)	0.0108	0.0151	0.0233	0.0212	0.0132

Table 6.23: Comparison of the predicted and numerical lateral ultimate deformations

Sample notation	**Lateral ultimate strain, δ_u (mm)**		$\frac{\delta_u \textbf{(predicted)}}{\delta_u \textbf{(numerical)}}$
	Predicted	Numerical	
G3	93.1	28.4	3.28
G4(1)	52.6	16.1	3.27
G4(2)	51.9	150.0	0.35
G4(5)	52.0	9.1	5.72
G4(6)	51.3	15.6	3.29
G4(8)	51.0	19.0	2.69

(d) The lateral ultimate strength for the frames with fixed supports

The predicted lateral ultimate strengths are established using the proposed analytical relationships provided in Table 6.8 and the results are presented in Table 6.24. The G4 samples have ultimate capacity of 150 kN while sample G3 has ultimate capacity of 130 kN. The predicted strength is compared with the bare frame capacity obtained from both the experimental data and the numerical analysis (see Table 6.25). The overall mean of the analytical to numerical strength ratios is 3.08 with Cov of 99.45%, while the mean ratio reduces to 1.71 with Cov of 4.48% when sample G3 is removed. The overall mean of the analytical-to-the-experimental strength ratios is 2.68 with Cov of 308.77%, while the mean ratio reduces to 1.42 with Cov of 0.48% when sample G3 is removed. Considering the experimental data and ignoring the prediction from the sample G3, a correction factor of 0.70 can be used (1/1.42).

Table 6.24: Bare frame ultimate strengthfrom analytical models

Sample notation	**Calculated ultimate strength from the four cases (kN)**				**Predicted strength (interpolated), kN**
	Case A- $F_u(A)$	Case B - $F_u(B)$	Case C - $F_u(C)$	Case D - $F_u(D)$	
G3	150.5	120.1	94.9	75.4	130.3
G4(1)	153.2	148.1	133.5	132.3	150.3
G4(2)	153.7	148.6	138.2	137.0	150.8
G4(5)	153.6	148.5	137.3	136.0	150.7
G4(6)	155.0	148.3	139.6	133.9	151.3
G4(8)	155.2	148.5	141.8	136.0	151.6

Table 6.25: Comparison of the predicted and numerical lateral ultimate strength

Sample notation	**Lateral ultimate strength, F_u (kN)**			$\frac{F_u \textbf{(analytical)}}{F_u \textbf{(numerical)}}$	$\frac{F_u \textbf{(analytical)}}{F_u \textbf{(experimental)}}$
	Analytical	Numerical	Experimental		
G3	130.3	14.0	14.5	9.31	8.99
G4(1)	150.3	92.6	106.0*	1.62	1.42
G4(2)	150.8	84.1	106.0*	1.79	1.42
G4(5)	150.7	65.1	106.0*	2.31	1.42
G4(6)	151.3	86.2	106.0*	1.76	1.43
G4(8)	151.6	90.4	106.0*	1.68	1.43

*One bare frame was tested, the rest had similar material and cross-sectional properties

6.5 DICUSSIONS AND CONCLUSION

The parametric evaluation of both the fixed and pinned bare frames is conducted, considering variations in the second moment of area and the length of the beam and the columns. The results and the analytical relations derived from the parametric studies can be assumed to represent the specified limits, based on the range of second moment of areas and the span of the beam and the columns. From the observations of the results of the parametric studies, the following restrictions should be observed when using the analytical expressions:

(a) The minimum ratio of I_b/I_c (i.e. either $I_b/I_c\,(I_b)$ or $I_b/I_c\,(I_c)$ should be 1.0;

(b) The maximum ratio of I_b/I_c should be 40;

(c) The minimum allowable aspect ratio, r_a (i.e. either $r_a(L_b)$ or $r_a(L_c)$ should be 0.2;

(d) The maximum allowable aspect ratio, r_a should be about 1.5; and

(e) The longitudinal reinforcement ranges from 2.0% to 4.0%, based on the amount of reinforcement considered in the reinforced frame sections.

Using the above restrictions, sample G3, with about 1.4% of reinforcement, is not qualified for the use of the analytical models under this Chapter.

The linearised approximation for the *F-δ* curve, assumed in the derivation of the analytical relations, enables generation of simplified analytical relationships for the diagonal strut. The linearised approximations may be useful in the seismic evaluation of structure. Notwithstanding its usefulness, the use of linearised curves generates possible model uncertainty. For example, sample G4(5) has challenges in numerical convergence, with the finite element model aborting just after reaching the 'peak' strength. The *F-δ* curve for the sample indicates less stiffness degradation to reach the peak than the other samples. Based on the linearised approximation for the *F-δ* curve, the yield strength and deformation for sample G4(5) are far lower than the rest of the same group samples.

CHAPTER 7

7.0 SIMPLIFIED INFILL FRAME NONLINEAR ANALYSIS USING THE TRUSS ANALOGY

7.1 INTRODUCTION

A simplified infill frame nonlinear analysis, using a truss analogy is proposed, and verified using experimental data for the infill RC frames. Using a stiffness formulation, force-displacement behaviour of a structural system is evaluated through adjustment in stiffness that is based on the stress-strain state and resulting changes in nodal forces and displacements. The stiffness adjustment is based on strain state of an element and force equilibrium principles using simplified stress-strain material law. In the proceeding sections, Young's modulus adjustment procedures at material level and overall structural system evaluation procedure are provided. When a framed structure has been transformed into a truss system, the diagonal struts used for this transformation can be combined with equivalent diagonal struts derived from the infills as discussed in Chapter 4. Thus, an overall trussed system can be used to evaluate the structural behaviour of the infilled RC frames for seismic evaluation of structure where the method is used to establish a capacity curve. Two formulations for the determination of the diagonal strut properties that represent the bare frame flexural mechanism are considered, namely:

(a) Diagonal properties derived from the column material properties as discussed in Section 5.5. A perfect plastic bilinear material model is assumed; and
(b) Diagonal properties derived from the parametric evaluation of the bare frames reported in Section 6.4. A bilinear material model is used.

For the infill RC frame, the idealised truss system comprises the diagonal strut that combines the contributions from the frame and the infill. In this study these contributions are added. While the frame-infill resistance mechanism is not depicted by the summation of resistance from the individual system, it is assumed that the analytical models that are used to determine equivalent infill strut properties account for the synergetic effects of the frame-infill mechanism. This is reflected in the determination of the geometric properties for the equivalent infill struts as discussed in Section 2.3.1. The truss-based evaluation of the infill RC frames is implemented in finite element software (ABAQUS, 2011) and Matlab (through the development of specific pseudo-code provided in Appendix A2.2). A detailed structural evaluation process used for truss evaluation in Matlab is provided in Section 7.4, with material modelling discussed under Section 7.3.

7.2 COMBINATION OF MULTIPLE ELEMENTS INTO ONE SECTION

The proposed truss-based nonlinear evaluation of infill RC framed structures is based on converting the bare frame into a truss system and combining the infill contribution using an equivalent infill diagonal strut. This means that a bare frame can be represented by either a double diagonal strut system or by a single diagonal strut system (see Figure 7.1). When a single diagonal is used for the bare frame, the equivalent single strut should be used. Double diagonals representation of the frame is combined with double equivalent struts. This ensures that the system's stiffness remains representative of the actual structure over a large stress (loading) range.

The objective of combining elements that are identified by the same coordinates is to have a single material property definition. The elements may have different stiffness values and there is need to have a homogenised material property. The elements' combination and homogenisation are based on the following assumptions:

(a) The elements are bar elements. i.e. they can only resist axial forces;
(b) The elements are defined by the same coordinates. i.e. they have the same coordinates defining the start of element and end of element respectively; and
(c) All the assumptions for homogenisation of composite sections, stated in Section 5.2.

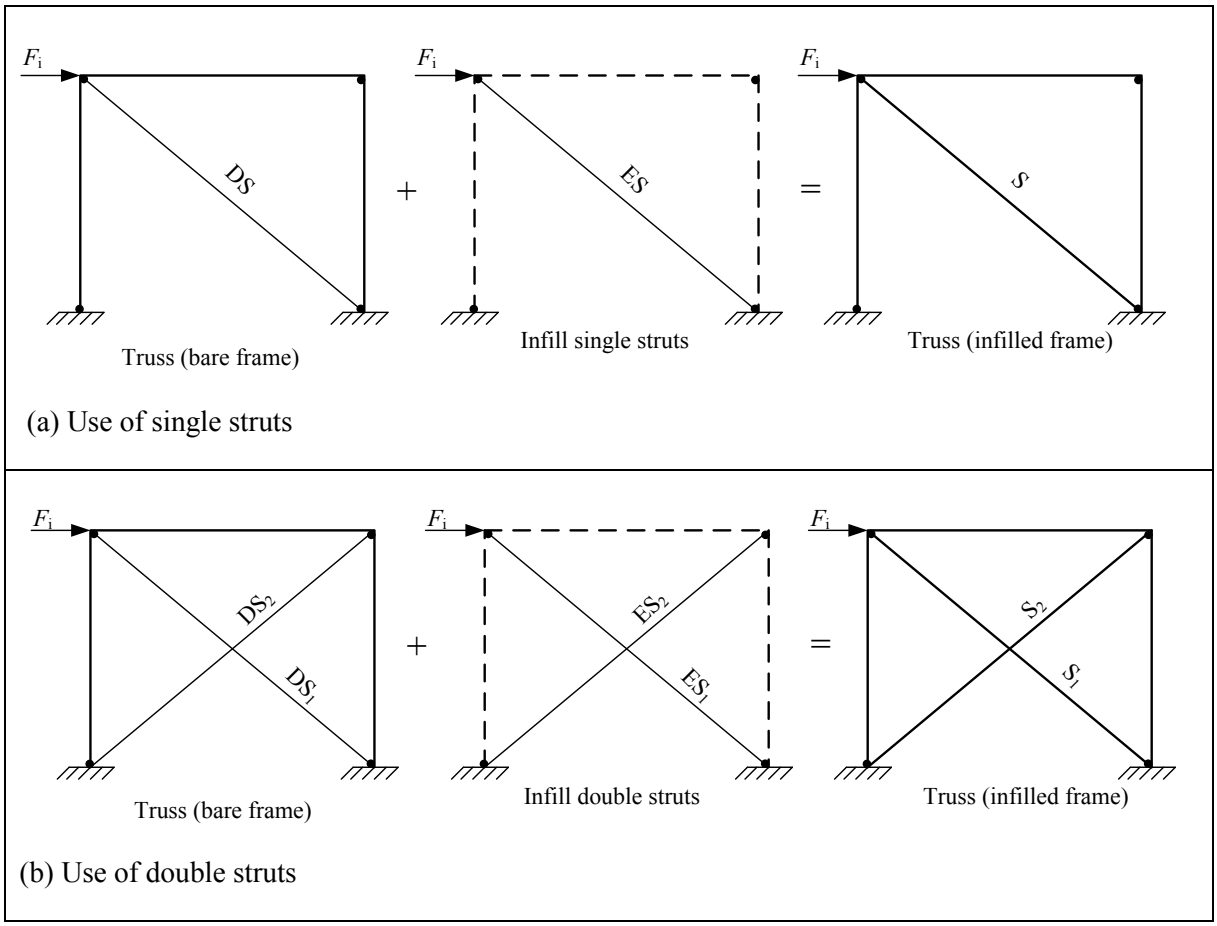

Figure 7.1: Truss configuration using (a) single diagonal strut, (b) double diagonal struts

Consider that two elements are to be combined whose respective material and geometric properties are denoted by subscripts 1 and 2 respectively as shown in Figure 7.2. The strain points, *j*, for materials 1 and 2 are defined by strains ε_{1j} and ε_{2j} respectively. Linearised instantaneous Young's moduli are related to initial moduli E_1 and E_2 respectively and are defined by $\alpha_{1j}E_1$ and $\alpha_{2j}E_2$ respectively. For Figure 7.2, $\alpha_{1j}E_1 > \alpha_{2j}E_2$. The cross-sectional areas for the respective elements are A_1 and A_2. Let the cross-sectional area for the combined element be represented by A_1, if element 1 is more ductile than, or at least as ductile as, element 2. The relationships for the combination of the elements are used:

For a constant instantaneous strain, $\Delta\varepsilon_j$, within the common strain state (see Figure 7.2), change in axial force, ΔF_j, is defined as:

$$\Delta F_j = \alpha_{1j}E_1\Delta\varepsilon_j A_1 + \alpha_{2j}E_2\Delta\varepsilon_j A_2 \qquad (7.1)$$

Defining parameters ρ and m as follows:

$$\rho = \frac{A_2}{A_1}, \quad m = \frac{E_2}{E_1}$$

Equation 7.1 can be rewritten as:

$$\Delta F_j = E_1 \Delta \varepsilon_j A_1 \left(\alpha_{1j} + \alpha_{2j} m \rho\right) \tag{7.2}$$

Dividing the incremental force with area, A_1, generates an incremental stress, $\Delta\sigma_j$:

$$\Delta \sigma_j = E_1 \Delta \varepsilon_j \left(\alpha_{1j} + \alpha_{2j} m \rho\right) \tag{7.3}$$

The new homogenised combined element can be assumed to have a cross-sectional area of A_1 and instantaneous Young's modulus, $\eta_j E_1$, where η_j is defined as

$$\eta_j = \alpha_{1j} + \alpha_{2j} m \rho \tag{7.4}$$

With the material and geometric behaviour for the diagonal strut known, finite element models can be used to evaluate the structural performance for the infill RC frames. Truss elements are used to model all the elements of the structural system. The procedure is validated as reported in Section 7.5.

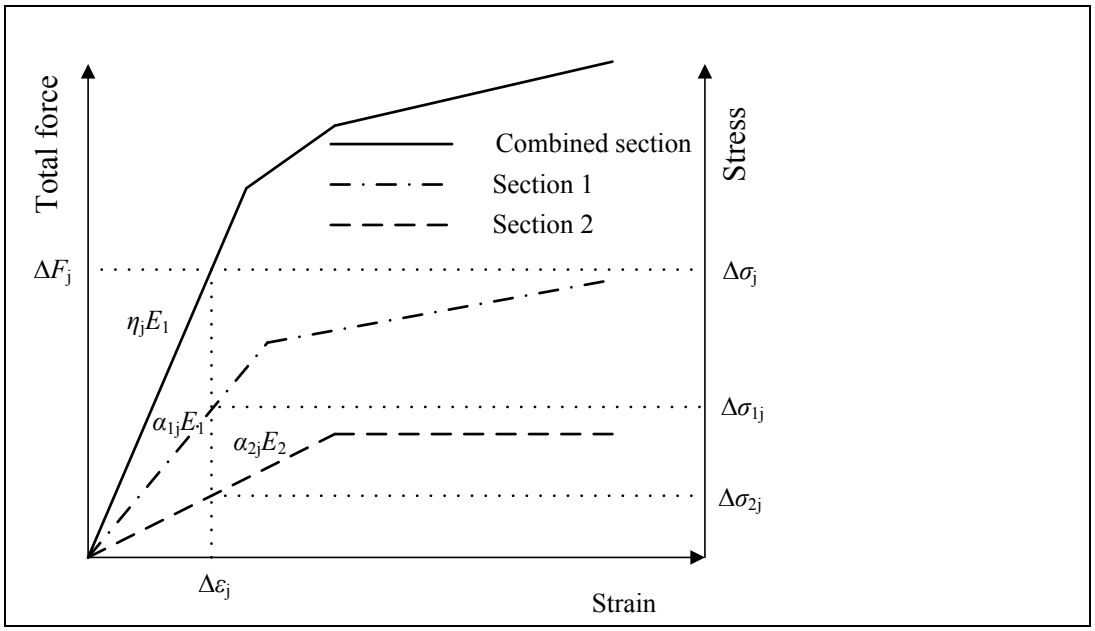

Figure 7.2: Typical material behaviour combination for two truss sections

7.3 MATERAIL BEHAVIOUR MODELLING

Implementation of the truss-based structural system evaluation in Matlab involves parametric consideration of the truss material behaviour for both force-deformation evaluations. Structural materials under axial loading display either strain hardening, strain softening or perfect plastic behaviour. A modified modulus of elasticity is introduced as secant stiffness, E_{ij} (see Figure 7.3) together with tangential modulus of elasticity to model the nonlinear behaviour of the structural system. Both secant modulus and tangential modulus are expressed as functions of initial elastic modulus. The

stiffness method, as used in this procedure, involves the use of two components of system stiffness derived from these two moduli; namely, secant stiffness (which is the normal stiffness but derived from secant modulus and it depends on the strain state at a specific displacement/deformation) and tangential stiffness (which is derived using normal stiffness formulations but uses tangential modulus of elasticity and is valid for a specific range of strain state/region for an element).

Secant modulus derivation for structural performance evaluation (nonlinear behaviour)
The phenomenon of modification of modulus of elasticity is based on the premise that the behaviour of an element that is undergoing inelastic behaviour following a simplified multi-linear stress-strain can be modelled by replacing an equivalent elastic material with appropriate secant modulus of elasticity. This is true when the required output is equivalent force (see Figure 7.3). Information about specific stress-strain at a given loading point for the modification of modulus of elasticity is required. Secant modulus for a stress-strain state for the force (E_{ij}) and energy (E'_{ij}) evaluation is derived from the initial modulus of elasticity (E) using force equilibrium principle and strain balance principle respectively for the two material systems.

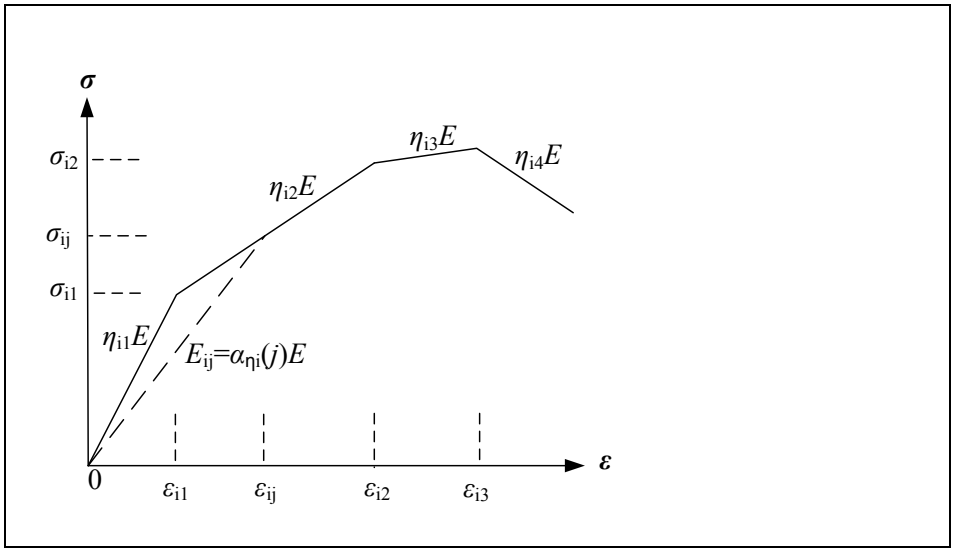

Figure 7.3: Typical stress-strain relationship for a homogenised RC truss element

With respect to Figure 7.3, the secant modulus for the force deformation evaluation (E_{ij}) is derived as:

The force or stress at strain ε_{i1} for an equivalent elastic material is the same as that of a multi-linear material and can be written as

$$\eta_{i1}E\varepsilon_1 + \eta_{i2}E(\varepsilon_{i2} - \varepsilon_{i1}) = E_{i1}\varepsilon_{i1} \tag{7.5}$$

Relating the secant modulus for the first stress-strain state after elastic state (point j =1) with initial elastic modulus gives

$$E_{i1} = \frac{E(\eta_{i1}\varepsilon_{i1} + \eta_{i2}(\varepsilon_{i2} - \varepsilon_{i1}))}{\varepsilon_{i1}} = \alpha_{\eta i}(1)E \tag{7.6}$$

where

$$\alpha_{\eta i}(1) = \frac{\eta_{i1}\varepsilon_{i1} + \eta_{i2}(\varepsilon_{i2} - \varepsilon_{i1})}{\varepsilon_{i1}} \tag{7.7}$$

The generalised factor $\alpha_{\eta i}(j)$ for the j^{th} state can be rewritten as:

$$\alpha_{\eta i}(j) = \frac{\sum_{k=1}^{j+1} \eta_{ik}(\varepsilon_{ik} - \varepsilon_{ik-1})}{\varepsilon_{ij}} \tag{7.8}$$

where

$$\varepsilon_{i0} = 0$$

Note that factor $\alpha_{\eta i}(j)$ can define whether the material is strain-softening ($\alpha_{\eta i}(j) < 0$), strain-hardening ($\alpha_{\eta i}(j) > 0$) or perfect plastic ($\alpha_{\eta i}(j) = 0$). Implementation of the solution procedure involves an iterative process where a trial solution is first performed, and its results are evaluated to determine the strain state. The stiffness of each element is modified through the modification of its Young's modulus. This means that for an element with initial elastic stiffness, K_e, will have its stiffness modified to $\alpha_{\eta i}(j)K_e$ when the element is undergoing plastic deformation.

7.4 STRUCTURAL SYSTEM PERFORMANCE EVALUATION

This procedure offers a systematic identification of the most probable alternative load path after an element failure or change in material strength for nonlinear material. The use of the proposed methodology is premised on the following assumptions:

(a) The individual elements will not buckle but will experience full strength behaviour as characterised by its conventional material law both in tension and compression. Otherwise consideration for buckling will result in complex structural behaviour that cannot be modelled by this procedure, if a simplified procedure is to be maintained.

(b) Applied load is proportionally increased as prescribed by the user and the corresponding nodal displacements and subsequent materials strain and stress states are derived. The change in loading can be varied according to the perceived loading conditions. For push over analysis, existing procedures for load proportioning can be adopted and a push over curve can be derived for a structural system.

(c) Material properties of the elements are modelled as multi-linear stress-strain with known modulus of elasticity and tangent modulus for all lines.

Derivation of key parameters

Figure 7.4 is a schematic presentation of force vs. displacement curve for a multi-degree of freedom system (MDOF). The figure is used to illustrate the development of methodological procedure in MDOF systems. The proposed algorithm identifies points where there is a change in gradient due to an element changing its material properties (elastic to plastic or plastic to ultimate failure for the derived homogenised material law as shown in Figure 7.3).

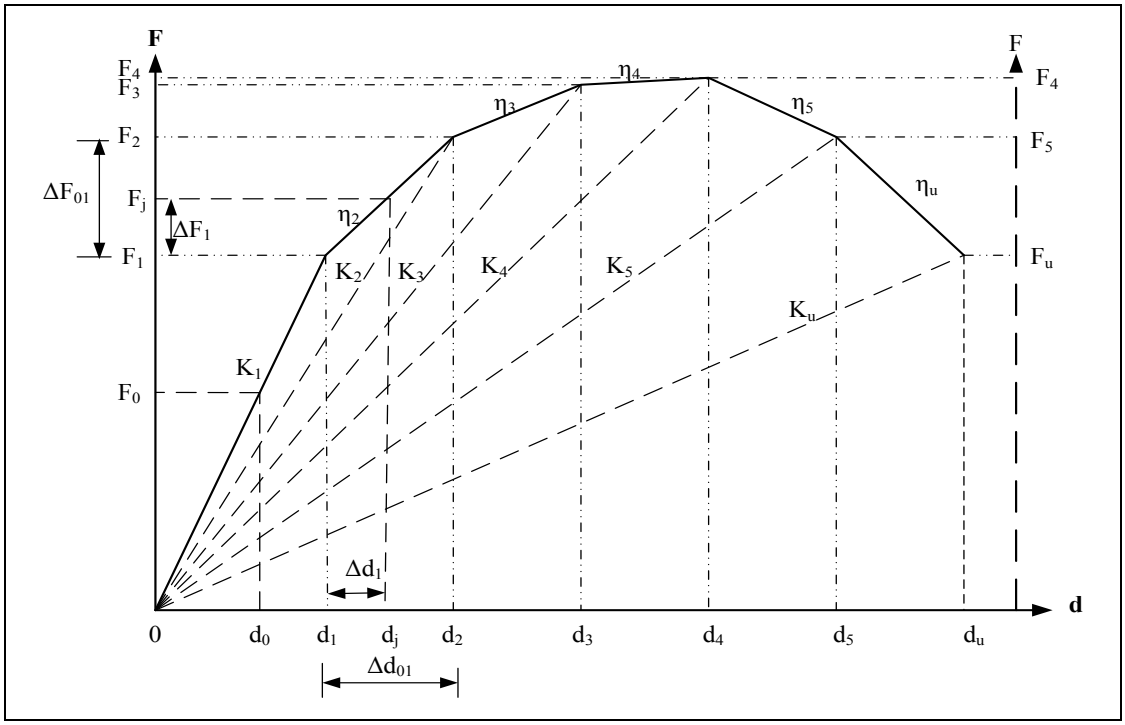

Figure 7.4: Assumed force vs displacement for a multi-degree of freedom structural system

With reference to Figure 7.4, consider that initial loading occurs within fully elastic range at point (F_0, d_0). Initial small force, F_0, is applied to the system and the corresponding nodal displacement is derived from stiffness equation as follows:

$$F_0 = K_e d_0 \tag{7.9}$$

A scaling factor, β_{min}, is used to identify initial yielding point based on the strains of elements at the initial loading point (ε_0) and the earliest element to yield. Initial strains are determined from a general axial strain-displacement relationship for a system in elastic state as follows:

$$\{\varepsilon\} = [C_\varepsilon]\{d\} \tag{7.10}$$

Where $[C_\varepsilon]$ is a system matrix assembled from individual element, i, transformation as follows:

$C_{\varepsilon(i)}$	First node		Second node	
	$-\frac{Cos\theta}{L}$	$-\frac{Sin\theta}{L}$	$\frac{Cos\theta}{L}$	$\frac{Sin\theta}{L}$

(7.11)

Considering $\{\varepsilon_1\}$ as a vector of yield strains for all elements and $\{\varepsilon_0\}$ the initial loading strains, the scaling factor, β_{min}, is determined as a least value of the ratio of yield strains and initial loading strains expressed as follows:

$$\beta_{min} = Min\left(\frac{\{\varepsilon_1\}}{\{\varepsilon_0\}}\right) \tag{7.12}$$

Initial yielding nodal force $\{F_1\}$, displacements $\{d_1\}$ and elements' strains $\{\varepsilon_1\}$ can be determined respectively as:

$$\{F_1\} = \beta_{\min}\{F_0\},\ \{d_1\} = \beta_{\min}\{d_0\} \text{ and } \{\varepsilon_1\} = \beta_{\min}\{\varepsilon_0\} \quad (7.13)$$

Force-displacement evaluation at subsequent points after initial element(s) yielding considers the tangential stiffness and its corresponding vectors of change in force (ΔF_j), nodal displacement change (Δd_j) and elements' strain change ($\Delta \varepsilon_j$). An additional change in force vector (ΔF_j) is applied to a system undergoing a reduced stiffness (tangential stiffness, η_j, as shown in Figure 7.4). Balancing internal and overall external loads (F_j), the following stiffness equation can be used:

$$F_j = K_{j-1}d_{j-1} + \Delta F_j \quad (7.14)$$

where

$$\Delta F_j = K_{\alpha j}\Delta d_j = F_j - K_{j-1}d_{j-1} \quad (7.15)$$

Δd_j can be determined from the relationship/or from the first part of equation 7.15 with change in force vector taking the form of the applied load (for the applied load part).

$$\Delta d_j = \frac{F_j - K_{j-1}d_{j-1}}{K_{\alpha j}} \quad (7.16)$$

Equation 7.16 is valid when the determinant of instantaneous stiffness matrix $K_{\alpha j}$ is not zero (i.e. for a system that displays strain hardening and strain softening only). A scaling factor, $\beta_{\min,}$ for subsequent yielding points, or ultimate strain point in elements can be determined as follows:

$$\beta_{\min} = Min\left(\frac{\{\varepsilon_j\} - \{\varepsilon_{ij}\}}{\{\Delta\varepsilon_j\}}\right) \quad (7.17)$$

where the change in strain vector, $\Delta \varepsilon_j$, is determined in the same way as that of normal strain vector, ε_{ij}, using change in nodal displacement, Δd_j (i.e. $\Delta \varepsilon_j = [C_\varepsilon]\{\Delta d_j\}$), ε_j is element strain where stress-strain gradient changes. Nodal forces at any change in stress-strain gradient of elements, $\{F_j\}$, corresponding nodal displacements $\{d_j\}$ and elements' strains $\{\varepsilon_{ij}\}$ can be determined respectively as:

$$\{F_j\} = \{F_{j-1}\} + \beta_{\min}\{\Delta F_j\},\ \{d_j\} = \{d_{j-1}\} + \beta_{\min}\{\Delta d_j\} \text{ and } \{\varepsilon_j\} = \{\varepsilon_{j-1}\} + \beta_{\min}\{\Delta\varepsilon_j\} \quad (7.18)$$

Structural performance evaluation procedure

Using the mathematical formulas derived above, an evaluation procedure for force vs displacement behaviour of a RC infilled frame with full stress-strain behaviour of all its constituent materials is summarised as follows:

Step 1: Structural idealisation of the RC infilled frame into an equivalent truss system;

Step 2: Determine the specific homogenised material model for each RC frame element and the material properties of all diagonal struts;

Step 3: Formulation of force equations using stiffness matrix formulation (assumes all members are fully elastic) and solve for all unknown forces and displacements;

Step 4: Establish the initial strain state of each member $\{\varepsilon_0\}$;

Step 5: Calculate a scaling factor for the first element yielding, β_{min}. Using the scaling factor adjust the nodal forces and displacement and elements' strains at first element(s)' yielding;

Step 6: Formulate the tangential stiffness considering the moduli of elasticity based on the existing strain state ($\eta_{ij}E$ as shown in Figure 7.3). Determine change in nodal displacement for a change in nodal forces;

Step 7: Determine the full new force vector, $\{F_1\}$ and nodal vector $\{d_1\}$. Establish the strains at this force. Determine the scaling factor. The new nodal displacements and forces at second element yielding and elements' strains are then determined;

Repeat steps 6 and 7 until the system reaches ultimate capacity. The proposed algorithm allows evaluation of the structural system using reduced system's stiffness using tangential stiffness of elements and the reduction of redundancy up to attainment of static determinacy or substantial reduction of carrying capacity of the system. Since the incremental analysis uses tangential parameters, the post peak evaluation is carried out by maintaining the nodal displacement at the applied load node in the same direction as the original direction (during first elastic evaluation stage). When a member reaches ultimate strain, it is completely removed from the analysis.

7.5 VALIDATION OF THE PROPOSED METHOD FOR LATERAL LOAD RESISTANCE

This section validates the structural evaluation procedure that utilises the truss-analogy approach using both the experimental and numerical data for the RC infill frames. All elements of the frame are modelled as a truss with an additional diagonal strut modelled to represent both the flexural mechanism and the equivalent infill behaviour. The diagonal strut behaviour representing the frame flexural behaviour is calibrated using the two procedures discussed in Section 5.5 (based on column properties) and Section 6.4 (based on parametric evaluation of the bare frames). The infill strut is calibrated using the procedure summarised in Section 4.5. Finite element models are used to evaluate and verify the behaviour of both the fixed and the pin supported infill frames as predicted by the proposed modelling procedures. Apart from the use of numerical models, available experimental data for the fixed RC infill frames is used for the validation exercise. Experimental data from both Crisafulli (1997) and Mehrabi et al. (1996) are used for the verification exercise. These experiments involved fixed infill frames. A code is developed in Matlab for both the infill frame characterisation and structural system evaluation for the proposed procedure as outlined in Section 7.4. The proposed evaluation procedure utilising the truss analogy is also implemented in ABAQUS (2011). Preliminary evaluation of the infill frame, using the consistency factor, $\overline{N}_f$, defined in Section 4.4.1 is provided first before the truss-based evaluation procedure, involving material behaviour characterisation and overall structural system evaluation is validated.

7.5.1 Preliminary evaluation of the infill frames

The capacity of the bare frames, using analytical relations developed in Sections 5.5 and 6.4 are established. A consistency factor, $\overline{N}_f$, that is proposed in Section 4.4.1 is used to generate preliminary results for the infill capacity (using equation 4.85). The consistency factor, $\overline{N}_f$ is determined for the infill frames with fixed supports, thus only the fixed supported frames are considered in this section. Table 7.1 summarises the results of the preliminary evaluation for the infill frames. $\overline{N}_f$ values determined from the experimental data, considering whether the infill is made of hollow or solid

masonry (categorised masonry) are used. The appropriate correction factors are used for the bare frame capacity prediction using the analytical models derived from the parametric studies.

Mean ratio of the predicted bare frame strength-to-experimental strength is 1.00 (Cov of 0.28%) for predictions based on the procedure from Section 6.4 and 0.92 (Cov of 9.84%) for predictions based on the procedure from Section 5.5. Mean ratios of the predicted infill frame strength-to-experimental strength is 0.95 (Cov of 21.21%) and 0.86 (Cov of 21.74%) for predictions based on the procedure from Sections 6.4 and 5.5 respectively.

Table 7.1: Preliminary evaluation results for the fixed frames

Item	Sample notation								
	G3	G4(1)	G4(2)	G4(3)	G4(4)	G4(5)	G4(6)	G4(7)	G4(8)
F_{bare} (pred)[1] – kN	-	105.2	105.6	105.6	105.6	105.5	105.9	105.9	106.1
F_{bare} (pred)[2] – kN	15.4	105.4	95.0	95.0	95.0	77.2	101.4	101.4	98.4
f_{cw} -MPa	16.0	13.2	9.3	8.3	9.3	12.1	9.3	11.9	10.0
r_w	0.79	0.67	0.67	0.67	0.67	0.67	0.48	0.48	0.48
$\overline{N}_f$	0.13	0.13	0.09	0.09	0.13	0.13	0.09	0.13	0.13
$F_{\inf ra}$ (pred)[1] - kN	-	278.5	136.4	122.3	196.5	256.3	188.9	348.3	293.8
$F_{\inf ra}$ (pred)[2] - kN	41.5	278.8	122.7	110.0	176.8	187.5	180.7	333.2	272.5
F_{bare} (pred)[1] / F_{bare} (exp)	-	0.99	1.00	1.00	1.00	1.00	1.00	1.00	1.00
F_{bare} (pred)[2] / F_{bare} (exp)	1.06	0.99	0.90	0.90	0.90	0.73	0.96	0.96	0.93
$F_{\inf ra}$ (pred)[1] / $F_{\inf ra}$ (exp)	-	1.00	0.89	0.64	0.67	1.10	1.21	0.98	1.06
$F_{\inf ra}$ (pred)[2] / $F_{\inf ra}$ (exp)	0.91	1.00	0.80	0.58	0.61	0.81	1.16	0.94	0.99

[1]Analytical models derived from the parametric studies (Section 6.4); [2]Analytical models derived from the column properties (Section 5.5)

7.5.2 Material behaviour characterisation

Evaluation of the infill frame using the truss system involves characterising the material behaviour of the truss elements so that they represent the frame lateral behaviour. The RC column and beam sections are converted into homogeneous sections using the procedure provided in Section 5.2. Based on the material characterisation for the infill strut summarised in Section 4.5, material characteristic behaviours for the RC beams and columns and the infill struts are evaluated for samples G3, G4(1), G4(4), G4(5), G4(7) and G4(8). Detailed information involving all the steps carried out for the determination of the homogenised truss elements is provided for sample G3 while summarised information is provided for the rest of the samples.

(a) Sample G3

A tri-linear material model is used for both the concrete and the reinforcement compressive stress behaviour. For the unconfined concrete, the yield, peak and residual stresses are 22.5 MPa, 22.5 MPa and 4.5 MPa and their respective strains are 0.0010, 0.0028 and 0.0144. The confined concrete yield, peak and residual stresses are 24.77 MPa, 24.77 MPa and 4.95 MPa and their respective strains are 0.0011, 0.0031 and 0.0124. The stresses for the reinforcing bars are 323 MPa, 323 MPa and 441 MPa with respective strains of 0.0016, 0.0260, and 0.253. A summary of the total stress-strain behaviour for the homogenised column and beam sections is provided in Table 7.2.

Table 7.2: Stress-strain behaviour for the homogenised RC beam and RC column sections for the sample G3

jth stress-strain state	**Homogenised RC column section**			**Homogenised RC beam section**		
	η_j x10^{-3}	ε_{cj}	σ_{cj} (MPa)	η_j x10^{-3}	ε_{cj}	σ_{cj} (MPa)
1	1113.6	0.0011	27.59	1085.2	0.0010	24.42
2	127.6	0.0016	28.94	95.7	0.0016	25.65
3	0.0	0.0031	28.94	0.0	0.0028	25.65
4	-94.5	0.0124	9.40	-69.2	0.0144	7.84
5	0.0	0.0260	4.51	0.0	0.0260	3.38
6	0.3	0.2530	6.17	0.2	0.2530	4.63

Using the procedure summarised in Section 4.5, the key parameters used for the evaluation of the infill strut behaviour are generated as summarised in Table 7.3. Using the parameters provided in Table 7.3, the equivalent strut characterisation is performed using a programme developed in Matlab (see pseudo-code in appendix A2.1). The choice of the compression and shear strength factors, γ_{cc} and γ_{ss} has minimal effects on the overall performance of the equivalent strut as observed in Section 4.4.3. In this case, γ_{cc} and γ_{ss} are chosen such that the ratio of the compressive strength factor to the shear strength factor is about $2/3$. The stress-strain results for the diagonal strut are shown in Figure 7.5.

Table 7.3: Key parameters established for the determination of infill strut behaviour

Item	f_{cw} **definition**	$f_{m\theta}$ **definition**
$f_{m\theta}$ (equation 2.19) or f_{cw} (MPa)	16.0	15.5
E_θ (equation 2.18) (MPa)	11161	11161
$\gamma_{cc}+\gamma_{ss}$ (equations 4.98 and 4.99)	0.19	0.17
F_{sa} (equation 4.97) (kN)	69.7	65.3
ε_{cp} (equation 4.96)	0.0029	0.0028
ε_1 (equation 4.96)	0.0019	0.0018
ε_2 (equation 4.96)	0.0039	0.0038
ε_{1c} (equation 4.95)	0.0016	0.0015
$F_{a\varepsilon}$ (equations 4.93 and 4.97) (kN)	364.3	385.6
$a_u = a_v$ (mm)	230	230
d_{cc} (equation 4.2 and 4.3) (mm)	325	325
d_{dc} (equation 4.2 and 4.3) (mm)	2566	2566
Strut cross-sectional area, A_d (equation 4.94) (mm^2)	20447	22730
Infill strut strength - ($F_{a\varepsilon}/A_d$) (kN)	3.41	2.87

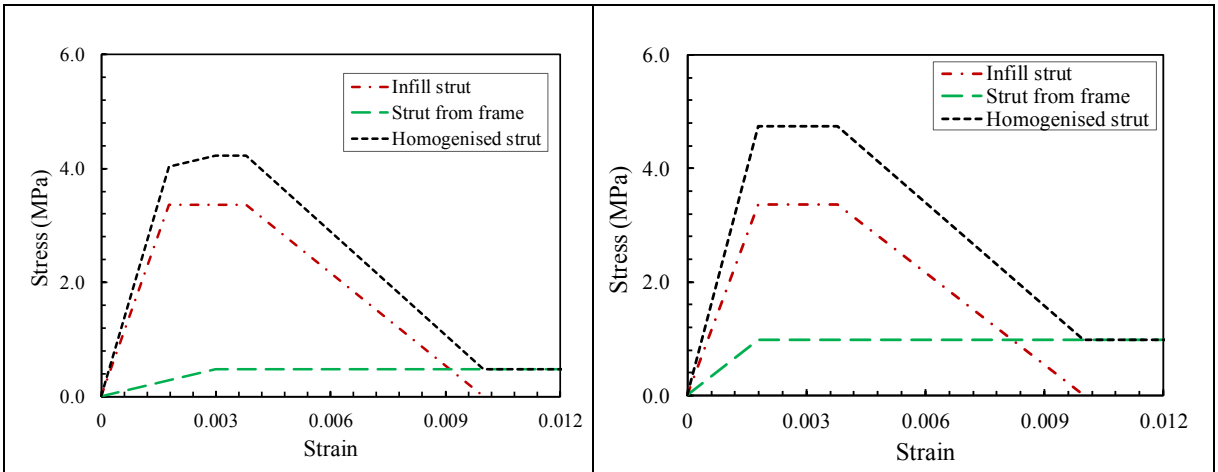

(a) Stress-strain for the pinned sample G3

(b) Stress-strain for the fixed sample G3

Figure 7.5: Typical stress-strain behaviour for the diagonal strut homogenisation

The infill strut stress-strain data is used, together with the diagonal struts stress-strain data obtained from the bare frame, to generate the homogenised diagonal strut material properties for both the pinned and fixed frames as summarised in Tables 7.4 and 7.5 respectively.

Table 7.4: Homogenised equivalent diagonal strut material behaviour for the pinned sample G3

jth stress-strain state	**Diagonal strut-frame**		**Diagonal strut-infill**		**Homogenised diagonal strut**		
	ε_{cj}	σ_{cj} (MPa)	ε_{cj}	σ_{cj} (MPa)	η_j	ε_{cj}	σ_{cj} (MPa)
1	0.0030	0.47	0.0018	3.36	14.43	0.0018	4.04
2	0.0225[1]	0.47	0.0038	3.36	1.00	0.0030	4.23
3			0.01	0.00	0.00	0.0038	4.23
4					-3.84	0.0100	0.47
5					0.00	0.0225	0.47

[1]Ultimate strain of $7.5\varepsilon_{de}$ is assumed

Table 7.5: Homogenised equivalent diagonal strut material behaviour for the fixed sample G3

jth stress-strain state	**Diagonal strut-frame**		**Diagonal strut-infill**		**Homogenised diagonal strut**		
	ε_{cj}	σ_{cj} (MPa)	ε_{cj}	σ_{cj} (MPa)	η_j	ε_{cj}	σ_{cj} (MPa)
1	0.0018	0.99	0.0018	3.36	4.82	0.0018	4.7
2	0.0134[1]	0.99	0.0038	3.36	1.00	0.0018	4.7
3			0.01	0.00	0.00	0.0038	4.7
4					-1.09	0.0100	1.0
5					0.00	*0.0134*	1.0

[1]Ultimate strain of $7.5\varepsilon_{de}$ is assumed

(b) Mehrabi et al. (1996) ***data Samples G4(1), G4(4), G4(5),G4(7) and G4(8)***

Using the homogenisation procedure proposed in Section 5.2, RC beam and column elements are converted to truss elements and the results are summarised in Tables 7.6 and 7.7 respectively. In subsequent analysis, the Young's modulus for each element is determined by the first stress-strain

provided in the Tables 7.6 and 7.7. The homogenised stress-strain behaviours for the beam and the column elements are applicable for both the fixed and the pinned frames.

Table 7.6: Homogenised RC beam sections for samples G4(1), G4(4), G4(5), G4(7) and G4(8)

Sample G4(1)		**Sample G4(4)**		**Sample G4(5)**		**Sample G4(7)**		**Sample G4(8)**	
ε_{cj}	σ_{cj} -MPa	ε_{cj}	σ_{cj} -MPa	ε_{cj}	σ_{cj} -MPa	ε_{cj}	σ_{cj} -MPa	ε_{cj}	σ_{cj} -MPa
0.0014	29.02	0.0016	33.64	0.0012	24.76	0.0013	27.96	0.0014	30.33
0.0020	31.26	0.0020	35.79	0.0020	28.63	0.0020	30.70	0.0020	33.00
0.0027	31.27	0.0027	35.80	0.0027	28.64	0.0027	30.71	0.0027	33.01
0.0297	12.77	0.0313	15.49	0.0324	13.70	0.0303	13.25	0.0316	14.52
0.0365	8.15	0.0384	10.41	0.0399	9.96	0.0372	8.89	0.0389	9.90
0.2500	11.88	0.2500	15.11	0.2500	14.42	0.2500	12.93	0.2500	14.36
0.3000	0.00	0.3000	0.00	0.3000	0.00	0.3000	0.00	0.3000	0.00

Table 7.7: Homogenised RC column sections for samples G4(1), G4(4), G4(5), G4(7) and G4(8)

Sample G4(1)		**Sample G4(2-4)**		**Sample G4(5)**		**Sample G4(6-7)**		**Sample G4(8)**	
ε_{cj}	σ_{cj} -MPa	ε_{cj}	σ_{cj} -MPa	ε_{cj}	σ_{cj} -MPa	ε_{cj}	σ_{cj} -MPa	ε_{cj}	σ_{cj} -MPa
0.0016	46.04	0.0019	43.52	0.0014	35.02	0.0016	41.82	0.0017	41.43
0.0020	48.20	0.0020	44.26	0.0020	38.53	0.0020	44.33	0.0020	43.20
0.0032	48.24	0.0032	44.30	0.0032	38.57	0.0032	44.37	0.0032	43.24
0.0297	21.11	0.0295	20.32	0.0306	19.21	0.0299	20.35	0.0295	20.11
0.0363	14.33	0.0360	14.33	0.0375	14.37	0.0365	14.34	0.0361	14.33
0.2500	21.18	0.2500	21.18	0.2500	21.18	0.2500	21.18	0.2500	21.18
0.3000	0.00	0.3000	0.00	0.3000	0.00	0.3000	0.00	0.3000	0.00

Homogenisation of the equivalent infill strut involves combination of the frame-based diagonal strut and the infill strut as discussed in Section 7.2. Using the respective procedures in Section 4.5 and Section 6.4, infill strut and bare frame strut behaviours for each sample are determined. The results for the individual stress-strain behaviour are summarised in Tables A4.1 – A4.6 in the Appendix A4.1. The stress-strain behaviour for each of the strut is combined and summarised in Tables A4.7 and A4.8. A summary of homogenised stress-strain behaviour for the equivalent struts is provided in Table 7.8 and Table 7.9 for the pinned and fixed infill frames respectively. Note that the infill properties for the samples G4(2), G4(3) and G4(4) are the same and for samples G4(6) and G4(7) are the same. Similar homogenised stress-strain behaviours for the equivalent struts for both the pinned and the fixed frames, with bare frame properties established from the column properties (based on Section 5.5), are provided in Appendix A4.2.

Table 7.8: A summary of the homogenised equivalent diagonal strut material behaviour for the pinned samples G4(1), G4(4), G4(5), G4(7) and G4(8)

Sample G4(1)		**Sample G4(4)**		**Sample G4(5)**		**Sample G4(7)**		**Sample G4(8)**	
(23800mm^2)[1]		(26100mm^2) [1]		(23200mm^2) [1]		(26200mm^2) [1]		(21900mm^2) [1]	
ε_{cj}	σ_{cj} -MPa	ε_{cj}	σ_{cj} -MPa	ε_{cj}	σ_{cj} -MPa	ε_{cj}	σ_{cj} -MPa	ε_{cj}	σ_{cj} -MPa
0.0018	12.70	0.0013	15.14	0.0017	14.97	0.0022	14.47	0.0011	17.88
0.0024	13.03	0.0018	15.43	0.0023	15.29	*0.0038*	15.30	0.0031	19.11
0.0038	10.20	*0.0040*	8.99	0.0037	11.64	0.0042	15.30	*0.0038*	17.73
0.0041	9.61	0.0033	11.62	*0.0040*	10.52	0.0100	2.01	0.0100	2.41
0.0070	2.30	0.0060	2.09	0.0053	5.84	*0.0168*	2.07	*0.0166*	2.48
0.0177	2.54	*0.0173*	2.33	0.0062	2.35				
				0.0174	2.62				

[1]Effective cross-sectional area for the homogenised equivalent diagonal strut; strains for bare frames in italics

Table 7.9: A summary of the homogenised equivalent diagonal strut stress-strain behaviour for the fixed samples for G4(1), G4(4), G4(5), G4(7) and G4(8)

Sample G4(1)		**Sample G4(4)**		**Sample G4(5)**		**Sample G4(7)**		**Sample G4(8)**	
(23800mm^2)[1]		(26100mm^2) [1]		(23200mm^2) [1]		(26200mm^2) [1]		(21900mm^2) [1]	
ε_{cj}	σ_{cj} -MPa	ε_{cj}	σ_{cj} -MPa	ε_{cj}	σ_{cj} -MPa	ε_{cj}	σ_{cj} -MPa	ε_{cj}	σ_{cj} -MPa
0.00178	15.41	0.00125	16.90	0.0017	17.6	*0.0016*	12.65	0.0011	19.9
0.00182	15.48	0.0018	17.94	*0.0018*	17.9	0.0022	16.73	*0.0016*	21.0
0.0024	15.66	*0.0018*	17.95	0.0023	18.0	0.0042	17.40	0.0031	21.6
0.0038	12.52	0.0033	13.47	*0.0066*	6.1	*0.0056*	14.77	*0.0055*	16.5
0.0066	6.20	0.0060	4.71						
		0.0065	4.86						

[1]Effective cross-sectional area for the homogenised equivalent diagonal strut; strains for bare frames in italics

7.5.3 Implementation and validation of the proposed structural system modelling in ABAQUS

The two approaches of idealising and modelling the infill frame lateral behaviour proposed in this study are validated in this section using FE in ABAQUS (2011). The two approaches are:

(a) the infill frame idealisation that comprises of the frame elements and the infill diagonal strut representing the infill behaviour; and

(b) the infill idealisation that comprises RC beam and column elements as truss elements and the diagonal strut representing the infill behaviour (through infill strut). Properties of the diagonal strut representing flexural behaviour is derived from both the column properties (column-based) and parametric evaluation of bare frames (frame-based).

Both experimental data and numerical data for samples G3, G4(1), G4(4), G4(5), G4(7) and G4(8) are used for validation.

7.5.3.1 Use of a frame and an infill strut (frame-strut) for the fixed frames

Fixed RC infill frames modelled with frame and infill strut are analysed using ABAQUS (2011). The results of the analysis are compared with the experimental data, considering the key data points of yield

and ultimate values for the *F-δ* curve. Figure 7.6 show a typical deformed model in ABAQUS and Figure 7.7 shows a typical *F-δ* curve generated from the numerical results. The numerical models consider the loading mechanism employed during the actual experiment.

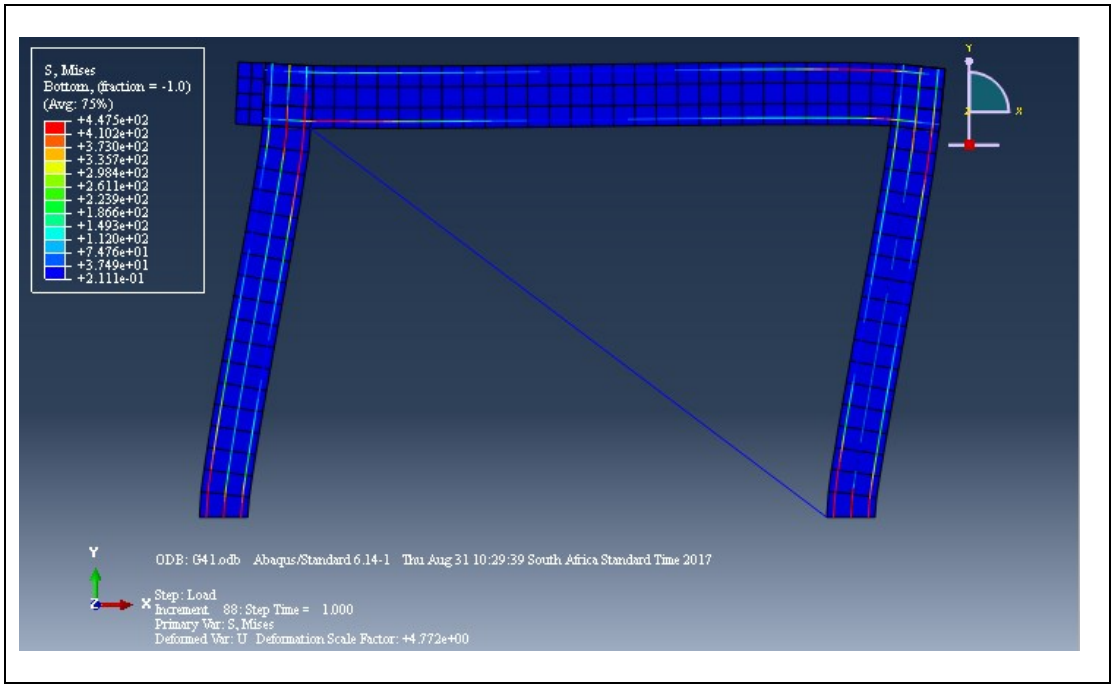

Figure 7.6: Typical deformation diagram for the infill frame modelled with equivalent infill strut (sample G41)

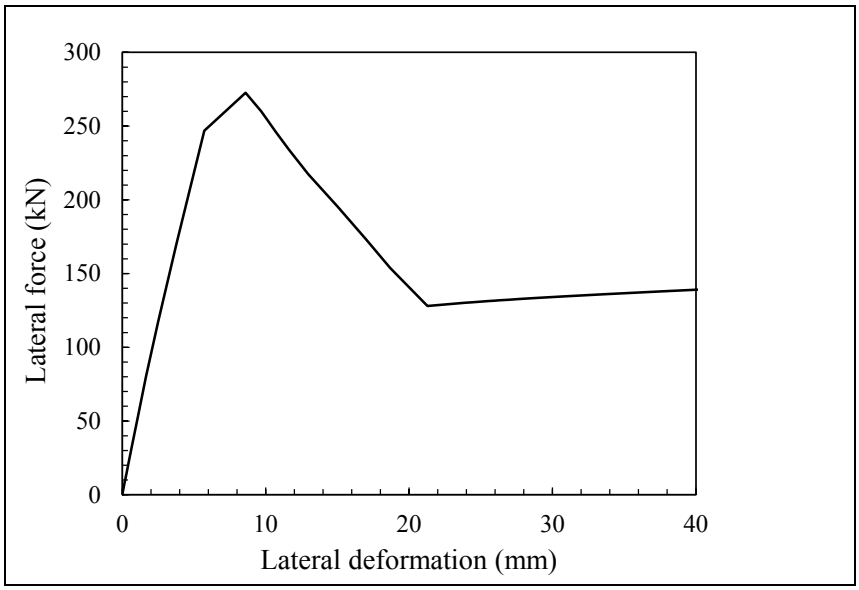

Figure 7.7: Typical force-deformation curve for the infill frame modelled with equivalent infill strut (sample G41)

(a) Lateral yield strength and yield deformation

The predicted lateral yield strength and corresponding deformation is presented in Table 7.10. The yield strength and deformation are established from the *F-δ* curve, using the actual curve points as discussed

in Section 3.4.5. The results from the numerical analyses are compared with the experimental data (see Table 7.11). Available experimental data specified the strength and corresponding deformation at first major crack in panel. As noted during the element section homogenisation in Section 7.5.2, most of the times the first strain change for the homogenised section is due to change in strain in the infill. Thus, the behaviour of the infill frame at first major crack is assumed to correspond to the yield point. The model fairly predicts the yield strength while there is greater variability in the yield deformation. The mean of the ratios of the predicted yield strength to the experimental yield strength for the first run and second run points is 1.05 (with Cov of 16.75%) and 1.07 (with Cov of 10.25%) respectively. The mean of the ratios of the predicted yield deformation to the experimental yield deformation for the first run and second run points are 1.10 (with Cov of 30.55%) and 1.72 (with Cov of 52.24%).

Table 7.10: Yield strength and deformation prediction results from the numerical models

Sample notation	**Yield strength (kN)**	**Yield deformation (mm)**
G3	53.4	6.8
G4(1)	218.5	5.0
G4(4)	243.1	3.5
G4(5)	261.3	5.6
G4(7)	335.1	7.3
G4(8)	291.0	4.0

Table 7.11: Yield strength and deformation comparison with experimental data

Sample notation	$F_e(\text{exp})$**(kN)**		$\frac{F_e(a)\textbf{(num)}}{F_e\textbf{(exp)}}$		$\delta_e(\text{exp})$ **(mm)**		$\frac{\delta_e(a)\textbf{(num)}}{\delta_e\textbf{(exp)}}$	
	1st run[1]	2nd run	1st run[1]	2nd run	1st run[1]	2nd run	1st run[1]	2nd run
G3	45.5	-	1.17	-	-	-	-	-
G4(1)	277	-	0.79	-	3.3	-	1.52	-
G4(4)	261.2	-	0.93	-	5.1	-	0.69	-
G4(5)	204.7	218.9	1.28	1.19	4.6	2.0	1.22	2.76
G4(7)	332	329.7	1.01	1.02	5.8	5.6	1.26	1.30
G4(8)	262.6	292.8	1.11	0.99	4.8	3.6	0.83	1.11

[1]The only data for quasi-static experiment

(b) Lateral ultimate strength and deformation

The predicted lateral ultimate strengths and corresponding deformations, taken from the actual *F-δ* curve are presented in Table 7.12. The results from the numerical analyses are compared with the experimental data as shown in Table 7.13. There is variability in the model predictions for the ultimate strength, with all the samples except samples G3, G45 and G4(8) showing close values to the experimental ultimate strength. There is greater variability with the ultimate deformations, even within the experimental data as noted with the variations in the values for the two runs (loading directions from which the data was taken). The mean of the ratios of the predicted ultimate strength to the experimental ultimate strength for the first run and second run points is 1.20 (with Cov of 15.67%) and 1.12 (with Cov of 13.17%) respectively. The mean of the ratios of the predicted ultimate deformation to the experimental ultimate deformation for the first run and second run points is 1.29 (with Cov of 68.19%) and 1.62 (with Cov of 40.22%).

Table 7.12: Ultimate and deformation prediction results from the numerical models

Sample notation	Ultimate strength (kN)	Ultimate deformation (mm)
G3	65.0	16.0
G4(1)	272.6	8.6
G4(4)	347.9	6.8
G4(5)	304.7	7.9
G4(7)	348.4	14.4
G4(8)	366.7	11.0

Table 7.13: Ultimate strength and deformation comparison with experimental data

Sample notation	F_u (exp) (kN)		$\frac{F_u(a)(\text{num})}{F_u(\text{exp})}$		δ_u (mm)		$\frac{\delta_u(a)(\text{num})}{\delta_u(\text{exp})}$	
	1st run[1]	2nd run	1st run[1]	2nd run	1st run[1]	2nd run	1st run[1]	2nd run
G3	45.5	-	1.43	-	-	-	-	-
G4(1)	277.7	-	0.98	-	3.3	-	2.61	-
G4(4)	292.8	-	1.19	-	7.4	-	0.92	-
G4(5)	232.3	267	1.31	1.14	15.2	9.1	0.52	0.87
G4(7)	355.6	362.7	0.98	0.96	8.13	7.11	1.77	2.03
G4(8)	275.9	292.8	1.33	1.25	17	5.6	0.65	1.96

[1]The only data for quasi-static experiment

7.5.3.2 Use of truss system for the fixed frames

A truss-based structural system idealisation for the infill frame as proposed in this study is used to evaluate the infill frame behaviour subjected to incremental lateral load. The results of the analysis are compared with the experimental data, considering the key data points of yield and ultimate values for the *F-δ* curve. Figure 7.8 shows a typical deformed model in ABAQUS and Figure 7.9 shows a typical *F-δ* curve generated from the numerical results.

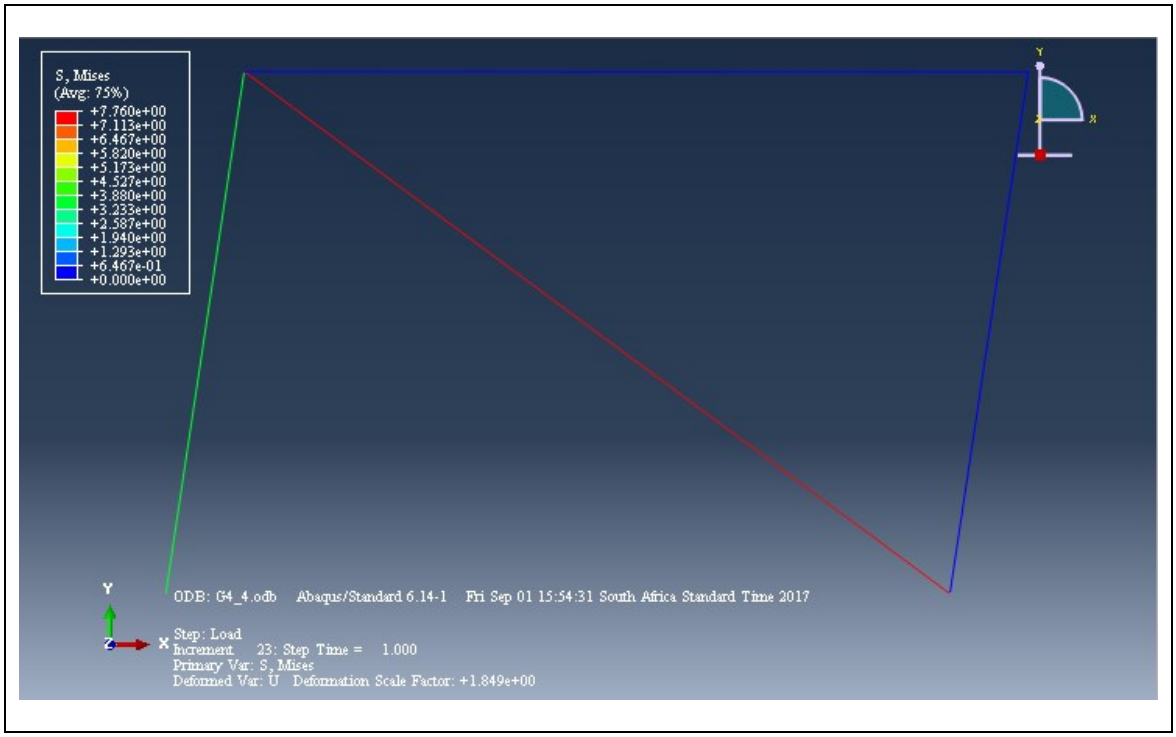

Figure 7.8: Typical deformation diagram for the infill frame modelled with equivalent infill strut (sample G41)

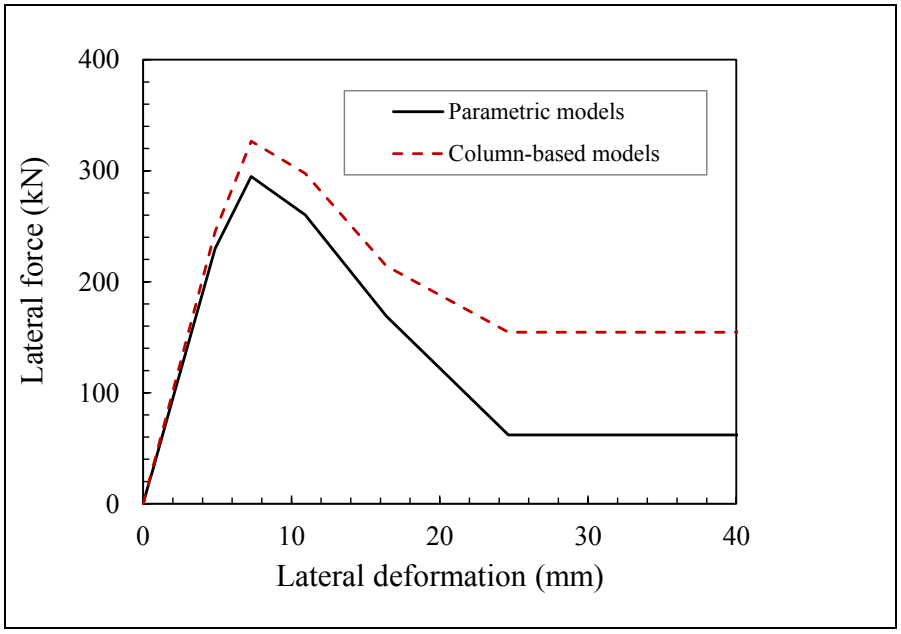

Figure 7.9: Typical force-deformation curve for the infill frame modelled with truss-based system (sample G41)

(a) Lateral yield strength and yield deformation

The predicted lateral yield strengths and corresponding deformations (from actual F-δ curve) are presented in Table 7.14. The results from the numerical analyses are compared with the experimental data (see Tables 7.15 and 7.16). Mean of the ratios of the predicted yield strength to the experimental yield strength for the first run and second run points is 1.18 (with Cov of 26.69%) and 1.16 (with Cov

of 22.77%) respectively for parametric-based models and 1.26 (with Cov of 19.19%) and 1.21 (with Cov of 12.89%) respectively for the column-based models. The mean of the ratios of the predicted yield deformation to the experimental yield deformation for the first run and second run points is 1.18 (with Cov of 21.79%) and 1.75 (with Cov of 33.23%) respectively for parametric-based models and 1.15 (with Cov of 18.55%) and 1.68 (with Cov of 36.67%) respectively for the column-based models.

Table 7.14: Yield strength and deformation prediction results from the numerical models

Sample notation	**Yield strength (kN)**		**Yield deformation (mm)**	
	Parametric models	Column-based models	Parametric models	Column-based models
G3	-	63.2	-	9.8
G4(1)	231.0	245.2	4.9	7.3
G4(4)	355.5	366.5	4.6	7.3
G4(5)	278.4	277.1	4.9	7.3
G4(7)	283.4	341.1	8.2	10.9
G4(8)	396.0	389.9	4.9	10.9

Table 7.15: Yield strength comparison with experimental data

Sample notation	$F_e(\text{exp})$**(kN)**		$\frac{F_e(\text{num})^1}{F_e(\text{exp})}$		$\frac{F_e(\text{num})^2}{F_e(\text{exp})}$	
	1st run[3]	2nd run	1st run[3]	2nd run	1st run[3]	2nd run
G3	45.5	-	-	-	1.39	-
G4(1)	277	-	0.83	-	0.89	-
G4(4)	261.2	-	1.36	-	1.40	-
G4(5)	204.7	218.9	1.36	1.27	1.35	1.27
G4(7)	332	329.7	0.85	0.86	1.03	1.03
G4(8)	262.6	292.8	1.51	1.35	1.48	1.33

[1]Parametric models; [2]Column-based models; [3]The only data for quasi-static experiment

Table 7.16: Yield deformation comparison with experimental data

Sample notation	$\delta_e(\text{exp})$**(mm)**		$\frac{\delta_e(\text{num})^1}{\delta_e(\text{exp})}$		$\frac{\delta_e(\text{num})^2}{\delta_e(\text{exp})}$	
	1st run[3]	2nd run	1st run[3]	2nd run	1st run[3]	2nd run
G3	-	-	-	-	-	-
G4(1)	3.3	-	1.48	-	1.47	-
G4(4)	5.1	-	0.90	-	0.95	-
G4(5)	4.6	2.0	1.07	2.41	1.05	2.43
G4(7)	5.8	5.6	1.41	1.46	1.26	1.30
G4(8)	4.8	3.6	1.02	1.36	1.01	1.35

[1]Parametric models; [2]Column-based models; [3]The only data for quasi-static experiment

(b) Lateral ultimate strength and deformation

The predicted lateral ultimate strengths and corresponding deformations are presented in Table 7.17. The results from the numerical analyses are compared with the experimental data as shown in Tables 7.18 and 7.19. Mean of the ratios of the predicted ultimate strength to the experimental ultimate strength for the first run and second run is 1.26 (with Cov of 20.95%) and 1.21 (with Cov of 22.74%) respectively for parametric-based models and 1.40 (with Cov of 15.15%) and 1.32 (with Cov of 13.11%) respectively for the column-based models. The mean of the ratios of the predicted ultimate deformation to the experimental ultimate deformation for the first run and second run points is 1.27 (with Cov of 62.89%) and 1.69 (with Cov of 46.62%) respectively for parametric-based models and 1.13 (with Cov of 60.71%) and 1.43 (with Cov of 40.79%) respectively for the column-based models.

Table 7.17: Ultimate and deformation prediction results from the numerical models

Sample notation	**Ultimate strength (kN)**		**Ultimate deformation (mm)**	
	Parametric models	Column-based models	Parametric models	Column-based models
G3	144.2	75.0	14.8	9.8
G4(1)	294.7	326.6	7.3	7.3
G4(4)	373.1	374.8	7.3	7.3
G4(5)	345.9	349.7	7.3	7.3
G4(7)	328.9	417.5	16.4	10.9
G4(8)	422.0	438.2	10.9	10.9

Table 7.18: Ultimate strength comparison with experimental data

Sample notation	F_u **(kN)**		$\frac{F_u(\text{num})^1}{F_u(\text{exp})}$		$\frac{F_u(\text{num})^2}{F_u(\text{exp})}$	
	1st run[3]	2nd run	1st run[3]	2nd run	1st run[3]	2nd run
G3	45.5	-		-	1.65	-
G4(1)	277.7	-	1.06	-	1.18	-
G4(4)	292.8	-	1.27	-	1.28	-
G4(5)	232.3	267	1.49	1.30	1.51	1.31
G4(7)	355.6	362.7	0.92	0.91	1.17	1.15
G4(8)	275.9	292.8	1.53	1.44	1.59	1.50

[1]Parametric models; [2]Column-based models; [3]The only data for quasi-static experiment

Table 7.19: Ultimate deformation comparison with experimental data

Sample notation	$\delta_u(\text{exp})$ **(mm)**		$\frac{\delta_u(\text{num})^1}{\delta_u(\text{exp})}$		$\frac{\delta_u(\text{num})^2}{\delta_u(\text{exp})}$	
	1st run[3]	2nd run	1st run[3]	2nd run	1st run[3]	2nd run
G3	-	-	-	-	-	-
G4(1)	3.3	-	2.21	-	2.21	-
G4(4)	7.4	-	0.99	-	0.98	-
G4(5)	15.2	9.1	0.48	0.80	0.48	0.80
G4(7)	8.13	7.11	2.02	2.31	1.34	1.54
G4(8)	17	5.6	0.64	1.95	0.64	1.95

[1]Parametric models; [2]Column-based models; [3]The only data for quasi-static experiment

7.6 DISCUSSIONS AND CONCLUSIONS

A truss-based nonlinear structural system evaluation for the infill RC frames is provided. An infill RC frame is converted into a truss, by considering the contribution of the bare frame and the infill separately. Appropriate truss elements for each system are developed and combined to form a complete system. The infill is represented by the diagonal infill strut, whose material characteristic properties are assumed to capture any synergetic effects of the frame-infill behaviour. The bare frame is converted to a truss by introducing a diagonal strut. The diagonal strut for the bare frame is derived using either the column-based material behaviour or the parametric evaluation of bare frames. It should be noted that in the literature, the macro-models for the RC infill frames are implemented in such a way that the diagonal strut is connected to the frame using pin connections, and sometimes more than one strut can be used. This work validates both the use of a frame with diagonal strut system and the complete truss system. A single strut system is used for both the frame-strut and full truss systems. It should be noted that the systems behave similarly when a double strut mechanism is used (when two struts of similar material properties but with halved cross-sectional areas are connected for the opposite diagonals as shown in Figure 7.1b).

The frame-strut model gives better predictions than the truss model. For example, the ratios of the predicted-to-experimental yield strength ranges from 0.79 to 1.28 for the frame-strut model and from 0.83 to 1.51 for the truss model. With masonry properties that are generally more variable, the variability in the prediction, especially for the yield strength can be assumed to be within acceptable range. However, the challenge in the model prediction lies with the deformation predictions. While the yield deformation over-prediction mean ratio is 1.10 for the first run (with Cov of 31%) the yield deformation over-prediction and its variability for the second run is indicative of how variable the experimental data is. Both the yield and ultimate deformation data obtained from the experiments vary across the infill RC frames of similar material properties, with variability observed even within different runs of the same frame. Nevertheless, the proposed model generates more consistent deformation values across infill frame made from similar material properties.

The truss-based models, based on the column and the parametric study fairly predicts the yield and ultimate strength. While both models give slightly higher strength values than the frame-strut models, the variability of their prediction is less than 30% and is acceptable for the infill frame behaviour. The column-based approach generates higher strength values. The predictions for both the yield deformation is fairly good for the first run experimental results (with mean ratio and Cov of 1.18 and 21.79% respectively for the parametric-based truss model, and 1.15 and 18.55% respectively for the column-based truss models respectively). Like the frame model, the ultimate deformation predictions are more variable, even within same sample across different runs for cyclic loaded infill frames.

CHAPTER 8

8.0 TOWARDS SUSTAINABILITY-BASED STRUCTURAL SYSTEM PERFORMANCE EVALUATION FOR RESIDENTIAL BUILDINGS

8.1 INTRODUCTION

A simplified approach for the determination of the structural performance of infill RC framed structures subjected to seismic loading is discussed in the preceding chapters. With the variability in structural performance prediction known, a simplified probabilistic approach is adopted in evaluating the overall structural performance under seismic loading. Overall structural performance that includes performance under both normal loading and seismic loading is performed using reliability based design. This allows capturing of the structural performance and the timeline within which it is assessed (through the structural reliability index and probability of failure). Sustainability performance of the structure is assessed using LCA methods. Probabilistic approaches are used to determine both the timeline and the impact of each activity within its timeline. An integration of the structural performance and sustainability performance of residential buildings is proposed, and its implementation illustrated in this Chapter. A case study based approach is used to illustrate the implementation of the integrated structural performance and sustainability evaluation. Due to the limitation of the available data, some parameters are assumed such as distribution functions and Cov.

8.2 INTEGRATION OF THE STRUCTURAL PERFORMANCE AND SUSTAINABILITY ASSESSMENT

In Section 2.3, structural repair strategy that integrates structural performance with sustainability is reviewed. The repair strategy, developed by Lepech et al. (2015), highlighted how sustainability and structural performance through service life design can be integrated. In order to consider the whole building life, pre-use phase is added to the framework proposed by Lepech et al. (2015) (see Figure 8.1). The objective of this framework is to develop sustainable structural systems, building envelopes and repair strategies for the building infrastructure. Iterative processes are involving in achieving each set goal.

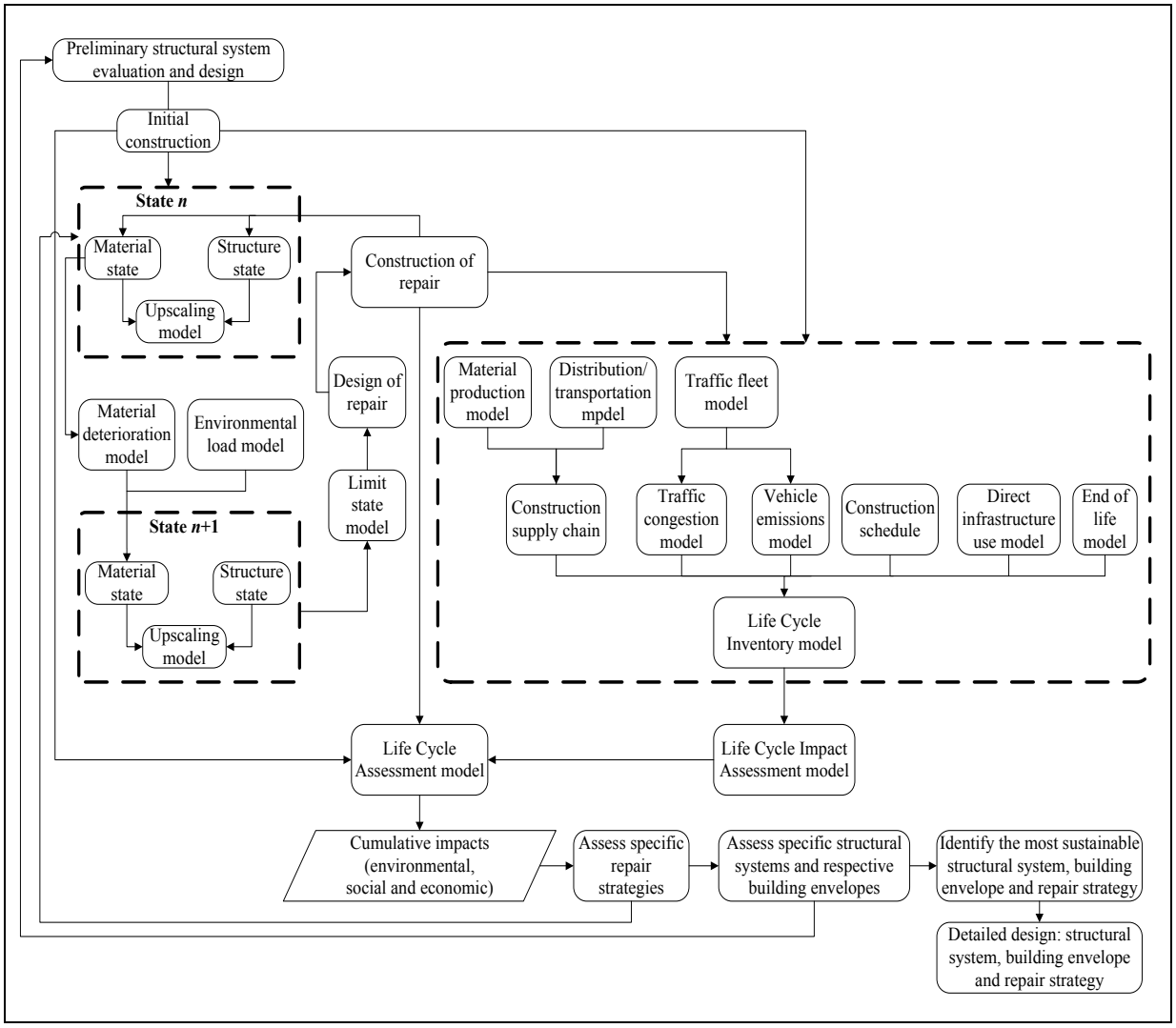

Figure 8.1: An integrated structural performance and sustainability of building infrastructure evaluation framework (modified from the Lepech et al. (2015) model)

8.3 CASE STUDY BUILDING STRUCTURE, INPUT PARAMETERS AND BOUNDARY CONDITIONS

Implementation of the proposed structural evaluation procedure together with the sustainability evaluation is illustrated through a case study. The description of the selected structure, inputs for both the seismic and sustainability assessment and the boundary conditions within which the sustainability assessment is conducted are provided in this section.

8.3.1 Case study structure and seismic performance assessment input parameters

A three-storey residential building, assumed to exist in the Western Cape, South Africa is selected (see Figure 8.2). Low rise residential buildings in the Western Cape are constructed using mostly reinforced and unreinforced load-bearing masonry and sometimes infill frames. For this case, an infill RC framed structure is adopted for evaluation of the proposed procedure. Masonry infills are constructed without openings in all the bays that are resisting the loading (as indicated in Figure 8.2a). Seismic assessment of the structure subjected to a PGA of 0.15g (typical for some parts of the Western Cape as shown in Figure 3.12). Probabilistic evaluation of the structure requires statistical data of all the input variables, some of which may not be available for this case. The variable data characteristics comprise a median

value, a coefficient of variation and a distribution function. Appropriate assumptions for the missing data are made and all the required input is summarised in Table 8.1. Infill properties, similar to that of sample G3 are assumed. A single strut derived from the frame properties and the infill properties is also provided in Table 8.1.

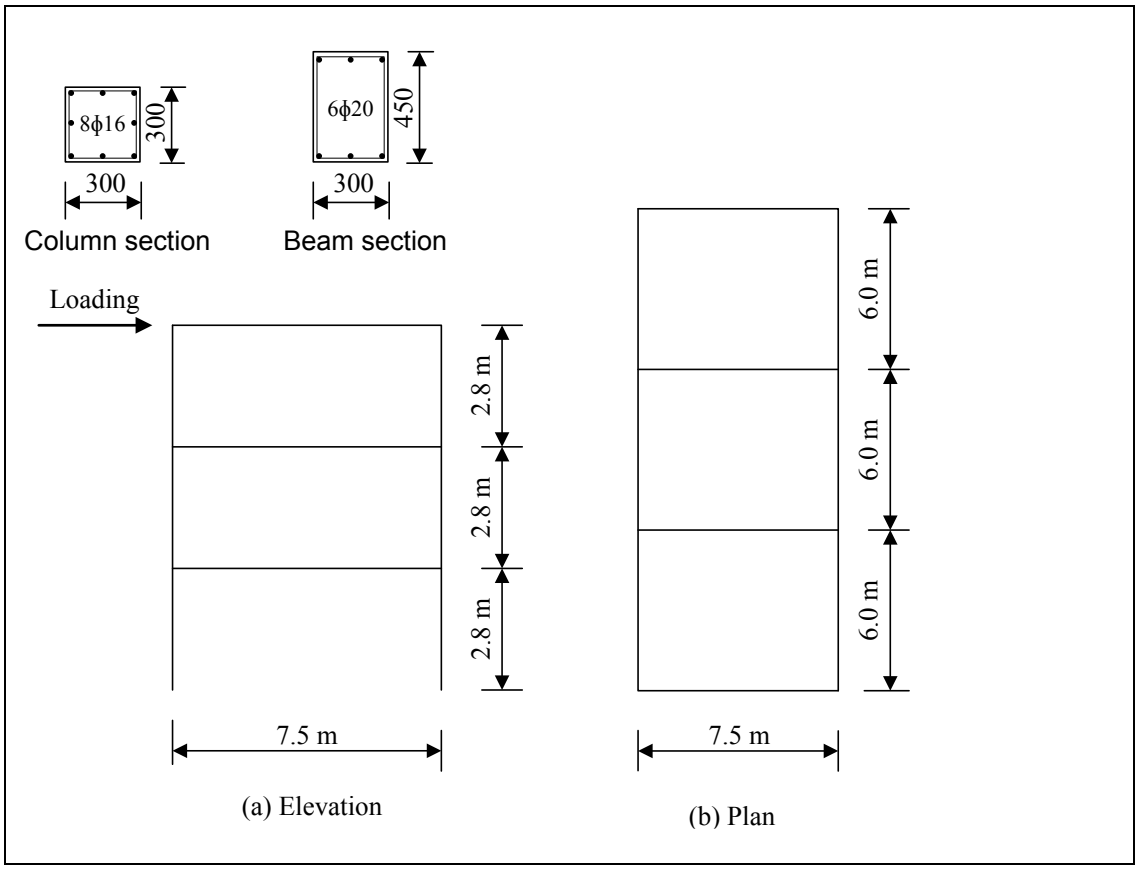

Figure 8.2: Layout for the case study structure (units in mm unless otherwise indicated)

Table 8.1: A summary of input variables for the seismic assessment

Variable	Median	Statistical characteristics	
		Cov	Assumed distribution
Concrete compressive strength	30.0 MPa	0.20	Normal
Concrete Young's modulus	33.0 GPa		Normal
Reinforcement yield strength	460.0 MPa	0.05	Lognormal
Reinforcement Young's modulus	200.0 GPa	0.05	Lognormal
Mass per storey floor per bay	39.0 tonnes	0.10	Normal
Mass for the roof slab per bay	20.0 tonnes	0.10	Normal
Yield strength of infill RC frame	169.1 kN	0.19	Lognormal
Ultimate strength of infill RC frame	171.8 kN	0.15	Lognormal
Post-peak residual of infill RC frame	131.4 kN	0.19	Lognormal
Yield deformation of infill RC frame	14.3	0.19	Lognormal
Ultimate deformation of infill RC frame	32.7	0.61	Lognormal
Post peak residual of infill RC frame	74.9	0.19	Lognormal
Compressive strength of masonry infill	18.3 MPa	0.30	Lognormal
Masonry infill Young's modulus, E_{90}	16.6 GPa	0.40	Lognormal
Masonry infill Poisson ratio	0.3		

8.3.2 Goal, scope and boundary conditions for the sustainability assessment

The objective of the LCA for the case study building is to assess the specific environmental impacts associated with the structural system of the building. The sustainability performance is not compared with the target or acceptable impact levels. The LCA is carried out for academic purposes (targeting academic researchers) and aims at illustrating the proposed integration of structural performance (seismic performance inclusive) with sustainability performance. The following are the boundary conditions within which the sustainability assessment is conducted:

(a) Environmental impacts associated with structural elements are assessed. Brewis (2011) identified three indicators as relevant for the built environment consideration in South Africa as emissions, waste generation and resource depletion. For this assessment, only emissions are considered. Carbon footprint (CF) and acidification potential (AP) are used to measure the impact of carbon dioxide, methane and Nitrogen oxide on global warming, and sulphur dioxide and oxides of nitrogen on acidification of water and soil.

(b) The environmental impact associated with structural repair is assessed on the following conditions:
   a. Appropriate structural repair is performed when the structure deteriorates to a specified performance;
   b. Structural deterioration associated with corrosion of reinforcement is considered as dominant since the building is within the coastal region;
   c. Crack filling and re-plastering are the repair methods for the building structure; and
   d. Other maintenance activities like painting for the internal walls and re-tiling the floors are not considered.

(c) The impact is calculated for the building shown in Figure 8.2 whose typical functional unit (residential flat) is shown in Figure A5.1 in Appendix A5.1. Some of the data for the building is adopted from a typical low-cost housing assessed for environmental performance by Brewis (2011). The area of the functional unit assessed by Brewis (2011) is 40 m^2. The calculated impacts and the timelines for each activity are assumed as the most probable and treated as mean or median while the Cov are assumed as provided in Table 8.1.

(d) The building structural system is designed for a 50-year period after which a major maintenance is expected. The assessment considers the regular maintenance works only.

(e) All the impacts associated with the usage of the building are not considered. Non-structural systems such as building services are ignored.

8.3.3 Input data for sustainability assessment

Each sustainability indicator, measured as life cycle assessment impact, i_{rk} is characterised in terms of its median value, coefficient of variation and distribution function. The timeline over which the impact is assessed, t_{rk}, is also described in terms of the median value, coefficient of variation and the distribution function. The structural performance of a new system or a repair event directly influences the timeline, t_{rk}. This section discusses the data required in characterising sustainability impacts and their respective timelines

(a) Environmental impacts for the structure at initial construction

As stated earlier, carbon footprint and the acidification potential are the environmental impact indicators selected for this assessment. Residential building structures are usually designed for a 50-year period (SANS 10160-1, 2011). This is assumed as the mean value for the service life. The building is divided into foundation, walling and roofing components. The calculated impacts are assumed to be lognormally distributed with a Cov of 20% (Lepech, et al., 2015). The building structure is an infill RC

framed. Cement and steel are the major constituents of the building materials used. The production of cement produces Nitrogen oxides (NO_x), sulphur dioxide (SO_2), carbon monoxide (CO) while steel production generates carbon dioxide (CO_2), and CO_2, CO, SO_x and NO_x respectively.

As noted from the calculations of the impacts as provided in Table 2.8 (Section 2.5.3), characterisation factors such as GWP_{100} and AP are required. These factors are regional-based and are calibrated based on several factors such as production processes used and incorporate the whole supply chain to produce the specific item. Ecoinvent database is used to obtain the characterisation factors in this study. Various methodologies such as EDIP-2003, CML-2001, IPCC-2013 and ReCipe Midpoint (H) are available in the Ecoinvent (2007). The characterisation factors vary based on regional input parameters and methodologies used to calibrate them. For example, GWP_{100} for ordinary cement production is 1.1724 $kgCO_{2e}$/kg, 1.1712 $kgCO_{2e}$/kg, 1.1708 $kgCO_{2e}$/kg, 1.1704 $kgCO_{2e}$/kg, 1.1724 $kgCO_{2e}$/kg or 1.112 $kgCO_{2e}$/kg using CML-2001, EDIP, EDIP-2003, IPCC-2001, IPCC-2007 or IPC-2013 respectively for the rest of the world (Ecoinvent, 2007).

(b) Environmental impact of structural repairs

Various structural repair strategies exist that depend on the nature of deterioration. Measuring the sustainability of each repair event from extraction of the raw materials to the end of life requires data that can quantify the impact and its respective timeline of all products involved. For building infrastructure, the impact can be established from data provided in the bills of quantities (BoQs). Table 8.2 summarises the general description of the required data. Where data is not readily available in the BoQs, appropriate estimates and assumptions can be made. Each presented quantity should consist of mean, standard deviation and the distribution function. In this study, quantities of the construction works, incorporating most of the materials used for selected structural repair are calculated and treated as mean values while standard deviation and the distribution function are assumed.

Table 8.2: Data requirements for the impact assessment

Item name	Quantity		Location of source	Mode of transport	Cost	Product information	Material safety data
	Amount	Other					
All construction works	Volume/ mass	Dim[1]	×	×	✓	×	×
All installed products	✓	×	✓	✓	✓	✓	✓
All materials used	✓	×	✓	✓	✓	✓	✓
Construction crew	✓	Prod[2]	×	×	✓	×	×
Construction equipment used	✓[3]	×	×	×	✓	✓	×

✓ Information is required; × Information not required; [1]Dimensions; [2] Productivity; [3]Rating of equipment

(c) Timelines for structural repair events

Structural deterioration through corrosion of reinforcement is assumed as the dominating deteriorating action. The *fib* model (2006) is used to establish the initiation of corrosion, a period that is assumed as the time at which repairs are to be conducted. The model requires the following data:

(a) Critical chloride content
(b) Initial chloride content
(c) Chloride content at depth, Δx, time t, $C_{\Delta x}$
(d) Depth of convection zones, Δx
(e) Apparent coefficient of chloride diffusion of all repair layers, Dapp.C

8.4 SEISMIC PERFORMANCE ASSESSMENT

Design of structures subjected to seismic loading involves initial consideration of the performance of the structure under normal loading and then assessing and design for seismic resistance. Only the seismic performance is reported. A nonlinear static procedure utilises less data and involves less effort than the dynamic methods hence it is adopted. This section illustrates the use of the proposed nonlinear structural evaluation procedure for seismic performance evaluation of the structure discussed in the case study. The simplified probabilistic approach using the IN2 method discussed in Section 2.4 is adopted. The F-δ curve is generated from the proposed structural evaluation procedure. As noted in Sections 6.5 and 7.6, the proposed procedure is developed from minimal amount of data and has some variability due to both model and material data uncertainty. Thus, the use of probabilistic method is essential as it incorporates the model and material uncertainty using standard deviations. Furthermore, any future improvements in both the data and analytical models can be captured through corresponding improvements in the material and model uncertainties. Evaluation of the structural performance to a target level of reliability is possible.

For this assessment a target displacement of the first-floor is considered while an F-δ curve for a single internal bay is used for the capacity curve for illustration of the procedure. While the region under consideration has a peak ground acceleration (PGA) of 0.15g, PGA of 0.10g, 0.15g, 0.20g and 0.25g are considered for an IN2 method. Ground type 2 (SANS 10160-4, 2011) (equivalent to ground type B for the Eurocode 8 (2004) is selected. The importance class II is considered for the building. Elastic spectral response in the format of A-D is established for each PGA as shown in Figure 8.3. The capacity curve is determined for both the mean values and the characteristic values, calculated at 5% fractile (95% fractile for the floor mass). The calculated period for the structure is 0.06 second and 0.05 second when mean and characteristic values are used respectively.

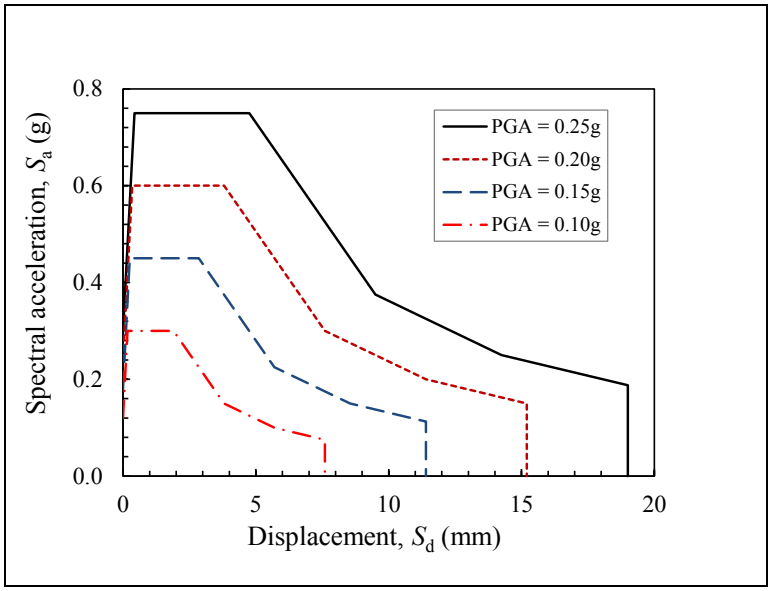

Figure 8.3: A-D response spectra for the selected PGA

Steps provided in Section 2.4.1 are followed to illustrate the whole procedure. For each of the A-D curves, a radial line of the period, T, is drawn and its intersection with the A-D curve provides an elastic spectral seismic demand in terms of elastic spectral acceleration, S_{ae} and elastic spectral displacement, S_{de}. The capacity curve (F-δ curve) is drawn in the A-D format (see Figure 8.4). From the capacity curve, the yield acceleration, S_{ay} and yield displacement, S_{dy} are identified.

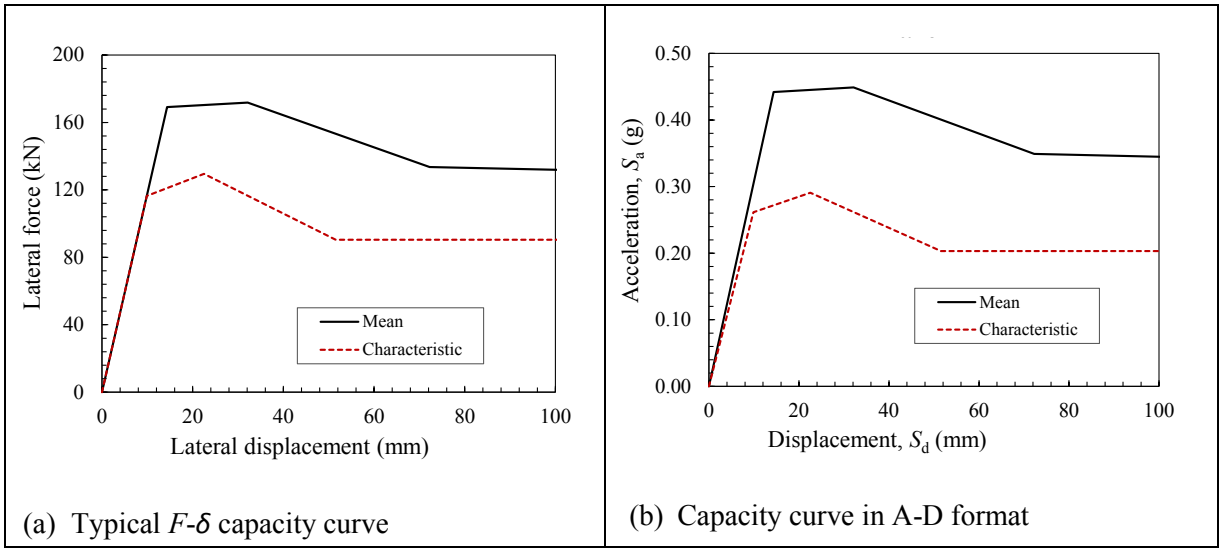

(a) Typical F-δ capacity curve

(b) Capacity curve in A-D format

Figure 8.4: Capacity curve for the single storey single bay

Strength reduction factor is determined using equation 2.25. For all the PGAs considered, the R values are less than 1.0. Furthermore, the yield strength-to-mass ratio of the structure is less than the elastic spectral acceleration, S_{ae}. The structure is within the short period range and its response is within elastic regime according to the conditions set in the Eurocode 8 (2004). The displacement values are not modified, and the inelastic spectral curve is not required. Figure 8.5 illustrates the IN2 curve (linear) for the mean and characteristic cases.

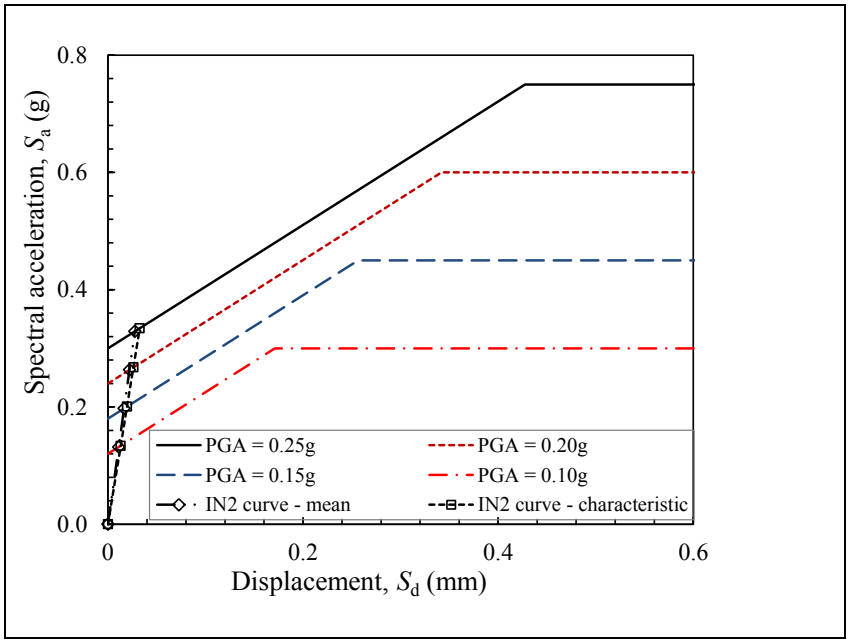

Figure 8.5: IN2 curve for the case study structure

8.5 STRUCTURAL PERFORMANCE AND SUSTAINABILITY ASSESSMENT

The role of structural performance in the integrated structural performance and sustainability assessment procedure is the establishment of the timelines for the structural system. Using appropriate models, a building service life is established together with the timelines of repair activities for the selected repair strategy. The following parameters and assumption are used for this study:

(a) The service life for the building is assumed to be 50 years and is deterministic
(b) A single repair of crack filling and re-plastering is adopted, with the durability of each repair assumed as 15 years (time when corrosion initiates), with a Cov of 0.2 and distribution assumed as lognormal.

A summary of the life cycle inventory is provided in Table 8.3. The structure is divided in parts, namely foundation, external walls, internal walls, ground and upper floor slabs, and roof. Carbon footprint (CF) and acidification potential (AP) are calculated. CF of 79339 CO_{2e}kg and AP of 235 SO_{2e}kg for initial construction are generated while each repair generates CF of 3534 CO_{2e} kg and AP of 6.6 SO_{2e}kg. These values are assumed as mean and using appropriate Cov and distribution, a cumulative impact curve for each impact is established. Figure 8.6 shows the structural repair impacts over the entire life of the building. An envelope of the cumulative impacts for the structural repairs is generated for a 5% fractile and a 95% fractile. A cumulative impact envelope for the whole building comprising of initial construction and structural repairs is shown in Figure 8.7.

Table 8.3: A summary of impact for each activity

Building part	Carbon footprint (CO_{2e} kg)		Acidification potential (SO_{2e} kg)	
	Initial construction	Single repair	Initial construction	Single repair
Foundation	17122.4	-	38.60	-
Ground floor slab	5003.9	-	10.4	-
External wall-ground floor	12136.6	1174.5	29.4	2.2
Internal walls-ground floor	129.2	3.3	0.3	0.0
Upper floors slab	18409.5	-	40.5	-
External wall-upper floors	24149.2	2349.0	57.3	4.4
Internal walls-upper floors	258.3	6.6	0.6	0.0
Roofing	2130.0	-	57.7	-

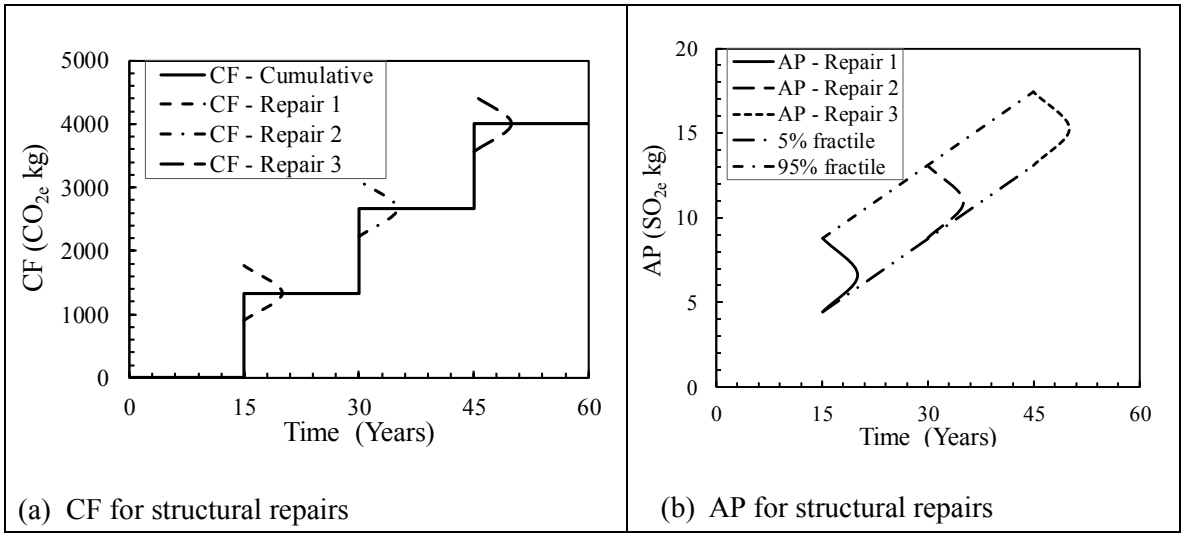

(a) CF for structural repairs (b) AP for structural repairs

Figure 8.6: Environmental impacts for the structural repairs over time

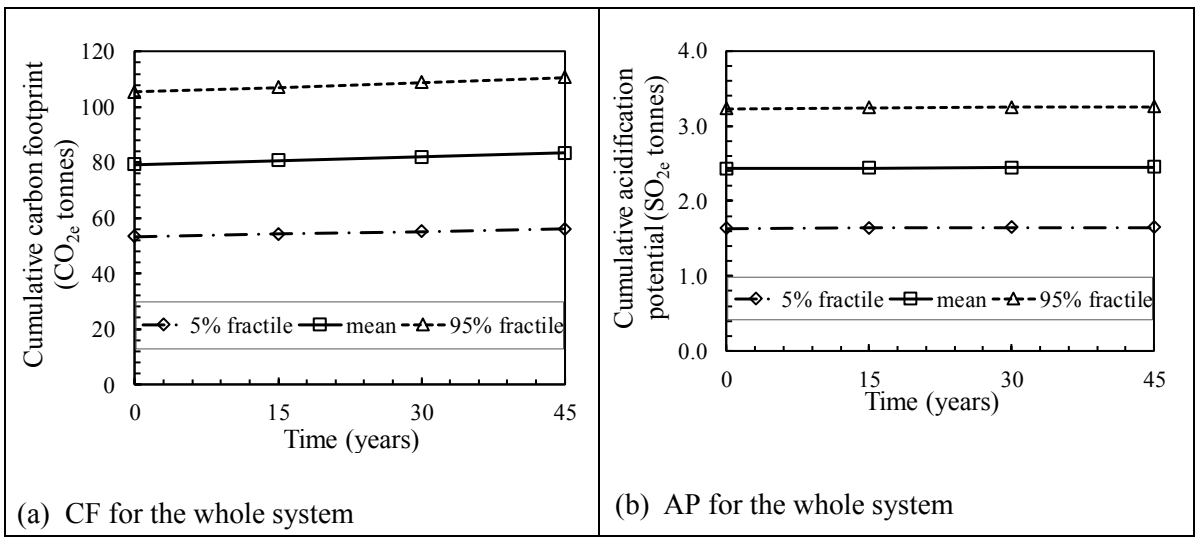

(a) CF for the whole system (b) AP for the whole system

Figure 8.7: Cumulative environmental impact for the whole structural system over time

8.6 DISCUSSIONS AND CONCLUSIONS

Seismic assessment of infill RC frames using the proposed procedure is performed. Although the data used is not taken from experiment, the typical values used provided adequate information to conduct the assessment. The structure has a short period of dynamic movement and is in the elastic regime. The chapter also provides a general framework of integrating structural performance with sustainability performance. Using the sustainability framework developed by Lepech et al. (2015) and incorporating the proposed structural performance models, a case study based sustainability evaluation is implemented for a typical RC infill framed residential buildings in the Western Cape. Cumulative environmental impacts of implementing typical repair strategies, considering the nature of the buildings under study are established. A case study-based evaluation allows definition of the boundary conditions for the specified case regarding a specific number of repair events, repair strategy, nature of the structure, environment within which it exists and the loading it is subjected to through it life span. While the framework allows for comparison of the impact of various repair strategies, in this research the impact of a single structural system, without optimisation of the system is considered for illustration purposes only. Nonetheless, the integrated approach affords selection of better structural systems and repair strategies through optimisation as noted with the following:

(a) Any change in repair strategy can change the repair timeline and or impact of the repair event and hence affect overall sustainability
(b) If the structural systems are constructed for a specified service life and performance level, any change in the choice of the structural system may have influence on the impact from initial construction. Furthermore, the change can affect the appropriate repair strategies which also influence the sustainability as noted in (a).

CHAPTER 9

9.0 CONCLUSIONS, RECOMMENDATION AND RESEARCH CONTRIBUTION

Provision of sustainable building infrastructure requires integration of the structural performance with the sustainability performance. This includes both the structural systems and the structural repair strategies. The proposed integration of structural performance with sustainability performance requires interactive evaluation of various structural systems and repair strategies as illustrated in Section 8.2. Such an iterative process may require simple but robust structural performance evaluation processes. Infill RC framed structures can promote material resource efficiency when the contribution of the infill is considered in the design. Use of macro-modelling provides a possible means of simplified structural performance evaluation process for the infill RC framed structures subjected to seismic loading. From the evaluation of the infill capacity, the bare frame behaviour, the infill RC frame behaviour to the integration of structural performance with building sustainability assessment, various analytical models are developed and validated. Main conclusions and recommendations for each of the specific objectives are provided in this chapter.

9.1 CONCLUSIONS

A simplified structural evaluation macro-modelling procedure is used for the infill RC framed structures subjected to seismic loading. Various analytical models are developed for the evaluation of the infill behaviour, the bare frame behaviour and the infill RC frame behaviour. In understanding the validity and applicability of any of these models, it is worthwhile noting that analytical models can be categorised into three groups based on the formulation process, namely:

(a) Expressions that are derived based on general experimental observations and are purely empirical approximations without any scientific relationship;
(b) Expressions that link some physical phenomena but uses generalised calibrated parameters to match the experimental results with analytical results; and
(c) Expressions that are derived based on scientific relationship and provides comprehensive detail of the physical phenomena involved.

The ability of the analytical model to reliably and accurately predict the outcome usually depends on the best way the analytical models are developed and are modelled on the actual behaviour and scientific relationships. Category (a) is usually easier to use and requires fewer input but due to its generality, it is difficult to calibrate reliably the output of the model while the level of accuracy and ability to reliably calibrate improves through (b) to (c) with (c) providing the best outcome. However, category (c) involves complex physical relationships and may require significant input parameters

9.1.1 Infill behaviour evaluation

The infill behaviour is modelled using an equivalent infill strut whose properties are derived based on both the infill properties and the frame properties. The infill is divided into stress zones depicting some of the main infill failure mechanism, namely corner crushing, diagonal cracking/compression and sliding shear failures. A parametric evaluation of the infill behaviour is conducted, through which infill strut behaviour is characterised using the target strut resistance, F_{sa}, the compression zone strength factor, γ_{cc}, and the shear sliding strength factor, γ_{ss}. These values are established from the transformed diagonal strut infill strength and the transformed diagonal strut Young's modulus (see equations 2.18 and 2.19). The transformed diagonal strut infill strength and the transformed diagonal strut Young's modulus are determined from the following data:

(a) Infill Young's modulus parallel to the bed;
(b) Infill Young's modulus perpendicular to the bed;

(c) Poisson ratio;
(d) Infill shear modulus; and
(e) Infill compressive strength
(f) Infill compressive strain at peak stress

With the above information available, infill strut stress-strain behaviour is established considering the stress zoning, where each stress zone element is represented by a nonlinear spring. The generated stress-strain behaviour obtained from the evaluation of the infill subsystem indicates infill degradation with possible modes of failure. Where shear sliding is experienced very early in the analysis, there is a possibility for frame failure as shear sliding generates stress concentration where there is contact with the frame.

9.1.2 Bare frame behaviour evaluation

A parametric study conducted to evaluate the structural behaviour of the RC bare frames generated notable trends in the yield and ultimate strength and their deformations across the aspect ratios and the second moment of area ratios of the beam and columns. These trends are used to develop analytical relationships for both the bare frames and the diagonal struts used to convert the frame into a truss. These analytical models are calibrated and validated using both the numerical and experimental data available in literature. Apart from the use of parametric study for the bare frame to generate diagonal strut properties, column-based material calibration for the diagonal is used. With the column-based diagonal strut behaviour evaluation, an important factor comprising of the product of the Young's modulus for the column E_{ce} and the stiffness factor k_{TM} is used to establish the yield strength and deformation ratios. These ratios are used to generate the diagonal strut yield stress and strain.

Evaluation of the bare frames using the proposed analytical models shows good correlation. For the column-based formulation, elastic stiffness transformation utilises the stiffness method formulation while elastic strength and deformation is calibrated for the diagonal strut. Both the fixed and pinned frames are used to validate the model column-based truss models. The mean predicted strength-to-experimental strength ratios of 1.13 (with Cov of 9.58%) and 0.81 (with Cov of 8.87%) for the parametric-based and the column-based truss models respectively are acceptable. Likewise, the mean predicted deformation-to-experimental deformation ratios of 1.32 (Cov of 11.53%) and 0.78 (with Cov of 13.66%) for the parametric based model and the column-based truss model respectively may be considered acceptable

It is worth noting that the analytical models developed from the parametric studies are applicable with the boundary definition of the parametric study. The limitation comprises range of second moment of area ratios, the range of the aspect ratio of the frame and the range of the amount of reinforcement in the RC frame elements. Furthermore, these analytical relationships are developed from the F-δ curve involving linearised data points, which are always higher than the actual data points. This is one of the reasons the predictions from these models are then calibrated.

9.1.3 Infill RC frame behaviour evaluation

A truss-based structural evaluation of the nonlinear behaviour of the infill RC frames subjected to seismic loading is presented. Using the simplified analytical relations, an infill RC frame is converted to a truss. The simplification of both the frame and the infill brings uncertainties arising from ignoring contribution of shear and self-weight, and the linearization of the stress-strain behaviour for the truss elements. Notwithstanding the uncertainties that come with the simplification, the simplified evaluation process generates reasonable predictions for the yield and ultimate strengths. Apart from the truss-based

modelling, a frame-strut macro-model is also used to evaluate the infill RC frame behaviour. In this model, the infill frame behaviour is represented by the diagonal strut characterised using the procedure provided in Section 4.5. The frame-strut model provides better predictions than the truss model, with better results observed for the yield strength as compared to the ultimate strength. It should be noted that the variability in prediction may arise from both the model and the experimental data. With masonry properties that are generally more variable, the variability in the prediction for the yield and ultimate strength can be assumed to be within acceptable range (with the predicted-to-experimental strength ratios ranging from 1.05 for Cov of 16.75% to 1.2 for Cov of 15.67%). However, the challenge in the model prediction lies with the deformation predictions as the experimental data is very variable across frames with statistically similar properties. The yield and ultimate deformation variability of the experimental data is notable even within the same frame across different runs (for the experiments conducted under cyclic loading). The proposed model generates more consistent deformation values across infill frame made from similar material properties.

The truss-based model provides less conservative predictions as compared to the frame-truss model. This variation may be a result of uncertainties in the conversion parameters for the truss while experimental data variability also contributes to model predictions. Both column-based and parametric based diagonal strut material calibrations are used. The column-based models generate higher values for the strength and similar values for the yield deformation with the parametric-based material models. The variation of both the yield and ultimate strength over-prediction ratios is less than 30% for both models. However, there is greater variability in the deformations with the yield deformation having lower variability over-prediction ratios and lower variability while the ultimate deformation having higher over-prediction ratios and the higher Cov. For example, the yield deformation over-prediction ratio for the column-based model is 1.15 (with Cov of 18.53%) for the first run and 1.68 (with Cov of 36.6%) for the second run. The ultimate deformation predictions are more variable, even within same sample across different runs for cyclic loaded infill frames. The variability in the experimental data across different runs is expected for highly nonlinear materials that degrade with each run such as masonry. Though the column-based models require the least effort amongst the models evaluated, they can fairly predict both the yield and ultimate strength and the corresponding deformations.

9.1.4 Sustainability assessment and structural performance integration

Integration of structural performance and sustainability performance is based on the establishment of activity timelines from structural performance methods and using the timelines for establishing the impacts of each activity. A probabilistic approach for the evaluation of the sustainability impact enables proper capturing of the variability of the data used. Furthermore, it enables interpretation of the sustainability indicator impacts based on selected confidence levels and target reliability. A case study involving an infill RC framed residential building from Western Cape is used to illustrate the implementation of the evaluation process for seismic performance and sustainability performance. While significant amount of data is assumed, the process offers opportunities for integration of sustainability and structural performance for sustainable infrastructure development.

9.2 RECOMMENDATIONS

An extensive study of the infill frame behaviour while providing some knowledge for use and evaluation of the infill RC framed structures has also generated opportunities for further studies. There is variability in the model predictions from strut characterisation, frame-to-truss elements transformation and infill RC frame modelling using both the frame-strut and truss systems. The variations in predictions may be as results of uncertainties arising from the analytical model uncertainty, material properties uncertainty,

the uncertainty in both the numerical and experimental data for model calibration and validation. The following recommendations are made:

9.2.1 Structural performance evaluation

(a) Infill frame characterisation

More relevant data for calibration of the analytical models is required. With different construction methodologies adopted to strengthen infill RC frames, evaluation of the proposed procedure considering various construction methodologies is required. Furthermore, the amount of uncertainty in the model prediction and the input characterisation material data can be improved by using improved material characterisation data and model calibration data. A full reliability calibration exercise is needed to establish appropriate structural resistance factors and capture statistical variability of the model.

(b) Evaluation of multi-bay and multi-storey infill frames

The structural evaluation models are developed based on single bay single storey infill and their application to a multi-storey structural system is illustrated by using a single frame mimicking a SDOF system. There is need for a comprehensive study on the applicability of the proposed model with various structural topologies. Data of the behaviour of various structural topologies of the infill RC framed structures from both experimental and refined FE models can be used to refine the proposed analytical models.

(c) Evaluation of the infill frames with openings

The models developed in this study only consider a fully infilled RC frame. However, in practice framed structures can be either fully or partially infilled with masonry. A study on the effects of the opening on the behaviour of the infill frames conducted by Dawe and Seah (1989) indicated that openings affect both the strength and stiffness of the infill frames. Further work is required to incorporate the effects of openings (size and location) on the strength, stiffness and general deformation characteristics of the infill frame. Thus, a parametric study should be conducted with the target of identifying parameters that can be used to modify the behaviour of the infill and frame as a result of openings in the infill. Possible change in failure patterns of the infill frame should also be examined as there is a possibility of experiencing short column effects when partially filled frames are used.

9.2.2 Sustainability evaluation and structural performance integration

Some of data used for sustainability performance in this research is assumed. More work is required to establish both the impact characterisation data and the structural performance characterisation data, comprising mean value, standard deviation and the distribution function for the infill RC framed buildings. Furthermore, incorporation of most of the sustainability and structural performance indicators for the infill RC framed buildings is required.

9.3 RESEARCH CONTRIBUTION

The overall goal of the research work is to promote building sustainability through integration of the structural performance with sustainability indicators evaluation. Key to the achievement of this goal is the optimum use of structural materials through design and execution of appropriate structural systems and repair strategies. A simplified structural performance evaluation procedure for seismic assessment of infill RC framed structures is developed and can be used at conceptual stage as various material and structural system options are considered. From the evaluation of the infill capacity, the bare frame

behaviour, the infill RC frame behaviour to the integration of structural performance with building sustainability assessment, key research contributions are developed and summarised as follows:

(a) Equivalent strut characterisation for the masonry infilled in the RC frames. A simplified code for equivalent strut evaluation is developed in Matlab;
(b) Simplified analytical relationships for the bare frame that can be used for framed structures subjected to seismic loading;
(c) A simplified nonlinear structural performance evaluation for infill RC frames subjected to seismic loading. A simplified programme for the structural performance evaluation that generates the F-δ curve is developed in Matlab; and
(d) Integrated structural performance and sustainability performance evaluation is proposed.

REFERENCES

ABAQUS, 2011. *Abaqus documentation,* Providence, RI, USA: Dassault Systèmes.

Abdel-Hafez, L., Abouelezz, A. & Elzefeary, F., 2015. Behaviour of masonry strengthened infilled reinforced concrete frames under in-plane load. *HBRC Journal,* Volume 11, pp. 213-223.

ACI 318, 1999. *Building code requirements for structural concrete.* Michigan: American Concrete Institute.

ACI, 1992. *Specifications for masonry structures-ACI 530.1-92/ASCE 6-92.* Michigan: ACI/ASCE.

Adukadukam, A. & Sengupta, A., 2013. Equivalent strut method for modelling of masonry infill walls in the nonlinear static analysis. *Journal of Institution of Engineers (India) series A,* 94(2), pp. 99-108.

Ameny, P., Loov, R. & Shrive, N., 1983. Prediction of elastic behaviour of masonry. *International journal of masonry construction,* 3(1), pp. 1-9.

Amrhein, J., 1992. *Reinforced masonry engineering handbook.* 5th ed. Los Angels: Masonry Institute of America.

Asteris, P., Kakaletsis, D., Chrysostomou, C. & Smyrou, E., 2011. Failure Modes of In-filled Frames. *Electronic Journal of Structural Engineering ,* 11(1), pp. 11-20.

ASTM C1006, 2013. *Standard test method for splitting tensile strength of masonry units.* Philadelphia: ASTM International.

ASTM C140/C140-17a, 2017. *Standard test methods for sampling and testing concrete masonry units and related units.* Philadelphia: ASTM International.

Atkinson, R., Amadei, B., Saeb, S. & Sture, S., 1989. Response of masonry bed joints in direct shear. *Journal of Structural Engineering,* 115(9), pp. 2276-2296.

Atkinson, R., Amadei, B., Saeb, S. & Stute, S., 1989. Response of masonry bed joints in direct shear. *Journal of Structural Engineering, ASCE,* 115(9), pp. 2276-2296.

Azapagic, A., Perdan, S. & Clift, R., 2004. *AZAPAGIC, A. Sustainable Development in Practice: Case Studies for Engineers and Scientists.* Chichester: John Wiley & Sons.

Bayer, C., Gamble, N., Gentry, R. & Joshi, S., 2010. *AIA Guide to Building Life Cycle Assessment in Practice.* New York: The American Institute of Architects.

Bazant, Z., 1976. Instability, ductility and sizew effect in strain-softening concrete. *Journal of Engineering Mechanbics division, ASCE,* 102(EM2), pp. 331-344.

Bazant, Z., 1985. Fracture in Concrete and Reinforced concrete. In: Bazant, ed. *Mechanics of Geomaterials.* New Jersey: John Wiley & Sons, pp. 259-303.

Bazant, Z. & Oh, B., 1983. Crcak band thery for fracture of concrete. *Materials and structures,* 16(93), pp. 155-177.

Beebay, A., Scott, R. & Jones, A., 2005. Revised code provisions for long-term deflection calculations. *Proceedings of the Institute of Civil Engineers, Structures and Buildings,* 158(1), pp. 71-75.

Binda, L., Fontana, A. & Frigerio, G., 1988. Mechanical behaviour of brick masonries derived from unit and mortar characteristics. *Proceedings of the eighth international brick and block masonry conference,* September, Volume 1, pp. 205-216.

Branson, D., 1968. Design procedures for computing deflection. *ACI Journal,* 65(9), pp. 730-742.

BRE Global, 2008. *BREEAM Offices 2008 Assessors Manual.* London: BRE Global.

Brewis, C., 2011. *Quantifying the environmental dimension of sustainability for the built environment: with a focus on low-cost housing in South Africa,* Stellenbosch: Stellenbosch University.

Brewis, C. & Boshoff, W., 2010. *A Holistic Approach for Measuring the Environmental Impact of the Built Environment.* Pretoria, Concrete Society of Southern Africa.

Brits, J., 2012. *Quantifying the sustainability of the built environment: Model for the determination of the environmental impact of the end-of-life phase,* Stellenbosch: Stellenbosch University.

BS EN 1504-9, 2008. *Products and systems for the protection and repair of concrete structures. Definitions, requirements, quality control and evaluation of conformity. General principles for use of products and systems.* London: British Standards Institution.

Catherin, J., Jayalekshmi, B. & Katta, V., 2013. Modelling of masonry infills-A review. *American Journal of Engineering Research,* Volume 2, pp. 59-63.

CEB-FIP, 1993. *Model Code 1990, Bulletin D'Information 213/214.* London: Thomas Telford.

Cervenka, V. & Gerstle, K., 1972. Inelastic analysis of reinforced concrete panels: experimental verification and application. *International Association of bridge and structural engineering publications,* Volume 32, pp. 25-39.

Chaudhary, M. & Piracha, A., 2013. Examining the role of structural engineers in green building ratings and sustainable development. *Australian Journal of Structural Engineering,* 14(3), pp. 217-228.

Chopra, A. K., 2007. *Dynamics of Structures: Theory and applications to earthquake engineering.* 3rd ed. New Jersey: Pearson Prentice Hall.

Cornell, C., Jalayar, F., Hamburger, R. & Foutch, D., 2002. Probabilistic basis for 2000 SAC Federal Emergency Management Agency steel moment frame guidelines. *Journal of Structural Engeering ASCE,* 128(4), pp. 526-533.

Crisafulli, F. J., 1997. *Seismic behaviour of reinforced concrete structures with masonry infills,* Christchurch: University of Canterbury.

Dawe, J. & Seah, C., 1989. Behaviour of masonry infilled steel frames. *Canadian Journal of Civil Engineering,* Volume 16, pp. 865-876.

De Beer, L., 2016. *Developing and testing a sprayable overlay of strain hardening cement-based composite for retrofitting of unreinforced load bearing masonry walls,* Stellenbosch: Stellenbosch University (M-thesis).

De Meester, B. et al., 2009. Exegetic life cycle assessment (ELCA) for resource consumption evaluation in the built environment. *Building and Environment,* Volume 44, pp. 11-17.

De Villiers J, P., 2015. *Bond Behaviour of Deformed Steel Reinforcement in Lightweight Foamed Concrete,* Stellenbosch: Stellenbosch University (M-thesis).

De Villiers, W. I., 2012. *Regulation of Alternative Building Materials and Systems in South Africa.* Cape Town, The Southern African Housing Foundation international.

Dewulf, J. et al., 2009. Quantification of the impact of the end-of-life scenario on the overall resource consumption for a dwelling house. *Resources, Conservation and Recycling,* Volume 53, p. 231–236.

Dolšek, M. & Fajfar, P., 2004. *IN2-A simple alternative for the IDA.* Vancouver, Canada, World Conference on Earthquake Engineering, p. 3353.

Dolšek, M. & Fajfar, P., 2005. Simplified nonlinear seismic analysis of infilled reinforced concrete frames. *Earthquake Engineering and Structural Dynamics,* 34(1), pp. 49-66.

Dolšek, M. & Fajfar, P., 2007. Simplified probabilistic seismic performance assessment of plan-asymmetric buildings. *Earthquake Engineering and Structural Dynamics,* Volume 36, pp. 2021-2041.

Dolšek, M. & Fajfar, P., 2008. The effect of masonry infills on the seismic response of a four storey reinforced concrete frame-a probabilistic assessment. *Engineering Structures,* Volume 30, pp. 3186-3192.

Drysdale, R., Hamid, A. A. & Baker, L. R., 1994. *Masonry structures: Behaviour and design.* Englewood Cliffs, N.J: Prentice-Hall.

Ecoinvent, 2007. *Life Cycle Inventories of Production Systems. Ecoinvent data v2.0.* [Online] Available at: http://www.ecoinvent.ch
[Accessed 16 February 2016].

El-Dakhakhni, W., Elgaaly, M. & A, H., 2003. Three-Strut model for concrete masonry-infilled steel frames. *Journal of structural Engineering,* 129(2), pp. 177-185.

Elkington, J., 1994. Towards the sustainable corporation: Win-win-win business strategies for sustainable development. *California Management Review,* 36(2), pp. 90-100.

EN 1052-1, 1998. *Methods of test for masonry - Part 1: Determination of compressive strength.* Brussels: European Committee for Standardization.

EN 1052-2, 2016. *Methods of test for masonry- Part 2: Determination of flexural strength.* Brussels: European committee for Standardization.

EN 1052-3, 2007. *Methods of test for masonry- Part 3: Determination of initial shear strength.* Brussels: European Committee for Standardization.

EN 1052-5, 2005. *Methods of test for masonry- Part 5: Determination of bond strength by bond wrench method.* Brussels: European committee for Standardization.

EN 1992-1-1, 2004. *Eurocode 2: Design of concrete structures - Part 1-1: General rules and rules for buildings.* Brussels: European Committee for Standardization.

EN 772-1, 2011. *Methods of test for masonry units-Part 1: Determination of compressive strength.* Brussels: European Committee for Standardization.

Eurocode 2, 2004. *BS EN 1992-1-1:2004 Design of concrete structures. General rules and rules for buildings.* Brussels: CEN.

Eurocode 8, 2004. *Design of structures for earthquake resistance. Part 1:General rules, seismic action and rules for buildings.* Brussels: CEN.

Ewing, B. & Kowalsky, M. J., 2004. Compressive behaviour of unconfined and confined clay brick masonry. *Journal for Structural Engineering,* 130(4), p. 650–661.

Fajfar, P., 2000. A nonlinear analysis method for performance-based seismic design. *Earthquake spectra,* 16(3), pp. 573-592.

FEMA 350, 2000. *Recommended Seismic Design Criteria for New Steel Moment Frame Buildings.* Washington DC: SAC Joint Venture, Federal Emergency Management Agency.

FEMA 356, 2000. *Prestandard and commentary for the seismic rehabilitation of buildings.* Washington : Federal Emergency Management Agency.

fib, 2006. *Model Code for Service Life Design – Bulletin 34.* Lausanne, Switzerland: *fib*.

fib, 2012. *2010 Model Code - Bulletin 65,66.* Lausanne, Switzerland: *fib*.

Flamant, A., 1892. Sur la répartition des pressions dans un solide rectangulaire chargé transversalement. *CR Acad. Sci.,* Volume 114, pp. 1465-1468.

Flint, M., Michel, A., Billington, S. & Geiker, M., 2013. Influence of temporal resolution and processing of exposure data on modeling of chloride ingress and reinforcement corrosion in concrete. *Materials and Structures,* Volume 47, pp. 729-748.

GBCA, 2008. *Technical Manual Green Star Office Design & Office As Built, Version 3.* Sydney, Australia: Green Building Council of Australia .

GBCSA, 2009. *Green Building Council of South Africa.* [Online]
Available at: https://www.gbcsa.org.za/rating-tools/green-star-sa-rating-system/
[Accessed 10 October 2014].

Gilbert, R. & Warner, R., 1978. Tension stiffening in reinforced concrete slabs. *Journal of Structural Division,* 104(12), pp. 1885-1900.

Gopalaratnam, V. & Shah, S., 1985. Sofetning response of plain concrete in direct tension. *ACI Journal,* 82(3), pp. 310-323.

Grimm, C., 1984. *Elastic modulus of clay brick masonry.* Edinburg, University of Edinburgh, Department of Civil Engineering.

Hamid, A., Ziab, G. & El Naway, O., 1987. *Modulus of elasticity of concrete block masonry.* Los Angels, Masonry Society, pp. 7/1-7/13.

Han, S. & Chopra, A., 2006. Approximate incremental dynamic analysis using the modal pushover analysis procedure. *Earthquake Engineering and Structural Dynamics ,* Volume 35, p. 1853–1873.

Hendry, A., 1990. *Structural masonry.* London: MacMillan Education Ltd.

Hischier, R. & Weidema, B., 2010. *Implementation of Life Cycle Impact Assessment Methods,* Switzerland: Swiss Centre for Life Cycle Inventories.

Hischier, R. et al., 2010. *Implementation of Life Cycle Impact Assessment Methods,* Dübendorf: Swiss Centre for Life Cycle Inventories.

Holmes, M., 1961. Steel frames with brick and concrete filling. *Proceedings of Institute of Civil Engineers,* 19(4), pp. 473-478.

Ibrahim, K. & Suter, G., 1994. *Smeared crack model for reinforced concrete masonry shear wall analysis.* Calgary, Canada, s.n.

ISO 14040, 2006. *Environmental management- Life cycle assessment – Principles and framework.* Geneva, Switzerland: International Organization for Standards.

ISO 14044, 2006. *Environmental management - Life cycle assessment - Requirements and guidelines.* Geneva, Switzerland: International Organization for Standards.

Kaushik, H., Rai, D. & Jain, S., 2007. Stress-strain characteristics of clay brick masonry under axial compression. *Journal of materials in civil engineering,* 19(9), pp. 728-737.

Kent, D. & Park, R., 1971. Flexural members with confined concrete. *Journal of Structural Division,* 97(7), pp. 1969-1990.

Khalaf, F., Hendry, A. & Fairbairn, D., 1992. The strength of blockwork prisms tested parallel to the bed face. *Masonry Internaltional journal,* 6(1), pp. 29-35.

Lam, J., Ng, P. & Kwan, A., 2010. Tension stiffening in reinforced concrete beams: part 2 - section and member analysis. *Proceedings of the Institution of Civil Engineers, Structures and Buildings,* 163(1), pp. 29-39.

Lavanya, L., Rowena, K., Anuradha, P. & Krishna, N., 2015. Analysis of infill using neural networks. *International Journal of research in Engineering and Technology,* 4(1), pp. 110-115.

Lepech, M., Stang, H. & Michel, A., 2015. *Sustainable Rehabilitation of Civil and Building Structures,* Kongens Lyngby: DTU.

LIANE, 2015. *Liane-network, Case studies.* [Online]
Available at: http://www.liane-network.org/?project=sustainable-development-step-1-assessment-criteria
[Accessed 10 August 2017].

Liauw, T. & Kwan, K., 1985. Unified plastic analysis for infilled frames. *Journal of Structural Engineering,* 111(7), pp. 1427-1448.

Lin, C. & Scordelis, A., 1975. Nonlinear analysis of RC shells of general form. *Journal of Structural Division,* 101(3), pp. 523-538.

Liu, M., Li, B. & Yao, R., 2010. A generic model of Exergy Assessment for the Environmental Impact of Building Lifecycle. *Energy and Buildings,* 42(9), pp. 1482-1490.

Lofti, H. & Shing, P., 1994. An interface model applied to fracture of masonry structures. *Journal of Structural engineering, ASCE,* 120(1), pp. 63-80.

Lourenco, P., Alvarenga, R. & Silva, R., 2006. Validation of a simplified model for the design of masonry infilled frames. *Masonry International,* 19(1), pp. 15-26.

Lourenço, P., 1996. *Computational strategies for masonry structures.* Delft: Delft University Press.

Mainstone, R., 1971. On the stiffnesses and strengths of infills. *Proceedings of the Institution of Civil engineers,* Volume Supplement IV, pp. 57-90.

Mander, J., Priestley, M. & Park, R., 1988. Observed stress-strain behaviour of confined concrete. *Journal of Structural Engineering,* 114(8), pp. 1827-1849.

Markulak, D., Radic, I. & Sigmund, V., 2013. Cyclic testing of single bay steel frames with various types of masonry infill. *Engineering structures,* Volume 51, pp. 2676-277.

Mathworks, 2015. *Matlab.* Massachusetts: The MathWorks, Inc.

Mehrabi, A., Shing, P., Schuller, M. & Noland, J., 1996. Experimental evaluation of masonry-infilled RC frames. *Journal of Structural Engineering,* 122(3), pp. 228-237.

Michel, A., Geiker, M., Stang, H. & Olesen, J., 2012. Modelling Reinforcement Corrosion in Concrete. *MicroDurability.*

Mohamad, G. et al., 2017. Strength, behavior, and failure mode of hollow concrete masonry constrcuted with mortars of different strengths. *Constrcution and Building Materials,* Volume 134, pp. 489-496.

Murty, C. & Jain, A., 2000. *Beneficial influence of masonry infill walls on seismic performance of RC frame buildings.* Auckland, Upper Hutt.

Ng, P., Lam, J. & Kwan, A., 2010. Tension stiffening in concrete beams. Part 1: FE analysis. *Proceedings Of The Institution Of Civil Engineers: Structures and Buildings,* 163(1), pp. 19-18.

Pachauri, R. & Reisinger, A., 2007. *Climate Change 2007: Synthesis Report. Contribution of Working Groups I, II and III to the Fourth Assessment Report of the Intergovernmental Panel on Climate Change,* Geneva: IPCC.

Page, A., 1981. The biaxial compressive strength of brick masonry. *Proceedings of the Institution of Civil Engineers,* 2(71), pp. 893-906.

Page, A., 1983. The strength of brick masonry under biaxial compression-tension. *Page AW 1983. Journal of Masonry Construction,* Volume 31, pp. 26-31.

Page, A. & Marshall, R., 1985. The influence of brick and blockwork prism aspect ratio on the evaluation of the compressive strength. *Proceedings of the seventh international brick and masonry conference,* Volume 1, pp. 653-664.

Park, R., Priestley, M. & Wayne, D., 1982. Ductility of square confined concrete columns. *Journal of Structural Division,* Volume 108, pp. 929-950.

Paulay, T. & Priestley, M., 1992. *Seismic design of reinforced concrete and masonry buildings.* New Jersey: John Wiley & Sons Inc.

Pease, B., Michel, A., Geiker, M. & Stang, H., 2012. Modelling Moisture Ingress through Simplified Concrete Geometries. *International Congress on Durability of Concrete.*

Polyakov, S., 1963. Masonry in framed buildings. *Godsudarstvenoe Isdatel' syvo Literatury Po Stroidal stvui Architecture.*

Priestley, M. J. N. & Elder, D. M., 1983. Priestley, M. J.Stress-strain curves for unconfined and confined concrete masonry. *ACI J,* 80(3), pp. 192-201.

Radić, I., Markulak, D. & Sigmund, V., 2016. Analytical modelling of masonry-infilled steel frames. *Technical Gazette*, 23(1), pp. 115-127.

Rodrigues, H., Varum, H. & Costa, A., 2010. Simplified Macro-Model for Infill Masonry panels. *Journal of Erthquake Engineering,* 14(3), pp. 390-416.

Rosa, L. V. & Haddad, A. N., 2013. Assessing the sustainability of existing buildings using the analytic hierarchy process. *American Journal of Civil Engineering,* 1(1), pp. 24-30.

Rots, J. & Blaauwendraad, J., 1989. *Crack models for concrete: discrete or smeared? fixed, multi-directional or rotating?,* Delft: Heron, Delft University of Technology.

Saneinejad, A. & Hobbs, B., 1995. Inelastic design of infilled frames. *Journal of Structural Engineering,* 121(4), pp. 634-650.

SANS 10160-1, 2011. *Basis of structural design and actions for buildings and inductrial structures. Part 1: Basis of structural desgn.* Pretoria: SABS Styabdards Division.

SANS 10160-4, 2011. *Basis of structural design and actions for buildings and industrial structures — Part 4: Seismic actions and general requirements for building.* Pretoria: SABS Standards Division.

Sawko, F. & Rouf, M. A., 1984. On the stiffness properties of masonry. *Proc. Inst. Civ. Eng., Part 2. Res. Theory ,* Volume 77, pp. 1-12.

Schnobrich, W., 1985. *Role of finite element analysis of reinforced concrete structures.* New York, ASCE, pp. 1-24.

Sheikh, S. & Uzumeri, S., 1982. Analytical Model for Concrete Confinement in Tied Columns. *Journal of Structural division (ASCE),* 108(12), pp. 2703-2722.

Sinha, B. & Pedreschi, R., 1983. Compressive strength and some elastic properties of brickwork. *Internal Journal of Masonry Construction,* 3(1), p. 19–27.

Smith, S., 1962. Lateral stiffness of infilled frames. *Journal of the Structural Division, ASCE,* 88(6), pp. 183-199.

Solis-Guzman, J., Marrero, M., Montes-Delgado, M. & Ramirez-de-Arellano, A., 2009. A Spanish model for quantification and management of construction waste. *Waste Management,* Volume 29, pp. 2542-2548.

Stavridis, A. & Shing, P., 2008. *Calibration of numerical model for masonry infilled RC frames.* Beijing, WCEE.

USGBC, 2009. *LEED Reference Guide for Green Building Design and Construction, Version 3.0.* Washington, DC: US Green Building Council.

Vallenas, J., Bertero, V. & Popov, E., 1977. *Concrete confined by rectangular hoops subjected to axial loads,* California: University of California.

Vamvatsikos, D. & Cornell, C., 2002. Incremental dynamic analysis. *Earthquake Engineering and Structural Dynamics,* Volume 31, pp. 491-514.

Vamvatsikos, D. & Cornell, C. A., 2005. Direct estimation of seismic demand and capacity of multi-degree-of-freedom systems through incremental dynamic analysis of single degree of freedom approximation. *Journal of Structural Engineering (ASCE),* Volume 131, p. 589–599.

Van der Pluijm, R., 1993. *Shear behaviour of bed joints.* Philadelphia, Pennsylvania, Drexel University, pp. 125-136.

Van der Pluijm, R., 1998. *Overview of deformation controlled combined tensile and shear tests ,* Eindhoven: Eindhoven University of Technology.

Vecchio, F. & Colins, M., 1986. The Modified Compression-Filed Theory for Reinforced Concrete Elements subjected to Shear. *ACI Journal,* 83(22), pp. 219-231.

Wang, W., Zmeureanu, R. & Rivard, H., 2005. Applying multi-objective genetic algorithms in green building design optimization. Building design optimization. *Building and Environment,* Volume 40, pp. 1512-1525.

Watermeyer, R., 2006. Poverty reduction responses to the Millenium Development Goals. *The Structural Engineer,* 84(9), pp. 27-34.

Watermeyer, R. & Pham, L., 2011. A framework for the assessment of the structural performance of the 21st century buildings. *The Structural Engineer,* 89(1), pp. 19-25.

WCED, 1987. *Our Common Future,* Oxford: Oxford University Press.

Weisenberger, G., 2011. Sustainability and the Structural Engineer. *Practice Periodicals on Structural Design and Construction*, 16(4), pp. 146-150.

Yun, S.-Y., Hamburger, R., Cornell, C. & Foutch, D., 2002. Seismic performance evaluation for steel moment frames. *Journal of Structural Engineering (ASCE) ,* 128(4), p. 534–545.

APPENDICES

APPENDIX A1: Parametric inputs and calibration

APPENDIX A1.1: Parameter inputs for the bare frame evaluation

Table A1.1: Parameters for Case A parametric study

$\frac{I_b}{I_c}$	Item	Span ratio, r_a and beam length, L_b (c/c in mm)					
		r_a=1.5	r_a=1.0	r_a=0.75	r_a=0.665	r_a=0.5	r_a=0.2
		L_b=1025	L_b=1537	L_b=2049	L_b=2311	L_b=3074	L_b=7685
1.0	I_{b0} x10^8 (mm^4)	1.421	1.421	1.421	1.421	1.421	1.42
	I_ρ x10^7 (mm^4)	8.904	8.904	8.904	8.904	8.904	8.90
	Beam size: b=d (mm)	203.2	203.2	203.2	203.2	203.2	203.2
	d_1 (mm)	76.6	76.6	76.6	76.6	76.6	76.6
	A_s for rebars (mm^2)	1583	1583	1583	1583	1583	1583
	Rebar radius* (mm)	15.9	15.9	15.9	15.9	15.9	15.9
2.5	I_{b0} x10^8 (mm^4)	3.552	3.552	3.552	3.552	3.552	3.552
	I_ρ x10^8 (mm^4)	2.226	2.226	2.226	2.226	2.226	2.226
	Beam size: b=d (mm)	255.5	255.5	255.5	255.5	255.5	255.5
	d_1 (mm)	102.8	102.8	102.8	102.8	102.8	102.8
	A_s for rebars (mm^2)	2200	2200	2200	2200	2200	2200
	Rebar radius* (mm)	18.7	18.7	18.7	18.7	18.7	18.7
5.0	I_{b0} x10^8 (mm^4)	7.104	7.104	7.104	7.104	7.104	7.104
	I_ρ x10^8 (mm^4)	4.452	4.452	4.452	4.452	4.452	4.452
	Beam size: b=d (mm)	303.9	303.9	303.9	303.9	303.9	303.9
	d_1 (mm)	126.9	126.9	126.9	126.9	126.9	126.9
	A_s for rebars (mm^2)	2884	2884	2884	2884	2884	2884
	Rebar radius* (mm)	21.4	21.4	21.4	21.4	21.4	21.4
10.0	I_{b0} x10^9 (mm^4)	1.421	1.421	1.421	1.421	1.421	1.421
	I_ρ x10^8 (mm^4)	8.904	8.904	8.904	8.904	8.904	8.904
	Beam size: b=d (mm)	361.3	361.3	361.3	361.3	361.3	361.3
	d_1 (mm)	155.7	155.7	155.7	155.7	155.7	155.7
	A_s for rebars (mm^2)	3834	3834	3834	3834	3834	3834
	Rebar radius* (mm)	24.7	24.7	24.7	24.7	24.7	24.7
20.0	I_{b0} x10^9 (mm^4)	2.841	2.841	2.841	2.841	2.841	2.841
	I_ρ x10^9 (mm^4)	1.781	1.781	1.781	1.781	1.781	1.781
	Beam size: b=d (mm)	429.7	429.7	429.7	429.7	429.7	429.7
	d_1 (mm)	189.9	189.9	189.9	189.9	189.9	189.9
	A_s for rebars (mm^2)	5155	5155	5155	5155	5155	5155
	Rebar radius* (mm)	28.6	28.6	28.6	28.6	28.6	28.6

Table A1.2: Parameters for Case B parametric study

$\frac{I_b}{I_c}$	Item	Span ratio, r_a and column length, L_c (c/c in mm)					
		r_a=1.5	r_a=1.0	r_a=0.75	r_a=0.665	r_a=0.5	r_a=0.2
		L_c=3467	L_c=2311	L_c=1733	L_c=1537	L_c=1156	L_c=462
1.0	I_{b0} x10^8 (mm^4)	1.421	1.421	1.421	1.421	1.421	1.421
	I_ρ x10^7 (mm^4)	8.904	8.904	8.904	8.904	8.904	8.904
	Beam size: b=d (mm)	203.2	203.2	203.2	203.2	203.2	203.2
	d_1 (mm)	76.6	76.6	76.6	76.6	76.6	76.6
	A_s for rebars (mm^2)	1583	1583	1583	1583	1583	1583
	Rebar radius* (mm)	15.9	15.9	15.9	15.9	15.9	15.9
2.5	I_{b0} x10^8 (mm^4)	3.552	3.552	3.552	3.552	3.552	3.552
	I_ρ x10^8 (mm^4)	2.226	2.226	2.226	2.226	2.226	2.226
	Beam size: b=d (mm)	255.5	255.5	255.5	255.5	255.5	255.5
	d_1 (mm)	102.8	102.8	102.8	102.8	102.8	102.8
	A_s for rebars (mm^2)	2200	2200	2200	2200	2200	2200
	Rebar radius* (mm)	18.7	18.7	18.7	18.7	18.7	18.7
5.0	I_{b0} x10^8 (mm^4)	7.104	7.104	7.104	7.104	7.104	7.104
	I_ρ x10^8 (mm^4)	4.452	4.452	4.452	4.452	4.452	4.452
	Beam size: b=d (mm)	303.9	303.9	303.9	303.9	303.9	303.9
	d_1 (mm)	126.9	126.9	126.9	126.9	126.9	126.9
	A_s for rebars (mm^2)	2884	2884	2884	2884	2884	2884
	Rebar radius* (mm)	21.4	21.4	21.4	21.4	21.4	21.4
10.0	I_{b0} x10^9 (mm^4)	1.421	1.421	1.421	1.421	1.421	1.421
	I_ρ x10^8 (mm^4)	8.904	8.904	8.904	8.904	8.904	8.904
	Beam size: b=d (mm)	361.3	361.3	361.3	361.3	361.3	361.3
	d_1 (mm)	155.7	155.7	155.7	155.7	155.7	155.7
	A_s for rebars (mm^2)	3834	3834	3834	3834	3834	3834
	Rebar radius* (mm)	24.7	24.7	24.7	24.7	24.7	24.7
20.0	I_{b0} x10^9 (mm^4)	2.841	2.841	2.841	2.841	2.841	2.841
	I_ρ x10^9 (mm^4)	1.781	1.781	1.781	1.781	1.781	1.781
	Beam size: b=d (mm)	429.7	429.7	429.7	429.7	429.7	429.7
	d_1 (mm)	189.9	189.9	189.9	189.9	189.9	189.9
	A_s for rebars (mm^2)	5155	5155	5155	5155	5155	5155
	Rebar radius* (mm)	28.6	28.6	28.6	28.6	28.6	28.6

Table A1.3: Parameters for Case C parametric study

$\frac{I_b}{I_c}$	Item	Span ratio, r_a and beam length, L_b (c/c in mm)					
		r_a=1.5	r_a=1.0	r_a=0.75	r_a=0.665	r_a=0.5	r_a=0.2
		L_b=1025	L_b=1537	L_b=2049	L_b=2311	L_b=3074	L_b=7685
1.0	I_{c0} x10^9 (mm^4)	2.841	2.841	2.841	2.841	2.841	2.841
	I_ρ x10^9 (mm^4)	1.781	1.781	1.781	1.781	1.781	1.781
	Column size: b=d (mm)	429.7	429.7	429.7	429.7	429.7	429.7
	d_1 (mm)	189.9	189.9	189.9	189.9	189.9	189.9
	A_s for rebars (mm^2)	5155	5155	5155	5155	5155	5155
	Rebar radius* (mm)	28.6	28.6	28.6	28.6	28.6	28.6
2.5	I_{c0} x10^9 (mm^4)	1.137	1.137	1.137	1.137	1.137	1.137
	I_ρ x10^8 (mm^4)	7.123	7.123	7.123	7.123	7.123	7.123
	Column size: b=d (mm)	341.7	341.7	341.7	341.7	341.7	341.7
	d_1 (mm)	145.9	145.9	145.9	145.9	145.9	145.9
	A_s for rebars (mm^2)	3493	3493	3493	3493	3493	3493
	Rebar radius* (mm)	23.6	23.6	23.6	23.6	23.6	23.6
5.0	I_{c0} x10^8 (mm^4)	5.683	5.683	5.683	5.683	5.683	5.683
	I_ρ x10^8 (mm^4)	3.561	3.561	3.561	3.561	3.561	3.561
	Column size: b=d (mm)	287.4	287.4	287.4	287.4	287.4	287.4
	d_1 (mm)	118.7	118.7	118.7	118.7	118.7	118.7
	A_s for rebars (mm^2)	2638	2638	2638	2638	2638	2638
	Rebar radius* (mm)	20.5	20.5	20.5	20.5	20.5	20.5
10.0	I_{c0} x10^8 (mm^4)	2.841	2.841	2.841	2.841	2.841	2.841
	I_ρ x10^8 (mm^4)	1.781	1.781	1.781	1.781	1.781	1.781
	Column size: b=d (mm)	241.6	241.6	241.6	241.6	241.6	241.6
	d_1 (mm)	95.8	95.8	95.8	95.8	95.8	95.8
	A_s for rebars (mm^2)	2024	2024	2024	2024	2024	2024
	Rebar radius* (mm)	17.9	17.9	17.9	17.9	17.9	17.9
20.0	I_{c0} x10^8 (mm^4)	1.421	1.421	1.421	1.421	1.421	1.421
	I_ρ x10^7 (mm^4)	8.904	8.904	8.904	8.904	8.904	8.904
	Column size: b=d (mm)	203.2	203.2	203.2	203.2	203.2	203.2
	d_1 (mm)	76.6	76.6	76.6	76.6	76.6	76.6
	A_s for rebars (mm^2)	1583	1583	1583	1583	1583	1583
	Rebar radius* (mm)	15.9	15.9	15.9	15.9	15.9	15.9

Table A1.4: Parameters for Case D parametric study

$\frac{I_b}{I_c}$	Item	Span ratio, r_a and column length, L_c (c/c in mm)					
		r_a=1.5	r_a=1.0	r_a=0.75	r_a=0.665	r_a=0.5	r_a=0.2
		L_c=3467	L_c=2311	L_c=1733	L_c=1537	L_c=1156	L_c=462
1.0	I_{c0} x10^9 (mm^4)	2.841	2.841	2.841	2.841	2.841	2.841
	I_ρ x10^9 (mm^4)	1.781	1.781	1.781	1.781	1.781	1.781
	Column size: b=d (mm)	429.7	429.7	429.7	429.7	429.7	429.7
	d_1 (mm)	189.9	189.9	189.9	189.9	189.9	189.9
	A_s for rebars (mm^2)	5155	5155	5155	5155	5155	5155
	Rebar radius* (mm)	28.6	28.6	28.6	28.6	28.6	28.6
2.5	I_{c0} x10^9 (mm^4)	1.137	1.137	1.137	1.137	1.137	1.137
	I_ρ x10^8 (mm^4)	7.123	7.123	7.123	7.123	7.123	7.123
	Column size: b=d (mm)	341.7	341.7	341.7	341.7	341.7	341.7
	d_1 (mm)	145.9	145.9	145.9	145.9	145.9	145.9
	A_s for rebars (mm^2)	3493	3493	3493	3493	3493	3493
	Rebar radius* (mm)	23.6	23.6	23.6	23.6	23.6	23.6
5.0	I_{c0} x10^8 (mm^4)	5.683	5.683	5.683	5.683	5.683	5.683
	I_ρ x10^8 (mm^4)	3.561	3.561	3.561	3.561	3.561	3.561
	Column size: b=d (mm)	287.4	287.4	287.4	287.4	287.4	287.4
	d_1 (mm)	118.7	118.7	118.7	118.7	118.7	118.7
	A_s for rebars (mm^2)	2638	2638	2638	2638	2638	2638
	Rebar radius* (mm)	20.5	20.5	20.5	20.5	20.5	20.5
10.0	I_{c0} x10^8 (mm^4)	2.841	2.841	2.841	2.841	2.841	2.841
	I_ρ x10^8 (mm^4)	1.781	1.781	1.781	1.781	1.781	1.781
	Column size: b=d (mm)	241.6	241.6	241.6	241.6	241.6	241.6
	d_1 (mm)	95.8	95.8	95.8	95.8	95.8	95.8
	A_s for rebars (mm^2)	2024	2024	2024	2024	2024	2024
	Rebar radius* (mm)	17.9	17.9	17.9	17.9	17.9	17.9
20.0	I_{c0} x10^8 (mm^4)	1.421	1.421	1.421	1.421	1.421	1.421
	I_ρ x10^7 (mm^4)	8.904	8.904	8.904	8.904	8.904	8.904
	Column size: b=d (mm)	203.2	203.2	203.2	203.2	203.2	203.2
	d_1 (mm)	76.6	76.6	76.6	76.6	76.6	76.6
	A_s for rebars (mm^2)	1583	1583	1583	1583	1583	1583
	Rebar radius* (mm)	15.9	15.9	15.9	15.9	15.9	15.9

Table A1.5: Column-based elastic material properties of diagonal strut for the fixed bare frames

Sample notation	Column properties										
	E_{ce} (GPa)	σ_{cy} (MPa)	ε_{cy}	A_d (mm^2)	k_{TM}	$k_{TM}.E_{ce}$ (GPa)	F_{eR}	δ_{eR}	σ_{de} (MPa)	ε_{de}	E_d (MPa)
G4(1)	21.91	46	0.0016	2280	0.7252	20.25	0.955	0.747	48.18	0.0021	22487
G4(5)	18.05	35.02	0.0014	2438	0.7238	17.51	1.075	0.827	32.58	0.0017	19239
G4(6)	20.12	41.82	0.0016	2345	0.7246	18.98	1.006	0.781	41.58	0.0020	20293
G4(8)	18.12	41.43	0.0017	2434	0.7238	17.56	1.072	0.825	38.63	0.0021	18750

Table A1.6: Column-based elastic material properties of diagonal strut for the pinned bare frames

Sample notation	Column properties										
	E_{ce} (GPa)	σ_{cy} (MPa)	ε_{cy}	A_d (mm^2)	k_{TM}	$k_{TM}.E_{ce}$ (GPa)	F_{eR}	δ_{eR}	σ_{de} (MPa)	ε_{de}	E_d (GPa)
G4(1)	21.91	46	0.0016	545	0.1732	3.795	0.484	0.463	95.05	0.0035	27485
G4(5)	18.05	35.02	0.0014	582	0.1729	3.121	0.550	0.526	63.67	0.0027	23909
G4(6)	20.12	41.82	0.0016	560	0.1731	3.483	0.512	0.489	81.69	0.0033	24985
G4(8)	18.12	41.43	0.0017	581	0.1729	3.133	0.549	0.524	75.51	0.0032	23293

Appendix A1.2: Parametric results for Cases B – D for the fixed bare frames

Case B numerical results and discussions

Case B numerical simulations involve bare frames with constant second moment of area for the column (I_c) and constant beam length (L_b). The results and discussions for each of the four lateral strength resistance indicators for the frames (F_e, δ_e, F_u and δ_u) are summarised in subsequent paragraphs.

(a) Yield strength (F_e) results and discussions for Case B

The variations of the yield strength with various ratios of the $I_b/I_c(I_b)$ are presented in Figure A1.1. The yield strength gradually increases with increase in the $I_b/I_c(I_b)$ ratio for $I_b/I_c(I_b)$ less than 5.0, while there is very minimal or no increase for $I_b/I_c(I_b)$ > 5.0 (see Figure A1.1). Figure A1.2 illustrates the scatter of the yield strength across various values of the aspect ratio, $r_a(L_c)$. There is consistent reduction in the yield strength with increase in the aspect ratio, $r_a(L_c)$. A summary of mean values, standard deviation and coefficient of variation for the yield strength under each category of aspect ratio, $r_a(L_c)$ across the $I_b/I_c(I_b)$ ratio is provided in Table 6.3. There is lower variability of the yield strength for each sample category based on aspect ratio than the overall variability. This may imply that the aspect ratio, $r_a(L_c)$, has more significant influence on the yield strength than the $I_b/I_c(I_b)$ ratio. The Cov ranges from 4.98% to 10.93% for linearised curve points and 4.41% to 8.23% for the actual curve points. The overall Cov for all the samples altogether is 32.54% for the linearised curve points and 34.18% for the actual curve points.

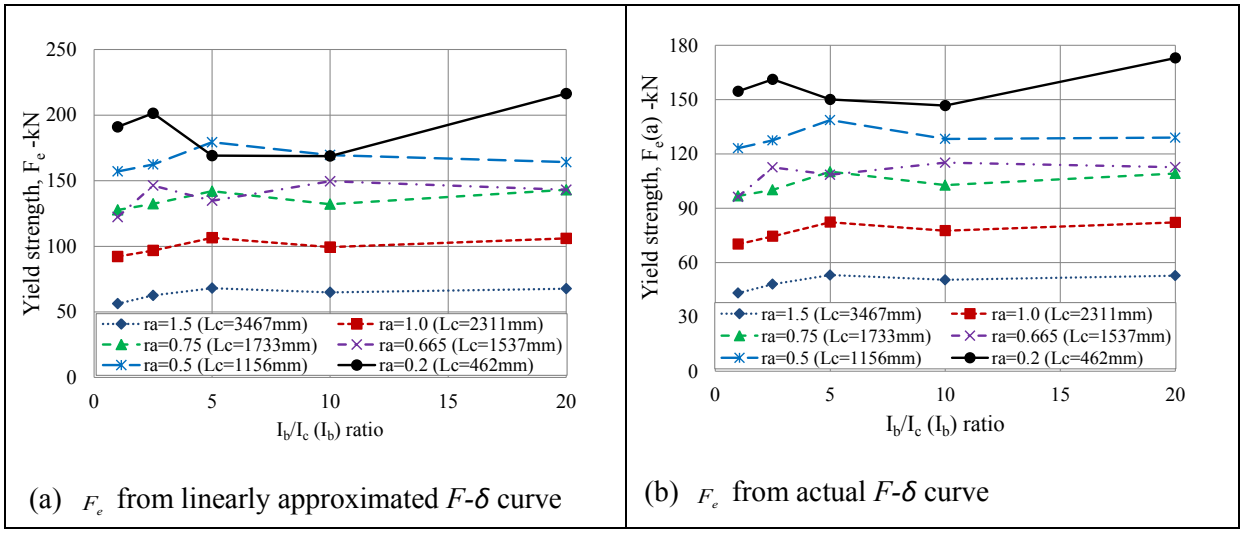

(a) F_e from linearly approximated *F-δ* curve (b) F_e from actual *F-δ* curve

Figure A1.1: Typical variation of the yield strength with the $I_b/I_c(I_b)$ ratio for Case B

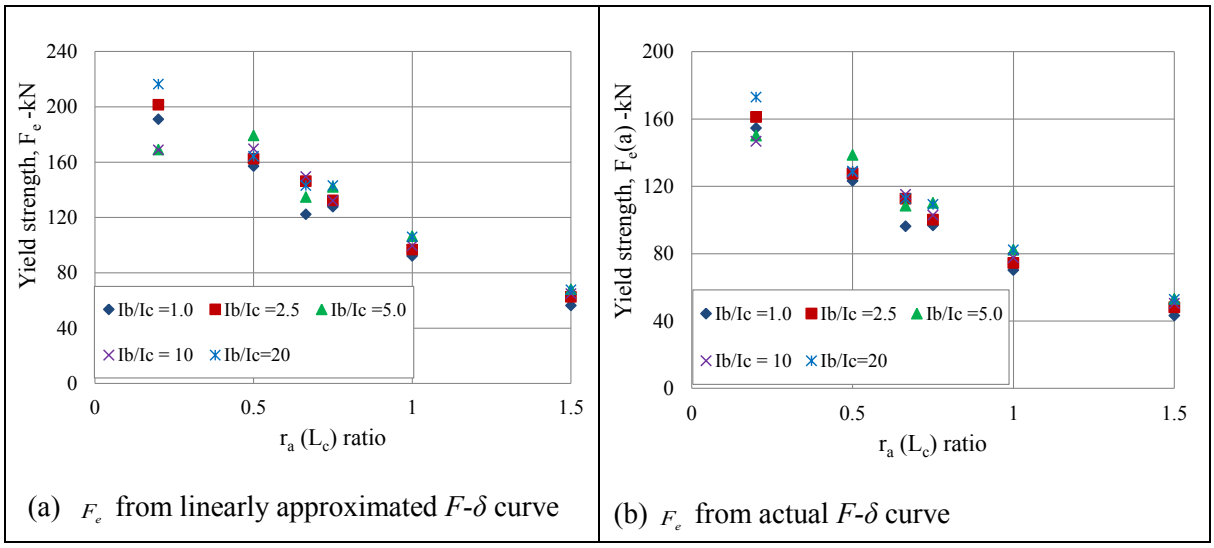

(a) F_e from linearly approximated *F-δ* curve (b) F_e from actual *F-δ* curve

Figure A1.2: Typical variation of the yield strength with the aspect ratio, $r_a(L_c)$ for Case B

Table A1.7: Yield strength mean values, standard deviation and coefficient of variation for each aspect ratio, $r_a(L_c)$ sample category

Sample category	***F*e from linearly approximated *F-δ* curve**			***F*e (a) from the actual *F-δ* curve**		
	Mean (kN)	Std dev	Cov	Mean (kN)	Std dev	Cov
B_{i1}	63.9	4.81	0.0752	49.5	4.08	0.0823
B_{i2}	100.2	6.11	0.0610	77.4	5.18	0.0670
B_{i3}	135.5	6.75	0.0498	103.8	5.77	0.0555
B_{i4}	139.2	10.94	0.0786	109.1	7.53	0.0690
B_{i5}	166.5	8.42	0.0506	129.3	5.70	0.0441
B_{i6}	189.3	20.69	0.1093	157.1	10.40	0.0662
B_{ij}*	132.4	43.09	0.3254	104.4	35.68	0.3418

*Overall results

(b) Yield deformation (δ_e) results and discussions for Case B

Results from the numerical analysis for the yield deformations are plotted against the $I_b/I_c(I_b)$ ratios and aspect ratios, $r_a(L_c)$ as shown in Figure A1.3. There is a reduction in the yield deformation with increase in the ratio $I_b/I_c(I_b)$ while the yield deformation increases with increase in the aspect ratio, $r_a(L_c)$. The aspect ratio, $r_a(L_c)$, has more significant effect on the yield deformation than the $I_b/I_c(I_b)$ for the values considered.

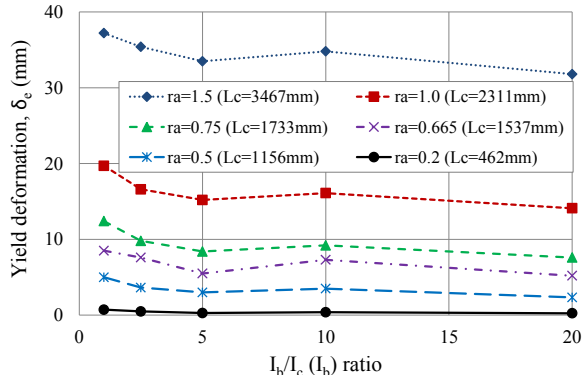

(a) Variation of the yield deformation with the $I_b/I_c(I_b)$ ratio

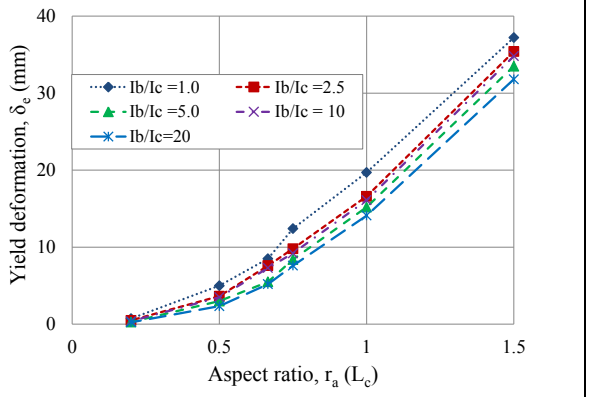

(b) Variation of the yield deformation with the aspect ratio, $r_a(L_c)$

Figure A1.3: Typical variation of the yield deformation with $I_b/I_c(I_b)$ and aspect ratio, $r_a(L_c)$ for Case B

(c) Ultimate strength (F_e) results and discussions for Case B

The ultimate strength for each numerical simulation data is determined using both the linearised *F-δ* curve and the actual *F-δ* curve (see Figure 3.11). Results of the ultimate strength variations with the $I_b/I_c(I_b)$ ratio are shown in Figure A1.4. The ultimate strength slightly increases with increase in the $I_b/I_c(I_b)$ ratio for $I_b/I_c(I_b) < 5.0$ while there is no increase for $I_b/I_c(I_b) > 5.0$. Figure A1.5 illustrates the scatter of the ultimate strength across various values of the aspect ratio of the frame, $r_a(L_c)$. There is consistent reduction in the ultimate strength with increase in the aspect ratio, $r_a(L_c)$. A summary of mean values, standard deviation and coefficient of variation for the ultimate strength under each category of aspect ratio, $r_a(L_c)$ across the $I_b/I_c(I_b)$ ratio is provided in Table A1.8. There is lower variability of the yield strength for each sample category based on aspect ratio while overall variability is very high. Cov ranges from 3.21% to 10.82% for linearised curve points and 3.88% to 5.04% for the actual curve points. The overall Cov for all the samples altogether is 33.15% for the linearised curve points and 32.40% for the actual curve points.

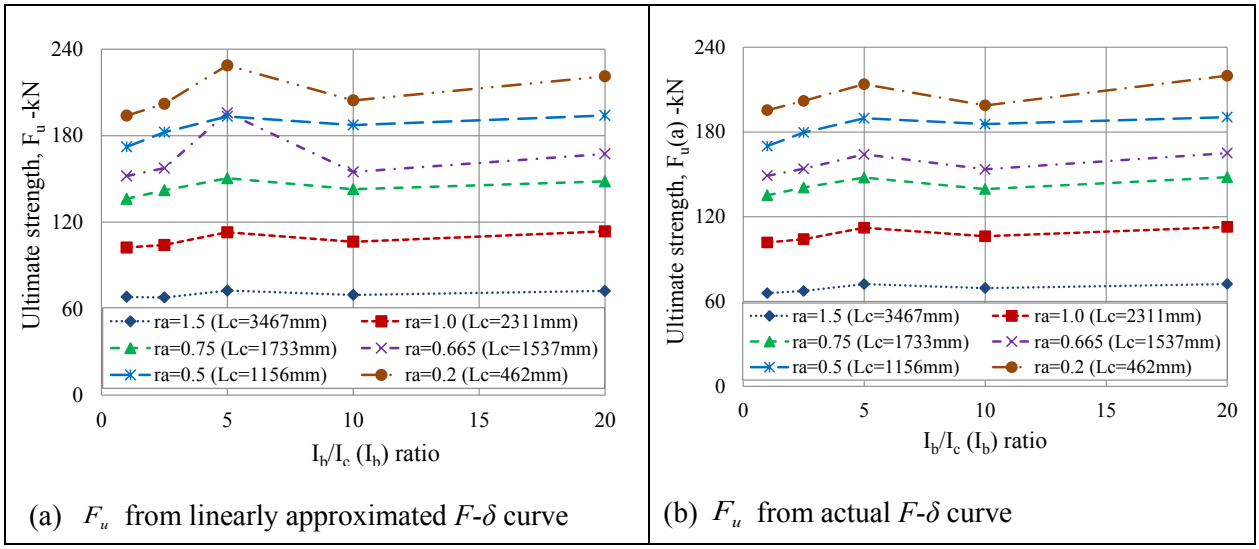

(a) F_u from linearly approximated F-δ curve (b) F_u from actual F-δ curve

Figure A1.4: Typical variation of the ultimate strength with $I_b/I_c(I_b)$ ratio for Case B

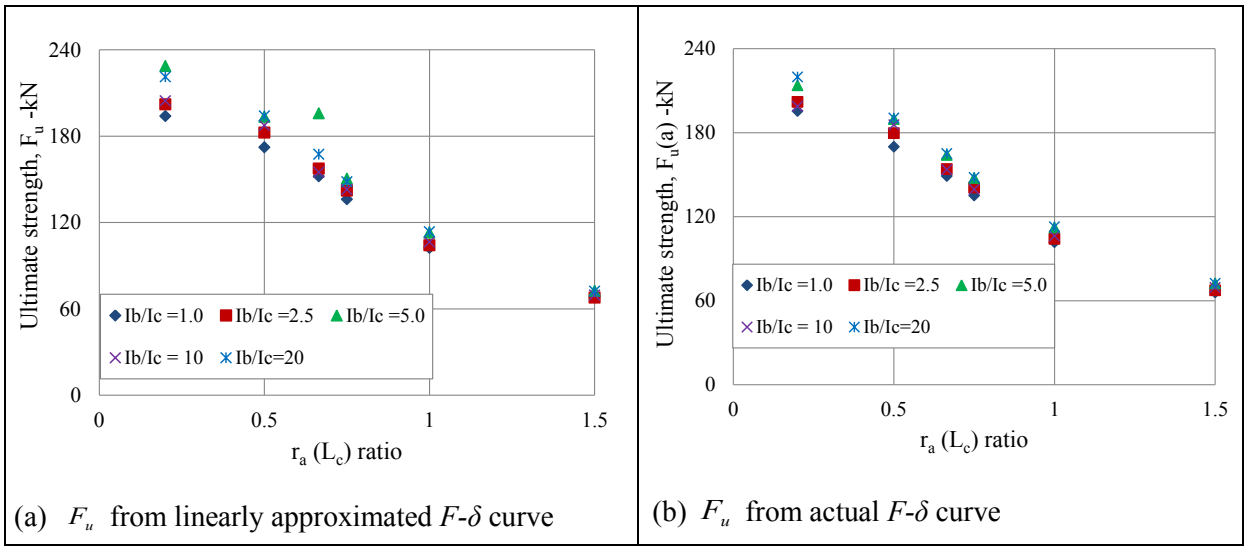

(a) F_u from linearly approximated F-δ curve (b) F_u from actual F-δ curve

Figure A1.5: Typical variation of the ultimate strength with aspect ratio, $r_a(L_c)$ for Case B

Table A1.8: Ultimate strength mean values, standard deviation and coefficient of variation for each aspect ratio, $r_a(L_c)$ sample category

Sample category	***F*u from linearly approximated *F*-δ curve**			***F*u (a) from the actual *F*-δ curve**		
	Mean (kN)	Std dev	Cov	Mean (kN)	Std dev	Cov
B_{i1}	70.1	2.25	0.0321	69.5	2.90	0.0417
B_{i2}	107.9	5.12	0.0474	107.4	4.90	0.0456
B_{i3}	144.0	5.62	0.0390	142.2	5.52	0.0388
B_{i4}	165.6	17.91	0.1082	157.2	7.08	0.0450
B_{i5}	185.9	9.00	0.0484	183.1	8.49	0.0464
B_{i6}	210.1	14.41	0.0686	206.0	10.39	0.0504
B_{ij}*	147.3	48.82	0.3315	144.2	46.73	0.3240

*Overall results

(d)Ultimate deformation (δ_u) results and discussions for Case B

The ultimate deformation results from Case B numerical analyses are plotted against the $I_b/I_c(I_b)$ ratio and the aspect ratio, $r_a(L_c)$ as shown in Figure A1.6. Apart from samples with $r_a(L_c)$ of 1.5 and 1.0, the rest of the samples show steeper reduction in the ultimate deformation with increase in $I_b/I_c(I_b)$ for the $I_b/I_c(I_b)$ ratio less than 5.0 while there is a slower or no reduction in the ultimate deformation for $I_b/I_c(I_b)$ ratio > 5.0 (see Figure A1.6a). There is increase in the ultimate deformation with increase in the aspect ratio, $r_a(L_c)$ (see Figure A1.6b).

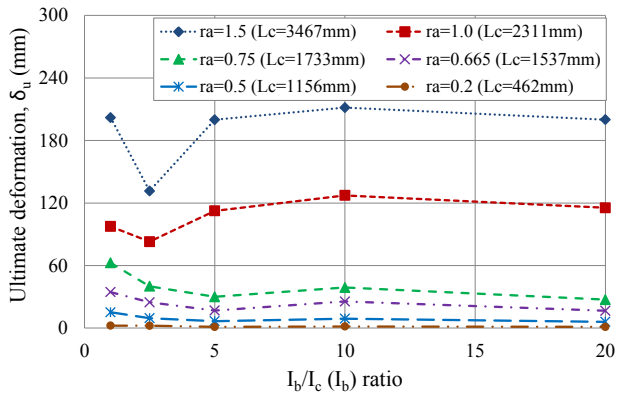

(a) Variation of the ultimate deformation with the $I_b/I_c(I_b)$ ratio

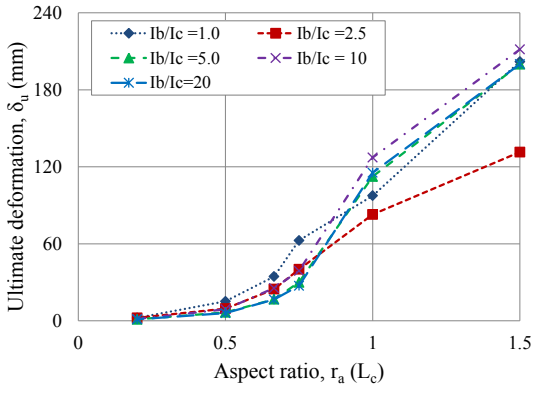

(b) Variation of the ultimate deformation with the aspect ratio, $r_a(L_c)$

Figure A1.6: Typical ultimate deformation variation with $I_b/I_c(I_b)$ and aspect ratio, $r_a(L_c)$ for Case B

Case C numerical results and discussions

Case C numerical simulations involve bare frames with constant second moment of area for the beam (I_b) and constant column height (L_c). The results and discussions for each of the four lateral strength resistance indicators for the frames (F_e, δ_e, F_u and δ_u) are summarised in subsequent paragraphs.

(a) Yield strength (F_e) resultsand discussions for Case C

The variations of the yield strength with the $I_b/I_c(I_c)$ ratios are provided in Figure A1.7. The yield strength increases with increase in the $I_b/I_c(I_c)$ ratio. Figure A1.8 illustrates the scatter of the yield strength across various values of the aspect ratio, $r_a(L_b)$. Despite the variability in the scatter, there is gradual reduction in the yield strength across the aspect ratio, $r_a(L_b)$. A summary of mean values, standard deviation and coefficient of variation for the yield strength under each category of aspect ratio, $r_a(L_b)$ across the $I_b/I_c(I_c)$ ratio is provided in Table A1.9. There is considerable variability of the yield strength for both the sample categories based on aspect ratio and all the samples altogether. The Cov ranges from 39.74% to 59.39% for linearised curve points and 43.91% to 57.71% for the actual curve points. The overall Cov for all the samples altogether is 48.58% for the linearised curve points and 49.46% for the actual curve points.

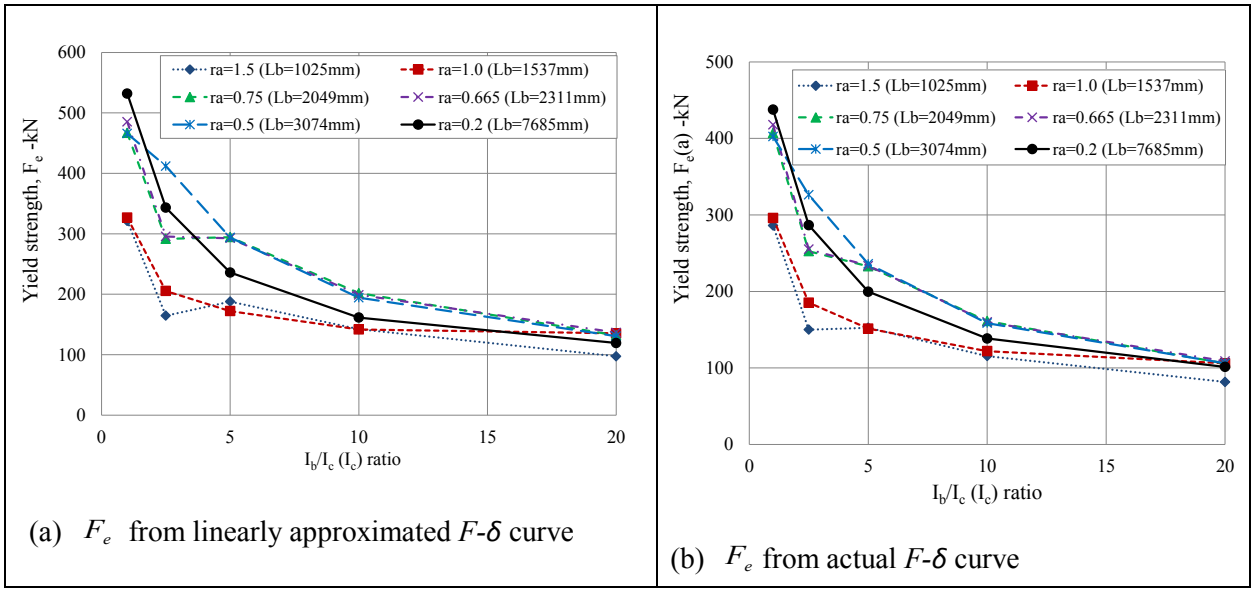

(a) F_e from linearly approximated *F-δ* curve

(b) F_e from actual *F-δ* curve

Figure A1.7: Typical variation of the yield strength with the $I_b/I_c\,(I_c)$ ratio for Case C

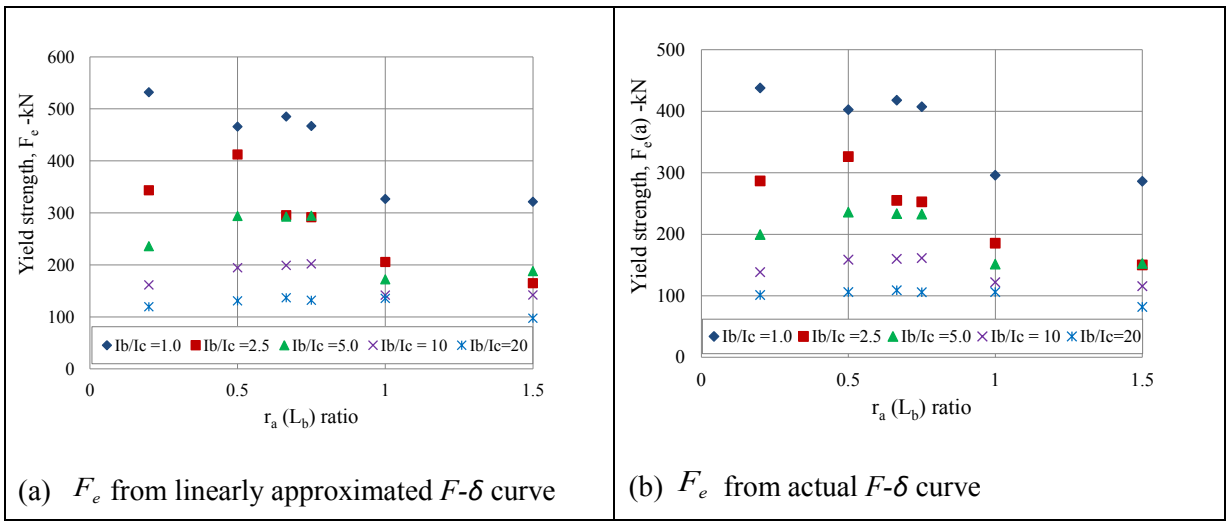

(a) F_e from linearly approximated *F-δ* curve

(b) F_e from actual *F-δ* curve

Figure A1.8: Typical variation of the yield strength with the aspect ratio, $r_a\,(L_b)$ for Case C

Table A1.9: Yield strength mean values, standard deviation and coefficient of variation for each aspect ratio, $r_a\,(L_b)$ sample category

Sample category	***F*e from linearly approximated *F-δ* curve**			***F*e (a) from the actual *F-δ* curve**		
	Mean (kN)	Std dev	Cov	Mean (kN)	Std dev	Cov
C_{i1}	182.6	84.36	0.4619	157.2	77.71	0.4944
C_{i2}	196.3	78.02	0.3974	172.1	75.57	0.4391
C_{i3}	277.4	125.74	0.4533	231.9	114.03	0.4917
C_{i4}	281.8	131.90	0.4680	235.1	117.66	0.5005
C_{i5}	299.3	141.37	0.4723	245.8	120.71	0.4910
C_{i6}	278.4	165.32	0.5939	232.7	134.32	0.5771
C_{ij}*	252.6	122.73	0.4858	212.5	105.10	0.4946

*Overall results

(b) Yield deformation (δ_e) results and discussions for Case C

Yield deformation results from the numerical analyses for Case C samples are plotted against the $I_b/I_c(I_c)$ ratios and aspect ratios, $r_a(L_b)$ as shown in Figure A1.9. The yield deformation increases with increase in the $I_b/I_c(I_c)$, with a steeper increase observed for $I_b/I_c(I_c)$ ratio < 5.0 (see Figure A1.9a). The yield deformation reduces with increase in the aspect ratio, $r_a(L_b)$ (see Figure A1.9b).

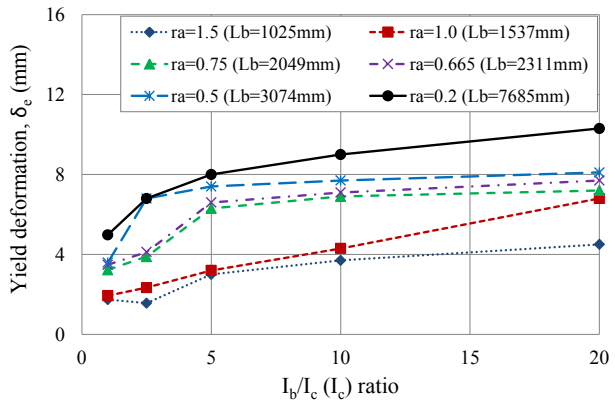

(a) Variation of the yield deformation with the $I_b/I_c(I_c)$ ratio

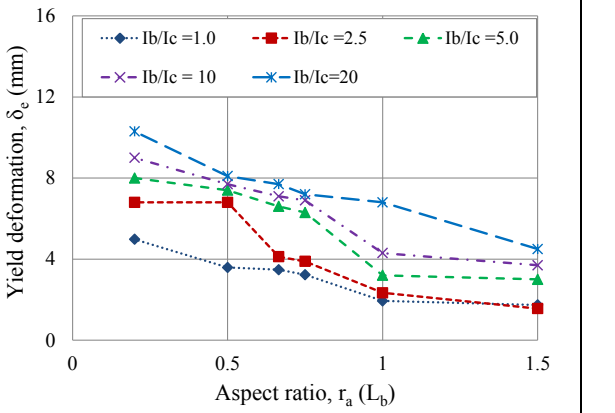

(b) Variation of the yield deformation with the aspect ratio, $r_a(L_b)$

Figure A1.9: Typical variation of the yield deformation with $I_b/I_c(I_c)$ ratio and aspect ratio, $r_a(L_b)$ for Case C

(c) Ultimate strength (F_u) results and discussions for Case C

Ultimate strength values from Case C samples are plotted against the $I_b/I_c(I_c)$ ratio as shown in Figure A1.10. There is reduction in the ultimate strength with increase in the $I_b/I_c(I_c)$ ratio, with steeper increase for $I_b/I_c(I_c) < 5.0$. Figure A1.11 illustrates the scatter of the ultimate strength across various values of the aspect ratio, $r_a(L_b)$. While there is notable variability in the scatter, there is gradual or no reduction in the ultimate strength with increase in the aspect ratio, $r_a(L_b)$. A summary of mean values, standard deviation and coefficient of variation for the ultimate strength under each category of aspect ratio, $r_a(L_b)$ across the $I_b/I_c(I_c)$ ratio is provided in Table A1.10. There is considerable variability of the ultimate strength for both the sample categories based on aspect ratio and all the samples altogether. The Cov ranges from 48.06% to 77.65% for linearised curve points and 49.97% to 77.92% for the actual curve points. The overall Cov for all the samples altogether is 56.56% for the linearised curve points and 57.03% for the actual curve points.

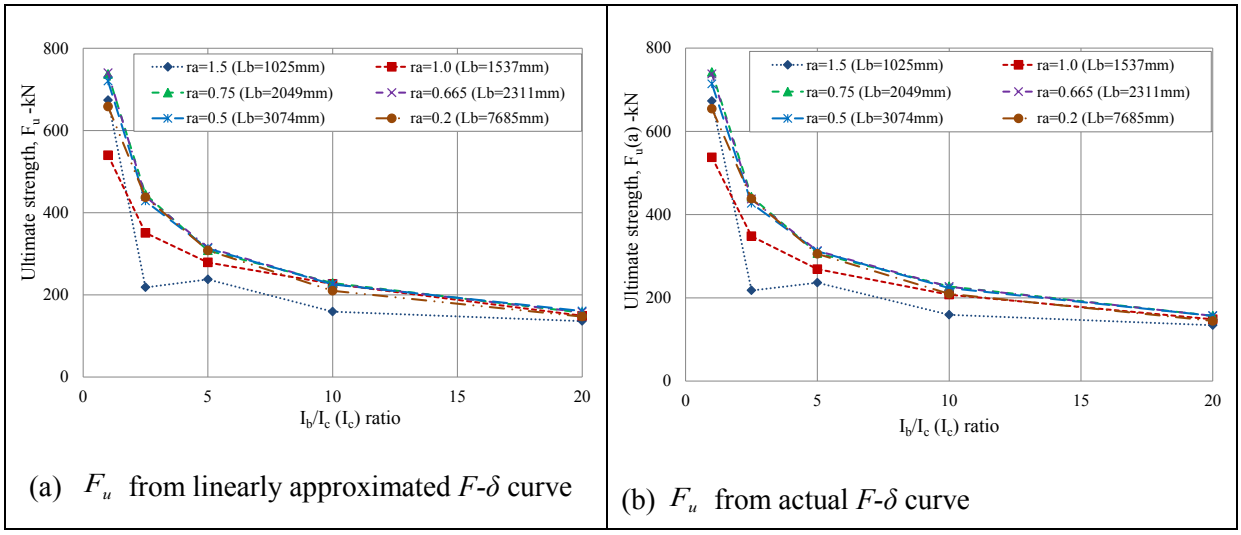

(a) F_u from linearly approximated F-δ curve

(b) F_u from actual F-δ curve

Figure A1.10: Typical variation of the ultimate strength with $I_b/I_c\,(I_c)$ ratio for Case C

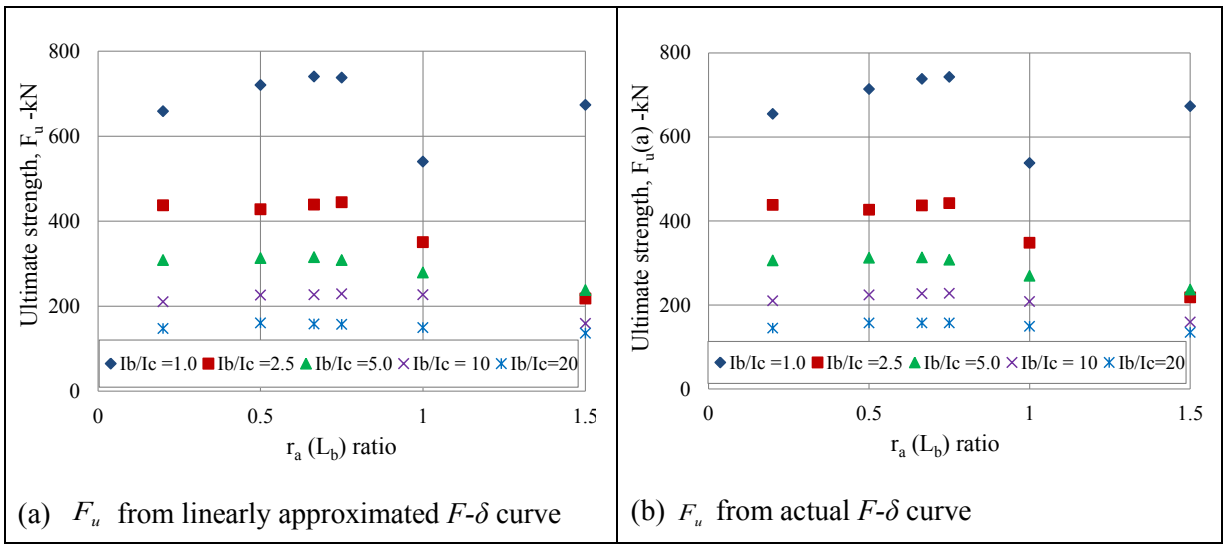

(a) F_u from linearly approximated F-δ curve

(b) F_u from actual F-δ curve

Figure A1.11: Typical variation of the ultimate strength with aspect ratio, $r_a\,(L_b)$ for Case C

Table A1.10: Ultimate strength mean values, standard deviation and coefficient of variation for each aspect ratio, $r_a\,(L_b)$ sample category

Sample category	***F*u from linearly approximated *F*-δ curve**			***F*u (a) from the actual *F*-δ curve**		
	Mean (kN)	Std dev	Cov	Mean (kN)	Std dev	Cov
C_{i1}	284.8	221.15	0.7765	284.1	221.33	0.7792
C_{i2}	309.0	148.51	0.4806	302.2	151.01	0.4997
C_{i3}	375.0	228.94	0.6106	375.3	231.00	0.6155
C_{i4}	375.7	229.25	0.6101	374.2	228.53	0.6107
C_{i5}	369.3	220.27	0.5964	366.5	218.85	0.5971
C_{i6}	352.2	203.28	0.5772	350.5	202.60	0.5781
C_{ij}*	344.3	194.77	0.5656	342.1	195.12	0.5703

*Overall results

(d) Ultimate deformation (δ_u) results and discussions for Case C

Ultimate deformation results from the numerical analyses for Case C samples are plotted against the $I_b/I_c(I_c)$ ratio and aspect ratio, $r_a(L_b)$ as shown in Figure A1.12. There is variability in the trends of the ultimate deformation with either the $I_b/I_c(I_c)$ ratio or the aspect ratio, $r_a(L_b)$. Nevertheless, there is a general increase in the ultimate deformation with increases in the $I_b/I_c(I_c)$ ratio, with steeper increase for $I_b/I_c(I_c) < 5.0$ (see Figure A1.12a). The yield deformation reduces with increase in the aspect ratio, $r_a(L_b)$ (see Figure A1.12b).

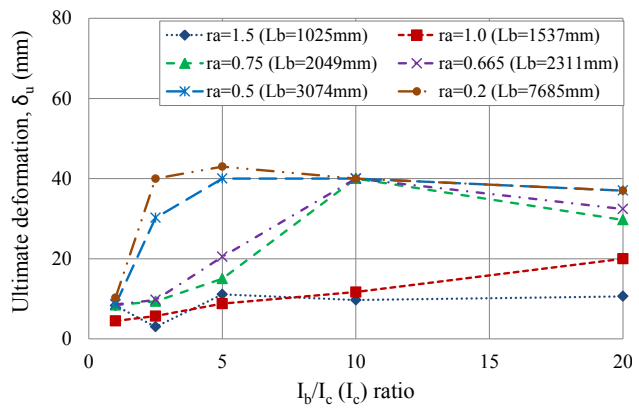

(a) Variation of the ultimate deformation with the $I_b/I_c(I_c)$ ratio

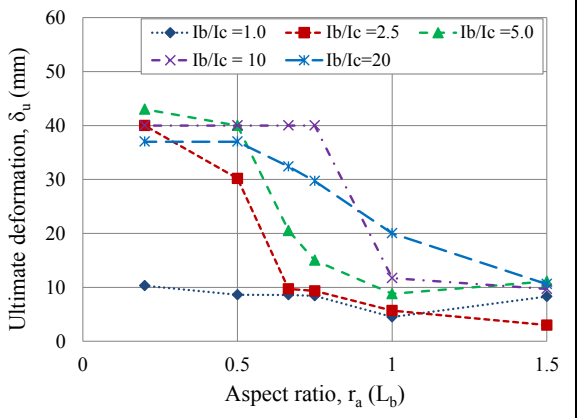

(c) Variation of the ultimate deformation with the aspect ratio, $r_a(L_b)$

Figure A1.12: Typical ultimate deformation variation with $I_b/I_c(I_c)$ and aspect ratio, $r_a(L_b)$ for Case C

Case D numerical results and discussions

Case D numerical simulations involve bare frames with constant second moment of area and length of the beam (I_b and L_b). The results and discussions for each of the four lateral strength resistance indicators for the frames (F_e, δ_e, F_u and δ_u) are summarised in subsequent paragraphs.

(a) Yield strength (F_e) results and discussions for Case D

The results of the yield strength variations with the $I_b/I_c(I_c)$ ratios are shown in Figure A1.13. The yield strength reduces with increase in the $I_b/I_c(I_c)$ ratio, with steeper reduction for $I_b/I_c(I_c)$ <5.0. Figure A1.14 illustrates the scatter of the yield strength across various values of the aspect ratio, $r_a(L_c)$. There is reduction in the yield strength with increase in the aspect ratio, $r_a(L_c)$. A summary of mean values, standard deviation and coefficient of variation for the yield strength under each category of aspect ratio, $r_a(L_c)$ across the $I_b/I_c(I_c)$ ratio is provided in Table A1.11. There is considerable variability of the yield strength for both the sample categories based on aspect ratio and all the samples altogether. The Cov ranges from 34.98% to 56.70% for linearised curve points and 39.80% to 56.06% for the actual curve points. The overall Cov for all the samples altogether is 64.38% for the linearised curve points and 64.32% for the actual curve points.

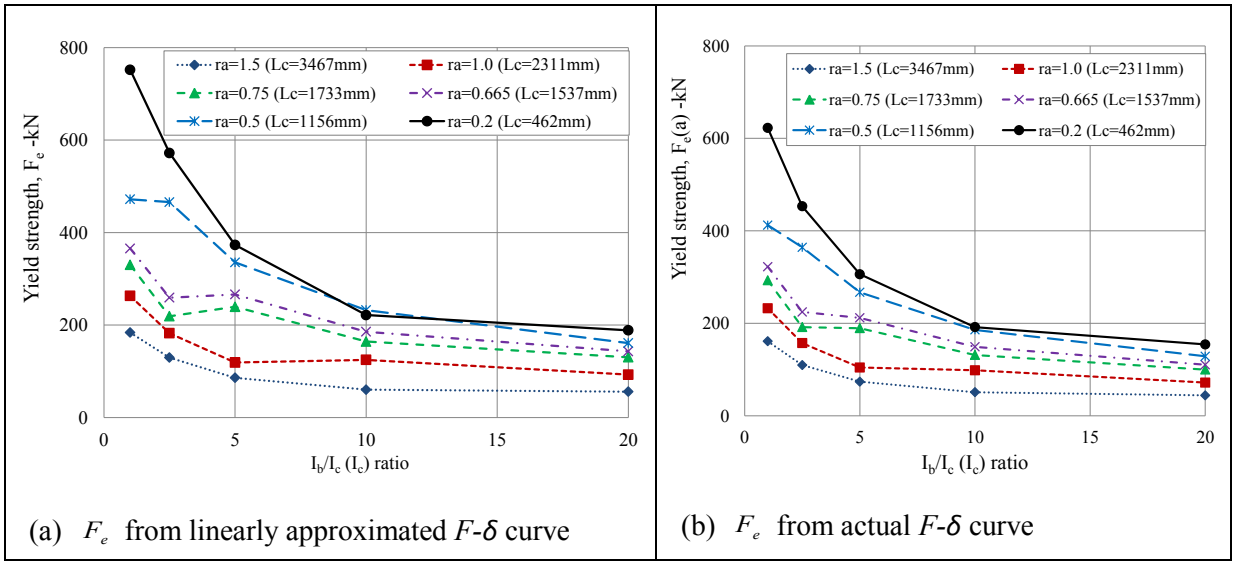

Figure A1.13: Typical variation of the yield strength with the $I_b/I_c\,(I_c)$ ratiofor Case D

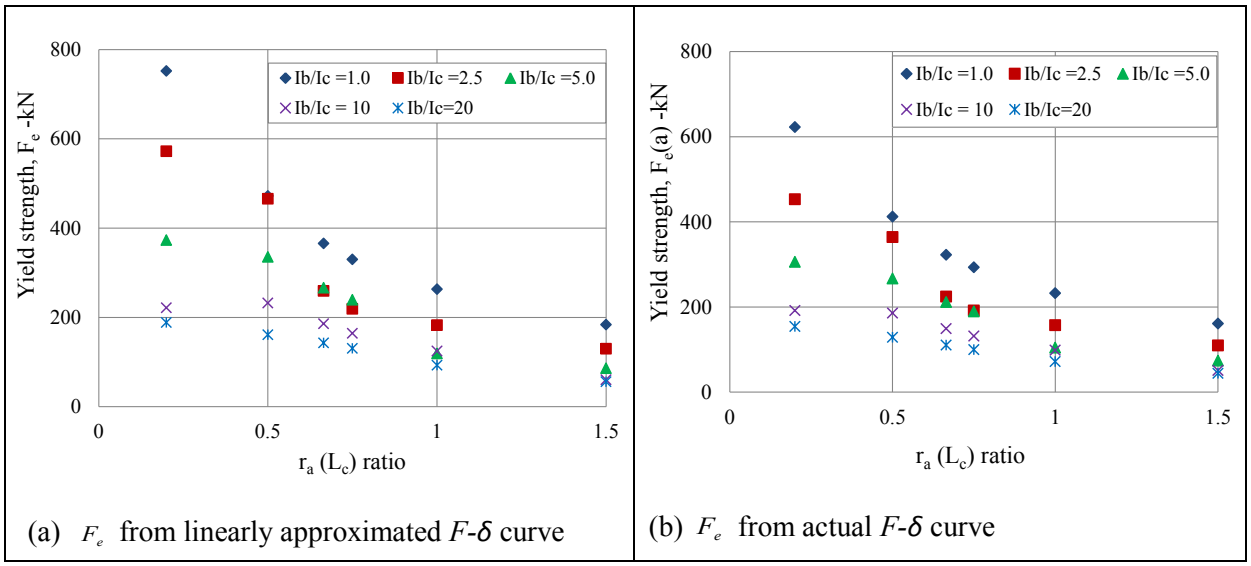

Figure A1.14: Typical variation of the yield strength with the aspect ratio, $r_a\,(L_c)$ for Case D

Table A1.11: Yield strength mean values, standard deviation and coefficient of variation for each aspect ratio, $r_a\,(L_c)$ sample category

Sample category	F_e from linearly approximated F-δ curve			F_e (a) from the actual F-δ curve		
	Mean (kN)	Std dev	Cov	Mean (kN)	Std dev	Cov
D_{i1}	103.1	53.79	0.5217	87.9	48.23	0.5485
D_{i2}	156.4	68.04	0.4350	132.8	63.80	0.4803
D_{i3}	216.7	76.76	0.3542	181.2	73.79	0.4073
D_{i4}	243.9	85.33	0.3498	203.6	81.06	0.3980
D_{i5}	333.4	138.41	0.4152	271.6	118.53	0.4364
D_{i6}	421.5	238.96	0.5670	345.6	193.73	0.5606
D_{ij}*	245.8	158.28	0.6438	203.08	131.09	0.6432

*Overall results

(b) ***Yield deformation (δ_e) results and discussions for Case D***

Yield deformation results from the numerical analyses for Case D samples are plotted against the $I_b/I_c(I_c)$ ratio and aspect ratio, $r_a(L_c)$ as shown in Figure A1.15. Apart from samples with $I_b/I_c(I_c)$ ratio of 1.5 and 1.0, there is a gradual increase in the yield deformation with increase in the $I_b/I_c(I_c)$ ratio (see Figure A1.15a). The yield deformation increases with increase in the aspect ratio, $r_a(L_c)$ (see Figure A1.15b).

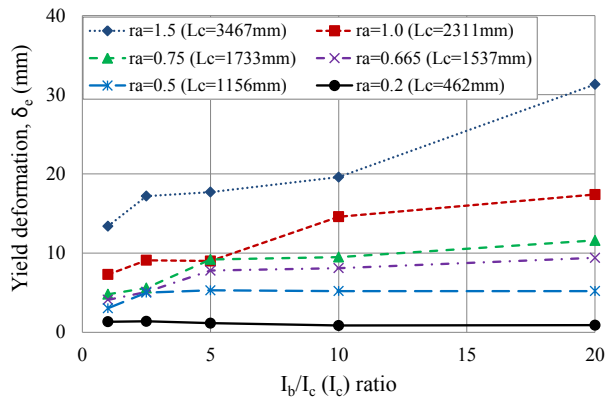

(a) Variation of the yield deformation with the $I_b/I_c(I_c)$ ratio

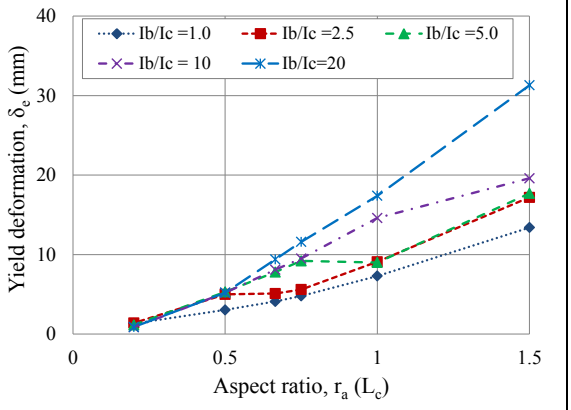

(b) Variation of the yield deformation with the aspect ratio, $r_a(L_c)$

Figure A1.15: Typical variation of the yield deformation with $I_b/I_c(I_c)$ and aspect ratio, $r_a(L_c)$ for Case D

(c) ***Ultimate strength (F_u) results and discussions for Case D***

Results of the ultimate strength for various values of the $I_b/I_c(I_c)$ ratio are plotted in Figure A1.16. The ultimate strength reduces with increase in the $I_b/I_c(I_c)$ ratio, with steeper reduction for $I_b/I_c(I_c) < 5.0$. Figure A1.17 illustrates the scatter of the ultimate strength across various values of the aspect ratio, $r_a(L_c)$. There is reduction in the yield strength with increase in the aspect ratio, $r_a(L_c)$. A summary of mean values, standard deviation and coefficient of variation for the yield strength under each category of aspect ratio, $r_a(L_c)$ across the $I_b/I_c(I_c)$ ratio is provided in Table A1.12. The coefficient of variation of the ultimate strength for both the sample categories based on aspect ratio and all the samples altogether are high. The Cov ranges from 55.39% to 62.82% for linearised curve points and 55.58% to 62.24% for the actual curve points. The overall Cov for all the samples altogether is 67.22% for the linearised curve points and 66.20% for the actual curve points.

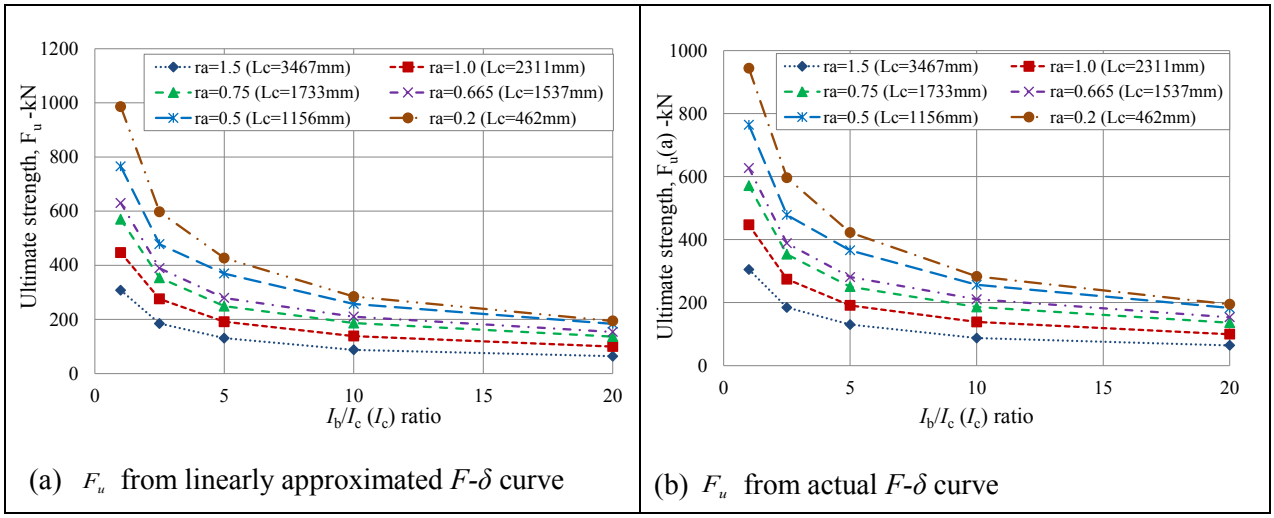

Figure A1.16: Typical variation of the ultimate strength with $I_b/I_c\,(I_c)$ ratio for Case D

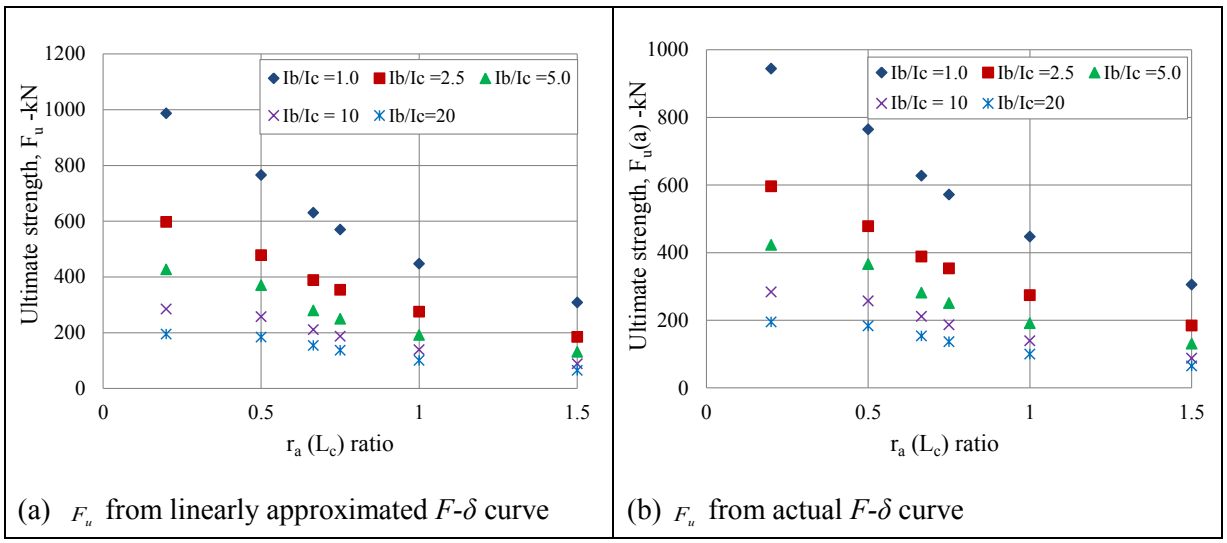

Figure A1.17: Typical variation of the ultimate strength with aspect ratio, $r_a\,(L_c)$ for Case D

Table A1.12: Ultimate strength mean values, standard deviation and coefficient of variation for each aspect ratio, $r_a\,(L_c)$ sample category

Sample category	***F*u from linearly approximated *F-δ* curve**			***F*u (a) from the actual *F-δ* curve**		
	Mean (kN)	Std dev	Cov	Mean (kN)	Std dev	Cov
D_{i1}	155.0	97.00	0.6258	154.2	95.96	0.6224
D_{i2}	230.3	137.79	0.5982	229.9	137.72	0.5989
D_{i3}	299.0	171.58	0.5738	299.3	172.19	0.5753
D_{i4}	332.4	188.01	0.5655	331.9	186.70	0.5625
D_{i5}	410.6	227.43	0.5539	409.4	227.55	0.5558
D_{i6}	497.7	312.66	0.6282	487.9	296.52	0.6077
D_{ij}*	320.8	215.67	0.6722	318.8	211.02	0.6620

*Overall results

(d) ***Ultimate deformation (δ_u) results and discussions for Case D***

Ultimate deformation results from the numerical analyses for Case D samples are plotted against the $I_b/I_c(I_c)$ ratio and aspect ratio, $r_a(L_c)$ as shown in Figure A1.18. There is variability in the trends of the ultimate deformation with either the $I_b/I_c(I_c)$ ratio or the aspect ratio, $r_a(L_c)$. Nevertheless, there is general increase in the ultimate deformation with increase in the $I_b/I_c(I_c)$ ratio for most of the samples while other samples show no significant change in the ultimate deformation with increase in the $I_b/I_c(I_c)$ ratio. The ultimate deformation increases with increase in the aspect ratio, $r_a(L_c)$.

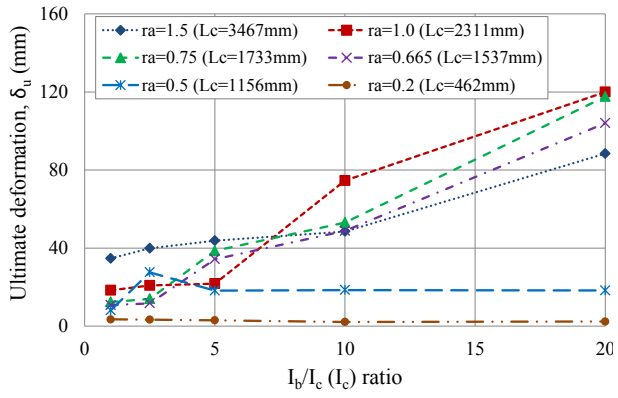

(a) Variation of the ultimate deformation with the $I_b/I_c(I_c)$ ratio

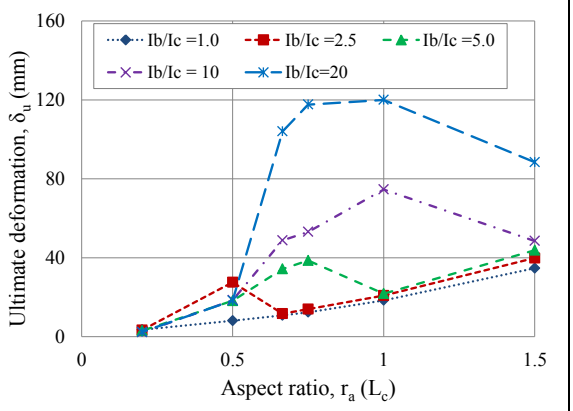

(b) Variation of the ultimate deformation with the aspect ratio, $r_a(L_c)$

Figure A1.18: Typical ultimate deformation variation with $I_b/I_c(I_c)$ and aspect ratio, $r_a(L_c)$ for Case D

Appendix A1.3: Parametric results for Cases B – D for pinned bare frames

Case B numerical results and discussions

Case B numerical simulations involve bare frames with constant second moment of area for the column (I_c = 2.31x10^8 mm^4) and constant beam length (L_b = 2311 mm). The results and discussions for each of the four lateral strength resistance indicators for the frames (F_e, δ_e, F_u and δ_u) are summarised in subsequent paragraphs.

(a) Yield strength (F_e) results and discussionsfor Case B

Yield strength results from the finite element analyses for Case B frames respect to the $I_b/I_c(I_b)$ ratiosare presented in Figure A1.19. The yield strength slightly increases with increase in the $I_b/I_c(I_b)$ ratio, with almost no increase for $I_b/I_c(I_b) > 5.0$ for most of the samples. Figure A1.20 illustrates the scatter of the yield strength across various values of the aspect ratio, $r_a(L_c)$. There is consistent reduction in the yield strength with increase in the aspect ratio, $r_a(L_c)$. A summary of mean values, standard deviation and coefficient of variation for the yield strength under each category of aspect ratio, $r_a(L_c)$ across the $I_b/I_c(I_b)$ ratio is provided in Table A1.13. There is lower variability of the yield strength for each sample category based on aspect ratio while overall variability is very high. The Cov ranges from 6.51% to 9.43% for linearised curve points and 7.47% to 10.26% for the actual curve points. The overall Cov for all the samples altogether is 55.91% for the linearised curve points and 58.63% for the actual curve points.

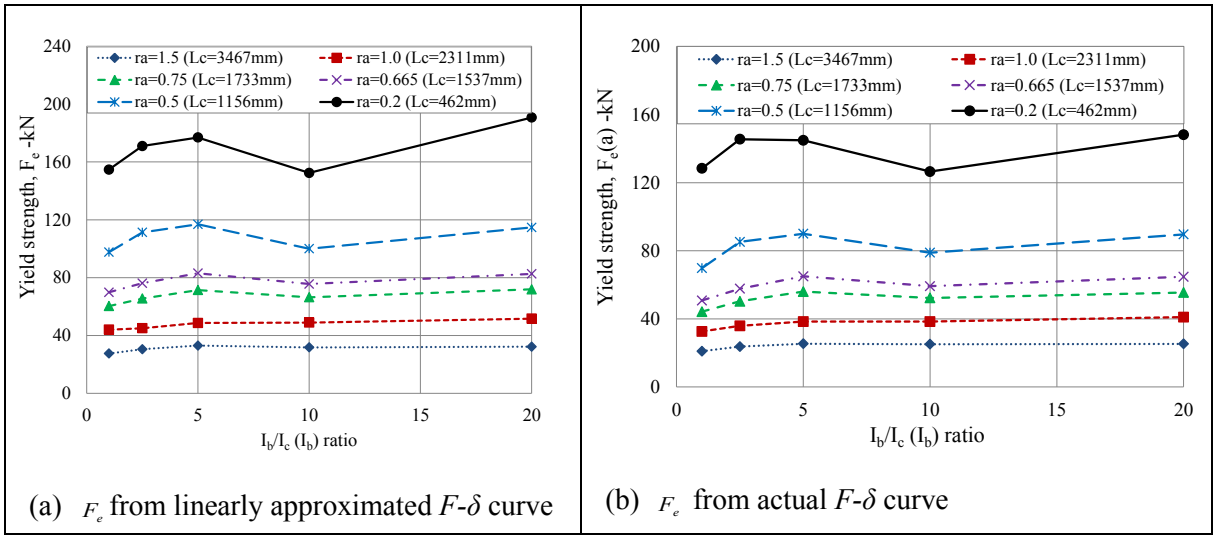

(a) F_e from linearly approximated *F-δ* curve (b) F_e from actual *F-δ* curve

Figure A1.19: Typical variation of the yield strength with the $I_b/I_c(I_b)$ ratio for Case B

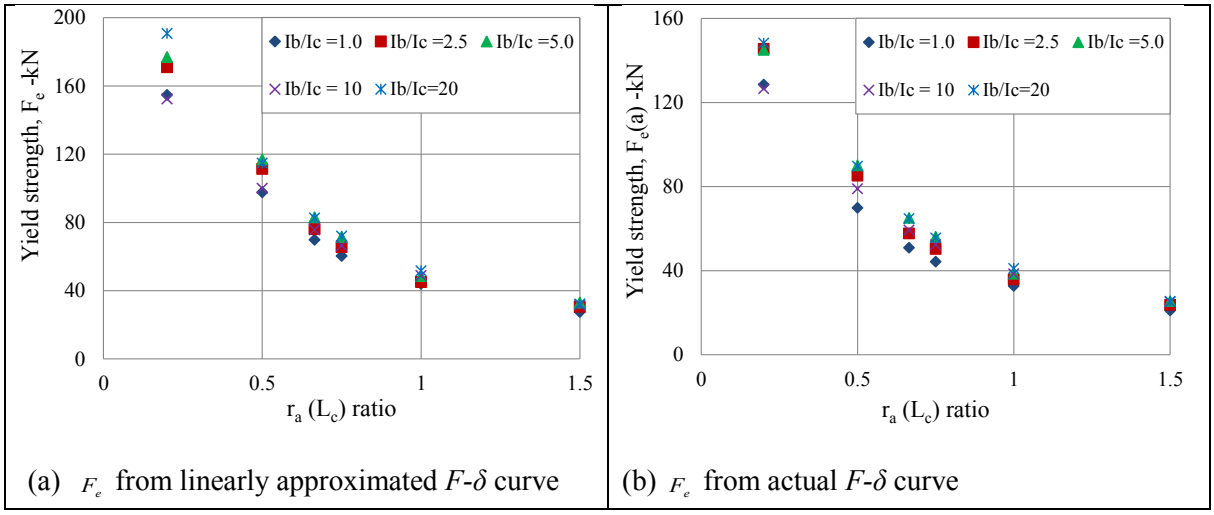

(a) F_e from linearly approximated *F-δ* curve (b) F_e from actual *F-δ* curve

Figure A1.20: Typical variation of the yield strength with the aspect ratio, $r_a(L_c)$ for Case B

Table A1.13: Yield strength mean values, standard deviation and coefficient of variation for each aspect ratio, $r_a(L_c)$ sample category

Sample category	***F*e from linearly approximated *F-δ* curve**			***F*e (a) from the actual *F-δ* curve**		
	Mean (kN)	Std dev	Cov	Mean (kN)	Std dev	Cov
B_{i1}	31.0	2.15	0.0693	24.1	1.86	0.0774
B_{i2}	47.6	3.10	0.0651	37.3	3.17	0.0850
B_{i3}	67.1	4.76	0.0710	51.7	4.78	0.0926
B_{i4}	77.4	5.50	0.0711	59.5	5.84	0.0981
B_{i5}	108.1	8.76	0.0811	82.7	8.49	0.1026
B_{i6}	169.1	15.95	0.0943	138.7	10.37	0.0747
B_{ij}*	83.4	46.63	0.5591	65.7	38.49	0.5863

*Overall results

(b) Yield deformation (δ_e)results and discussions for Case B

Results from the numerical analysis for the yield deformations are plotted against the $I_b/I_c(I_b)$ ratio and aspect ratio, $r_a(L_c)$ as shown in Figure A1.21. There is a general reduction in the yield deformation with increase in the $I_b/I_c(I_b)$ ratio while the yield deformation increases with increase in the aspect ratio, $r_a(L_c)$.

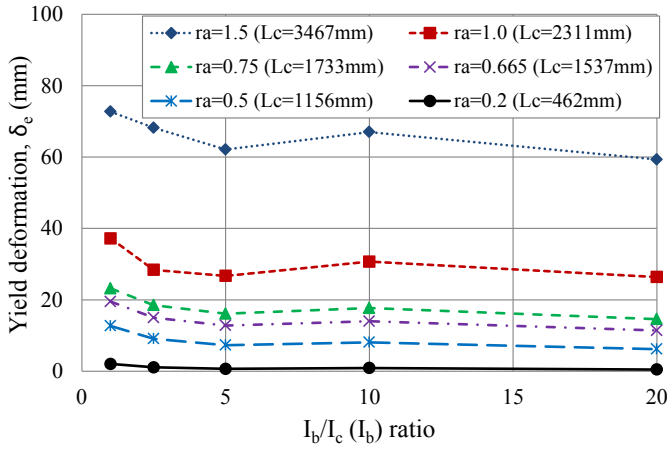

(a) Variation of the yield deformation with the $I_b/I_c(I_b)$ ratio

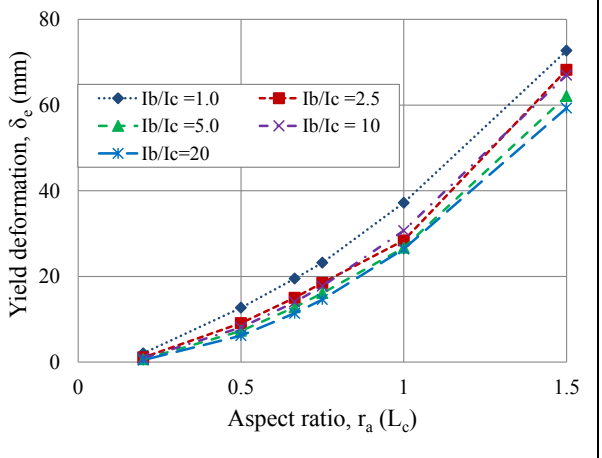

(b) Variation of the yield deformation with the aspect ratio, $r_a(L_c)$

Figure A1.21: Typical variation of the yield deformation with $I_b/I_c(I_b)$ ratio and aspect ratio, $r_a(L_c)$ for Case B

(c) Ultimate strength (F_u) results and discussions for Case B

Results for the ultimate strength variation with $I_b/I_c(I_b)$ ratio for Case B samples are shown in Figure A1.22. With minimal variability within each aspect ratio category, there is a gradual increase in the ultimate strength with increase in the $I_b/I_c(I_b)$. Figure A1.23 illustrates the scatter of the ultimate strength across various values of the aspect ratio of the frame, $r_a(L_c)$. There is consistent reduction in the ultimate strength across the aspect ratio, $r_a(L_c)$. A summary of mean values, standard deviation and coefficient of variation for the ultimate strength under each category of aspect ratio, $r_a(L_c)$ across the $I_b/I_c(I_b)$ ratio is provided in Table A1.14. There is lower variability of the yield strength for each sample category based on aspect ratio while overall variability is very high. Cov ranges from 2.96% to 7.03% for linearised curve points and 3.75% to 7.14% for the actual curve points. The overall Cov for all the samples altogether is 56.13% for the linearised curve points and 55.74% for the actual curve points

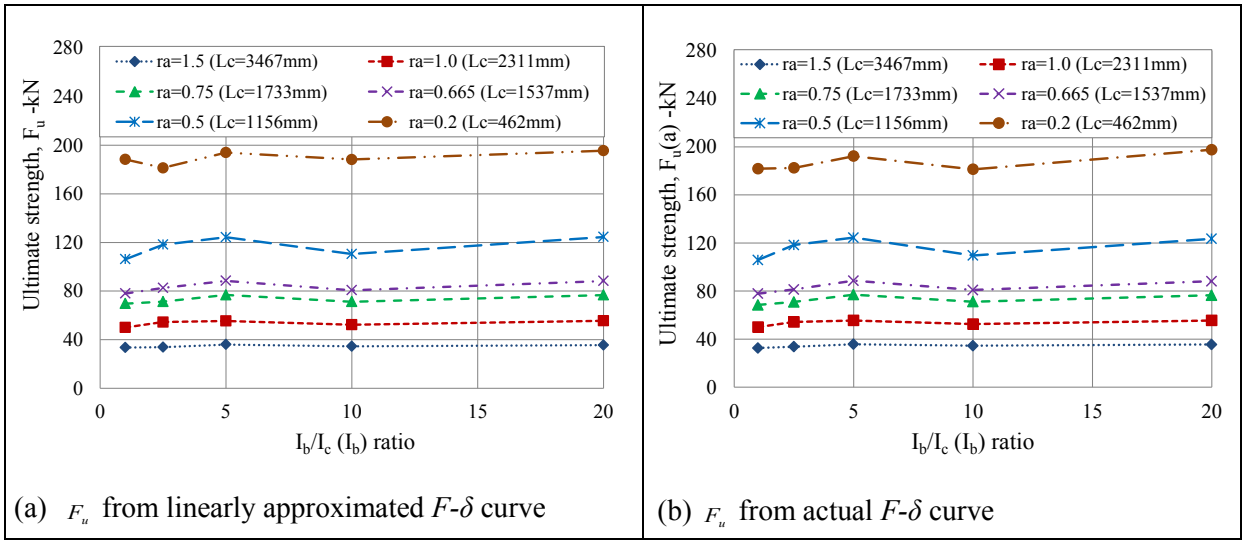

(a) F_u from linearly approximated *F-δ* curve

(b) F_u from actual *F-δ* curve

Figure A1.22: Typical variation of the ultimate strength with $I_b/I_c(I_b)$ ratio for Case B

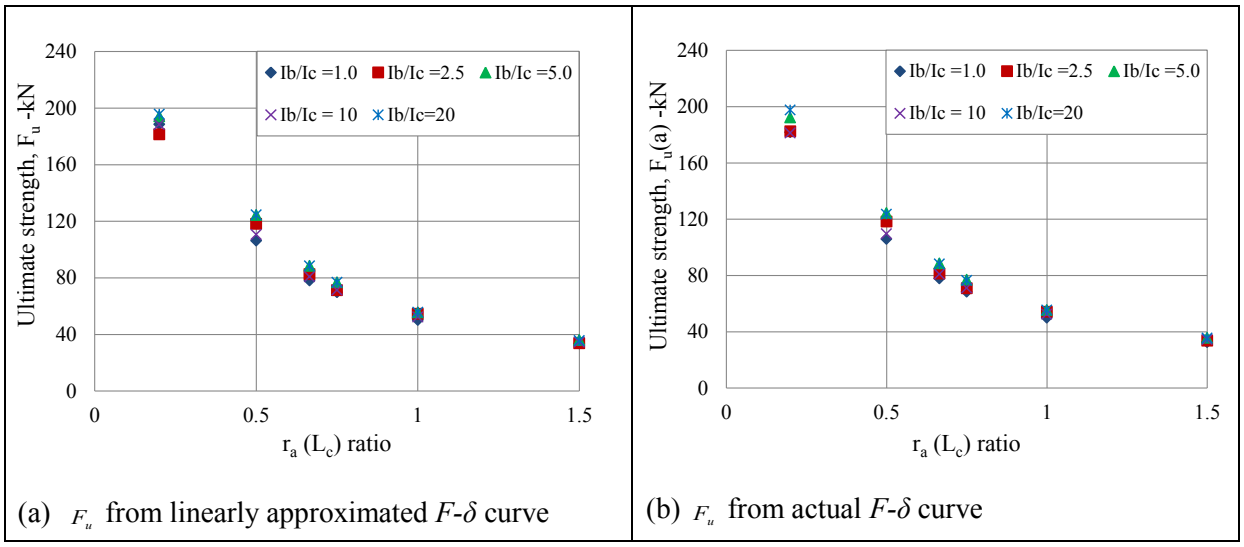

(a) F_u from linearly approximated *F-δ* curve

(b) F_u from actual *F-δ* curve

Figure A1.23: Typical variation of the ultimate strength with aspect ratio, $r_a(L_c)$ for Case B

Table A1.14: Ultimate strength mean values, standard deviation and coefficient of variation for each aspect ratio, $r_a(L_c)$ sample category

Sample category	***F*u from linearly approximated *F-δ* curve**			***F*u (a) from the actual *F-δ* curve**		
	Mean (kN)	Std dev	Cov	Mean (kN)	Std dev	Cov
B_{i1}	34.7	1.07	0.0310	34.4	1.29	0.0375
B_{i2}	53.6	2.34	0.0438	53.5	2.33	0.0435
B_{i3}	73.1	3.36	0.0459	72.8	3.78	0.0520
B_{i4}	83.6	4.63	0.0554	83.4	4.77	0.0572
B_{i5}	116.7	8.21	0.0703	116.4	8.31	0.0714
B_{i6}	189.5	5.61	0.0296	187.1	7.42	0.0397
B_{ij}*	91.9	51.57	0.5613	91.3	50.87	0.5574

*Overall results

(d) Ultimate deformation (δ_u) results and discussions for Case B

The ultimate deformation results from the numerical analyses are plotted against the $I_b/I_c(I_b)$ ratio and the aspect ratio, $r_a(L_c)$ as shown in Figure A1.24. Except for samples with aspect ratio, $r_a(L_c)$ of 1.5, all the other samples show minimal change with increase in $I_b/I_c(I_b)$ ratio. There is increase in the ultimate deformation with increase in the aspect ratio, $r_a(L_c)$ (see Figure A1.24b).

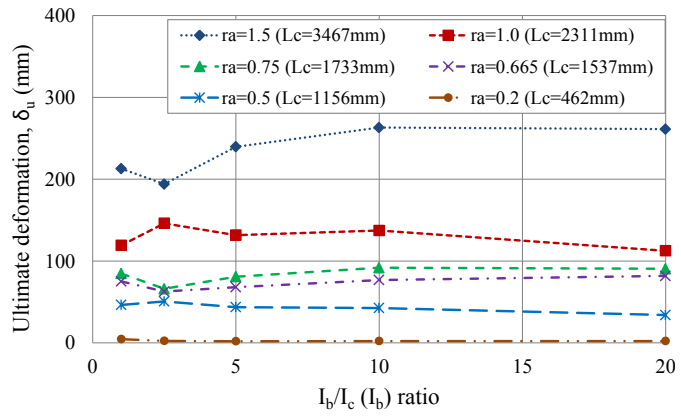

(a) Variation of the ultimate deformation with the $I_b/I_c(I_b)$ ratio

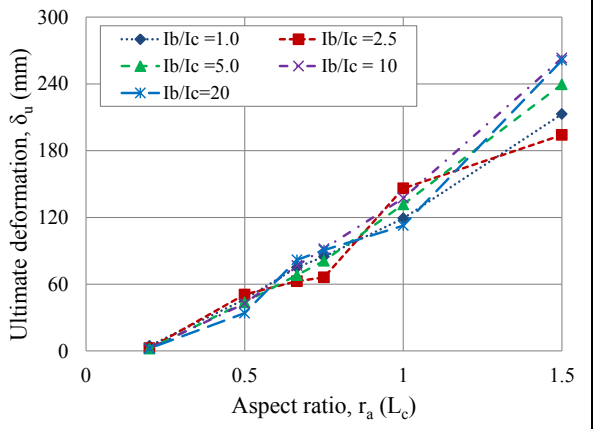

(b) Variation of the ultimate deformation with the aspect ratio, $r_a(L_c)$

Figure A1.24: Typical ultimate deformation variation with $I_b/I_c(I_b)$ ratio and aspect ratio, $r_a(L_c)$ for Case B

Case C numerical results and discussions

Case C numerical simulations involve bare frames with constant second moment of area for the beam (I_b = 46.2 x10^8 mm^4) and constant column height (L_c = 1537mm). The numerical results and discussions for each of the four lateral strength resistance indicators for the frames (F_e, δ_e, F_u and δ_u) are summarised in subsequent paragraphs.

(a) Yield strength (F_e)results and discussions for Case C

The yield strength for the frame across various ratios of $I_b/I_c(I_c)$ are given in Figure A1.25. While there is inconsistent variability in the yield strength with increase in the $I_b/I_c(I_c)$ ratio for $I_b/I_c(I_c) < 5.0$, there is a general reduction in the yield strength with increase in the $I_b/I_c(I_c)$ ratio. Figure A1.26 illustrates the scatter of the yield strength across various values of the aspect ratio, $r_a(L_b)$. Despite the variability in the scatter, there is gradual reduction in the yield strength across the aspect ratio, $r_a(L_b)$. A summary of mean values, standard deviation and coefficient of variation for the yield strength under each category of aspect ratio, $r_a(L_b)$ across the $I_b/I_c(I_c)$ ratio is provided in Table A1.15. There is some variability of the yield strength for both the sample categories based on aspect ratio and all the samples altogether. The Cov ranges from 5.16% to 21.94% for linearised curve points and 4.39% to 22.10% for the actual curve points. The overall Cov for all the samples altogether is 23.46% for the linearised curve points and 22.64% for the actual curve points.

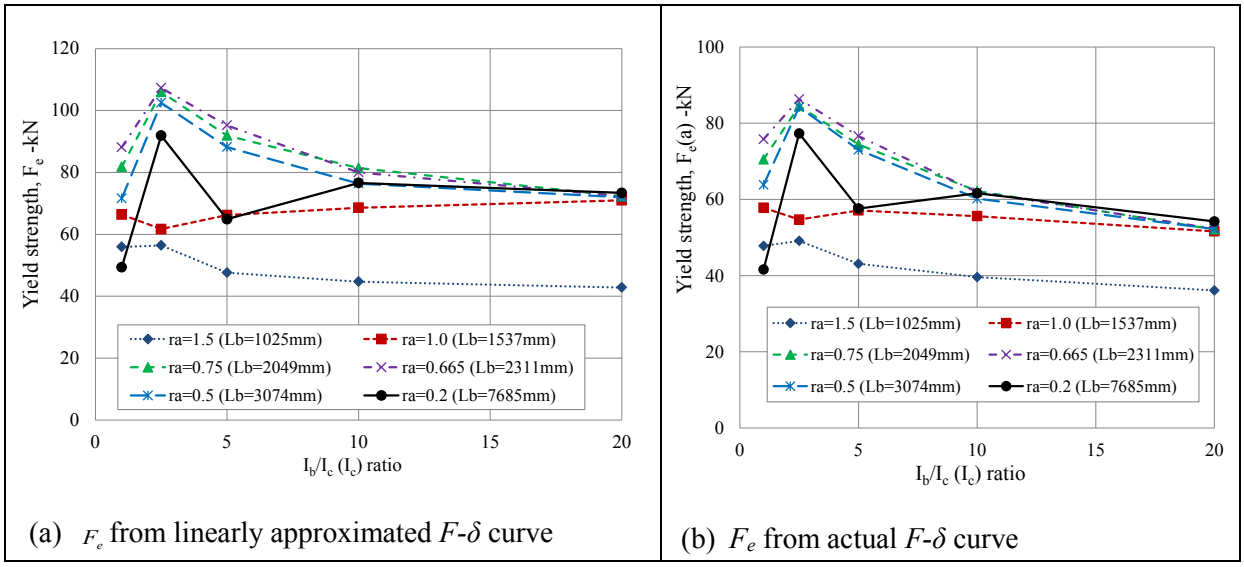

(a) F_e from linearly approximated *F-δ* curve (b) F_e from actual *F-δ* curve

Figure A1.25: Typical variation of the yield strength with the $I_b/I_c(I_c)$ ratio for Case C

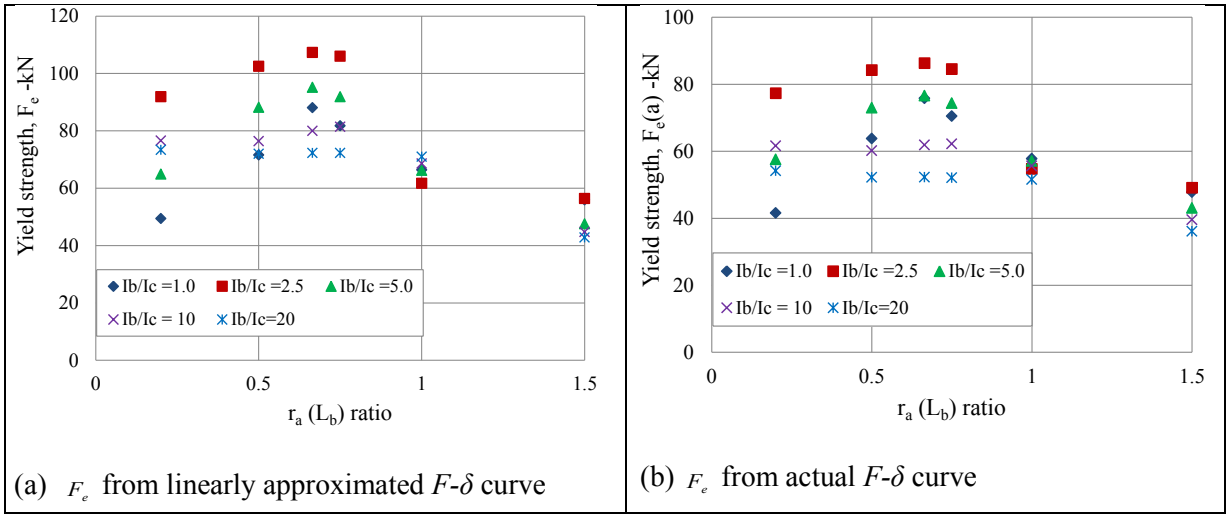

(a) F_e from linearly approximated *F-δ* curve (b) F_e from actual *F-δ* curve

Figure A1.26: Typical variation of the yield strength with the aspect ratio, $r_a(L_b)$ for Case C

Table A1.15: Yield strength mean values, standard deviation and coefficient of variation for each aspect ratio, $r_a(L_b)$ sample category

Sample category	F_e from linearly approximated *F-δ* curve			F_e (a) from the actual *F-δ* curve		
	Mean (kN)	Std dev	Cov	Mean (kN)	Std dev	Cov
C_{i1}	49.5	6.33	0.1279	43.1	5.46	0.1266
C_{i2}	66.8	3.44	0.0516	55.4	2.43	0.0439
C_{i3}	86.7	12.84	0.1481	68.7	12.28	0.1786
C_{i4}	88.6	13.54	0.1528	70.6	13.42	0.1901
C_{i5}	82.1	13.21	0.1608	66.7	12.32	0.1847
C_{i6}	71.2	15.63	0.2194	58.5	12.92	0.2210
C_{ij}*	74.2	17.40	0.2346	60.5	13.70	0.2264

*Overall results

(b) Yield deformation (δ_e) results and discussions considering I_b and L_c as constants

Yield deformation results from the numerical analyses for Case C samples are plotted against the $I_b/I_c(I_c)$ ratio and the aspect ratios, $r_a(L_b)$ as shown in Figure A1.27. Apart from samples with $r_a(L_b)$ = 0.2 (especially sample C_{26}), there is consistent increase in the yield deformation with increase in the $I_b/I_c(I_c)$ ratio. The yield deformation reduces with increase in the aspect ratio, $r_a(L_b)$.

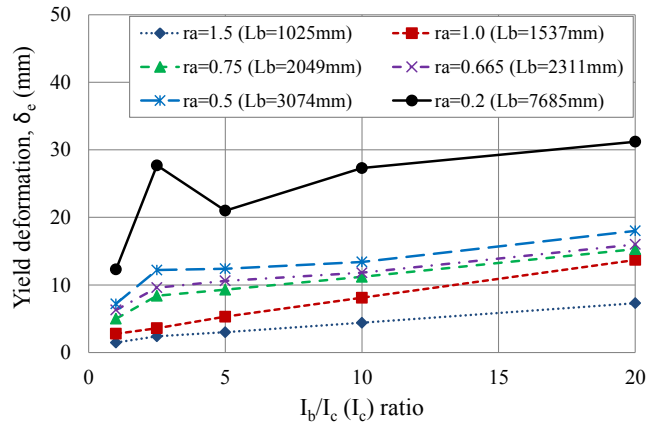

(a) Variation of the yield deformation with the $I_b/I_c(I_c)$ ratio

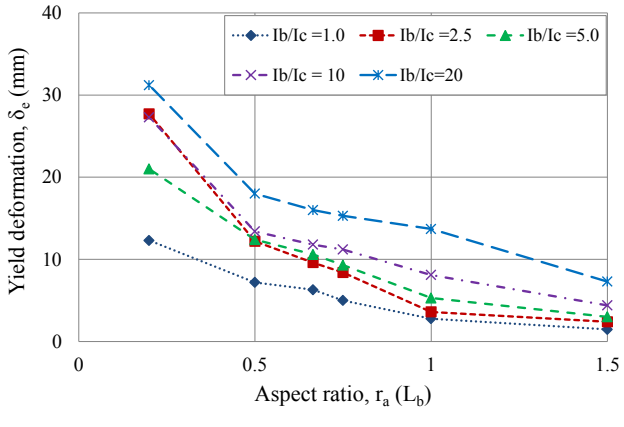

(b) Variation of the yield deformation with the aspect ratio, $r_a(L_b)$

Figure A1.27: Typical variation of the yield deformation with $I_b/I_c(I_c)$ and aspect ratio, $r_a(L_b)$ for Case C

(c) Ultimate strength (F_u) results and discussions for Case C

The results of the ultimate strength variation with the $I_b/I_c(I_c)$ ratios are presented in Figure A1.28. Except for samples with $r_a(L_b)$ of 1.5, there is a gradual reduction in the ultimate strength with increase in the $I_b/I_c(I_c)$ ratio, where the values seem to converge to a common strength for very high $I_b/I_c(I_c)$ ratios. Figure A1.29 illustrates the scatter of the ultimate strength across various values of the aspect ratio, $r_a(L_b)$. There is gradual or no reduction in the ultimate strength across the aspect ratio, $r_a(L_b)$. A summary of mean values, standard deviation and coefficient of variation for the ultimate strength under each category of aspect ratio, $r_a(L_b)$ across the $I_b/I_c(I_c)$ ratio is provided in Table A1.16. There is considerable variability of the ultimate strength for both the sample categories based on aspect ratio and all the samples altogether. The Cov ranges from 1.0% to 16.29% for linearised curve points and 0.45% to 16.25% for the actual curve points. The overall Cov for all the samples altogether is 22.31% for the linearised curve points and 20.69% for the actual curve points.

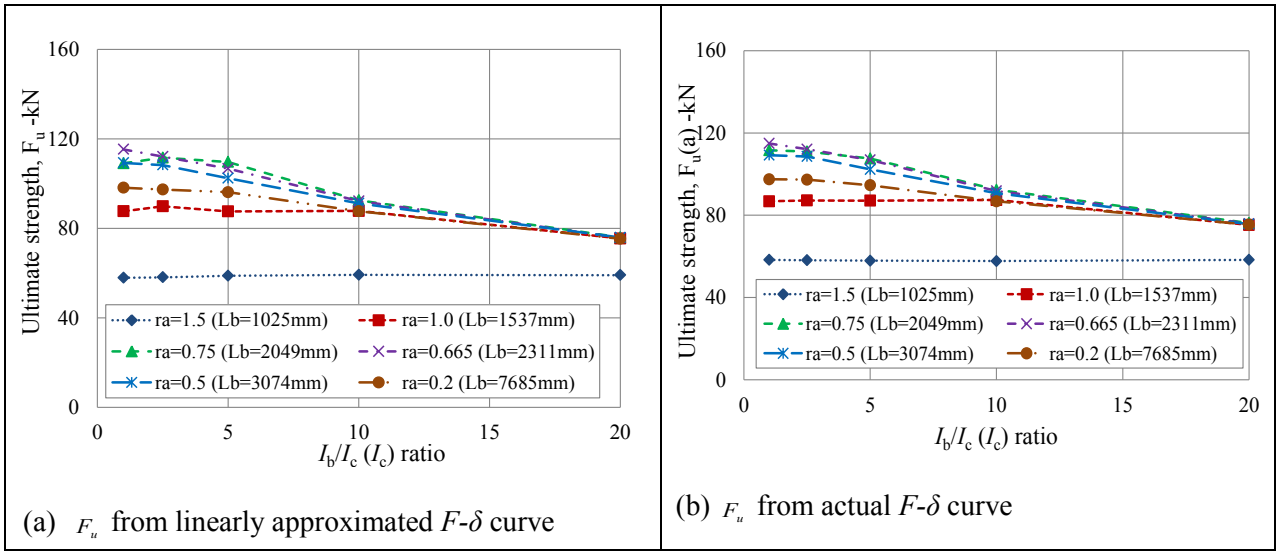

(a) F_u from linearly approximated *F-δ* curve

(b) F_u from actual *F-δ* curve

Figure A1.28: Typical variation of the ultimate strength with $I_b/I_c(I_c)$ ratio for Case C

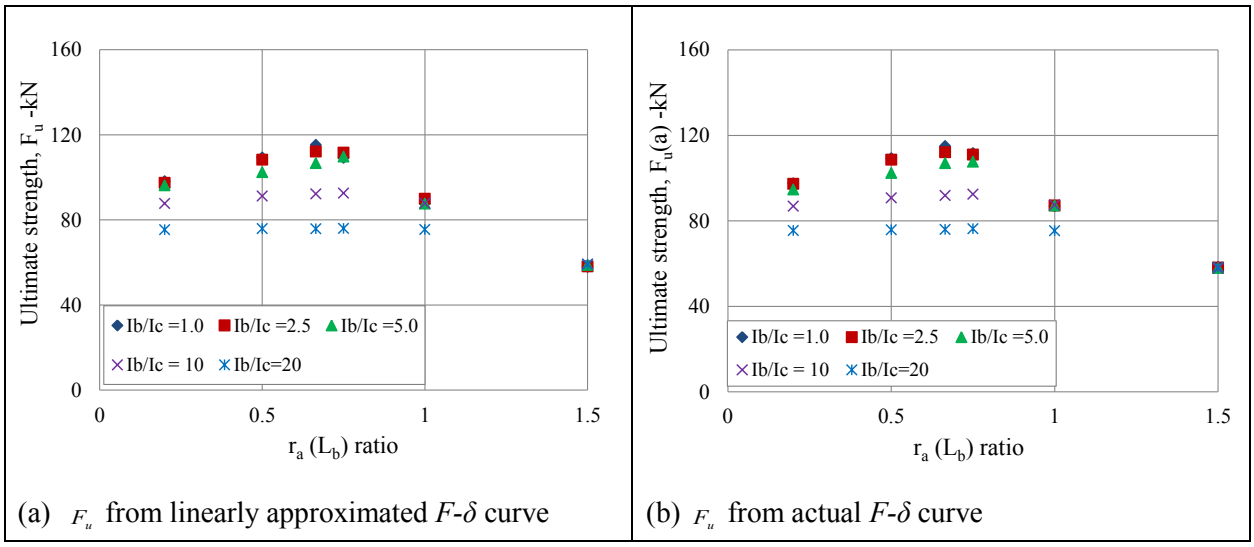

(a) F_u from linearly approximated *F-δ* curve

(b) F_u from actual *F-δ* curve

Figure A1.29: Typical variation of the ultimate strength with aspect ratio, $r_a(L_b)$ for Case C

Table A1.16: Ultimate strength mean values, standard deviation and coefficient of variation for each aspect ratio, $r_a(L_b)$ sample category

Sample category	***F*u from linearly approximated *F-δ* curve**			***F*u (a) from the actual *F-δ* curve**		
	Mean (kN)	Std dev	Cov	Mean (kN)	Std dev	Cov
C_{i1}	58.6	0.59	0.0100	58.1	0.26	0.0045
C_{i2}	85.7	5.78	0.0675	84.8	5.29	0.0624
C_{i3}	99.8	15.35	0.1538	99.8	15.31	0.1534
C_{i4}	100.4	16.36	0.1629	100.3	16.31	0.1625
C_{i5}	97.4	14.02	0.1439	97.3	14.18	0.1457
C_{i6}	91.0	9.67	0.1063	90.3	9.40	0.1041
C_{ij}*	88.8	18.18	0.2047	88.4	18.30	0.2069

*Overall results

(d) Ultimate deformation (δ_u) results and discussions for Case C

Ultimate deformation results from the numerical analyses for Case C samples are plotted against the $I_b/I_c(I_c)$ ratio and aspect ratio, $r_a(L_b)$ as shown in Figure A1.30. There is inconsistent variability in the trends of the ultimate deformation with either the $I_b/I_c(I_c)$ ratio for $I_b/I_c(I_c) < 5.0$. Nevertheless, there is general increase in the ultimate deformation for the increase in the $I_b/I_c(I_c)$ ratio. The ultimate deformation reduces with increase in the aspect ratio, $r_a(L_b)$.

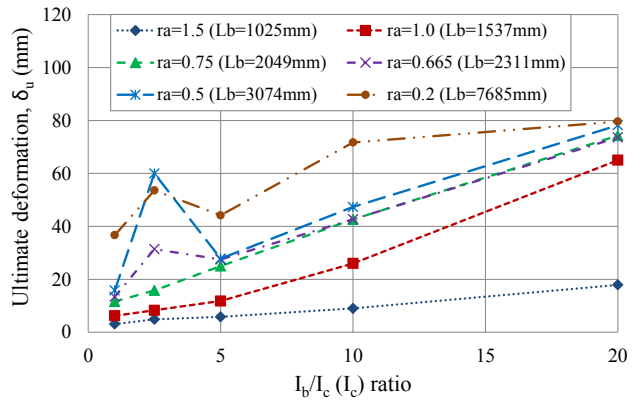

(a) Variation of the ultimate deformation with the $I_b/I_c(I_c)$ ratio

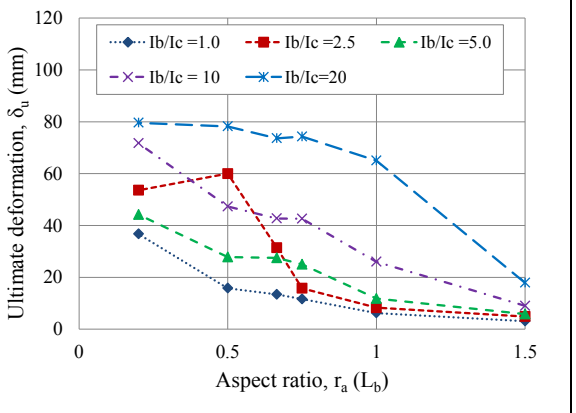

(b) Variation of the ultimate deformation with the aspect ratio, $r_a(L_b)$

Figure A1.30: Typical ultimate deformation variation with $I_b/I_c(I_c)$ and aspect ratio, $r_a(L_b)$ for Case C

Case D numerical results and discussions

Case D numerical simulations involve bare frames with constant second moment of area and length of the beam (I_b = 46.2x10^8 mm^4 and L_b = 2311 mm). The results and discussions for each of the four lateral strength resistance indicators for the frames (F_e, δ_e, F_u and δ_u) are summarised in subsequent paragraphs.

(a) Yield strength (F_e) results and discussions for Case D

The results of the yield strength with the $I_b/I_c(I_c)$ ratios are shown in Figure A1.31. Apart from samples with $r_a(L_c)$ = 0.2, there is a general reduction in the yield strength with increase in the $I_b/I_c(I_c)$ ratios. Figure A1.32 illustrates the scatter of the yield strength across various values of the aspect ratio, $r_a(L_c)$. There is reduction in the yield strength with increase in the aspect ratio, $r_a(L_c)$. A summary of mean values, standard deviation and coefficient of variation for the yield strength under each category of aspect ratio, $r_a(L_c)$ across the $I_b/I_c(I_c)$ ratio is provided in Table A1.17. There is some variability of the yield strength for both the sample categories based on aspect ratio and all the samples altogether. The Cov ranges from 10.99% to 32.17% for linearised curve points and 15.76% to 28.59% for the actual curve points. The overall Cov for all the samples altogether is 60.57% for the linearised curve points and 63.29% for the actual curve points.

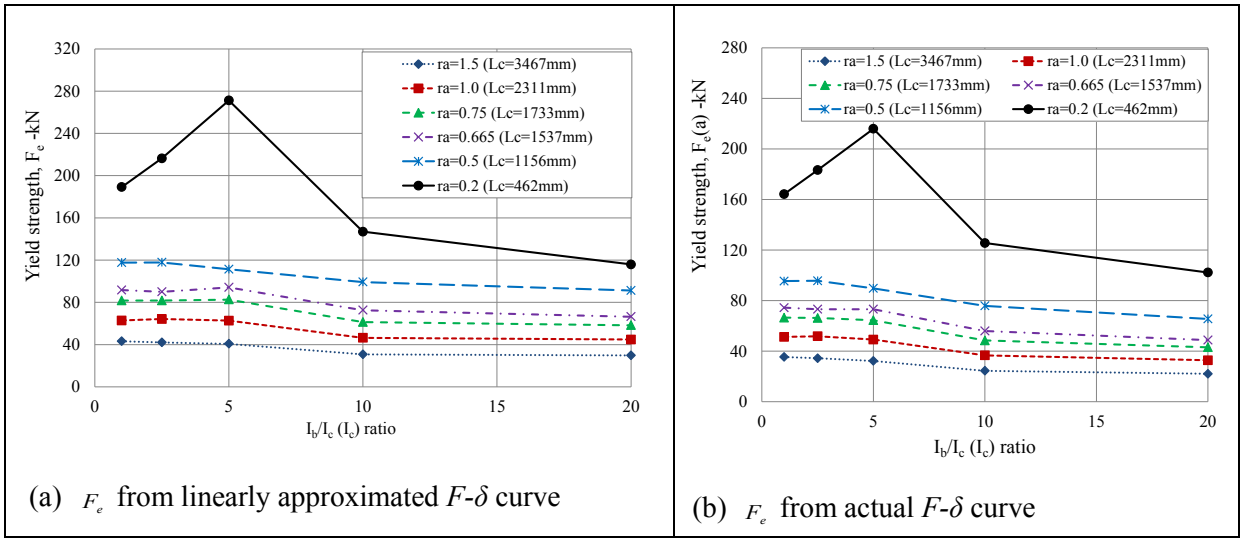

(a) F_e from linearly approximated *F-δ* curve

(b) F_e from actual *F-δ* curve

Figure A1.31: Typical variation of the yield strength with the $I_b/I_c(I_c)$ ratio for Case D

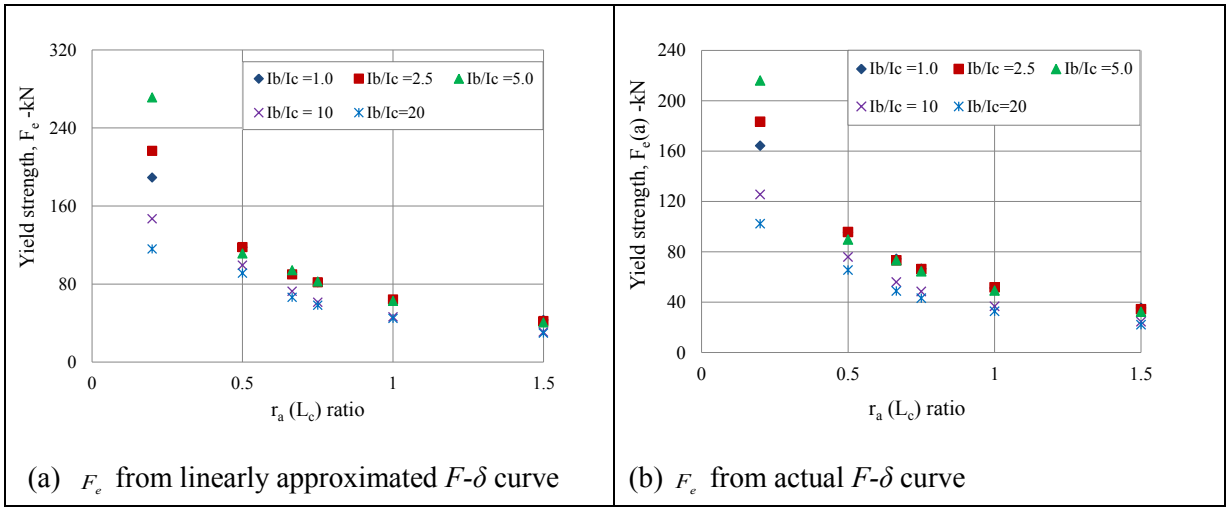

(a) F_e from linearly approximated *F-δ* curve

(b) F_e from actual *F-δ* curve

Figure A1.32: Typical variation of the yield strength with the aspect ratio, $r_a(L_c)$ for Case D

Table A1.17: Yield strength mean values, standard deviation and coefficient of variation for each aspect ratio, $r_a(L_c)$ sample category

Sample category	***F*e from linearly approximated *F-δ* curve**			***F*e (a) from the actual *F-δ* curve**		
	Mean (kN)	Std dev	Cov	Mean (kN)	Std dev	Cov
D_{i1}	37.2	6.49	0.1743	29.7	6.04	0.2032
D_{i2}	56.2	9.69	0.1725	44.4	8.93	0.2014
D_{i3}	73.1	12.21	0.1670	57.8	11.13	0.1926
D_{i4}	82.9	12.56	0.1515	65.1	11.90	0.1827
D_{i5}	107.4	11.80	0.1099	84.5	13.31	0.1576
D_{i6}	187.9	60.45	0.3217	158.3	45.26	0.2859
D_{ij}*	90.8	54.99	0.6057	73.3	46.38	0.6329

*Overall results

(b) ***Yield deformation (δ_e) results and discussions for Case D***

Yield deformation results from the numerical analyses for Case D samples are plotted against the $I_b/I_c(I_c)$ ratio and aspect ratio, $r_a(L_c)$ as shown in Figure A1.33. There is a steady increase in the yield deformation with increase in $I_b/I_c(I_c)$ ratio. The yield deformation increases with increase in the aspect ratio, $r_a(L_c)$.

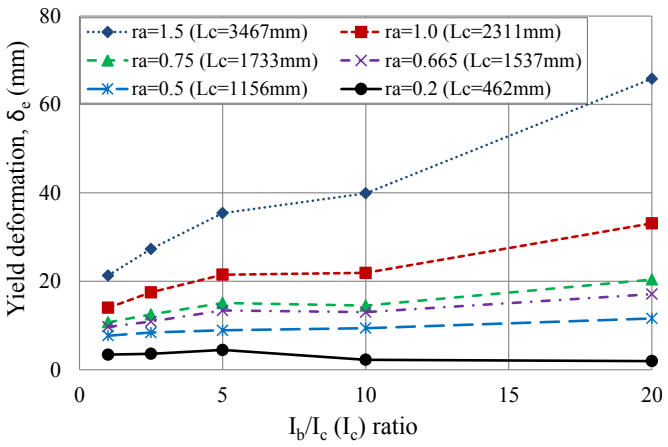

(a) Variation of the yield deformation with the $I_b/I_c(I_c)$ ratio

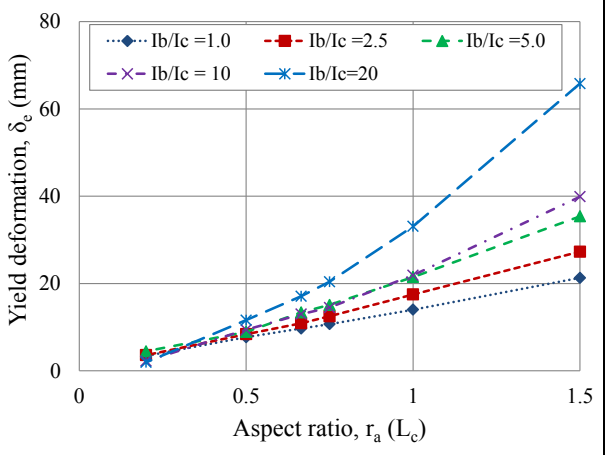

(b) Variation of the yield deformation with the aspect ratio, $r_a(L_c)$

Figure A1.33: Typical variation of the yield deformation with $I_b/I_c(I_c)$ and aspect ratio, $r_a(L_c)$ for Case D

(c) Ultimate strength (F_u) results and discussions for Case D

The results of the ultimate strength variation with the $I_b/I_c(I_c)$ ratios are shown in Figure A1.34. Apart from some samples from $r_a(L_c)$ of 0.2, there is a general decline in the ultimate strength with increase in the $I_b/I_c(I_c)$ ratio. Figure A1.35 illustrates the scatter of the ultimate strength across various values of the aspect ratio, $r_a(L_c)$. There is reduction in the yield strength with increase in the aspect ratio, $r_a(L_c)$. A summary of mean values, standard deviation and coefficient of variation for the yield strength under each category of aspect ratio, $r_a(L_c)$ across the $I_b/I_c(I_c)$ ratio is provided in Table A1.18. There is some variability in the ultimate strength for both the sample categories based on aspect ratio and all the samples altogether. The Cov ranges from 11.46% to 20.21% for linearised curve points and 11.31% to 19.70% for the actual curve points. The overall Cov for all the samples altogether is 64.72% for the linearised curve points and 64.64% for the actual curve points.

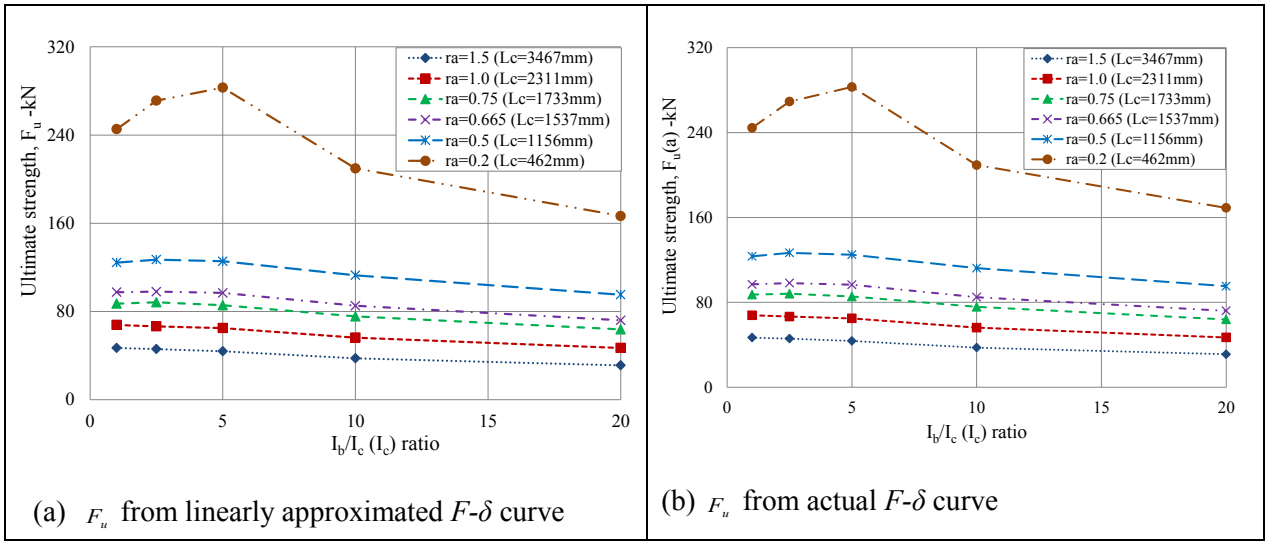

(a) F_u from linearly approximated *F-δ* curve

(b) F_u from actual *F-δ* curve

Figure A1.34: Typical variation of the ultimate strength with $I_b/I_c(I_c)$ ratio for Case D

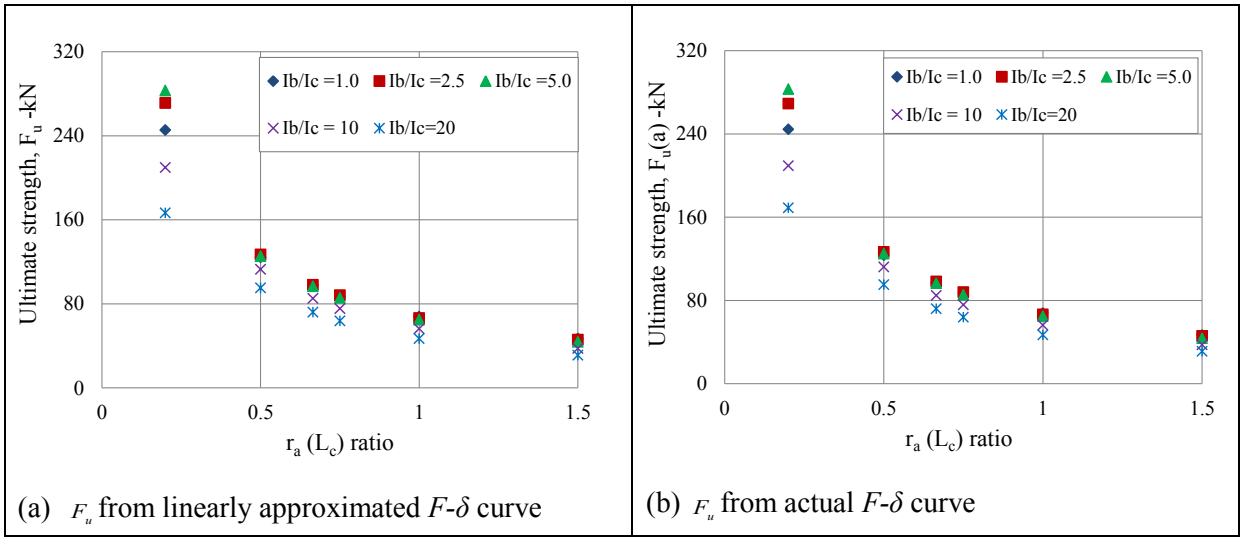

(a) F_u from linearly approximated *F-δ* curve

(b) F_u from actual *F-δ* curve

Figure A1.35: Typical variation of the ultimate strength with aspect ratio, $r_a(L_c)$ for Case D

Table A1.18: Ultimate strength mean values, standard deviation and coefficient of variation for each aspect ratio, $r_a(L_c)$ sample category

Sample category	***F*u from linearly approximated *F-δ* curve**			***F*u (a) from the actual *F-δ* curve**		
	Mean (kN)	Std dev	Cov	Mean (kN)	Std dev	Cov
D_{i1}	41.1	6.66	0.1622	40.9	6.62	0.1617
D_{i2}	60.5	8.82	0.1459	60.5	8.85	0.1463
D_{i3}	80.0	10.45	0.1305	80.1	10.32	0.1288
D_{i4}	89.9	11.33	0.1260	89.7	11.29	0.1258
D_{i5}	117.0	13.40	0.1146	116.5	13.18	0.1131
D_{i6}	235.2	47.53	0.2021	235.0	46.30	0.1970
D_{ij}*	103.9	67.27	0.6472	103.8	67.09	0.6464

*Overall results

(e) ***Ultimate deformation (δ_u) results and discussions for Case D***

Ultimate deformation results from the numerical analyses for Case D samples are plotted against the $I_b/I_c(I_c)$ ratio and aspect ratio, $r_a(L_c)$ as shown in Figure A1.36. There is variability in the trends of the ultimate deformation with either the $I_b/I_c(I_c)$ ratio or the aspect ratio, $r_a(L_c)$. Nevertheless, there is a general increase in the ultimate deformation with increase in the $I_b/I_c(I_c)$ ratio. The ultimate deformation increases with increase in the aspect ratio, $r_a(L_c)$.

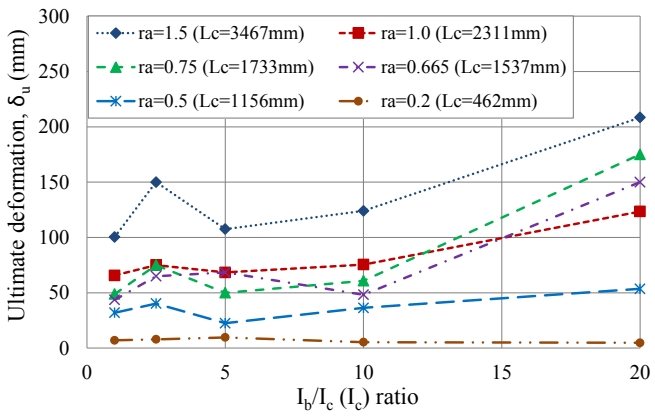

(a) Variation of the ultimate deformation with the $I_b/I_c(I_c)$ ratio

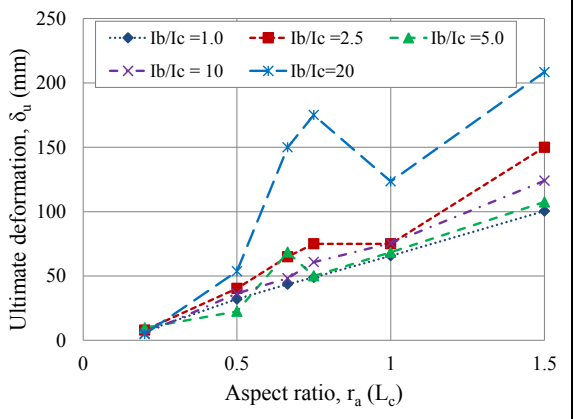

(b) Variation of the ultimate deformation with the aspect ratio, $r_a(L_c)$

Figure A1.36: Typical ultimate deformation variation with $I_b/I_c(I_c)$ and aspect ratio, $r_a(L_c)$ for Case D

Appendix A1.4: Calibration of the diagonal strut behaviour for pinned frames, Cases B-D

(a) Calibration of yield and ultimate strains for Case B

The mean values of the diagonal yield strains for Case B are plotted against the $I_b/I_c(I_b)$ ratio with the range in the yield strain for each data point indicated in Figure A1.37(a). Based on the similarity in the variation of the yield strain with $I_b/I_c(I_b)$ ratio to that of Case A, the expression used for Case A (equation 6.1) is adopted. Yield strain coefficient, ε_{der}, is:

$$\varepsilon_{der} = a_\varepsilon r_a^2(L_c) + b_\varepsilon r_a(L_c) + c_e \qquad \text{(A1.1)}$$

where a_e, b_e and c_e are coefficients for specific case and are defined as -0.003, 0.013 and -0.0019 respectively. The proposed analytical relationships show some correlation with typical values from the numerical data as shown in Figure A1.37.

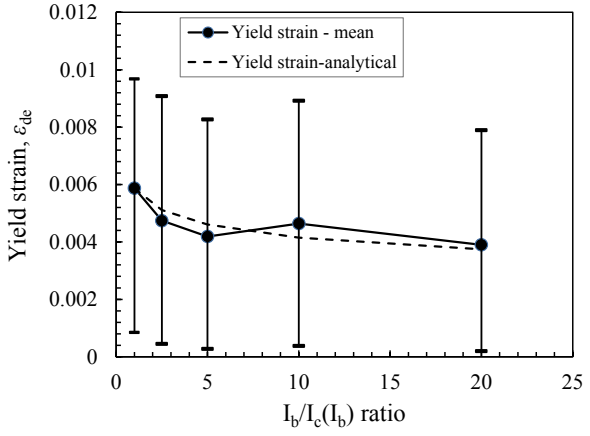

(a) Yield strain variation and relationship with the $I_b/I_c(I_b)$ ratio

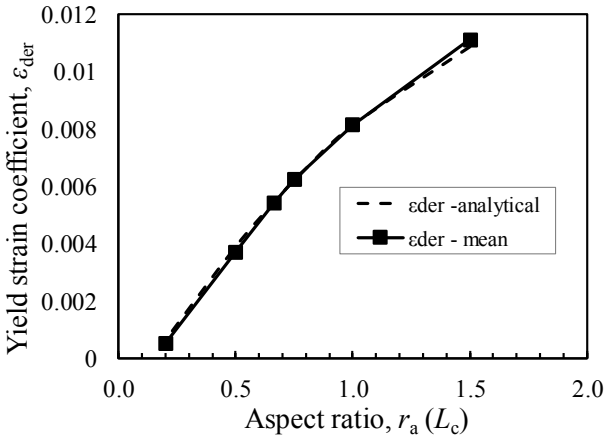

(b) Variation of the yield strain coefficient, ε_{er}, with the aspect ratio, $r_a(L_c)$

Figure A1.37: (a) Yield strain variation and relationship with the $I_b/I_c(I_b)$ ratio and, (b) the variation of the yield strain coefficient (ε_{er}) with the aspect ratio, $r_a(L_c)$ for Case B

(c) Calibration of ultimate strains for Case B

The mean values of the diagonal ultimate strains for Case B are plotted against the $I_b/I_c(I_b)$ ratio with the range in the ultimate strain for each data point indicated in Figure A1.38(a). Based on the similarity in the variation of the ultimate strain with $I_b/I_c(I_b)$ ratio to that of Case A, the expression used for Case A (equation 6.3) is adopted. Ultimate strain coefficient, ε_{dur}, is:

$$\varepsilon_{dur} = a_\varepsilon r_a^2(L_c) + b_\varepsilon r_a(L_c) + c_e \qquad \text{(A1.2)}$$

where a_e, b_e and c_e are coefficients for specific case and are defined as -0.003, 0.080 and -0.0128 respectively. The proposed analytical relationships show some correlation with typical values from the numerical data as shown in Figure A1.38.

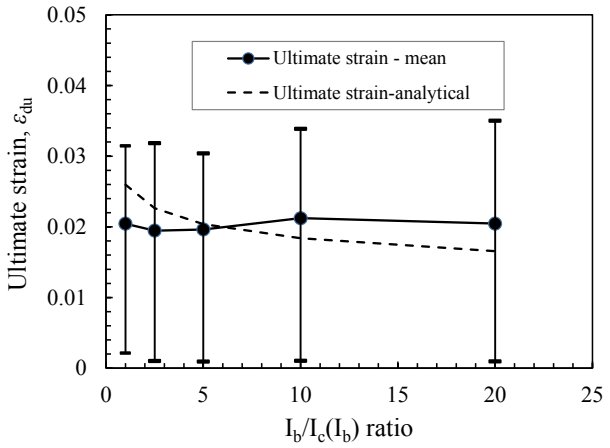

(a) Ultimate strain variation and relationship with the $I_b/I_c(I_b)$ ratio

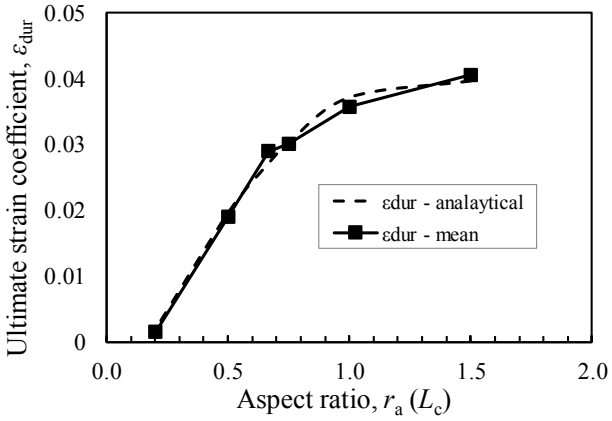

(b) Variation of the ultimate strain coefficient, ε_{ur}, with the aspect ratio, $r_a(L_c)$

Figure A1.38: (a) Ultimate strain variation and relationship with the $I_b/I_c(I_b)$ ratio and, (b) the variation of the ultimate strain coefficient (ε_{ur}) with the aspect ratio, $r_a(L_c)$ for Case B

(d) Calibration of yield strains for Case C

The mean values of the diagonal yield strains for Case C samples are plotted against the $I_b/I_c(I_c)$ ratio with the range in the yield strain for each data point indicated in Figure A1.39(a). Considering the pattern of variation of the mean yield strains, an analytical relationship is proposed to link the yield strains with the $I_b/I_c(I_c)$ ratio as follows:

$$\varepsilon_{de} = \varepsilon_{der}\left(\frac{I_b}{I_c}(I_c)\right)^{0.25} \qquad \text{(A1.3)}$$

where ε_{der} is the yield strain coefficient and is a function of the aspect ratio, $r_a(L_b)$, defined by equation 6.2 with the coefficients a_e, b_e and c_e as -0.0011, 0.0007 and 0.0020 respectively. The proposed analytical relationships show some correlation with typical values from the numerical data as shown in Figure A1.39.

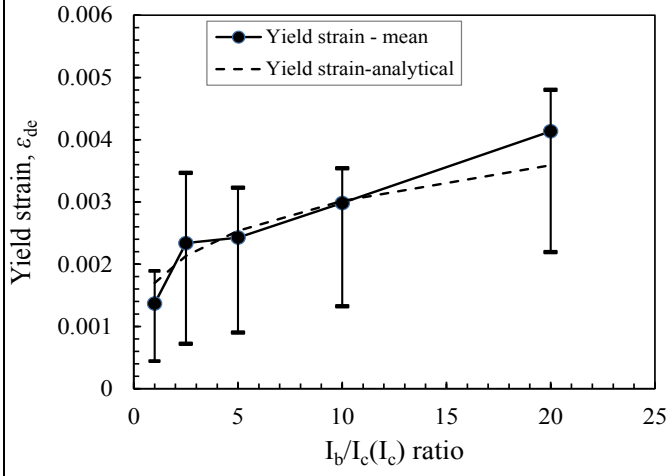

(a) Yield strain variation and relationship with the $I_b/I_c(I_c)$ ratio

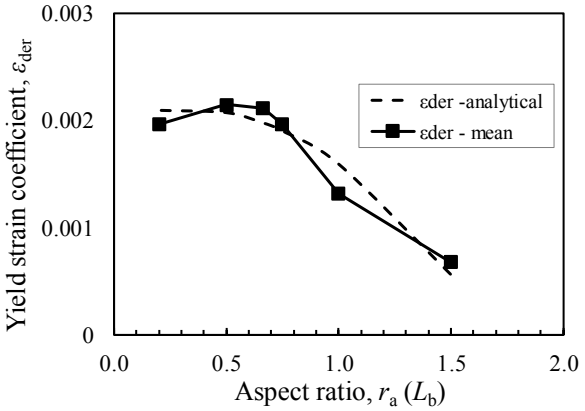

(b) Variation of the yield strain coefficient, ε_{er}, with the aspect ratio, $r_a(L_b)$

Figure A1.39:(a) Yield strain variation and relationship with the $I_b/I_c(I_c)$ ratio and, (b) the variation of the yield strain coefficient (ε_{er}) with the aspect ratio, $r_a(L_b)$ for Case C

(e) Calibration of ultimate strains for Case C

The mean values of the diagonal ultimate strains for Case C samples are plotted against the $I_b/I_c(I_c)$ ratio with the range in the ultimate strain for each data point indicated in Figure A1.40(a). Considering the pattern of variation of the mean ultimate strains, an analytical relationship is proposed to link the ultimate strains with the $I_b/I_c(I_c)$ ratio as follows:

$$\varepsilon_{du} = \varepsilon_{du0}\left(\frac{I_b}{I_c}(I_c)\right)^2 + \varepsilon_{du1}\left(\frac{I_b}{I_c}(I_c)\right) + \varepsilon_{dur} \qquad \text{(A1.4)}$$

where ε_{du0}, ε_{du1} and ε_{dur} are coefficients for specific case. For this case ε_{du0} and ε_{du1} are determined as 0.000006 and 0.0005 respectively. The coefficient ε_{dur} is a function of the aspect ratio, $r_a(L_b)$ and is defined by equation 6.4, with a_e, b_e and c_e established as -0.012, 0.0516 and 0.0007 respectively. The proposed analytical relationships show some correlation with typical values from the numerical data as shown in Figure A1.40.

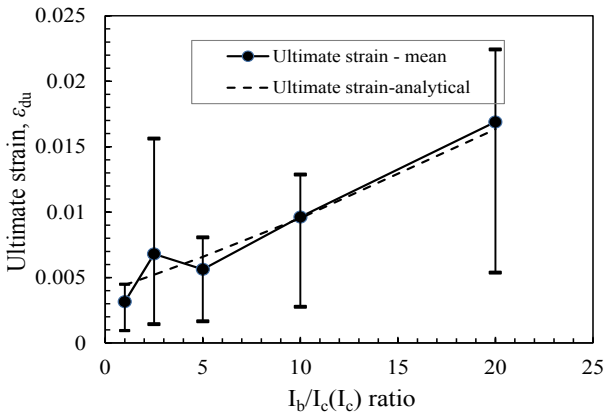

(a) Ultimate strain variation and relationship with the $I_b/I_c(I_c)$ ratio

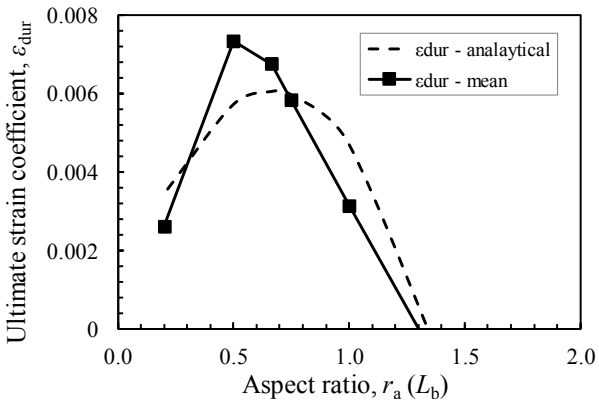

(b) Variation of the ultimate strain coefficient, ε_{ur}, with the aspect ratio, $r_a(L_b)$

Figure A1.40: (a) Ultimate strain variation and relationship with the $I_b/I_c(I_c)$ ratio and, (b) the variation of the ultimate strain coefficient (ε_{ur}) with the aspect ratio, $r_a(L_b)$ for Case C

(f) Calibration of yield strains for Case D

The mean values of the diagonal yield strains for Case D samples are plotted against the $I_b/I_c(I_c)$ ratio with the range in the yield strain for each data point indicated in Figure A1.41(a). Based on the similarity in the variation of the yield strain with $I_b/I_c(I_c)$ ratio to that of Case C, the expression used for Case C (equation A1.3) is adopted. The yield strain coefficient, ε_{dur}, is defined by equation A1.1 with the coefficients a_e, b_e and c_e as -0.002, 0.005 and 0.0001 respectively. The proposed analytical relationships show some correlation with typical values from the numerical data as shown in Figure A1.41.

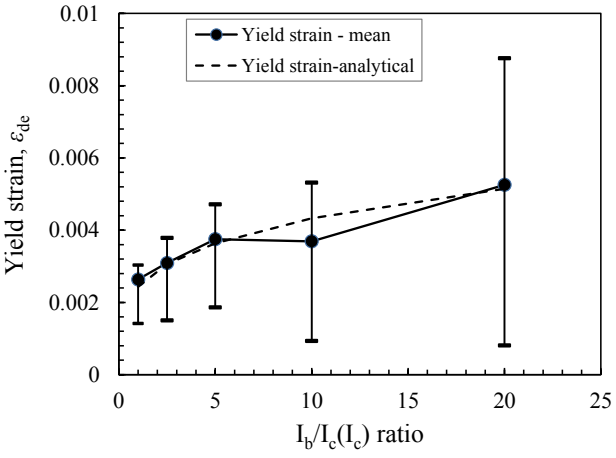

(a) Yield strain variation and relationship with the $I_b/I_c(I_c)$ ratio

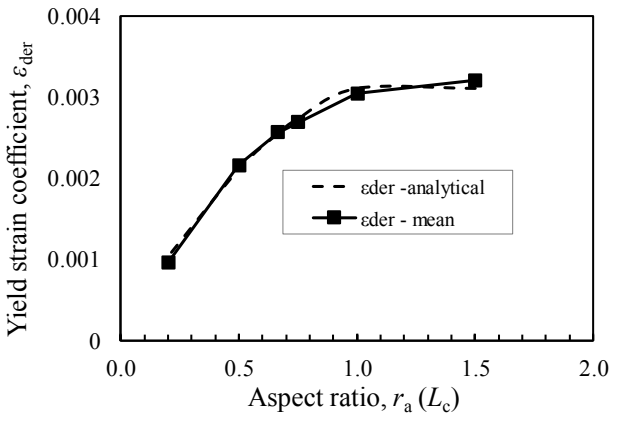

(b) Variation of the yield strain coefficient, ε_{er}, with the aspect ratio, $r_a(L_c)$

Figure A1.41: (a) Yield strain variation and relationship with the $I_b/I_c(I_c)$ ratio and, (b) the variation of the yield strain coefficient (ε_{er}) with the aspect ratio, $r_a(L_c)$ for Case D

(g) Calibration of ultimate strains for Case D

The mean values of the diagonal ultimate strains for Case D samples are plotted against the $I_b/I_c(I_c)$ ratio with the range in the ultimate strain for each data point indicated in Figure A1.42(a). Based on the similarity in the variation of the ultimate strain with $I_b/I_c(I_c)$ ratio to that of Case C, the expression used for Case C (equation A1.4) is adopted. The coefficients ε_{du0} and ε_{du1} are 0.00008 and -0.0008 respectively while ε_{dur} is a function of the aspect ratio and is defined by equation A1.2 for Case B with the coefficients a_e, b_e and c_e as -0.026, 0.055 and -0.0090 respectively. The proposed analytical relationships show some correlation with typical values from the numerical data as shown in Figure A1.42.

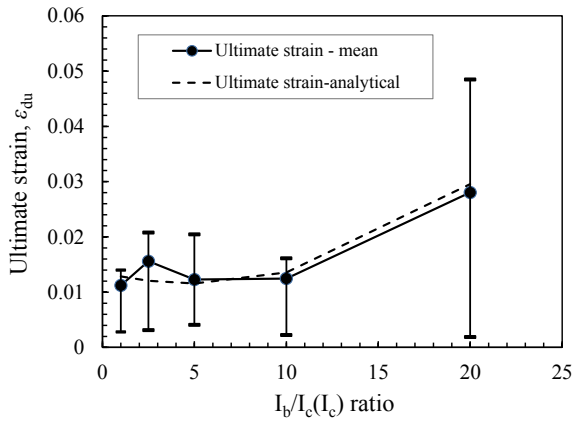

(a) Ultimate strain variation and relationship with the $I_b/I_c(I_c)$ ratio

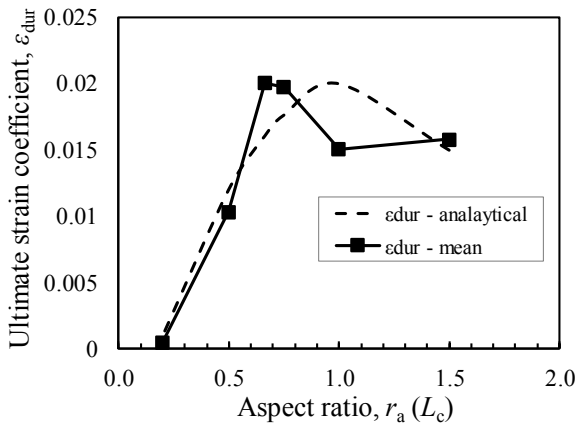

(b) Variation of the ultimate strain coefficient, ε_{ur}, with the aspect ratio, $r_a(L_c)$

Figure A1.42: (a) Ultimate strain variation and relationship with the $I_b/I_c(I_c)$ ratio and, (b) the variation of the ultimate strain coefficient (ε_{ur}) with the aspect ratio, $r_a(L_c)$ for Case D

Appendix A1.5: Diagonal strut yield strength and elastic stiffness calibration for pinned frames, Cases B - D

(a) Calibration of strut yield strength (F_{de}) and elastic stiffness (K_{de}) for Case B

The mean values of the diagonal yield strength for Case B samples are plotted against the $I_b/I_c(I_b)$ ratio with the range in the yield strength for each data point indicated in Figure A1.43(a). Due to the similarity in the pattern of the variation of the mean yield strength with the $I_b/I_c(I_b)$ ratio to that of Case A, the analytical relationship proposed for Case A is adopted (equation 6.6). Coefficient F_{der} is a function of the aspect ratio, $r_a(L_c)$ and is:

$$F_{der} = D_{fe1} r_a^2(L_c) + D_{fe} r_a(L_c) + D_{fe0} \qquad \text{(A1.5)}$$

where D_{fe1}, D_{fe} and D_{fe0} are constants and are established as 85.0 kN, -230.0 kN and 205.3 kN respectively for this case. The proposed analytical relationships show some correlation with typical values from the numerical data as shown in Figure A1.43.

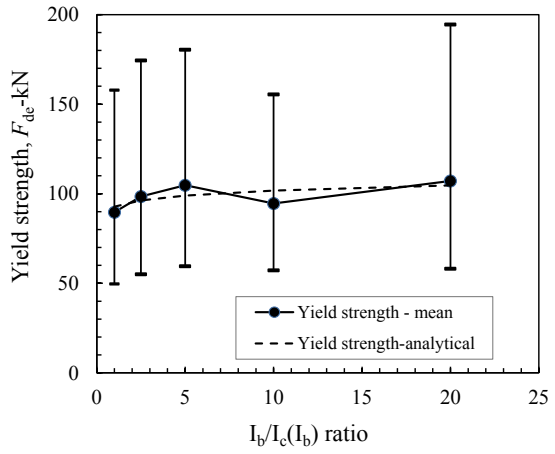

(a) Strut yield strength variation and relationship with the $I_b/I_c(I_b)$ ratio

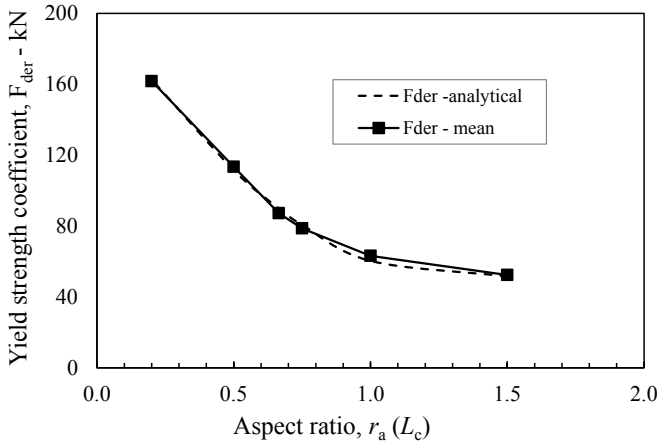

(b) Variation of the strut yield strength coefficient, F_{der}, with the aspect ratio, $r_a(L_c)$

Figure A1.43: (a) Diagonal strut yield strength variation and relationships with the $I_b/I_c(I_b)$ ratio and, (b) the variation of the strut yield strength coefficient with the aspect ratio, $r_a(L_c)$ for Case B

Mean values of the strut elastic stiffness calculated from both the numerical data and using elastic stiffness methods (equations 5.37 and 5.41) for Case B samples are plotted against the $I_b/I_c(I_b)$ ratio and the aspect ratio, $r_a(L_c)$ as shown in Figure A1.44. The variation of the elastic stiffness is similar for both methods of calculation, with that established using elastic stiffness being consistently higher than the numerical value except for the $I_b/I_c(I_b)$ ratio of 20.

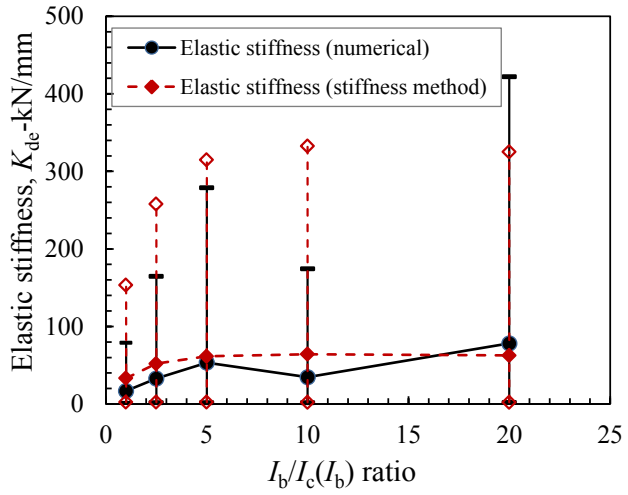

(a) Strut elastic stiffness variation with the $I_b/I_c(I_b)$ ratio

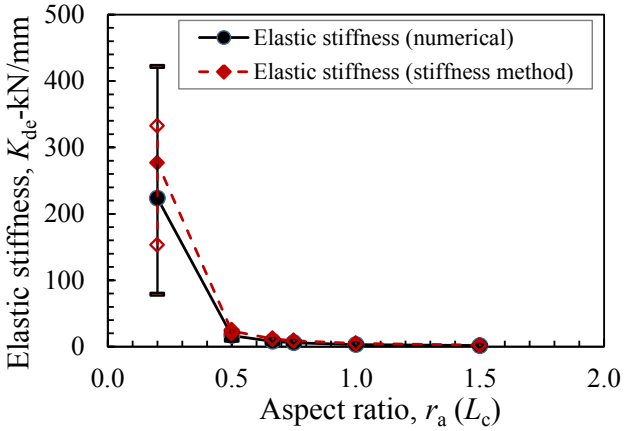

(b) Strut elastic stiffness variation with the aspect ratio, $r_a(L_c)$

Figure A1.44: (a) Diagonal strut elastic stiffness variation with the $I_b/I_c(I_b)$ ratio and, (b) diagonal strut elastic stiffness variation with the aspect ratio, $r_a(L_c)$ for Case B

The ratio of the elastic stiffness obtained from the numerical data to the elastic stiffness obtained using the stiffness method, K_{eF}, for each data point is established using equation 6.5. The variation of the elastic stiffness ratio K_{eF} is plotted against the $I_b/I_c(I_b)$ ratio as shown in Figure A1.45. Considering the similarity in the pattern of variation of the elastic stiffness ratio with the $I_b/I_c(I_b)$ ratio to that of Case A, equation 6.8 is adopted. The elastic stiffness ratio coefficient, K_{er} is a function of the aspect ratio, $r_a(L_c)$ and is defined as follows:

$$K_{er} = A_{ke} r_a(L_c) + K_{er0} \tag{A1.6}$$

where A_{ke} and K_{er0} are constants and are determined as -0.040 and 0.5276 respectively. The proposed analytical relationships show some correlation with typical values from the numerical data as shown in Figure A1.45.

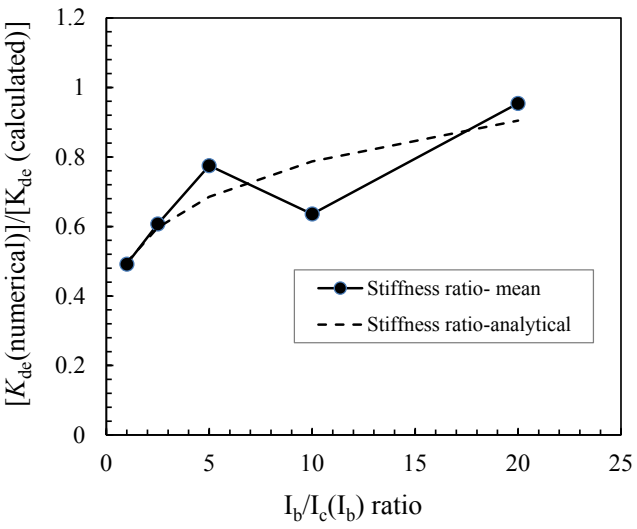

(a) Strut elastic stiffness ratio variation with the $I_b/I_c(I_b)$ ratio

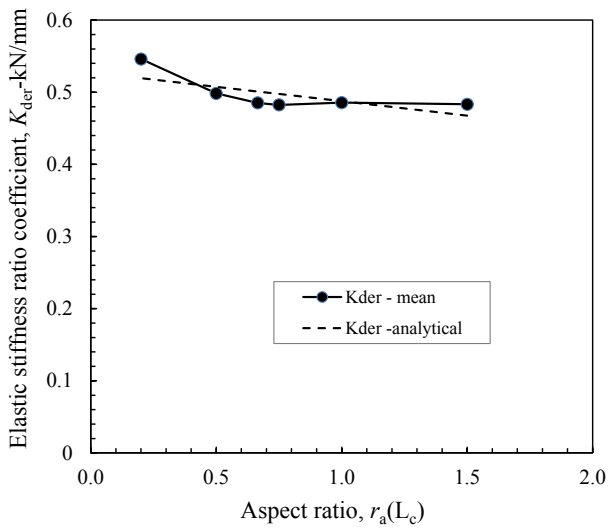

(b) Variation of the strut elastic stiffness ratio coefficient, K_{der}, with the aspect ratio, $r_a(L_c)$

Figure A1.45: (a) Diagonal strut elastic stiffness ratio variation and relationships with the $I_b/I_c(I_b)$ ratio and, (b) the variation of the strut elastic stiffness ratio coefficient with the aspect ratio, $r_a(L_c)$ for Case B

(b) Calibration of strut yield strength (F_{de}) and elastic stiffness (K_{de}) for Case C

The mean values of the diagonal yield strength for Case C samples are plotted against the $I_b/I_c(I_c)$ ratio with the range in the yield strength for each data point indicated in Figure A1.46(a). Considering the pattern of variation of the mean yield strength for the diagonal, an analytical relationship is proposed to link the yield strength with the $I_b/I_c(I_c)$ ratio as follows:

$$F_{de} = F_{der}\left(\frac{I_b}{I_c}(I_c)\right)^{-0.15} \tag{A1.7}$$

where F_{der} is the strut yield strength coefficient dependent on the aspect ratio, $r_a(L_b)$ and is:

$$F_{der} = D_{fe1} r_a^2(L_b) + D_{fe} r_a(L_b) + D_{fe0} \tag{A1.8}$$

and D_{fe1}, D_{fe} and D_{fe0} are constants and are -70.0 kN, 130.0 kN and 72.4 kN respectively for this case. The proposed analytical relationships show some correlation with typical values from the numerical data as shown in Figure A1.46.

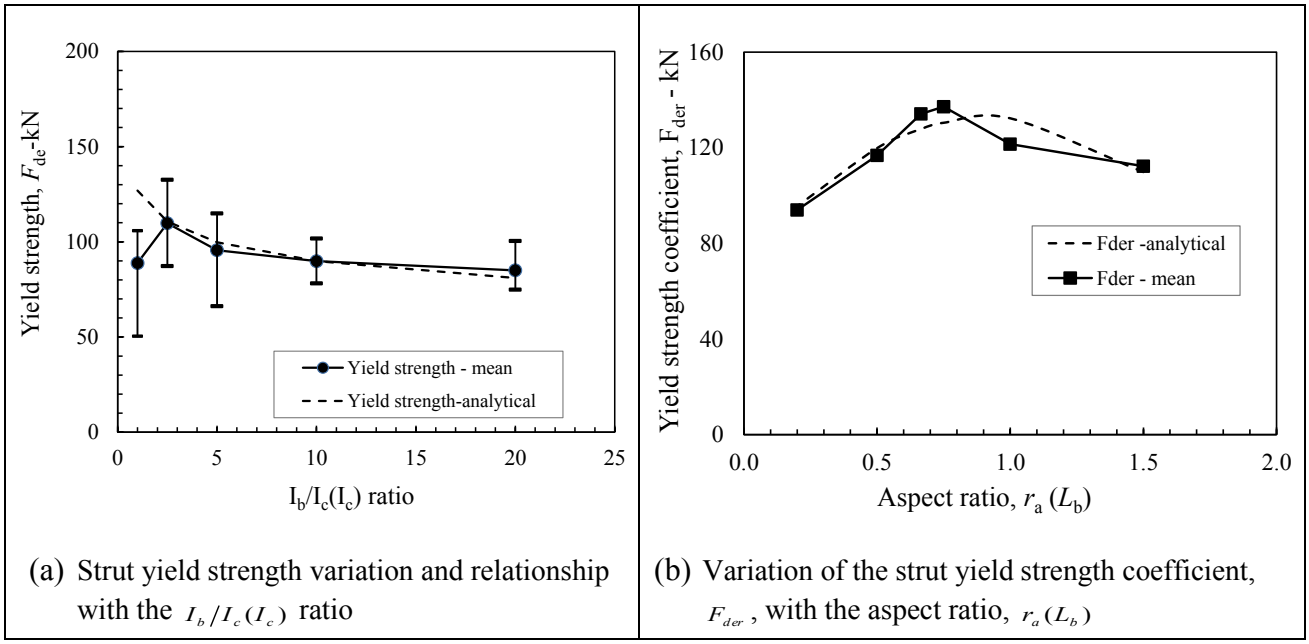

(a) Strut yield strength variation and relationship with the $I_b/I_c(I_c)$ ratio

(b) Variation of the strut yield strength coefficient, F_{der}, with the aspect ratio, $r_a(L_b)$

Figure A1.46: (a) Diagonal strut yield strength variation and relationships with the $I_b/I_c(I_c)$ ratio and, (b) the variation of the strut yield strength coefficient with the aspect ratio, $r_a(L_b)$ for Case C

Mean values of the strut elastic stiffness calculated from both the numerical data and using elastic stiffness methods for the Case C samples are plotted against the $I_b/I_c(I_c)$ ratio and the aspect ratio, $r_a(L_b)$ as shown in Figure A1.47. There is similar pattern in the variation of the elastic stiffness for both methods of calculation, with that established using elastic stiffness being consistently higher than the numerical value.

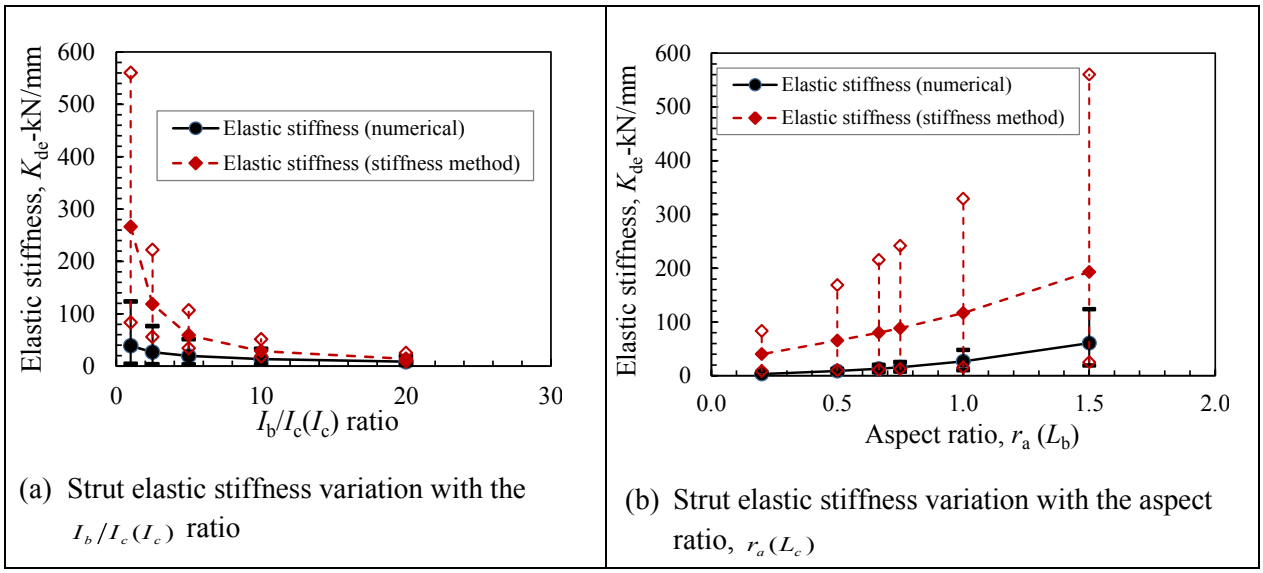

(a) Strut elastic stiffness variation with the $I_b/I_c(I_c)$ ratio

(b) Strut elastic stiffness variation with the aspect ratio, $r_a(L_c)$

Figure A1.47: (a) Diagonal strut elastic stiffness variation with the $I_b/I_c(I_c)$ ratio and, (b) diagonal strut elastic stiffness variation with the aspect ratio, $r_a(L_c)$ for Case C

The ratio of the elastic stiffness obtained from the numerical data to the elastic stiffness obtained using the stiffness method, K_{eF}, for each data point is established and plotted against the $I_b/I_c(I_c)$ ratio as shown in

Figure A1.48. Considering the pattern of variation of the elastic stiffness ratio, K_{eF}, an analytical relationship is proposed to link the elastic stiffness ratio, K_{eF} with the $I_b/I_c(I_c)$ ratio as follows:

$$K_{eF} = K_{er}\left(\frac{I_b}{I_c}(I_c)\right)^{0.50} \tag{A1.9}$$

where K_{er} is the elastic stiffness ratio coefficient dependent on the aspect ratio, $r_a(L_b)$ and is defined by equation 6.9, with constants A_{ke} and K_{er0} determined as 0.12 and 0.0313 respectively. The proposed analytical relationships show some correlation with typical values from the numerical data as shown in Figure A1.48.

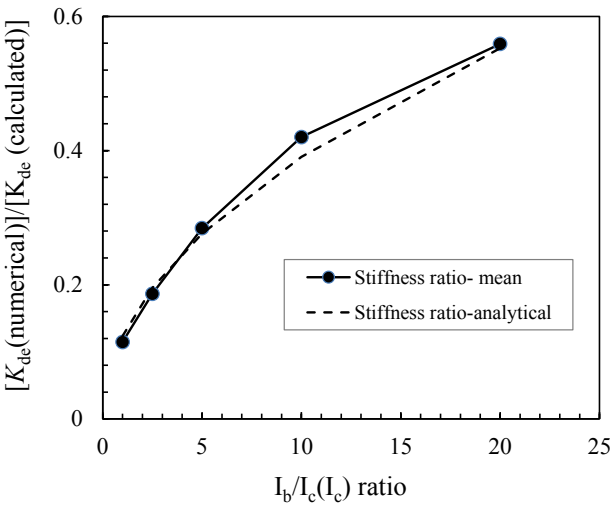

(a) Strut elastic stiffness ratio variation with the $I_b/I_c(I_c)$ ratio

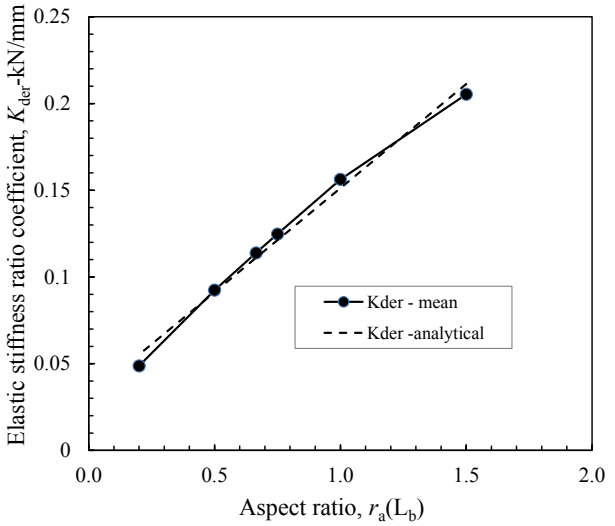

(b) Variation of the strut elastic stiffness ratio coefficient, K_{der}, with the aspect ratio, $r_a(L_b)$

Figure A1.48: (a) Diagonal strut elastic stiffness ratio variation and relationships with the $I_b/I_c(I_c)$ ratio and, (b) the variation of the strut elastic stiffness ratio coefficient with the aspect ratio, $r_a(L_b)$ for Case C

(c) Calibration of strut yield strength (F_{de}) and elastic stiffness (K_{de}) for Case D

The mean values of the diagonal yield strength for Case D samples are plotted against the $I_b/I_c(I_c)$ ratio with the range in the yield strength for each data point indicated in Figure A1.49(a). Considering the similarity in the pattern of variation of the diagonal yield strength with the $I_b/I_c(I_c)$ ratio to that of Case C, equation A1.7 is adopted. The strut yield strength coefficient, F_{der}, is dependent on the aspect ratio, $r_a(L_c)$ and is:

$$F_{der} = D_{fe1}r_a^2(L_c) + D_{fe}r_a(L_c) + D_{fe0} \tag{A1.10}$$

where D_{fe1}, D_{fe} and D_{fe0} are constants are established as 136.0 kN,-345.0 kN and 298.0 kN respectively for this case. The proposed analytical relationships show some correlation with typical values from the numerical data as shown in Figure A1.49.

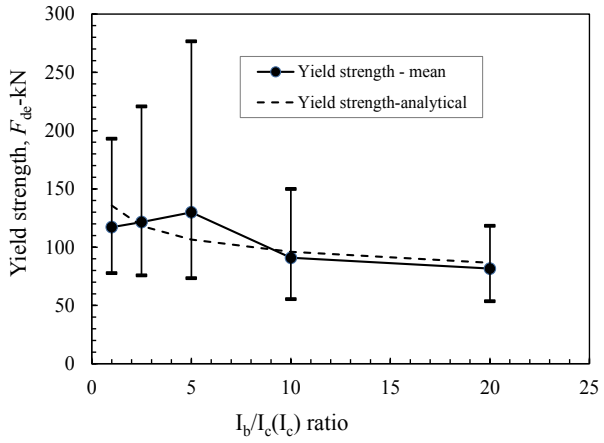

(a) Strut yield strength variation and relationship with the $I_b/I_c(I_c)$ ratio

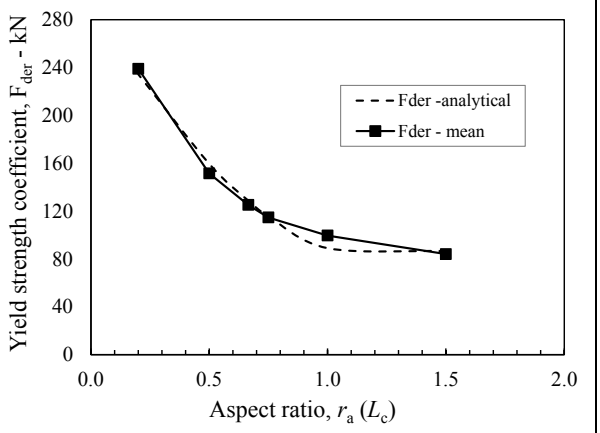

(b) Variation of the strut yield strength coefficient, F_{der}, with the aspect ratio, $r_a(L_c)$

Figure A1.49: (a) Diagonal strut yield strength variation and relationships with the $I_b/I_c(I_c)$ ratio and, (b) the variation of the strut yield strength coefficient with the aspect ratio, $r_a(L_c)$ for Case D

Mean values of the strut elastic stiffness calculated from both the numerical data and using elastic stiffness methods for Case C samples are plotted against the $I_b/I_c(I_c)$ ratio and the aspect ratio, $r_a(L_c)$ as shown in Figure A1.50. There is similar pattern in the variation of the elastic stiffness for both methods of calculation, with that established using elastic stiffness being consistently higher than the numerical value. However, the Elastic stiffness calculated from the stiffness method is excessively high for lower $I_b/I_c(I_c)$ and $r_a(L_c)$ ratios.

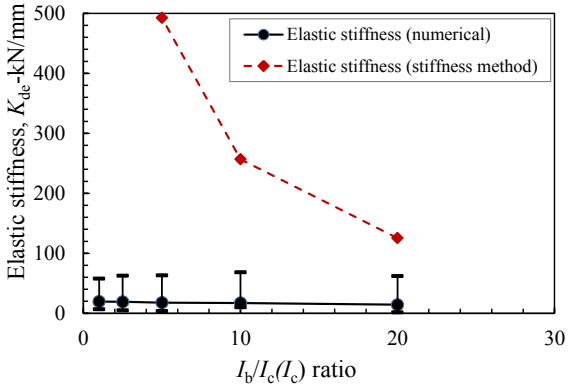

(a) Strut elastic stiffness variation with the $I_b/I_c(I_c)$ ratio

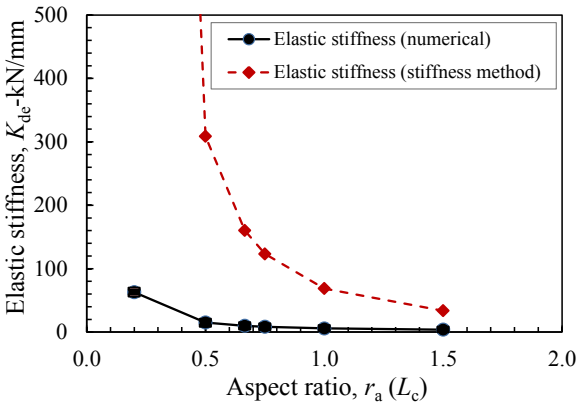

(b) Strut elastic stiffness variation with the aspect ratio, $r_a(L_c)$

Figure A1.50: (a) Diagonal strut elastic stiffness variation with the $I_b/I_c(I_c)$ ratio and, (b) diagonal strut elastic stiffness variation with the aspect ratio, $r_a(L_c)$ for Case D

The ratio of the elastic stiffness obtained from the numerical data to the elastic stiffness obtained using the stiffness method, K_{eF}, for each data point is established and plotted against the $I_b/I_c(I_c)$ ratio as shown in

Figure A1.51. Considering the pattern of variation of the elastic stiffness ratio, K_{eF}, an analytical relationship is proposed to link the elastic stiffness ratio, K_{eF} with the $I_b/I_c(I_c)$ ratio as follows:

$$K_{eF} = K_{er}\left(\frac{I_b}{I_c}(I_c)\right)^{0.60} \quad \text{(A1.11)}$$

where K_{er} is the elastic stiffness ratio coefficient dependent on the aspect ratio, $r_a(L_c)$ and is defined by equation A1.6, with constants A_{ke} and K_{er0} determined as 0.087 and 0.0131 respectively. The proposed analytical relationships show some correlation with typical values from the numerical data as shown in Figure A1.51.

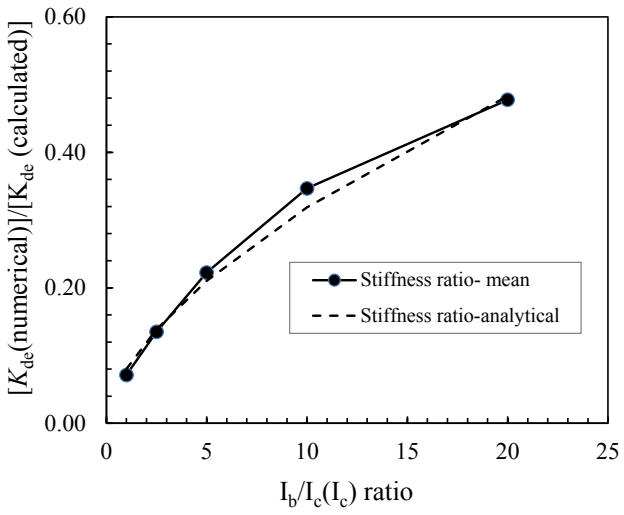

(a) Strut elastic stiffness ratio variation with the $I_b/I_c(I_c)$ ratio

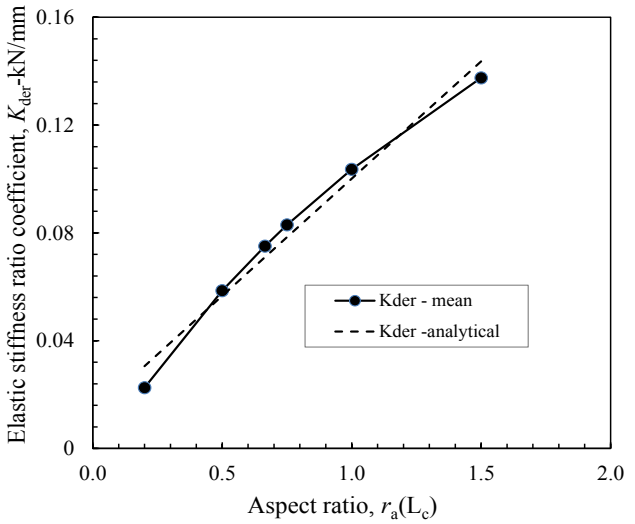

(b) Variation of the strut elastic stiffness ratio coefficient, K_{der}, with the aspect ratio, $r_a(L_c)$

Figure A1.51: Diagonal strut elastic stiffness ratio variation and relationships with the $I_b/I_c(I_c)$ ratio and, (b) the variation of the strut elastic stiffness ratio coefficient with the aspect ratio, $r_a(L_c)$ for Case D

Appendix A1.6: Diagonal strut ultimate strength and plastic stiffness calibration for pinned frames, Cases B - D

(a) Calibration of strut ultimate strength (F_{du}) and plastic stiffness (K_{du}) for Case B

The mean values of the diagonal ultimate strength for Case B samples are plotted against the $I_b/I_c(I_b)$ ratio with the range in the ultimate strength for each data point indicated (see Figure A1.52(a)). Considering the similarity in the pattern of the variation of the mean ultimate strength with the $I_b/I_c(I_b)$ ratio to that of Case A, equation 6.11 is adopted. The strut ultimate strength coefficient is a function of the aspect ratio, $r_a(L_c)$ and is:

$$F_{dur} = D_{fu1}r_a^2(L_c) + D_{fu}r_a(L_c) + D_{fu0} \quad \text{(A1.12)}$$

where D_{fu1}, D_{fu} and D_{fu0} are constants and are determined as 101.0 kN, -265.0 kN and 230.0 kN respectively for this case. The proposed analytical relationships show some correlation with typical values from the numerical data as shown in Figure A1.52.

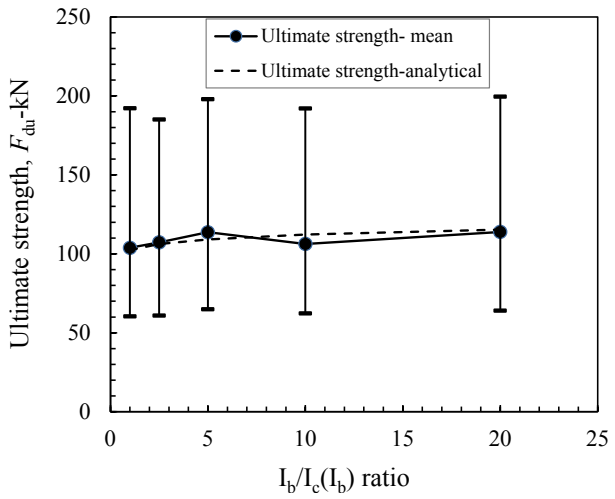

(a) Strut ultimate strength variation and relationship with the $I_b/I_c(I_b)$ ratio

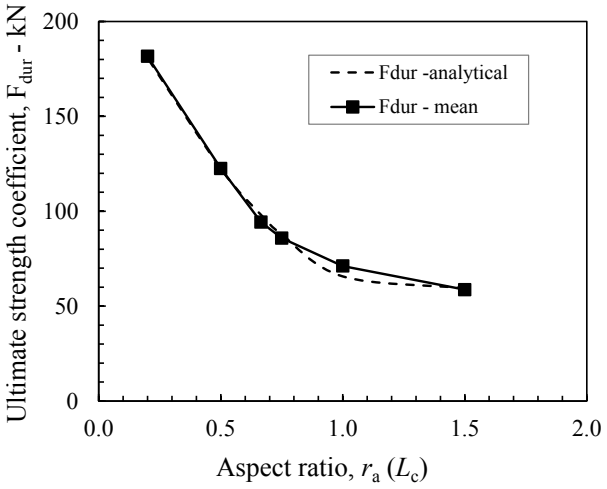

(b) Variation of the strut ultimate strength coefficient, F_{dur}, with the aspect ratio, $r_a(L_c)$

Figure A1.52: Diagonal strut ultimate strength variation and relationships with the $I_b/I_c(I_b)$ ratio and, (b) the variation of the strut ultimate strength coefficient with the aspect ratio, $r_a(L_c)$ for Case B

Mean values of the strut plastic stiffness for Case B samples are plotted against the $I_b/I_c(I_b)$ ratio and the aspect ratio, $r_a(L_c)$ with the range in the plastic stiffness for each data point indicated as shown in Figure A1.53. The plastic stiffness increases with the increase in the $I_b/I_c(I_b)$ ratio, with steeper increase for $I_b/I_c(I_b) < 5.0$. Increase in the aspect ratio, $r_a(L_c)$ reduces the plastic stiffness for the diagonal, with very steep reduction occurring for $r_a(L_c) < 0.5$ (see Figure A1.53b).

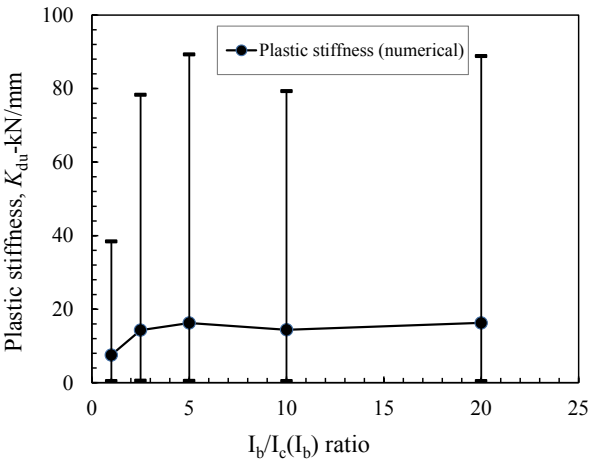

(a) Strut plastic stiffness variation with the $I_b/I_c(I_b)$ ratio

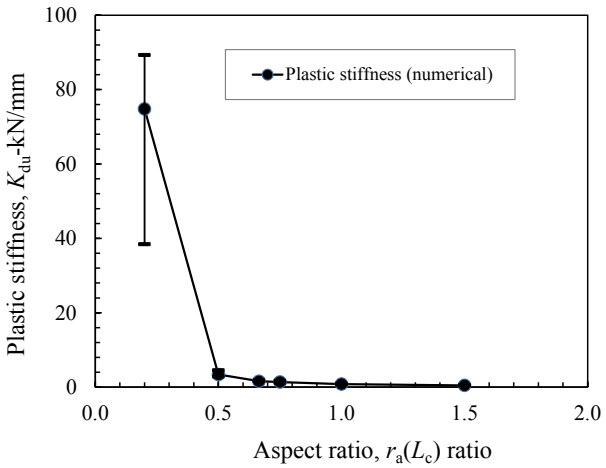

(b) Strut plastic stiffness variation with the $r_a(L_c)$ ratio

Figure A1.53: Diagonal strut plastic stiffness variation with (a) the $I_b/I_c(I_b)$ ratio and, (b) the aspect ratio, $r_a(L_c)$ for Case B

The ratio of the plastic stiffness to the elastic stiffness, K_{pF}, for each data point is established and plotted against the $I_b/I_c(I_b)$ ratio as shown in Figure A1.54. Considering the similarity in the pattern of variation of the plastic stiffness ratio, K_{pF}, with the $I_b/I_c(I_b)$ ratio to that of Case A, equation 6.13 is adopted. The plastic stiffness ratio coefficient is a function of the aspect ratio, $r_a(L_c)$ and is:

$$K_{pr} = A_{kp1} r_a^2(L_c) + A_{kp} r_a(L_c) + A_{kp0} \quad \text{(A1.13)}$$

A_{kp1}, A_{kp} and A_{kp0} are constants and are established as 0.380, -0.670 and 0.567 respectively for this case. The proposed analytical relationships show some correlation with typical values from the numerical data as shown in Figure A1.54.

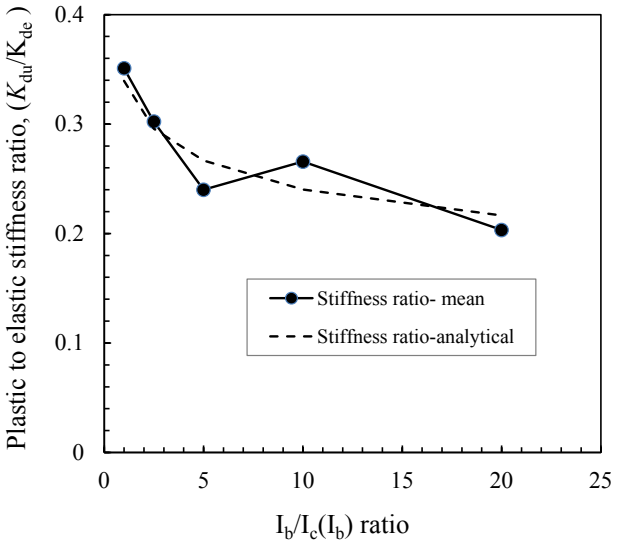

(a) Strut plastic stiffness ratio variation and relationship with the $I_b/I_c(I_b)$ ratio

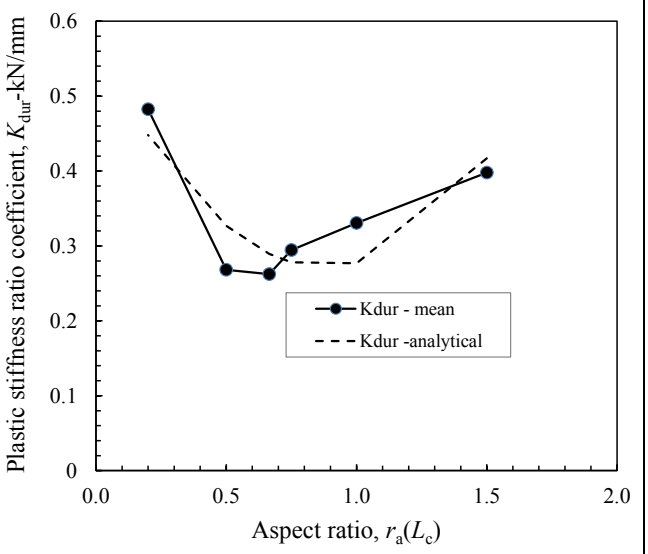

(b) Variation of the strut plastic stiffness ratio coefficient, K_{dur}, with the aspect ratio, $r_a(L_c)$

Figure A1.54: Diagonal strut plastic stiffness ratio variation and relationships with the $I_b/I_c(I_b)$ ratio and, (b) the variation of the strut plastic stiffness ratio coefficient with the aspect ratio, $r_a(L_c)$ for Case B

(b) Calibration of strut ultimate strength (F_{du}) and plastic stiffness (K_{du}) for Case C

The mean values of the diagonal ultimate strength for Case C samples are plotted against the $I_b/I_c(I_c)$ ratio with the range in the ultimate strength for each data point indicated (see Figure A1.55(a)). Considering the pattern of variation of the mean ultimate strength for the diagonal, an analytical relationship is proposed to link the ultimate strength with the $I_b/I_c(I_c)$ ratio as follows:

$$F_{du} = F_{dur}\left(\frac{I_b}{I_c}(I_c)\right)^{-0.15} \quad \text{(A1.14)}$$

where F_{dur} is the strut ultimate strength coefficient and is dependent of the aspect ratio, $r_a(L_b)$ and is:

$$F_{dur} = D_{fu1} r_a^2(L_b) + D_{fu} r_a(L_b) + D_{fu0} \quad \text{(A1.15)}$$

and D_{fu1}, D_{fu} and D_{fu0} are constants and are determined as -70.0 kN, 133.0 kN and 92.6 kN respectively for this case. The proposed analytical relationships show some correlation with typical values from the numerical data as shown in Figure A1.55.

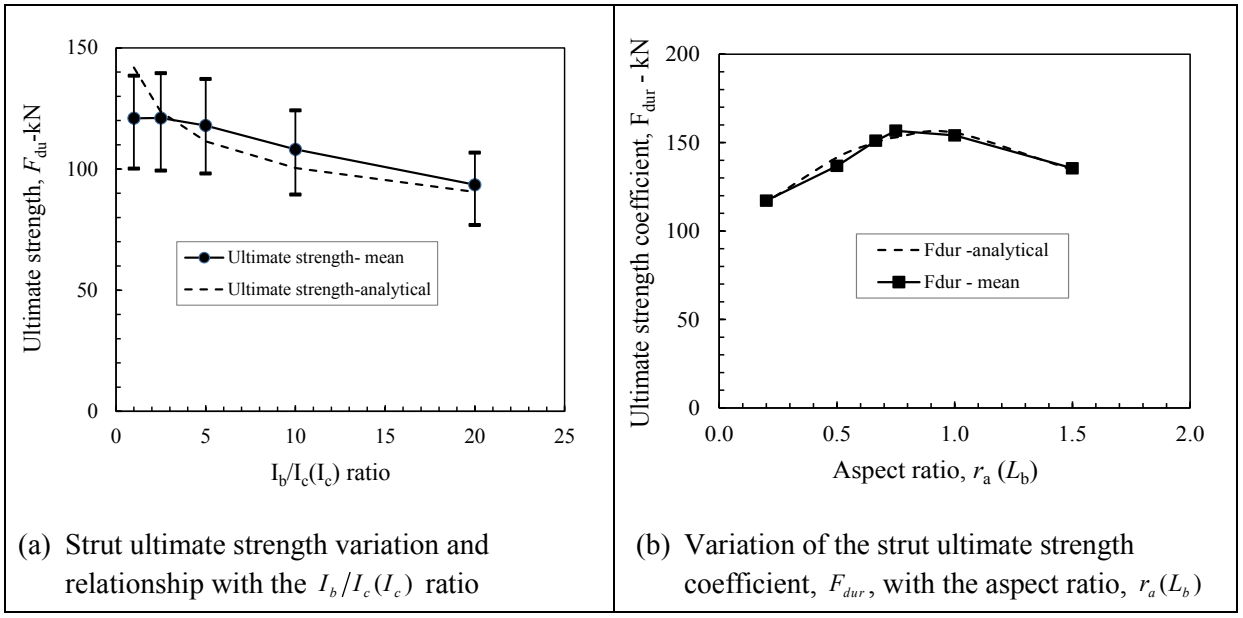

(a) Strut ultimate strength variation and relationship with the $I_b/I_c(I_c)$ ratio

(b) Variation of the strut ultimate strength coefficient, F_{dur}, with the aspect ratio, $r_a(L_b)$

Figure A1.55: Diagonal strut ultimate strength variation and relationships with the $I_b/I_c(I_c)$ ratio and, (b) the variation of the strut ultimate strength coefficient with the aspect ratio, $r_a(L_b)$ for Case C

Mean values of the strut plastic stiffness for Case C samples are plotted against the $I_b/I_c(I_c)$ ratio and the aspect ratio, $r_a(L_b)$ with the range in the plastic stiffness for each data point indicated as shown in Figure A1.56. The plastic stiffness reduces with the increase in the $I_b/I_c(I_c)$ ratio while it increases with the increase in the aspect ratio, $r_a(L_b)$.

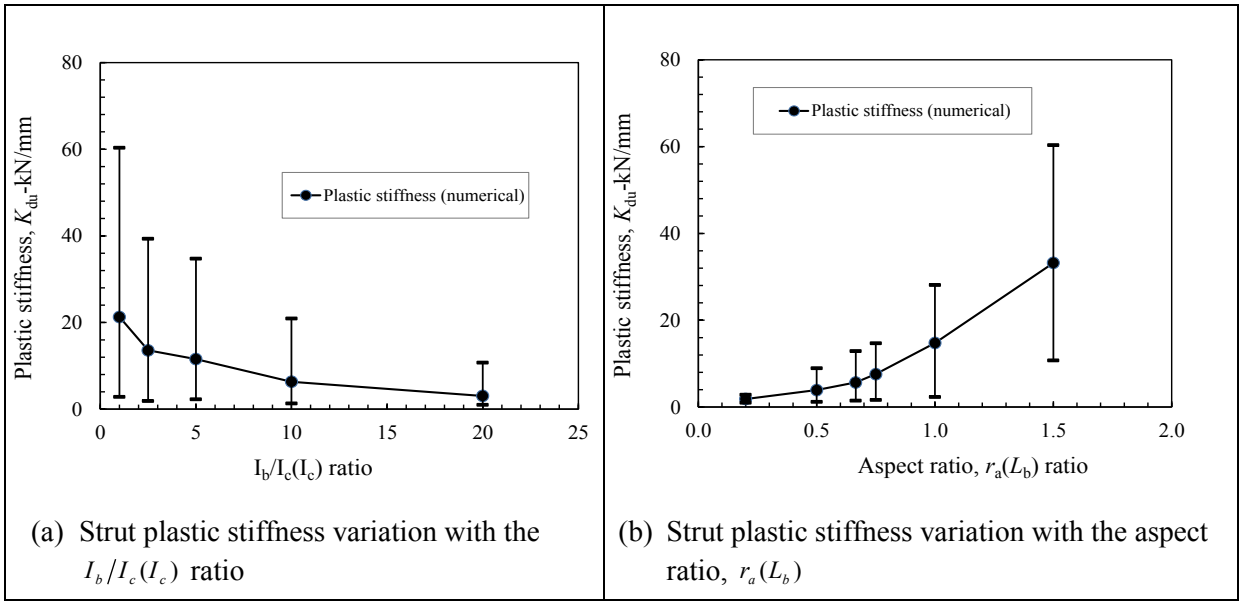

(a) Strut plastic stiffness variation with the $I_b/I_c(I_c)$ ratio

(b) Strut plastic stiffness variation with the aspect ratio, $r_a(L_b)$

Figure A1.56: Diagonal strut plastic stiffness variation with (a) the $I_b/I_c(I_c)$ ratio and, (b) the aspect ratio, $r_a(L_b)$ for Case C

The ratio of the plastic stiffness to the elastic stiffness, K_{pF}, for each data point is established and plotted against the $I_b/I_c(I_c)$ ratio as shown in Figure A1.57. Considering the pattern of variation of the plastic stiffness ratio, K_{pF}, with the $I_b/I_c(I_c)$ ratio, an analytical relationship is proposed to link the plastic stiffness ratio, K_{pF} with the $I_b/I_c(I_c)$ ratio as follows:

$$K_{pF} = K_{pr}\left(\frac{I_b}{I_c}(I_c)\right)^{-0.20} \tag{A1.16}$$

where the plastic stiffness ratio coefficient is a function of the aspect ratio, $r_a(L_b)$ and is defined using equation 6.27. The constants A_{kp1}, A_{kp} and A_{kp0} for the plastic stiffness ratio coefficient for this case are 0.530, -0.815 and 0.861 respectively. The proposed analytical relationships show some correlation with typical values from the numerical data as shown in Figure A1.57.

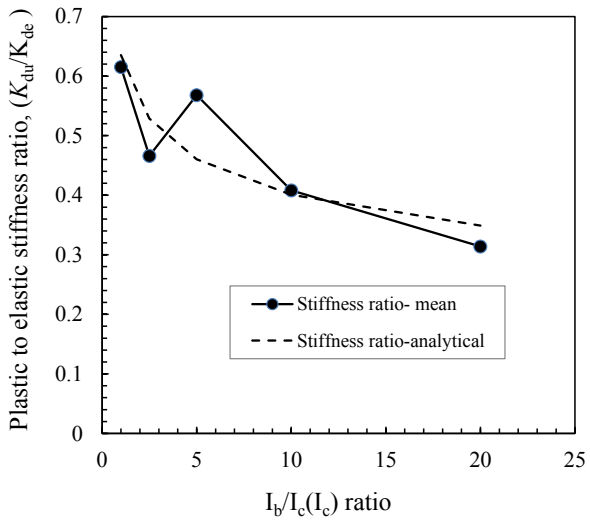

(a) Strut plastic stiffness ratio variation and relationship with the $I_b/I_c(I_c)$ ratio

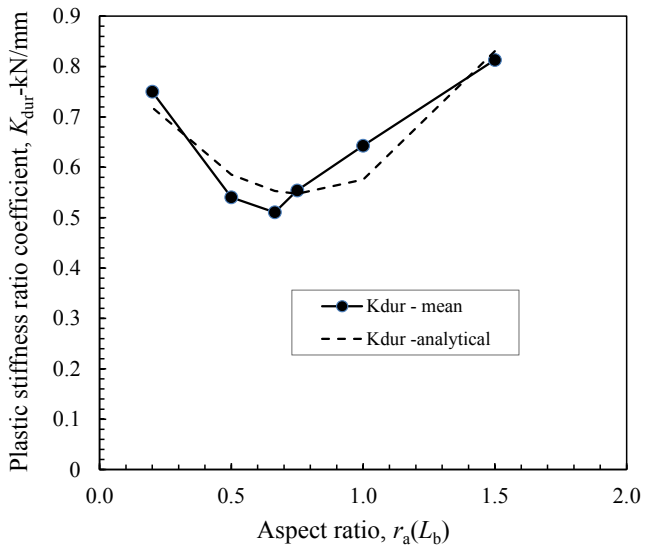

(b) Variation of the strut plastic stiffness ratio coefficient, K_{dur}, with the aspect ratio, $r_a(L_b)$

Figure A1.57: Diagonal strut plastic stiffness ratio variation and relationships with the $I_b/I_c(I_c)$ ratio and, (b) the variation of the strut plastic stiffness ratio coefficient with the aspect ratio, $r_a(L_b)$ for Case C

(c) Calibration of strut ultimate strength (F_{du}) and plastic stiffness (K_{du})for Case D

The mean values of the diagonal ultimate strength for Case D samples are plotted against the $I_b/I_c(I_c)$ ratio with the range in the ultimate strength for each data point indicated (see Figure A1.58(a)). Considering the similarity in the pattern of variation of the mean ultimate strength with the $I_b/I_c(I_c)$ ratio to that of Case C, equation A1.14 is adopted. The strut ultimate strength coefficient, F_{dur}, is the function of the aspect ratio, $r_a(L_c)$ and is defined by equation A1.12 similar to Case B. Constants D_{fu1}, D_{fu} and D_{fu0} for this case are 206.0 kN, -500.0 kN and 383.2 kN respectively. The proposed analytical relationships show some correlation with typical values from the numerical data as shown in Figure A1.58.

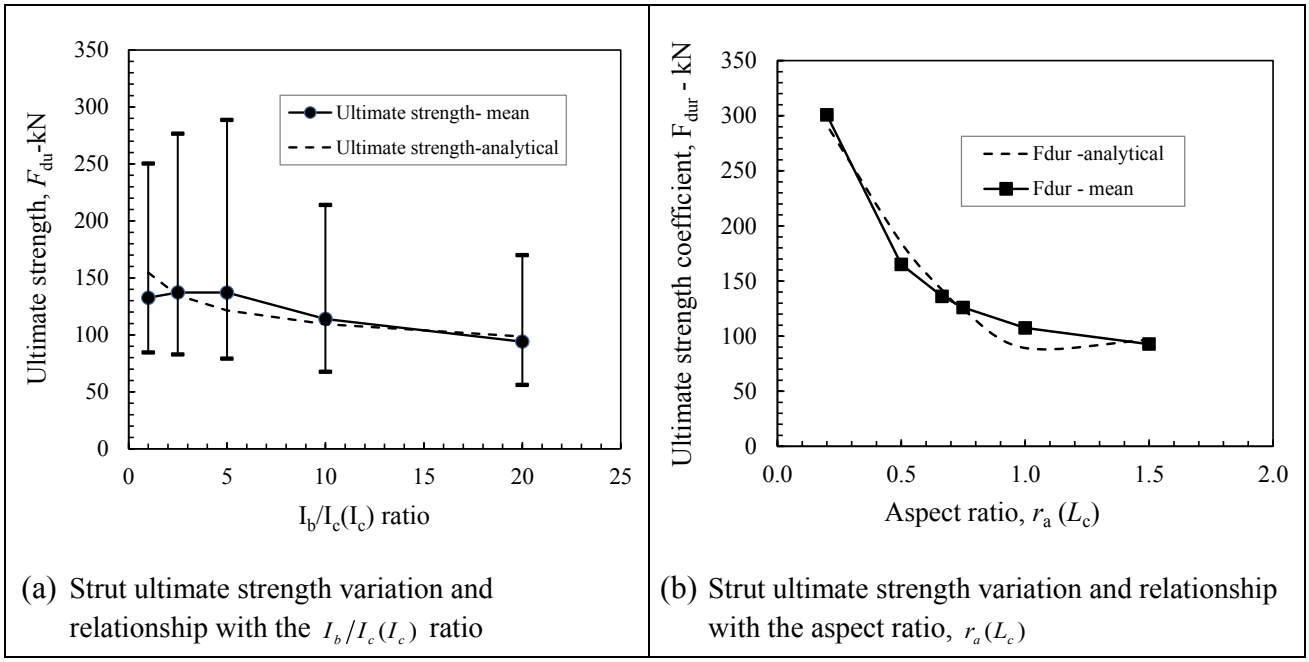

(a) Strut ultimate strength variation and relationship with the $I_b/I_c(I_c)$ ratio

(b) Strut ultimate strength variation and relationship with the aspect ratio, $r_a(L_c)$

Figure A1.58: Diagonal strut ultimate strength variation and relationships with the $I_b/I_c(I_c)$ ratio and, (b) the variation of the strut ultimate strength coefficient with the aspect ratio, $r_a(L_c)$ for Case D

Mean values of the strut plastic stiffness for Case D samples are plotted against the $I_b/I_c(I_c)$ ratio and the aspect ratio, $r_a(L_c)$ with the range in the plastic stiffness for each data point indicated as shown in Figure A1.59. There is no significant change in the plastic stiffness with increase in the $I_b/I_c(I_c)$ ratio while the plastic stiffness significantly reduces with increase in the aspect ratio, $r_a(L_c)$.

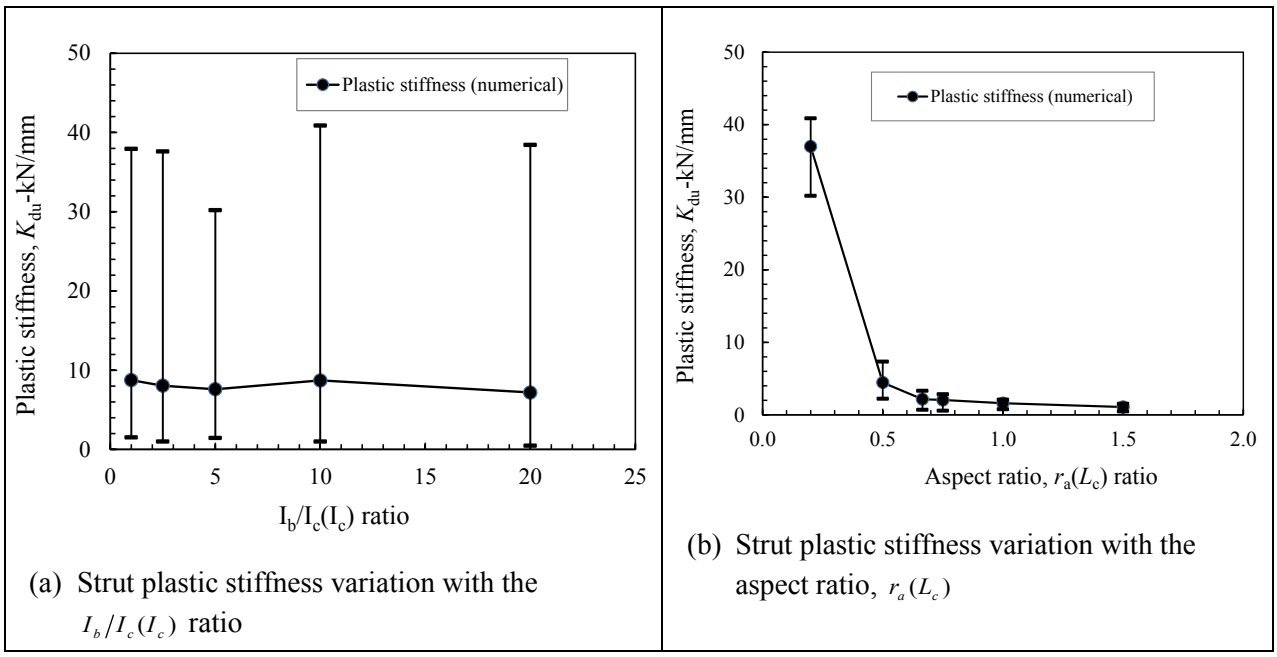

(a) Strut plastic stiffness variation with the $I_b/I_c(I_c)$ ratio

(b) Strut plastic stiffness variation with the aspect ratio, $r_a(L_c)$

Figure A1.59: Diagonal strut plastic stiffness variation with (a) the $I_b/I_c(I_c)$ ratio and, (b) the aspect ratio, $r_a(L_c)$ for Case D

The ratio of the plastic stiffness to the elastic stiffness, K_{pF}, for each data point is established and plotted against the $I_b/I_c(I_c)$ ratio as shown in Figure A1.60. Considering the pattern of variation of the plastic stiffness ratio, K_{pF}, with the $I_b/I_c(I_c)$ ratio, an analytical relationship is proposed to link the plastic stiffness ratio, K_{pF} with the $I_b/I_c(I_c)$ ratio as follows:

$$K_{pF} = A_{pr1}\left(\frac{I_b}{I_c}(I_c)\right)^2 + A_{pr}\left(\frac{I_b}{I_c}(I_c)\right) + K_{dur} \qquad \text{(A1.17)}$$

where A_{pr1} and A_{pr} are constants and are established as -0.001 and 0.024 respectively and the plastic stiffness ratio coefficient, K_{dur}, is a function of the aspect ratio, $r_a(L_c)$ and is defined by equation A1.13 for Case B. Constants A_{kp1}, A_{kp} and A_{kp0} for the K_{dur} function are 0.530, 1.080 and 0.674 respectively for this case. The proposed analytical relationships show some correlation with typical values from the numerical data as shown in Figure A1.60.

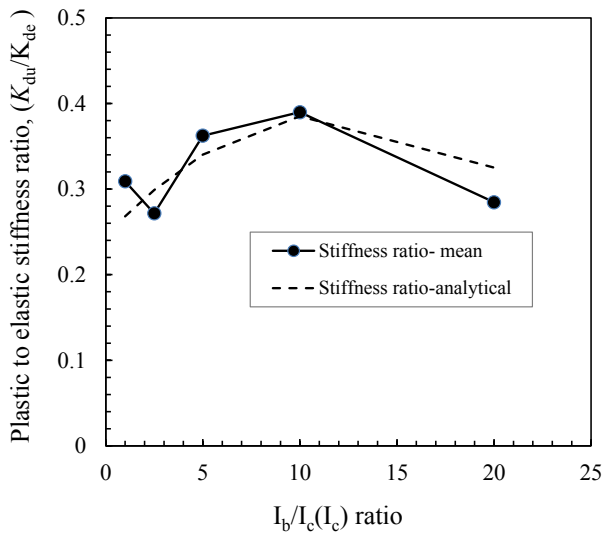

(a) Strut plastic stiffness ratio variation and relationship with the $I_b/I_c(I_c)$ ratio

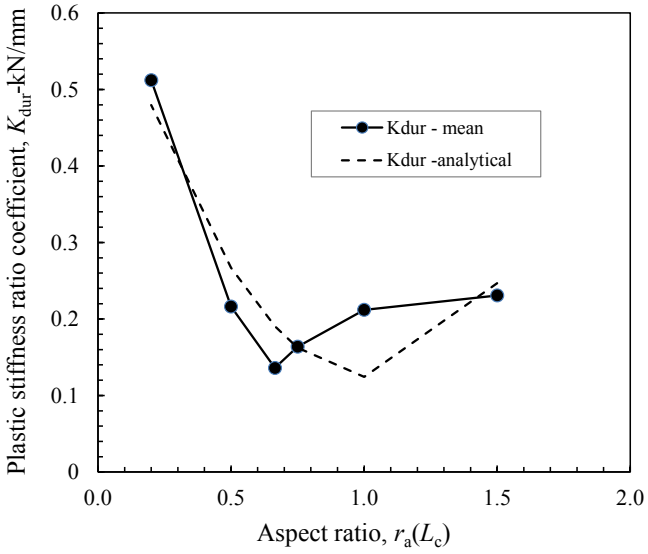

(b) Variation of the strut plastic stiffness ratio coefficient, K_{dur}, with the aspect ratio, $r_a(L_c)$

Figure A1.60: Diagonal strut plastic stiffness ratio variation and relationships with the $I_b/I_c(I_c)$ ratio and, (b) the variation of the strut plastic stiffness ratio coefficient with the aspect ratio, $r_a(L_c)$ for Case D

Appendix A1.7: Calibration of the diagonal strut behaviour for fixed frames

(a) Case A, yield strength for the frame

Based on the variation of the yield strength with the I_b/I_c (I_b) ratio and the r_a (L_b) ratio, an expression is developed to link these behaviours. A power function is proposed to relate the yield strength with the I_b/I_c (I_b) ratio while a linear relationship is used to link the coefficients of the proposed power function with the aspect ratio, r_a (L_b) as provided in equations A1.18 and A1.19.

$$F_e = F_{er}\left(\frac{I_b}{I_c}(I_b)\right)^{0.04} \qquad \text{(A1.18)}$$

where coefficient F_{er} is a linear relationship dependent on the aspect ratio, r_a (L_b) and is:

$$F_{er} = D_{fe} r_a(L_b) + D_{fe0} \quad \text{(A1.19)}$$

and constants D_{fe} and D_{fe0} that may be dependent on specific structural configuration. For this case, A_{fe0} and C_{fe} are -3.8 kN and 133.0 kN respectively for the linearised curve and -0.6 kN and 102.6 kN respectively for the actual curve. The analytical relationships show good correlation with typical values from the numerical data as shown in Figure A1.61.

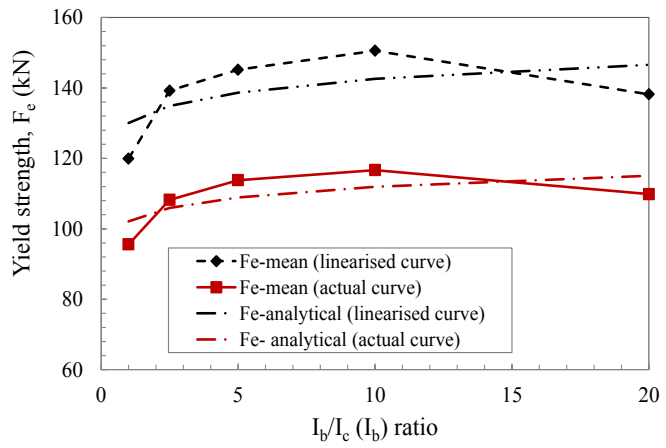

(a) Possible relationship for the ultimate strength with I_b/I_c (I_b) ratio

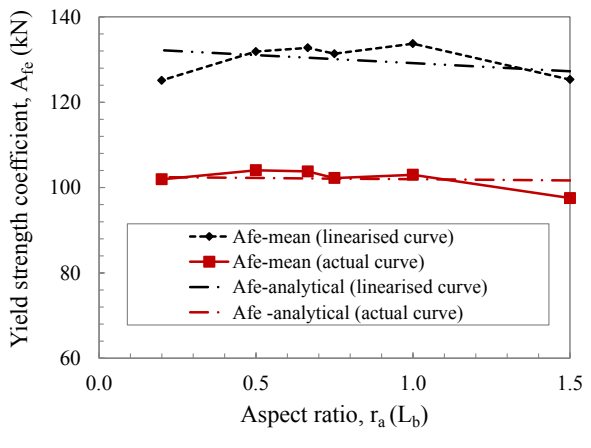

(b) Possible relationship for the yield strength with aspect ratio, $r_a(L_b)$

Figure A1.61: Yield strength relationships with the aspect ratio, r_a (L_b) and the I_b/I_c (I_b) ratio for Case A

(b) Case A, yield deformation for the frame

From the patterns observed for the yield deformation variation with either the $I_b/I_c(I_b)$ ratio or the $r_a(L_b)$ ratio, an expression can be used to link these behavioural patterns. A power function is proposed to relate the yield deformation with the $I_b/I_c(I_b)$ ratio (see equation A1.20) while a linear relationship is used to link the coefficients of the proposed power function with the aspect ratio, $r_a(L_b)$.

$$\delta_e = \delta_{er}\left(\frac{I_b}{I_c}(I_b)\right)^{-0.15} \quad \text{(A1.20)}$$

where δ_{er} is yield deformation coefficient and is defined using a linear relationship as follows:

$$\delta_{er} = b_e r_a(L_b) + C_e \quad \text{(A1.21)}$$

and b_ε and C_ε are constants. For this data set, the values of constants δ_{0er} and D_{fe} are -1.85 mm and 10.0 mm respectively. The analytical relationships show some correlation with typical values from the numerical data as shown in Figure A1.62.

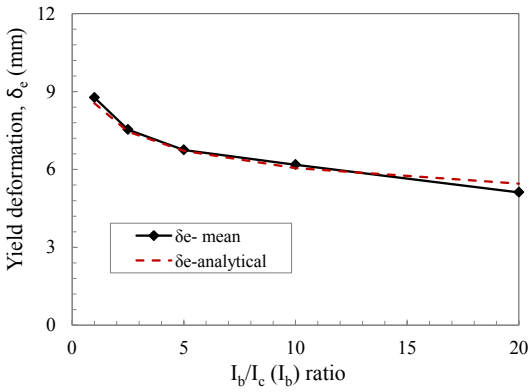

(a) Typical yield deformation variation with I_b/I_c (I_b) ratio

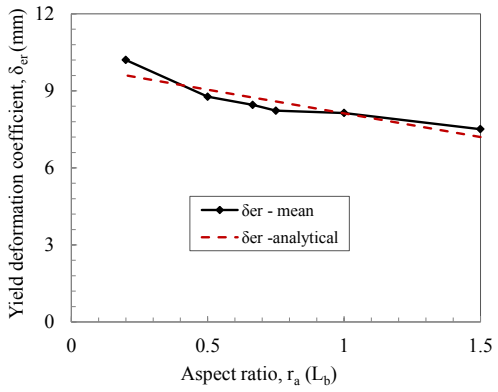

(b) Variation of the yield deformation coefficient (δ_{er}) with the aspect ratio, $r_a(L_b)$

Figure A1.62: Yield deformation relationships with the $I_b/I_c(I_b)$ ratio and aspect ratio, r_a (L_b) for Case A

(c) Case A, ultimate strength for the frame

Based on the variation of the ultimate strength with the I_b/I_c (I_b) ratio and the r_a (L_b) ratio, an expression is developed to link these behaviour patterns. A power function, used for the yield strength is adopted due to the similarity in the behaviour patterns for the ultimate strength variation with the I_b/I_c (I_b) ratio while a linear relationship is also used to link the coefficient of the proposed power function with the aspect ratio, r_a (L_b) as provided in equations A1.22 and A1.23.

$$F_u = A_{fu}\left(\frac{I_b}{I_c}(I_b)\right)^{0.04} \qquad \text{(A1.22)}$$

where coefficient A_{fu} is a linear function of the aspect ratio, r_a (L_b) (see Figure A1.63b) and is:

$$A_{fu} = A_{fu0} r_a(L_c) + C_{fu} \qquad \text{(A1.23)}$$

and A_{fu0} and C_{fu} are coefficients for case. For linearly defined ultimate strength, A_{fu0} and C_{fu} for this material and structural configuration are -9.6 kN and 160.3 kN respectively. The coefficients A_{fu0} and C_{fu} for the actual curve values for this problem are -3.8 kN and 150.2 kN respectively. The analytical relationships show good correlation with typical values from the numerical data as shown in Figure A1.63.

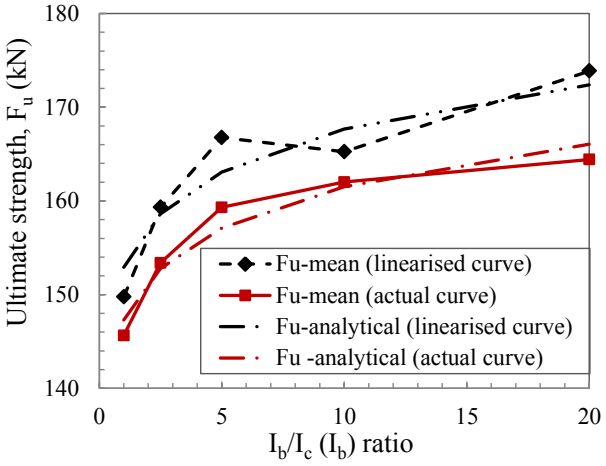

(a) Possible relationship for the ultimate strength with I_b/I_c (I_b) ratio

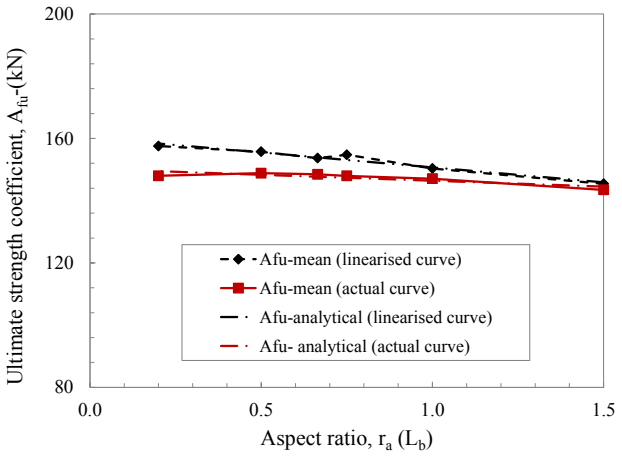

(a) Possible relationship for the ultimate strength with aspect ratio

Figure A1.63: Ultimate strength relationships with the aspect ratio, r_a (L_b) and the I_b/I_c(I_b) ratio for Case A

(d) Case A, ultimate deformation for the frame

Based on the variation of the ultimate deformation with the I_b/I_c (I_b) ratio and the r_a (L_b) ratio, an expression is developed to link these behaviour patterns. A power function, used for the yield deformation is adopted due to the similarity in the behaviour patterns for the ultimate deformation variation with the I_b/I_c (I_b) ratio while a linear relationship is also used to link the coefficient of the proposed power function with the aspect ratio, r_a (L_b) (see equations A1.24 and A1.25).

$$\delta_u = \delta_{ur}\left(\frac{I_b}{I_c}\right)^{-0.15} \tag{A1.24}$$

where coefficient δ_{ur} is a linear function of the aspect ratio, r_a (L_b) and is:

$$\delta_{ur} = \delta_{0ur} r_a(L_b) + D_{fu} \tag{A1.25}$$

and δ_{0ur} and D_{fu} are constants. For this data set, the values of constants δ_{0ur} and D_{fu} are -11.0 mm and 36.2 mm respectively. The analytical relationships show some correlation with typical values from the numerical data as shown in Figure A1.64.

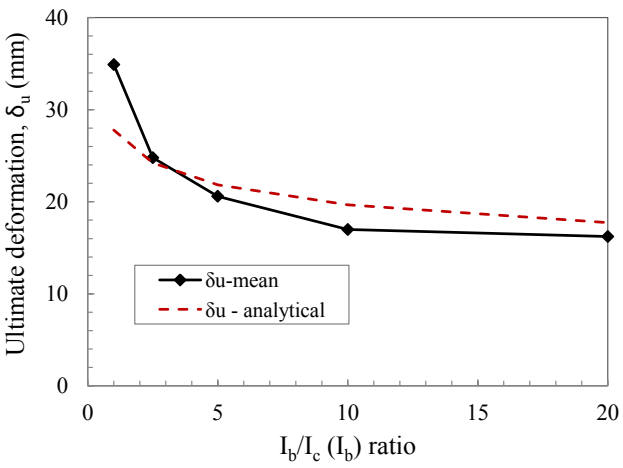

(a) Typical ultimate deformation variation with I_b/I_c (I_b) ratio

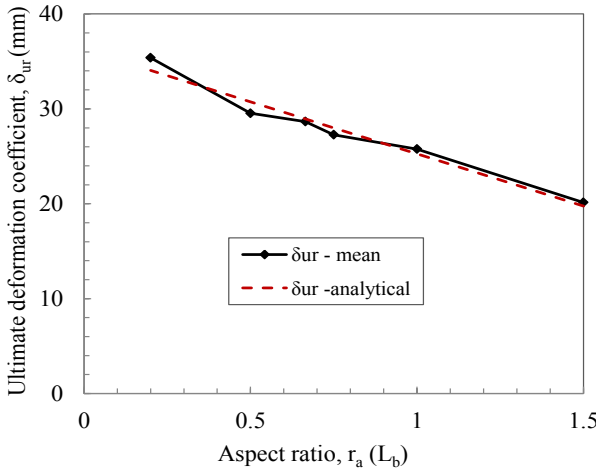

(b) Variation of the ultimate deformation coefficient (δ_{ur}) with aspect ratio, r_a(L_b)

Figure A1.64: Ultimate deformation relationship with the I_b/I_c(I_b) ratio and the aspect ratio, r_a(L_b) for Case A

Case B frames

(a) Case B, yield strength for the frame

Based on similar variation of the yield strength with the I_b/I_c (I_b) ratio and the r_a (L_c) ratio to that of Case A, the same expression (equations A1.18) used in Case A. Since the aspect ratio under this section is a function of column length, the coefficient A_{fe} for the adopted expression is defined as follows:

$$A_{fe} = A_{fe0} r_a(L_c) + C_{fe} \qquad \text{(A1.26)}$$

where constants A_{fe0} and C_{fe} are case dependent. For this case, A_{fe0} and C_{fe} are -94.0 kN and 196.7 kN respectively for the linearised curve points and -79.0 kN and 158.8 kN respectively for the actual curve points. The analytical relationships show good correlation with typical values from the numerical data as shown in Figure A1.65.

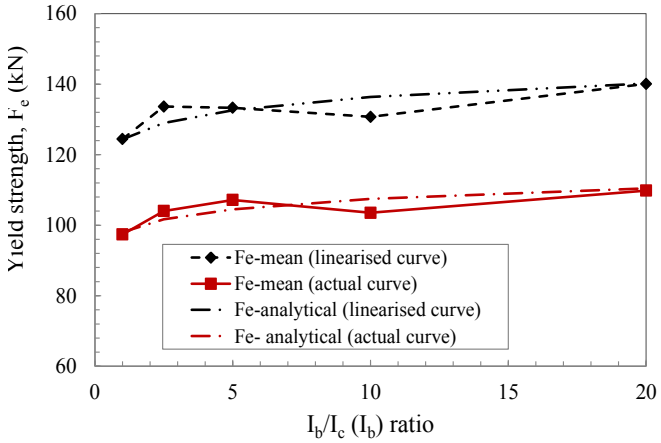

(a) Possible relationship for the ultimate strength with I_b/I_c (I_b) ratio

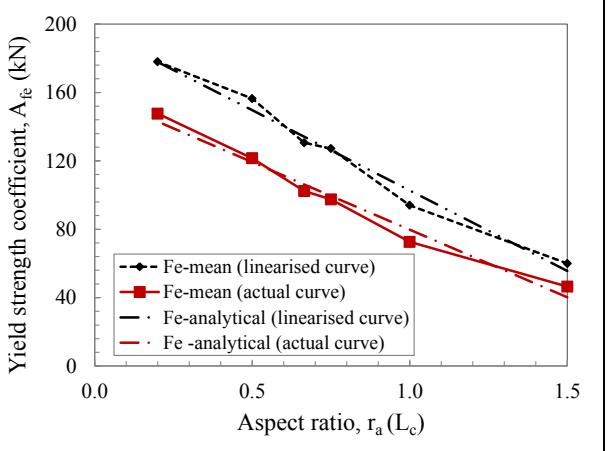

(b) Possible relationship for the yield strength with aspect ratio, r_a (L_c)

Figure A1.65: Yield strength relationships with the I_b/I_c (I_c) ratio and the aspect ratio, r_a (L_c) for Case B

(b) Case B, yield deformation for the frame

Based on similarity in the patterns of the variation of the yield deformation with the I_b/I_c (I_b) ratio to that of Case A, the same expression (equation A1.20) used in Case A is adopted. Since the aspect ratio under this section is a function of column length, the coefficientδ_{er} for the adopted expression is modified for this case and is:

$$\delta_{er} = \delta_{0er} r_a(L_c) + D_{fe} \qquad \text{(A1.27)}$$

where δ_{0er} and D_{fe} are constants. For this data set, the values of constants δ_{0er} and D_{fe} are 34.4 mm and -11.5 mm respectively. The analytical relationships show some correlation with typical values from the numerical data as shown in Figure A1.66.

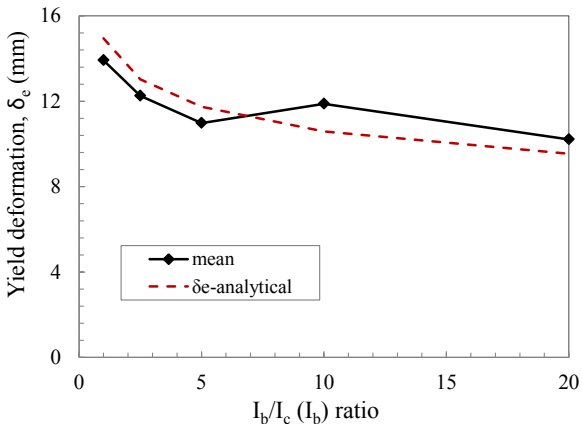

(a) Typical yield deformation variation with I_b/I_c (I_b) ratio

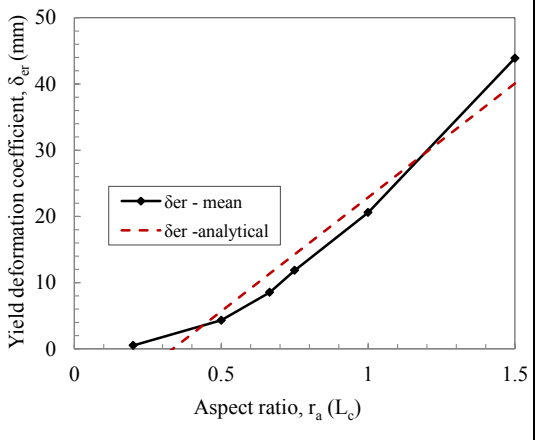

(b) Variation of the yield deformation coefficient (δ_{er}) with aspect ratio, r_a(L_c)

Figure A1.66: Yield deformation relationships with I_b/I_c (I_b) ratio and aspect ratio, r_a (L_c) for Case B

(c) Case B, ultimate strength for the frame

Based on similar variation of the ultimate strength with the I_b/I_c (I_b) ratio and the r_a (L_c) ratio to that of Case A, the same expression (equations A1.22) used in Case A is adopted here. Since the aspect ratio under this section is a function of column length, the coefficient A_{fu0} for the adopted expression is defined as follows:

$$A_{fu} = A_{fu0} r_a(L_c) + C_{fu} \qquad \text{(A1.28)}$$

where A_{fu0} and C_{fu} are coefficient for each case. For linearly defined ultimate strength, A_{fu0} and C_{fu} for this material and structural configuration are -104 kN and 218 kN respectively. The coefficients A_{fu0} and C_{fu} for the ultimate strength defined from the actual curve values for this problem are -104 kN and 215 kN respectively. The analytical relationships show some correlation with typical values from the numerical data as shown in Figure A1.67.

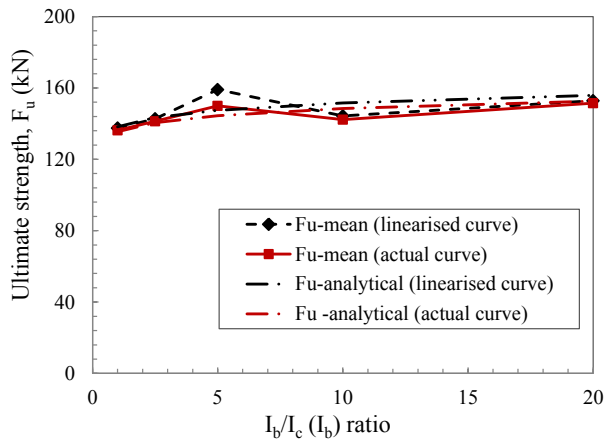

(a) Possible relationship for the ultimate strength with I_b/I_c (I_b) ratio

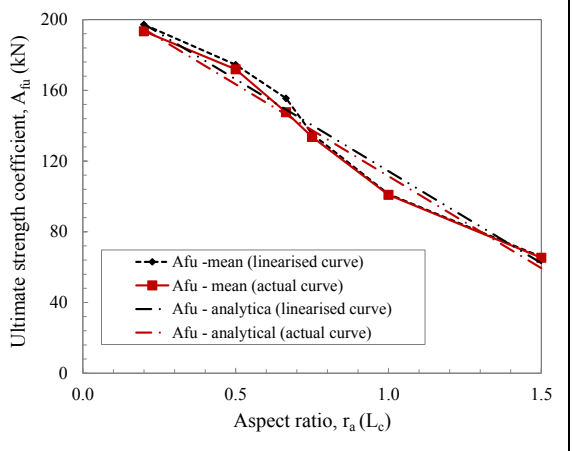

(b) Possible relationship for the ultimate strength with aspect ratio, r_a (L_c)

Figure A1.67: Ultimate strength relationships with I_b/I_c (I_b) and aspect ratio, r_a (L_c) for Case B

(d) Case B, yield deformation for the frame

The patterns of the variation of the ultimate deformation with the I_b/I_c (I_b) ratio is similar to that of Case A. Thus, the expression (equation A1.24) used in Case A is adopted. Since the aspect ratio under this section is a function of column length, the coefficient δ_{ur} for the adopted expression is modified for this case and is:

$$\delta_{er} = \delta_{0ur} r_a(L_c) + D_{fu} \qquad \text{(A1.29)}$$

where δ_{0ur} and D_{fu} are constants. For this data set, the values of constants δ_{0ur} and D_{fu} are 196.3 mm and -72.5 mm respectively. The analytical relationships show some correlation with typical values from the numerical data as shown in Figure A1.68.

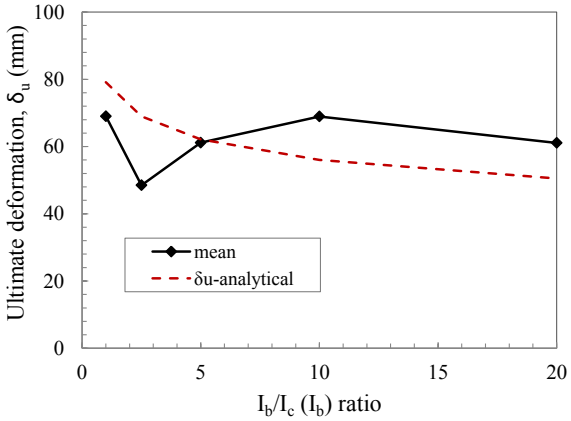

(a) Typical ultimate deformation variation with I_b/I_c (I_b) ratio

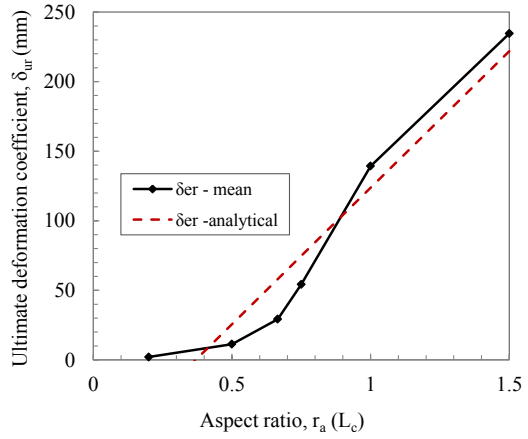

(b) Variation of the ultimate deformation coefficient (δ_{ur}) with aspect ratio, r_a(L_c)

Figure A1.68: Ultimate deformation relationship with I_b/I_c (I_b) ratio and aspect ratio, r_a (L_c) for Case B

Case C frames

(a) Case C, yield strength for the frame

Based on the variation of the yield strength with the I_b/I_c (I_c) ratio and the r_a (L_b) ratio, an expression is developed to link these behaviour patterns. A power function is proposed to relate the yield strength with the I_b/I_c (I_c) ratio while a linear relationship is used to link the coefficients of the proposed power function with the aspect ratio, r_a (L_b) as provided in equations A130 and A1.31.

$$F_e = A_{fe}\left(\frac{I_b}{I_c}(I_c)\right)^{-0.40} \qquad \text{(A1.30)}$$

where A_{fe} is a yield strength coefficient based on the aspect ratio. A linear relationship is chosen for the yield strength coefficient as follows:

$$A_{fe} = A_{fe0} r_a(L_c) + C_{fe} \qquad \text{(A1.31)}$$

and constants A_{fe0} and C_{fe} are case dependent. For this case, A_{fe0} and C_{fe} are -142.0 kN and 542.0 kN respectively for the linearised curve points and -112.0 kN and 446.6 kN respectively for the actual curve points. The analytical relationships show some correlation with typical values from the numerical data as shown in Figure A1.69.

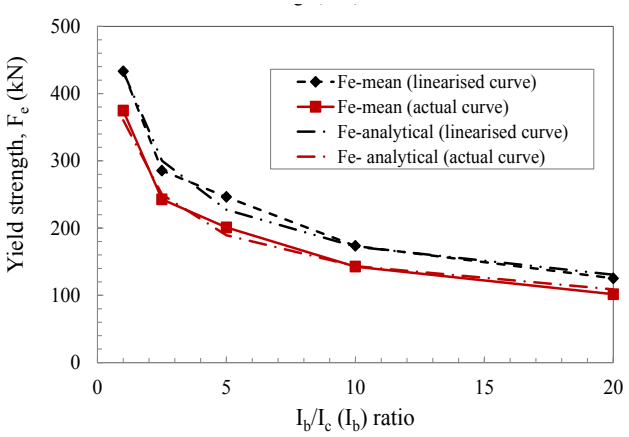

(a) Possible relationship for the ultimate strength with I_b/I_c (I_b) ratio

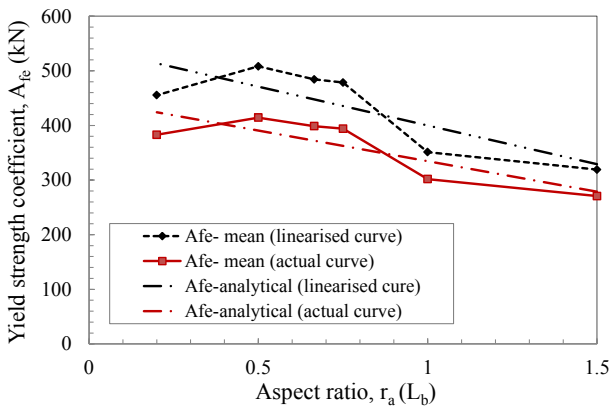

(b) Yield strength coefficient variation with the aspect ratio, r_a (L_b)

Figure A1.69: Yield strength relationships with the I_b/I_c (I_c) ratio and the aspect ratio, r_a (L_c) for Case C

(b) Case C, yield deformation for the frame

From the patterns observed for the yield deformation variation with either the I_b/I_c (I_c) ratio or the r_a (L_b) ratio, an expression is developed to link these behavioural patterns. A power function is proposed to relate the yield deformation with the I_b/I_c (I_c) ratio (see equation A1.32) while a linear relationship is used to link the coefficients of the proposed power function with the aspect ratio, r_a (L_b).

$$\delta_e = \delta_{er}\left(\frac{I_b}{I_c}(I_c)\right)^{0.25} \tag{A1.32}$$

where

δ_{er} is yield deformation coefficient and is defined using a linear relationship with the aspect ratio, r_a (L_b) as:

$$\delta_{er} = \delta_{0er} r_a(L_b) + D_{fe} \tag{A1.33}$$

and δ_{0er} and D_{fe} are constants. For this data set, the values of δ_{0er} and D_{fe} are -2.2 mm and 4.5 mm respectively. The analytical relationships show some correlation with typical values from the numerical data as shown in Figure A1.70.

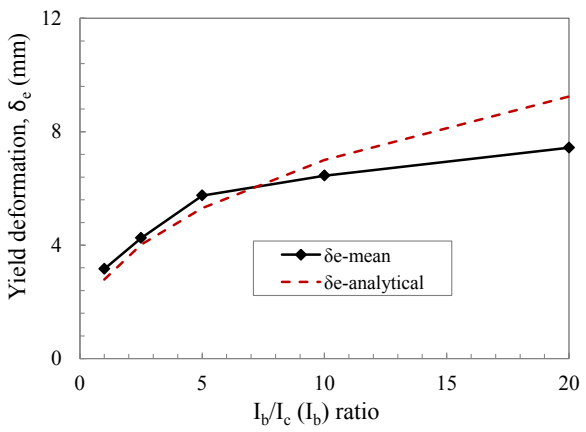

(a) Typical yield deformation variation with I_b/I_c (I_b) ratio

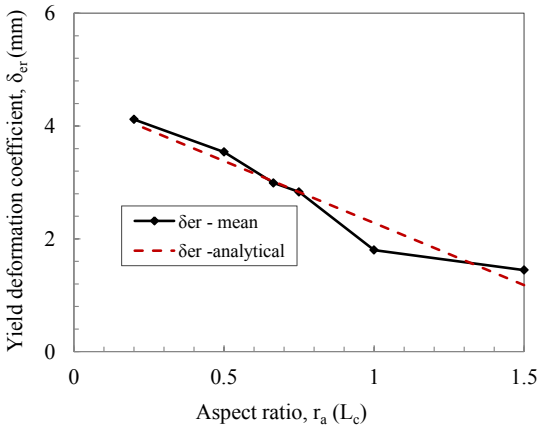

(b) Variation of the yield deformation coefficient (δ_{er}) with aspect ratio, $r_a(L_c)$

Figure A1.70: Yield deformation relationships with I_b/I_c (I_b) ratio and aspect ratio, r_a (L_c) for Case C

(c) Case C, ultimate strength for the frame

Based on the variation of the ultimate strength with the I_b/I_c (I_c) ratio and the r_a (L_b) ratio, an expression is developed to link these behaviour patterns. A power function, used for the yield strength has been adopted due to the similarity in the behaviour patterns for the ultimate strength variation with the I_b/I_c (I_c) ratio while a linear relationship is also used to link the coefficient of the proposed power function with the aspect ratio, r_a (L_b) as provided in equations A1.34 and A1.35.

$$F_u = A_{fu}\left(\frac{I_b}{I_c}(I_c)\right)^{-0.40} \qquad \text{(A1.34)}$$

where coefficient A_{fu} is a linear function of the aspect ratio, r_a (L_b) and is:

$$A_{fu} = A_{fu0} r_a(L_b) + C_{fu} \qquad \text{(A1.35)}$$

and, A_{fu0} and C_{fu} are coefficients for each case. For linearly defined ultimate strength, A_{fu0} and C_{fu} for this material and structural configuration are -112.0 kN and 652.0 kN respectively. The coefficients A_{fu0} and C_{fu} for the actual curve values for this problem are -112.0 kN and 647.3 kN respectively. The analytical relationships show some correlation with typical values from the numerical data as shown in Figure A1.71.

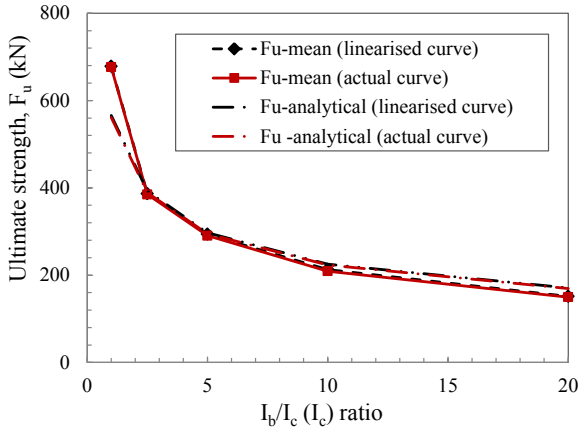

(a) Possible relationship for the ultimate strength with I_b/I_c (I_c) ratio

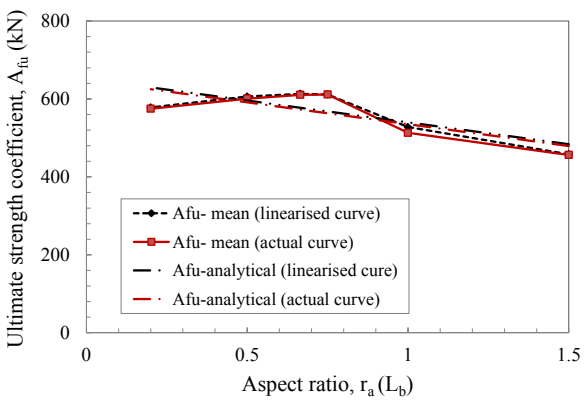

(b) Ultimate strength coefficient variation with the aspect ratio, r_a (L_b)

Figure A1.71: Ultimate strength relationships with I_b/I_c (I_c) and aspect ratio, r_a (L_b) for Case C

(d) Case C, ultimate deformation for the frame

Based on the variation of the ultimate deformation with the I_b/I_c (I_c) ratio and the r_a (L_b) ratio, an expression is developed to link these behaviour patterns. A power function, used for the yield deformation has been adopted due to the similarity in the behaviour patterns for the ultimate deformation variation with the I_b/I_c (I_c) ratio while a linear relationship is also used to link the coefficient of the proposed power function with the aspect ratio, r_a (L_b) (see equations A1.36 and A.37).

$$\delta_u = \delta_{ur}\left(\frac{I_b}{I_c}\right)^{0.4} \tag{A1.36}$$

where δ_{ur} is the ultimate deformation coefficient and is defined as a linear function of the aspect ratio, r_a (L_c):

$$\delta_{ur} = \delta_{0ur} r_a(L_c) + D_{fu} \tag{A1.37}$$

and, δ_{0ur} and D_{fu} are constants. For this data set, the values of constants δ_{0ur} and D_{fu} are -8.3 mm and 17.4 mm respectively. The analytical relationships show some correlation with typical values from the numerical data as shown in Figure A1.72.

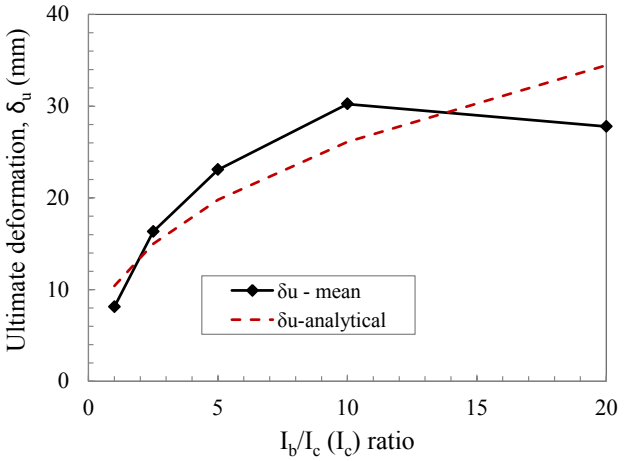

(a) Typical ultimate deformation variation with I_b/I_c (I_c) ratio

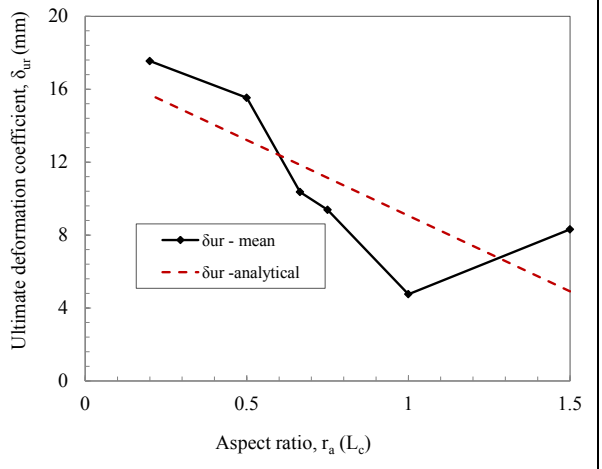

(b) Variation of the ultimate deformation coefficient (δ_{ur}) with aspect ratio, r_a(L_b)

Figure A1.72: Ultimate deformation relationship with I_b/I_c (I_c) ratio and aspect ratio, r_a (L_b) for Case C

Case D

(a) Case D, yield strength for the frame

Based on similar variation of the yield strength with the I_b/I_c (I_c) ratio and the r_a (L_b) ratio to that of Case C, the same expression (equation A1.30) used in Case C is adopted here. Since the aspect ratio under this section is a function of beam length, the coefficient A_{fe} for the adopted expression modified and is:

$$A_{fe} = A_{fe0} r_a(L_b) + C_{fe} \qquad \text{(A1.38)}$$

where constants A_{fe0} and C_{fe} are case dependent. For this case, the constants A_{fe0} and C_{fe} are -336.0 kN and 607.0 kN respectively for the linearised curve and -415.0 kN and 744.0 kN respectively for the actual curve. The analytical relationships show some correlation with typical values from the numerical data as shown in Figure A1.73.

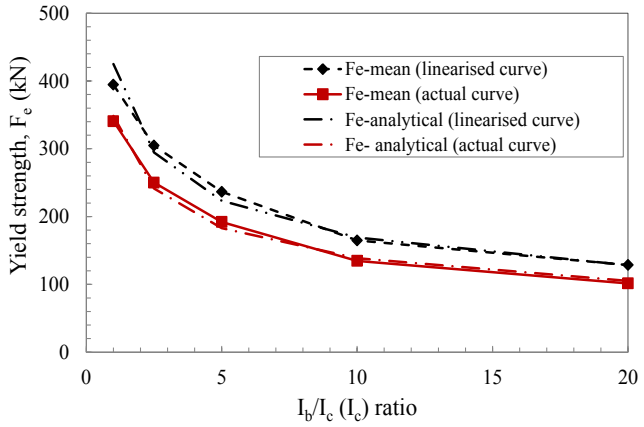

(a) Possible relationship for the ultimate strength with I_b/I_c (I_c) ratio

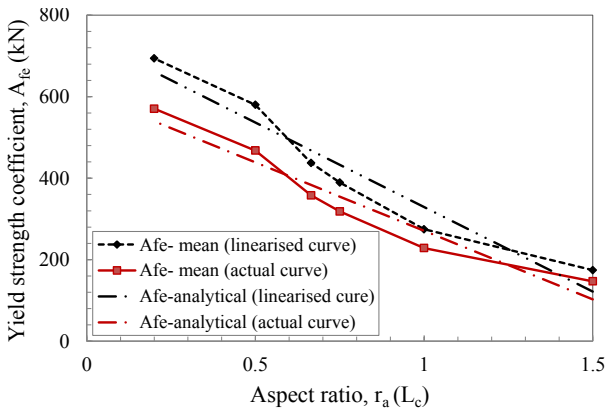

(b) Yield strength coefficient variation with the aspect ratio, r_a (L_c)

Figure A1.73: Yield strength relationships with the I_b/I_c (I_c) ratio and the aspect ratio, r_a (L_c) for Case D

(b) Case D, yield deformation for the frame

Based on similar variation of the yield deformation with the I_b/I_c (I_c) ratio and the r_a (L_c) ratio to that of Case C, the same expression (equation A1.32) used in Case C is adopted. Since the aspect ratio under this section is a function of column length, the coefficient δ_{er} for the adopted expression is modified and is:

$$\delta_{er} = \delta_{0er} r_a (L_b) + D_{fe} \qquad \text{(A1.39)}$$

where δ_{0er} and D_{fe} are constants. For this data set, the values of δ_{0er} and D_{fe} are -7.4 mm and -1.2 mm respectively. The analytical relationships show some correlation with typical values from the numerical data (especially for $I_b/I_c(I_c) < 10.0$) as shown in Figure A1.74.

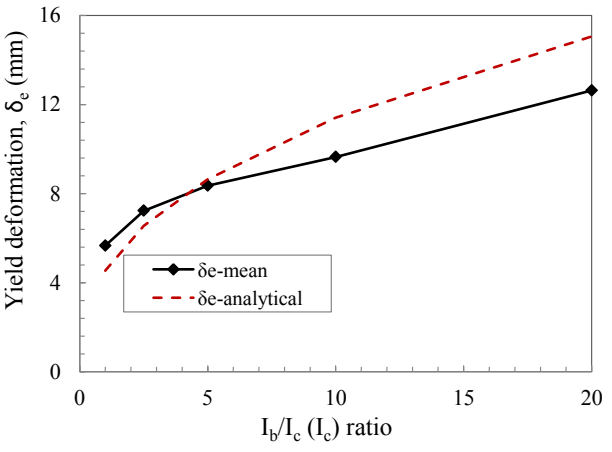

(a) Typical yield deformation variation with I_b/I_c (I_c) ratio

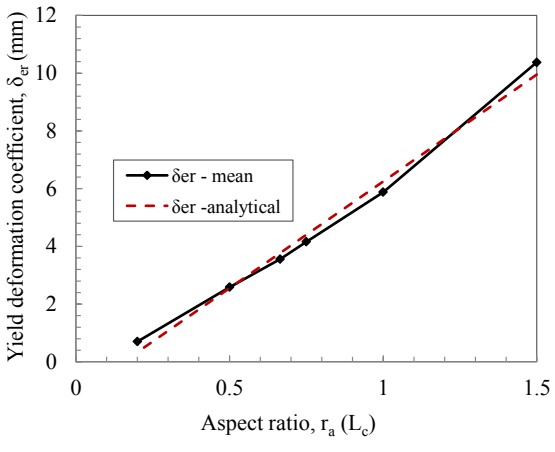

(b) Variation of the yield deformation coefficient (δ_{er}) with aspect ratio, $r_a(L_c)$

Figure A1.74: Yield deformation relationships with I_b/I_c (I_c) ratio and aspect ratio, r_a (L_c) for Case D

(c) Case D, ultimate deformation for the frame

Based on similar variation of the ultimate strength with the I_b/I_c (I_b) ratio and the r_a (L_b) ratio to that of Case C, the same expression (equations A1.34) used in Case C is adopted. Since the aspect ratio under this section is a function of beam height, the coefficient A_{fu} for the adopted expression is defined as follows:

$$A_{fu} = A_{fu0} r_a(L_b) + C_{fu} \qquad \text{(A1.40)}$$

where A_{fu0} and C_{fu} are coefficients for case. For linearly defined ultimate strength, A_{fu0} and C_{fu} for this material and structural configuration are -434.0 kN and 861.0 kN respectively. The coefficients A_{fu0} and C_{fu} for the actual curve values for this problem are -434.0 kN and 858.0 kN respectively. The analytical relationships show some correlation with typical values from the numerical data as shown in Figure A1.75.

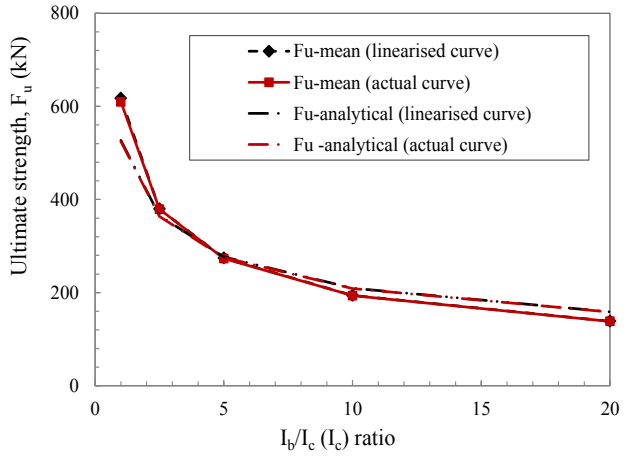

(a) Possible relationship for the ultimate strength with I_b/I_c (I_c) ratio

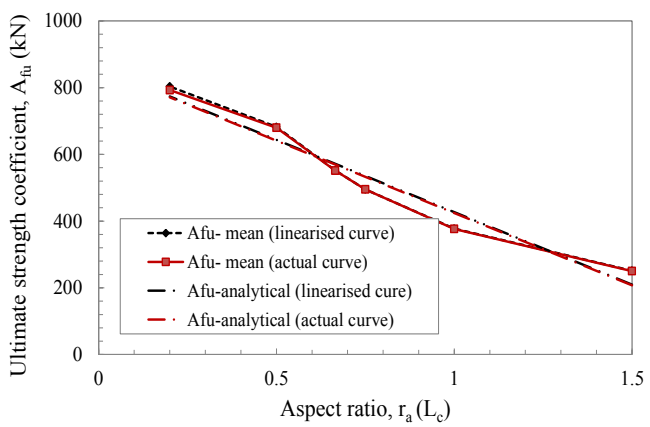

(b) The ultimate strength coefficient variation with the aspect ratio, r_a (L_b)

Figure A1.75: Ultimate strength relationships with I_b/I_c (I_c) and aspect ratio, r_a (L_c) for Case D

(d) Case D, ultimate deformation for the frame

Based on similar variation of the ultimate deformation with the I_b/I_c (I_c) ratio and the r_a (L_c) ratio to that of Case C, the same expression (equation A1.36) used in Case C is adopted. Since the aspect ratio under this section is a function of column length, the coefficient δer for the adopted expression is modified and is:

$$\delta_{ur} = \delta_{0ur} r_a(L_c) + D_{fu} \qquad \text{(A1.41)}$$

where δ_{0ur} and D_{fu} are constants. For this data set, the values of δ_{0er} and D_{fe} are 18.5 mm and 2.0 mm respectively. The analytical relationships show some correlation with typical values from the numerical data (especially for $I_b/I_c(I_c) < 10.0$) as shown in Figure A1.76.

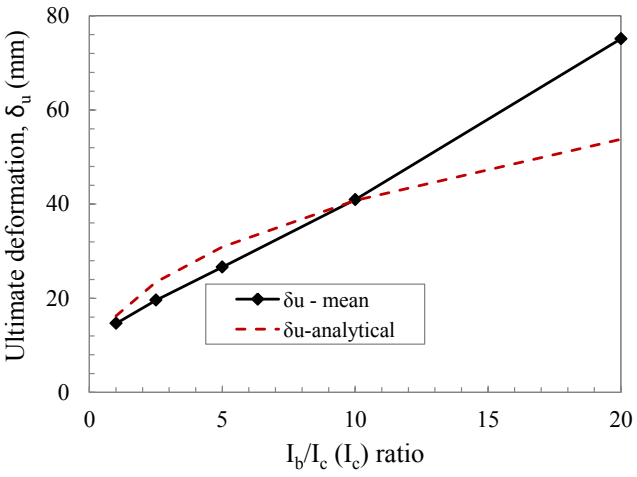

(a) Typical ultimate deformation variation with I_b/I_c (I_b) ratio

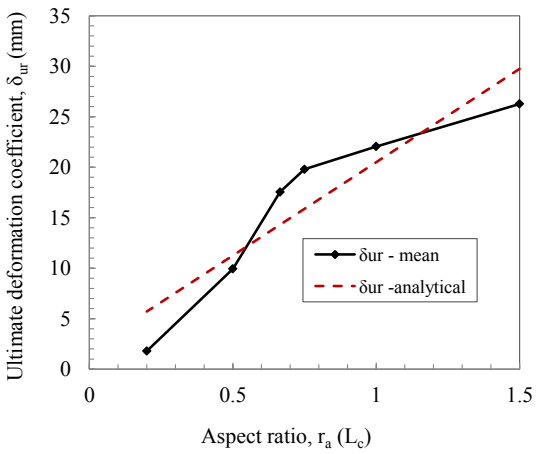

(b) Variation of the ultimate deformation coefficient (δ_{ur}) with aspect ratio, r_a(L_c)

Figure A1.76: Ultimate deformation relationship with I_b/I_c (I_b) ratio and aspect ratio, r_a (L_c) for Case D

Appendix A2: Pseudo-code for the material characterisation and truss-based system evaluation

A2.1: Pseudo-code for generating stress-strain behaviour of the equivalent strut (material characterisation procedure)

Main function

Input:

Enter geometric parameters for each elemental zone: $\{A_m\}$, $\{d_m\}$

Enter material model parameters matrices for each elemental zone: $\{E_m\}$, $[\varepsilon_m]$, $[\alpha_m]$

Enter effective cross-sectional area and length for the strut: A_s, d_s

Enter displacement step size and number of steps (yield points): Δu, NS

For j=1: NS

If j==1

For i=1:NE %NE=number of elements in the system

$f(i,j)=0$ %initial stress

$\varepsilon(i,j)=0$ %initial strain

$P(i,j)=0$ %initial force

$u(i,j)=0$ %/initial displacement

End

else

Establish tangential modulus

$E_t(i,j)=\alpha_m(k)E(i)$

Calculate element stiffness

For i=1:NE

$$K(i,j)=\frac{A(i)E_t(i,j)}{d(i)}$$

End

Compute system stiffness

$$K_s(j)=\frac{K(1,j)K(4,j)+K(1,j)K(2,j)+2K(2,j)K(4,j)}{K(1,j)+2K(2,j)}$$

Calculate effective tangential modulus for the system, E_s

$$E_s(j)=\frac{K_s(j)d_s}{A_s}$$

Compute change in element strains:

$\Delta\varepsilon(1,j)=\dfrac{-K(2)}{K(1)+2K(2)}\dfrac{\Delta u}{d(1)}$ %corner crushing zone 1

$\Delta\varepsilon(2,j)=\dfrac{-K(1)}{K(1)+2K(2)}\dfrac{\Delta u}{d(2)}$ % diagonal compression zone

$\Delta\varepsilon(3,j)=\dfrac{-K(2)}{K(1)+2K(2)}\dfrac{\Delta u}{d(1)}$ %corner crushing zone 2

$\Delta\varepsilon(4,j)=-\dfrac{\Delta u}{d(1)}$ % shear sliding zone

Establish instantaneous element's strains

For i=1:NE

$$\varepsilon_i(i,j) = \varepsilon(i,j) + \Delta\varepsilon(i,j)$$

End

Determine the strain scaling factor, β_{min1};

For i=1:NE,

$$\beta_{\min}(i) = \frac{\varepsilon_i(i,j) - \varepsilon_m(i,j)}{\Delta\varepsilon_c(i)}$$

End

$$\beta_{\min 1}(j) = Min\left(\beta_{\min}(i)\right)$$

Establish the next yielding point for the system

Recall previous yield strain vector, stress vector, displacement and force

Calculate yield point as follows:

For i=1:NE

$$\varepsilon(i,j) = \varepsilon(i,j-1) + \beta_{\min}(j)\Delta\varepsilon(i,j)$$

$$f(i,j) = f(i,j-1) + E_s(j)\frac{\beta_{\min}(j)\Delta u}{d_s}$$

$$u(i,j) = u(i,j-1) + \beta_{\min}(j)\Delta u$$

$$P(i,j) = P(i,j-1) + K_s(j)\beta_{\min}(j)\Delta u$$

End

End

End

End

Determine tangential modulus (E_t)

Recall system yield strain vector from previous step ($\varepsilon_{cj}(i,j-1)$)

Recall material and other properties from input (em,Etac2, Etac3,Etac4, NE,NS,E1)

For i=1:NE

Establish factor, $\alpha(i)$;

$E_t(i) = \alpha_m(i)E(i)$;

End

Determine the strain scaling factor, β_{min1};

Recall system yield strain vector from previous step ($\varepsilon_{cj}(i,j-1)$)

Recall material and other properties from input (em,Etac2, Etac3,Etac4,Etac5, Etac6 NE, NS, E1)

Recall current instantaneous strain (ej1)

Establish βmin1 as follows:

For i=1: NE

$$\beta_{\min}(i) = \frac{\varepsilon_i(i,j) - \varepsilon(i,j)}{\varepsilon_m(i)}$$

End

$$\beta_{\min 1}(j) = Min\left(\beta_{\min}(i)\right)$$

A2.2: Pseudo-code for 2D nonlinear evaluation of infill frame structures

Main function

Input data

(a) Enter topological data
   a. Number of nodes (NN)
   b. Coordinates of the nodes (x_i,y_i)
   c. Number of elements (columns (CE), beams (BE), diagonal struts (DS) and active equivalent diagonal struts (SE))

(b) Enter the material data
   a. Number of compressive yield strains for each material (CCS for concrete, RS for rebars and ESS for equivalent strut material)
   b. Compressive yield strain at yield point *j* for each material element *i* [$\varepsilon_c(i,j)$]
   c. Number of tensile yield strains for each material (CTS for concrete and RS for rebars)
   d. Tensile yield strain at yield point *j* for each material element *i* [$\varepsilon_t(i,j)$]

(c) Element definition and property assignment
   a. Define element using start node (n_1) and end node (n_2) notation [Dir(i,n_1) and Dir(i,n_2)]
   b. Enter the geometric data for each element (cross-sectional area, A(i))
   c. Enter material data for each element as defined in (b) [$E_k(i)$, $\alpha_j(i)$, $\varepsilon_{kj}(i)$]

(d) Define the boundary conditions and loading steps
   a. Number of constrained nodes (NC)
   b. Coordinates of the constrained nodes (x_{nc},y_{nc})
   c. Number of nodes for which the external load is applied (NF)
   d. Prescribe the size of incremental load (force [ΔF_{nf}] or displacement [Δd_{nf}])
   e. Prescribe the number of loading steps (NS)

(e) Pre-allocate storage space for input and output data

Preliminary analysis

(a) Homogenisation of material properties for all composite elements
   a. Assembly of material strains for homogenised element behaviour
   b. Assembly of material stress gradients (α_{cc1} and α_{sc1} sub function 1)
   c. Homogenised compressive stress gradients for frame elements (η_{c1} = sub function 2a)
   d. Homogenised tensile stress gradients for frame elements (η_{t1} = sub function 2b)
   e. Initial Young's modulus for homogenised frame elements in compression (E_{1c} =sub function 3a)
   f. Initial Young's modulus for homogenised frame elements in tension (E_{1t} =sub function 3b)
   g. Homogenised equivalent strut stress gradients (η_{c2} =sub function 4)
   h. Initial Young's modulus for homogenised equivalent struts and all the other elements (E_c =sub function 5)

(f) Establish element's length (use coordinates for the start and end nodes)

(g) Calculate element's cosines (use coordinates for the start and end nodes and element's length)

(h) Determine element's transformation matrix, T and its transpose, Tt.
For element *i*
   a. T(:,:,*i*) = [cos(*i*) sin(*i*);-sin(*i*) cos(*i*)]
   b. Tt(:,:,*i*) = transpose[T(:,:,*i*)]

(i) Establish the strain calculation matrix, C_ε, for each element. For element i, C_ε is defined as follows:

$$C_\varepsilon(:,:,i) = \frac{1}{L(i)}\left[-\cos(i)\ -\sin(i); \cos(i)\ \sin(i)\right]$$

Full analysis
Analysis is carried out for all prescribed steps (j^{th} analysis steps, from step 1 to step NS)

(a) Initialise the analysis (step j=1)
Assign zeros values for all key data outputs of each element and corresponding nodes in the first step of the analysis as follows:
   a. $f_k(i,j) = 0$ (initial force of element *i*; k denotes the axis of force, x or y)
   b. $\varepsilon(i,j) = 0$ (initial strain of element *i*)
   c. $P_k(n,j) = 0$ (initial force of node n; k denotes the axis of force, x or y)
   d. $d_k(n,j) = 0$ (initial displacement of node n; k denotes the axis of force, x or y)

(b) Determine tangential modulus (E_t = sub function 6)

(c) Establish the system's stiffness matrix using tangential modulus (K_t =sub function 7)

(d) Solve the system equilibrium equations for the unknown parameters
   a. Determine change in nodal displacement (Δd)
   b. Determine the change in strain, $\Delta\varepsilon$, for each element *i*:
   $\Delta\varepsilon(i) = \left[C_\varepsilon(i)\right]\{\Delta d\}$

(e) Establish the overall system's yield values for j^{th} step
   a. Determine the scaling factor (scaling=sub function 8)
   b. Establish element's instantaneous strains
   $\left[\varepsilon_c(:,j)\right] = \left[\varepsilon_c(:,j-1)\right] + \text{scaling}\left[\Delta\varepsilon_c(:,j)\right]$
   c. Establish instantaneous nodal displacement, d_{sk} for the structural system. For specific node, *r*, the instantaneous nodal displace at j^{th}step is defined as follows:
   $d_{sk}(r,j) = d_{sk}(r,j-1) + \text{scaling}\left(d_{sk}(r,j)\right)$
   d. Establish instantaneous nodal forces, P_{sk}, for the structural system. For specific node, *r*, the instantaneous nodal force at j^{th}step is defined as follows:
   $P_{sk}(r,j) = P_{sk}(r,j-1) + \text{scaling}\left(P_{sk}(r,j)\right)$

(f) Repeat steps (b) to (e) for NS times.

(b)<u>Sub function 1</u>: Homogenisation of compressive stress gradients (η_{c1}) for the frame elements

(a) Recall relevant input from the main function as follows:
   a. Frame element definitions and inactive (arbitrary) diagonal strut definitions;
   b. A vector of sorted compressive strains for both concrete and rebar materials (ε_{cm});
   c. Cross-sectional areas for each element (A(*i*) for frame elements and $A_s(i)$ for rebars);
   d. Initial compressive Young's modulus for concrete (E_1) and rebars (E_s);

e. Compressive stress gradients for nonlinear behaviour (α_{cc} for concrete and α_{sc} for rebars);

(b) Express the amount of rebar as a fraction of the cross-sectional area of the respective frame element (ρ_g)

$$\rho_g(i) = \frac{A_s(i)}{A(i)}$$

(c) Express the ratio of rebars Young's modulus to concrete Young's modulus (*m*). The homogenised material is defined in terms of concrete properties

$$m(i) = \frac{E_s(i)}{E_1(i)}$$

(d) Calculate the homogenised stress gradients, η_{c1}

$$\eta_{c1} = \alpha_{cc}(i,j) + \rho_g(i)\left[m(i)\alpha_{sc}(i,j) - \alpha_{cc}(i,j)\right]$$

The arbitrary diagonal strut uses the stress gradients, η_{c1} derived for the corresponding beam

(c)<u>Sub function 2</u>: Homogenisation of tensile stress gradients (η_{t1}) for the frame elements

(a) Recall relevant input from the main function as follows:

f. Frame element definitions;

g. A vector of sorted tensile strains for both concrete and rebar materials (ε_{tm});

h. Cross-sectional areas for each element (A(*i*) for frame elements and $A_{s(i)}$ for rebars);

i. Initial tensile Young's modulus for concrete (E_2) and rebars (E_s);

j. Tensile stress gradients for nonlinear behaviour (α_{ct} for concrete and α_{st} for rebars);

(b) Express the amount of rebar as a fraction of the cross-sectional area of the respective frame element (ρ_g)

$$\rho_g(i) = \frac{A_s(i)}{A(i)}$$

(c) Express the ratio of rebars Young's modulus to concrete Young's modulus (*m*). The homogenised material is defined in terms of concrete properties

$$m(i) = \frac{E_s(i)}{E_2(i)}$$

(d) Calculate the homogenised stress gradients, η_{t1}

$$\eta_{t1} = \alpha_{ct}(i,j) + \rho_g(i)\left[m(i)\alpha_{st}(i,j) - \alpha_{ct}(i,j)\right]$$

The arbitrary diagonal strut uses the stress gradients, $\eta_{t1} = \eta_{c1}$ as derived from previous sub function

<u>Sub function 3</u>: *Determine the tangential modulus of elasticity, E_t*

Recall system yield strain vector from previous step ($\varepsilon_{cj}(i, j-1)$)

Recall material and other properties from input (em, Etac2, Etac3, Etac4, NE, NS, E1)

For i=1: NE

Establish factor, $\alpha(i)$ % i.e. Etac (i);

$E_t(i) = \alpha_m(i)E(i)$; % tangential modulus

End

Sub function 4: *Establish system stiffness, Kt*

- *Input data:*
  Tangential modulus, Area of elements, Length of elements, directions, number of nodes, number of elements [Et(i), A(i), L(i), Dir(i,2), Dir(i,3), NN,NE]
  Kt=zeros (2*NN, 2*NN);
  kt11=zeros(); kt12=zeros();kt21=zeros();kt22=zeros();Kt11=zeros();…..
- *Analysis procedure:*
  For i=1:NE
  Establish element stiffness in local axis
  kt11(:,:,i)=A(i)*Et(i)/L(i)*[1 0; 0 0];
  kt12(:,:,i)=A(i)*Et(i)/L(i)*[-1 0; 0 0];
  kt21(:,:,i)=A(i)*Et(i)/L(i)*[-1 0; 0 0];
  kt22(:,:,i)=A(i)*Et(i)/L(i)*[1 0; 0 0];

  Define the element stiffness in global axis
  Kt11(:,:,i)=Tt(:,:,i)*kt11(:,:,i)*T(:,:,i);
  Kt12(:,:,i)=Tt(:,:,i)*kt12(:,:,i)*T(:,:,i);
  Kt21(:,:,i)=Tt(:,:,i)*kt21(:,:,i)*T(:,:,i);
  Kt22(:,:,i)=Tt(:,:,i)*kt22(:,:,i)*T(:,:,i);
  End

  Assemble global stiffness for the structural system
  For n=1:NE
  i=Dir(n,2);
  j=Dir(n,3);
  Kt(…..)
  End
- *Output data:*
  Kt

function→Kt=systemstiffness(Et(i), A(i), L(i), Dir(i,2), Dir(i,3), NN,NE);

Sub function 5: *Determining the scaling factor,* β_{min}

Recall system yield strain vector from previous step ($\varepsilon_{cj}(i, j-1)$)

Recall material and other properties from input (em,Etac2, Etac3,Etac4,Etac5, Etac6 NE, NS, E1)
Recall current instantaneous strain (ej1)
Establish β_{min1} as follows:

For j=2:NS
  For i=1:NE

$$\beta_{\min}(i) = \frac{\varepsilon_i(i,j) - \varepsilon(i,j)}{\varepsilon_m(i)}$$

End

$\beta_{\min 1}(j) = Min(\beta_{\min}(i))$

End

function→Scalingfactor();

Establish the next yielding point for the system

Recall previous yield strain vector, stress vector, displacement and force

Calculate yield point as follows:

For i=1:NE

$\varepsilon(i,j) = \varepsilon(i,j-1) + \beta_{\min}(j)\Delta\varepsilon(i,j)$

$f(i,j) = f(i,j-1) + E_s(j)\dfrac{\beta_{\min}(j)\Delta u}{d_s}$

$u(i,j) = u(i,j-1) + \beta_{\min}(j)\Delta u$

$P(i,j) = P(i,j-1) + K_s(j)\beta_{\min}(j)\Delta u$

End

End

End

Appendix A3: Material characterisation and structural behaviour evaluation

A3.1: Material characterisation data - parametric study

Table A3.1: Overall strut characteristics - Maximum strut resistance for sample G4(1)

Shear factor, γ_{ss}	**Strut resistance (kN) at compression factor, γ_{cc}**									
	0.5	0.6	0.7	0.8	0.9	1	1.1	1.15	1.25	1.4
0.15	190.09	220.57	250.02	279.42	308.83	338.23	338.23	338.23	338.23	338.23
0.25	218.81	250.02	279.46	308.87	338.27	367.68	367.68	367.68	367.68	367.68
0.35	247.50	279.42	308.87	338.27	367.68	397.08	397.08	397.08	397.08	397.08
0.5	290.52	323.53	352.97	382.38	411.78	441.19	441.19	441.19	441.19	441.19
0.65	333.59	367.68	397.12	426.53	455.93	485.33	485.33	485.33	485.33	485.33
0.8	376.61	411.78	441.23	470.63	500.04	529.44	529.44	529.44	529.44	529.44

Table A3.2: Overall strut characteristics – Deformation at maximum strut resistance for sample G4(1)

Shear factor, γ_{ss}	**Deformation (m) at compression factor, γ_{cc}**									
	0.5	0.6	0.7	0.8	0.9	1	1.1	1.15	1.25	1.4
0.15	0.0044	0.0045	0.0045	0.0045	0.0045	0.0045	0.0045	0.0045	0.0045	0.0045
0.25	0.0044	0.0045	0.0045	0.0045	0.0045	0.0045	0.0045	0.0045	0.0045	0.0045
0.35	0.0044	0.0045	0.0045	0.0045	0.0045	0.0045	0.0045	0.0045	0.0045	0.0045
0.5	0.0044	0.0045	0.0045	0.0045	0.0045	0.0045	0.0045	0.0045	0.0045	0.0045
0.65	0.0044	0.0045	0.0045	0.0045	0.0045	0.0045	0.0045	0.0045	0.0045	0.0045
0.8	0.0044	0.0045	0.0045	0.0045	0.0045	0.0045	0.0045	0.0045	0.0045	0.0045

Table A3.3: Overall strut characteristics - Maximum strut resistance for sample G4(2)

shear factor, γ_{ss}	**Strut resistance (kN) at compression factor, γ_{cc}**									
	0.5	0.6	0.7	0.8	0.9	1	1.1	1.15	1.25	1.4
0.15	143.33	168.22	192.65	215.26	237.96	260.58	260.58	260.58	260.58	260.58
0.25	163.28	189.69	215.26	237.88	260.58	283.20	283.20	283.20	283.20	283.20
0.35	183.30	211.23	237.96	260.58	283.28	305.89	305.89	305.89	305.89	305.89
0.5	213.30	243.51	271.97	294.58	317.28	339.90	339.90	339.90	339.90	339.90
0.65	243.23	275.71	305.89	328.51	351.21	373.83	373.83	373.83	373.83	373.83
0.8	273.23	307.99	339.90	362.52	385.21	407.83	407.83	407.83	407.83	407.83

Table A3.4: Overall strut characteristics – Deformation at maximum strut resistance for sample G4(2)

Shear factor, γ_{ss}	**Deformation (m) at compression factor, γ_{cc}**									
	0.5	0.6	0.7	0.8	0.9	1	1.1	1.15	1.25	1.4
0.15	0.0069	0.0074	0.0078	0.0078	0.0078	0.0078	0.0078	0.0078	0.0078	0.0078
0.25	0.0069	0.0074	0.0078	0.0078	0.0078	0.0078	0.0078	0.0078	0.0078	0.0078
0.35	0.0069	0.0074	0.0078	0.0078	0.0078	0.0078	0.0078	0.0078	0.0078	0.0078
0.5	0.0069	0.0074	0.0078	0.0078	0.0078	0.0078	0.0078	0.0078	0.0078	0.0078
0.65	0.0069	0.0074	0.0078	0.0078	0.0078	0.0078	0.0078	0.0078	0.0078	0.0078
0.8	0.0069	0.0074	0.0078	0.0078	0.0078	0.0078	0.0078	0.0078	0.0078	0.0078

Table A3.5: Overall strut characteristics - Maximum strut resistance for sample G4(5)

Shear factor, γ_{ss}	**Strut resistance (kN) at compression factor, γ_{cc}**									
	0.5	0.6	0.7	0.8	0.9	1	1.1	1.15	1.25	1.4
0.15	169.52	196.81	223.03	249.30	275.53	301.76	301.76	301.76	301.76	301.76
0.25	195.04	223.03	249.26	275.53	301.76	327.98	327.98	327.98	327.98	327.98
0.35	220.60	249.30	275.53	301.79	328.02	354.25	354.25	354.25	354.25	354.25
0.5	259.91	288.66	314.89	341.16	367.38	393.61	393.61	393.61	393.61	393.61
0.65	299.27	328.02	354.25	380.52	406.74	432.97	432.97	432.97	432.97	432.97
0.8	338.64	367.38	393.61	419.88	446.11	472.33	472.33	472.33	472.33	472.33

Table A3.6: Overall strut characteristics – Deformation at maximum strut resistance for sample G4(5)

Shear factor, γ_{ss}	**Deformation (m) at compression factor, γ_{cc}**									
	0.5	0.6	0.7	0.8	0.9	1	1.1	1.15	1.25	1.4
0.15	0.0042	0.0044	0.0044	0.0044	0.0044	0.0044	0.0044	0.0044	0.0044	0.0044
0.25	0.0042	0.0044	0.0044	0.0044	0.0044	0.0044	0.0044	0.0044	0.0044	0.0044
0.35	0.0042	0.0044	0.0044	0.0044	0.0044	0.0044	0.0044	0.0044	0.0044	0.0044
0.5	0.0044	0.0044	0.0044	0.0044	0.0044	0.0044	0.0044	0.0044	0.0044	0.0044
0.65	0.0044	0.0044	0.0044	0.0044	0.0044	0.0044	0.0044	0.0044	0.0044	0.0044
0.8	0.0044	0.0044	0.0044	0.0044	0.0044	0.0044	0.0044	0.0044	0.0044	0.0044

Table A3.7: Overall strut characteristics - Maximum strut resistance for sample G4(9)

Shear factor, γ_{ss}	**Strut resistance (kN) at compression factor, γ_{cc}**									
	0.5	0.6	0.7	0.8	0.9	1	1.1	1.15	1.25	1.4
0.15	158.40	185.00	209.68	234.36	259.04	283.72	283.72	283.72	283.72	283.72
0.25	181.79	209.68	234.36	259.04	283.72	308.40	308.40	308.40	308.40	308.40
0.35	205.19	234.36	259.04	283.72	308.40	333.08	333.08	333.08	333.08	333.08
0.5	240.19	271.29	295.97	320.65	345.33	370.01	370.01	370.01	370.01	370.01
0.65	275.28	308.31	332.99	357.67	382.35	407.02	407.02	407.02	407.02	407.02
0.8	310.37	345.33	370.01	394.68	419.36	444.04	444.04	444.04	444.04	444.04

Table A3.8: Overall strut characteristics – Deformation at maximum strut resistance for sample G4(9)

Shear factor, γ_{ss}	**Deformation (m) at compression factor, γ_{cc}**									
	0.5	0.6	0.7	0.8	0.9	1	1.1	1.15	1.25	1.4
0.15	0.0078	0.0082	0.0082	0.0082	0.0082	0.0082	0.0082	0.0082	0.0082	0.0082
0.25	0.0078	0.0082	0.0082	0.0082	0.0082	0.0082	0.0082	0.0082	0.0082	0.0082
0.35	0.0078	0.0082	0.0082	0.0082	0.0082	0.0082	0.0082	0.0082	0.0082	0.0082
0.5	0.0078	0.0082	0.0082	0.0082	0.0082	0.0082	0.0082	0.0082	0.0082	0.0082
0.65	0.0078	0.0082	0.0082	0.0082	0.0082	0.0082	0.0082	0.0082	0.0082	0.0082
0.8	0.0078	0.0082	0.0082	0.0082	0.0082	0.0082	0.0082	0.0082	0.0082	0.0082

Table A3.9: Overall strut characteristics - Maximum strut resistance for sample G4(3)

Shear factor, γ_{ss}	**Strut resistance (kN) at compression factor, γ_{cc}**									
	0.5	0.6	0.7	0.8	0.9	1	1.1	1.15	1.25	1.4
0.15	128.05	149.67	169.63	189.59	209.55	229.51	229.51	229.51	229.51	229.51
0.25	146.91	169.63	189.59	209.55	229.51	249.48	249.48	249.48	249.48	249.48
0.35	165.76	189.59	209.55	229.51	249.48	269.44	269.44	269.44	269.44	269.44
0.5	194.07	219.56	239.52	259.48	279.44	299.40	299.40	299.40	299.40	299.40
0.65	222.32	249.48	269.44	289.40	309.36	329.32	329.32	329.32	329.32	329.32
0.8	250.63	279.44	299.40	319.37	339.33	359.29	359.29	359.29	359.29	359.29

Table A3.10: Overall strut characteristics – Deformation at maximum strut resistance for sample G4(3)

Shear factor, γ_{ss}	**Deformation (m) at compression factor, γ_{cc}**									
	0.5	0.6	0.7	0.8	0.9	1	1.1	1.15	1.25	1.4
0.15	0.0055	0.0058	0.0058	0.0058	0.0058	0.0058	0.0058	0.0058	0.0058	0.0058
0.25	0.0055	0.0058	0.0058	0.0058	0.0058	0.0058	0.0058	0.0058	0.0058	0.0058
0.35	0.0055	0.0058	0.0058	0.0058	0.0058	0.0058	0.0058	0.0058	0.0058	0.0058
0.5	0.0055	0.0058	0.0058	0.0058	0.0058	0.0058	0.0058	0.0058	0.0058	0.0058
0.65	0.0055	0.0058	0.0058	0.0058	0.0058	0.0058	0.0058	0.0058	0.0058	0.0058
0.8	0.0055	0.0058	0.0058	0.0058	0.0058	0.0058	0.0058	0.0058	0.0058	0.0058

Table A3.11: Overall strut characteristics - Maximum strut resistance sample G4(4)

Shear factor, γ_{ss}	**Strut resistance (kN) at compression factor, γ_{cc}**									
	0.5	0.6	0.7	0.8	0.9	1	1.1	1.15	1.25	1.4
0.15	132.09	152.42	172.72	193.05	213.38	233.71	233.71	233.71	233.71	233.71
0.25	152.42	172.75	193.05	213.38	233.71	254.04	254.04	254.04	254.04	254.04
0.35	172.75	193.08	213.38	233.71	254.04	274.37	274.37	274.37	274.37	274.37
0.5	203.23	223.56	243.86	264.19	284.51	304.84	304.84	304.84	304.84	304.84
0.65	233.71	254.04	274.34	294.66	314.99	335.32	335.32	335.32	335.32	335.32
0.8	264.19	284.51	304.81	325.14	345.47	365.80	365.80	365.80	365.80	365.80

Table A3.12: Overall strut characteristics – Deformation at maximum strut resistance for sample G4(4)

Shear factor, γ_{ss}	**Deformation (m) at compression factor, γ_{cc}**									
	0.5	0.6	0.7	0.8	0.9	1	1.1	1.15	1.25	1.4
0.15	0.0032	0.0032	0.0032	0.0032	0.0032	0.0032	0.0032	0.0032	0.0032	0.0032
0.25	0.0032	0.0032	0.0032	0.0032	0.0032	0.0032	0.0032	0.0032	0.0032	0.0032
0.35	0.0032	0.0032	0.0032	0.0032	0.0032	0.0032	0.0032	0.0032	0.0032	0.0032
0.5	0.0032	0.0032	0.0032	0.0032	0.0032	0.0032	0.0032	0.0032	0.0032	0.0032
0.65	0.0032	0.0032	0.0032	0.0032	0.0032	0.0032	0.0032	0.0032	0.0032	0.0032
0.8	0.0032	0.0032	0.0032	0.0032	0.0032	0.0032	0.0032	0.0032	0.0032	0.0032

Table A3.13: Overall strut characteristics - Maximum strut resistance for sample G4(6)

Shear factor, γ_{ss}	**Strut resistance (kN) at compression factor, γ_{cc}**									
	0.5	0.6	0.7	0.8	0.9	1	1.1	1.15	1.25	1.4
0.15	133.60	157.51	181.32	204.64	226.16	247.78	247.78	247.78	247.78	247.78
0.25	150.94	176.39	201.73	226.26	247.78	269.40	269.40	269.40	269.40	269.40
0.35	168.20	195.18	222.05	247.78	269.30	290.92	290.92	290.92	290.92	290.92
0.5	194.09	223.38	252.53	280.06	301.58	323.20	323.20	323.20	323.20	323.20
0.65	220.07	251.65	283.10	312.44	333.96	355.58	355.58	355.58	355.58	355.58
0.8	245.96	280.22	313.58	344.72	366.24	387.86	387.86	387.86	387.86	387.86

Table A3.14: Overall strut characteristics – Deformation at maximum strut resistance for sample G4(6)

Shear factor, γ_{ss}	**Deformation (m) at compression factor, γ_{cc}**									
	0.5	0.6	0.7	0.8	0.9	1	1.1	1.15	1.25	1.4
0.15	0.0097	0.0106	0.0114	0.0121	0.0121	0.0121	0.0121	0.0121	0.0121	0.0121
0.25	0.0097	0.0106	0.0114	0.0121	0.0121	0.0121	0.0121	0.0121	0.0121	0.0121
0.35	0.0097	0.0106	0.0114	0.0121	0.0121	0.0121	0.0121	0.0121	0.0121	0.0121
0.5	0.0097	0.0106	0.0114	0.0121	0.0121	0.0121	0.0121	0.0121	0.0121	0.0121
0.65	0.0097	0.0106	0.0114	0.0121	0.0121	0.0121	0.0121	0.0121	0.0121	0.0121
0.8	0.0097	0.0121	0.0114	0.0121	0.0121	0.0121	0.0121	0.0121	0.0121	0.0121

Table A3.15: Overall strut characteristics - Maximum strut resistance for sample G4(8)

Shear factor, γ_{ss}	**Strut resistance (kN) at compression factor, γ_{cc}**									
	0.5	0.6	0.7	0.8	0.9	1	1.1	1.15	1.25	1.4
0.15	126.14	145.55	164.95	184.37	203.76	223.18	223.18	223.18	223.18	223.18
0.25	145.53	164.95	184.34	203.76	223.16	242.57	242.57	242.57	242.57	242.57
0.35	164.95	184.37	203.76	223.18	242.57	261.99	261.99	261.99	261.99	261.99
0.5	194.04	213.46	232.85	252.27	271.67	291.09	291.09	291.09	291.09	291.09
0.65	223.16	242.57	261.97	281.39	300.78	320.20	320.20	320.20	320.20	320.20
0.8	252.27	271.69	291.09	310.50	329.90	349.32	349.32	349.32	349.32	349.32

Table A3.16: Overall strut characteristics – Deformation at maximum strut resistance for sample G4(8)

Shear factor, γ_{ss}	**Deformation (m) at compression factor, γ_{cc}**									
	0.5	0.6	0.7	0.8	0.9	1	1.1	1.15	1.25	1.4
0.15	0.0035	0.0035	0.0035	0.0035	0.0035	0.0035	0.0035	0.0035	0.0035	0.0035
0.25	0.0035	0.0035	0.0035	0.0035	0.0035	0.0035	0.0035	0.0035	0.0035	0.0035
0.35	0.0035	0.0035	0.0035	0.0035	0.0035	0.0035	0.0035	0.0035	0.0035	0.0035
0.5	0.0035	0.0035	0.0035	0.0035	0.0035	0.0035	0.0035	0.0035	0.0035	0.0035
0.65	0.0035	0.0035	0.0035	0.0035	0.0035	0.0035	0.0035	0.0035	0.0035	0.0035
0.8	0.0035	0.0035	0.0035	0.0035	0.0035	0.0035	0.0035	0.0035	0.0035	0.0035

Table A3.17: Overall strut characteristics - Maximum strut resistance for sample G4(7)

Shear factor, γ_{ss}	**Strut resistance (kN) at compression factor, γ_{cc}**									
	0.5	0.6	0.7	0.8	0.9	1	1.1	1.15	1.25	1.4
0.15	154.86	182.39	209.85	234.62	259.35	284.04	284.04	284.04	284.04	284.04
0.25	175.78	205.16	234.48	259.30	284.04	308.72	308.72	308.72	308.72	308.72
0.35	196.74	227.98	259.16	284.04	308.77	333.45	333.45	333.45	333.45	333.45
0.5	228.43	262.12	296.07	321.03	345.77	370.45	370.45	370.45	370.45	370.45
0.65	265.49	298.24	333.07	358.08	382.82	407.50	407.50	407.50	407.50	407.50
0.8	302.54	335.29	370.12	395.13	419.87	444.55	444.55	444.55	444.55	444.55

Table A3.18: Overall strut characteristics – Deformation at maximum strut resistance for sample G4(7)

Shear factor, γ_{ss}	**Deformation (m) at compression factor, γ_{cc}**									
	0.5	0.6	0.7	0.8	0.9	1	1.1	1.15	1.25	1.4
0.15	0.0062	0.0067	0.0073	0.0073	0.0073	0.0073	0.0073	0.0073	0.0073	0.0073
0.25	0.0062	0.0067	0.0073	0.0073	0.0073	0.0073	0.0073	0.0073	0.0073	0.0073
0.35	0.0062	0.0067	0.0073	0.0073	0.0073	0.0073	0.0073	0.0073	0.0073	0.0073
0.5	0.0073	0.0067	0.0073	0.0073	0.0073	0.0073	0.0073	0.0073	0.0073	0.0073
0.65	0.0073	0.0073	0.0073	0.0073	0.0073	0.0073	0.0073	0.0073	0.0073	0.0073
0.8	0.0073	0.0073	0.0073	0.0073	0.0073	0.0073	0.0073	0.0073	0.0073	0.0073

Table A3.19: Overall strut characteristics - Maximum strut resistance for sample G3

Shear factor, γ_{ss}	**Strut strength (kN) at compression factor, γ_{cc}**									
	0.5	0.6	0.7	0.8	0.9	1	1.1	1.15	1.25	1.4
0.15	225.81	266.29	306.78	343.52	379.72	415.88	415.88	415.88	415.88	415.88
0.25	255.81	299.18	342.55	379.68	415.88	452.04	452.04	452.04	452.04	452.04
0.35	285.81	332.06	378.31	415.84	452.04	488.19	488.19	488.19	488.19	488.19
0.5	333.85	381.37	431.94	470.05	506.25	542.41	542.41	542.41	542.41	542.41
0.65	388.11	435.49	486.00	524.31	560.51	596.67	596.67	596.67	596.67	596.67
0.8	442.32	489.71	540.22	578.53	614.73	650.88	650.88	650.88	650.88	650.88

Table A3.20: Overall strut characteristics – Deformation at maximum strut resistance for sample G3

Shear factor, γ_{ss}	**Deformation (m) at compression factor, γ_{cc}**									
	0.5	0.6	0.7	0.8	0.9	1	1.1	1.15	1.25	1.4
0.15	0.0047	0.0052	0.0056	0.0057	0.0057	0.0057	0.0057	0.0057	0.0057	0.0057
0.25	0.0047	0.0052	0.0056	0.0057	0.0057	0.0057	0.0057	0.0057	0.0057	0.0057
0.35	0.0047	0.0052	0.0056	0.0057	0.0057	0.0057	0.0057	0.0057	0.0057	0.0057
0.5	0.0057	0.0052	0.0056	0.0057	0.0057	0.0057	0.0057	0.0057	0.0057	0.0057
0.65	0.0057	0.0057	0.0057	0.0057	0.0057	0.0057	0.0057	0.0057	0.0057	0.0057
0.8	0.0057	0.0057	0.0057	0.0057	0.0057	0.0057	0.0057	0.0057	0.0057	0.0057

Appendix A4: Stress-strain characterisation data for model verification

Appendix A4.1: Diagonal strut characterisation - column-based

Table A4.1: Stress-strain behaviour for Sample G3

j^{th} state	Infill strut		Pinned bare frame strut		Fixed bare frame strut	
	ε_j	σ_j - MPa	ε_j	σ_j - MPa	ε_j	σ_j - MPa
1	0.0018	3.36	0.0030	0.47	0.0018	0.99
2	0.0038	3.36	0.0225	0.47	0.0134	0.99
3	0.0100	0.00				

Table A4.2: Stress-strain behaviour for Sample G4(1)

j^{th} state	Infill strut		Pinned bare frame strut		Fixed bare frame strut	
	ε_j	σ_j - MPa	ε_j	σ_j - MPa	ε_j	σ_j - MPa
1	0.0018	12.28	0.0040	2.55	0.0024	5.45
2	0.0024	12.28	0.0300	2.55	0.0181	5.45
3	0.0038	8.51				
4	0.0070	0.00				

Table A4.3: Stress-strain behaviour for Samples G4(2), G4(3) and G4(4)

j^{th} state	Infill strut - G4(2)		Infill strut - G4(3)		Infill strut - G4(4)		Pinned bare frame strut*		Fixed bare frame strut*	
	ε_j	σ_j - MPa	ε_j	σ_j - MPa	ε_j	σ_j - MPa	ε_j	σ_j -MPa	ε_j	σ_j - MPa
1	0.0030	11.95	0.0023	8.86	0.0013	14.47	0.0041	2.07	0.0026	4.49
2	0.0039	11.95	0.0029	8.86	0.0018	14.47	0.0308	2.07	0.0193	4.49
3	0.0100	0.00	0.0043	6.25	0.0033	9.57				
4			0.0059	2.45	0.0060	2.89				

*Same bare frame properties are used

Table A4.4: Stress-strain behaviour for Sample G4(5)

j^{th} state	Infill strut		Pinned bare frame strut		Fixed bare frame strut	
	ε_j	σ_j - MPa	ε_j	σ_j - MPa	ε_j	σ_j - MPa
1	0.0017	14.05	0.0031	1.90	0.0019	4.10
2	0.0023	14.05	0.0233	1.90	0.0145	4.10
3	0.0037	9.56				
4	0.0053	3.52				
5	0.0100	0.00				

Table A4.5: Stress-strain behaviour for Samples G4(6) and G4(7)

j[th] state	Infill strut - G4(6)		Infill strut - G4(7)		Pinned bare frame strut*		Fixed bare frame strut*	
	ε_j	σ_j - MPa	ε_j	σ_j - MPa	ε_j	σ_j - MPa	ε_j	σ_j - MPa
1	0.0037	11.10	0.0022	16.58	0.0038	2.05	0.0023	4.42
2	0.0051	12.35	0.0042	16.58	0.0285	2.05	0.0174	4.42
3	0.0057	11.18	0.0100	0.00				
4	0.0073	6.90						

*Same bare frame properties are used

Table A4.6: Stress-strain behaviour for Sample G4(8)

j[th] state	Infill strut		Pinned bare frame strut		Fixed bare frame strut	
	ε_j	σ_j - MPa	ε_j	σ_j - MPa	ε_j	σ_j - MPa
1	0.0011	13.51	0.0038	2.26	0.0024	5.13
2	0.0031	13.51	0.0285	2.26	0.0177	5.13
3	0.0100	0.00				

Appendix A4.2: Homogenised material data

Table A4.7: A summary of the homogenised equivalent diagonal strut material behaviour for the pinned samples G4(1), G4(4), G4(5), G4(7) and G4(8) - column-based properties

Sample G4(1)		Sample G4(4)		Sample G4(5)		Sample G4(7)		Sample G4(8)	
(23800mm^2)[1]		(26100mm^2) [1]		(23200mm^2) [1]		(26200mm^2) [1]		(21900mm^2) [1]	
ε_{cj}	σ_{cj} -MPa	ε_{cj}	σ_{cj} -MPa	ε_{cj}	σ_{cj} -MPa	ε_{cj}	σ_{cj} -MPa	ε_{cj}	σ_{cj} -MPa
0.0018	12.86	0.0013	15.13	0.0017	15.04	0.0022	14.54	0.0011	17.86
0.0024	13.23	0.0018	15.42	0.0023	15.39	*0.0038*	15.39	0.0031	19.05
0.0038	10.53	0.0033	11.23	*0.0031*	13.29	0.0042	15.39	*0.0038*	17.70
0.0040	10.11	*0.0041*	8.76	0.0037	11.43	0.0100	2.05	0.0100	2.26
0.0070	2.55	0.0060	2.07	0.0053	5.41	*0.0285*	2.05	*0.0285*	2.26
0.0300	2.55	*0.0308*	2.07	0.0062	1.90				
				0.0233	1.90				

[1]Effective cross-sectional area for the homogenised equivalent diagonal strut; strains for bare frames are in italics

Table A4.8: A summary of the homogenised equivalent diagonal strut stress-strain behaviour for the fixed samples for G4(1), G4(4), G4(5), G4(7) and G4(8) - column-based properties

Sample G4(1)		**Sample G4(4)**		**Sample G4(5)**		**Sample G4(7)**		**Sample G4(8)**	
(23800mm^2)[1]		(26100mm^2) [1]		(23200mm^2) [1]		(26200mm^2) [1]		(21900mm^2) [1]	
ε_{cj}	σ_{cj} -MPa	ε_{cj}	σ_{cj} -MPa	ε_{cj}	σ_{cj} -MPa	ε_{cj}	σ_{cj} -MPa	ε_{cj}	σ_{cj} -MPa
0.0018	15.74	0.0013	16.69	0.0017	17.6	0.0022	17.57	0.0011	19.6
0.0024	17.05	0.0018	17.68	*0.0019*	18.1	*0.0023*	17.76	*0.0024*	22.3
0.0024	17.03	*0.0026*	16.43	0.0023	18.1	0.0042	17.76	0.0031	22.3
0.0038	13.58	0.0033	14.08	0.0037	13.6	0.0100	4.42	0.0100	5.1
0.0061	7.80	0.0060	7.39	*0.0053*	7.6	*0.0174*	4.42	*0.0177*	*5.1*
0.0181	7.80	*0.0193*	7.39	0.0145	7.6				

[1]Effective cross-sectional area for the homogenised equivalent diagonal strut; strains for bare frames are in italics

Appendix A5: Data for the case study building structure

Appendix A5.1: Input data for sustainability assessment

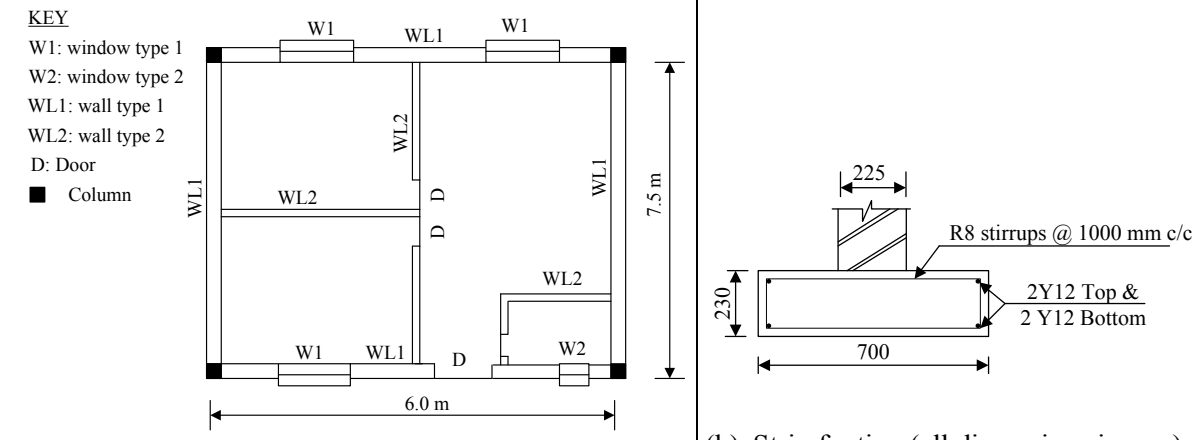

(a) Layout for a single housing unit

(b) Strip footing (all dimensions in mm)

Figure A5.1: Typical single housing unit used for LCA

Table A5.1: Details for the case study building structure

Building part	Item	Dimensions (mm)			Comments
		Length	Height or width	Thickness	
Foundation	Pad footing	3000	3000	400	8No.; rebar = 41.0 kg/m^3
	Strip footing	63600	700	230	Rebar = 26.6 kg/m^3
	Brickwork	63500	1000	225	10 mm plaster; brick force
	Column	300	1000	300	8No.; rebar = 40.4 kg/m^3
Floor slabs (2No.)	Ground floor (G/floor)	7725	18225	120	Rebar = 16.1 kg/m^3; 250-micron DPM
	Upper floor	7725	18225	200	Rebar = 37.3 kg/m^3
G/floor walling	Brickwork-external*		2800	225	39.6 m^3; brick force; 10 mm plaster; DPC
	Column	300	2800	300	8No.; rebar = 40.4 kg/m^3
	Brickwork-internal**		2800	115	0.5 m^3; brick force; 10 mm plaster
Upper floor walling (2No.)	Brickwork-external*		2800	225	39.6 m^3;brick force; 10 mm plaster
	Column	300	2800	300	8No.; rebar = 40.4 kg/m^3
	Brickwork-internal**		2800	115	0.5 m^3;brick force; 10 mm plaster
Roofing	Roof truss				2.2 m^3
	Coverings and other				827 kg iron sheets; ceiling and thermal insulation

* Volume excluding windows and doors; ** Volume excluding doors

Table A5.2: LCI for the initial construction

Building part	**Unit**	**Quantity**	**CF factors**	**CF (CO_{2e} kg)**	**AP factors**	**AP (SO_{2e} kg)**
(a) Foundations				***17122***		***38.60***
Pad footing-concrete	m^3	28.8	264.1	7606	0.5066	14.59
Pad footing-reinforcement	kg	1180.0	1.6841	1987	0.0057	6.73
Strip footing-concrete		10.2	264.1	2704	0.5066	5.19
Strip footing-reinforcement		272.0	1.6841	458	0.0057	1.55
Brickwork	kg	30051.0	0.1212	3642	0.0003	9.02
Plaster	kg	2645.8	0.1605	425	0.0003	0.79
Brick force	kg	28.0	2.1555	60	0.0078	0.22
Column - concrete	m^3	0.7	264.1	190	0.5066	0.36
Column - reinforcement		29.1	1.6841	49	0.0057	0.17
(b) Ground floor slab				***5004***		***10.40***
Concrete	m^3	16.9	264.1	4462	0.5066	8.56
250-micron DPM	kg	32.4	2.6085	84	0.0098	0.32
Steel mesh reinforcement 193	kg	271.7	1.6841	458	0.0057	1.55
(c) G/floor external walls				***12137***		***29.40***
Brickwork	kg	83117.5	0.1212	10074	0.0003	24.94
Brick force	kg	72.6	2.1555	156	0.0078	0.57
Plaster	kg	7317.9	0.1605	1175	0.0003	2.20
DPC	kg	23.8	2.6085	62	0.0098	0.23
Column -concrete	m^3	2.0	264.1	532	0.5066	1.02
Column-reinforcement	kg	81.5	1.6841	137	0.0057	0.46
(d) G/floor internal walls				***129***		***0.30***
Brickwork	kg	1038.6	0.1212	126	0.0003	0.31
Plaster	kg	20.6	0.1605	3	0.0003	0.01
(e) Upper floors slab				***18409***		***40.50***
Concrete	m^3	56.3	264.1	14873	0.5066	28.53
Reinforcement	kg	2100.0	1.6841	3537	0.0057	11.97
(f) Upper floors external walls				***24149***		***57.30***
Brickwork	kg	166235.0	0.1212	20148	0.0003	49.87
Brick force	kg	145.2	2.1555	313	0.0003	0.04
Plaster	kg	14635.7	0.1605	2349	0.0003	4.39
Column -concrete	m^3	4.0	264.1	1065	0.5066	2.04
Column -reinforcement	kg	163.1	1.6841	275	0.0057	0.93
(g) Upper floors internal walls				***258***		***0.60***
Brickwork	kg	2077.1	0.1212	252	0.0003	0.62
Plaster	kg	41.2	0.1605	7	0.0003	0.01
(h) Roofing				***2130***		***57.70***
Roof truss	m^3	2.2	88.873	91	0.5546	1.20
Roof covering	kg	826.7	2.1191	829	0.0082	6.78
Other (galvanised, steel sheet)	m^2	164.4	4.4401	169	0.28458	46.77
Ceiling and thermal insulation						
Gypsum plasterboard	kg	769.5	0.354	770	0.0012	0.92
Glass wool-insulation	kg	270.0	1.4934	271	0.0074925	2.02

Table A5.3: LCI for a typical repair event (re-plastering)

Building part	**Unit**	**Quantity**	**CF factors**	**CF (CO_{2e} kg)**	**AP factors**	**AP (SO_{2e} kg)**
(a) G/floor external walls				***1175***		***2.20***
Plaster	kg	7317.9	0.1605	1175	0.0003	2.20
(b) G/floor internal walls				***3***		***0.01***
Plaster	kg	20.6	0.1605	3	0.0003	0.01
(c) Upper floors external walls				***2349***		***4.39***
Plaster	kg	14635.7	0.1605	2349	0.0003	4.39
(d) Upper floors internal walls				***7***		***0. 01***
Plaster	kg	41.2	0.1605	7	0.0003	0.01